PhD Dissertation

RATIONAL DESIGN OF METAL-MEDIATED DNA G-QUADRUPLEXES AS DNAZYMES

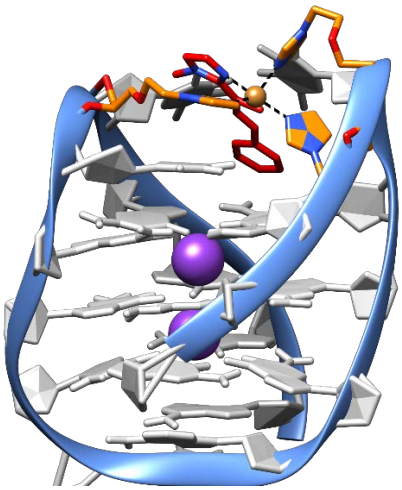

This dissertation is submitted for the degree of

“Doctor rerum naturalium”

TU Dortmund 2020

Fakultät für Chemie und Chemische Biologie

Philip Punt

This work has been prepared from August 2017 to November 2020 at the Faculty of Chemistry and Chemical Biology at TU Dortmund University under supervision of Prof. Dr. Guido H. Clever.

Examiner: **Prof. Dr. Guido H. Clever**

Faculty of Chemistry and Chemical Biology,
TU Dortmund University,
Otto-Hahn-Str. 6, 44227 Dortmund

Coexaminer: **Prof. Dr. Hannes Mutschler**

Faculty of Chemistry and Chemical Biology,
TU Dortmund University,
Otto-Hahn-Str. 4a, 44227 Dortmund

Submission Date: 19.11.2020

Eidesstattliche Versicherung (Affidavit)

Name, Vorname
(Surname, first name)

Matrikel-Nr.
(Enrolment number)

Belehrung:

Wer vorsätzlich gegen eine die Täuschung über Prüfungsleistungen betreffende Regelung einer Hochschulprüfungsordnung verstößt, handelt ordnungswidrig. Die Ordnungswidrigkeit kann mit einer Geldbuße von bis zu 50.000,00 € geahndet werden. Zuständige Verwaltungsbehörde für die Verfolgung und Ahndung von Ordnungswidrigkeiten ist der Kanzler/die Kanzlerin der Technischen Universität Dortmund. Im Falle eines mehrfachen oder sonstigen schwerwiegenden Täuschungsversuches kann der Prüfling zudem exmatrikuliert werden, § 63 Abs. 5 Hochschulgesetz NRW.

Die Abgabe einer falschen Versicherung an Eides statt ist strafbar.

Wer vorsätzlich eine falsche Versicherung an Eides statt abgibt, kann mit einer Freiheitsstrafe bis zu drei Jahren oder mit Geldstrafe bestraft werden, § 156 StGB. Die fahrlässige Abgabe einer falschen Versicherung an Eides statt kann mit einer Freiheitsstrafe bis zu einem Jahr oder Geldstrafe bestraft werden, § 161 StGB.

Die oben stehende Belehrung habe ich zur Kenntnis genommen:

Official notification:

Any person who intentionally breaches any regulation of university examination regulations relating to deception in examination performance is acting improperly. This offence can be punished with a fine of up to EUR 50,000.00. The competent administrative authority for the pursuit and prosecution of offences of this type is the chancellor of the TU Dortmund University. In the case of multiple or other serious attempts at deception, the candidate can also be unenrolled, Section 63, paragraph 5 of the Universities Act of North Rhine-Westphalia.

The submission of a false affidavit is punishable.

Any person who intentionally submits a false affidavit can be punished with a prison sentence of up to three years or a fine, Section 156 of the Criminal Code. The negligent submission of a false affidavit can be punished with a prison sentence of up to one year or a fine, Section 161 of the Criminal Code.

I have taken note of the above official notification.

Ort, Datum
(Place, date)

Unterschrift
(Signature)

Titel der Dissertation:
(Title of the thesis):

Ich versichere hiermit an Eides statt, dass ich die vorliegende Dissertation mit dem Titel selbstständig und ohne unzulässige fremde Hilfe angefertigt habe. Ich habe keine anderen als die angegebenen Quellen und Hilfsmittel benutzt sowie wörtliche und sinngemäße Zitate kenntlich gemacht.
Die Arbeit hat in gegenwärtiger oder in einer anderen Fassung weder der TU Dortmund noch einer anderen Hochschule im Zusammenhang mit einer staatlichen oder akademischen Prüfung vorgelegen.

I hereby swear that I have completed the present dissertation independently and without inadmissible external support. I have not used any sources or tools other than those indicated and have identified literal and analogous quotations.

The thesis in its current version or another version has not been presented to the TU Dortmund University or another university in connection with a state or academic examination.*

*Please be aware that solely the German version of the affidavit ("Eidesstattliche Versicherung") for the PhD thesis is the official and legally binding version.

Ort, Datum
(Place, date)

Unterschrift
(Signature)

I like the night. Without the dark, we'd never see the stars.

Bella Swan, Twilight

Parts of this dissertation were published in the following articles

“Imidazole-modified G-quadruplex DNA as metal-triggered peroxidase” Philip M. Punt, Guido H. Clever, *Chem. Sci.* **2019**, *10*, 2513.

“Tailored Transition-Metal Coordination Environments in Imidazole-Modified DNA G-Quadruplexes” Philip M. Punt, Guido H. Clever, *Chem. Eur. J.* **2019**, *25*, 13987.

“Heteroleptic Coordination Environments in Metal-Mediated DNA G-Quadruplexes” Philip M. Punt, Lukas M. Stratmann, Sinem Sevim, Lena Knauer, Carsten Strohmann, Guido H. Clever, *Front. Chem.* **2020**, *8*, 26.

“Modular Design of G-Quadruplex MetalloDNAzymes for Catalytic C-C Bond Formations with Switchable Enantioselectivity” Philip M. Punt, Marie D. Langenberg, Okan Altan, Guido H. Clever, manuscript submitted.

ABSTRACT

A correct folding of DNA and proteins is fundamental for their function.[1] While it can be challenging to predict the secondary structure of proteins, DNA has much better self-recognition properties and folds into various secondary structures[2,3] such as hairpin loops, triplex DNA, three- and four-way junctions, i-motifs and G-quadruplexes.[4–8] Latter assemble from guanine-rich sequences to form planar tetrameric G-tetrads, which form by π-π stacking interactions the G-quadruplex with central cations.[9,10] In recent years, G-quadruplexes received increasing interest in medicinal chemistry for their involvement in various diseases[10–16] and in DNA nanotechnology.[17–23] Our research group expanded the concept of metal-mediated base pairing to DNA G-quadruplexes by incorporation of pyridine ligandosides in G-quadruplex structures, allowing the complexation of transition metal cations such as Cu^{II} or Ni^{II}. The metal-mediated G-quadruplexes then found useful applications as EPR-based distance rulers or for Cu^{II}-responsive topology switching.[24–28] Motivated by these results, the aim of this thesis was to use metal-mediated G-quadruplexes for the design of DNAzymes. Inspired by natural metalloproteins and the amino acid histidine, a first generation of imidazole ligandosides in tetramolecular G-quadruplexes allowed the complexation of various transition metal cations such as Cu^{II}, Ni^{II}, Zn^{II} and Co^{II}. Especially Cu^{II} lead to unprecedented high thermal stabilizations, which culminated in the design of a Cu^{II} responsive DNAzyme, that catalysed peroxidase like reactions in presence of hemin.[29] Expanding the concept to unimolecular G-quadruplexes allowed the design of tailored coordination environments for different transition metal cations in accordance with the preferred coordination geometry e.g. a square planar coordination for Cu^{II} and a tetrahedral coordination environment for Zn^{II}.[30,31] Even more interesting was the design of unsaturated coordination environments for Cu^{II}, allowing a substrate to coordinate. Indeed, G-quadruplexes with unsaturated coordination environments could then be utilized for a Cu^{II} catalysed asymmetric Michael-Addition, in which Cu^{II} was acting as Lewis-acid. The high modularity of the approach then allowed in iterative rounds of sequence design and screening the design of highly active G-quadruplex structures, catalysing the Michael-Addition in excellent conversions (94 %) and enantioselectivities of up to, 99 % *ee*. More exciting, it allowed the design of G-quadruplexes for the enrichment of both enantiomers without completely inverting the chirality of DNA. As future prospect it is planned to expand the system to other reaction types including Diels-Alder reactions, cyclopropanation reactions and sulfoxidations and to further improve the efficiency of the system, aided by computational studies.

ZUSAMMENFASSUNG

Für die Funktion von DNA und Proteinen ist eine korrekte Faltung der Sekundär- und Tertiärstruktur notwendig.[1] Im Gegensatz zu Proteinen ist die Sekundärstruktur von DNA besser voraus zu sagen und eine Vielzahl von Sekundärstrukturen[2,3], einschließlich Triplex DNA, Vier-Wegkreuzungen, i-Motiven und G-Quadruplexen sind bekannt.[4–7] Die zuletzt genannten falten sich aus Guanin-reichen Sequenzen zu planaren tetrameren G-Tetraden, welche über π-π Stapel-Wechselwirkungen den G-Quadruplex mit einem zentralen Kation bilden.[9,10] Seit einigen Jahren erfahren G-Quadruplexe aufgrund ihrer Relevanz in verschiedenen Krankheiten ein steigendes Interesse aus der medizinischen Chemie[10–16] und der DNA Nanotechnologie.[17–23] Vor kurzem etablierte unsere Arbeitsgruppe die metall-vermittelte Basenpaarung in DNA G-Quadruplexen. Der Einbau von Pyridin Ligandosiden erlaubte die Komplexierung verschiedener Übergangsmetalle, einschließlich Cu^{II} oder Ni^{II}. Diese metall-vermittelten G-Quadruplex Strukturen konnten als ESR-basierte molekulare Lineale oder für die Cu^{II} vermittelte Schaltung von G-Quadruplex Topologien genutzt werden.[24–27] Diese Arbeit war motiviert, um metall-vermittelte G-Quadruplexe als Mimikry für Metalloproteine zu designen. Inspiriert von der Aminosäure Histidin wurde eine erste Generation von Imidazol Ligandosiden in tetramolekularen G-Quadruplexen eingebaut, welche die Komplexierung von verschiedenen Metallkationen wie Cu^{II}, Ni^{II}, Zn^{II} und Co^{II} erlaubte. Insbesondere Cu^{II} zeigte deutliche Stabilisierungen, welche das Design eines Cu^{II} schaltbaren DNAzymes erlaubte, dass in Gegenwart von Hämin Peroxidase ähnliche Reaktionen katalysierte.[29] In unimolekularen G-Quadruplexen konnten maßgeschneiderte Koordinationsumgebungen für verschiedene Übergangsmetalle designt werden. So bevorzugte Cu^{II} quadratisch planare Koordinationsumgebungen, wohingegen Zn^{II} tetraedrische Geometrien bevorzugte.[30,31] Die Entwicklung mündete im Design von G-Quadruplexen für eine Cu^{II} katalysierte Michael-Addition. Die hohe Modularität des Systems erlaubte schließlich in iterativen Runden von Sequenz-Design und Screening das Design von hoch effizienten G-Quadruplex Strukturen, welche eine Michael-Addition mit exzellenten Umsätzen (94 %) und Enantioselektivitäten von bis zu ≥ 99 % *ee* katalysierten. Wesentlich interessanter war es, dass Sequenzen designt werden konnte, welche beide Enantiomere anreicherten, ohne die Chiralität der DNA komplett zu invertieren. Als Ausblick ist geplant, das hier etablierte System auf neue Reaktionstypen, wie Cyclopropanierungen, Diels-Alder Reaktionen oder Sulfoxidierungen auszudehnen und die weitere computergestützte Optimierung der Sequenzen voranzutreiben.

LIST OF PUBLICATION AND CONFERENCE CONTRIBUTIONS

Publications

- "Cation–Anion Arrangement Patterns in Self-Assembled $Pd_2\mathbf{L}_4$ and $Pd_4\mathbf{L}_8$ Coordination Cages" Guido H. Clever, Philip M. Punt, *Acc. Chem. Res.* **2017**,*50*, 2233.
- "Imidazole-modified G-quadruplex DNA as metal-triggered peroxidase" Philip M. Punt, Guido H. Clever, *Chem. Sci.* **2019**, *10*, 2513.
- "Tailored Transition-Metal Coordination Environments in Imidazole-Modified DNA G-Quadruplexes" Philip M. Punt, Guido H. Clever, *Chem. Eur. J.* **2019**, *25*, 13987.
- "Heteroleptic Coordination Environments in Metal-Mediated DNA G-Quadruplexes" Philip M. Punt, Lukas M. Stratmann, Sinem Sevim, Lena Knauer, Carsten Strohmann, Guido H. Clever, *Front. Chem.* **2020**, *8*, 26.
- "Modular Design of G-Quadruplex MetalloDNAzymes for Catalytic C-C Bond Formations with Switchable Enantioselectivity" Philip M. Punt, Marie D. Langenberg, Okan Altan, Guido H. Clever, manuscript submitted.

Awards

- Poster Price at the "Tag der Chemie", **2018**, *Dortmund*, Germany
- Poster Price at the "RESOLV Klausurtagung", **2018**, *Velen*, Germany
- Poster Price at the "RESOLV Klausurtagung", **2019**, *Marienfeld*, Germany

Conference Contribution

- Poster, 6th International Meeting on Quadruplex Nucleic Acids, **2017**, Prague, Czech Republic
- Talk, KCT – Koordinationschemie-Treffen, **2018**, Heidelberg, Germany
- Poster, RESOLV Klausurtagung, **2018**, *Velen*, Germany
- Poster, Tag der Chemie, **2018**, *Dortmund*, Germany
- Poster, 14th EuroBIC, **2018**, Birmingham, Great Britain
- Poster, KCT – Koordinationschemie-Treffen, **2019**, München, Germany
- Poster, RESOLV Klausurtagung, **2019**, *Marienfeld*, Germany
- Poster, GRK Confinement-controlled Chemistry, **2019**, *Bochum*, Germany
- Poster, 19th ICBIC – International Conference on Biological Inorganic Chemistry, **2019**, *Interlaken*, Switzerland

CONTENT

1 INTRODUCTION

1.1 DNA

Proteins and DNA are among the most important and abundant biopolymers and have been extensively studied for decades. Apart from their primary sequence, the correct folding of the secondary and tertiary structure is crucial for the function and misfolded proteins can cause severe diseases like Alzheimer and Parkinson.[32–34] While the prediction of secondary protein structures is highly demanding,[3] DNA folds into defined secondary structures from only a few nucleobases and even isolated nucleobases can form hydrogen bonded pairs.[2,35–37] The highly specific hydrogen bonding pairs in DNA, the so-called Watson-Crick pairs, form between the DNA bases cytosine (C) and guanine (G) or thymine (T) and adenine (A).[38–40] The DNA bases are connected to 2-deoxyribose, a pentose sugar, which forms with phosphate the phosphodiester backbone of DNA.[41] Although the structural biology of DNA is very rich, the most known secondary structure is the right handed helical duplex B-DNA.[38,41,42] While the genetic code is stored as B-DNA, two other types of helical duplex DNA are known, the right-handed A-DNA and the left-handed Z-DNA. Although they are much less abundant, it is assumed that they are relevant e. g. during transcription and under desiccation in bacteria.[43–45]

Next to duplex DNA, a number of other secondary DNA structures are known, such as three-way junctions, triplex DNA, i-motifs and G-quadruplexes.[6,10,46–48] The latter ones assemble from guanine rich sequences with the common pattern of $G_{\geq 2}N_xG_{\geq 2}N_xG_{\geq 2}N_xG_{\geq 2}$ *via* Hoogsteen base pairing to form planar tetrameric G-tetrads, which stack *via* π-π interactions to from the G-quadruplex.[9,10,49–51] Hoogsteen base pairing in G-tetrads has a distinct difference to Watson-Crick base pairs and involves the N7 Nitrogen in guanine as a hydrogen-bond acceptor and it was shown, that replacement of the N7 nitrogen with carbon inhibits the formation of G-tetrads.[28,52–55] The formation of G-tetrads is resulting in an accumulation of partial negative charges from the negatively polarized carbonyl oxygen atoms, pointing in the central cavity of the G-quadruplex. To compensate this, cations are incorporated in the central pockets between the G-tetrads. Under physiological conditions this is mostly K^+ or Na^+ but also other cations including Tl^I and Pb^{II} were found (**Figure 1)**.[10,16,53,56–58]

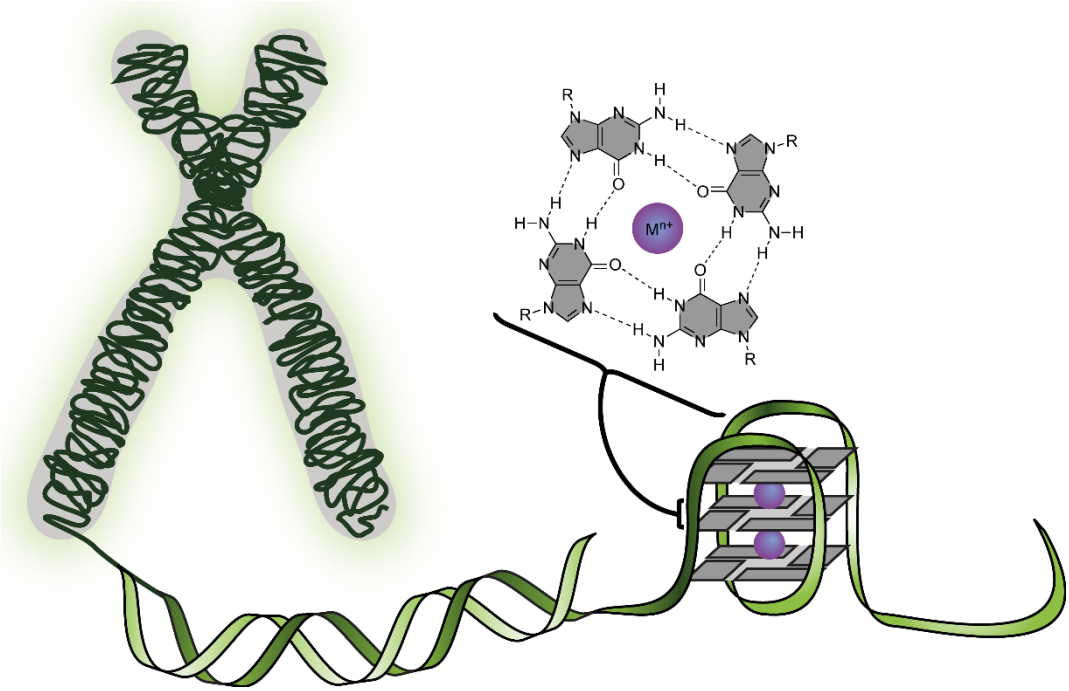

Figure 1. From chromosomes to the G-quadruplex. Schematic representation of a G-quadruplex, forming from the G-rich single stranded overhangs of the telomers.

1.2 Structural diversity and structure determination of G-quadruplex structures

Although the pattern of G-quadruplex forming sequences follows the common scheme $G_{\geq 2}N_xG_{\geq 2}N_xG_{\geq 2}N_xG_{\geq 2}$, G-quadruplexes can fold into a large variety of structures and often, for a given sequence, mixtures of structures are observed.[9,51,59,60] The large variety of G-quadruplex structures arises from different factors.[10,24,61] First, for G-quadruplexes, different molecularities are known, including tetra-, bi- and monomolecular (**Figure 2**) structures and in a few cases trimolecular examples were reported, although a special sequence design was required.[62] Further, the glycosidic angle of guanine can be *syn*- and *anti*-oriented. Directly connected to the glycosidic angles are the relative arrangements of the G-tracts to each other, adopting antiparallel or parallel orientations, depending on their glycosidic angle. This gives rise to different topologies including parallel, 2+2 antiparallel or 3+1 hybrid topologies. Which glycosidic angles the guanines adopt, strongly depends on the sequence, but also on the exact electrolyte composition. For this reason, different electrolytes can lead to different topologies e.g. the human telomeric repeat forms in sodium and potassium containing buffers different topologies, such as a 3+1 hybrid-type or mixtures of topologies are observed.[61,63–66] Next to the topology, also the thermal stability of G-quadruplexes

strongly depends on the size of the cations and was found to be ideal for K^+, whereas Li^+ is too small and Mg^{2+} too big. In general, the order $Li^+ > Na^+ > Rb^+ > K^+$ was found for the G-quadruplex stability.[67–70] At last, the G-tracts in bi- and unimolecular G-quadruplexes are connected by flexible loop regions and can be as short as one or up to seven or more nucleotides and adopt different orientations such as lateral, diagonal or propeller-shaped (**Figure 2**).[9,16,51] Together, these properties result in a diverse repertoire of different G-quadruplex structures and in many cases, a given G-quadruplex-forming sequence folds not into a single but in multiple different structures, rendering structure determination difficult. A selection of common folding patterns is shown in **Figure 2**.[53,71]

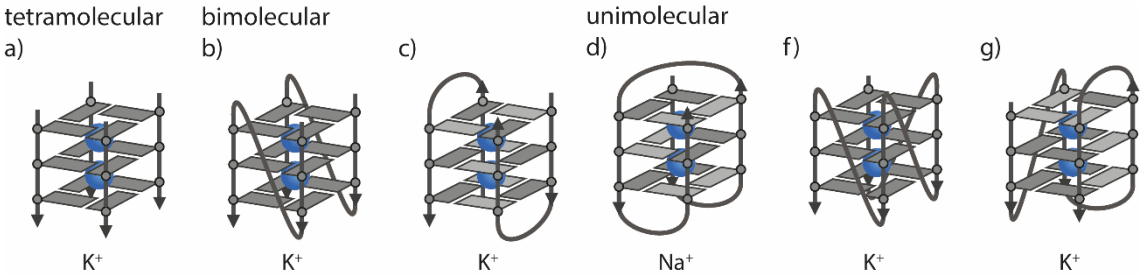

Figure 2. Structural diversity of DNA G-quadruplex structures. a) parallel stranded tetramolecular topology, b) bimolecular parallel topology with propeller shaped loops, c) antiparallel bimolecular G-quadruplex with lateral and diagonal loops, d) unimolecular antiparallel basket-type topology with lateral and diagonal loops, f) parallel topology with propeller loops and g) hybrid topology with lateral and propeller loops.[71]

As the landscape of G-quadruplex topologies is very diverse, structure determination can be difficult. To shed light on G-quadruplex properties and topology, the most common techniques are CD spectroscopy (Circular Dichroism), thermal denaturation experiments and thermal difference spectra (TDS) (**Figure 3**).[72–79] In thermal denaturation experiments, the stability of G-quadruplexes is determined, expressed as the melting temperature T_m. It is based on a decrease of the absorption at 295 nm upon heating, resulting from a denaturation of the G-quadruplex structure. It is often used to investigate G-quadruplex binding small molecules, which induce a change of the thermal stability upon binding.[80,81] In TDS specific maxima at ~240 and ~273 nm and a minimum at ~295 nm indicates a G-quadruplex formation and is used for the differentiation from other secondary structures. TDS are derived from subtraction of a low temperature spectrum from a high temperature spectrum, corresponding to a folded and unfolded G-quadruplex structure, respectively.[72]

In CD spectroscopy of G-quadruplexes, mostly the guanine residues contribute to the CD spectrum, while other bases are neglectable. How guanine contributes to the CD spectrum depends on the glycosidic angle and the relative arrangement to the next

guanine, resulting in specific CD signatures for parallel (type I), antiparallel (type II) and hybrid (type III) topologies.[78,79] As a rule of thumb, type I spectra have a positive Cotton effect at ~295 nm and a minimum at ~260 nm, type II spectra a positive Cotton effect at ~264 nm and a minimum at ~245 nm and type III spectra a positive Cotton effect at ~295 nm, a maximum at ~260 nm and a minimum at ~245 nm.[82] In addition, CD spectra are often compared to the CD spectra of G-quadruplexes with a known structure, allowing the qualitative assignment of a structure. Although CD spectroscopy is a fast and easy method to assess the topology of G-quadruplexes, it becomes complicated, if mixtures of topologies are observed or to differentiate between subtypes of the same topology, e.g. antiparallel chair-and basket-type.[63,65,83]

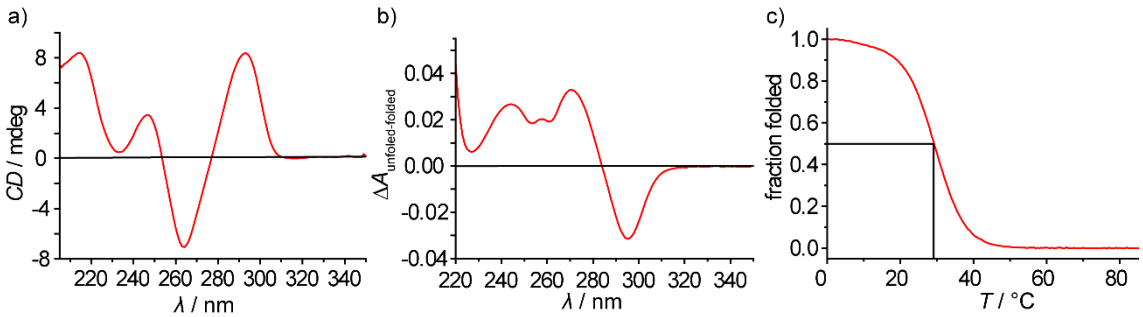

Figure 3. Examples for a CD spectrum, TDS and melting profile of a G-quadruplex. The CD spectrum indicates an antiparallel topology, while the signature of the TDS indicates G-quadruplex formation. The melting profiles provide information about the thermal stability.

While CD spectroscopy, thermal denaturation experiments and TDS are commonly the primary techniques to investigate G-quadruplexes, they give no atomistic information about the structure. For atomistic insights NMR, spectroscopy and X-ray crystallography are widely applied[84,85] and over the last decade a large number of structures was published.[86–89] In this dissertation, it is focussed on the structures formed from the human telomeric repeat, called htel, as most of the investigated sequences are based on htel. For this repeat alone, several distinct G-quadruplex structures was published, showing the high structural diversity.[63–65,83] Which structure forms, depends on small differences such as the electrolyte composition or single point mutations. In **Figure 4** three different structures formed from the human telomeric repeat are shown, the crystal structures of a parallel and antiparallel chair-type topology and the NMR solution structure of an antiparallel basket-type topology. Especially the latter two antiparallel topologies cannot be reliably differentiated by CD spectroscopy.

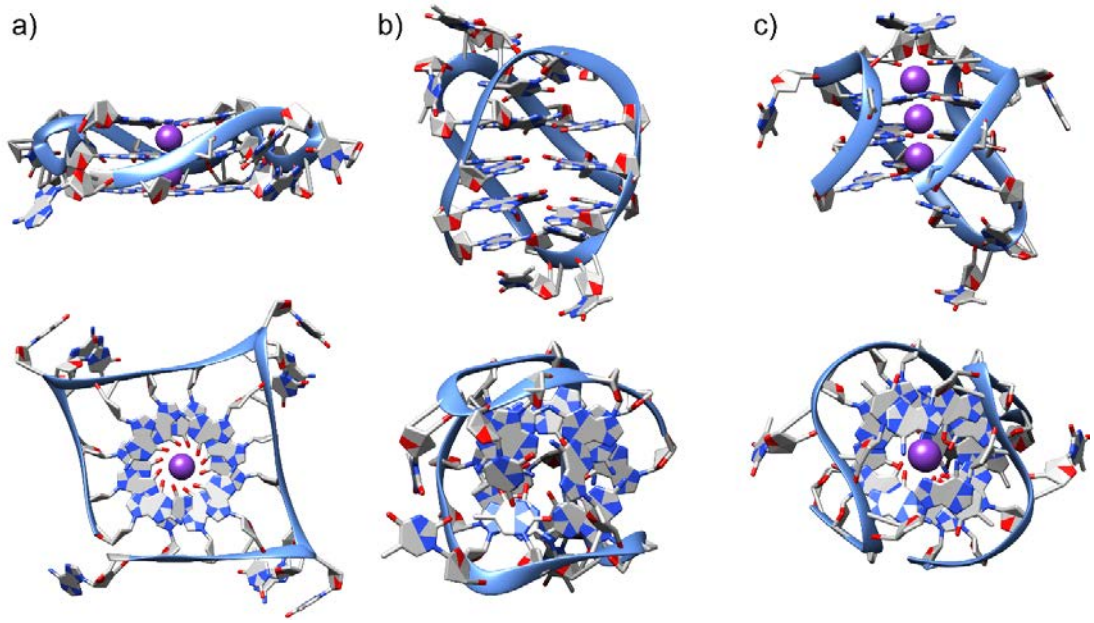

Figure 4. Structures of G-quadruplexes formed from the human telomeric repeat. a) Crystal structure of a parallel topology (1KF1), b) NMR solution structure of an antiparallel basket-type topology (143D) and c) crystal structure of an antiparallel chair-type topology. The central ions are not detected in NMR spectroscopy and therefore missing in b).[64,65,83]

1.3 Biological Relevance

Since the first report of isolated G-tetrads formed in guanosine monophosphate gels, it took decades to realize that DNA G-quadruplexes are more than just a laboratory curiosity.[90] It is proposed that the human genome contains >300,000 sequences, that potentially form G-quadruplexes, however for a long time it was difficult to proof the formation of G-quadruplexes not only *in vitro* with isolated sequences, but *in vivo* and therefore to proof a biological relevance.[9,91,92] The breakthrough was achieved with the development of G-quadruplex specific antibodies allowing to visualize G-quadruplexes *in vivo*. Interestingly, it was found that the number of G-quadruplexes was varying during the different phases of the cell cycle indicating a regulatory function (**Figure 5**).[92]

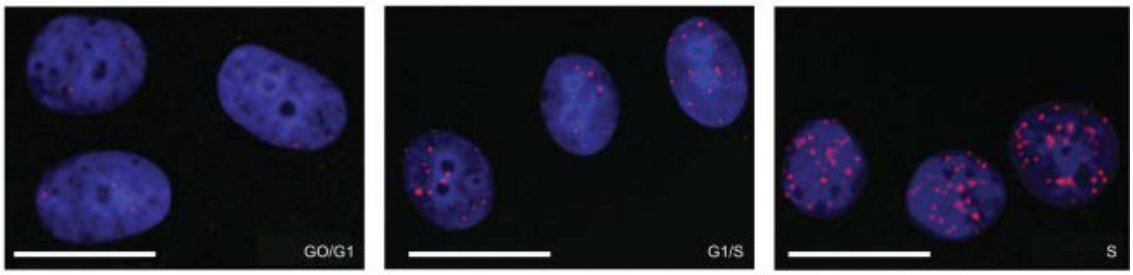

Figure 5. Antibody stained (red dots) MCF-7 mammary adenocarcinoma cells in the G0/G1, G1/S and during the S phase. Nuclei are stained with DAPI. Different amounts of G-quadruplexes were observed during the phases. Reprinted with permission from ref.**[92]** Copyright © 2013, Nature Publishing Group.

Nowadays, it is known that G-quadruplexes are involved in a wide range of regulatory processes and consequently also in diseases. The abundance of the G-quadruplex forming tandem repeats $(TTAGGG)_n$ in the telomeric regions early on promoted the idea of a regulating function during the elongation of the telomers in cancer.[93] Indeed, it was found that the telomerase activity was strongly dependent on the formation of G-quadruplexes.[94–98] This led to the idea for the development G-quadruplex stabilizing small molecules, which could inhibit the activity of telomerase.[53,93,99] A typical design for G-quadruplex binding molecules often involves planar aromatic molecules, allowing π-π stacking interactions with the G-tetrads in combination with additional cationic functionalities for strong electrostatic interactions with the negatively charged phosphate backbone (**Figure 6**).[53,99–103] A classic example for this approach was quarfloxin that showed strong antiproliferative activities in cancer cell lines and reached clinical phase II trials.[104] Pleasingly, it showed very little adverse side effects during clinical trials.[53,105,106]

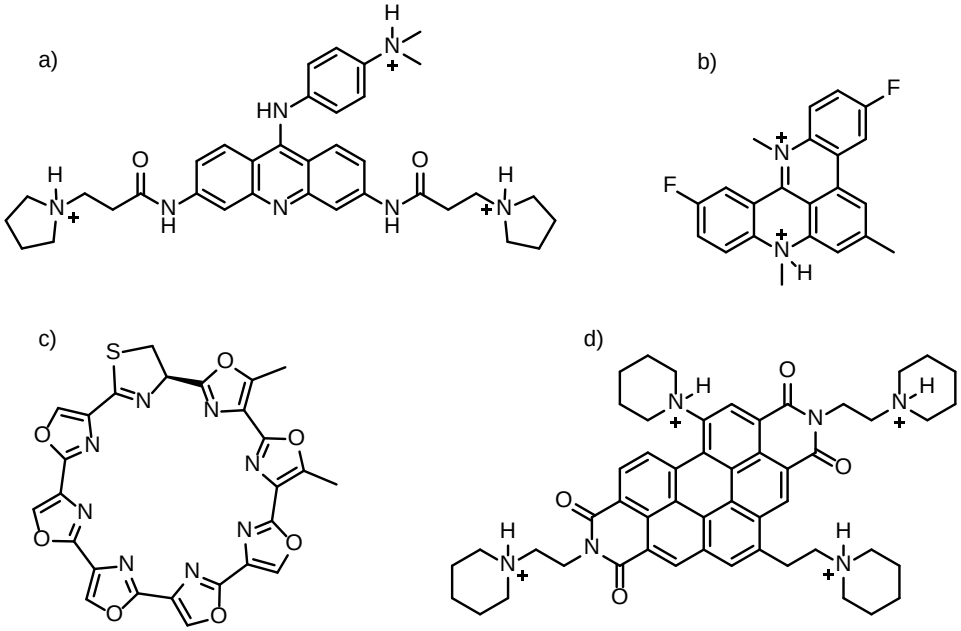

Figure 6. Selection of G-quadruplex targeting molecules. Commonly they are aromatic planar structures and have a high content of nitrogen atoms that can be protonated under physiological pH leading to strong electrostatic interactions with the negatively charged phosphate backbone. a) BRACO-19 b) RHPS4 c) Telomestatin d) EMICORON.[53,99,101–103]

Apart from the telomeric repeats, G-quadruplex forming sequences were found in the promoter regions of a large number of well-known proto-oncogenes, including *cMyc*, *KRAS*, *HRAS* and *KIT*.[107–111] As for the telomers, it was shown, that a stabilization of G-quadruplexes in these promotor regions induced a downregulation of the corresponding genes.[107–109] Although the approach to target G-quadruplexes in the oncogenes was promising, it raised the question, if a selectivity for certain G-quadruplex topologies could be achieved. While good selectivity's were shown for a series of small molecules to

differentiate between duplex DNA and G-quadruplexes, examples for compounds selectively binding a certain G-quadruplex topology over another, are very limited.[112–114] The reason is that although the topologies of G-quadruplexes are highly diverse they always share the common feature of a helical twist and G-tetrads allowing π-π stacking interactions, rendering the design of selective small molecules challenging.[16] Nevertheless, G-quadruplexes remain a vibrant target in medicinal chemistry and the future will show if this results in new therapeutic approaches.

1.4 Metal-mediated Base Pairing

In Watson-Crick pairs, two nucleobases form hydrogen bonds, leading to the highly selective formation of duplex DNA from two complementary sequences.[41,42] In metal-mediated base pairs the canonical hydrogen bonds are completely or partially replaced by metal coordination.[115–117] The first example was discovered in 1960 by Katz, when he investigated the reversible reaction of Hg^{II} with oligonucleotides.[118] Although no structural evidence was available at that time, he already correctly proposed that two thymine residues were binding a single Hg^{II} ion to forming a metal-mediated T-Hg^{II}-T metallo base pair (**Figure 7a**).[119]

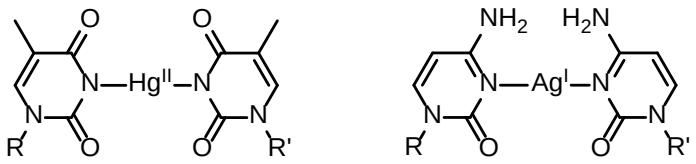

T-Hg^{II}-T C-Ag^{I}-C; *cisoid*

Figure 7. Metal-mediated base pairs of a) a T-T mismatch with Hg^{II} and b) a C-C mismatch with Ag^{I}. [120–122]

After the initial studies by Katz (T-Hg^{II}-T), different examples like the Ag^{I} mediated C-Ag^{I}-C metallo base pair (**Figure 7b**) followed.[123–125] Today, a broad variety of Ag^{I} and Hg^{II} mediated base pairs involving different nucleobases are known.[116] Even a crystal structure was recently published, where all canonical hydrogen bonds were replaced with Ag^{I} mediated base pairs, resembling a long silver nanowire.[126] Although numerous examples of metal-mediated base pairs comprising natural nucleobases were reported, they mostly involved Hg^{II} and Ag^{I}. This changed with the introduction of artificial nucleobase surrogates into DNA by solid phase DNA synthesis, enabling the complexation of a broad variety of transition metal cations such as Mn^{II}, Ag^{I}, $Pd^{II,}$ Ni^{II}, $Cu^{I/II}$ or Zn^{II}.[127–133] Some of these metallo base pairs were modifications of the canonical nucleobases, like a methylated cytosine in a ^{Me}C-Ag-T metallo base pair.[134] Others were designed from scratch for the complexation of a specific metal cation, such as a

hydroxypyridone ligandoside (HP) for the specific complexation of Cu^{II}, to from a HP-Cu^{II}-HP metallo base pair, resulting in strong thermal stabilizations of up to ΔT_m = + 13 °C.[135] Other, more exotic examples involved palladacycles as metal-mediated base pairs, which was one of only a few examples involving organometallic chemistry in metal-mediated base pairing.[136,137]

In 2005, the salen ligandoside (S) was introduced into duplex DNA. Special about the salen metallo base pair was, that for the first time, in addition to metal coordination the metallo base pair formed a covalent imine crosslink between two DNA strands, which formed in a condensation reaction with the salen ligandosides and ethylene diamine (**Figure 8**). The corresponding S-Cu^{II}-S metallo base pairs showed unprecedented high thermal stabilizations for metal-mediated duplex DNA.[138–141] The development then culminated in the programmable design of long mixed metal arrays (**Figure 8**). This was facilitated by the introduction of the salen base pair, that selectively bound Cu^{II}, combined with T:T mismatches, selectively forming T-Hg^{II}-T metallo base pairs.[142] With the design of long metal arrays inside DNA, the question was, if they could be used as nanowires and if it was possible to conduct electricity.[143] This question remained highly controversial until today, as it was assumed, that this was not directly due to the incorporation of the metal cations, but rather a structural change, which was induced after metal complexation. The rigidification of the duplex structure after metal complexation presumably allowed a better charge conductance between the nucleobases, therefore not directly involving the metal cations.[143,144] Further support for this explanation was published in a recent study, showing that the incorporation of a metal increased the conductance indeed through structural effects.[144] Besides applications as nano-wires, recent studies focused on applications for the selective detection of heavy metal contaminations such as Hg^{II}[145,146] or for the templating of defined metal nano-clusters by reduction of the incorporated metal cations.[147,148] In recent times, a growing number of examples is reported on metal-mediated base pairing in higher DNA structures, which will be discussed in the following chapter.

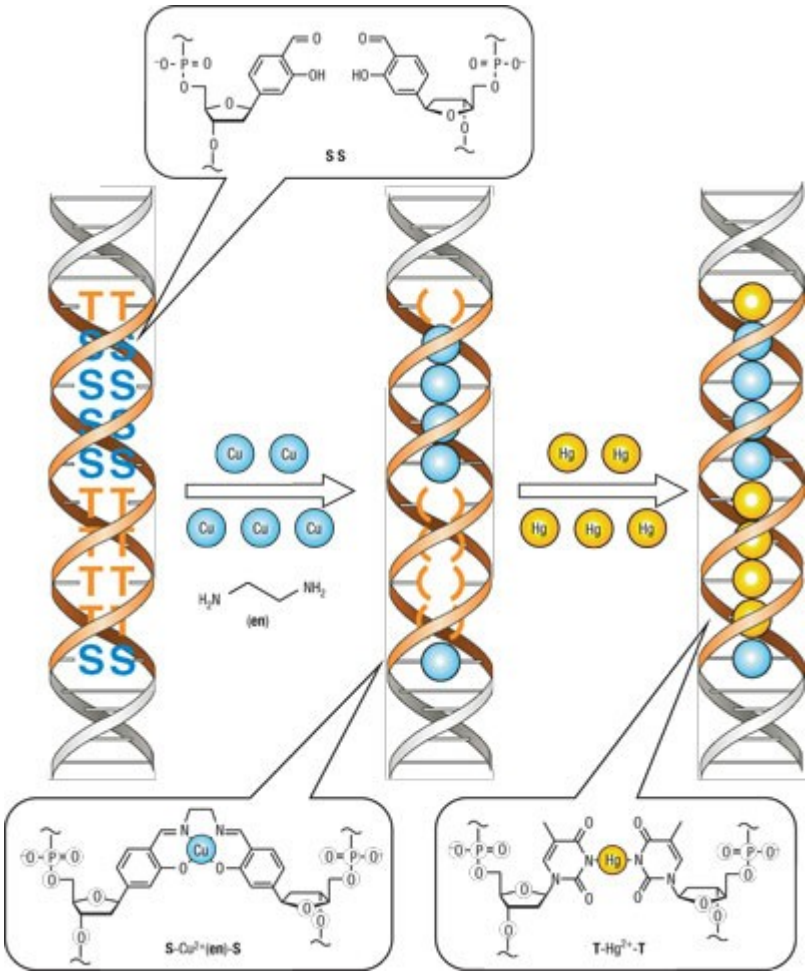

Figure 8. Formation of long mixed metal wires comprising of T-Hg^{II}-T and S-Cu^{II}-S or H-Cu^{II}-H base pairs. Successive addition of the respective metal cations resulted in a step wise stabilization. Reprinted with permission from ref.[142] Copyright © 2006, Nature Publishing Group.

1.5 Metal-mediated base pairs in higher DNA structures

A vast number of examples described metal-mediated base pairs in duplex DNA, involving different metal cations such as Mn^{II}, Ag^{I}, Ni^{II}, Cu$^{I/II}$ or Zn^{II}.[117,127,129,138,149] Though, only a limited number of studies was reporting on metal-mediated base pairs in higher structures such as three-way junctions, triplex DNA, i-motifs or G-quadruplexes.

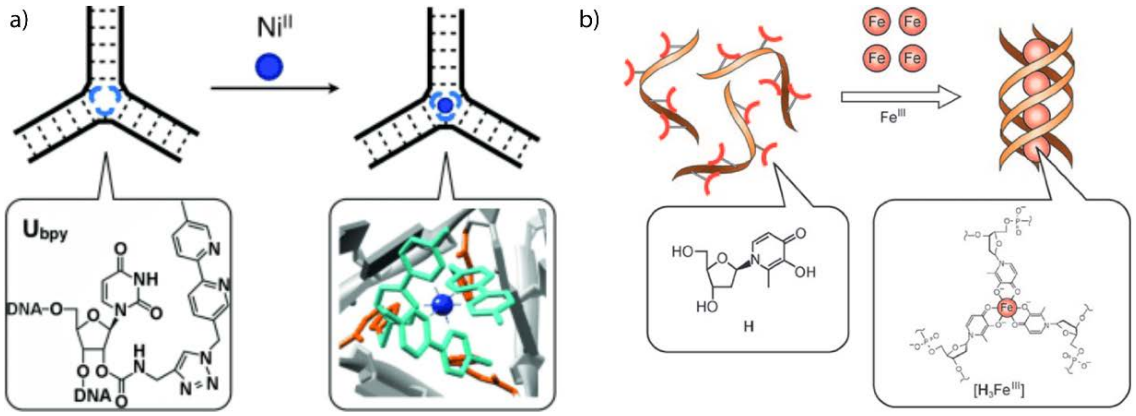

Figure 9. Metal-mediated three-way junction and triplex DNA. In a) the incorporation of a bipyridine ligand, covalently attached to uracil, allowed the complexation of Ni^{II} in the centre of the three-way junction and b) the incorporation of hydroxypyridone in a DNA sequence allowed the design of Fe^{III} wires inside a triplex structure. Reprinted with permission from ref.[150,151] Copyright © 2009, 2013 WILEY-VCH Verlag GmbH & Co. KGaA, Weinheim Inc.

An early example of a metal-locked three-way junctions was published in 2013 by Shionoya et al. The incorporation of alkyne-modified uracil at the junction position allowed in a click reaction the post-synthetic incorporation of a bipyridine ligand to complex one Ni^{II} cation in the central pocket.[151] Since three-way junctions are often used in DNA nanotechnology as branching units, this might show useful for the design of metal responsive nanostructures. In contrast to three-way junctions, where only one metal ion can be incorporated in the branching unit, triplex DNA offers the possibility of metal wires. The first example of a metal-mediated triplex DNA was reported already in 2002, involving a Pyridine-Ag^{I}-Pyridine metallo base pair.[152] In a different approach, the same group synthesized sequences containing only hydroxypyridone ligandosides, which allowed to design a triplex DNA with a central Fe^{III} array (**Figure 9b**).[150]

Only recently, the first example of a Cu^{I} mediated i-motif was reported.[153] i-motifs form from cytosine-rich sequences *via* an interlocked C-C^{+} base pairing mode (**Figure 10a,b**). Working under oxygen free conditions, the central protons could be replaced with Cu^{I} ions, leading to i-motifs with multiple incorporated Cu^{I} ions. Clue of the system was, that it allowed a redox regulated switching between the copper bound and unbound state. When Cu^{I} was oxidized to Cu^{II}, due to the different coordination geometry, Cu^{II} was released and the i-motif disassembled. Reducing Cu^{II} to Cu^{I} lead again to the formation of the metal-mediated i-motif.[154]

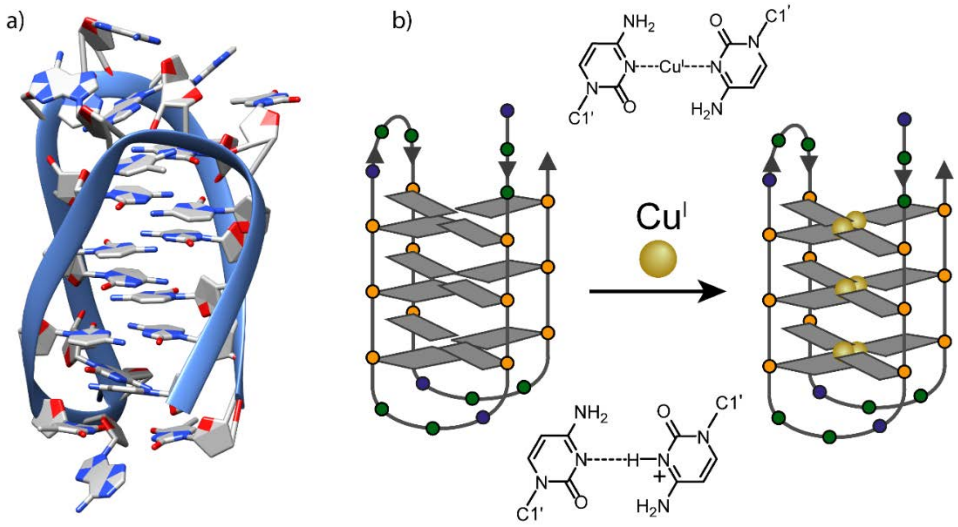

Figure 10. Structural features of the i-motif. In a) is the NMR solution structure of an unimolecular i-motif shown (1EL2). b) schematic representation of the i-motif with the interlocked C-C$^+$ base pairs and Cu^I mediated C-Cu^I-C metallo base pair.[153]

For G-quadruplexes, a number of examples was shown, in which metals were incorporated into the DNA, involving a T-Hg^{II}-T metallo base pair between the loops of a unimolecular G-quadruplex, a sequence-specific DNA-cleaving Ce^{IV} complex and a bimolecular G-quadruplex functionalized with bipyridine for the complexation of different metal ions.[121,155,156] In 2013, our group reported the first example of a G-quadruplex structure, where the 5'-terminal G-tetrad in a tetramolecular system was replaced with a pyridine$_4$-Cu^{II} quartet, allowing a Cu^{II} responsive G-quadruplex formation.[157,158] Iterative rounds of EDTA and Cu^{II} addition could show a high reversibility of the system without compromising the metal-mediated thermal stabilization. Incorporation of additional pyridine ligandosides at the 3'-ends allowed the complexation of a second Cu^{II}, which could be exploited for accurate distance measurements between the Cu^{II} centres by EPR-spectroscopy (**Figure 11**), showing extremely narrow distance distributions. Also, the measured distances were in very good agreement to the theoretical distances calculated from MD simulations.[159] This system was then further developed to investigate dimerization of tetramolecular G-quadruplexes and how this was affected by different small molecules. Interestingly, in the study it could be shown, that guanosine monophosphate could form an additional G-tetrad in between a G-quadruplex dimer, resulting in a distance increase, exactly corresponding to one π-stacking distance.[28]

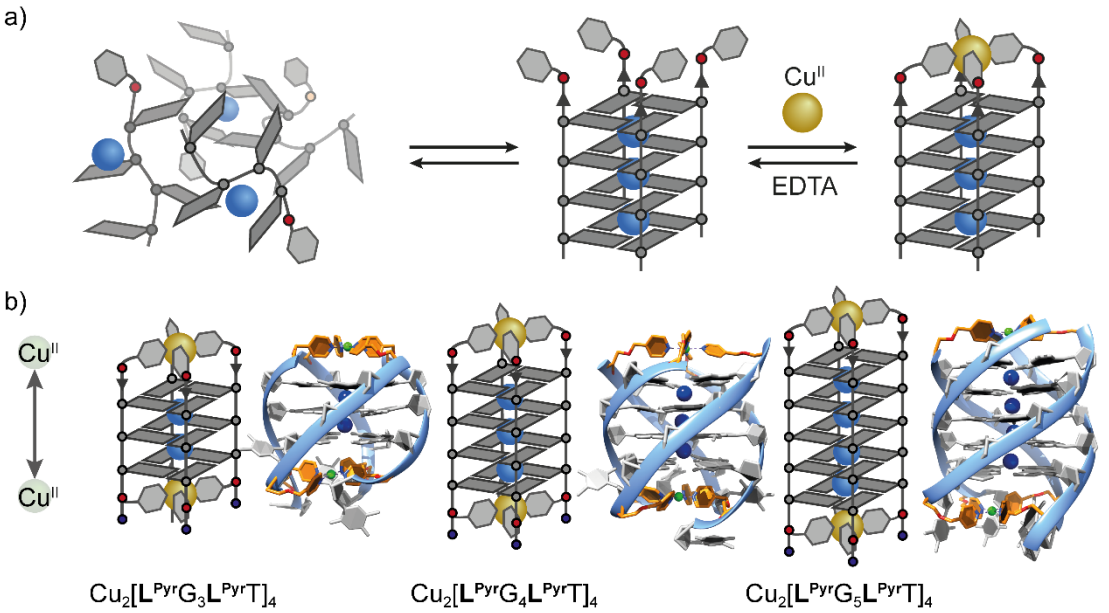

Figure 11. a) First example of metal-mediated G-quadruplexes. The introduction of 5'-terminal pyridine ligandosides in tetramolecular G-quadruplexes allowed the complexation of Cu^{II}, resulting in strong thermal stabilizations. b) Cu^{II} based EPR distance rulers and Snapshots of the corresponding MD simulations of the G-quadruplexes.

After the concept of metal-mediated tetramolecular G-quadruplexes was established, naturally the next step was to expand the concept to unimolecular G-quadruplexes. In contrast to tetramolecular G-quadruplexes, where the ligandosides can only be incorporated at the terminal sites, unimolecular G-quadruplexes offer more possibilities to incorporate the ligandosides anywhere in the sequence. Although unimolecular G-quadruplexes offer more possibilities, the determination of the formed topology is much more complex and a series of different folds can form. Nevertheless, incorporation of four pyridine ligandosides in the human telomeric repeat htel (AGG G $(TTAGGG)_3$) by replacement of one G-tetrad led to the formation of a clear antiparallel G-quadruplex, showing strong thermal stabilizations after Cu^{II} addition.[160]

When the same pyridine ligandoside was incorporated four times in the G-quadruplex forming sequence $ttel_{24}$, another interesting effect was observed. In absence of Cu^{II} the G-quadruplex formed a mixture of topologies, but addition of Cu^{II} induced a topology change towards a clear antiparallel topology. When Cu^{II} was then removed with EDTA, the topology was trapped in a metastable state, that could be reversed to the initial state by thermal de- and renaturation. Another example was shown, when four pyridine ligandosides were incorporated in the thrombin binding aptamer, which is known to inhibit the clotting reaction of thrombin. The pyridine modified aptamer was very unstable, but after Cu^{II} was added, the aptamer was stabilized, resulting in a significantly slower clotting reaction of thrombin (**Figure 12**).[160]

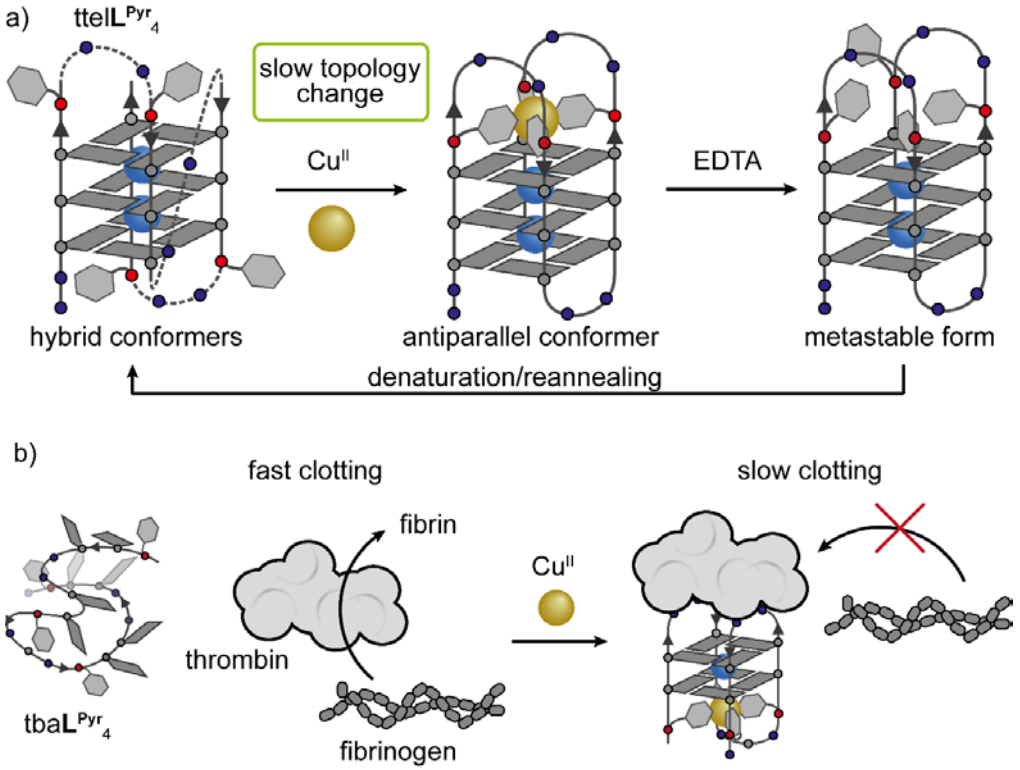

Figure 12. a) Cu^{II} mediated topology switch of ttel**L**$^{Pyr}_4$ from a mixture of topologies towards a clean antiparallel topology. b) Thrombin clotting assay with a Cu^{II} activated thrombin binding aptamer. Reprinted and adapted with permission from ref.[160] Copyright © 2017 WILEY-VCH Verlag GmbH & Co. KGaA, Weinheim Inc.

1.6 DNAzymes and DNA Based Asymmetric Catalysis

Over billions of years nature has evolved enzymes for variety of chemical transformations. Key to many of these enzymes are metal cations acting as Lewis-acids, redox cofactors, structural regulators and in other functions.[161–164] Due to the unique reactions enzymes are able to catalyse under ambient conditions, many efforts were undertaken to use them for biotechnological applications, focusing to further improve reaction rates and selectivity's or to make xenobiotic reactions – reactions unknown to nature – accessible.[165,166] In this context a widely used approach is directed evolution, which proofed highly successful and was awarded with the Nobel prize in 2018 to Frances H. Arnold, George P. Smith and Sir Gregory P. Winter.[167]

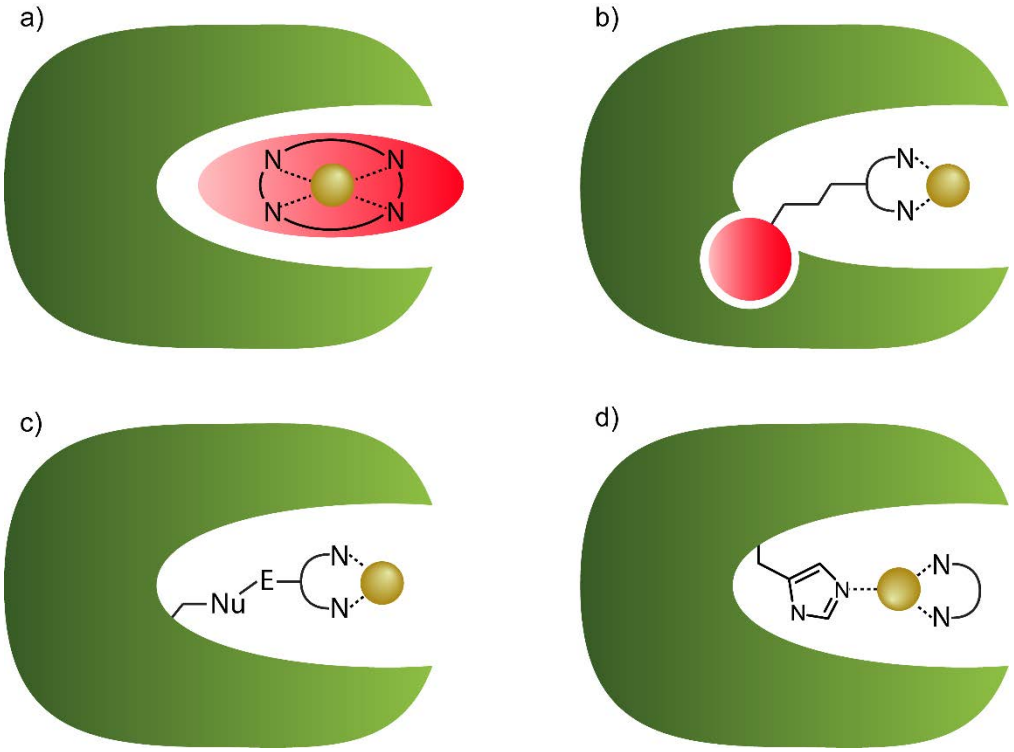

Figure 13. Approaches to anchor metal cations in protein scaffolds. a) non-covalent interactions between the metal complex and the protein scaffold, b) non-covalent anchoring with an affinity tag to the protein, c) covalent anchoring of the metal complex to the protein and d) dative bond of an amino acid to an unsaturated metal.[168]

While the approach of directed evolution was relying on existing metallo-enzymes, in a different approach new metallo-enzymes were designed by exchanging the metal cations in the catalytic centres or by the introduction of metal centres in metal free proteins, including four general approaches 1) non-covalent interactions or replacement of metals with other metals,[169,170] 2) anchoring metals with affinity tags like biotin in proteins[171] 3) covalent anchoring or 4) coordination of unsaturated coordination environments[172,173] (**Figure 13**).[166,174] This enabled the design of artificial enzymes for cyclopropanations,[170,174] Diels-Alder reactions,[175] Michael-Additions,[176] ring-closing metathesis[177] and others. While many of these approaches were depending on the modification of natural protein scaffolds, the *de novo* design of metallo-proteins remains highly challenging. Major difficulty is the design of discreate folding patterns to position ligands in a certain proximity to allow a chelation of metal cations.[178]

In this context, the folding patterns of DNA and RNA are much better predictable and since the discovery of catalytic nucleic acids in 1982, a large number of different nucleic acid enzymes was discovered.[179,180] With the discovery of catalytic RNA (RNAzymes), also the RNA world hypothesis was born, suggesting that in an early world RNA was acting in two functions as carrier of the genetic information and as catalyst.[182] However, the theory was contested with several shortcomings of an RNA only world, such as a

limited catalytic repertoire or insufficient concentrations of precursor molecules.[181] Today it is assumed, that a coevolution of RNA with DNA and peptides could have solved these shortcomings.[182] Although the theory of an RNA world is contested, ribozymes remain a vibrant field in prebiotic chemistry to understand the origins of life.[183] Besides the origin of life catalytic nucleic acids are also extensively investigated for their biological function. One of the most prominent examples is the ribosome. Build from ribosomal RNA and ribosomal proteins, the ribosomes catalyse the synthesis of proteins from mRNA.[184,185] Other examples are the hammerhead ribozyme, catalysing the reversible cleavage of RNA strands or the self-splicing group II intron, catalysing the excision of the intron and the ligation of the flanking exons, an important step in RNA maturation.[186–188] The role of metal cations in ribozymes is very important and in the latter mentioned self-splicing group II intron, Mg^{II} ions were found to lock the exons in place.[188]

In the early 90's first examples of Pb^{II}- and Zn^{II}-dependent DNAzymes were found, which showed RNA cleavage and DNA ligation activities.[189,190] Other DNAzymes were shown to catalyse the metalation of porphyrins or were used as sensors for heavy metals.[191–197] In a more recent study, the group around Shionoya could combine the concept of artificial metallo base pairs with a DNAzyme. The incorporation of a hdroxypyridone (HP) mismatch in a RNA cleaving DNAzyme allowed a Cu^{II}-responsive cleavage of RNA, however switching between the on/off state remained challenging.[198] To circumvent this issue, they replaced the HP mismatch with a recently published bidentate 4-carboxyimidazole (IMC) mismatch, which formed with Cu^{II} a square planar metallo base pair.[132] Clue about this system was the additional electrostatic repulsion from the carboxylates, that completely prevented the formation of the DNAzyme in absence of Cu^{II}. Cycles of Cu^{II} and GHL (Cu^{II} chelating tripeptide) addition could show a reversible and sharp on/off switching of the DNAzyme.[199]

Another class of DNAzymes is based on DNA G-quadruplexes with hemin, acting as cofactor. It was shown that hemin could bind to G-quadruplexes *via* π-π stacking interactions to form a DNAzyme with a strong peroxidase-like activity, that catalysed the oxidation of organic substrates in presence of H_2O_2.[20–22,201] A proposed mechanism is shown in **Figure 14**. In a first step H_2O_2 binds to hemin and following an O-O bond cleavage in a two-electron oxidation a ferryl species (Fe^{IV}=O) and a cationic porphyrin radical are produced. The activated state then oxidizes two substrate molecules in two consecutive one-electron transfers and hemin is reduced again to the initial Fe^{III} state.[200] After it's discovery, the hemin/G-quadruplex DNAzyme was applied in large number of studies for the detection of heavy metals, organic catalysis, in DNA nanotechnology for the design of stimuli responsive gels, in logic gates and for MOF-DNA (metal organic

framework) hybrid materials to name just a few examples.[19,202–206] The group around Itamar Willner recently conjugated the hemin/G-quadruplex DNAzyme to SELEX (Systematic Evolution of Ligands by EXponential Enrichment) selected aptamers, which was termed as nucleoapzymes.[207–209] Due to the very high affinities of the aptamers to the substrate, this resulted in locally increased substrate concentrations at the catalytic hemin/G-quadruplex DNAzyme, leading to strongly enhanced catalytic activities, displaying saturation kinetics.[209]

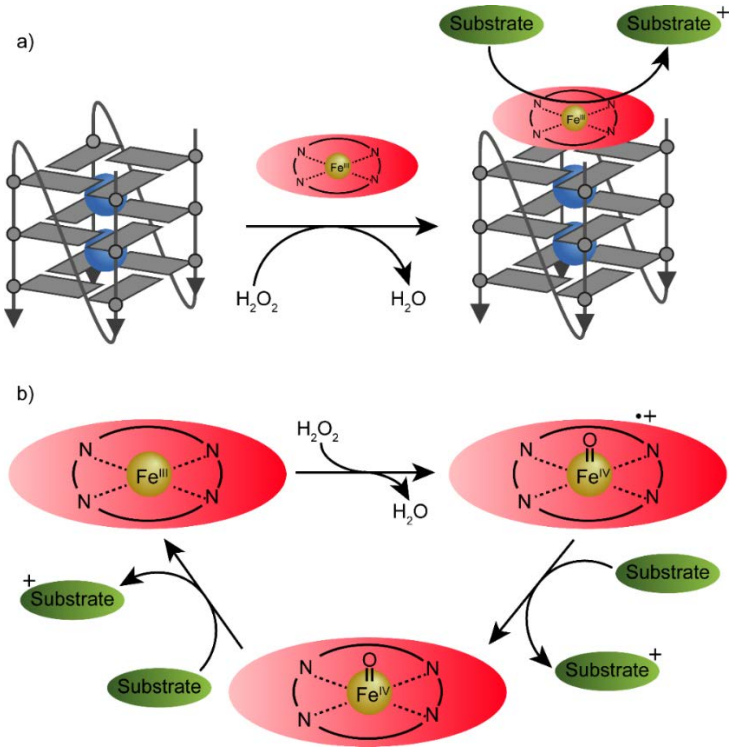

Figure 14. Hemin/G-quadruplex DNAzyme with a peroxidase activity. a) Schematic representation of a unimolecular parallel G-quadruplex, that forms with hemin the active DNAzyme to catalyse the oxidation of organic substrates in presence of H_2O_2. b) Proposed peroxidation cycle of the DNAzyme.[200]

Next to the design of DNAzymes, in an increasing number of studies, DNA was used as a chiral scaffold for asymmetric catalysis.[210] Although in these systems DNA was shown to strongly enhance the catalytic reactions, the DNA is considered as a chiral scaffold and not as a DNAzyme. In DNA based asymmetric catalysis, a metal complex is embedded into the chiral environment of DNA *via* covalent or non-covalent interactions. This concept could be applied for enantioselective Diels-Alder reactions, Michael-Additions, *syn*-hydrations, Friedel-Crafts reactions, cyclopropanations and others (**Figure 15**).[210–226] The first example was a Diels-Alder reaction of azachalcone with cyclopentadiene reported by Roelfes and Feringa (**Figure 15b**) in 2005. It was shown that undefined salmon testis DNA with an intercalating 9-aminoacridine-Cu^{II} complex catalysed the Diels-Alder reaction with high conversions and enantioselectivities of up to

90 % *ee*, proving that the chirality of the DNA was transferred to the product.[227] In **Figure 15a** is the generalized mechanism for the substrate activation shown. After the duplex DNA has formed, Cu^{II} salt and complexing ligand are added to the solution and are incubated for a certain time to allow a Cu^{II} complexation and the intercalation of the complex into the DNA. The substrate then coordinates with the pyridine nitrogen and carbonyl oxygen atom to Cu^{II} and is activated for the Diels-Alder reaction. Later the enantioselectivity was improved to 99 % *ee* by simply changing 9-aminoacridine to bipyridine based ligands.[216] The same system was then applied in an enantioselective Michael-additions of chalcone derivatives with dimethyl malonate or nitromethane, again showing high enantioselectivities of up to 99 % (**Figure 15c**).[215] Interestingly, they found that the same substrate could undergo under a slightly acidic pH a *syn*-hydration, which was previously unreported (**Figure 15d**). Although the product was not stable, due to a slow dehydration, it was possible to fully characterize it and to show quantitative conversions in good enantioselectivities of 72 % *ee*.[223] Later also a Friedel-Crafts reaction using the same substrates with several pyrroles and indoles was reported (**Figure 15e**).[214] Interestingly, unsubstituted indoles and pyrroles were selectively undergoing the Friedel-Crafts reaction in high enantiomeric ratios. Although a variety of reactions was accessible for DNA based asymmetric catalysis, they were mostly based on very similar substrates, all containing next to the α, β-unsaturated ketone an aromatic heterocycle. The heterocycle, typically imidazole or pyridine, was acting as an affinity tag, as it was coordinating to the metal centre and bringing the α, β-unsaturated ketone to the metal centre for activation. Consequently, substrates where the imidazole or pyridine was replaced with phenyl were not undergoing the discussed reactions, strongly limiting the accessible substrate scope.

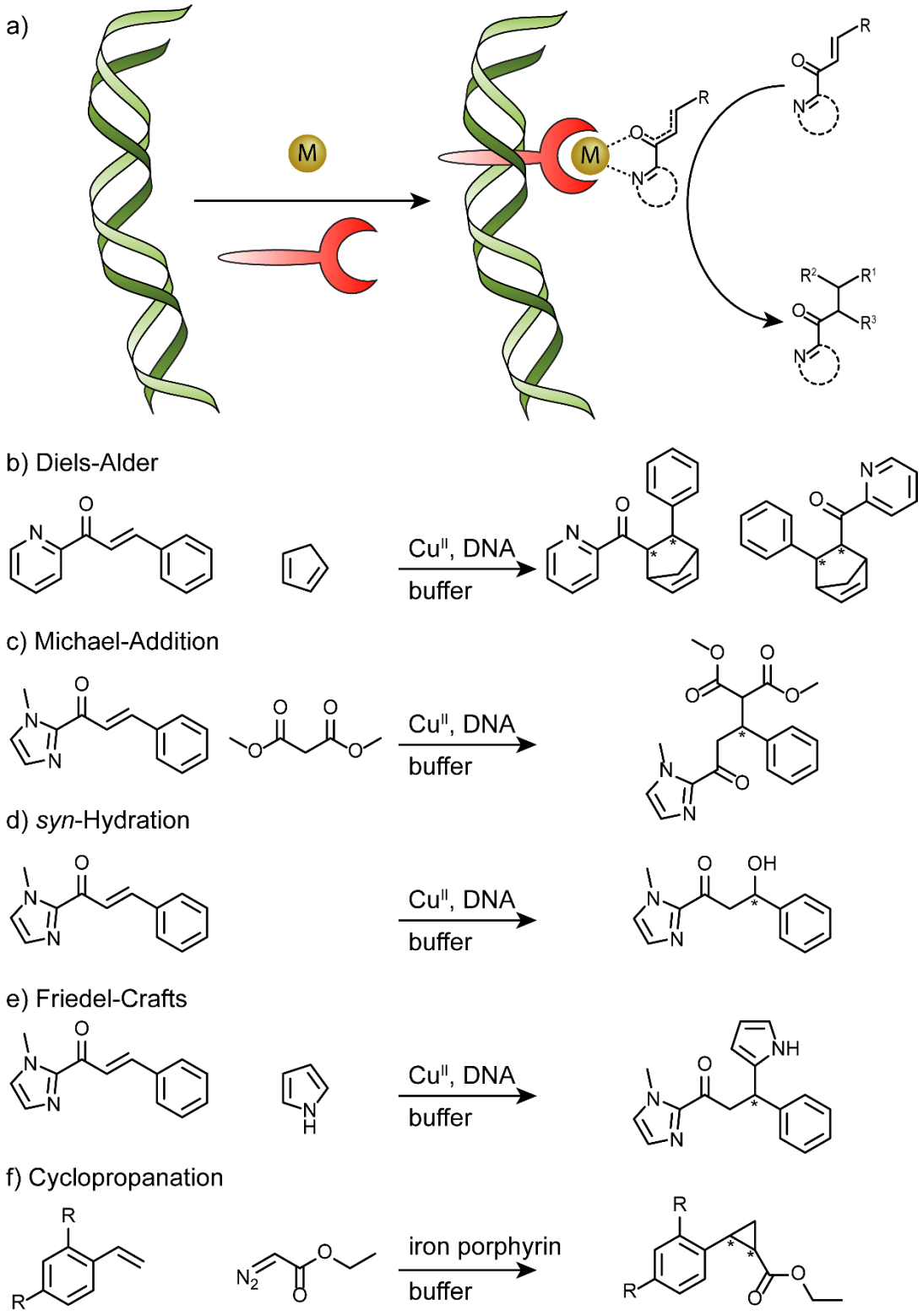

Figure 15. Examples of reactions used in DNA based asymmetric catalysis. a) Proposed and generalized reaction mechanism for the reaction in b-e). To the assembled duplex DNA, a metal (M) salt and a complexing chelate ligand are added. The formed metal complex then binds *via* intercalation into the duplex DNA. The substrates are then activated by coordination to the metal centre (M), acting as a Lewis-acid. b) Diels-Alder reaction of azachalcone with cyclopentadiene, c) Michael-Addition with imidazole chalcone and dimethyl malonate (DMM), d) *syn*-hydration of imidazole chalcone under acidic pH values, Friedel-Crafts reaction of imidazole chalcone with pyrrole and f) cyclopropranation reaction of styrene with a ethyl diazoacetate, catalysed by an iron porphyrin.[210–226]

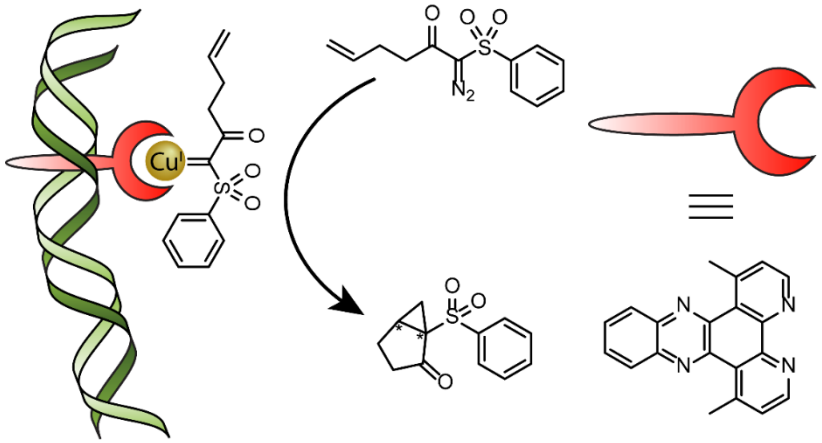

Figure 16. Asymmetric cyclopropanation reaction of a diazo-compound in presence of DNA and Cu^{I}.[226]

Examples beyond Lewis-acid based catalysis are scarce in the context of DNA and only a few examples were reported. One example was showing the allylic amination using a DNA–Diene–$Iridium^{I}$ hybrid catalyst and in another example the Cu^{I} catalysed cyclopropanation reaction of a diazo-compound was shown (**Figure 16**), which was activated through the formation of a Cu^{I}-carbene complex.[226,228] As Cu^{I} is prone to disproportionation in water, instead of Cu^{I} a Cu^{II} salt was used and it was suggested, that Cu^{II} was reduced *in situ* to Cu^{I}. Nevertheless, it was necessary to work in a glovebox under strict inert conditions avoiding oxygen. After conditions were optimized, good yields and enantioselectivities' of up to 84 % *ee* were shown.[226] When instead of copper, positively charged iron-porphyrin derivatives were used, the cyclopropanation of methoxy styrene with ethyl diazoacetate was catalysed. Remarkably the reaction was complete after only 5 minutes, however only low yields and enantioselectivities' between 40-55 % *ee*, depending on the substrate, were observed.[217]

The examples discussed so far, were based on duplex DNA, but in recent years DNA G-quadruplexes became increasingly popular in asymmetric catalysis. The first example was published by Moses et al. in 2010, five years after the pioneering works of Feringa and Roelfes.[227,229] They investigated the Diels-Alder reaction of azachalcone with cyclopentadiene in presence of the G-quadruplex forming sequences $htel_{21}$ or c-kit with different Cu^{II} complexes (**Figure 17**). Although good conversions were observed, the enantioselectivity was considerably low (*ee* = 34 %).[230]

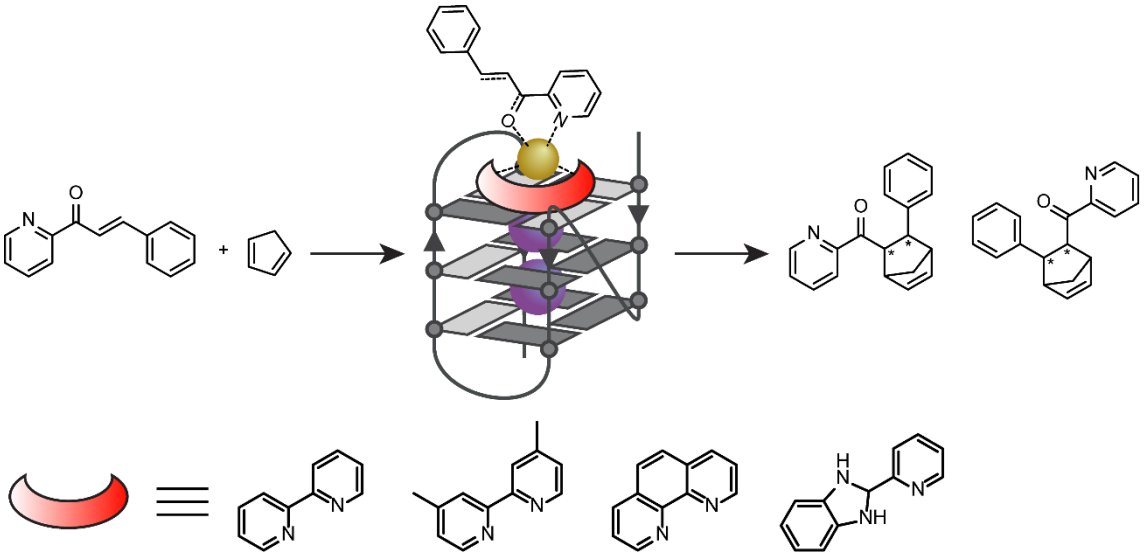

Figure 17. Asymmetric catalysis of a Diels-Alder reaction with azachalcone and cyclopentadiene. The Cu^{II} complex is assumed to bind *via* π-π stacking interactions to the G-quadruplex.[230]

Lately, Hennecke and co-workers could show improved enantioselectivities of 54 % *ee* for the same Diels-Alder reaction, using a tetra cationic Cu^{II}-Porphyrin in combination with htel. Replacing adenine at position 13 in the sequence with thymine improved the enantioselectivity to 68 % *ee*, but when a single adenine was added to the 3'-end, a strong corrosion of the *ee* to 29 % was observed, suggesting that the Cu^{II} Porphyrin was binding to the 3'-face of the G-quadruplex.[231] In other examples, G-quadruplexes were employed in Michael-Additions, cyclopropanations, Friedel-Crafts reactions, sulfoxidations and others, mostly based on the same substrates shown in **Figure 15**.[232–236] For more details it is referred to a comprehensive review on G-quadruplexes as DNAzymes and in asymmetric catalysis.[237]

2 MOTIVATION

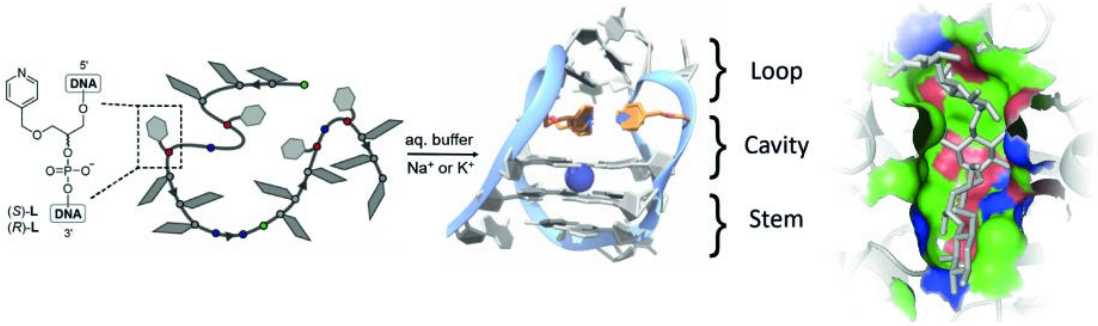

Figure 18. Pyridine modified G-quadruplex. Pyridine ligandosides were incorporated by DNA solid phase synthesis into G-quadruplex forming sequences. In aqueous electrolyte containing buffers the formed G-quadruplexes complex different transition metal cations.[24,26]

In recent years, there has been a growing interest to use DNA in asymmetric catalysis and for the design of DNAzymes.[20,22,199,233,236,238–242] In most of these examples the catalytic activity relies on transition metal cations as catalytic centre, structural element or redox cofactor. Since DNA is made from only four nucleobases, the possibilities for metal complexation are very limited.[243,244] To circumvent this limitation, in different approaches metal chelating ligands were introduced into DNA *via* covalent or non-covalent interactions, however the exact position and coordination environment of the metal cation remained often elusive.

This thesis is motivated by the development of a new approach, tackling this problem by combining the concept of metal-mediated base pairing with the unique folding properties of DNA G-quadruplexes. It is based on previous work of David M. Engelhard, who established the concept of metal-mediated G-quadruplexes in the group, using a pyridine ligandoside.[24,26] When inspecting the MD simulations of pyridine modified G-quadruplexes, the structure can be split into a rigid stem region, where the G-quartets are located, a cavity with the pyridine ligandosides, that can coordinate a metal cation and a flexible loop region, allowing substrate uptake (**Figure 18**).[24] The idea was to incorporate amino acid inspired ligandosides, such as carboxylates and imidazoles by DNA solid phase synthesis, to design tailored coordination environments for transition metal cations. Due to the high modularity of DNA solid phase synthesis, ligandosides can be incorporated at any position, allowing iterative rounds of sequence design and screening for the development of metallo DNAzymes, mimicking the functions of different metallo proteins, such as hydrolases, peroxidases or electron carriers.

3 IMIDAZOLE-BASED LIGANDOSIDES IN TETRAMOLECULAR G-QUADRUPLEXES

3.1 Design and Synthesis

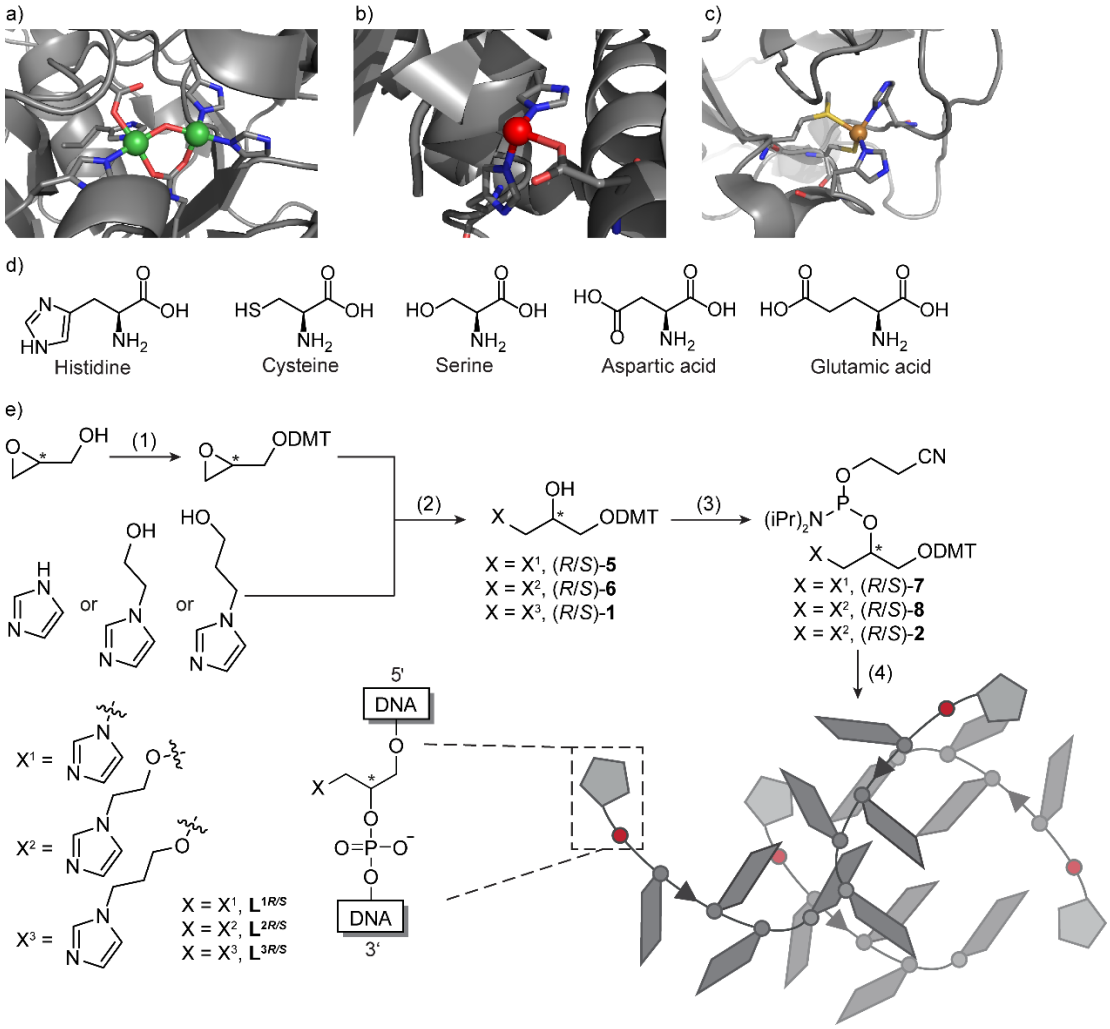

Figure 19. a)-c) Examples of selected metalloproteins. a) Urease with a dinuclear Ni^{II} centre, (pdb: 5g4h), b) Peptidase with a Zn^{II} centre (pdb: 5e33), c) Single electron shuttle protein Plastocyanin with a $Cu^{I/II}$ centre (pdb: 4dp0)[245–247] and d) amino acids commonly involved in metal coordination. e) Synthetic route to access the phosphoramidite building blocks (*R*/*S*)-**7**, (*R*/*S*)-**8** and (*R*/*S*)-**2**. (1) DMT-protection of (*R*/*S*)-glycidol with DMT-Cl and NEt_3 in CH_2Cl_2 at rt; (2) nucleophilic ring opening with imidazole in dioxane at 70 °C (X = X^1) or with N-hydroxyethyl-imidazole (X = X^2) and N-hydroxypropyl-imidazole (X = X^3), NaH in DMF at 40 °C; (3) phosphitylation of (*R*/*S*)-**5**, (*R*/*S*)-**6** and (*R*/*S*)-**1** with CEDIP-Cl and DIPEA in CH_2Cl_2 at rt; (4) automated solid-phase DNA synthesis. DMT = 4,4′-Dimethoxytrityl, DMF = dimethylformamide, CEDIP-Cl = 2-Cyanoethyl N,N-diisopropylchlorophosphoramidite, DIPEA = Diisopropylethylamine.

The work shown in this chapter was published in the journals Chemistry – A European Journal and Chemical Science.[29,31] Results regarding **L^3** are part of the Bachelor thesis of Katharina Rohlf.[248]

As explained in the motivation, this thesis is based on the pioneering work of David M. Engelhard, who incorporated pyridine ligandosides into tetramolecular and unimolecular G-quadruplexes.[24,26,249] In this proof of concept study, it was shown that tetramolecular G-quadruplexes, which were modified pyridine ligandosides at the 5'-end, complexed Cu^{II} and Ni^{II}, indicated by thermal stabilization.[26] When pyridine ligandosides were incorporated at both ends of tetramolecular G-quadruplexes, this led to the design of highly precise Cu^{II}-based EPR (electron paramagnetic resonance) distance rulers.[25] Later the concept was expanded to unimolecular G-quadruplexes for the design of a Cu^{II}-switchable thrombin binding aptamer, that inhibited the thrombin-catalysed clotting reaction after addition of Cu^{II}. Also, it could be used to reversibly switch the topology of the G-quadruplex forming sequence ttel (*Tetrahymena* telomeric repeat) in alternating rounds of Cu^{II} and EDTA addition.[24] When the unimolecular G-quadruplexes were closely investigated, they appeared to share some common properties with enzymes, as they have G-tetrads as rigid stem region, a cavity where the pyridine ligandosides are located and flexible loop regions, that can open and close, therefore acting as a gate. From this impression, the idea was born to utilize this system for the design of DNA-based metallo-protein mimics, which was also the starting point for this thesis.

It is commonly known that proteins are made from the 20 canonical amino acids. Less known is, that roughly half of all proteins rely for their correct structure and functions on metal cations.[162,250] In **Figure 19**, a selection of metallo-proteins is shown, including a) urease with a dinuclear nickel centre, b) a zinc peptidase and c) the electron carrier protein plastocyanin in its oxidized Cu^{II} state.[245–247] When zooming into their metal centres and carefully analysing the coordination environments, the most ubiquitous amino acids involved are glutamic/aspartic acid, cysteine and histidine (**Figure 19d**), which usually coordinate to the metal with the side chains, but also a coordination of the amide backbone to metal cations such as Cu^{II} was observed e.g. in the ATCUN (amino terminal Cu^{II}- and Ni^{II}-binding) coordination motif.[251] Inspired by histidine, an imidazole-based ligandoside was designed. Although, in histidine the linker is attached to the imidazole C4-carbon, for synthetic simplification, the linker was attached to the N1-nitrogen to avoid the need of protecting groups. To further simplify the synthesis, the ribose backbone was replaced with an acyclic chiral glycol backbone, leading to the design of the imidazole ligandosides **L^1**, **L^2** and **L^3** each as *R* and *S* enantiomer (**Figure 19**).[29–31] When incorporated into DNA, the superscript *R* or *S* indicates the stereo

configuration of the ligandoside e.g. **L**^{2R} for the *R* enantiomer. Note that the incorporation of the *R* and *S* enantiomer into DNA leads to diastereomeric DNA sequences due to the inherent chirality of DNA. If incorporated at terminal positions into G-quadruplexes, the stereo descriptor of the ligandosides is formally inverted, but for reasons of clarity, the stereo configuration of the ligandosides in DNA always refers to the here given configuration of the corresponding phosphoramidite building block.

To access the phosphoramidite building blocks for DNA solid-phase synthesis, a three-step synthesis was performed, which was adapted from literature.[252,253] First, the hydroxy group of (*R*/*S*)-glycidol was DMT-protected (4,4′-dimethoxytrityl). Therefore, a modified literature procedure was followed using 4,4′-dimethoxytrityl chloride and NEt_3 in CH_2Cl_2 at rt under nitrogen atmosphere. Triethylammonium chloride formed in large quantities, which required a vigorous stirring to avoid solidification of the reaction mixture.[253] Since decomposition of the starting materials caused a corrosion of the yield, chemicals were stored under argon in a *GS-systems* Glovebox. After completion, the reaction was washed with concentrated aq. $NaHCO_3$ to maintain a slightly basic pH and extracted once with CH_2Cl_2. The product was purified by column chromatography to obtain DMT-(*R*/*S*)-glycidol as a highly viscous colourless oil in 60 - 80 % yield. Quantitative yields, as they were reported in literature, could not be reproduced.[253] The protected DMT-(*R*/*S*)-glycidol was then reacted with imidazole in dioxane at 70 °C, resulting in a nucleophilic ring opening reaction at the primary carbon atom. The selectivity for the primary carbon atom results from a higher electrophilicity and a better steric accessibility of the primary carbon compared to the secondary one. After completion, the reaction mixture was washed with concentrated aq. $NaHCO_3$ to maintain a slightly basic pH and extracted once with CH_2Cl_2. The product was purified by column chromatography to obtain (*R*/*S*)-**5**, but a small impurity (ca. 5 %) was observed, which was assumed to be the regioisomer, where the ring was opened at the secondary carbon atom. The resulting by-product had a very similar polarity compared to (*R*/*S*)-**5**, rendering it difficult to separate it by column chromatography. Therefore, the product was purified by gel permeation chromatography (GPC) to afford the clean product (*R*/*S*)-**5** as a white foamy solid. In case of N-hydroxyethyl-imidazole and N-hydroxypropyl-imidazole, the hydroxy group was not reactive enough and no reaction was observed. Therefore, the hydroxy groups were first deprotonated with NaH in DMF leading to the alkoxide and then a solution of DMT-(*R*/*S*)-glycidol in DMF was added to the alkoxides. The mixture was heated to 40 °C leading to compound (*R*/*S*)-**6** and (*R*/*S*)-**1**. The workup procedure was the same as for compound (*R*/*S*)-**5**. The reaction mixture was washed with

concentrated aq. $NaHCO_3$ and the aqueous layer was extracted once with CH_2Cl_2 and the crude reaction mixture was purified by column chromatography followed by GPC.

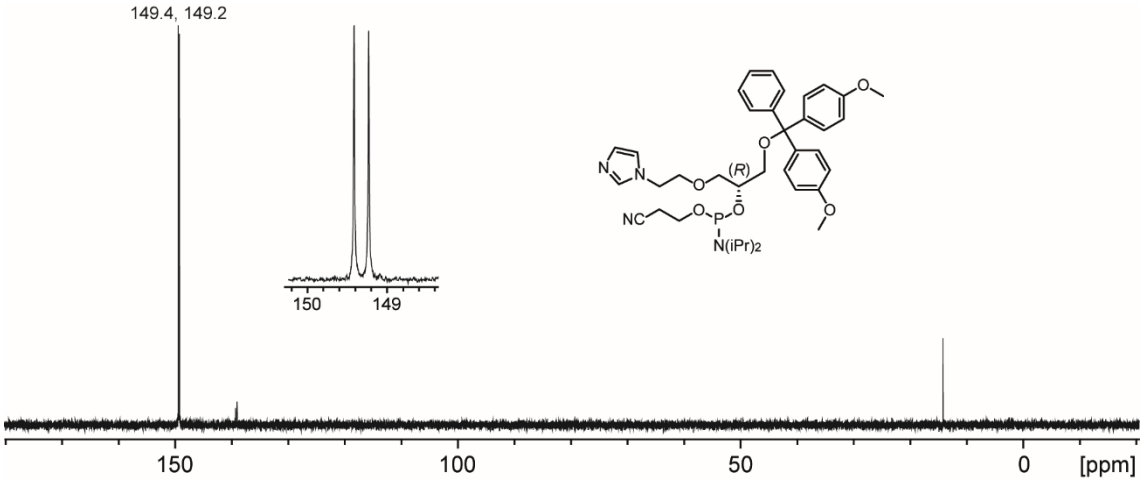

Figure 20. ^{31}P NMR (202 MHz, 298 K, $CDCl_3$) spectrum of phosphoramidite (*R*)-**8** in $CDCl_3$. The inset shows the two diastereomeric pairs. The signal at ~14 ppm belongs to oxidized or hydrolysed phosphitylating agent.

In the last step, (*R*/*S*)-**5**, (*R*/*S*)-**6** and (*R*/*S*)-**1** were dissolved in CH_2Cl_2 and phosphitylated with CEDIP-Cl (2-cyanoethyl *N*,*N*-diisopropylchlorophosphoramidite) in presence of an excess of DIPEA (*N*,*N*-diisopropylethylamin). DIPEA was added to trap the formed HCl and to avoid the acid-promoted cleavage of the DMT-group. After 90 min, the solvent was removed under reduced pressure and the crude products were directly used for DNA solid-phase synthesis assuming a yield of 80 %. A purification was omitted, since the phosphoramidites were highly sensitive to oxidation and hydrolysis. The integrity of the product was controlled by ^{31}P-NMR spectroscopy showing two characteristic peaks belonging to the two diastereomers at around 149 ppm (**Figure 20**). The pair of diastereomers results from the introduction of the racemic P^{III} centre. Since the P^{III} atom is oxidized in DNA to an achiral P^{V} species, the use of an enantiopure phosphitylating agent is not necessary. Oxidized and hydrolysed phosphoramidite or phosphitylating agent are detected at upfield shifted values (typically 2-15 ppm).[254–256] For DNA solid-phase synthesis, the phosphoramidites (*R*/*S*)-**7**, (*R*/*S*)-**8** and (*R*/*S*)-**2** were dissolved in acetonitrile at a concentration of 0.1 M. For higher coupling efficiencies, the coupling time was elongated to 10 min compared to 3 min of the standard phosphoramidites. The observed coupling efficiencies were usually higher than 99 % according to the trityl monitor, although the total yield of purified oligonucleotides was usually lower, if (*R*/*S*)-**7**, (*R*/*S*)-**8** and (*R*/*S*)-**2** were incorporated multiple times. Details on DNA solid-phase synthesis and purification can be found in chapter **9.1.1**.[29,31]

3.2 G-quadruplex Formation of Imidazole-Modified Sequences

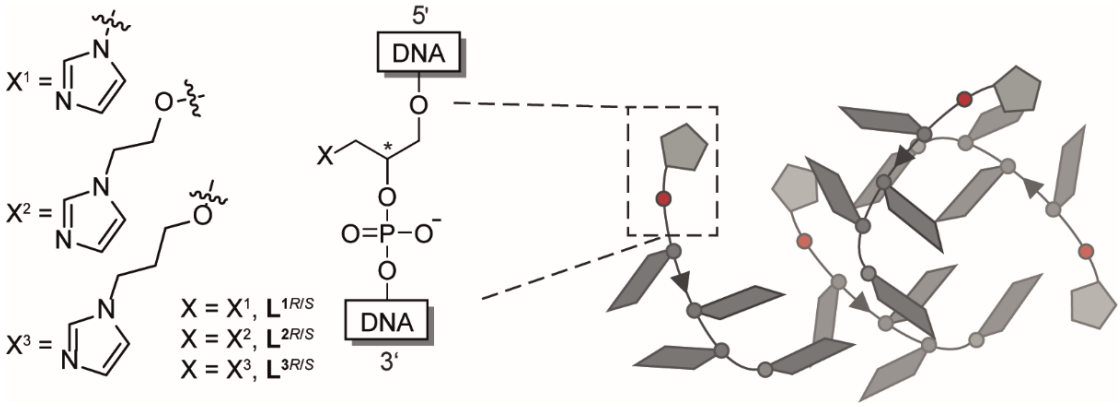

Figure 21. Schematic representation of **L$^{1\text{-}3R/S}$** at 5'-terminal positions in short oligonucleotides.

With the synthesized phosphoramidite building blocks (*R*/*S*)-**7**, (*R*/*S*)-**8** and (*R*/*S*)-**2**, the next step was DNA solid-phase synthesis using previously published protocols.[24,157,254,255] Extended coupling times for the ligandoside phosphonamidites were used to maximize coupling efficiencies. For details see chapter **9.1.1.** Coupling efficiencies were typically > 99 % for the ligandoside phosphoramidites. Once incorporated into oligonucleotides, the imidazole ligandosides are called **L$^{1\text{-}3R/S}$** where *R*/*S* indicates the stereo configuration at the glycol backbone (**Figure 21**). Note that the incorporation of the *R*- or *S*-enantiomer results in diastereomeric DNA due to the inherent chirality of DNA.

Table 1. Thermal stabilities expressed as melting temperatures $T_{1/2}$ and thermal stabilizations $\Delta T_{1/2}$ after addition of $CuSO_4$, $NiSO_4$, ZnI_2 and $Co(NO_3)_2$ of the investigated tetramolecular G-quadruplex structures. Conditions: 3.75 µM ssDNA, 100 mM NaCl, 10 mM LiCaco pH 7.2 and 0.98 µM of the respective transition metal salt.

Sequence	**-**	**Cu^{II}**	**Ni^{II}**	**Zn^{II}**	**Co^{II}**
L^{1S}G$_3$	/	40	n. d.	/	/
L^{1R}G$_3$	/	38	n. d.	/	/
L^{1S}G$_4$	31	79 (+ 48)	77 (+ 46)	54 (+ 23)	64 (+ 33)
L^{1R}G$_4$	32	83 (+ 51)	81 (+ 49)	61 (+ 29)	73 (+ 41)
L^{2S}G$_4$	36	76 (+ 40)	73 (+ 37)	52 (+ 16)	63 (+ 27)
L^{2R}G$_4$	34	74 (+ 40)	68 (+ 34)	46 (+ 12)	54 (+ 20)
L^{3S}G$_4$	45	83 (+ 38)	82 (+ 37)	62 (+ 17)	73 (+ 18)
L^{3R}G$_4$	45	77 (+ 32)	76 (+ 31)	54 (+ 9)	63 (+ 18)
L^{1S}G$_5$	78	> 95	> 95	87 (+ 9)	> 95
L^{1R}G$_5$	77	> 95	> 95	86 (+ 9)	> 95

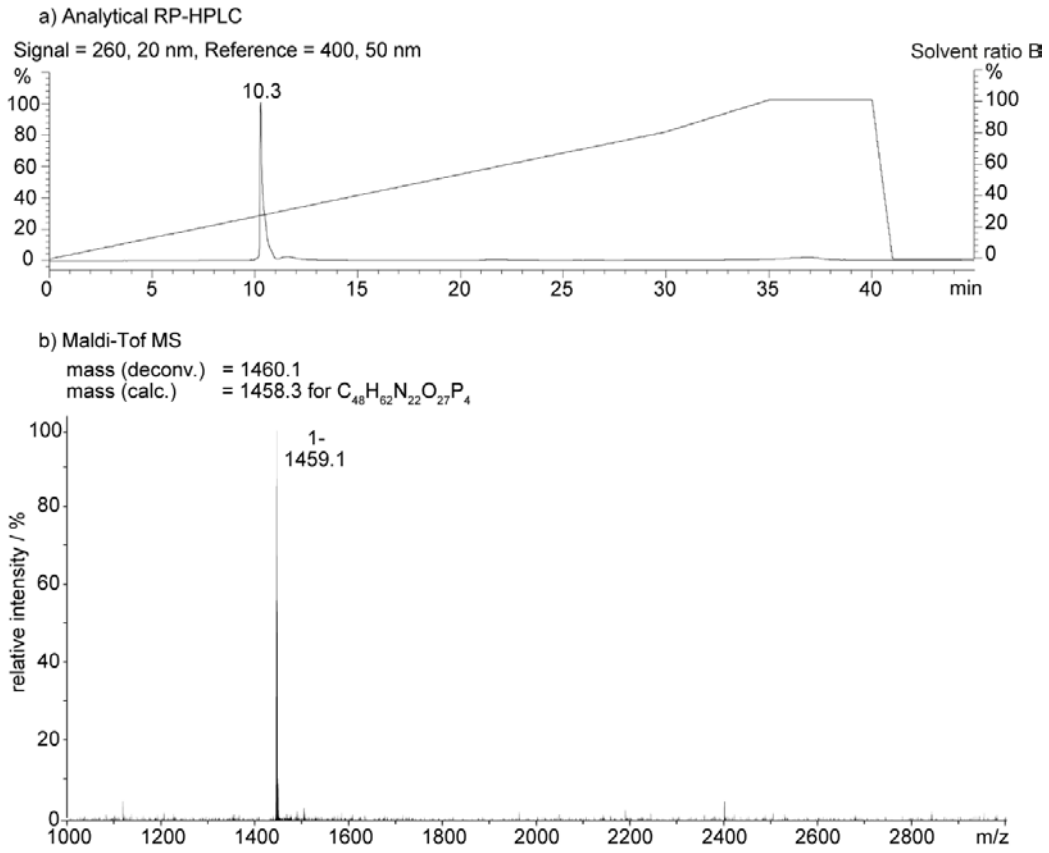

Figure 22. Analytical data of **L^{1S}G$_4$**. a) Analytical reversed-phase HPLC with a buffer gradient going from 100 % buffer A (0.05 mM TEAA pH 7) to 100 % buffer B (30 % 0.05 mM TEAA pH 7, 70 % acetonitrile) and b) MALDI-TOF spectrum using a 3-hydroxypicolinic acid (3-HPA) matrix.

After DNA solid-phase synthesis, the oligonucleotides were cleaved from the solid support and deprotected at 55 °C in concentrated aq. NH_4OH for 16 h. The deprotected oligonucleotides were purified by reversed-phase HPLC with the DMT-group still attached. The DMT-group was acting as a purification tag, since it caused longer retention times for oligonucleotides due to the increased hydrophobicity. After purification, the oligonucleotides were treated with 2 % aq. TFA to remove the DMT-group. The integrity of the samples was analysed by analytical HPLC and ESI or MALDI mass spectrometry. As an example, in **Figure 22** the analytical data of **L^{1S}G$_4$** is shown. The remaining stock solutions were lyophilized and stored at -20 °C until usage.

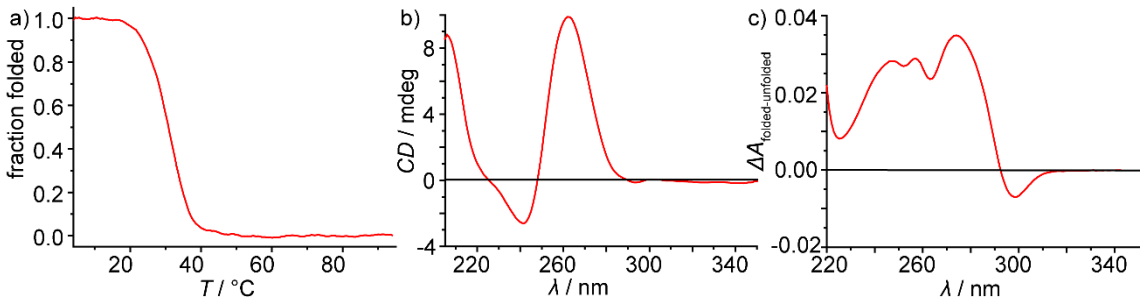

Figure 23. Analytical data of **L^{1S}G$_4$**. a) Melting profile converted to fraction folded, b) CD spectrum and c) TDS. Conditions: 3.75 µM ssDNA, 100 mM NaCl, 10 mM LiCaco pH 7.2.

To show, that the imidazole ligandosides still allowed the formation of G-quadruplexes, short sequences of the type 5'-**L**GG GG-3', called **L**G_4, were investigated. These sequences are known to form tetramolecular G-quadruplexes in a parallel topology and only in a few special cases the formation of other topologies was observed.[257,258] To investigate the G-quadruplex formation, Circular Dichroism spectroscopy (CD), Thermal Difference Spectra (TDS) and thermal denaturation experiments were recorded. Each of these techniques gives a unique information about the investigated DNA structure. While a TDS tells, whether a G-quadruplex has formed, indicated by specific minima and maxima, CD spectra give an information about the actual topology and in thermal denaturation experiments the thermal stability is determined (for details see **Chapter 1.2** and **9.3.2**).[72,73,76,78,79] To form tetramolecular G-quadruplexes, samples containing 3.75 µM ssDNA, 100 mM NaCl, and 10 mM LiCaco pH 7.2 were prepared and heated to 85 °C, slowly cooled to 4 °C with 0.5 °C min^{-1} and left at 4 °C for several hours. To ensure a full G-quadruplex formation, samples were then frozen for 1 h at -20 °C.[259] Slowly freezing the samples results in local hotspots with high DNA concentrations, that strongly accelerate G-quadruplex formation.[259,260] Unless otherwise stated, samples of tetramolecular G-quadruplexes were always prepared in this way. In **Figure 23**, the spectroscopic data of **L**$^{1S}G_4$ is shown, proving the formation of a tetramolecular G-quadruplex with two maxima at 247 and 274 nm and a minimum at 298 nm in the TDS and a positive Cotton effect at 263 nm in the CD spectrum, consistent with a parallel topology. From the melting profile a thermal stability of $T_{1/2}$ = 31 °C was determined.

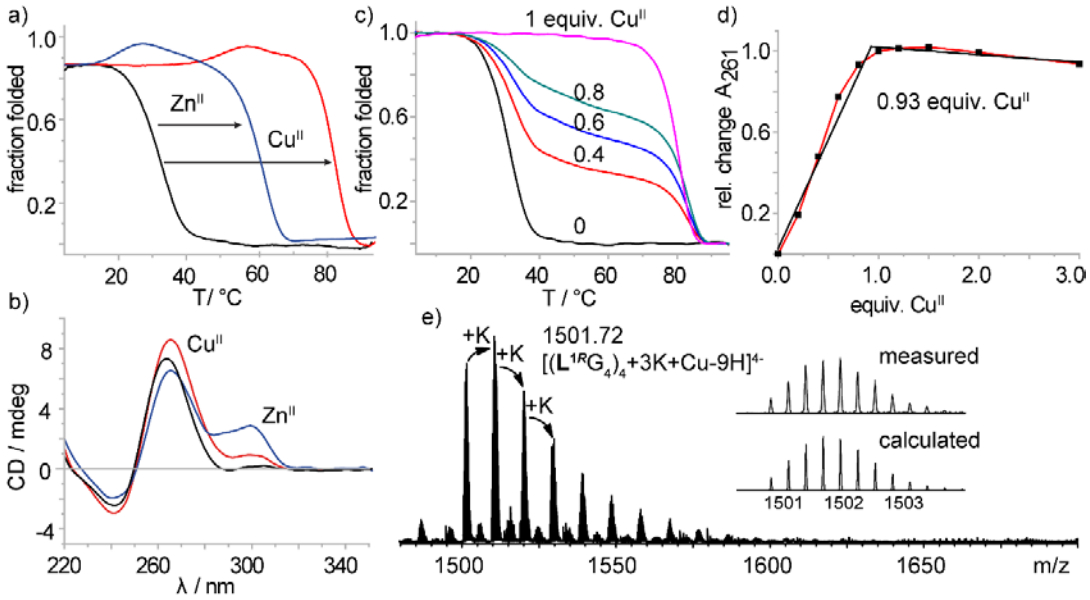

Figure 24. Analytical data of **L**$^{1R}G_4$. a) Melting profiles in absence and presence of 1 equiv. Cu^{II} and Zn^{II}, b) CD spectra in absence and presence of 1 equiv. Cu^{II} and Zn^{II}, c) melting profiles with sub equimolar amounts of Cu^{II} and d) native ESI-MS of **L**$^{1R}G_4$ in presence of Cu^{II}, showing a main species corresponding to the folded G-quadruplex in complex with Cu^{II}. Reproduced from Ref.[29] Copyright © 2019 The Royal Society of Chemistry.

Likewise, for **L**^{1R}G$_4$, **L**^{2S}G$_4$, **L**^{2R}G$_4$, **L**^{3S}G$_4$, and **L**^{3R}G$_4$, the formation of tetramolecular G-quadruplexes in a parallel topology was observed. The melting temperatures of **L**^{2S}G$_4$ and **L**^{2R}G$_4$ ($T_{1/2}$ = 36 °C, $T_{1/2}$ = 34 °C) were slightly higher compared to **L**^{1S}G$_4$ and **L**^{1R}G$_4$ ($T_{1/2}$ = 31 °C, $T_{1/2}$ = 32 °C). In case of **L**^{3R}G$_4$ and **L**^{3R}G$_4$, where the linker was the longest, the melting temperature was even higher with a $T_{1/2}$ = 45 °C for both sequences. This trend of increasing thermal stabilities with longer linker chains is in accordance with a previous report (**Figure 25**). It was explained by better π-π stacking interactions between the 5'-G-tetrad and the imidazole ring with an increasing linker length.[158] When the sequences were extended to five consecutive guanine residues in **L**^{1S}G$_5$, a drastic increase of the thermal stability to $T_{1/2}$ = 78 °C ($\Delta T_{1/2}$ = +47 °C) was observed compared to $T_{1/2}$ = 31 °C in **L**^{1S}G$_4$. This was the result of the additional G-tetrad which had formed. In contrast, reducing the sequence to only three consecutive guanine residues in **L**^{1S}G$_3$ prevented the formation of a G-quadruplex and only single-stranded DNA was observed as indicated by the CD spectrum (**Figure 35**).

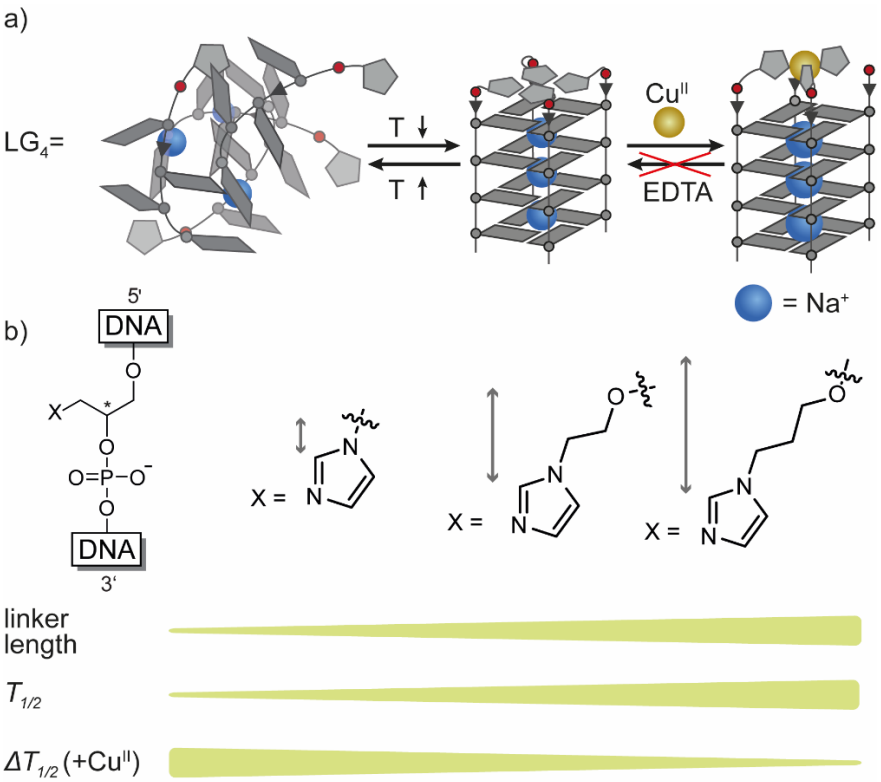

Figure 25. Linker length-dependent thermal stability and metal-mediated thermal stabilization. a) Schematic representation of denatured single strand **L**G$_4$, formed G-quadruplex from **L**G$_4$ in absence of Cu^{II} and in presence of Cu^{II} b) Illustration of the linker length dependency on the thermal stability.

After proving the formation of parallel tetramolecular G-quadruplexes, the question was whether the imidazole modification allowed the complexation of transition metal cations, as it was reported for a pyridine ligandoside, called **L**^{Pyr}.[24,26] Indeed, different transition

metal cations such as Cu^{II} ($\Delta T_{1/2}$ = +48 °C), Ni^{II} ($\Delta T_{1/2}$ = +46 °C), Zn^{II} ($\Delta T_{1/2}$ = +23 °C) and Co^{II} ($\Delta T_{1/2}$ = +33 °C) were complexed by $\mathbf{L^{1S}}G_4$ as indicated by very strong thermal stabilizations, while retaining a clear parallel topology (**Figure 24a,b**). As the complexation of Cu^{II} and Ni^{II} was already shown with a pyridine ligandoside in $\mathbf{L^{Pyr}}G_4$,[24,26] complexation of Zn^{II} and Co^{II} was unprecedented in G-quadruplex structures. For Zn^{II}, in general only one recent example in literature showed a specific complexation in the context of metal-mediated base pairs.[261] Comparing the thermal stabilization of $\mathbf{L^{1S}}G_4$ and $\mathbf{L^{Pyr}}G_4$, addition of Cu^{II} stabilized $\mathbf{L^{1S}}G_4$ by $\Delta T_{1/2}$ = +48 °C, more than two times higher as observed for $\mathbf{L^{Pyr}}G_4$ ($\Delta T_{1/2}$ = +20 °C).[26] This was unprecedented high in the field of metal-mediated base pairs and offered the potential to switch the G-quadruplex formation as it will be shown later (**Figure 36**). An explanation for the much higher stabilization of $\mathbf{L^{1S}}$ compared to $\mathbf{L^{Pyr}}$ could be the higher basicity of imidazole compared to pyridine. While in pyridine, six π-electrons are delocalized on six atoms, in imidazole six π-electrons are delocalized on five atoms resulting in a higher electron density and stronger coordination ability.[262,263] Surprisingly, while for $\mathbf{L^{Pyr}}G_4$ the metal-mediated thermal stabilization could be reversed with EDTA, addition of 10 equiv. EDTA to $\mathbf{L^{1S}}G_4$ could not remove Cu^{II} or Ni^{II}, although in case of Zn^{II} and Co^{II} EDTA addition led to an immediate reversal of the metal-induced thermal stabilization. This effect was attributed to kinetically trapped states, since no metal-mediated stabilization could be observed, when EDTA was added to the Cu^{II} or Ni^{II}-containing samples before the G-quadruplexes had formed.

The stereo configuration of $\mathbf{L^{1R/S}}$ was also shown to influence the metal-mediated stabilization, thus for $\mathbf{L^{1R}}G_4$ in general higher thermal stabilizations were observed compared to $\mathbf{L^{1S}}G_4$. More interesting was the influence of the different linker length in $\mathbf{L^{1R/S}}$, $\mathbf{L^{2R/S}}$ and $\mathbf{L^{3R/S}}$. As mentioned previously, in absence of transition metal cations the order of thermal stability was $\mathbf{L^{3R}}G_4 > \mathbf{L^{2R}}G_4 > \mathbf{L^{1R}}G_4$. In fact, when it comes to metal-mediated stabilizations this order turns around showing the highest thermal stabilisation $\Delta T_{1/2}$ for $\mathbf{L^{1R}}G_4 > \mathbf{L^{2R}}G_4 > \mathbf{L^{3R}}G_4$. Thus, addition of Cu^{II} leads to stabilizations of $\Delta T_{1/2}$ = +51 °C ($\mathbf{L^{1R}}G_4$), $\Delta T_{1/2}$ = +40 °C ($\mathbf{L^{2R}}G_4$) and $\Delta T_{1/2}$ = +32 °C ($\mathbf{L^{3R}}G_4$). This effect can be explained in agreement with a previous publication.[27] In absence of transition metal cations, a longer linker facilitates better π-π stacking interactions between the imidazole ligandosides and the terminal 5'-G-tetrad.[27] When it comes to metal complexation, these π-π stacking interactions need to break up to complex the transition metal cation, leading to an energetic penalty and eventually to lower metal-mediated thermal stabilizations (**Figure 25**).[27,29]

To confirm a 1:1 stoichiometry of G-quadruplex:transition metal cation, two types of titrations were performed with Cu^{II}. First, increasing amounts of Cu^{II} were added to the formed G-quadruplex **L^{1R}**G$_4$ and after every addition a full UV spectrum from 205 to 350 nm was recorded. From this it became clear that the strongest change in absorption was occurring at 261 nm, although the reason remained unanswered. The change of absorption at 261 nm was then plotted against the equivalents of Cu^{II} showing a maximum absorption after ~ 0.93 equiv. Cu^{II}, consistent with a 1:1 complex (**Figure 24d**). The second titration was based on thermal denaturation experiments with sub-equimolar ratios of Cu^{II} showing two clear transitions corresponding to metal free **L^{1R}**G$_4$ and **L^{1R}**G$_4$ in complex with Cu^{II}. After 1 equiv. Cu^{II} was added, only one transition corresponding to **L^{1R}**G$_4$ in complex with Cu^{II} was observed, again consistent with a 1:1 complex (Figure 24**c**).

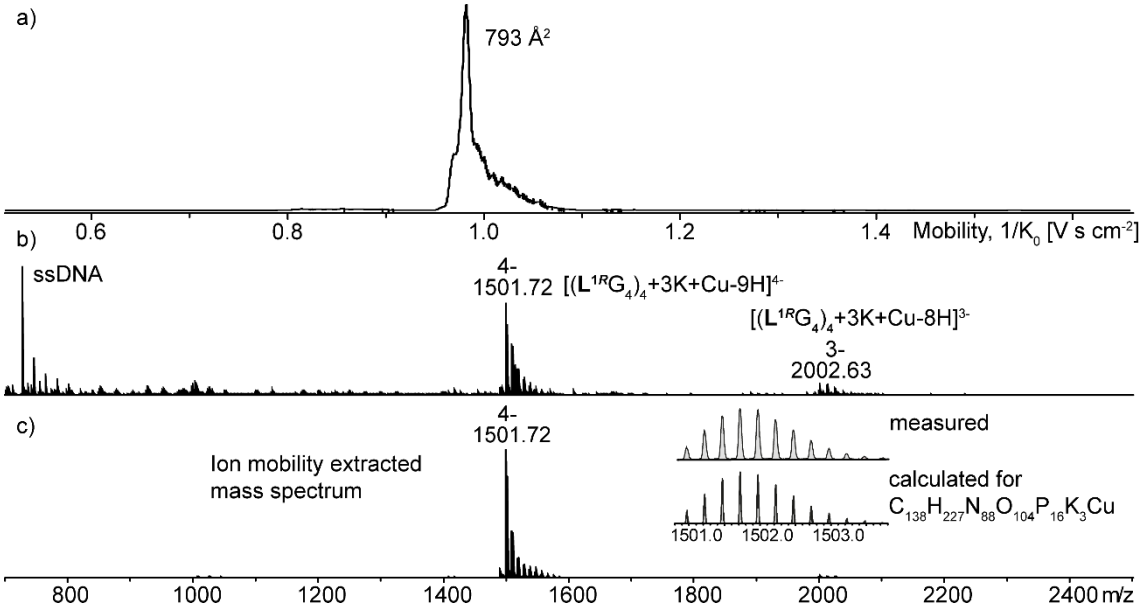

Figure 26. Native ESI-tims-TOF MS of **L^{1R}**G$_4$ in presence of Cu^{II}. a) Ion mobility trace showing one sharp ion mobility distribution from which a CCS of 793 Å^2 was calculated. b) Full mass-spectrum of **L^{1R}**G$_4$ where [**L^{1R}**G$_4$+3K+Cu-9H]$^{4-}$ was observed as the main species. c) Ion mobility-extracted mass spectrum for [**L^{1R}**G$_4$+3K+Cu-9H]$^{4-}$. Conditions: 50 µM ssDNA, 12.5 µM $CuSO_4$, 0.5 mM KCl and 50 mM TMAA pH 6.8 in H_2O:ACN, 1:1.

To further proof the proposed G-quadruplex metal complexes, native ESI-MS studies were performed. In native ESI-MS, mild conditions are applied during the ionization process to keep the secondary structure folded. To distinguish, whether a G-quadruplex remains folded during ionization, two intrinsic properties are exploited. First, in case of tetramolecular G-quadruplexes signals corresponding to a tetramer are observed and single-stranded DNA corresponds to denatured G-quadruplexes. Second, in their native state G-quadruplexes always bind n-1 monovalent cations (n = number of G-tetrads) in their central pockets followed by a statistical distribution of additional unspecific adducts.

For a denatured species, a statistical distribution of adducts would be expected, starting with zero cations.[264–266]

Equation 1.

$$\Omega = \frac{(18\pi)^{\frac{1}{2}}}{16} \frac{ze}{(k_B T)^{\frac{1}{2}}} \left[\frac{1}{\mu}\right]^{\frac{1}{2}} \frac{1}{K_0} \frac{1}{N_0}$$

In addition, ESI-MS can be coupled to trapped ion mobility spectrometry (tims) to measure the mobility K_0 of an ion in a drift gas. Different techniques to measure ion mobilities are available with the drift tube as the most classic one, where the ions are pushed by an electric field against a drift gas resulting in higher ion mobilities for ions with a smaller surface area. In contrast, for the here used trapped ion mobility technique, the ion is trapped in an electric field and then pushed forward by a drift gas. For this reason ions with a larger surface area are pushed faster through the drift cell.[267] Using the Mason-Schamp **Equation 1**, from the ion mobility K_0 and charge state, the collisional cross section (CCS) can be calculated in Å^2, describing the area of the ion, that is exposed to the drift gas.[268,269] Accordingly, larger ions have larger CCS values.[270–272] When **L^{1RS}**G$_4$ was subjected to native ESI-tims-TOF, only signals corresponding to single-stranded DNA were observed. As soon as Cu^{II} was added, **L^{1R}**G$_4$ was stabilized and remained folded during the ionization process. A main species [(**L^{1R}**G$_4$)$_4$+3K+Cu-9H]$^{4-}$ was observed, corresponding to the folded G-quadruplex in complex with one Cu^{II} (**Figure 26**). From K_0 a CCS of 793 Å^2 was calculated which was in the same range as reported for similar unmodified G-quadruplexes.[264]

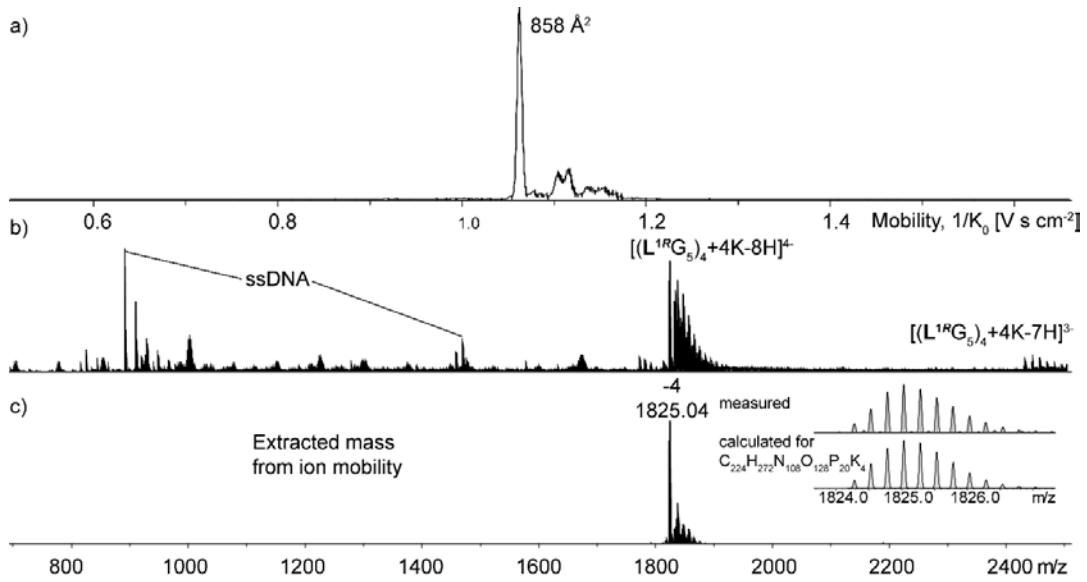

Figure 27. Native ESI-tims-TOF MS of **L^{1R}**G$_5$. a) Ion mobility trace shows one sharp ion mobility distribution from which a CCS of 858 Å^2 was calculated. b) Full mass-spectrum of **L^{1R}**G$_5$ where [(**L^{1R}**G$_5$)$_4$+4K-8H]$^{4-}$ was observed as the main species. c) Ion mobility-extracted mass spectrum for [(**L^{1R}**G$_5$)$_4$+4K-8H]$^{4-}$. Conditions: 50 µM ssDNA, 0.5 mM KCl and 50 mM TMAA pH 6.8 in H$_2$O:ACN, 1:1.

Unfortunately, since **L^{1R}**G$_4$ was denaturing during the ionization process in absence of Cu^{II}, it was not possible to compare the CCS in absence and presence of Cu^{II} and to analyse, how Cu^{II} binding was affecting the G-quadruplex size. It was assumed, that Cu^{II} would restrain the freely moving imidazole ligandosides, resulting in a smaller CCS. For this purpose, **L^{1R}**G$_5$ was investigated, which forms one additional G-tetrad. Due to the additional G-tetrad it was stable enough in absence of Cu^{II} to survive the ionization process and as main species [(**L^{1R}**G$_5$)$_4$+4K-8H]$^{4-}$ (**Figure 27**) was observed, corresponding to the folded G-quadruplex. The ion mobility spectrum showed a very sharp signal with a CCS of 858 Å^2.

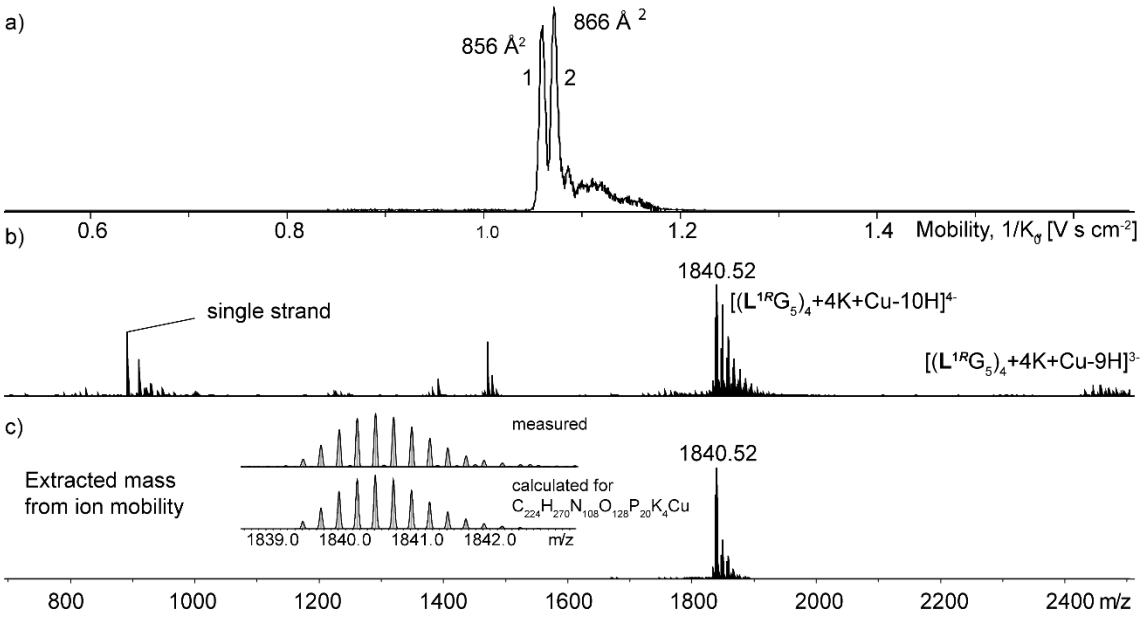

Figure 28. Native ESI-tims-TOF MS of **L^{1R}**G$_5$ in presence of 1 equiv. Cu^{II}. a) Ion mobility trace shows two sharp ion mobility distributions from which a CCS of 856 and 866 Å^2 were calculated. b) Full mass-spectrum of **L^{1R}**G$_5$ where [(**L^{1R}**G$_5$)$_4$+4K+Cu-10H]$^{4-}$ was observed as the main species. c) Ion-mobility-extracted mass spectrum for [(**L^{1R}**G$_5$)$_4$+4K+Cu-10H]$^{4-}$. Conditions: 50 µM ssDNA, 0.5 mM KCl and 50 mM TMAA pH 6.8, 12.5 µM CuSO$_4$, H$_2$O:ACN, 1:1.

When Cu^{II} was added to **L^{1R}**G$_5$, the resulting mass spectrum showed as expected the main species [(**L^{1R}**G$_5$)$_4$+4K+Cu-10H]$^{4-}$ (**Figure 28**). The corresponding ion mobility showed two sharp signals with CCS values of 856 Å^2 and 866 Å^2 and for both ion mobility distributions, the extracted mass spectrum showed as main species [(**L^{1R}**G$_5$)$_4$+4K+Cu-10H]$^{4-}$. There was no experimental evidence found, why signals were observed, but it was hypothesized that the 3'-G-tetrad was flipping between a *syn*- and *anti*-orientation or that the imidazole ligandosides were coordinating in two different motifs, e.g. the imidazole H2 proton pointing up in one and down in the other case. Interestingly, for other sequences including **L^{1R}**G$_4$ (**Figure 26**) and **L^{2R}**G$_5$ (**Figure 29**) only one ion mobility distribution was observed. In addition, the increased CCS of 866 Å^2 was contradicting the hypothesis, that addition of Cu^{II} would catch the freely moving imidazole ligandosides

and therefore reducing the CCS. Instead, it was hypothesized that the imidazole ligandosides are either found inside the G-quadruplex grooves or flat on top of the 5'-G-tetrad. Cu^{II} forces the imidazole ligandosides out from the grooves or the 5'-G-tetrad and arranges them in a propeller shaped square planar coordination, resulting in a slight increase of the CCS. This observation was consistently also made for $\mathbf{L^{2R}}G_5$ (**Figure 29**) where the same small increase of the CCS from 868 Å^2 $[(\mathbf{L^{2R}}G_5)_4+4K\text{-}8H]^{4-}$ to 876 Å^2 $[(\mathbf{L^{2R}}G_5)_4+4K+Cu\text{-}10H]^{4-}$ was observed. This time, however, only one sharp ion mobility distribution in presence of Cu^{II} was observed.

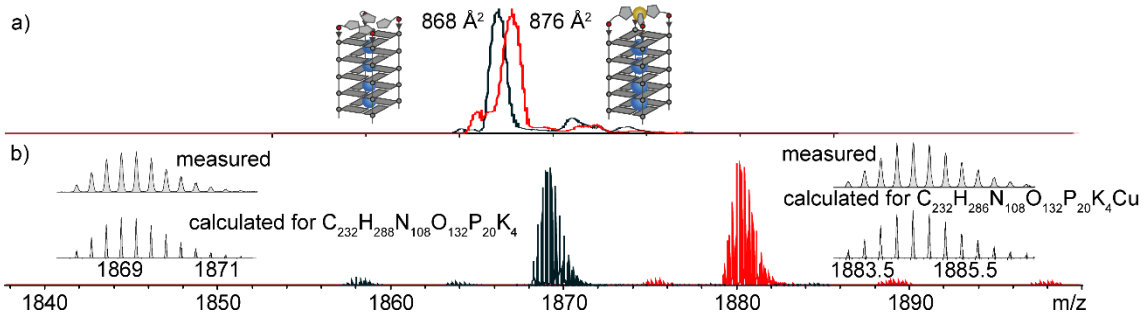

Figure 29. Native ESI-tims-TOF MS of $\mathbf{L^{2R}}G_5$ in presence of 1 equiv. Cu^{II}. a) Ion mobility trace shows two sharp ion mobility distributions from which a CCS of 868 and 876 Å^2 were calculated. b) Ion mobility-extracted mass spectrum of $[(\mathbf{L^{2R}}G_5)_4+4K\text{-}8H]^{4-}$ and $[(\mathbf{L^{2R}}G_5)_4+4K+Cu\text{-}10H]^{4-}$. Conditions: 50 µM ssDNA, 0.5 mM KCl and 50 mM TMAA pH 6.8, 12.5 µM $CuSO_4$, H_2O:ACN, 1:1. Reprinted and adapted from ref.[31] Published under the terms of the Creative Commons CC BY license.

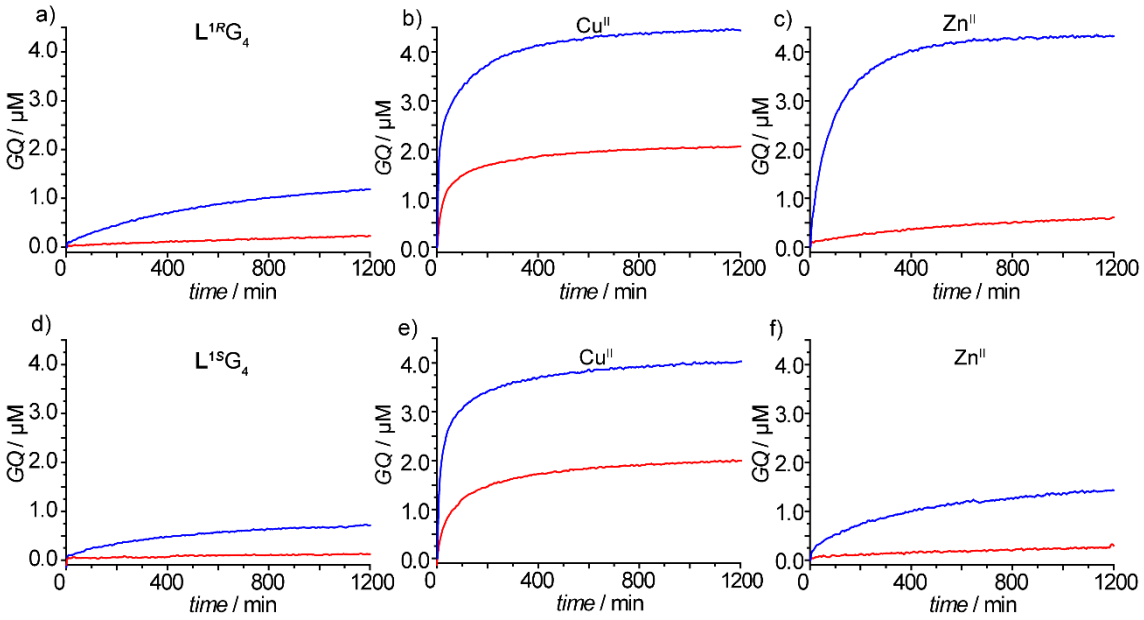

Figure 30. Association kinetics of $\mathbf{L^{1R}}G_4$ and $\mathbf{L^{1S}}G_4$ at 8 (red) and 16 (blue) µM single strand concentration. Conditions: 8 and 16 µM ssDNA, respectively, 10 mM LiCaco pH 7.2, 100 mM NaCl and 8 or 16 µM $CuSO_4$ and ZnI_2, 7°C.

Besides the strong thermal stabilization, another effect after addition of Cu^{II} to **L^{1S}**G_4 and **L^{1R}**G_4 was discovered. When TDS spectra were recorded, the minima and maxima of the samples in presence of Cu^{II} always showed significantly lower intensities compared to the sample without Cu^{II}, which often indicates an incomplete G-quadruplex formation. Since Cu^{II} was shown to tremendously stabilize the G-quadruplex structures, this explanation was ruled out. At this point it is important to know that the low-temperature spectrum for the TDS was recorded at 4 °C, while for the high-temperature spectrum, the sample was heated to 85 °C and then cooled back to 20 °C before a spectrum was recorded. Normally this is no issue, since the formation of tetramolecular G-quadruplexes is at low concentrations extremely slow and cooling the sample down to 20 °C for a short period should not allow the formation of significant amounts of G-quadruplexes.[260] However, in this case a strongly accelerated G-quadruplex formation in presence of Cu^{II} was assumed, which would explain the smaller intensities in the TDS. To probe this, the high-temperature spectrum was now recorded at 85 °C and indeed now the TDS in absence and presence of Cu^{II} showed nearly the same intensities. To get even more insights into the accelerated folding kinetics, UV/Vis-based studies were performed. Therefore, G-quadruplex solutions were heated to 95 °C and then quickly transferred to cuvettes in UV/Vis spectrometers and cooled to 4°C. The change of absorbance at 295 nm was recorded, which is indicative for the formation of G-quadruplexes. However, water condensation on the cuvettes and unspecific changes of absorption upon cooling were interfering with these experiments rendering interpretations difficult.

Equation 2.

$$\frac{d[A]}{dt} = -4\frac{d[A_4]}{dt} = -k_{on} * [A]^4$$

For this reason, the experiments were repeated using a CD spectrometer by measuring the change of the positive Cotton-effect at 262 nm at 7°C for 20 h (**Figure 30**). From this, k_{on} for the G-quadruplex association kinetics was calculated using **Equation 2**.[260,275] Advantage here is, that the Cotton-effect at 262 nm is not significantly affected by water condensation and unspecific temperature-dependent changes. Indeed, while in absence of Cu^{II} only an extremely slow G-quadruplex formation was observed, addition of Cu^{II} resulted in strongly accelerated formations. From the slope using **Equation 2**, k_{on} values of 2.5 x 10^9 M^{-3} s^{-1} for **L^{1R}**G_4 and 1.4 x 10^9 M^{-3} s^{-1} for **L^{1S}**G_4 could be calculated. A drastic increase of k_{on} by two orders of magnitude to k_{on} = 4.2 x 10^{11} M^{-3} s^{-1} and 3.2 x 10^{11} M^3 s^{-1} was observed when Cu^{II} was added to **L^{1R}**G_4 and **L^{1S}**G_4, respectively. Interestingly, an excess of 10 equiv. Cu^{II} slowed down the G-quadruplex formation again (**L^{1R}**G_4: k_{on} = 1.8 x 10^{11} M^{-3} s^{-1}, **L^{1S}**G_4: k_{on} = 1.3 x 10^{11} M^{-3} s^{-1}). A possible explanation for these findings could be a templating effect of Cu^{II} (**Figure 31c**). When Cu^{II} is present the

imidazole ligandosides quickly coordinate to Cu^{II} and preorganise four DNA strands. These then quickly assemble to a tetramolecular G-quadruplex. This is consistent with the observation made in excess Cu^{II}. In an excess situation of Cu^{II}, it becomes statistically less probable that four strands are organized around a single Cu^{II}, but more likely that only a single DNA strand is coordinated per Cu^{II} centre which is not sufficient for the formation of a G-quadruplex. Addition of Zn^{II} resulted only for $\mathbf{L^{1R}}G_4$ in a 10-fold accelerated formation (k_{on} = 1.9 x 10^{10} M^{-3} s^{-1}) being one order of magnitude lower compared to Cu^{II}. In **Figure 31** the results are summarised. In absence of Cu^{II}, the G-quadruplexes form very slow. As soon as Cu^{II} is added the G-quadruplex formation is highly accelerated and the resulting metal-mediated G-quadruplexes are thermally stabilized.

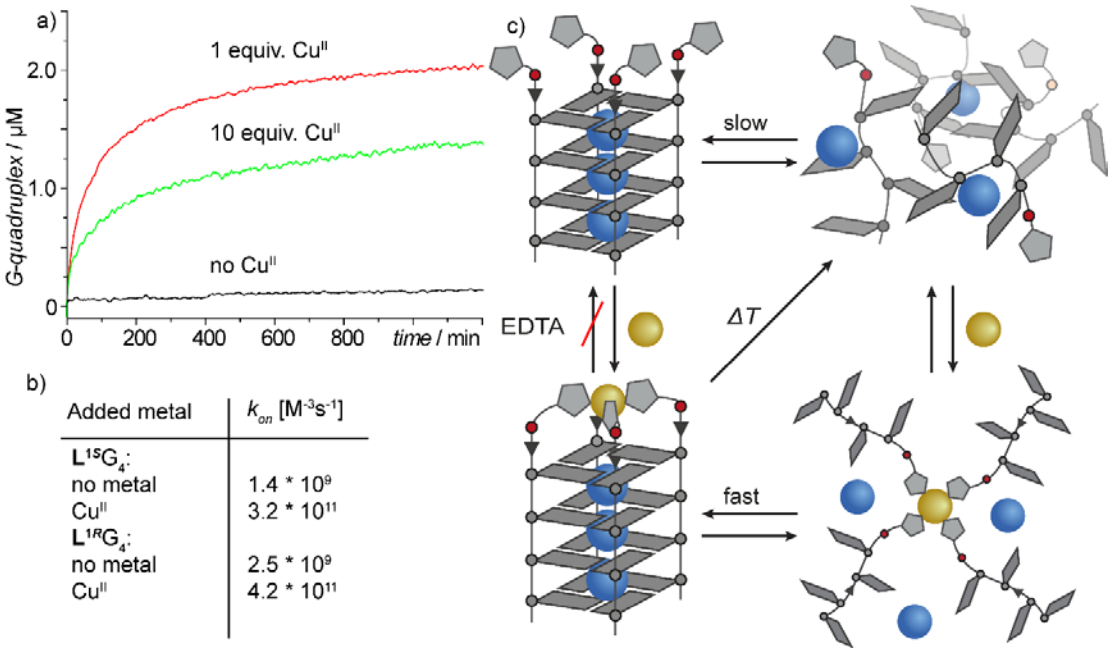

Figure 31. G-quadruplex formation kinetics. a) Formation of the G-quadruplex $\mathbf{L^{1S}}G_4$ in absence (black) and in presence of 1 (red) and 10 (green) equiv. Cu^{II} indicated as the increase of the CD band at 262 nm. b) Calculated k_{on} values for the formation of $\mathbf{L^{1S}}G_4$ using **Equation 2**. c) Proposed scheme for the formation of tetramolecular G-quadruplexes of the type $\mathbf{L}G_4$. In absence of transition metal cations, a slow G-quadruplex formation is observed. After addition of Cu^{II}, this formation is strongly accelerated by a proposed template effect. The resulting G-quadruplexes are thermally highly stabilized and Cu^{II} cannot be removed with EDTA which was dedicated to a kinetically trapped state. Reproduced from Ref.[25] Copyright © 2019 The Royal Society of Chemistry.

For more detailed structural insights into the metal-mediated G-quadruplex structures, MD simulations were performed (**Figure 32**). For the imidazole-metal complex, a bonded model was chosen in which the metal-ligand bonds and angles are fixed.[24,276] Although this does not allow ligands to dissociate from the metal or ligand exchange, this model is widely used in the context of metallo-proteins and the easiest to apply. For details on the forcefield parameterization see **Chapter 9.6**. In absence of transition metal cations,

the imidazole ligandoside **L^{1}** was observed to mostly interact with the G-quadruplex grooves. When MD simulations were performed with Cu^{II} and Zn^{II}, the G-quadruplexes were very well suited to adopt both geometries, square planar for Cu^{II} and tetrahedral for Zn^{II} (**Figure 32**). Also, the G-quadruplexes showed no signs of distortions when the metal ions were coordinated.

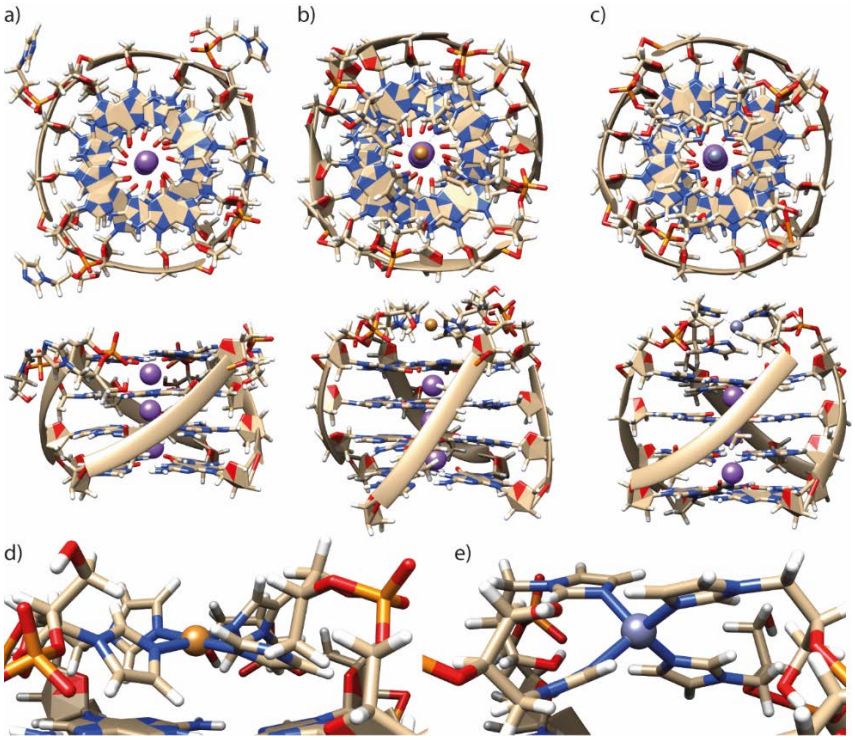

Figure 32. MD simulations of **L^{1R}**G_4 in a) absence of transition metal cations, b,d) in presence of Cu^{II} and c,e) in presence of Zn^{II}. Shown are representative screenshots from the MD simulations. Reproduced from Ref.[29] Copyright © 2019 The Royal Society of Chemistry.

After exploring the transition metal interactions, the aim was to make use from the accelerated assembly and the high metal-mediated thermal stabilizations to design a Cu^{II} responsive DNAzyme, catalysing peroxidase-like reactions. From literature, it is known that DNA G-quadruplexes can bind the iron containing macrocycle hemin *via* π-π stacking interactions.[277–279] This complex then forms a DNAzyme, which catalyses peroxidase-like reactions and the DNAzyme was utilized for a vast number of applications.[278,280–286] As a start, it was investigated whether **L^{1S}**G_4 was able to bind hemin and to catalyse peroxidase-like reactions. To probe this, the ABTS-assay was chosen due to its simple set up. In the ABTS-assay a peroxidase catalyses the oxidization of the organic compound ABTS (2,2′-Azino-bis(3-ethylbenzothiazoline-6-sulfonic acid) diammonium salt) by one electron, leading to the formation of the ABTS radical, which has a strong absorption band at 414 nm (**Figure 33**).[287]

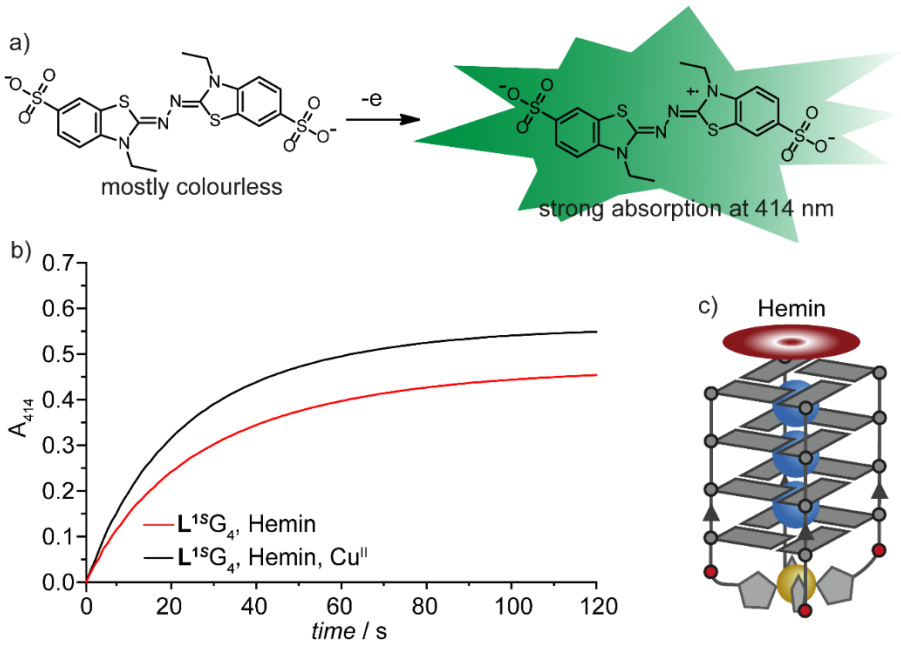

Figure 33. ABTS peroxidase assay. a) Oxidation of the organic substrate ABTS to the ABTS radical with a strong absorption at 414 nm, b) ABTS assay of **L**^{1S}G$_4$ in absence (red) and presence (black) of Cu^{II}. The change of absorption at 414 nm was followed over 120 seconds. c) Schematic representation of the active DNAzyme. Conditions: 625 nm G-quadruplex, 625 nm transition metal salt, 50 mM NaCl, 5 mM HEPES pH 8, 500 nM Hemin, 2 mM ABTS, 0.5 mM H_2O_2, 1 % v/v DMSO.

To start, a sample of **L**^{1S}G$_4$ containing NaCl and HEPES buffer pH 8 was prepared. To this solution, hemin and ABTS were added and the sample was incubated for 10 min to allow hemin binding. After 10 min, the reaction was initiated by the addition of H_2O_2 (**Figure 33**). Indeed, a strong increase of the absorption at 414 nm was observed, showing the oxidation of ABTS to the ABTS radical. When the same reaction was performed with **L**^{1S}G$_4$ in presence of 1 equiv. Cu^{II}, a small increase of the reaction rate from V_0 = 390 nM s^{-1} to V_0 = 523 nM s^{-1} was observed. Although a small increase was observed, the aim was to design a switchable DNAzyme that is only active in presence of Cu^{II}. Therefore, it was necessary to further destabilize the G-quadruplex structure in a way that it forms only in presence of Cu^{II}.

In a first attempt to destabilise **L**^{1S}G$_4$, thermal denaturation experiments were performed where the NaCl concentration was stepwise reduced to decrease the thermal stability. Decreasing the ionic strength is well known to destabilize DNA G-quadruplexes.[288,289] Although indeed a drastic decrease of the thermal stability was observed from $T_{1/2}$ = 31 °C in 100 mM NaCl to $T_{1/2}$ = ~17 °C in 1 mM NaCl (**Figure 34**), addition of hemin stabilized **L**^{1S}G$_4$ by $\Delta T_{1/2}$ = + 20 °C. Due to the high stabilizing effect of hemin no Cu^{II} was needed as switch, but this was at least proving that hemin was binding strongly to **L**^{1S}G$_4$. For this reason, a new strategy was chosen to decrease the G-quadruplex stability by reducing the number of G-tetrads from four in **L**^{1S}G$_4$ to only three in **L**^{1S}G$_3$.

Indeed, **L^{1S}G$_3$** was not able to form a G-quadruplex under the investigated conditions and, at 7 °C, only CD signatures corresponding to unfolded DNA were observed (**Figure 35**). Pleasingly, Cu^{II} addition triggered the G-quadruplex formation of **L^{1S}G$_3$** with a melting temperature of $T_{1/2}$ = 40 °C and a CD signature which clearly corresponded to the formation of a parallel G-quadruplex (**Figure 35**).

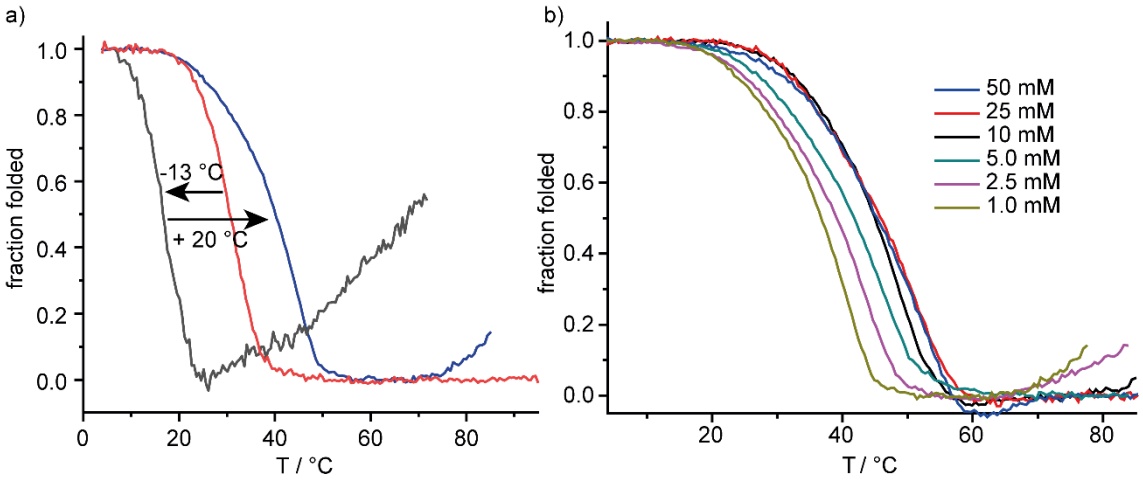

Figure 34. Stability screening of **L^{1S}G$_4$** under different conditions. a) Thermal denaturation profiles of **L^{1S}G$_4$** with 100 mM NaCl (red, $T_{1/2}$ = 31 °C), 1 mM NaCl (black, $T_{1/2}$ = 17 °C) and 1 mM NaCl and 1 µM hemin (blue, T_m = 37 °C). b) Melting profiles of **L^{1S}G$_4$** in presence of 1 equiv. hemin and varying concentrations of NaCl. Conditions: 3.75 µM ssDNA, 1 µM hemin, 10 mM LiCaco pH 7.2 and the respective NaCl concentration. No Cu^{II} was added.

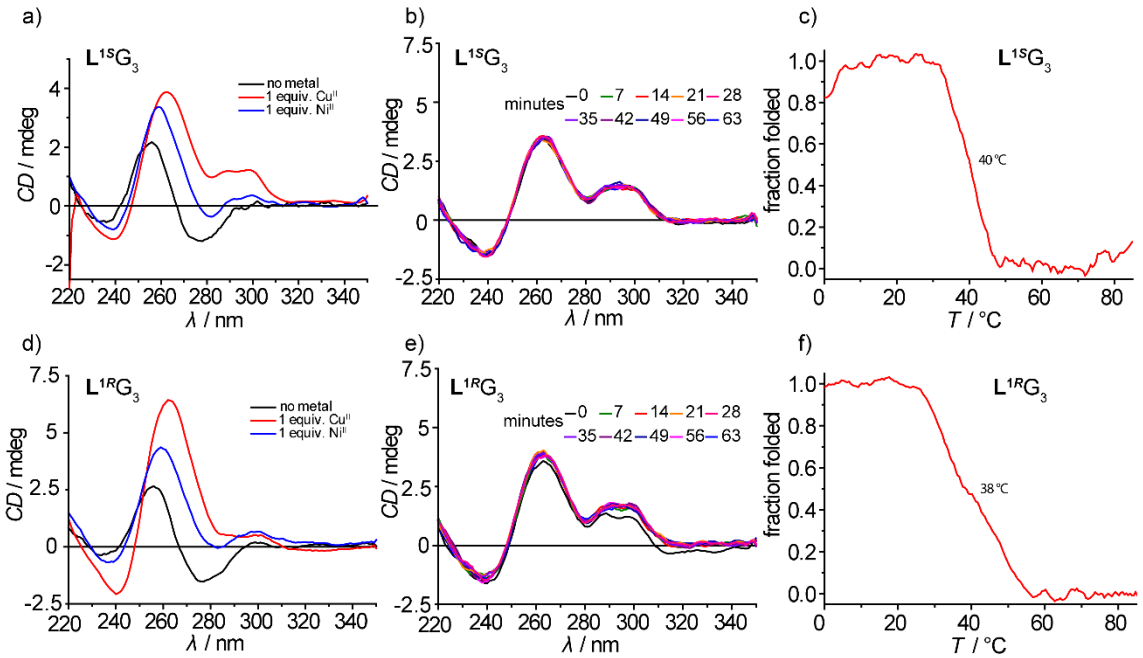

Figure 35. CD spectra of a) **L^{1S}G$_3$** and d) **L^{1R}G$_3$** in absence of transition metal cations (black), in presence of $CuSO_4$ (red) and $NiSO_4$ (blue). Time resolved CD spectroscopy of b) **L^{1S}G$_3$** and e) **L^{1R}G$_3$** in presence of Cu^{II} and after addition of 10 equiv. EDTA (with respect to Cu^{II}). Melting profiles of c) **L^{1S}G$_3$** and f) **L^{1R}G$_3$** in presence of 1 equiv. Cu^{II}. Conditions: 3.75 µM DNA, 0.98 µM transition metal cation, 100 mM NaCl, 10 mM LiCaco pH 7.2.

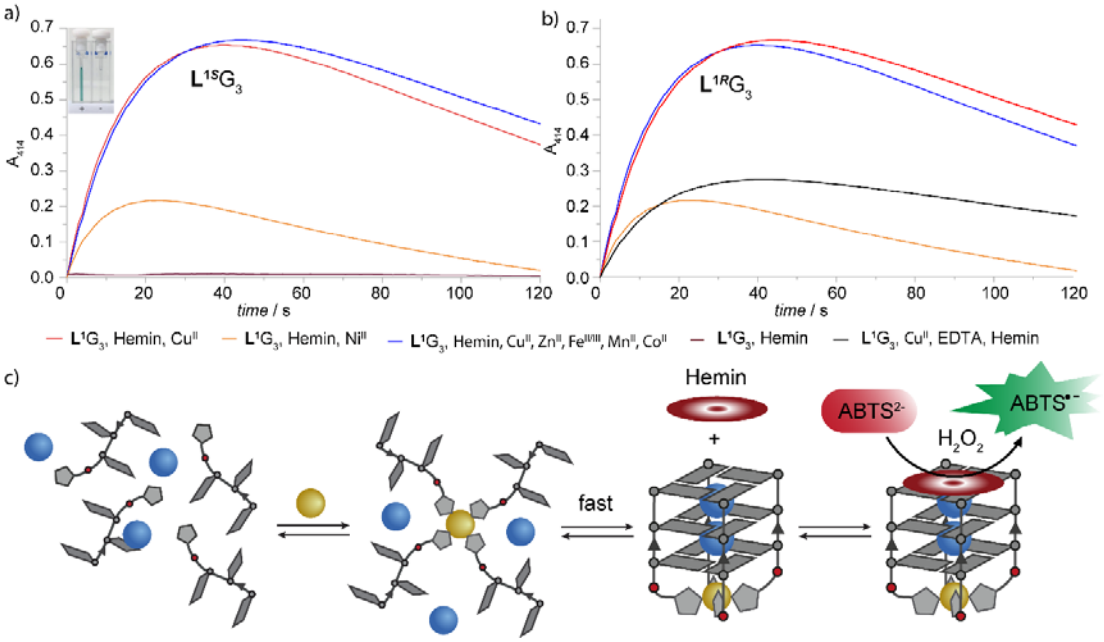

Figure 36. ABTS assay in presence of a) **L^{1S}G$_3$** and b) **L^{1R}G$_3$**. c) Schematic representation of the Cu^{II}-switchable formation of the hemin-DNAzyme complex. Conditions: 625 nm G-quadruplex, 625 nm transition metal salt, 50 mM NaCl, 5 mM HEPES pH 8, 500 nm Hemin, 1 % v/v DMSO, 2 mM ABTS, 0.5 mM H_2O_2. Reproduced and adapted from Ref.[29] Copyright © 2019 The Royal Society of Chemistry.

When the ABTS assay was now performed with **L^{1S}G$_3$** in presence of hemin, no change of the absorption at 414 nm was observed, showing that hemin was not inducing a G-quadruplex formation. Only when Cu^{II} was added, **L^{1S}G$_3$** formed a G-quadruplex and consequently could bind to hemin. This complex was then showing a strong catalytic activity (**Figure 36**) in the ABTS assay (V_0 = 615 nM s^{-1}). The DNAzyme was also stable in presence of EDTA (V_0 = 353 nM s^{-1}), although a decreased activity was observed, which was ascribed to the previously discussed kinetically inert G-quadruplex-Cu^{II} complex. Further time resolved CD spectroscopy showed after addition of EDTA to **L^{1S}G$_3$** and **L^{1R}G$_3$** no denaturation of the G-quadruplex structures (**Figure 35b,e**). When considering this system as a sensor for Cu^{II} ions it is important to show a selectivity for Cu^{II} ions and that it works in complex mixtures with other competing transition metal cations. To show this, several transition metal cations where tested if they could trigger the formation of the DNAzyme out of which only Ni^{II} showed an activity, although it was less efficient (V_0 = 369 nM s $^{-1}$). This was explained with an incomplete G-quadruplex formation in presence of Ni^{II} as it was indicated by the CD spectrum showing characteristics of unfolded ssDNA and of a parallel G-quadruplex (**Figure 35**). When the ABTS assay was performed in a complex mixture with other competing metal cations including Zn^{II}, Fe$^{II/III}$, Mn^{II}, and Co^{II}, the reaction rate was almost unaffected (V_0 = 641 nM s $^{-1}$), showing a high tolerance towards complex mixtures of transition metal cations. The stereo configuration of the imidazole ligandosides showed only a neglectable influence

on the activity and consequently **L**^{1S}G$_3$ and **L**^{1R}G$_3$ showed in the ABTS assay very similar activities (**Figure 36**).

After establishment of the ABTS-assay, ESI-MS studies were performed to further investigate the DNAzyme and to proof that hemin binds to the G-quadruplex. Since the G-quadruplex formed from **L**^{1R}G$_3$ was rather unstable, for native ESI-MS studies **L**^{1R}G$_4$ was used instead as it was shown to stay intact in presence of Cu^{II} during ionization (**Figure 26**). As expected, in presence of hemin and Cu^{II} the species [(**L**^{1R}G$_4$)$_4$+3K+Cu+hemin-10H]$^{4-}$ was observed corresponding to a folded G-quadruplex with one Cu^{II} and one hemin adduct. This was supporting the hypothesis that hemin could only bind at the 3'-end and that the Cu^{II} complex at the 5'-end was preventing hemin from binding. Interestingly, for [(**L**^{1R}G$_4$)$_4$+3K+Cu+hemin-10H]$^{4-}$ a distinct increase of the CCS to 860 Å^2 compared to [(**L**^{1R}G$_4$)$_4$+3K+Cu-9H]$^{4-}$ (793 Å^2) was observed, almost exactly matching the increase of an additional G-tetrad in [(**L**^{1R}G$_5$)$_4$+4K+Cu+10H]$^{4-}$ (858 Å^2).

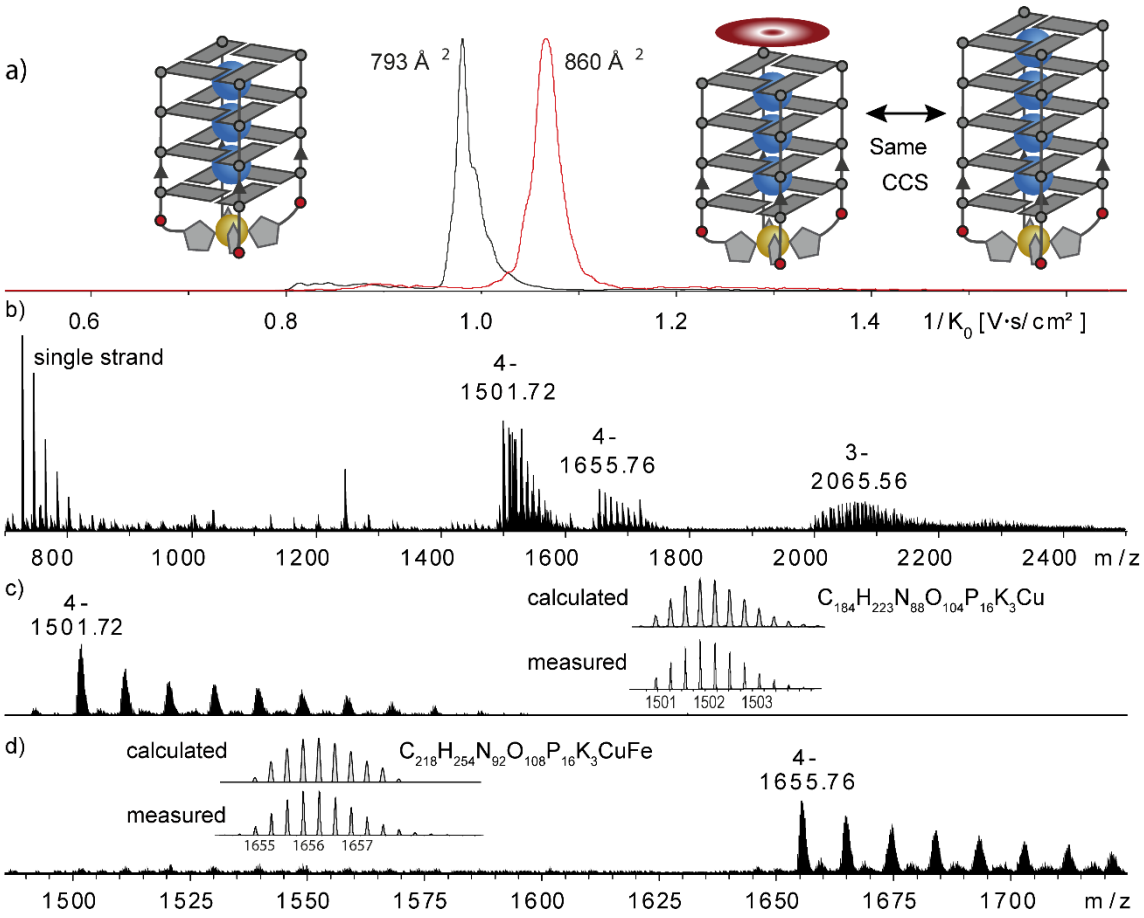

Figure 37. Native ESI-timsTOF MS of **L**^{1R}G$_4$ in presence of Cu^{II} and hemin. a) Ion mobility trace shows two sharp ion mobility distributions corresponding to [(**L**^{1R}G$_4$)$_4$+3K+Cu-9H]$^{4-}$ (793 Å^2) and [(**L**^{1R}G$_4$)$_4$+3K+Cu+hemin-10H]$^{4-}$ (860 Å^2). b) Full mass spectrum, c) and d) Ion mobility-extracted mass spectrum corresponding to [(**L**^{1R}G$_4$)$_4$+3K+Cu-9H]$^{4-}$ and [(**L**^{1R}G$_4$)$_4$+3K+Cu+hemin-10H]$^{4-}$. Conditions: 50 µM ssDNA, 0.5 mM KCl and 50 mM TMAA pH 6.8, 12.5 µM CuSO$_4$, 12.5 µM hemin, H$_2$O:ACN, 1:1. Reproduced from Ref.[29] Copyright © 2019 The Royal Society of Chemistry.

3.3 Summary

In this chapter, the incorporation of three nature-inspired imidazole ligandosides **L**$^{1-3}$ in both enantiomeric forms (*R*/*S*) into tetramolecular G-quadruplex structures was reported. All three ligandosides allowed the formation of tetramolecular G-quadruplexes in a parallel topology with thermal stabilities, that were increasing with the linker length from **L**^{1} to **L**^{3}. This was explained by better π-π stacking interactions between the imidazole ligandosides and the 5'-G-tetrad due to the longer linker. For the modified G-quadruplexes a series of transition metal cations was found to be complexed including Cu^{II}, Ni^{II}, Zn^{II} and Co^{II}, as it was indicated by strong thermal stabilizations. Interestingly, now for **L**^{1} with the shortest linker the highest thermal stabilisation was found. This was – in accordance with literature – explained by the π-π stacking interactions that had to break up to facilitate a metal coordination resulting in a stronger energetic penalty for **L**^{3}.[27] Cu^{II} addition to **L**$^{1R}G_4$ resulted in an unprecedented high thermal stabilization of ΔT_m = + 51 °C and highly accelerated G-quadruplex association kinetics by two orders of magnitude. These enhanced properties culminated in the design of a Cu^{II}-switchable and hemin-dependent DNAzyme with a peroxidase-like activity, that catalysed the oxidation of ABTS in presence of H_2O_2. Further ESI-tims-TOF experiments could show the formation of complexes in a 1:1 ratio between the G-quadruplex and hemin. Interestingly, binding of hemin to the G-quadruplex resulted in a size increase, that exactly matched the increase of an additional G-tetrad. Together, these results open new possibilities for the design of transition metal-dependent DNAzymes and future applications in DNA nanotechnology are thinkable. Nevertheless, this was just a starting point and future research will show the applicability of this concept.

4 IMIDAZOLE BASED LIGANDOSIDES IN UNIMOLECULAR G-QUADRUPLEXES

4.1 Introduction

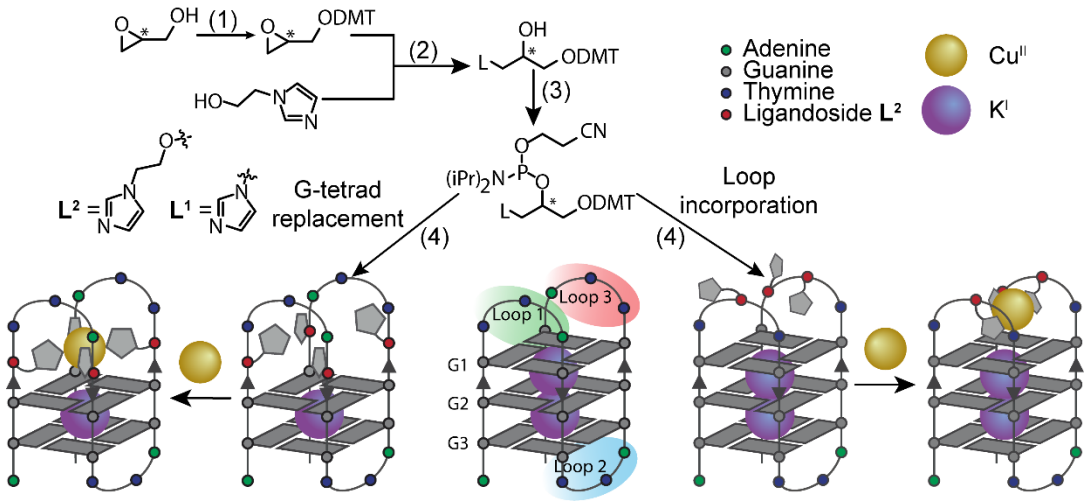

Figure 38. Synthetic route to access the phosphoramidite building blocks (*R*/*S*)-**7** and (*R*/S)-**8**. (1) DMT-protection of (*R*/*S*)-**1** (glycidol) with DMT-Cl and NEt_3 in CH_2Cl_2 at rt (2) Nucleophilic ring opening with imidazole in dioxane at 70 °C (X = X1) or with N-hydroxyethyl-imidazole and NaH in DMF at 40 °C (X = X2) (3) Phosphitylation of (*R*/*S*)-**5** and (*R*/*S*)-**6** with CEDIP-Cl and DIPEA in CH_2Cl_2 at rt (5) DNA-solid-phase synthesis. DMT = 4,4′-Dimethoxytrityl, CEDIP-Cl = 2-Cyanoethyl *N*,*N*-diisopropylchlorophosphoramidite, DIPEA = Diisopropylethylamine.[29,31]

The work shown in this chapter was published in the journals Chemistry – A European Journal and Chemical Science.[29,31]

After $\mathbf{L^1}$ and $\mathbf{L^2}$ were established in tetramolecular G-quadruplexes, the next step was the incorporation in unimolecular G-quadruplexes. While in tetramolecular G-quadruplexes $\mathbf{L^1}$ and $\mathbf{L^2}$ were only incorporated at the 5'-terminal positions, unimolecular G-quadruplexes allow to incorporate $\mathbf{L^1}$ and $\mathbf{L^2}$ in varying numbers and positions in the sequence. However, this comes at the price of a higher structural complexity, making the structure determination of unimolecular G-quadruplexes more challenging. Compared to tetramolecular G-quadruplexes, which elusively form a parallel topology, unless a special sequence design was chosen, unimolecular G-quadruplexes can fold into a wide variety of different topologies.[82,258,290,291] More detailed information's on the different unimolecular topologies of can be found in **Chapter 1.2**.

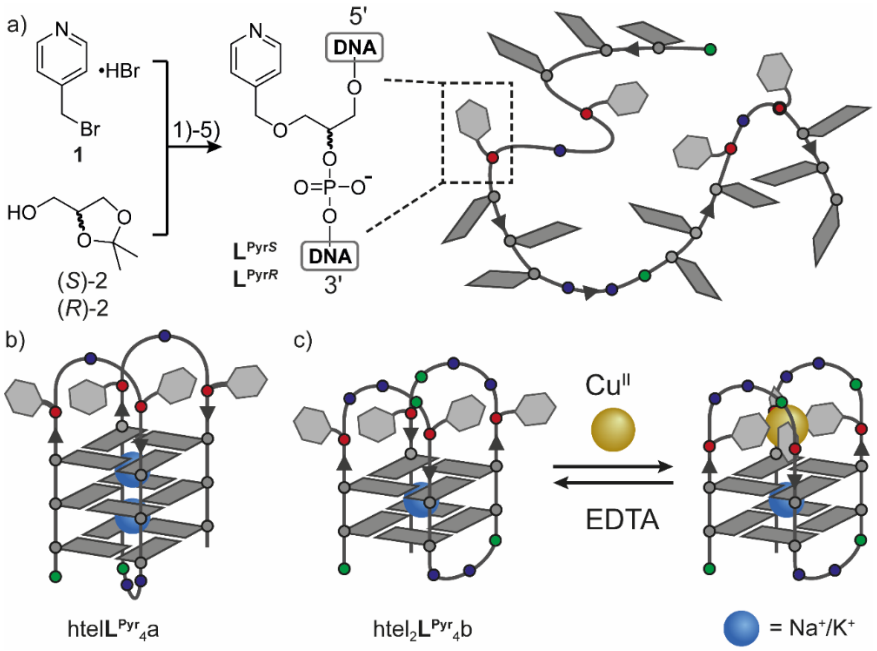

Figure 39. a) Synthesis of the pyridine phosphoramidite building block suitable for DNA-solid-phase synthesis. Schematic representation of b) htel**L**$^{Pyr}_4$a and c) htel**L**$^{Pyr}_4$b in presence and absence of Cu^{II}. Binding of Cu^{II} was found to be reversible upon EDTA addition. Reprinted and adapted with permission from ref.[24] Copyright © 2017 WILEY-VCH Verlag GmbH & Co. KGaA, Weinheim Inc.

As for the tetramolecular system the pioneering studies on metal-mediated unimolecular G-quadruplexes were based on the work of David M Engelhard. He established a pyridine ligandoside in unimolecular G-quadruplexes, here called **L**^{Pyr}, (**Figure 39**).[24] **L**^{Pyr} was incorporated into the well characterized G-quadruplex forming sequence htel (human telomeric repeat, A $(GGG\ TTA)_3\ G_3$) by either replacing four bases from the loop regions (htel**L**$^{Pyr}_4$a) or by replacement of one G-tetrad (htel**L**$^{Pyr}_4$b) with four pyridine ligandosides. Although both modified G-quadruplex structures were shown to fold in an antiparallel topology, only the latter one, with a ligandoside replaced G-tetrad was able to complex Cu^{II} and Ni^{II}, as it was indicated by increased thermal stabilities (**Figure 39**). This complexation was reversible upon addition of equimolar amounts of EDTA. Incorporation of pyridine ligandosides into the *Tetrahymena* telomeric repeat $(TTGGGG)_4$ made the Cu^{II} responsive switching from a mixture to an antiparallel topology possible.[24,292] Interestingly, when Cu^{II} was removed with EDTA, the topology was not switched back to the initial mixture of topologies, but was trapped in a metastable state. After denaturation and reannealing the sample could be transferred back to the initial state. Also, it was shown, that the incorporation of **L**^{Pyr} in the thrombin binding aptamer (**tba**), allowed a Cu^{II} switchable formation of the aptamer structure. This could be exploited for the Cu^{II} mediated inhibition of the thrombin catalysed proteolysis of fibrinogen (**Figure 40**).[24,293–295]

4.2 Results

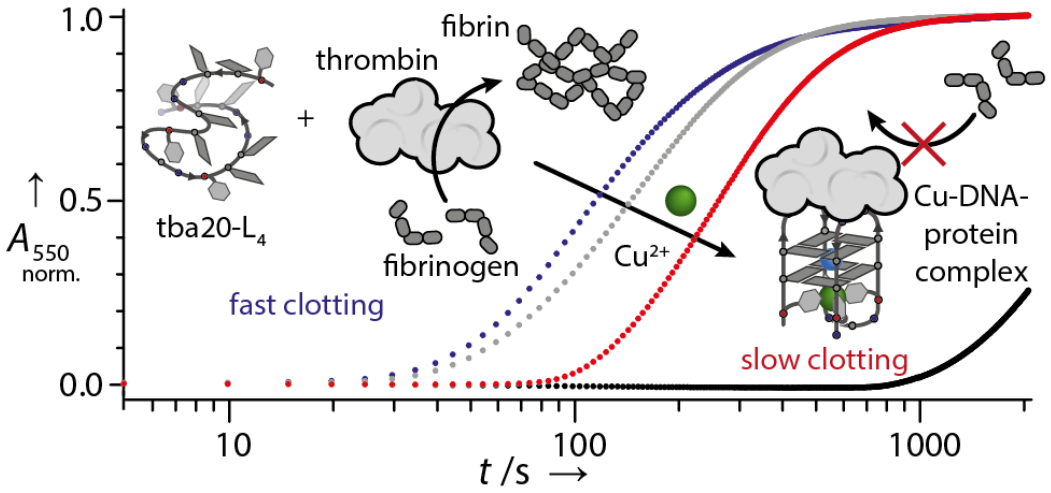

Figure 40. Clotting assay with thrombin and tba. Cu^{II} addition resulted in a significant slowdown of the clotting reaction. Reprinted with permission from ref.[24] Copyright © 2017 WILEY-VCH Verlag GmbH & Co. KGaA, Weinheim Inc.

Similarly, one G-tetrad in htel was herein replaced with the imidazole based ligandosides **L¹** and **L²**, leading to the design of htel**L**$^{1R}_4$ and htel$_{22}$**L**$^{1S}_4$. Thermal denaturation experiments showed much higher thermal stabilities for htel**L**$^{1S}_4$ (ΔT_m = 37 °C) (**Figure 41**) in compared to htel**L**$^{Pyr}_4$b (T_m = 12 °C).[24] The lower stability of the pyridine structure compared to the analogous imidazole system, is probably caused by less favourable interactions between the pyridine ligandosides and the G-quadruplex loops. Further, CD spectroscopy could clearly show the formation of an antiparallel G-quadruplex (**Figure 41**). Surprisingly, addition of various transition metal cations showed no signs of complexation in thermal denaturation experiments (**Figure 41**) or by CD spectroscopy. Since tetramolecular G-quadruplexes with four **L¹** showed strong complexations for a series of transition metal cations, the question was, why for htel**L**$^{1S}_4$ no interactions were observed, and the only reasonable explanation was the very short linker in **L¹**.

Table 2. Melting temperatures T_m and metal-mediated thermal stabilizations (ΔT_m) of unimolecular G-quadruplex forming sequences. Conditions: 1.88 µM ssDNA, 100 mM KCl, 10 mM LiCaco pH 7.2 and 1.88 µM transition metal cation. *NaCl was used as electrolyte.

Name	Sequence	-	$CuSO_4$	$NiSO_4$	ZnI_2	$Co(NO_3)_2$
htel**L**$^{2S}_2$B*	AGG GT**L** TGG GTT AGG GT**L** TGG G	53	55 (+2)	53 (+0)	54 (+1)	53 (+0)
htel**L**$^{2S}_3$B*	AGG GT**L** TGG GTT AGG G**L**T **L**GG G	50	56 (+6)	51 (+1)	52 (+2)	50 (+0)
htel**L**$^{2S}_4$	AGG **L**TT A**L**G GTT AGG **L**TT A**L**G G	33	56 (+23)	45 (+12)	36 (+3)	35 (+2)
htel**L**$^{2S}_4$B	AGG T**L**T **L**GG TTA GG**L** T**L**A GG	37	60 (+23)	n.d.	56 (+19)	n.d.
htel**L**$^{2S}_4$C	AGG T**L**T **L**GG TTA GGT **L**T**L** GG	42	63 (+21)	n.d.	63 (+21)	n.d.
htel**L**$^{2S}_5$	AGG **L**T**L** T**L**G GTT AGG **L**TT A**L**G G	33	54 (+21)	55 (+22)	37 (+4)	37 (+4)
htel**L**$^{2S}_6$	AGG **L**T**L** T**L**G GTT AGG **L**T**L** T**L**G G	36	54 (+18)	59 (+23)	44 (+8)	44 (+8)
htel**L**$^{2S}_7$A	AGG **L**T**L** **L**T**L** GGT TAG G**L**T **L**T**L** GG	28	43 (+15)	46 (+18)	36 (+8)	36 (+8)

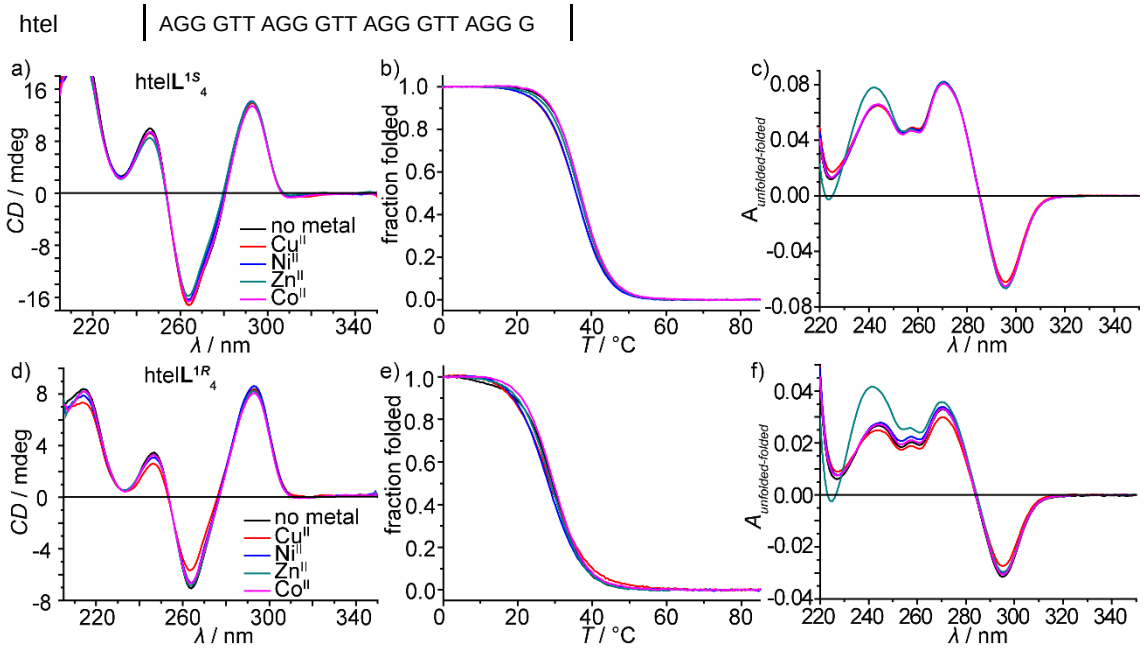

Figure 41. CD spectra, melting profiles and TDS of a-c) htel**L**$^{1S}_4$ and d-f) htel**L**$^{1R}_4$. Conditions: 1.88 µM ssDNA, 100 mM KCl, 10 mM LiCaco pH 7.2 and if present 1.88 µM transition metal cation.

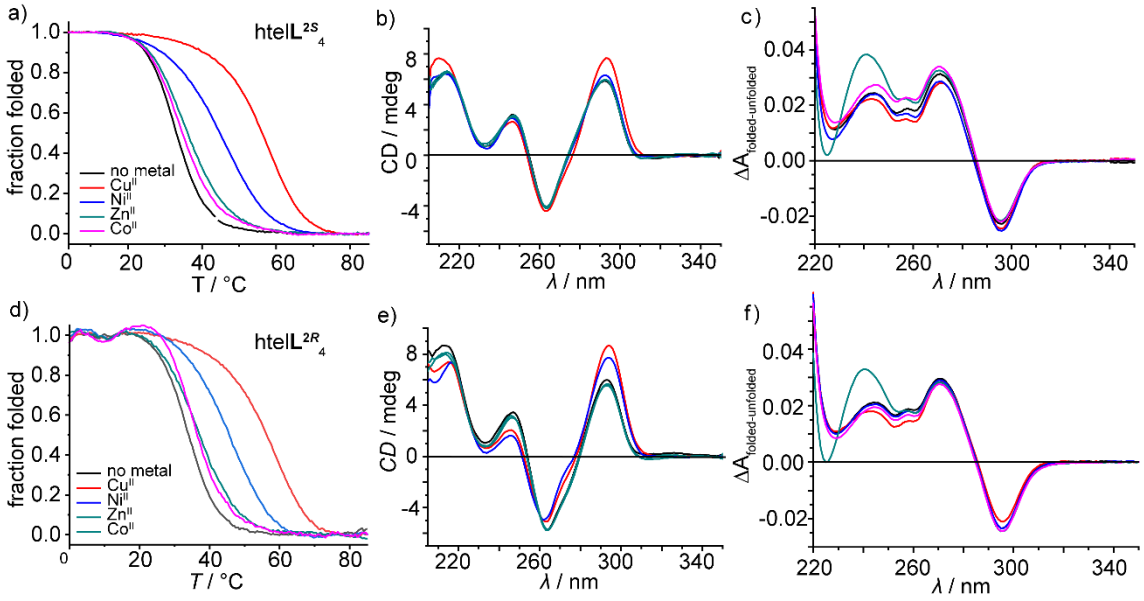

Figure 42. Thermal denaturation profiles, CD spectra and TDS of a-c) htel**L**$^{2S}_4$ and d-f) htel**L**$^{2R}_4$. Conditions: 1.88 µM ssDNA, 100 mM KCl, 10 mM LiCaco pH 7.2 and if present 1.88 µM transition metal cation.

For this reason, **L**^{2} – containing a longer linker – was incorporated into htel**L**$^{2S}_4$ and htel**L**$^{2R}_4$. Again, CD spectroscopy was consistent with the formation of a clear antiparallel topology as it was indicated by a positive Cotton effect at ~ 293 nm (**Figure 42**). Thermal denaturation experiments showed similar melting temperatures (htel**L**$^{2S}_4$, T_m = 33 °C, htel**L**$^{2R}_4$, T_m = 34 °C) compared to htel**L**$^{1S}_4$ (T_m = 37 °C) and htel**L**$^{1R}_4$ (T_m = 29 °C). In contrast to **L**^{1}, this time addition of Cu^{II} and Ni^{II} resulted in strong thermal stabilizations

for both sequences htel**L**$^{2S}_4$ (ΔT_m Cu^{II} = 23 °C, ΔT_m Ni^{II} = + 12 °C) and htel**L**$^{2R}_4$ (ΔT_m Cu^{II} = 22 °C, ΔT_m Ni^{II} = + 11 °C), while the presence of Zn^{II} and Co^{II} caused only weak stabilizations (**Table 2**). CD spectroscopy (**Figure 42**) confirmed the clear formation of an antiparallel topology. Native ESI-MS experiments could further proof the formation of a 1:1 complex with Cu^{II} or Ni^{II}, showing in each case the main species [htel**L**$^{2R}_4$+K+Cu-7H]$^{4-}$ and [htel**L**$^{2R}_4$+K+Ni-7H]$^{4-}$ accompanied by additional unspecific potassium adducts (**Figure 43**), consistent with folded G-quadruplexes in complex with Cu^{II} or Ni^{II}. As a reminder, a folded G-quadruplex shows in the mass spectrum always n-1 (n = number of G-tetrads) potassium adducts followed by additional unspecific potassium adducts.[264,265,296]

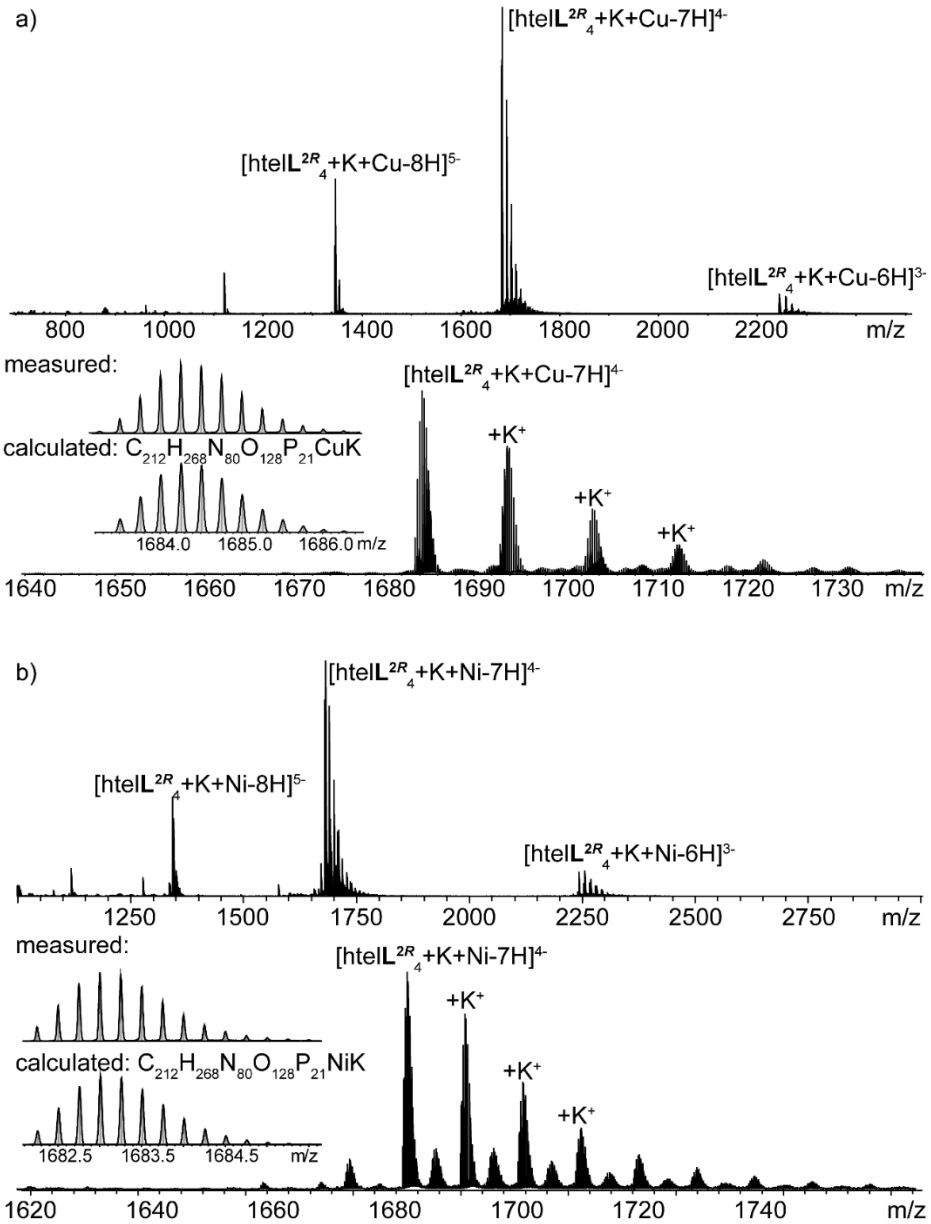

Figure 43. Native ESI-MS spectra of htel**L**$^{2R}_4$ in presence of a) Cu^{II} and b) Ni^{II}. Conditions: 12.5 µM DNA, 12.5 µM $CuSO_4$, 0.5 mM KCl and 50 mM TMAA pH 6.8, H_2O:ACN, 1:1.

In case of Zn^{II} or Co^{II} the mass spectra were more complex. While [htel**L**$^{2R}_4$+K+Zn-7H]$^{4-}$ or [htel**L**$^{2R}_4$+K+Co-7H]$^{4-}$ were observed as the main species in both cases, the species [htel**L**$^{2R}_4$-4H]$^{4-}$ showed a much higher intensity, as well. This led to the conclusion that Zn^{II} or Co^{II} stabilized the G-quadruplex structure not enough to survive the ionization process during the ESI-MS experiments and therefore a mixture of folded G-quadruplexes and ssDNA was observed. If no stabilizing transition metal cation was present, the mass spectrum was clearly corresponding to a fully denatured G-quadruplex, showing as main species [htel**L**$^{2R}_4$-4H]$^{4-}$ followed by additional unspecific potassium adducts (**Figure 89**).

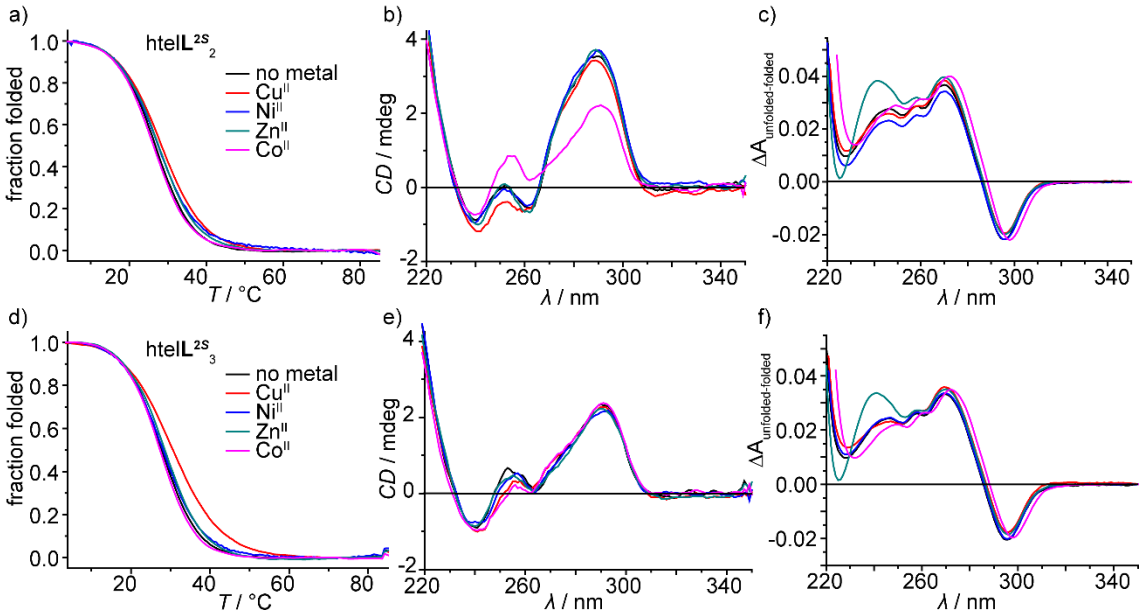

Figure 44. Thermal denaturation profiles, CD spectra and TDS of a-c) htel**L**$^{2S}_2$ and d-f) htel**L**$^{2S}_3$. Conditions: 1.88 µM ssDNA, 100 mM KCl, 10 mM LiCaco pH 7.2 and if present 1.88 µM transition metal cation.

Since the differences between **L**^{2S} and **L**^{2R} were minor in htel**L**$^{2S}_4$ and htel**L**$^{2R}_4$ and very similar observations were made, the following paragraph focuses on the observations for **L**^{2S} containing G-quadruplexes. The melting temperatures T_m for the **L**^{2R} containing sequences can be found in **9.3.2**. After **L**^{2S} was incorporated four times into htel by replacing one G-tetrad with **L**^{2S}, the next step was to change number and positions of the ligandosides and to explore, how this would affect the coordination chemistry. For the beginning, the amount of **L**^{2S} was reduced from four to two or three **L**^{2S} per G-quadruplex, resulting in an unsaturated coordination environment. Latter is crucial for catalytic applications, since unsaturated coordination environments are required to allow a substrate binding to the metal centre. The two sequences htel**L**$^{2S}_2$ and htel**L**$^{2S}_3$ with two or three **L**^{2S}, respectively, were synthesized with additional thymine bases, replacing ligandoside positions. TDS and thermal denaturation experiments were in accordance

with previous findings and confirmed the formation of G-quadruplexes for both sequences. However, CD spectroscopy provided inconclusive results giving rise to the assumption of mixed coexisting topologies, causing low signal intensities due to overlapping spectra with opposite Cotton effects (**Figure 44**). After addition of different transition metal cations, the CD spectra were not changing, although for htel**L**$^{2S}_3$ a weak thermal stabilization of ΔT_m = + 3°C after Cu^{II} addition was observed. Since CD spectroscopy was inconclusive, two new sequences were designed, called htel**L**$^{2S}_2$B and htel**L**$^{2S}_3$B, where all three G-tetrads from htel were left intact. Instead, adenine and thymine in the loop regions were replaced with **L**^{2S} (**Figure 38**). Initially, CD spectroscopy showed again no clear antiparallel topology with potassium chloride as electrolyte. Interestingly, upon addition of Cu^{II}, the CD spectra changed towards a more pronounced antiparallel topology (**Figure 45**). This is most likely caused by a templating effect of Cu^{II}, which could only be coordinated by all three **L**^{2S}, if an antiparallel topology was adopted.

Native ESI-MS further proofed the complexation of Cu^{II} for both sequences htel**L**$^{2S}_2$B **(Figure 101**) and htel**L**$^{2S}_3$B (**Figure 99**). Compared to the experiments in presence of KCl, with NaCl CD spectroscopy showed a clear antiparallel topology for both sequences, in absence and presence of Cu^{II} (**Figure 45**). This electrolyte dependent topology change is well known for G-quadruplexes and especially for htel different topologies in different electrolytes were reported.[63,64,83,297,298] Since only in presence of NaCl a clear antiparallel topology was formed from htel**L**$^{2S}_2$B and htel**L**$^{2S}_3$B, further investigations were performed with NaCl as electrolyte. Thermal denaturation experiments could only show a complexation for Cu^{II} and Zn^{II}, indicated by weak thermal stabilizations (htel**L**$^{2S}_2$B (Cu^{II}) ΔT_m = + 2°C, htel**L**$^{2S}_3$B (Cu^{II}) ΔT_m = + 6°C (**Figure 45b**), htel**L**$^{2S}_3$B (Zn^{II}) ΔT_m = + 2°C).

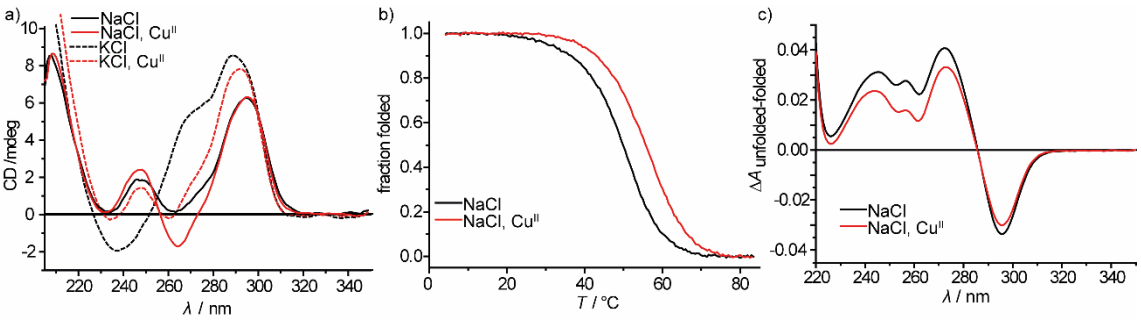

Figure 45. CD spectra, melting profiles and TDS of htel**L**$^{2S}_3$B. a) CD spectra in NaCl and KCl, b) melting profiles in NaCl and c) TDS in NaCl. Conditions: 1.88 µM ssDNA, 100 mM electrolyte, 10 mM LiCaco pH 7.2 and if present 1.88 µM Cu^{II}.

After reducing the amount of **L**^{2S} within G-quadruplexes, sequences with increasing numbers of **L**^{2S} (>4) were investigated. The amount of **L**^{2S} ranged from five to seven in a single sequence. Additional **L**^{2S} were either incorporated by replacing one G-tetrad

and/or by replacing further bases in the loop regions. In the case of the htel**L**$^{2S}_7$A containing seven **L**^{2S}, one ligandoside was incorporated without the replacement of an existing base, extending the sequence to 23 bases. The new sequences htel**L**$^{2S}_5$, htel**L**$^{2S}_6$ and htel**L**$^{2S}_7$A all showed a clear formation of G-quadruplexes in an antiparallel topology, indicated by a positive Cotton-effect at ~ 293 nm in the CD spectra. Addition of Cu^{II} to htel**L**$^{2S}_5$ showed a strong thermal stabilization of ΔT_m = + 21 °C, but lower compared to htel**L**$^{2S}_4$ (ΔT_m = + 23 °C). In contrast, for Ni^{II} the opposite effect was observed, showing a higher stabilization for htel**L**$^{2S}_5$ (ΔT_m = + 22 °C) compared to htel**L**$^{2S}_4$ (ΔT_m = + 12 °C). With htel**L**$^{2S}_6$ this trend continued showing for Cu^{II} a further reduced thermal stabilization (ΔT_m = + 18 °C) and for Ni^{II} a further increase to (ΔT_m = + 23 °C). In contrast to **L**^{1S}G$_4$ the metal-mediated thermal stabilization of htel**L**$^{2S}_6$ was found to be reversible upon EDTA addition (**Figure 48**), illustrating the reversibility of the system upon alternating additions of transition metal cations and EDTA. When seven **L**^{2S} were incorporated in htel**L**$^{2S}_7$A for Cu^{II} (ΔT_m = + 15 °C) and Ni^{II} (ΔT_m = + 18 °C) a lower thermal stabilization was observed compared to htel**L**$^{2S}_6$.

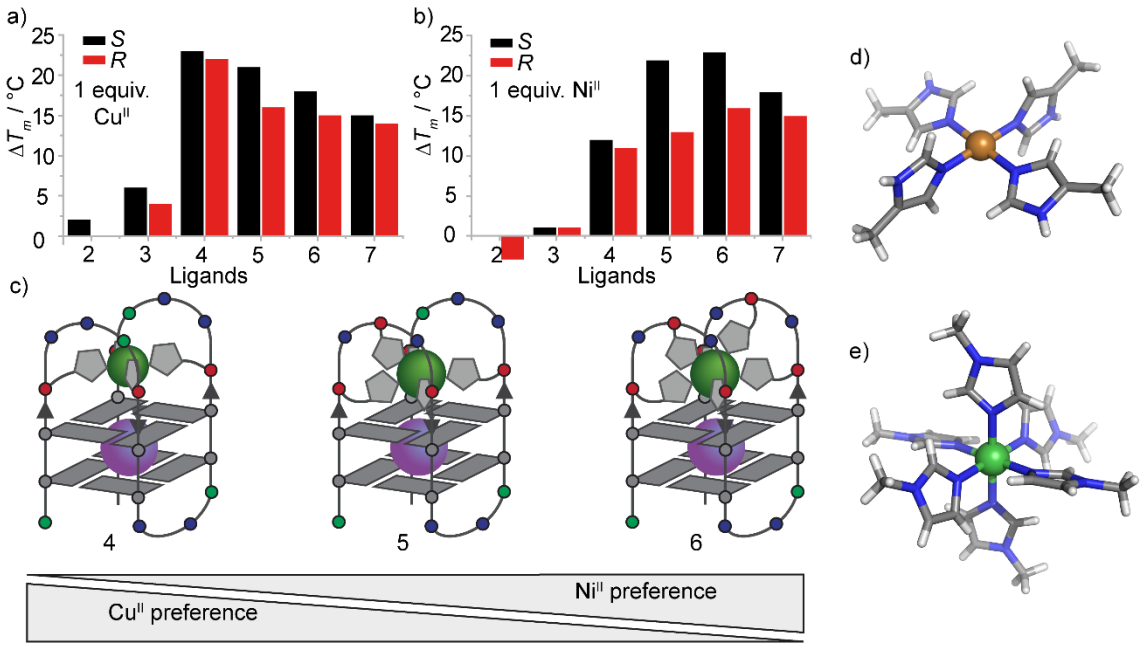

Figure 46. Fine tuning of metal affinities. The bar diagrams show the thermal stabilization after addition of 1 equiv. a) Cu^{II} and b) Ni^{II}. c) Schematic representations of G-quadruplexes with 4 – 6 ligandosides. Crystal structure of d) dichlorotetrakis(4-methylimidazole)copper(II). and e) hexakis(1-methyl-1H-imidazole-[kappa]N3)nickel(II) dichloride dihydrate. The counter ions were omitted for clarity.[273,274] Reprinted and adapted from ref.[31] Published under the terms of the Creative Commons CC BY license.

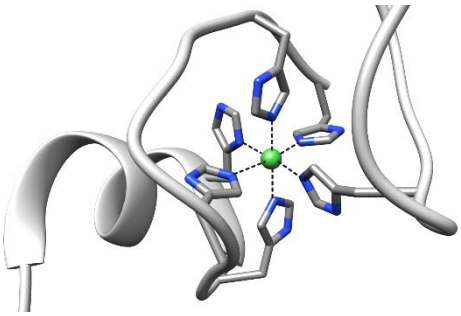

Figure 47. Crystal structure of the Metallochaperone SlyD from *thermus thermophilus* (pdb: 3CGM). One histidine residue (HIS 153) on the right side is from a neighbouring SlyD protein in the crystal structure.[299]

To explain these tendencies a closer look at the coordination chemistry of Cu^{II} and Ni^{II} is advisable. Cu^{II} is typically found coordinated in a square planar fashion with additional weakly coordinating Jahn-Teller distorted axial ligands and crystal structures of square planar Cu^{II}-imidazole complexes (**Figure 46d**) are well known.[300] The coordination environment is perfectly preorganized in htel**L**$^{2S}_4$, but as soon as the number of **L**^{2S} is increased from five to seven, an overcrowded system is created, offering more ligandosides than needed, in which different coordination geometries can be adopted. This might be the reason for the decreasing thermal stabilization with additional **L**^{2S}. In contrast Ni^{II} has a much more divers coordination chemistry and can form complexes with four to six ligands, but especially in case of Ni-imidazole complexes an octahedral crystal structure is known.[274] Even a crystal structure of the Metallochaperone SlyD from *thermus thermophilus* is known, where nickel is coordinated by six histidine residues, although one histidine comes from a second SlyD protein.[299] We therefore see a stepwise increase of the thermal stability from four to six **L**^{2S} in case of Ni^{II}, although the difference between five **L**^{2S} in htel**L**$^{2S}_5$ (ΔT_m = + 22 °C) and six **L**^{2S} in htel**L**$^{2S}_6$ (ΔT_m = + 23 °C) was rather small. These findings are summarized in the bar diagrams in **Figure 46**, nicely illustrating the highest thermal stabilization for Cu^{II} with four **L**^{2S} followed by a stepwise decrease with additional **L**^{2S}, while for Ni^{II} the opposite effect is observed.

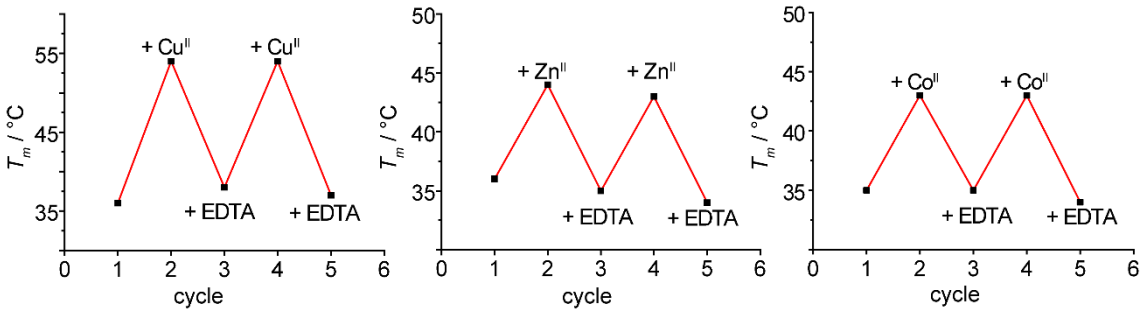

Figure 48. Iterative rounds of Cu^{II}/Zn^{II}/Co^{II} and EDTA addition with htel**L**$^{2S}_6$. The metal complexes were shown to be highly reversible after EDTA addition. Conditions: 1.88 µM ssDNA, 100 mM KCl, 10 mM LiCaco pH 7.2 and 1.88 µM transition metal salt or EDTA per addition.

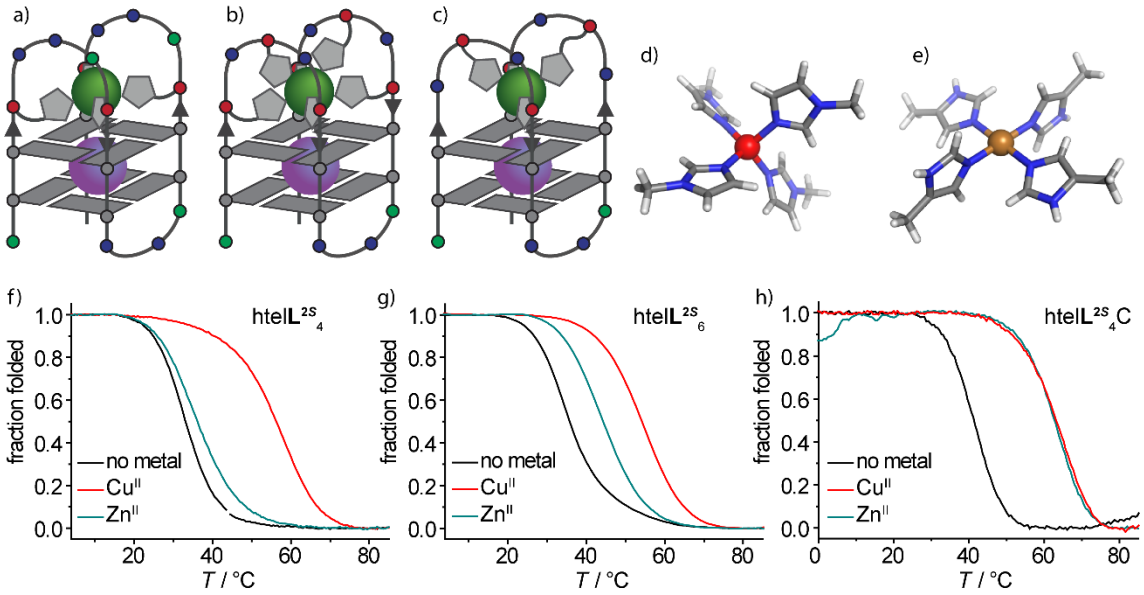

Figure 49. a-c) Schematic representation of htel**L**$_4$, htel**L**$_6$ and htel**L**$_4$C, crystal structure of d) tetrakis(1-methyl-1Himidazole-κN3)zinc(II) bis(tetrafluoridoborate) and e) dichlorotetrakis(4-methylimidazole)copper(II).[300,301] The counter ions were omitted for clarity.

For Zn^{II} and Co^{II} similar observations were made. While for htel**L**$^{2S}_4$ only weak stabilizations (ΔT_m (Zn^{II}) = + 3 °C, ΔT_m (Co^{II}) = + 2 °C) were observed, this stepwise increased with more incorporated **L**^{2S} in htel**L**$^{2S}_5$ (ΔT_m (Zn^{II}) = + 4 °C, ΔT_m (Co^{II}) = + 4 °C) and htel**L**$^{2S}_6$ (ΔT_m (Zn^{II}) = + 8 °C, ΔT_m (Co^{II}) = + 8 °C). For Co^{II}, this was explained with a possible oxidation to Co^{III}, preferring an octahedral coordination. For Zn^{II} this was not as simple, since the coordination chemistry is very dynamic and complexes with coordination numbers ranging from 4 – 6 are well known. Also, a crystal structure of a Zn^{II}-imidazole complex with a tetrahedral geometry is known (**Figure 49**).[301] The question was if the increased thermal stabilization in htel**L**$^{2S}_6$ was due to the six **L**^{2S} or due to a better preorganization. To answer this question two new sequences htel**L**$^{2S}_4$B and htel**L**$^{2S}_4$C were synthesized. In these two sequences two **L**^{2S} were lifted from the former G-tetrad to offer a preorganized tetrahedral coordination environment for Zn^{II}. Indeed, this small change caused a drastic increase of the metal-mediated thermal stabilization after Zn^{II} addition to ΔT_m (htel**L**$^{2S}_4$B) = + 19 °C and ΔT_m (htel**L**$^{2S}_4$C) = + 21 °C compared to only ΔT_m = + 3 °C for htel**L**$^{2S}_4$. Compared to that addition of Cu^{II} to htel**L**$^{2S}_4$B and htel**L**$^{2S}_4$C showed stabilizations of ΔT_m = + 23 °C and ΔT_m = + 21 °C, respectively. This means, that for htel**L**$^{2S}_4$C the Zn^{II} mediated thermal stabilisation was now as strong as for Cu^{II}. This was remarkable, considering that Cu^{II} forms according to the Irving-Williams series usually much more stable complexes than Zn^{II} and that this was achieved by simply rearranging the position **L**^{2S}.[302] This also led to the conclusion that the increased thermal stabilization observed for htel**L**$^{2S}_6$ (ΔT_m (Zn^{II}) = + 8 °C) compared

to htel**L**$^{2S}_4$ (ΔT_m (Zn^{II}) = + 3 °C) was most likely due to a better preorganization of the two **L**^{2S} in the loop regions.

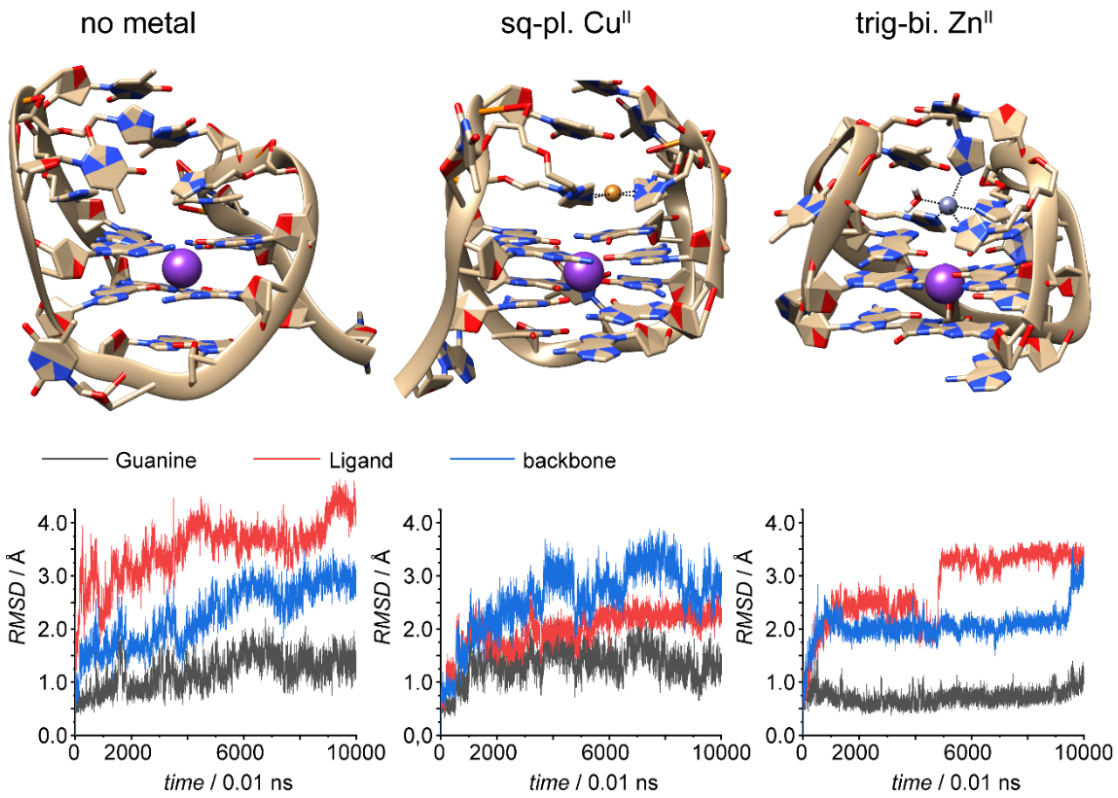

Figure 50. Representative Snapshots from the MD simulations of htel**L**$^{2S}_4$C in complex with Cu^{II} and Zn^{II}. The respective RMSD plots are shown below each snapshot. Reprinted from ref.[31] Published under the terms of the Creative Commons CC BY license.

Native ESI-MS could further proof the complexation of Zn^{II} by htel**L**$^{2S}_4$C as the main species observed [htel**L**$^{2S}_4$C+K+Zn-7H]$^{4-}$ was corresponding to the folded G-quadruplex in complex with Zn^{II} (**Figure 51b**). Interestingly, htel**L**$^{2S}_4$C was even in absence of Zn^{II} stable enough not to unfold during ionization and [htel**L**$^{2S}_4$C+K-5H]$^{4-}$ was observed as the main species (**Figure 51a**). This was in contrast to htel**L**$^{2S}_4$, for which only denatured ssDNA was observed in the mass spectrum. The reason was the higher thermal stability of htel**L**$^{2S}_4$C (T_m = 42 °C) compared to htel**L**$^{2S}_4$ (T_m = 33 °C), although the reason for the higher thermal stability remained unclear. Nevertheless, for G-quadruplexes it is well known, that seemingly small changes in the sequence can cause strong changes of the thermal stability e.g. due to the formation of additional base pairs in the loop regions. For further structural insights, MD simulations were performed using the bonded model approach. Although in this approach the coordination environment is fixed by the chosen parameters, it can be useful for a better understanding of the investigated systems. In **Figure 50** snapshots from the MD simulations of htel**L**$^{2S}_4$C are represented in complex

with Cu^{II} or Zn^{II}. Interestingly, in the case of Zn^{II}, a thymine base, located at the loops, was found to participate in coordination.

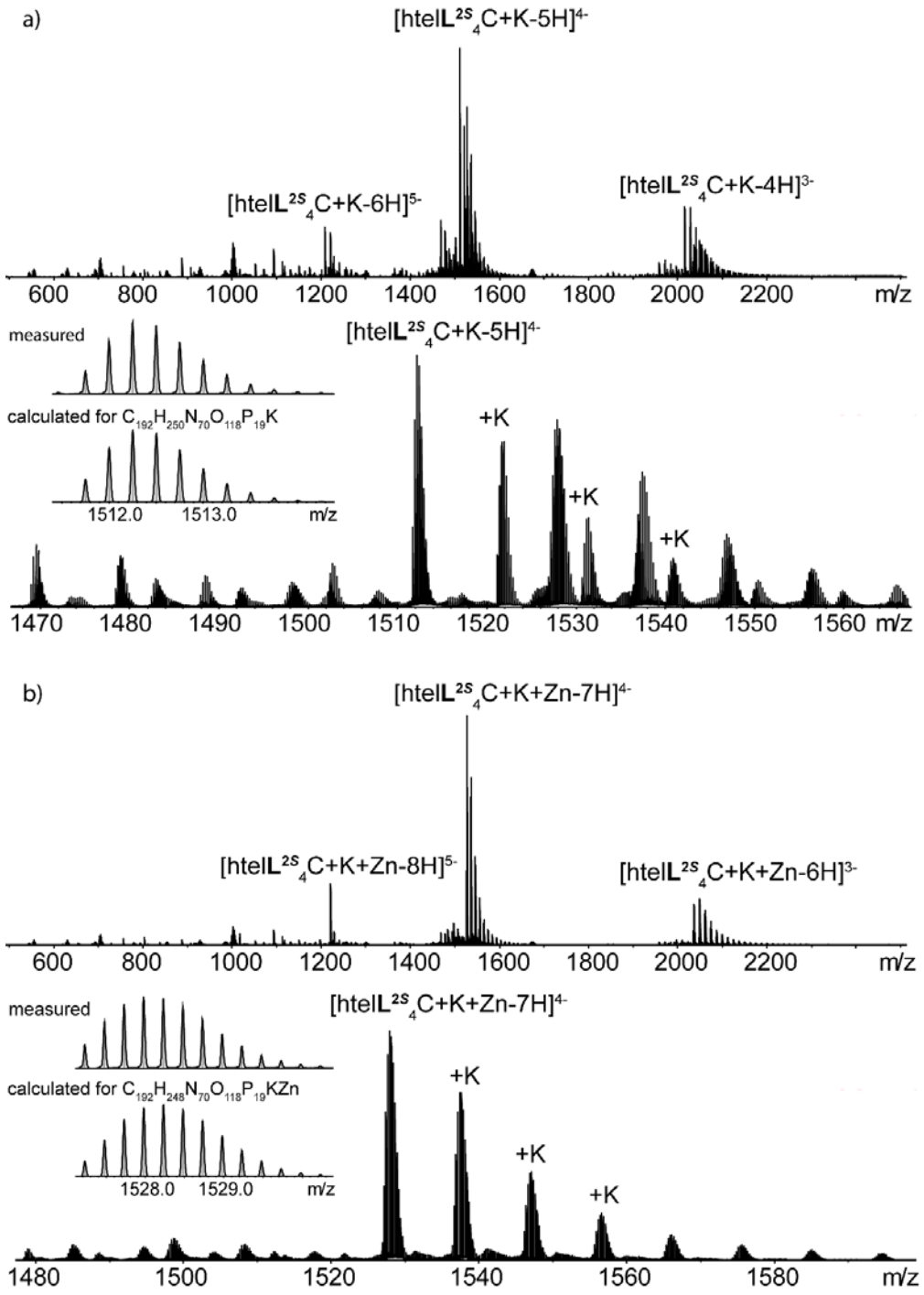

Figure 51. Native ESI-MS spectra of a) htel**L**$^{2S}_4$C and b) in presence of Zn^{II}. Conditions: 12.5 µM G-quadruplex, 12.5 µM ZnI_2, 0.5 mM KCl and 50 mM TMAA pH 6.8, H_2O:ACN, 1:1. Reprinted from ref.[273,274] Published under the terms of the Creative Commons CC BY license.

Another interesting observation was made for htel**L**$^{2S}_7$A after Cu^{II} addition (ΔT_m = + 15°C). A second equivalent Cu^{II} resulted in a second small thermal stabilization (ΔT_m =

+ 3 °C). This finding prompted the idea, that a dinuclear Cu^{II} complex could have formed. To elucidate this assumption, native ESI-MS experiments were performed and indeed a main species, assignable to a dinuclear Cu^{II} complex [htel**L**$^{2R}{}_7$+K+2Cu-9H]$^{4-}$ was observed.

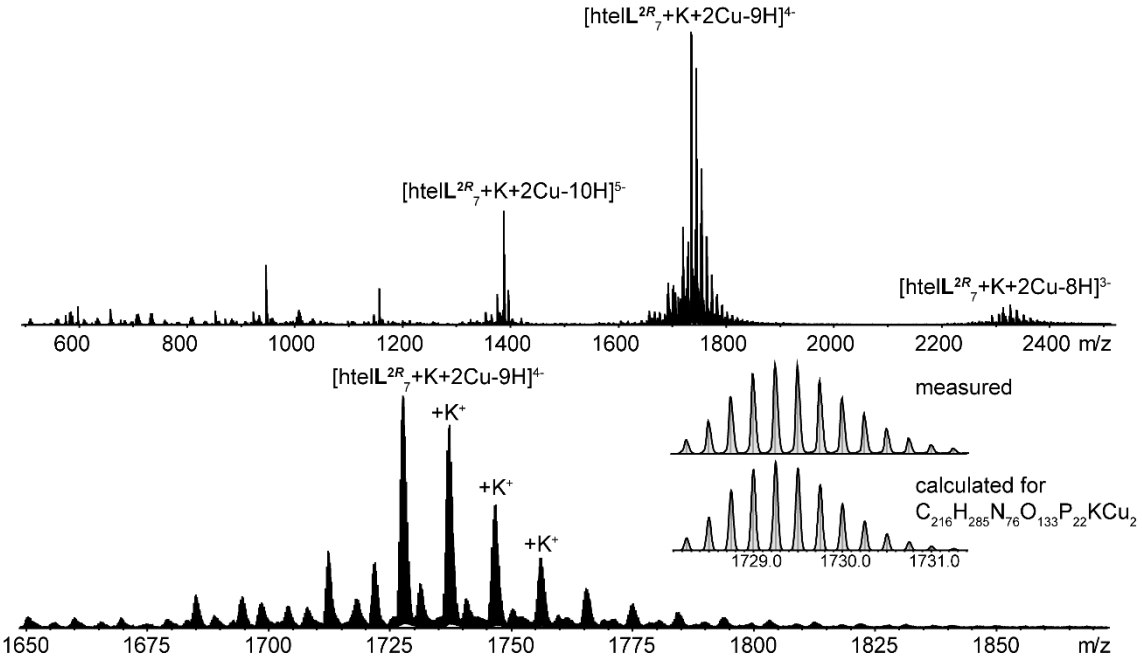

Figure 52. Native ESI-MS of htel**L**$^{2R}{}_7$A in presence of two equiv. Cu^{II}. Conditions: 12.5 µM ssDNA, 25 µM $CuSO_4$ 0.5 mM KCl and 50 mM TMAA pH 6.8 and, H_2O:ACN, 1:1.

This was interesting, since in nature proteins with dimeric Cu^{II} centres are well known. Copper proteins are classified in three types, blue copper proteins (Type I), non-blue copper proteins (type II) and dimeric copper proteins (Type III).[303] Type III copper proteins are involved in the transport (hemocyanin) and activation of molecular oxygen e.g. in tyrosinases or catechol oxidases.[304] The active sites of both, the oxygen transporting or the oxygen activating protein, share of a very similar coordination environment around the dinuclear copper centre. Each Cu^{II} is coordinated by three histidine's and the copper centres are bridged by oxygen in a μ-η^2:η^2 mode. Due to the antiferromagnetic coupling of electron spins within the dinuclear Cu^{II} centre, the protein is EPR silent.[305,306] Whether molecular oxygen is activated for an oxidative process or just bound for transportation purposes, depends on small differences in the coordination environment including the secondary coordination sphere.[303]

To probe whether htel**L**$^{2S}{}_7$A in complex with two Cu^{II} was able to activate molecular oxygen, the oxidation reaction of *D*- or *L*-DOPA to dopachrome was investigated. In a first step, DOPA is oxidized to dopaquinone, followed by a quick cyclization reaction resulting in dopachrome, which has a strong absorption at 475 nm, easily detectable by

UV/Vis spectroscopy.[307,308] Dopachrome then spontaneously decarboxylates and polymerizes to melanin, which is indicated by brown precipitates in the test tubes (**Figure 54**).[309]

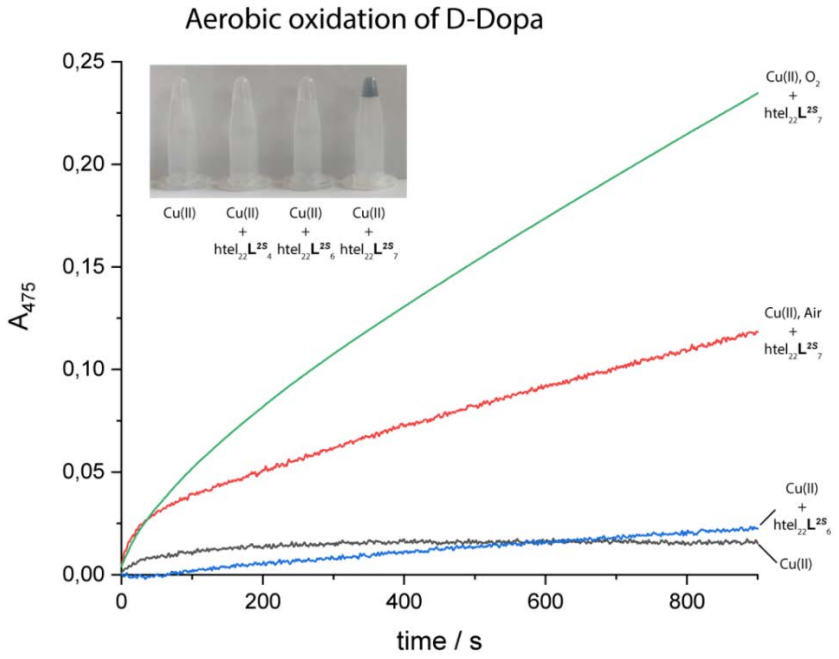

Figure 53. Aerobic oxidation of *D*-Dopa. Conditions: 0.25 mM DNA, 0.5 mM $CuSO_4$, 10 mM MOPS pH 6.5, 100 mM KCl, 2.5 mM *D*-Dopa.

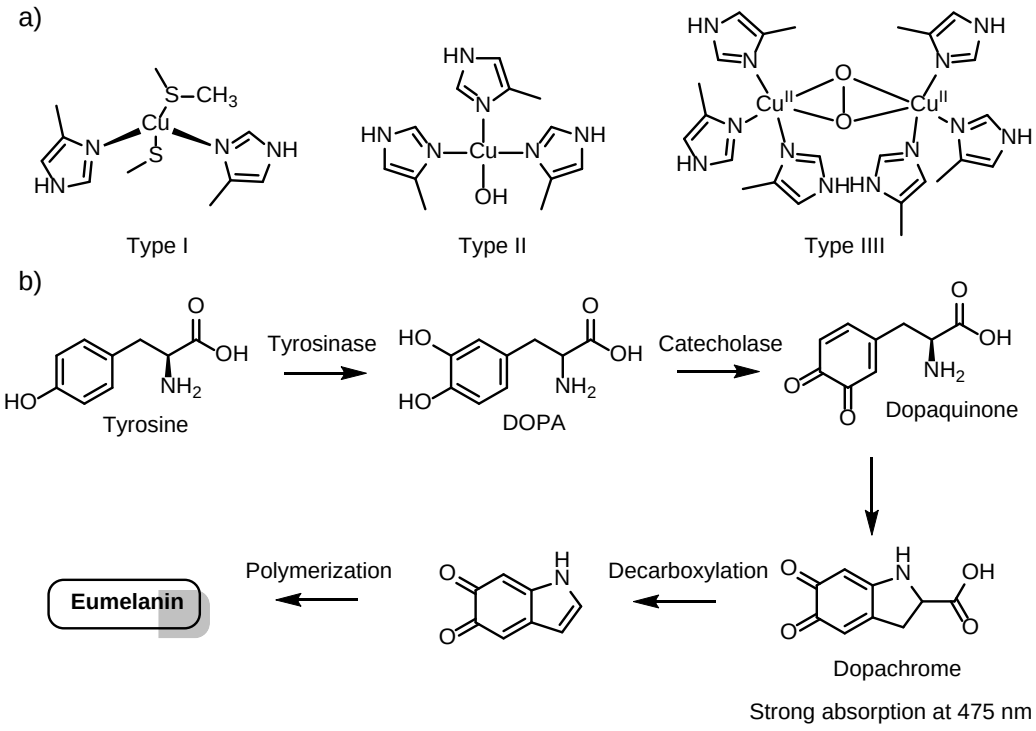

Figure 54. a) Types of copper proteins. b) Reaction pathway from the amino acid tyrosine to melanin. Tyrosine is hydroxylated in meta position by tyrosinases, which is then further oxidized by a tyrosinase or a catechol oxidase to dopaquinone. This spontaneously cyclizes to dopachrome which has a strong absorption at 475 nm. Dopachrome spontaneously decarboxylates and polymerizes to melanin.[310,311]

As illustrated in **Figure 53**, the presence of two equiv. Cu^{II} htel**L**$^{2R}_7$A showed a significant oxidation of *D*-DOPA, indicated by an increase of the absorbance at 475 nm. When the sample was flushed with pure O_2 an even faster oxidation was observed, proving the necessity of oxygen for the investigated reaction step. For sequences with less than seven **L**^{2S} or only with Cu^{II} no oxidation was observable. When *L*-DOPA was used instead, the same increase of absorption at 475 nm was observed, indicating that reaction kinetics are independent of the used Dopa stereoisomer.

From literature many model complexes are known, which mimic catechol oxidases, with mixed donor functionalities.[312–314] For this reason, a series of new sequences with mixed donor sites was synthesized, containing six and seven ligandosides with varying ratios of **L**^{2S} and **L**^{PyrS}. Both ligandosides were incorporated as the *S*-enantiomer. In **Figure 55** the results of the *D*-Dopamine oxidation are presented. The newly designed sequences showed no improved oxidation rates compared to the htel**L**$^{2S}_7$A, thereof, it remains one of the best performing sequences along with htel**L**$_7$C, providing nearly the same oxidation rates.

htel**L**$_7$A	AGG **L**^{2S}T**L**^{2S} **L**^{2S}T**L**^{2S} GGT TAG G**L**^{2S}T **L**^{2S}T**L**^{2S} GG
htel**L**$_7$B	AGG **L**^{2S}T**L**^{PyS} **L**^{2S}T**L**^{PyS} GGT TAG G**L**^{2S}T **L**^{2S}T**L**^{2S} GG
htel**L**$_7$C	AGG **L**^{2S}T**L**^{PyS} **L**^{2S}T**L**^{PyS} GGT TAG G**L**^{2S}T **L**^{PyS}T**L**^{2S} GG
htel**L**$_7$D	AGG **L**^{2S}T**L**^{PyS} **L**^{2S}T**L**^{2S} GGT TAG GLT **L**^{PyS}T**L**^{2S} GG
htel**L**$_7$E	AGG G**L**^{2S}T **L**^{2S}T**L**^{2S} GGG TT AGG G**L**^{2S}T **L**^{2S}T**L**^{2S} GGG
htel**L**$_7$F	AGG G**L**^{PyS}T **L**^{2S}T**L**^{2S} GGG TT AGG G**L**^{2S}T **L**^{PyS}TL GGG
htel**L**$_7$G	AGG GT**L**^{2S} **L**^{2S}**L**^{2S}T GGG TT AGG GT**L**^{2S} **L**^{2S}**L**^{2S}T GGG
htel**L**$_7$H	AGG GT**L**^{2S} **L**^{PyS}**L**^{2S}T GGG TT AGG GT**L**^{2S} **L**^{PyS}LT GGG

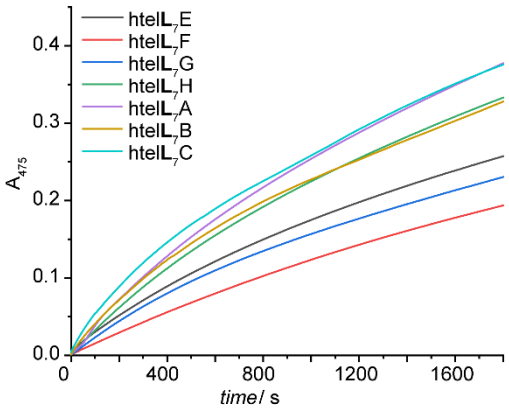

Figure 55. Oxidation of *D*-Dopa under oxygen atmosphere. Conditions: 0.1 mM DNA, 0.2 mM $CuSO_4$, 10 mM MOPS pH 6.5, 100 mM KCl, 2.5 mM *D*-Dopa.

4.3 Summary

In this chapter two imidazole-based ligandosides, **L**^{1} and **L**^{2}, were incorporated in both of their enantiomeric forms (*R*/*S*) into various unimolecular G-quadruplexes. A metal complexation could only be observed for G-quadruplexes containing **L**^{2}, which was assumed to be the reason of the longer linker. As for the tetramolecular G-quadruplex **L**^{2S}G$_4$, htel**L**$^{2S}_4$ was shown to form stable complexes with Cu^{II}, Ni^{II}, Zn^{II} and Co^{II}. The formation of specific 1:1 complexes between htel**L**$^{2S}_4$ and transition metal cation was confirmed by thermal denaturation and native ESI-MS experiments. The highly predictable folding pattern of unimolecular G-quadruplexes was then exploited for the

design of tailored coordination environments with improved metal affinities, indicated by higher thermal stabilizations. In this respect for Cu^{II} a preference for G-quadruplexes offering four $\mathbf{L^{2S}}$ in a square planar arrangement (htel$\mathbf{L^{2S}}_4$) was found while Ni^{II} showed a tendency to prefer G-quadruplexes with five to six $\mathbf{L^{2S}}$ (htel$\mathbf{L^{2S}}_5$ and htel$\mathbf{L^{2S}}_6$). Further for Zn^{II} highly improved coordination environments were designed by prearranging $\mathbf{L^{2S}}$ in a tetrahedral coordination environment in htel$\mathbf{L^{2S}}_4$C. Addition of Cu^{II} and Zn^{II} to htel$\mathbf{L^{2S}}_4$C led to equal thermal stabilizations. This was remarkable, considering that Cu^{II} forms according to the Irving-Williams series in general much more stable complexes than Zn^{II}.[302] Also, the concept allowed the design G-quadruplexes with unsaturated coordination environments for Cu^{II}, potentially allowing a coordination of substrates to the Cu^{II} centre. This was interesting, when considering catalytic applications and indeed the proof of concept will be discussed in **Chapter 6**.

Finally, the design culminated in the development of a series of sequences with dimeric Cu^{II} centres, as it is often found in oxygen activating enzymes such as catechol oxidases. Inspired by that it was found that these G-quadruplexes were able to catalyse the oxidation of DOPA under an oxygen atmosphere, although the reaction rates were rather slow compared to their natural counterparts. Nevertheless, this approach represents a promising starting point for to design DNAzymes inspired by their natural counterparts.

5 HETEROLEPTIC COORDINATION ENVIRONMENTS IN UNIMOLECULAR G-QUADRUPLEXES

5.1 Introduction

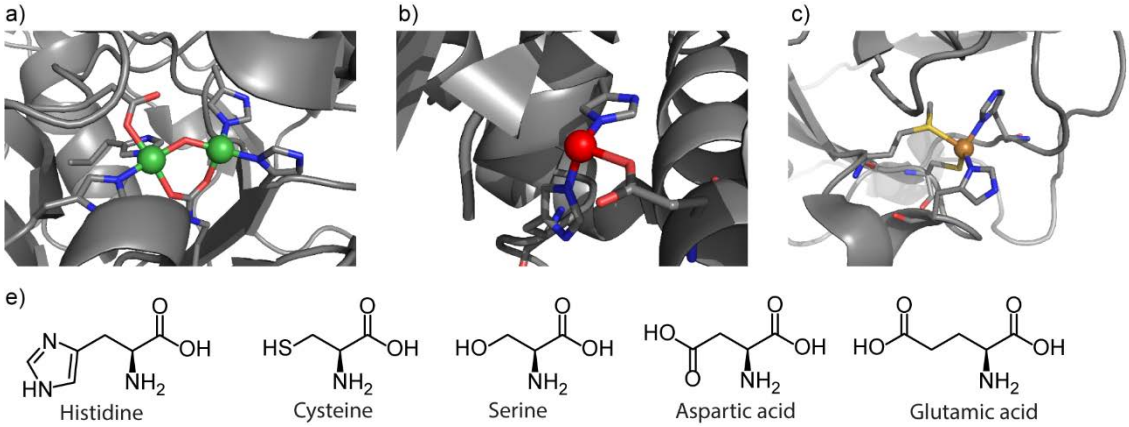

Figure 56. Examples of selected metalloproteins. a) Urease with a dimeric Ni^{II} centre, pdb: 5g4h, b) Peptidase with a Zn^{II} centre, pdb: 5e33, c) Single electron shuttle protein Plastocyanin with a $Cu^{I/II}$ centre, pdb: 4dp0 and e) amino acids that are mostly involved in metal coordination.

The work shown in this chapter was published in the journal Frontiers in Chemistry and is also part of the dissertation of Lukas M. Stratmann.[30]

In the previous chapter, it was discussed how the histidine-inspired ligandoside **L^2** was incorporated in unimolecular G-quadruplexes and how it was used to design tailored coordination environments for various transition metal cations.[30] Naturally, the next step was to expand the concept to other ligands with new functionalities and to design novel heteroleptic coordination environments. A combination of amino acids found in many metallo-proteins is histidine and the carboxylic acids aspartate and glutamate. Examples include ureases with a dimeric Ni^{II} centre or the human dipeptidyl peptidase III (DPP3) where the catalytically active Zn^{II} is coordinated by two histidine and one glutamate residue (**Figure 56**).[245,246] Inspired by glutamate a benzoate-based ligandoside **L^B** was designed and synthesized by Lukas M. Stratmann (**Figure 57**).[30] The reason for introducing a benzoic acid instead of an aliphatic carboxylic acid was dedicated to an simpler synthetic access.

5.2 Results

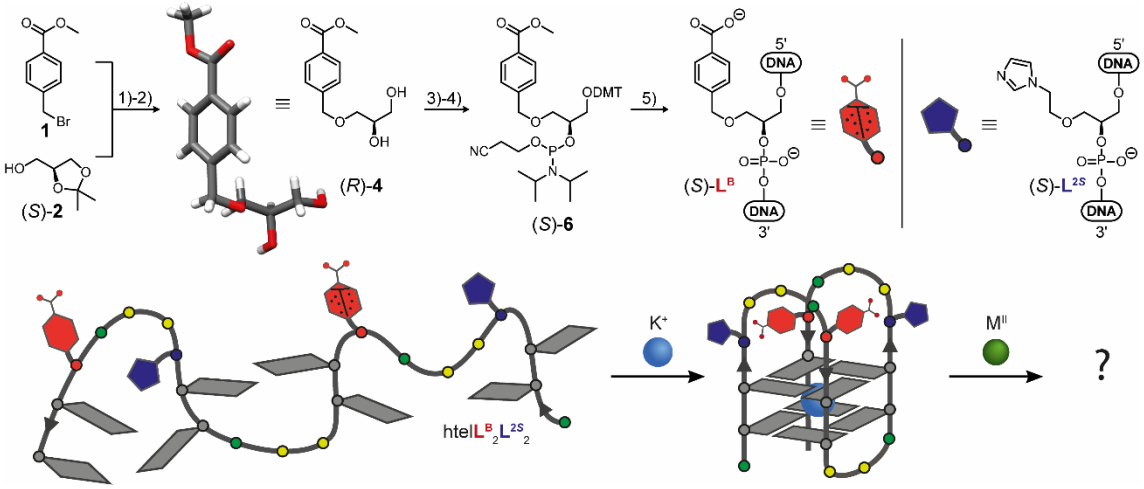

Figure 57. Synthetic route to access the phosphoramidite building block of $\mathbf{L^B}$ 1) NaH, dry ACN, rt 2) THF/acetic acid/H_2O, 2/1/1, rt 3) DMT-Cl, DMAP, DIPEA in THF, rt 4) DIPEA and CEDIP-Cl in CH_2Cl_2 5) DNA solid-phase synthesis. The scheme below shows the schematic formation of the G-quadruplex htel$\mathbf{L^B}_2\mathbf{L^{2S}}_2$. Reprinted from ref.[30] Published under the terms of the Creative Commons CC BY license.

The following experiments were performed in equal parts by Lukas M. Stratmann.[30] Both ligandosides $\mathbf{L^{2S}}$ and $\mathbf{L^B}$ contain a single stereo centre and can be accessed as the *S* and *R* enantiomer. Nevertheless, in this chapter only the *S* enantiomers of both ligandosides were investigated. This is because – although in the previous studies (**Chapter 3.2**) differences between $\mathbf{L^{2S}}$ and $\mathbf{L^{2R}}$ were observed – the general effects and tendencies were the same for the *S* and *R* enantiomer. Also, mixing both enantiomers in unimolecular G-quadruplexes would have resulted in such a large number of possible sequences that could not be investigated. All investigated sequences and melting temperatures can be found in (**Table 3**). Before starting with unimolecular sequences, $\mathbf{L^B}$ was investigated in the tetramolecular G-quadruplexes $\mathbf{L^B}G_3$, $\mathbf{L^B}G_4$ and $\mathbf{L^B}G_5$. In absence of transition metal cations, CD spectroscopy could show for $\mathbf{L^B}G_5$ the formation of a tetramolecular G-quadruplex with a positive Cotton-effect at ~261 nm, while the CD spectrum of $\mathbf{L^B}G_4$ indicated only a partial G-quadruplex formation and in case of $\mathbf{L^B}G_3$, only single-stranded DNA was observed (**Figure 58**). The melting temperature of $\mathbf{L^B}G_4$ at $T_{1/2}$ = 27 °C was significantly lower compared to $\mathbf{L^{2S}}G_4$ ($T_{1/2}$ = 36 °C), which was explained with a repulsion of the negatively charged benzoate $\mathbf{L^B}$ (**Figure 58b**). Since CD spectroscopy could show for $\mathbf{L^B}G_4$ a G-quadruplex formation with a parallel topology, next the interactions with a series of transition metal cations, including Cu^{II}, Ni^{II} and Zn^{II} were investigated, however in contrast to $\mathbf{L^{2S}}G_4$, no signs of a complexation were observed, neither by CD spectroscopy nor by thermal denaturation experiments (**Figure 58d-f**). As the benzoate is a hard Lewis base like water and cacodylate and on the other

hand, imidazole is a softer Lewis base, this was explained with a strong competition between the benzoate ligandoside with cacodylate, water and chloride ions. For this reason, more oxophilic metal cations such as Ce^{III} and Gd^{III} were investigated but still no signs for a complexation were observed.

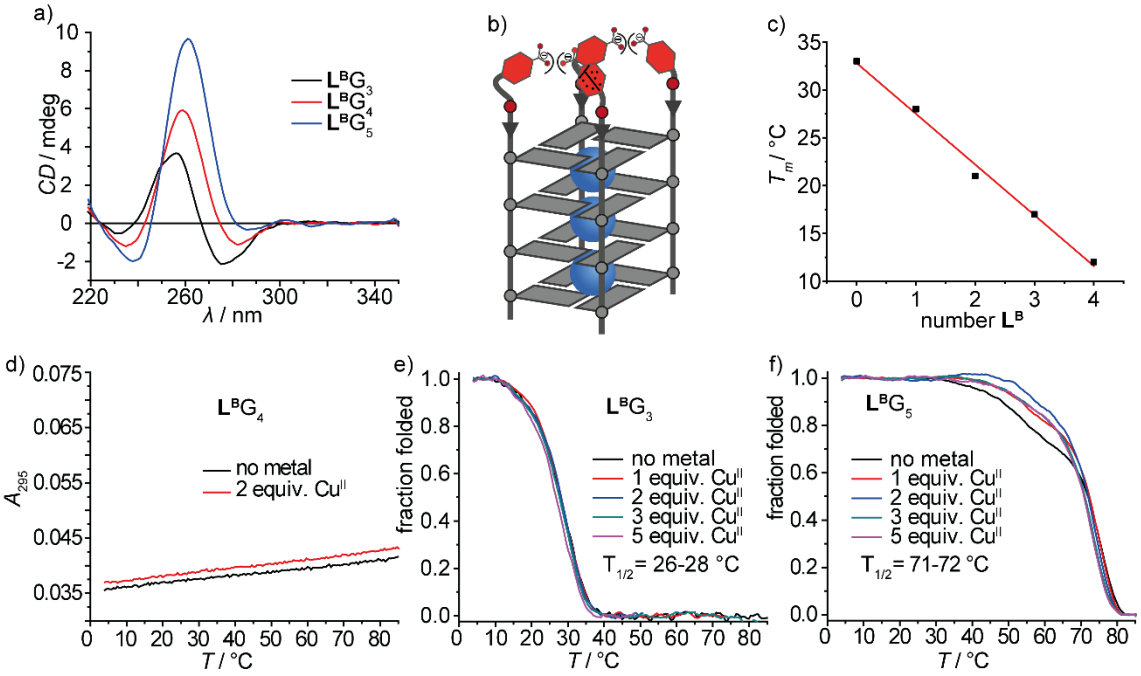

Figure 58. a) CD spectroscopy of $\mathbf{L^B}G_3$, $\mathbf{L^B}G_4$ and $\mathbf{L^B}G_5$, b) Schematic representation of the repulsing negative charges from $\mathbf{L^B}$, c) Correlation of the melting temperature T_m with the number of incorporated $\mathbf{L^B}$, d-f) Melting profiles of $\mathbf{L^B}G_3$, $\mathbf{L^B}G_4$ and $\mathbf{L^B}G_5$ with varying amounts of Cu^{II}. Conditions: 4 µM ss DNA, 100 mM NaCl, 10 mM LiCaco pH 7.2.

Although no metal complexation was found in tetramolecular G-quadruplexes, $\mathbf{L^B}$ was incorporated in unimolecular G-quadruplexes. At first, the sequence htel$\mathbf{L^B}_4$ was synthesized, where four $\mathbf{L^B}$ were incorporated in the former G-tetrad of htel. As for htel$\mathbf{L^{2S}}_4$, the formation of a clear antiparallel G-quadruplex was observed indicated by a positive Cotton effect at ~294 nm in the CD spectrum. Again, incorporation of $\mathbf{L^B}$ resulted in a strong destabilization of htel$\mathbf{L^B}_4$ (T_m = 12 °C) compared to htel$\mathbf{L^{2S}}_4$ (33 °C) and no interactions with a series of transition metal cations (Cu^{II}, Ni^{II}, Zn^{II}, Co^{II}) were observed. Then $\mathbf{L^B}$ was successively replaced with $\mathbf{L^{2S}}$ in htel$\mathbf{L^B}_3\mathbf{L^{2S}}$, htel$\mathbf{L^B}_2\mathbf{L^{2S}}_2$, htel$\mathbf{L^B}\mathbf{L^{2S}}_3$ and htel$\mathbf{L^{2S}}_4$. While for all sequence's CD spectroscopy showed a clear antiparallel topology, an interesting trend of the thermal stabilities was observed. With each replacement of $\mathbf{L^B}$, a linear increase of the thermal stability by ~ 5°C was observed (**Figure 58c**). This was dedicated to the reduction of negative charges from $\mathbf{L^B}$. As for htel$\mathbf{L^B}_4$, the sequences htel$\mathbf{L^B}_3\mathbf{L^{2S}}$, htel$\mathbf{L^B}_2\mathbf{L^{2S}}_2$ showed no signs for the complexation of Cu^{II}, Ni^{II}, Zn^{II} and Co^{II} but for htel$\mathbf{L^B}\mathbf{L^{2S}}_3$, a weak but distinct stabilization of ΔT_m = +4 °C after addition of 1 equiv. Cu^{II} was observed (**Figure 59**). Additional equivalents of Cu^{II} resulted in no further stabilization, consistent with a specific Cu^{II} complexation. Open remains the

question whether **L^{B}** was involved in Cu^{II} coordination. Further investigations by EPR spectroscopy might help to answer this question but are not part of this dissertation.

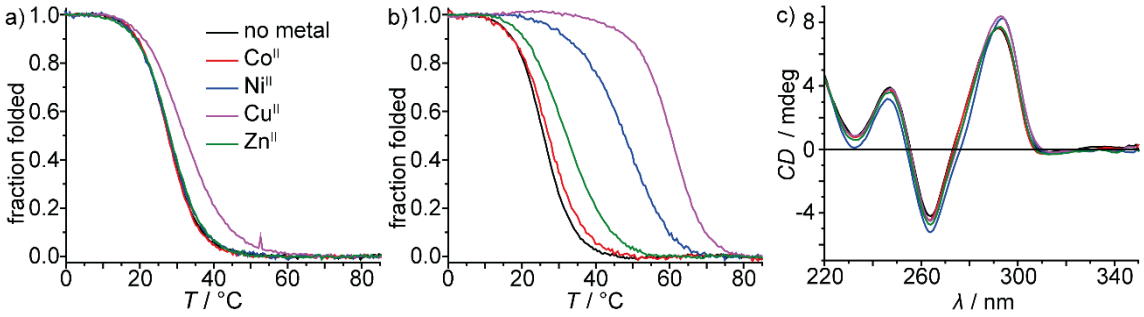

Figure 59. Thermal denaturation profiles normalized to fractions folded of a) htel**L^{B}L^{2S}$_3$** and b) htel**L^{B}$_2$L^{2S}$_4$** in absence and presence of 1 equiv. Cu^{II}, Ni^{II}, Zn^{II} and Co^{II} c) CD spectra of htel**L^{B}$_2$L^{2S}$_4$** in absence and presence of 1 equiv. Cu^{II}, Ni^{II}, Zn^{II} and Co^{II}. Conditions: 1.88 µM ssDNA, 100 mM KCl, 10 mM LiCaco pH 7.2 and 1.88 transition metal cation.

Table 3. Melting temperatures T_m in absence of transition metal cations and thermal stabilizations (ΔT_m) of unimolecular G-quadruplex forming sequences. Conditions: 1.88 (unimolecular) or 4 (tetramolecular) µM ssDNA, 100 mM NaCl (tetramolecular) or KCl (unimolecular), 10 mM LiCaco pH 7.2 and 1.88 or 1 µM transition metal cation.

Name	Sequence	-	$CuSO_4$	$NiSO_4$	ZnI_2	$Co(NO_3)_2$
L^{2S}G$_n$	**L^{2S}G$_n$**	36	76 (+40)	73 (+37)	52 (+16)	63 (+27)
L^{B}G$_n$	**L^{B}G$_n$**	27	27 (0)	27 (0)	27 (0)	27 (0)
htel**L^{2S}$_4$**A	AGG **L^{2S}**TT A**L^{2S}**G GTT AGG **L^{2S}**TT A**L^{2S}**G G	33	56 (+23)	45 (+12)	36 (+3)	35 (+2)
htel**L^{B}$_4$**	AGG **L^{B}**TT A**L^{B}**G GTT AGG **L^{B}**TT A**L^{B}**G G	12	12 (0)	12 (0)	12 (0)	12 (0)
htel**L^{2S}$_4$**D	AGG **L^{2S}**TT T**L^{2S}**G GTT AGG **L^{2S}**TT T**L^{2S}**G G	40	60 (+20)	46 (+6)	40 (0)	40 (0)
htel**L^{B}$_3$L^{2S}**	AGG **L^{2S}**TT A**L^{B}**G GTT AGG **L^{B}**TT A**L^{B}**G G	17	17 (0)	17 (0)	17 (0)	17 (0)
htel**L^{B}$_2$L^{2S}$_2$**	AGG **L^{2S}**TT A**L^{B}**G GTT AGG **L^{2S}**TT A**L^{B}**G G	23	24 (+1)	23 (+0)	23 (0)	23 (0)
htel**L^{B}L^{2S}$_3$**	AGG **L^{2S}**TT A**L^{2S}**G GTT AGG **L^{2S}**TT A**L^{B}**G G	28	32 (+4)	28 (+0)	28 (0)	28 (0)
htel**L^{2S}$_6$**	AGG **L^{2S}**T**L^{2S}** T**L^{2S}**G GTT AGG **L^{2S}**T**L^{2S}** T**L^{2S}**G G	36	54 (+18)	59 (+23)	44 (+8)	44 (+8)
htel**L^{B}$_4$L^{2S}$_2$**	AGG **L^{B}**T**L^{2S}** T**L^{B}**G GTT AGG **L^{B}**T**L^{2S}** T**L^{B}**G G	17	23 (+6)	18 (+1)	18 (+1)	17 (0)
htel**L^{B}$_3$L^{2S}$_3$**	AGG **L^{B}**T**L^{2S}** T**L^{2S}**G GTT AGG **L^{B}**T**L^{B}** T**L^{2S}**G G	26	35 (+9)	26 (+0)	31 (+5)	25 (-1)
htel**L^{B}$_2$L^{2S}$_4$**	AGG **L^{2S}**T**L^{B}** T**L^{2S}**G GTT AGG **L^{2S}**T**L^{B}** T**L^{2S}**G G	26	60 (+34)	48 (+22)	32 (+6)	27 (+1)

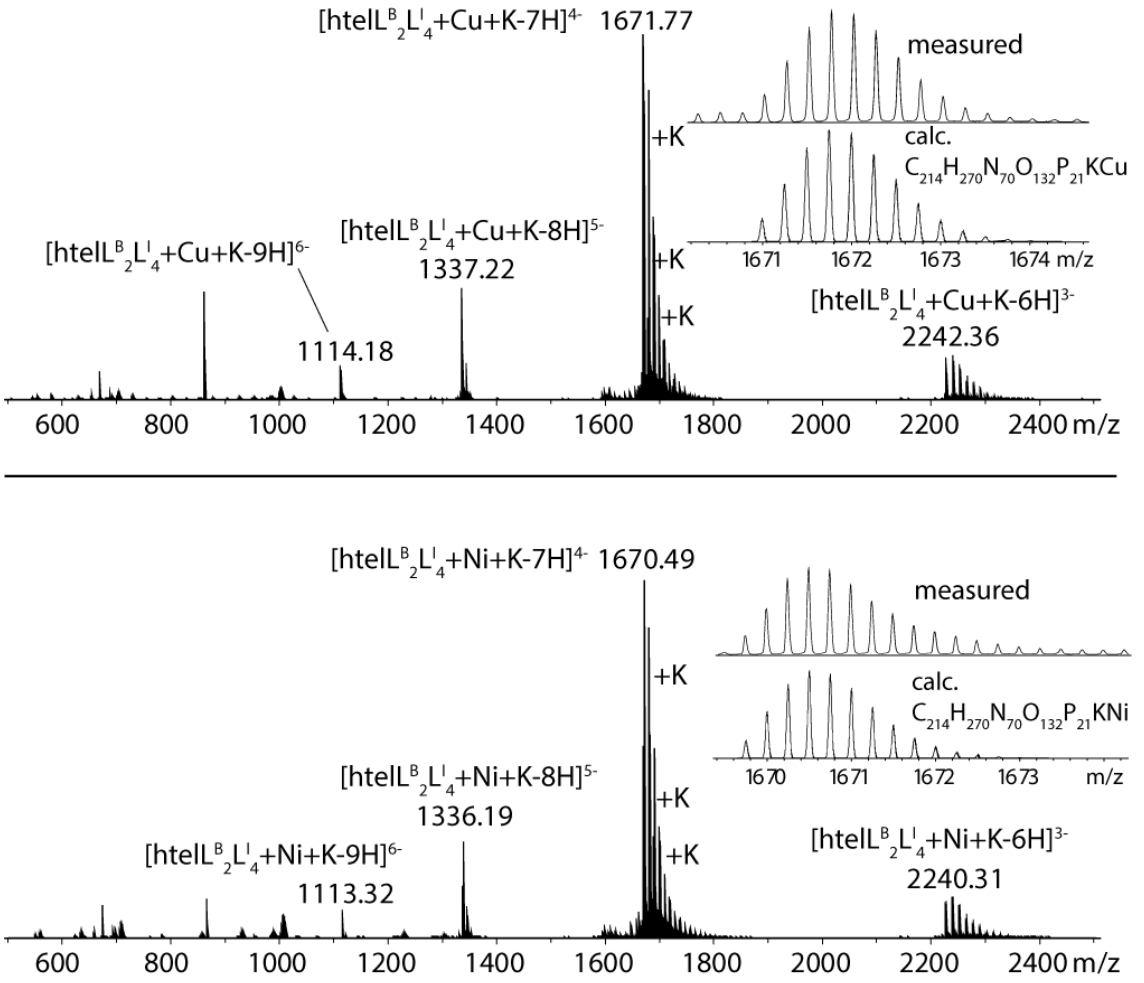

Figure 60. Native ESI-MS spectra of htel**L$^{B}_{2}$L$^{2S}_{4}$** in presence of Cu^{II} (upper spectrum) and Ni^{II} (lower spectrum). Conditions: 12.5 µM ssDNA, 12.5 µM $CuSO_4$ or $NiSO_4$, 0.5 mM KCl, 50 mM TMAA pH 6.8, H_2O:ACN, 1:1. Reprinted from ref.[30] Published under the terms of the Creative Commons CC BY license.

After showing that at least three **L^{2S}** were required for metal complexation, next DNA sequences with six ligandosides were investigated. For htel**L$^{B}_{4}$L$^{2S}_{2}$**, htel**L$^{B}_{3}$L$^{2S}_{3}$**, and htel**L$^{B}_{2}$L$^{2S}_{4}$**, again CD spectroscopy could show the same antiparallel topology as for htel**L$^{B}_{4}$**. Pleasingly, now a series of transition metal cations was shown to form stable complexes (**Table 3**). Interestingly, even for htel**L$^{B}_{4}$L$^{2S}_{2}$** addition of 1 equiv. Cu^{II} resulted in a distinct thermal stabilization of ΔT_m = +6 °C. Considering that previously it was found, that at least three **L^{2S}** were necessary to complex Cu^{II} it was concluded that in htel**L$^{B}_{4}$L$^{2S}_{2}$** at least one benzoate ligandoside was involved in coordination. In htel**L$^{B}_{3}$L$^{2S}_{3}$**, addition of Cu^{II} resulted in a slightly higher thermal stabilization (ΔT_m = +9 °C) due to the additional **L^{2S}**. More interesting was that now Zn^{II} was found to induce a stabilization of ΔT_m = +5 °C, while Ni^{II} showed no stabilization at all, which was the first time that Zn^{II} showed a higher stabilization. This becomes especially interesting in combination with another sequence called htel**L$^{2S}_{4}$**D. It was initially designed as a control sequence as it will be discussed later. But for htel**L$^{2S}_{4}$**D only a stabilization was observed after Ni^{II} addition (ΔT_m = +6 °C),

while after addition of Zn^{II} (ΔT_m = +0 °C), no effect was observed. This means that the pair of sequences htel$\mathbf{L^B}_3\mathbf{L^{2S}}_3$ and htel$\mathbf{L^{2S}}_4$D offers potential as an orthogonal system in which Zn^{II} and Ni^{II} selectively bind to one G-quadruplex over the other. But this could not be proofed yet and further studies, which include native ESI-MS will be necessary.

The last sequence investigated was htel$\mathbf{L^B}_2\mathbf{L^{2S}}_4$, which showed an unprecedented high thermal stabilization after addition of Cu^{II} (ΔT_m = +34 °C). The question was if this was the result of $\mathbf{L^B}$ being involved in coordination or if other effects were underlying. To answer this question a new sequence was designed in which the two $\mathbf{L^B}$ were replaced with two thymine, called htel$\mathbf{L^{2S}}_4$D. Addition of Cu^{II} resulted in a significantly lower thermal stabilization of ΔT_m = +20 °C, but the absolute melting temperature was T_m = 60 °C and therefore exactly the same as observed for htel$\mathbf{L^B}_2\mathbf{L^{2S}}_4$ ($T_m(Cu^{II})$= 60 °C). For this reason, it was concluded that the very high thermal stabilization observed for htel$\mathbf{L^B}_2\mathbf{L^{2S}}_4$ after addition of Cu^{II} (ΔT_m = +34 °C) was a compensation of the destabilizing electrostatic repulsion from $\mathbf{L^B}$. Similarly, for the addition of Ni^{II} to htel$\mathbf{L^B}_2\mathbf{L^{2S}}_4$ a very high thermal stabilization (ΔT_m = +22 °C) was observed. However, addition of Ni^{II} to htel$\mathbf{L^{2S}}_4$D (ΔT_m = +6 °C) resulted again in a much lower thermal stabilization but the absolute melting temperature ($T_m(Ni^{II})$= 46 °C) was almost the same. Therefore, as for Cu^{II}, this was explained with a compensation of the negative charges. The complexation of Cu^{II} and Ni^{II} by htel$\mathbf{L^B}_2\mathbf{L^{2S}}_4$ was further confirmed by native ESI-MS (**Figure 60**) showing for both metals a clear main species $[\text{htel}\mathbf{L^B}_2\mathbf{L^{2S}}_4\text{+Cu+K-7H}]^{4-}$ and $[\text{htel}\mathbf{L^B}_2\mathbf{L^{2S}}_4\text{+Ni+K-7H}]^{4-}$ corresponding to folded G-quadruplexes in complex with Cu^{II} and Ni^{II}, respectively. In case of Zn^{II} for htel$\mathbf{L^B}_2\mathbf{L^{2S}}_4$, no significant increase of ΔT_m compared to htel$\mathbf{L^B}_3\mathbf{L^{2S}}_3$ was observed indicating that the coordination environment of Zn^{II} is already saturated in htel$\mathbf{L^B}_3\mathbf{L^{2S}}_3$, which would in turn speak for an involvement of $\mathbf{L^B}$ in the coordination. Interestingly for Co^{II}, none of the G-quadruplexes containing $\mathbf{L^B}$ showed any signs of complexation.

5.3 Summary

As a conclusion, it is summarised that an imidazole-based ligandoside $\mathbf{L^{2S}}$ and a benzoate-based ligandoside $\mathbf{L^B}$ were incorporated into a series of G-quadruplex forming sequences to create heteroleptic coordination environments. Interestingly, incorporation of $\mathbf{L^B}$ showed a strongly destabilizing effect which linearly increased with the number of $\mathbf{L^B}$ and was therefore dedicated to a repulsion of the accumulating negative charges. When the interactions with a series of transition metal cations were investigated, it was found that sequences containing only $\mathbf{L^B}$ showed no signs of metal complexation. A minimum of two $\mathbf{L^{2S}}$ in htel$\mathbf{L^B}_4\mathbf{L^{2S}}_2$ was required to complex Cu^{II}. It was further found that

the incorporation of $\mathbf{L^B}$ allowed a further fine-tuning of metal affinities in which respect a pair of orthogonal sequences (htel$\mathbf{L^{2S}}_4$D and htel$\mathbf{L^B}_3\mathbf{L^{2S}}_3$) was found, that selectively complexed Ni^{II} over Zn^{II} and *vice versa*.[30] Conclusively, the design of heteroleptic coordination environments adds a third layer to fine-tune metal affinities besides the previously established concepts of varying ligandoside numbers as well as positions.[31] This represents another important step towards the overall goal to use this concept for the rational design of metallo-DNAzymes and will be further developed in the future. The results of this chapter were published in a scientific article and will also be part of the dissertation of Lukas M. Stratmann.[30]

6 G-QUADRUPLEX BASED ASYMMETRIC CATALYSIS

6.1 Sequence Design

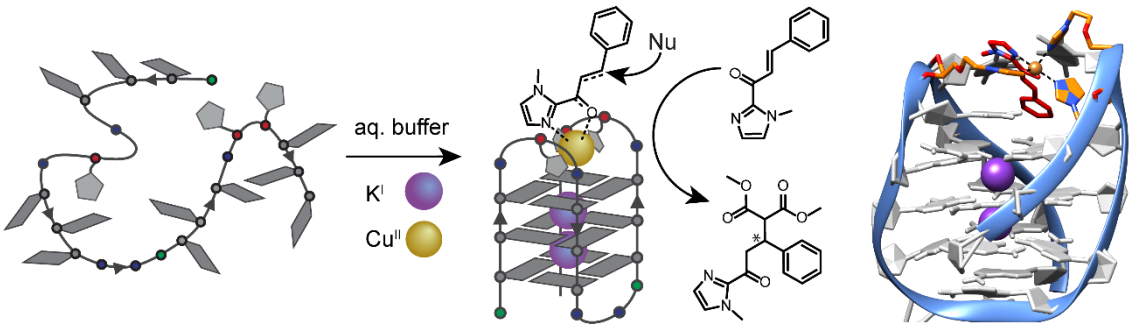

Figure 61. Schematic representation of the G-quadruplex formation and proposed mechanism of a Cu^{II}-catalysed Michael-Addition. On the right side a snapshot from a MD simulation of htel**L**$^{2S}_{3}$D with Michael-acceptor imidazole chalcone and Cu^{II} is shown.

The concept of metal-mediated G-quadruplexes was systematically studied in the previous chapters and here the concept is utilized to design G-quadruplexes for asymmetric catalysis. The field was established by the early works of Roelfes and Feringa in 2005. They used Cu^{II} complexes, that bound to undefined salmon testis DNA *via* non covalent interactions to catalyse an asymmetric Diels-Alder reaction in high enantiomeric ratios.[227] Later, they expanded the approach for enantioselective Friedel-Crafts reactions and Michael-Additions.[214,215,217] While the advantage of this approach was, that cheap salmon testis DNA with simple intercalating Cu^{II} complexes could be used, the nature of the undefined DNA sequence was impeding detailed atomistic studies. Therefore, novel systems with defined sequences were developed, using covalent approaches, where the metal chelating ligand was attached *via* a linker to the DNA. Although this was synthetically more demanding, advantage of these systems was, that the exact position of the chelating unit within the sequence was known, allowing to mutate the neighbouring nucleobases to optimize the efficiency and enantioselectivity.[315–318] As the first examples mostly used duplex DNA, later the concept was expanded to DNA G-quadruplexes, allowing the asymmetric oxidation of sulfides, Friedel-Crafts reactions, Michael-Additions and even cyclopropanation reactions.[213,219,234,235] Even if the ligands were covalently attached, a common drawback was a lack of knowledge about exact coordination environment, since the ligands were attached *via* long flexible linkers, allowing them to move into different positions. Also,

apart from a single recently published example,[316] the ligand moieties were always bi- or tridentate to ensure a strong Cu^{II} coordination, but it also restricted the possibilities to fine-tune the ligand arrangement. This is different in the here established system, in which the use of monodentate imidazole ligandosides allows much more control in the design of sequences. This way it was possible to optimize in iterative rounds of sequence design and screening highly efficient G-quadruplexes, that catalyse Michael-Additions in high enantiomeric ratios.

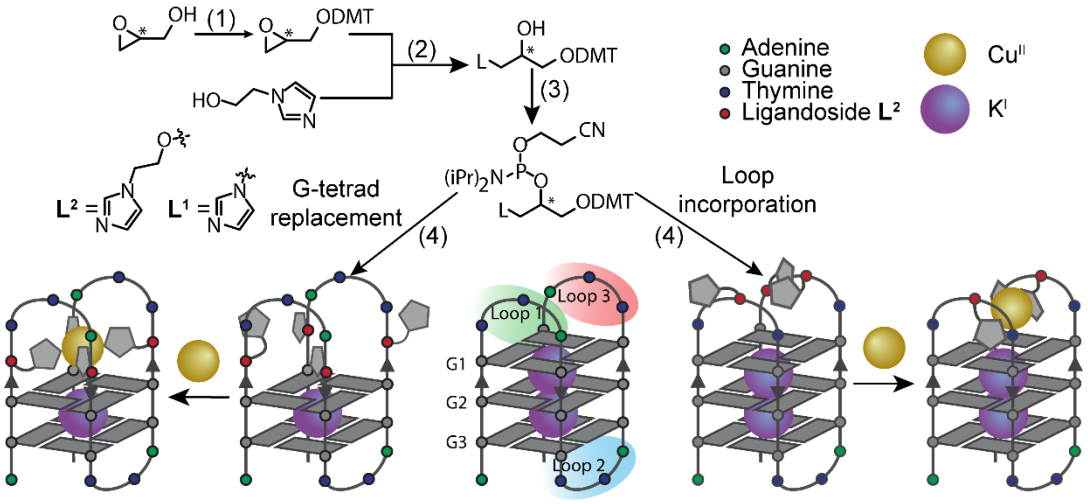

Figure 62. Synthetic route to access the phosphoramidite building blocks (*R*/*S*)-**7**, (*R*/*S*)-**8** and (*R*/*S*)-**32**. (1) DMT-protection of (*R*/*S*)-**1** with DMT-Cl and NEt_3 in CH_2Cl_2 at rt (2) Nucleophilic ring opening with imidazole in dioxane at 70 °C (**L¹**) or with N-hydroxyethyl-imidazole (**L²**), NaH in DMF at 40 °C (3) Phosphitylation of (*R*/*S*)-**5** and (*R*/*S*)-**6** with CEDIP-Cl and DIPEA in CH_2Cl_2 at rt. (4) DNA solid phase synthesis and schematic representations of G-quadruplexes where the imidazole ligandosides were either incorporated in the loop regions or by replacement of a G-tetrad. DMT = 4,4′-Dimethoxytrityl, DMF = dimethylformamide, CEDIP-Cl = 2-Cyanoethyl N,N-diisopropylchlorophosphoramidite, DIPEA = Diisopropylethylamine.

Here the proof of concept is shown, that our approach of metal-mediated G-quadruplexes can be used in asymmetric catalysis. As benchmark reaction, a Cu^{II}-catalysed Michael-Addition of a Michael-acceptor, here imidazole chalcone **MA1**, (**Table 4**) with DMM (dimethyl malonate) was investigated. In these systems, Cu^{II} activates as Lewis-acid the substrate for the attack of a nucleophile (**Figure 61**) and depending on the DNA secondary coordination sphere, the nucleophilic attack is preferred from either the *si* or *re* site, leading to an enantiomeric excess. For the sequence design of G-quadruplexes, two considerations were made. First, a coordinationally unsaturated Cu^{II} centre is mandatory to allow a substrate coordination, limiting the number of **L²** to ≤ 3, and second, the ligandosides must be arranged in a certain proximity to allow a chelation of Cu^{II}. For this purpose, the imidazole ligandoside **L²** was incorporated into the loops of htel by replacement of either adenine or thymine, leading to sequences of the type A GGG **TTA** GGG TTA GGG **TTA** GGG, where the

bold residues were replaced with **L²**. Sequences were synthesized, as previously described (**Chapter 3** and **9.1**), by DNA solid phase synthesis. At the end of this chapter in **Table 11** all investigated sequences can be found. Phosphoramidites of **L²** were accessed in a four steps synthesis (**Figure 62**).

6.2 Catalytic studies

The first two sequences designed were htel**L**$^{2S}_2$A and htel**L**$^{2S}_3$A. For catalytic studies, samples were prepared with 100 mM KCl, 10 mM HEPES pH 8, 1 mM substrate, 100 mM DMM, 1 % v/v DMSO, 120 µM DNA and 100 µM $CuSO_4$. This corresponded to a catalyst loading of 10 % with respect to Cu^{II}. An excess of DNA was used to ensure that no free Cu^{II} was left in solution, which could catalyse the Michael-Addition in a racemic fashion resulting in lower enantioselectivities. The slightly basic pH of 8 was important to allow a deprotonation of DMM. After G-quadruplexes were annealed (85 °C for 10 minutes, then cooling to 4°C with 0.5 °C min^{-1}), the substrates were added, and the reactions were incubated at 5 °C for 3 d. Samples were extracted with Et_2O, dried over $MgSO_4$ and the solvent was evaporated using a vacuum concentrator. Conversion and *ee* (enantiomeric excess) were analysed by chiral HPLC (**Figure 63**). For more details it is referred to **9.4**. Thee absolute stereo configuration of the Michael-adduct was determined with the optical activity [α] of the enantiopure product. Comparison with literature led to the conclusion, that the enantiomer eluting at ~ 14 min was the (*S*) enantiomer and at ~20 min the (*R*) enantiomer (**Figure 63**).[242]

Table 4. Initial screening of different G-quadruplex-forming sequences with 0-7 counts of **L**^{2S}. Conditions: 120 µM G-quadruplex, 100 µM $CuSO_4$, 10 mM HEPES pH 8, 100 mM KCl, 100 mM DMM, 1 mM substrate and 1 % v/v DMSO, 5° C, 3d. All experiments were performed in duplicate. The error was defined as the difference of two experiments and is within ± 5 %.

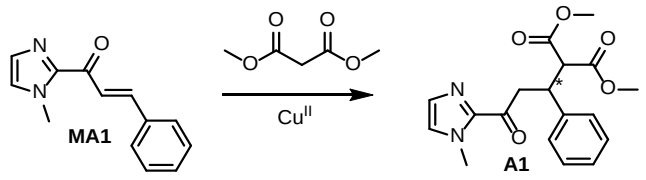

Entry	Sequence	**L**	Conversion	*ee*
0	-	-	23	1 (*S*)
1	cMyc	0	12	1 (*R*)
2	htel	0	10	5 (*S*)
3	htel**L**$^{S}_2$A	2	28	33 (*S*)
4	htel**L**$^{S}_3$A	3	23	29 (*R*)
5	htel**L**$^{S}_4$A	4	10	25 (*R*)
6	htel**L**$^{S}_6$	6	0	0
7	htel**L**$^{S}_7$	7	17	27 (*R*)

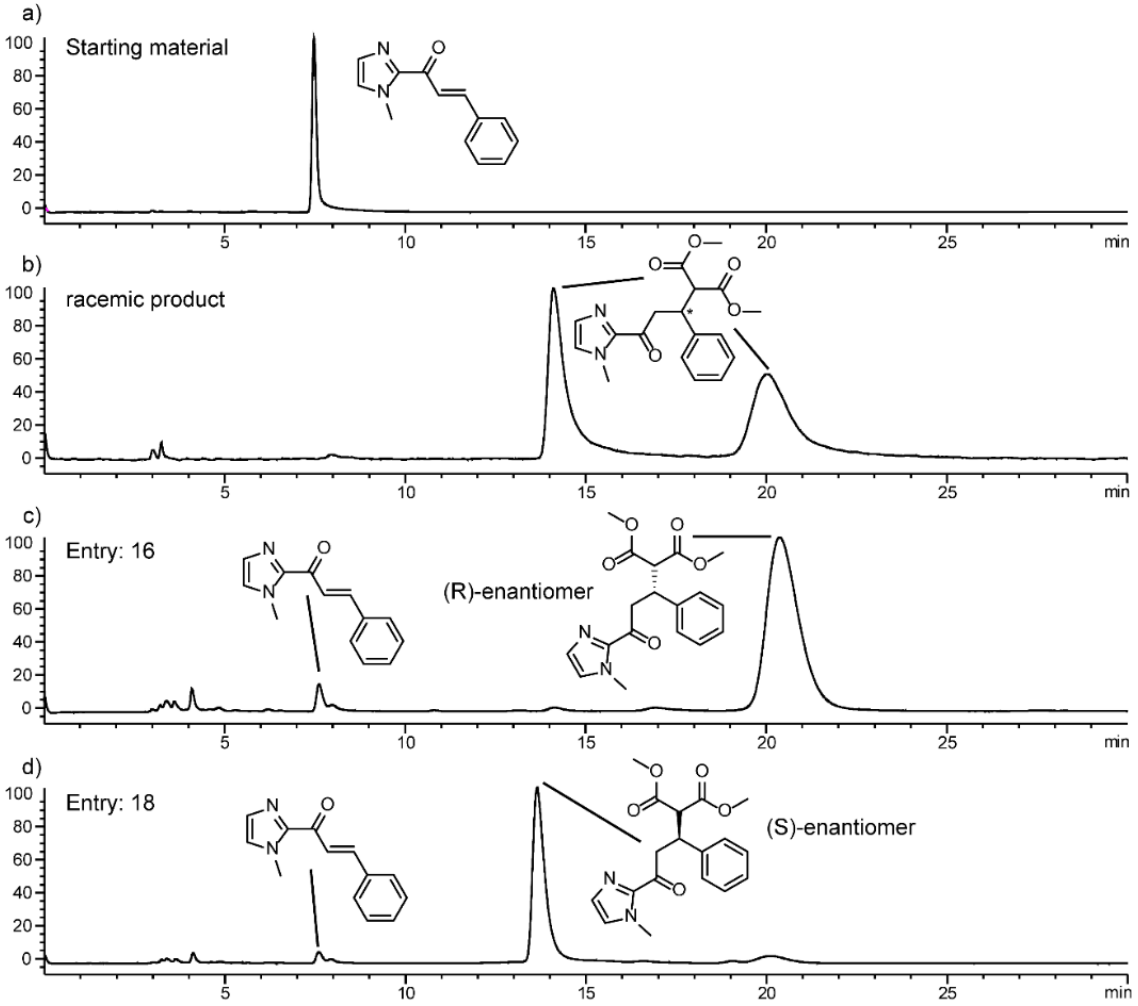

Figure 63. HPLC traces of a) imidazole chalcone **MA1**, b) the DMM Michael-adduct and c, d) the crude reaction mixtures of entry **16** (htel**L**$^{2R}{}_3$D) and **18** (htel**L**$^{2R}{}_3$G). HPLC Conditions: *Agilent Technologies 1260 Infinity* HPLC equipped with a chiral phase *CHIRALPAK IA-3* column (Amylose tris(3,5-dimethylphenylcarbamate) immobilized on 3 µM silica-gel) using a solvent mixture of *n*Hexane:*iso*Propanol, 80:20 with a flow rate of 1 mL min^{-1}, detection at 254 nm, bandwidth 8 nm.

After analysing the reactions, it became clear that htel**L**$^{2S}{}_2$A (28 % conversion, 33 % (*S*) and htel**L**$^{2S}{}_3$A (23 % conversion, 29 % (*R*)) significantly improved the reaction compared to unmodified htel (10 % conversion, 5 % (*S*)). Pleasingly, htel**L**$^{2S}{}_2$A and htel**L**$^{2S}{}_3$A enriched the opposite enantiomers showing the potential to design DNAzymes for both enantiomers without the need to invert the complete stereochemistry of the DNA backbone. To show that indeed ≤ 3 **L**^{2S} were needed a series of sequences containing ≥ 4 **L**^{2S} was screened and indeed they were shown to poorly perform in the Michael-Addition, as for all poor conversions were observed (< 17 %). As previously explained, this was the reason of a saturated Cu^{II} coordination environment, which prevents the substrate from coordination and therefore the substrate is not activated for the Michael-Addition.

Table 5. Conversions and enantioselectivities of different G-quadruplex forming sequences with 2 and 3 $\mathbf{L^{2S}}$ in presence of KCl and NaCl. Conditions:120 µM G-quadruplex, 100 µM $CuSO_4$, 10 mM HEPES pH 8, 100 mM KCl/NaCl, 100 mM DMM, 1 mM substrate and 1 % v/v DMSO. All experiments were performed in duplicate. The error was defined as the difference of two experiments and is within ± 5 %.

Entry	Seq.	L^S, Loop 1	L^S, Loop 2	Salt	Conversion	ee [%]
8	htel$\mathbf{L^S}_2$F	2	0	KCl	75	46 (*S*)
9	htel$\mathbf{L^S}_2$H	2	0	KCl	73	4 (*S*)
10	htel$\mathbf{L^S}_2$F	2	0	NaCl	78	71 (*S*)
11	htel$\mathbf{L^S}_2$H	2	0	NaCl	67	61 (*S*)
12	htel$\mathbf{L^S}_3$J	1	2	KCl	97	91 (*R*)
13	htel$\mathbf{L^S}_3$B	1	2	KCl	92	96 (*R*)
14	htel$\mathbf{L^S}_3$J	1	2	NaCl	25	46 (*R*)
15	htel$\mathbf{L^S}_3$B	1	2	NaCl	45	61 (*R*)

Encouraged by the results, a new series of sequences was synthesized all containing two and three $\mathbf{L^{2S}}$ incorporated in loop **1** and **3**, while retaining a constant loop length of three bases. Catalytic studies with the new set of sequences unveiled crucial structure-function relationships leading to highly efficient sequences. One group of sequences (htel$\mathbf{L^{2S}}_3$B, htel$\mathbf{L^{2S}}_3$H-M) was found to efficiently catalyse the reaction with conversions >80 % and enantioselectivities of up to 96 % *ee* (*R*). Common for this group of sequences was that $\mathbf{L^{2S}}$ was incorporated three times, one in loop **1** and two in loop **3**, separated by one base. Out of this group of sequences, the best performing sequence htel$\mathbf{L^{2S}}_3$B (92 % conversion, 96 % (*R*)) contained besides $\mathbf{L^{2S}}$ only thymine in loop **1** and **3**, whereas the others contained at least one adenine. This was suggesting, that the formation of A-T base pairs in the loop regions had a detrimental influence on the enantioselectivity. It was also found, that apparently small changes in the sequence could have a drastic influence on the catalysis. For example, after **T**18 and $\mathbf{L^{2S}}$19 in Loop **3** (htel$\mathbf{L^{2S}}_3$B (92 % conversion, 96 % (*R*)) were swapped to $\mathbf{L^{2S}}$18 and **T**19 (htel$\mathbf{L^{2S}}_3$C, 40 % conversion, 57 % (*S*)) an inversion of the enantioselectivity was observed, while changing **T**18 and $\mathbf{L^{2S}}$17 in Loop **3** (htel$\mathbf{L^{2S}}_3$B) to $\mathbf{L^{2S}}$18 and **T**17 in htel$\mathbf{L^{2S}}_3$D (80 %, conversion, 91 % *ee* (*R*)) had almost no influence.

Table 6. Melting temperatures of selected sequences with KCl and NaCl as electrolyte. Conditions: 1.88 µM DNA, 1.88 µM $CuSO_4$, 100 mM electrolyte, 10 mM HEPES pH 8.

Name	KCl	NaCl	KCl, Cu^{II}	NaCl, Cu^{II}
htel**L**$^{2S}_3$B	62	48	66 (+4)	53 (+5)
htel**L**$^{2S}_3$D	62	46	71 (+9)	55 (+9)
htel**L**$^{2S}_2$F	67	52	68 (-1)	52 (0)
htel**L**$^{2S}_2$G	58	46	58 (0)	46 (0)
htel**L**$^{2R}_3$D	63	-	68 (+5)	-
htel**L**$^{2R}_3$H	68	-	68 (0)	-
htel**L**$^{2R}_2$F	-	49	-	50 (+1)
htel**L**$^{2R}_2$G		47		47 (0)

More systematic was the effect, when **L**^{2S} was incorporated two times in loop **1** and once in loop **3** (htel**L**$^{2S}_3$A, htel**L**$^{2S}_3$E and htel**L**$^{2S}_3$F), which resulted in a strong corrosion of both conversion < 30 % and *ee* < 30 %. Also, sequences in which **L**^{2S} was incorporated two times, generally showed poor enantioselectivities, although for some very good conversions of up to 97 % were observed. Interestingly, this completely changed when NaCl instead of KCl was used as the electrolyte. Now, for the previously good performing sequences htel**L**$^{2S}_3$B, htel**L**$^{2S}_3$D and htel**L**$^{2S}_3$H-M a drastic drop of both, conversion (≤ 65 %) and *ee* (≤ 68 % (*R*)) was observed, but therefore another group of sequences (htel**L**$^{2S}_2$F-H) containing only two **L**^{2S} in loop **1** showed improved enantioselectivities of the opposite enantiomer of up to 71 % *ee* (*S*). An inversion of the enantioselectivity depending on the coordination number was previously described in a similar study, which used bi- and tridentate chelate ligands in a Diels-Alder reaction. DFT calculations suggested that two different chiral pockets were created from the bi- and tridentate ligands together with the DNA, although it could not be proofed.[319] However in this case, with the number of imidazole ligandosides it was not possible to explain the dependency of the enantioselectivity on the chosen electrolytes NaCl and KCl.

6.3 Structural Analysis

To investigate this question, htel**L**$^{2S}_2$G and htel**L**$^{2S}_2$D were investigated by UV/Vis and CD spectroscopy. As expected, TDS for both sequences in KCl and NaCl containing buffers were consistent with the formation of G-quadruplexes, indicated by a maximum at ~ 272 nm and a minimum at ~295 nm. Below 250 nm the spectra were dominated by the absorption of the HEPES buffer and could not be interpreted. Addition of Cu^{II} had only minor effects on the TDS. CD spectroscopy could proof for both htel**L**$^{2S}_2$G and htel**L**$^{2S}_3$D the formation of clear antiparallel topologies, when NaCl was used as electrolyte. Addition of Cu^{II} showed only minor effects on the CD spectra. With KCl as

electrolyte this picture changed. In absence of Cu^{II} the CD spectra appeared similar to a (3+1) hybrid topology but could also correspond to a mixture of topologies.[82,320] Addition of Cu^{II} induced a change towards an antiparallel topology. Although this effect was observed for both htel**L**$^{2S}_2$G and htel**L**$^{2S}_3$D, it was much stronger in case of htel**L**$^{2S}_3$D, which could be explained with a better templating effect. For htel**L**$^{2S}_3$D, only in case of an antiparallel topology all three **L**^{2S} are able to coordinate to Cu^{II}. In contrast, for htel**L**$^{2S}_2$G both **L**^{2S} are next to each other in the sequence and can always simultaneously coordinate to Cu^{II}, independent of the given topology.

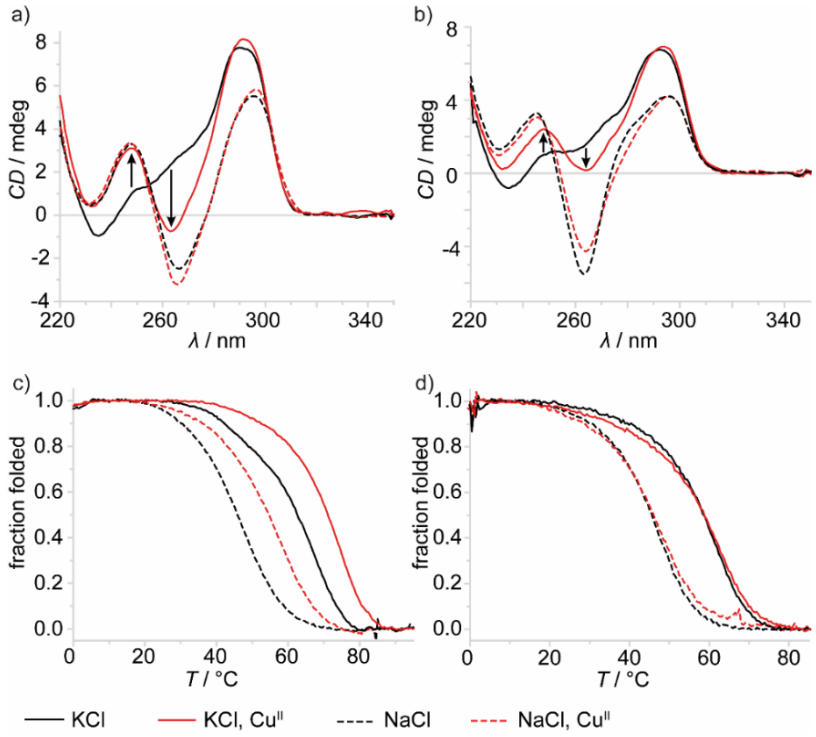

Figure 64. CD spectra and melting profiles of a, c) htel**L**$^{2S}_3$D and b, d) htel**L**$^{2S}_2$G with KCl (solid lines) and NaCl (dashed lines) in absence (black lines) and presence of Cu^{II} (red lines). Conditions: 1.88 µM DNA, 1.88 µM $CuSO_4$, 100 mM electrolyte, 10 mM HEPES pH 8.

Even more interesting was the finding that Cu^{II} still induced in htel**L**$^{2S}_2$G a topology change towards an antiparallel topology, highlighting once again, how sensible the topology of DNA G-quadruplexes reacts to external stimuli. Although CD spectroscopy of htel**L**$^{2S}_3$D (in KCl) and htel**L**$^{2S}_2$G (in NaCl) in presence of Cu^{II} could show for both sequences an antiparallel topology, the CD spectra still appeared slightly different. For htel**L**$^{2S}_3$D a very intense maximum at 292 nm but a very weak minimum at 263 nm was observed and for htel**L**$^{2S}_2$G the maximum at 297 nm was slightly shifted and showed a comparable intensity to the minimum at 265 nm. These differences in the CD spectra might be a hint to two different antiparallel topologies, in one case the basket-type and in the other case the chair-type.[63,66,83] These different types would result in different strand orientations of loop **1** and **3**. For the basket-type this would result in a parallel

orientation of loop **1** and **3** and for the chair-type in an antiparallel arrangement. As these different strand polarities could be the key to explain the different enantioselectivities of htel**L**^{2S}$_3$D (91 % (*R*)) and htel**L**^{2S}$_2$G (67 % (*S*)), at this stage it remains a hypothesis and further studies will be necessary to collect more evidence.

Thermal denaturation experiments of htel**L**^{2S}$_3$D showed in NaCl one clear transition with a corresponding melting temperature of T_m = 46 °C, indicating the formation of a single topology. In contrast with KCl, the melting profile indicated two transitions with a corresponding melting temperature of T_m = ~62 °C. Addition of Cu^{II} showed with both electrolytes a clear stabilization of ΔT_m = + 9 °C (NaCl) and ΔT_m = + 9 °C (KCl). Also, the melting profile in KCl showed after Cu^{II} addition only one transition indictive for a Cu^{II} induced shift towards a single topology (**Figure 64c**). For htel**L**^{2S}$_2$G with both electrolytes NaCl (T_m = ~46 °C) and KCl (T_m = ~58 °C) only one transition was observed. In contrast to htel**L**^{2S}$_3$D addition of Cu^{II} lead to no thermal stabilization, which was explained with two reasons. First, only two **L**^{2S} in htel**L**^{2S}$_2$G were available for Cu^{II} coordination, resulting in a weaker complexation, and second, in htel**L**^{2S}$_3$D the ligandoside **L**^{2S} is arranged in two opposite loops, once in loop **1** and twice in loop **3**. For this reason, Cu^{II} coordination leads to a crosslink between loop **1** and **3** resulting in a stabilization of the G-quadruplex. In htel**L**^{2S}$_2$G however, both **L**^{2S} are incorporated next to each other in loop **1** and accordingly Cu^{II} coordination is not leading to a stabilizing crosslink between the loops. The weaker Cu^{II} coordination of G-quadruplexes containing only two ligandosides was further supported by native ESI-MS with htel**L**^{2R}$_3$D and htel**L**^{2R}$_2$F (**Figure 66** and **Figure 68**). As a short reminder in case of folded G-quadruplexes a main species with n-1 potassium adducts would be observed, where n = number of G-tetrads, followed by a statistical distribution of additional unspecific potassium adducts.

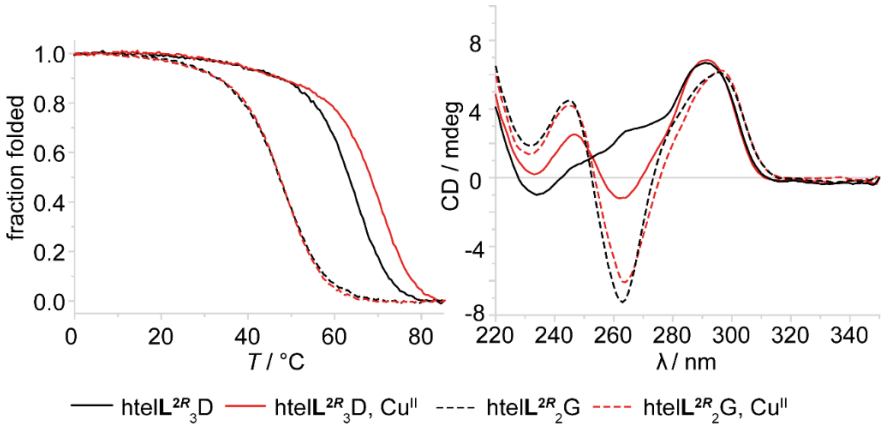

Figure 65. CD spectra and melting profiles of a, c) htel**L**^{2R}$_3$D and b, d) htel**L**^{2R}$_2$G with KCl (solid lines) and NaCl (dashed lines) in absence (black lines) and presence of Cu^{II} (red lines). Conditions: 2 µM DNA, 2 µM $CuSO_4$, 100 mM electrolyte, 10 mM HEPES pH 8.

While in absence of Cu^{II} for both sequences the species [htel**L**$^{2R}_3$D+2K-6H]$^{4-}$ and [htel**L**$^{2R}_2$F+2K-6H]$^{4-}$ were observed as main signals, corresponding to folded G-quadruplexes with three G-tetrads, in presence of Cu^{II} the spectra became more complex. For htel**L**$^{2R}_3$D as main species [htel**L**$^{2R}_3$D+Cu+2K-8H]$^{4-}$ was observed, in agreement with a folded G-quadruplex in complex with Cu^{II}. But with roughly half the intensity, another species [htel**L**$^{2R}_3$D+Cu+K-7H]$^{4-}$ could be observed with only one potassium ion bound. One possibility would be, that one potassium ion was lost during ionization, but this was rather unlikely since the potassium ions are usually strongly bound between the G-tetrads and can't be easily lost during ionization. Also, in absence of Cu^{II} the species htel**L**$^{2R}_3$D with only one bound potassium was a minor species. For this reason, another explanation was considered, in which Cu^{II} induced a structural change towards a topology with only two G-tetrads. Although two different G-quadruplex topologies were observed, both were mainly found in complex with Cu^{II}. This changed for htel**L**$^{2R}_2$F. In presence of Cu^{II} two main species [htel**L**$^{2R}_2$F+Cu+2K-8H]$^{4-}$ and [htel**L**$^{2R}_2$F+2K-6H]$^{4-}$ with almost identical intensities were observed. This was indicating, that htel**L**$^{2R}_2$F was losing Cu^{II} during the ionization process, pointing towards weaker interactions, in agreement with the thermal denaturation experiments previously discussed. The last open question was to what extent the stereo-configuration of **L**^{2} was affecting the catalysis, as until now only **L**^{2S} was incorporated.

Table 7. Influence of ligandoside stereo-configuration on conversion and enantioselectivity. 120 µM G-quadruplex, 100 µM $CuSO_4$, 10 mM HEPES pH 8, 100 mM electrolyte, 100 mM DMM, 1 mM substrate and 1 % v/v DMSO. The experiments were performed in duplicate. The error was defined as the difference of two experiments and is within ± 5 %.

Entry	Seq.	**L**	electrolyte	conversion	*ee*
16	htel**L**$^{R}_2$G	2	NaCl	92	90 (*S*)
17	htel**L**$^{R}_2$H	2	NaCl	93	56 (*S*)
18	htel**L**$^{R}_3$D	3	KCl	94	≥ 99 (*R*)
19	htel**L**$^{R}_3$B	3	KCl	97	84 (*R*)
20	htel**L**$^{R}_3$J	3	KCl	96	85 (*R*)
21	htel**L**$^{R}_3$K	3	KCl	94	67 (*R*)
22	htel**L**$^{R}_3$L	3	KCl	96	83 (*R*)

Therefore, a selection of the best performing sequences was resynthesized containing **L**^{2R}. Studies of the **L**^{2R} containing sequences could not show any systematic difference, i.e. sequences containing two **L**^{2R} in loop **1** enriched the (*S*) enantiomer while sequences containing one **L**^{2R} in loop **1** and twice in loop **3** enriched the (*R*) enantiomer. Although the stereo-configuration of **L**^{2} seemed to have only a minor influence, the two sequences htel**L**$^{R}_3$D (≥ 99 % (*R*) *ee*) and htel**L**$^{R}_2$G (90 % (*S*) *ee*) were identified with improved enantioselectivities as compared to htel**L**$^{S}_3$D (91 % (*R*) *ee*) and htel**L**$^{S}_2$G (67 % (*S*) *ee*).

From MD simulations of htel**L**^{2R}$_3$D (**Figure 70**) it is suggested, that neighbouring nucleobases were blocking the *Re* site for a nucleophilic attack, resulting in an exclusive nucleophilic attack from the *Si* site, giving rise to the high enantioselectivity.[215] Thermal denaturation experiments of htel**L**^{R}$_3$D and htel**L**^{R}$_2$G showed only for htel**L**^{R}$_3$D a thermal stabilization after Cu^{II} addition and CD spectroscopy proofed for both sequences in presence of Cu^{II} the formation of an antiparallel topology (**Figure 65, Table 6**). Compared to htel**L**^{S}$_3$D and htel**L**^{S}$_2$G these results were very similar, showing that the stereo-configuration had no significant effects on the topology and thermal stability.

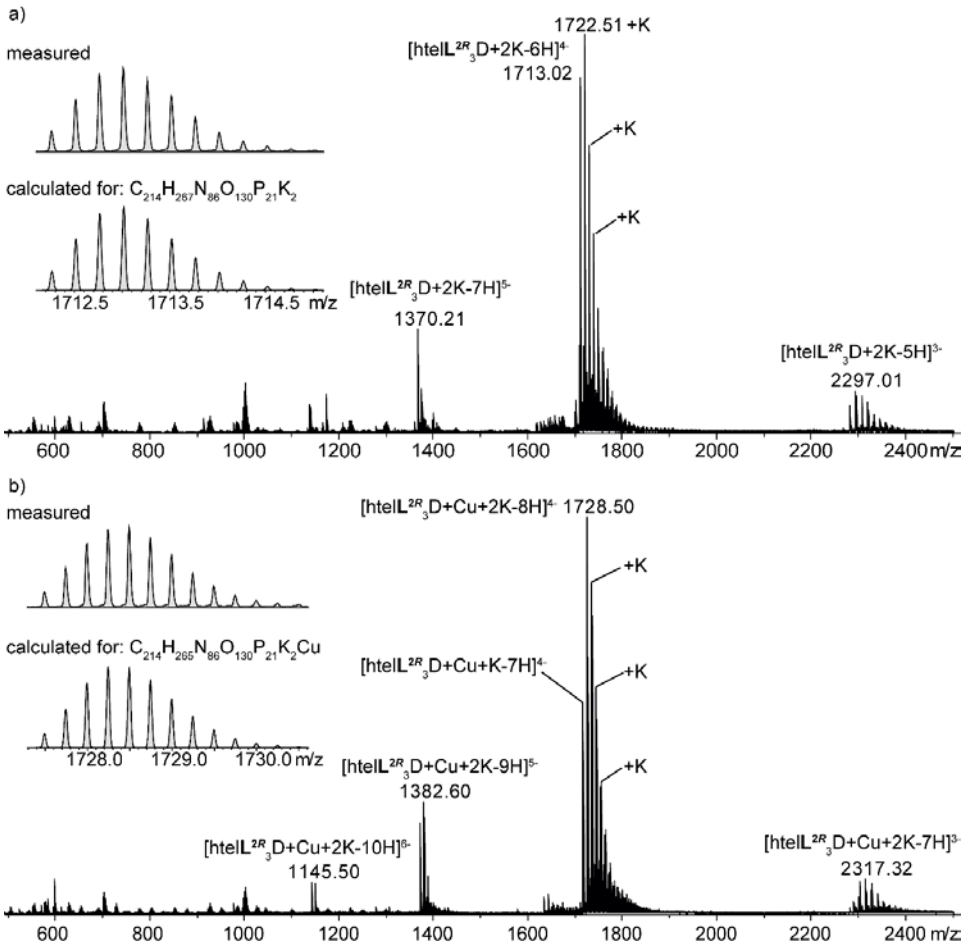

Figure 66. Native ESI-MS spectra of htel**L**^{2R}$_3$D in a) absence and b) presence of 1 equiv. Cu^{II}. Conditions: 12.5 µM G-quadruplex, 15 µM $CuSO_4$ 0.5 mM KCl and 50 mM TMAA pH 6.8, H_2O:ACN, 1:1.

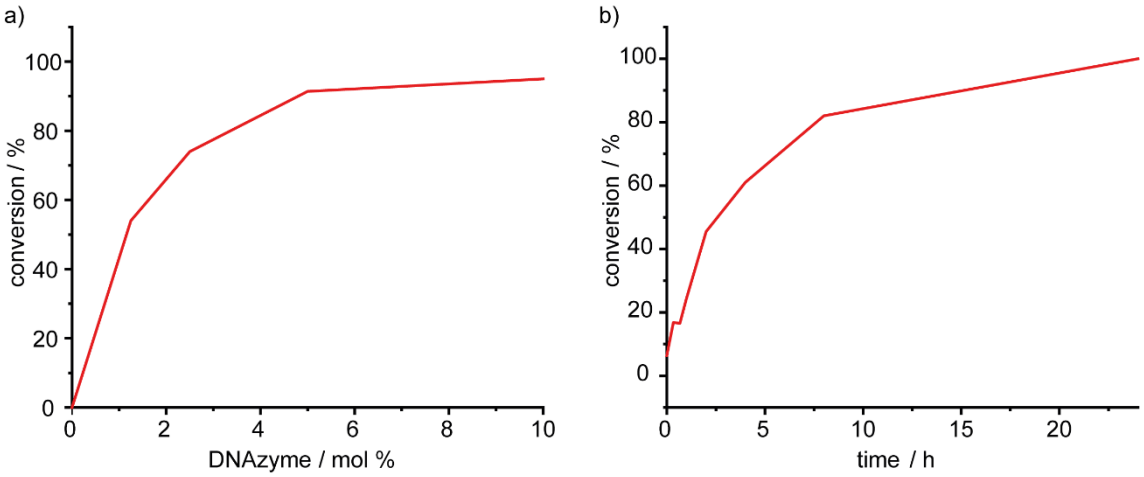

Figure 67. Optimization of the DNA concentration and reaction time with htel**L**$^{R}_{3}$D. a) The concentration of Cu^{II} is plotted against the conversion after two days at 5 °C. b) Aliquots from the reaction mixture with 120 uM htel**L**$^{R}_{3}$D and Cu^{II} were taken at different time steps. Conditions: 100 mM KCl, 10 mM HEPES pH 8, 1 mM substrate, 100 mM DMM, 1 % v/v DMSO.

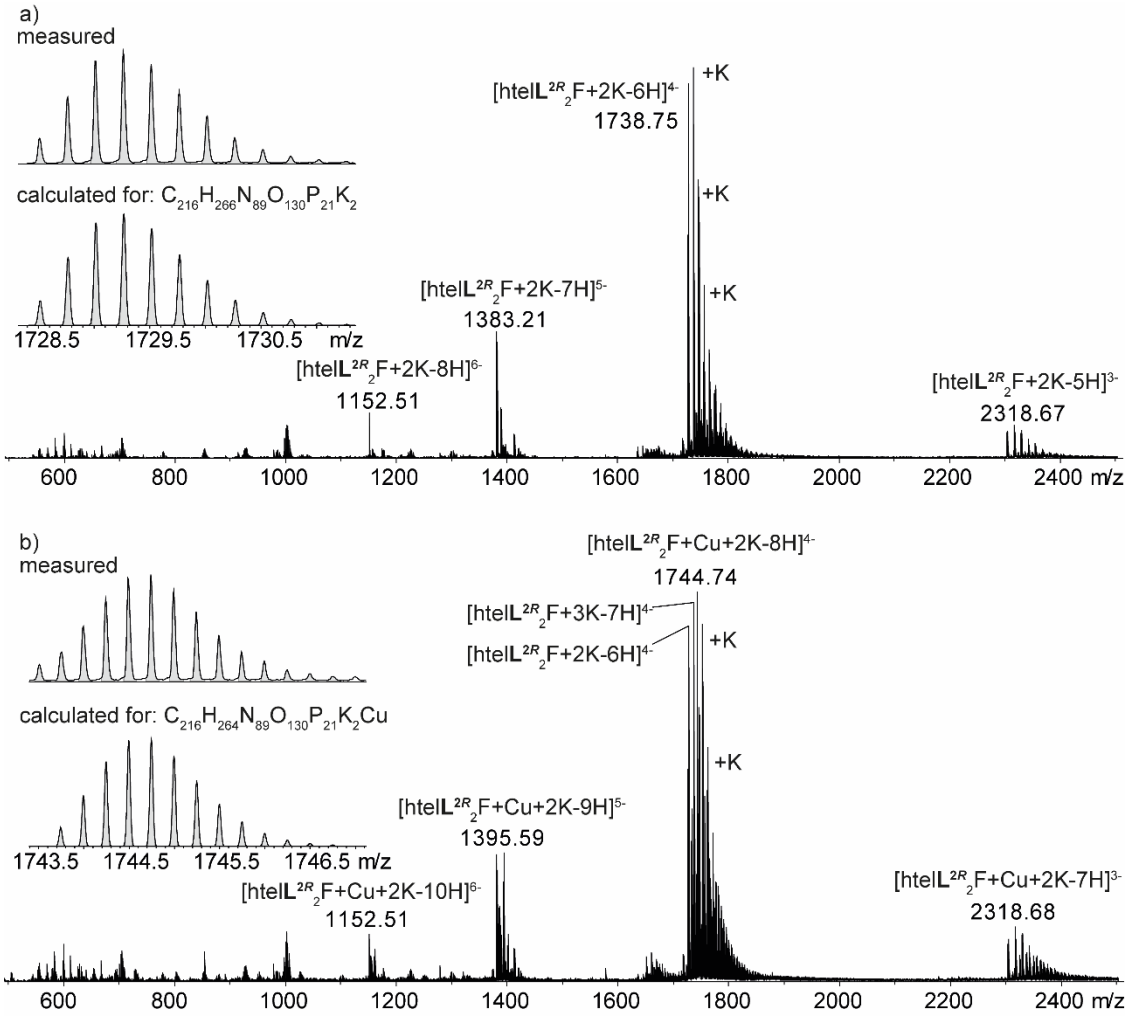

Figure 68. Native ESI-MS spectra of htel**L**$^{2R}_{2}$F in a) absence and b) presence of 1 equiv. Cu^{II}. Conditions: 12.5 µM G-quadruplex, 15 µM $CuSO_4$ 0.5 mM KCl and 50 mM TMAA pH 6.8, H_2O:ACN, 1:1.

6.4 Substrate scope

After the concept was established for the Michael-Addition, a substrate scope was investigated, to show the limits of the system. For this purpose, a series of substrates was synthesised with different substituents in para position of the phenyl ring. Also, one substrate was synthesized where N-methyl imidazole was replaced with pyridine.

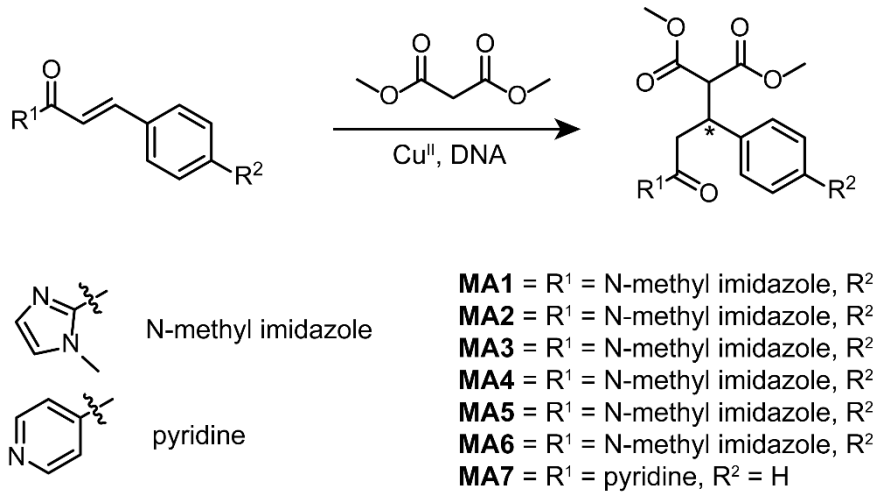

Figure 69. Substrate scope investigated for the Cu^{II} catalyzed Michael-Addition with the sequences htel**L**$^{2\boldsymbol{R}}$$_2$G and htel**L**$^{2\boldsymbol{R}}$$_3$D.

Stock solutions of all substrates were prepared as 100 mM stock solutions leading to 1% v/v DMSO in the sample mixture. Only exception was the nitro-substituted substrate **MA2**, which had a low solubility in DMSO. For this reason, a 25 mM stock solution in DMSO leading to a DMSO content of 4 % v/v in the sample. As shown later a concentration of up to 10 % v/v was not to interfering with the Michael-Addition. The absolute stereoconfiguration for the substrates was not assigned and the (+) refers to the earlier and (-) to the later eluting enantiomer.

For the substrate scope the two best sequences – in terms of the enantioselectivity – htel**L**$^{\boldsymbol{R}}$$_2$G and htel**L**$^{\boldsymbol{R}}$$_3$D were investigated. Substrate **MA2** with a nitro group in para position was shown to poorly react and only conversion of htel**L**$^{\boldsymbol{R}}$$_2$G: 10 %, htel**L**$^{\boldsymbol{R}}$$_3$D: 12 were observed compared to of 92 % (htel**L**$^{\boldsymbol{R}}$$_2$G) and 94 % (htel**L**$^{\boldsymbol{R}}$$_3$D) for the unsubstituted substrate **MA1**. The poor reactivity was attributed to the very low solubility of substrate **MA2**. Also, the electron withdrawing effect of the -NO_2 group could have a deactivating effect. This was supported from substrate **MA5** with an electron withdrawing -CF_3 group. Similarly, a lower conversion of only 49 % (htel**L**$^{\boldsymbol{R}}$$_2$G) and 59 % (htel**L**$^{\boldsymbol{R}}$$_3$D) was observed, but in very good enantioselectivities of 93 % (+) (htel**L**$^{\boldsymbol{R}}$$_2$G) and 98 % (-) (htel**L**$^{\boldsymbol{R}}$$_3$D). In agreement with these results for the substrates **MA3** (4-OCH_3) and **MA6** (4-CH_3) with electron donating groups higher conversions were observed, especially

substrate **MA6** with a conversion of 99 % for both sequences and 91 (+) (htel**L**$^{R}_{2}$G) and 99 (-) %(htel**L**$^{R}_{3}$D) *ee*. A bulky *tert* butyl group in **MA4** showed a lower reactivity compared to **MA1**, but interestingly for htel**L**$^{R}_{2}$G a better enantioselectivity of 95 % (+) was observed. This was probably due to the bulky *tert* butyl group, which caused a stronger induction from the chiral DNA. For **MA7**, where the N-methyl imidazole was replaced with pyridine very good conversions of 99 % for both sequences were observed, but this came with a strong decrease of the enantioselectivity 71 % (+) (htel**L**$^{R}_{2}$G) and 91 % (-) (htel**L**$^{R}_{3}$D). As a short summary, all investigated substrates, apart from **MA2**, showed very high enantioselectivities of ≥ 90 % *ee* and moderate to excellent conversion between 49 and 99 %. Interestingly, for all investigated substrates, again except for the poorly soluble substrate **MA2**, htel**L**$^{R}_{2}$G enriched the (+) enantiomer, while htel**L**$^{R}_{3}$D enriched the (-) enantiomer. Although the absolute stereo configuration was not determined, this might suggest, that the G-quadruplex properties leading to the (*R*) or (*S*) enantiomer of substrate **MA1**, were also valid for all substrates in the here investigated substrate scope.

Table 8. Conversion and enantioselectivities of the investigated Michael-acceptors **1** – **7**. Conditions: 120 µM DNA, 100 µM CuSO4, 10 mM HEPES pH 8, 100 mM electrolyte, 100 mM DMM, 1 mM substrate and 1 % v/v DMSO. 3 d incubation at 5°C. The experiments were performed in duplicate. The error was defined as the difference of two experiments. * 4 % v/v DMSO.

Seq.	electrolyte	L^{2R}	Substrate	conversion	*ee*
htel**L**$^{R}_{2}$G	NaCl	2	**MA1**	92 ± 5	90 (*S*) ± 1
htel**L**$^{R}_{2}$G	NaCl	2	**MA2**	10 ± 1	6 (-) ± 1
htel**L**$^{R}_{2}$G	NaCl	2	**MA3**	63 ± 31	84 (+) ± 1
htel**L**$^{R}_{2}$G	NaCl	2	**MA4**	69 ± 3	95 (+) ± 1
htel**L**$^{R}_{2}$G	NaCl	2	**MA5**	49 ± 4	93 (+) ± 1
htel**L**$^{R}_{2}$G	NaCl	2	**MA6**	97 ± 3	90 (+) ± 1
htel**L**$^{R}_{2}$G	NaCl	2	**MA7**	99 ± 1	71 (+) ± 1
htel**L**$^{R}_{3}$D	KCl	3	**MA1**	94 ± 5	99 (*R*) ± 1
htel**L**$^{R}_{3}$D	KCl	3	**MA2**	17 ± 2	88 (-) ± 10
htel**L**$^{R}_{3}$D	KCl	3	**MA3**	79 ± 4	98 (-)
htel**L**$^{R}_{3}$D	KCl	3	**MA4**	77 ± 4	95 (-) ± 1
htel**L**$^{R}_{3}$D	KCl	3	**MA5**	59 ± 6	98 (-) ± 1
htel**L**$^{R}_{3}$D	KCl	3	**MA6**	99 ± 1	99 (-) ± 1
htel**L**$^{R}_{3}$D	KCl	3	**MA7**	99 ± 1	91 (-) ± 1

6.5 Optimization of the Reaction Conditions

Table 9. Influence of the DNA and Cu^{II} concentration on conversion and *ee*. Conditions: DNA and $CuSO_4$ concentrations as mentioned, 10 mM HEPES pH 8, 100 mM electrolyte, 100 mM DMM,

1 mM substrate and 1 % v/v DMSO. 2 d incubation at 5°C. The experiments were performed in duplicate. The error was defined as the difference of two experiments and is within ± 5 %.

Seq.	DNA	Cu^{II}	L^{2R}	Electrolyte	Conversion	*ee*
htel**L**$^{R}_{2}$G	120	100	2	NaCl	92 ± 5	90 (*S*) ± 1
htel**L**$^{R}_{2}$G	60	50	2	NaCl	93 ± 3	92 (*S*) ± 1
htel**L**$^{R}_{2}$G	30	25	2	NaCl	65 ± 2	91 (*S*) ± 1
htel**L**$^{R}_{2}$G	12	10	2	NaCl	46 ± 1	89 (*S*) ± 1
htel**L**$^{R}_{3}$D	120	100	3	KCl	94 ± 5	≥ 99 (*R*) ± 1
htel**L**$^{R}_{3}$D	60	50	3	KCl	95 ± 2	≥ 99 (*R*) ± 1
htel**L**$^{R}_{3}$D	30	25	3	KCl	86 ± 10	≥ 99 (*R*) ± 1
htel**L**$^{R}_{3}$D	12	10	3	KCl	62 ± 1	≥ 96 (*R*) ± 2

After the proof of concept was established, further optimizations of the reaction conditions were anticipated. First the reaction time was optimized with htel**L**$^{R}_{3}$D (**Figure 67**). Therefore, aliquots were taken from the reaction mixture after different time steps, showing that the reaction was already completed after 1 d instead of 3 d (**Figure 67b**) and after only 8 h already ~80 % of the substrate were consumed. Much more important than a shorter reaction time, was to reduce the DNA concentration to save as much precious DNA as possible. So far concentrations of 120 µM DNA and 100 µM Cu^{II} were used, corresponding to a catalyst loading of 10 %. Considering the high molecular weight of the DNA of about ~6,000 g mol^{-1} vs 212.3 g mol^{-1} of the substrate, with 10 % catalyst loading roughly three times the mass of DNA was consumed compared to starting material. For this reason, the DNA concentration was stepwise reduced from 120 µM to 12 µM and the samples were incubated for 2 d at 5°C (**Figure 67 a**). For htel**L**$^{R}_{2}$G and htel**L**$^{R}_{3}$D no significant change of conversion and *ee* was observed, when the concentration was halved to 60 µM DNA. This changed after the concentration was further reduced to 30 µM DNA, showing a decreased conversion of 65 % for htel**L**$^{R}_{2}$G and 86 % for htel**L**$^{R}_{3}$D, while the enantioselectivity was unchanged. At 12 µM the conversion further decreased to 46 % for htel**L**$^{R}_{2}$G and 62 % for htel**L**$^{R}_{3}$D. Now, also the enantioselectivity became slightly worse (**Table 9**).

Table 10. Influence of cosolvents and molecular crowders on the conversion and enantioselectivity. 15 µM DNA, 12.5 µM $CuSO_4$, 10 mM HEPES pH 8, 100 mM KCl, 2d at 5 °C, 1 mM substrate, 100 mM DMM. The experiments were performed in duplicate. *[1]60 µM DNA, 50 µM $CuSO_4$,*[2] not reproduced.

Seq.	Cosolvent	Crowding agent	Conversion	*ee*
htel**L**$^{R}_{3}$D	-	-	64 ± 8	98 (*R*) ± 2
htel**L**$^{R}_{3}$D*[1,2]	-	PEG 8000 (5 % v/v)	0	0
htel**L**$^{R}_{3}$D*[1,2]	-	PEG 400 (5 % v/v)	40	89 (*R*)
htel**L**$^{R}_{3}$D	ACN (10 % v/v)	-	7 ± 1	0 ± 1
htel**L**$^{R}_{3}$D	DMSO (10 % v/v)	-	56 ± 5	97 (*R*) ± 1

htel**L**$^{R}_{3}$D*[2]	MeOH (10 % v/v)	-	64	97 (*R*)
htel**L**$^{R}_{3}$D	EtOH (10 % v/v)	-	45 ± 3	≥ 99 (*R*) ± 1
htel**L**$^{R}_{3}$D	THF (10 % v/v)	-	59 ± 6	≥ 99 (*R*) ± 1
htel**L**$^{R}_{3}$D	Acetone (10 % v/v)	-	6 ± 1	24 (*R*) ± 1
htel**L**$^{R}_{3}$D*[1,2]	Et_2O (50 % v/v)	-	0	0
htel**L**$^{R}_{3}$D	TMAO (0.5 M)	-	46 ± 1	95 (*R*) ± 1
htel**L**$^{R}_{3}$D	TMAO (1.0 M)	-	22 ± 1	87 (*R*) ± 2
htel**L**$^{R}_{3}$D	Urea (0.5 M)	-	70 ± 1	≥ 99 (*R*) ± 1
htel**L**$^{R}_{3}$D	Urea (1.0 M)	-	76 ± 10	≥ 99 (*R*) ± 1

For further optimization studies a concentration of 12 µM DNA and 10 µM Cu^{II} was chosen at an incubation time of 2 d. Since under these conditions no complete conversion was observed, it was ideal to evaluate new reaction conditions. A screening with different buffers and pH values clearly showed, that the slightly basic pH of 8 was highly beneficial for the reaction. When using a LiCaco buffer at a pH of 5.5, no conversion was observed and the optimal pH was found to be 8 (HEPES) or 7.5 (MOPS). Decreasing the buffer concentration to 1 mM resulted in a drastic decrease of the conversion. Presumably, the low buffer concentration was no sufficient to keep the pH at 8. A higher concentration of 50 mM resulted in a slightly higher conversion but also in a lower enantioselectivity.

After the reaction conditions were optimized, the effects of molecular crowders and organic co-solvents were investigated. They are known to exhibit strong effects on the structure and function of proteins and G-quadruplexes.[321,322] Also, co-solvents were successfully employed to strongly enhance the activity of different DNAzymes, e.g. a peroxidase like DNAzyme was strongly enhanced by addition of methanol or in a different study a DNAzyme showed strong RNA ligase activities in DMSO containing buffers.[239,241] More importantly, co-solvents were used in DNA based asymmetric catalysis and could significantly improve the yields, when reactions were scaled up from mg to g scales, dedicated to better substrate solubilities.[323]

Here a series of molecular crowders and co-solvents was investigated (**Table 10**), using imidazole chalcone as the substrate and htel**L**$^{2R}_{3}$D. Addition of the molecular crowders PEG400 or PEG8000 in 5 % v/v resulted in a drop of the conversion to 40 % and 89 % *ee* (PEG400) and in case of PEG8000 no product formation was observed. The reason was not further investigated, but it could depend on structural changes or to a Cu^{II} chelation. Since molecular crowders were not improving the reaction, the effects of organic co-solvents were investigated next. The idea was to increase the low solubility of imidazole chalcone in water to make it more accessible for the reaction. To test this a series of water miscible solvents namely ACN, MeOH, EtOH, DMSO, THF and acetone

were added at 10 % v/v. Addition of ACN, MeOH, EtOH, and acetone resulted in a strong decrease of the conversion and enantioselectivity. In contrast, addition of THF (59 %, 99 % *ee*) and DMSO (56 %, 97 % *ee*) showed only minor effects on the conversion and enantioselectivity, but none of the investigated co-solvents showed improved conversions. When plotting the dielectric constant of the co-solvents against the conversions no correlation between polarity and conversion was observed. THF with the lowest dielectric constant and DMSO with the highest showed the best conversions within the investigated cosolvents. Since the addition of classic organic co-solvents was unsuccessful, the effects of the osmolytes TMAO (Trimethylamine N-oxide) and urea were analysed. Both are known to strongly influence the stability of DNA G-quadruplexes and while Urea is a destabilizer, TMAO stabilizes G-quadruplex structures.[322,324–326] In case of TMAO addition of 0.5 M resulted in a decrease of both, conversion (46 %) and enantioselectivity (95 % (*R*)) and at 1.0 M a further decrease was observed (22 %, 87 % (*R*)). Interestingly, when urea was added at a concentration of 0.5 M, a conversion of 70 % with a high enantioselectivity (99 % (*R*)) and at 1.0 M and further increase to 76 % conversion was observed. This was contradicting the assumption that TMAO would stabilize the G-quadruplex structure and therefore improve the conversion, while urea would do the opposite. An explanation might be, that htel**L**$^{2R}_{3}$D folds into different topologies, which coexist in solution in an equilibrium. Addition of TMAO is shifting this equilibrium towards a catalytic inactive topology and urea to the active topology. Although this might sound reasonable, to verify this hypothesis further structural investigations by CD and UV/Vis spectroscopy are currently ongoing, but not discussed here.

6.6 Summary

The proof of concept was established, showing that monodentate imidazole ligandosides in DNA G-quadruplexes, can be used for asymmetric catalysis. Using the Cu^{II} catalysed Michael-Addition of imidazole chalcone as benchmark reaction, in iterative rounds of sequence design and screening highly efficient G-quadruplex structures were designed, catalysing the Michael-Addition in high conversion and up to 99 % *ee*. From these studies important structure activity relationships could be extracted, that will guide the further development of novel sequences. Accordingly, it was found, that ≤ 3 **L²** in a certain proximity were important to allow a chelation of Cu^{II} with an unsaturated coordination environment to allow a coordination of the substrate. In addition, it was found, that sequences enriching the (*S*) enantiomer required only two **L²** in the first loop and NaCl as electrolyte. In contrast, an enrichment of the (*R*) enantiomer was favoured, if one **L²**

was in loop 1 and two **L**^{2} in loop 3 with KCl as electrolyte. The reason for this finding was not elucidated but it was assumed, that two different antiparallel topologies could form, in one case the basket-type and in the other case the chair-type, resulting in opposite strand polarities of loop 1 and 3.

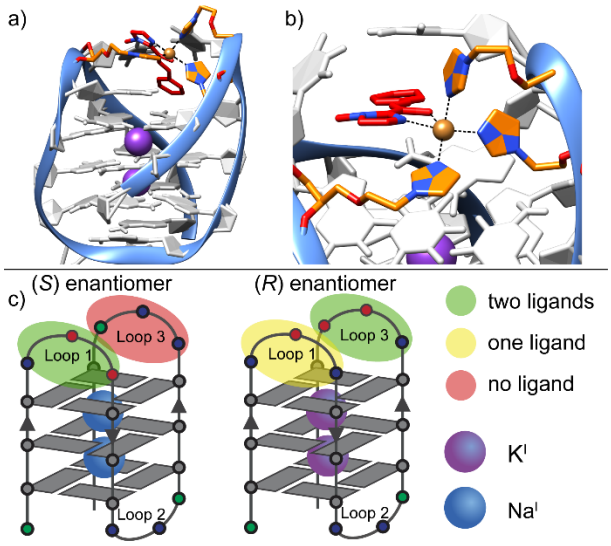

Figure 70. a and b) Snapshot from the MD of htel**L**$^{2R}{}_{3}$D in presence of Cu^{II} and the Michael-acceptor imidazole chalcone. c) Schematic representation of properties that lead to an enrichment of either the *S* or *R* enantiomer.

To further improve the reaction, the effects of molecular crowders and organic co-solvents were investigated. While molecular crowders (PEG400 and PEG8000) and water miscible solvents showed no improvement, addition of the osmolyte urea at 1.0 M significantly improved the reaction in presence of htel**IL**$^{2R}{}_{3}$D from 64 % to 76 % conversion with a high *ee* (98 % *R*). It is assumed, that addition of urea shifted an equilibrium of coexisting topologies towards the more active topology, but this question was not answered and further studies might shed light into this question. In the future, the concept is planned to be expanded to other reactions such as cyclopropanations and Friedel-Crafts reactions or sulfoxidations to show a wider applicability of the system. In preliminary results it was already found that the Diels-Alder reaction between imidazole chalcone **1** and cyclopentadiene was efficiently catalysed by G-quadruplexes in complex with Cu^{II}. Further improved sequences will be designed aided by computational studies, that are currently ongoing in a collaboration with the group of Prof. Sánchez-García from the university of Duisburg-Essen.

Table 11. G-quadruplex forming sequences used for the catalytic studies.

htel**L**$_2$A	AGG GTL TGG GTT AGG GLT TGG G
htel**L**$_2$B	AGG GTL TGG GTT AGG GTL TGG G
htel**L**$_2$C	AGG GTT LGG GTT AGG GTL TGG G
htel**L**$_2$D	AGG GLT TGG GTT AGG GTL TGG G
htel**L**$_2$E	AGG GTL TGG GTT AGG GTT LGG G
htel**L**$_2$F	AGG GLL TGG GTT AGG GTT AGG G
htel**L**$_2$G	AGG GTL LGG GTT AGG GTT AGG G
htel**L**$_2$H	AGG GLT LGG GTT AGG GTT AGG G
htel**L**$_2$I	AGG GTT AGG GTT AGG GTL LGG G
htel**L**$_2$J	AGG GTT AGG GTT AGG GLL TGG G
htel**L**$_2$K	AGG GTL AGG GTT AGG GTL TGG G
htel**L**$_2$L	AGG TTA LGG TTA GGL TTA GG
htel**L**$_3$A	AGG GLT LGG GTT AGG GTL TGG G
htel**L**$_3$B	AGG GTL TGG GTT AGG GLT LGG G
htel**L**$_3$C	AGG GTL TGG GTT AGG GLL TGG G
htel**L**$_3$D	AGG GTL TGG GTT AGG GTL LGG G
htel**L**$_3$E	AGG GLL TGG GTT AGG GTL TGG G
htel**L**$_3$F	AGG GTL LGG GTT AGG GTL TGG G
htel**L**$_3$G	AGG GTT LGG GTT AGG GLL TGG G
htel**L**$_3$H	AGG GTL AGG GTT AGG GLT LGG G
htel**L**$_3$I	AGG GAL TGG GTT AGG GLT LGG G
htel**L**$_3$J	AGG GTL TGG GTT AGG GLA LGG G
htel**L**$_3$K	AGG GTL AGG GTT AGG GLT LGG G
htel**L**$_3$L	AGG GAL TGG GTT AGG GLT LGG G
htel**L**$_3$M	AGG GTL TGG GTT AGG GLA LGG G
htel**L**$_3$N	AGG LTT ALG GTT AGG LTT AGG
htel**L**$_3$O	AGG LTT ALG GTT AGG TTA LGG
htel**L**$_4$A	AGG LTT ALG GTT AGG LTT ALG G
htel**L**$_4$B	AGG TLT LGG TTA GGL TLA GG
htel**L**$_4$C	AGG TLT LGG TTA GGT LTL GG
htel**L**$_6$	AGG LTL TLG GTT AGG LTL TLG G
htel**L**$_7$	AGG LTL LTL GGT TAG GLT LTL GG
htel$_{22}$	AGG GTT AGG GTT AGG GTT AGG G
c-myc	TGG GAG GGT GGG GAG GGT GGG GAAG G

7 NMR SPECTROSCOPY OF METAL-MEDIATED G-QUADRUPLEX STRUCTURES

In the previous chapters the development of metal-mediated G-quadruplex structures and early applications thereof were described. The structures of the modified G-quadruplexes were mainly investigated by CD spectroscopy and compared to the CD spectra of G-quadruplexes with a known structure. Although this procedure is widely accepted in the field of structural biology, it is only an indirect approach and can be easily misinterpreted. Furthermore, to understand the properties and functions of biomolecules, structural data on the atomic level is required. For this purpose, different techniques are utilized including X-ray crystallography, solution and solid-state NMR spectroscopy (Nuclear magnetic resonance spectroscopy).[64,294,327–331] For the G-quadruplex forming human telomeric repeat (htel), from which the here investigated sequence htel**L**^{2S}$_4$C was derived, only recently a novel topology was described by NMR spectroscopy. It could be shown, that a single mutation from adenine to thymine turned a mixture of G-quadruplex topologies to the formation of a previously undescribed chair-type antiparallel topology.[63,83]

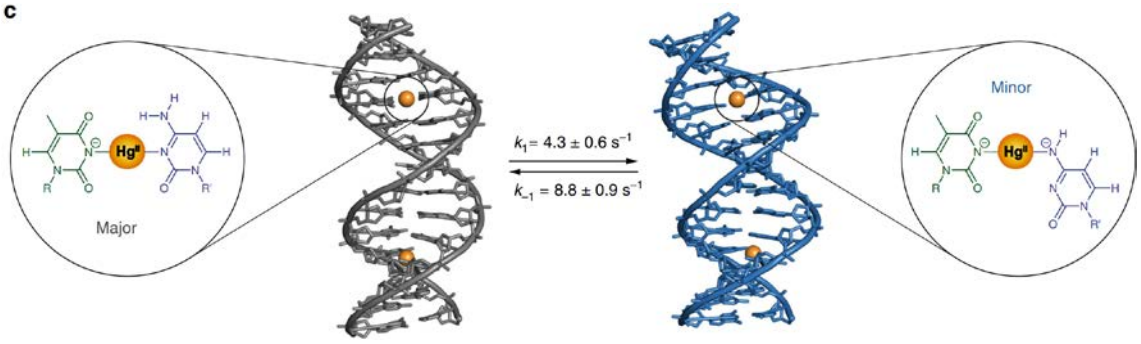

Figure 71. Major (left) and minor (right) duplex structure containing a Hg^{II} mediated base pairs. The rate constants were calculated based on cross-peaks and exchange-mediated NOE cross-peaks. Reprinted from Nature Communications.[332] Published under the terms of the Creative Commons CC BY license.

In the field metal-mediated base pairs, structures based on NMR spectroscopy or X-ray crystallography are very scarce. A first example of an Ag^{I} mediated base pair was reported in 2010 by Johannsen and Sigel et. al. using NMR spectroscopy.[333] Interestingly a similar ligandoside based on imidazole, as it used here, was investigated, although with a ribose backbone instead of glycol. Only recently another example by the

same group was reported on concerted dynamics in a Hg^{II} mediated T-Hg-T metallo-base pair, which was shown to adopt two distinct conformations (**Figure 71**).[332] NMR based studies on DNA structures containing GNA (glycol nucleic acids) are up to date unknown, but a crystal structure involving a GNA backbone and two hydroxypyridone-Cu^{II} (HP-Cu^{II}-HP) metallo base pairs was reported in 2008. While the ribose was completely replaced with glycol, the formed duplex DNA showed remarkable high thermal stabilities (T_m = 78 °C) compared to the metal free duplex (T_m = 40 °C).[334] Structural analysis of the glycol backbone could provide valuable geometric information for the structure calculation of htel**L**$^{2S}_4$C, in which the ligandoside **L**^{2S} was introduced with the same glycol modification.

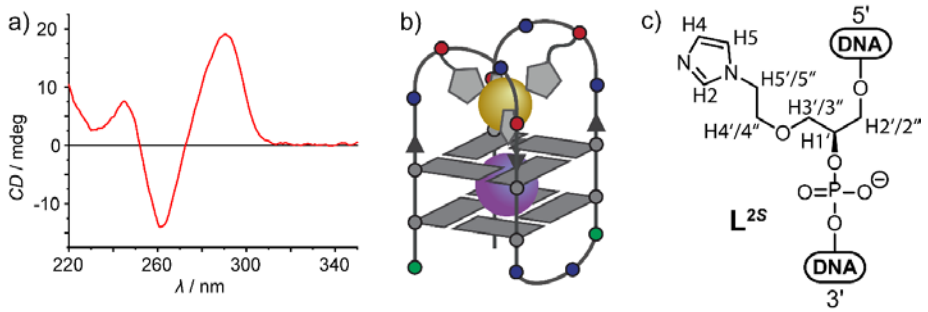

Figure 72. a) CD spectroscopy of htel**L**$^{2S}_4$C, showing a clear antiparallel topology. b) Schematic representation of the expected antiparallel chair-type topology. c) Numbering of the investigated imidazole ligandoside **L**^{2S}.

In this chapter, the NMR solution structure of the G-quadruplex forming sequence htel**L**$^{2S}_4$C (5'-AGG T**L**^{2S}T **L**^{2S}GG TTA GGT **L**^{2S}T**L**^{2S} GG-3') in absence and presence of Zn^{II} is investigated as benchmark to establish the procedure of NMR spectroscopy on metal-mediated G-quadruplexes. Later, this should be expanded to other likely more complex structures. For this purpose, the sequence htel**L**$^{2S}_4$C was chosen, because it folds, according to CD spectroscopy (**Figure 72**), into a clean antiparallel topology and shows very high thermal stabilizations after addition of 1 equiv. Zn^{II} (T_m = 63 °C, ΔT_m = +21 °C), indicating a strong complexation. The high thermal stabilization was attributed to a tetrahedral prearrangement of four **L**^{2S} inside the loop regions to facilitate an ideal coordination geometry for Zn^{II}.

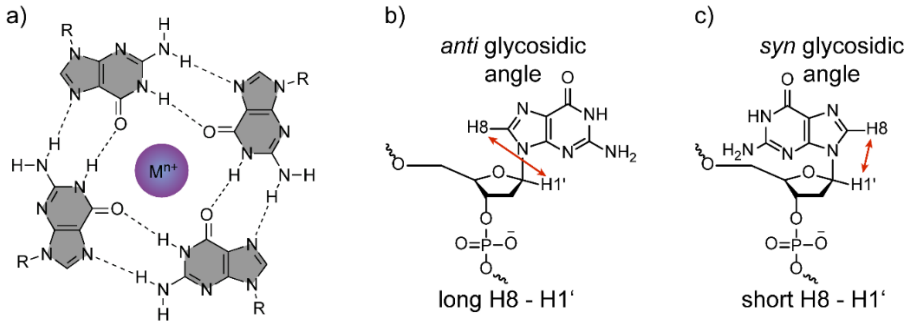

Figure 73. Schematic representation of a G-tetrad, showing the amino (-NH_2) and imino (-NH) protons involved in the Hoogsteen base pairing. b) and c) Dependence of the NOE contacts on the *syn*- and *anti*-glycosidic angle of guanine.[335]

Initial ^{1}H NMR experiments were performed using a very low electrolyte concentration of 2 mM KCl, to avoid a loss of sensitivity from a high conductivity of the solvent.[336–338] The pH value was adjusted to 7 with a deuterated solution of KOD in D_2O, while the use of an additional buffer was omitted, again to reduce the electrolyte concentration. Samples were measured in 9:1, H_2O:D_2O using excitation sculpting with gradients as water suppression.[339] Pleasingly, the very low electrolyte concentration was sufficient for a G-quadruplex formation, as it was proofed by CD spectroscopy (**Figure 72**) and ^{1}H NMR spectroscopy. To judge, whether a secondary structure forms, the imino-region (10 – 14 ppm) is indicative. Signals in the imino-region originate from the -NH protons of guanine and thymine, if they are involved in base pairing. While Watson-Crick base pairs (A-T and G-C) are typically found between 13 – 14 ppm, the imino-protons of a G-tetrad are found within 10 – 12 ppm.[335,340–342] According to that, for a G-quadruplex composed of two G-tetrads (**Figure 73**) with four guanine residues each, a total of eight imino-protons would be expected and indeed in the imino-region eight proton signals were observed (**Figure 74**), consistent with a folded G-quadruplex. To check, whether 2 mM KCl were sufficient, the KCl concentration was increased to 10 mM, showing no changes in the imino-region, concluding that 2 mM KCl were sufficient. Unfortunately, in the ^{1}H NMR spectrum two very intense signals at 1.18 and 3.10 ppm were observed, corresponding to triethylammonium (TEA). From integration of the signals a concentration of almost ~ 50 mM was estimated. When comparing the imino-signals in presence and absence of triethylammonium, only small shifts were observed, concluding that TEA had only a weak influence on the G-quadruplex structure. Nevertheless, samples were desalted two more times using *GE healthcare NAP-10* columns, to fully remove the TEA. TEA is a common impurity in oligonucleotides and originates from the HPLC purification, where triethylammonium acetate is commonly used in the liquid phase.

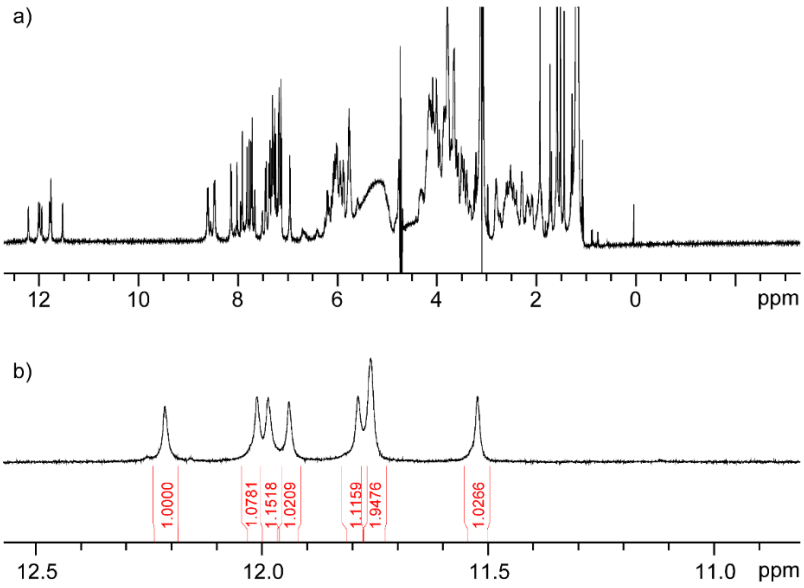

Figure 74. ^{1}H NMR spectrum (600 MHz, 298 K, H_2O:D_2O, 9:1) of htel**L**$^{2S}{}_4$C. a) Full spectrum and b) zoom into the imino-region of the G-quartets. Conditions: 0.5 mM htel**L**$^{2S}{}_4$C, 2 mM KCl, pH adjusted to pH 7, 300 µL.

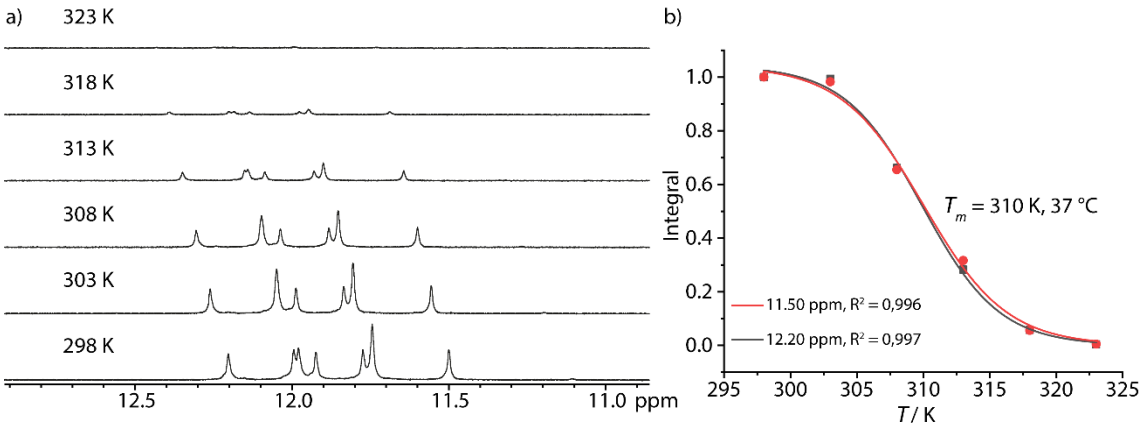

Figure 75. a) VT ^{1}H NMR (600 MHz, H_2O:D_2O, 9:1) of htel**L**$^{2S}{}_4$C. Spectra were recorded from 298 K (bottom) to 323 K (top). b) The integrals of the imino-protons at 11.50 and 12.20 were plotted against the temperature and fitted using a sigmoidal function (y = a/(1 + exp(-k*(x-xc)))). Conditions: 0.52 mM htel**L**$^{2S}{}_4$C, 9 mM K_2HPO_4/KH_2PO_4, 2 mM KOH, pH adjusted to pH 7.0, 300 µL.

VT (Various Temperatures) experiments (**Figure 75a**) of htel**L**$^{2S}{}_4$C could show a stepwise decrease of the imino-protons, that completely disappeared at 50 °C, indicative for a denaturation of the G-quadruplex structure. The integrals of the imino-protons at 11.50 and 12.50 ppm were plotted against the temperature and fitted using a sigmoidal function (**Figure 75b**). From this a melting temperature T_m = 37 °C was determined, which was only slightly lower compared to the T_m determined by UV/Vis spectroscopy

(T_m = 42 °C), showing that the reduced salt concentration (2 vs 100 mM KCl) had only a small influence on the thermal stability.

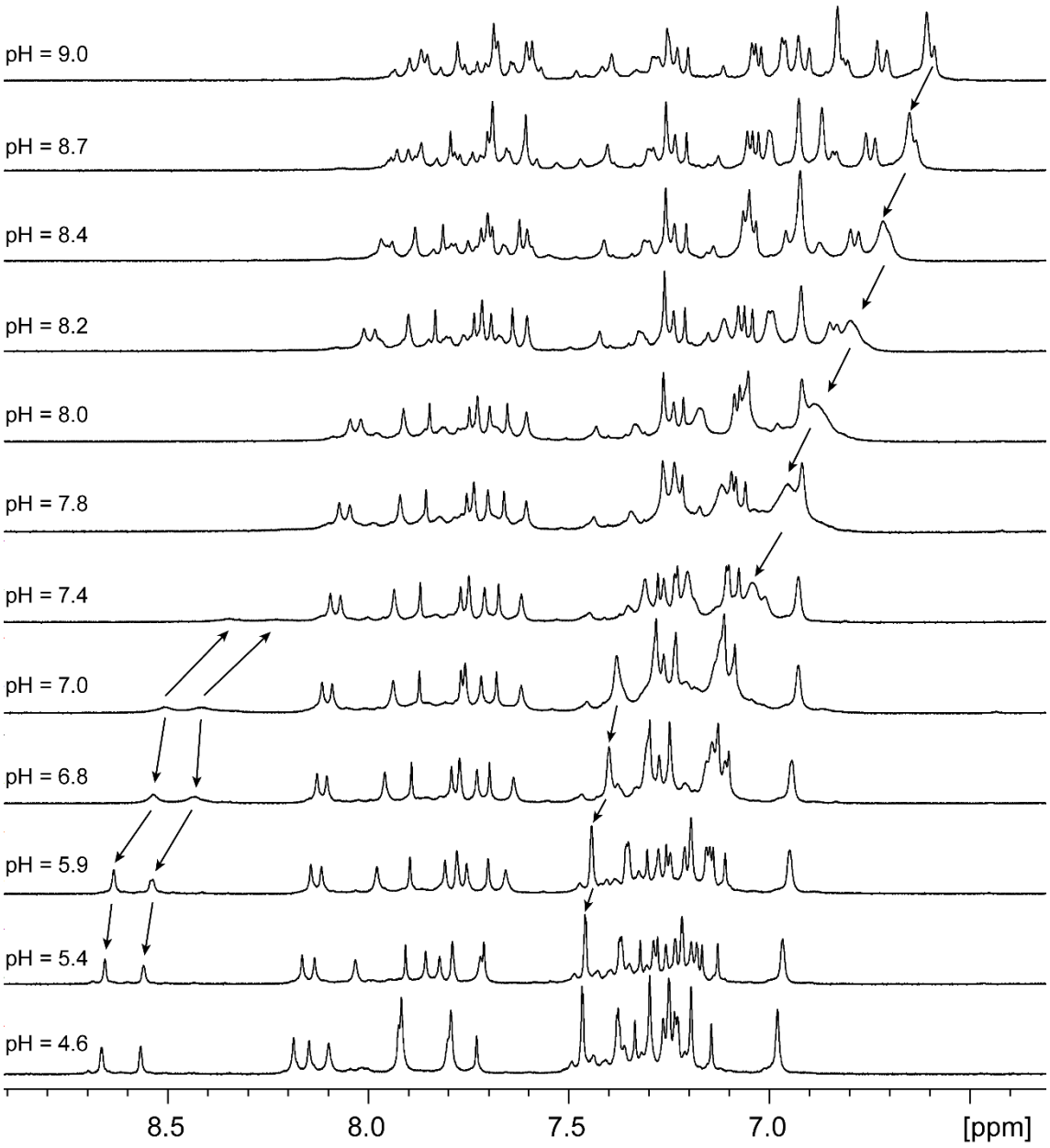

Figure 76. ^{1}H NMR (600 MHz, D_2O, 298 K) based pH titration of htel**L**$^{2S}_4$C. The pH was adjusted with diluted DCl (10 mM) and KOD (10 mM). Conditions: 0.625 mM htel**L**$^{2S}_4$C, 12.5 mM KCl, 240 µL.

To identify the imidazole protons a pH titration from 4.6 to 9 was performed (**Figure 76**). From literature it is known that the pK_a of imidazole is around 7.[343,344] For this reason, at a neutral pH an exchange of protonation and deprotonation on the NMR timescale can cause a broadening of the imidazole protons. Indeed, when stepwise acidifying the solution two broad signals at 8.46 and 8.55 ppm were downfield shifting and becoming much sharper, that were assigned to the H2 protons of imidazole. At a pH of 5.69 the peaks were very sharp and reached the maximum downfield shift at 8.66 and 8.56,

respectively. This was explained with a quantitative protonation of the imidazole N1 at acidic pH values. The H4 and H5 protons were not observed, as they were overlaying with other aromatic protons. Therefore, in another titration the pH value was stepwise increased (**Figure 76**). The H2 peaks became with lower pH values very broad and high field shifted until they overlaid with other aromatic protons. At a pH of 7.4 a broad peak appeared at 7.1 ppm which high field shifted with increasing pH values. At a pH of 9 it became relatively sharp and split into two peaks at 7.10 and 7.00 ppm. It is assumed that these signals were possibly the H4 or H5 protons from imidazole, however, it could not be confirmed from the ^{1}H NMR spectra alone.

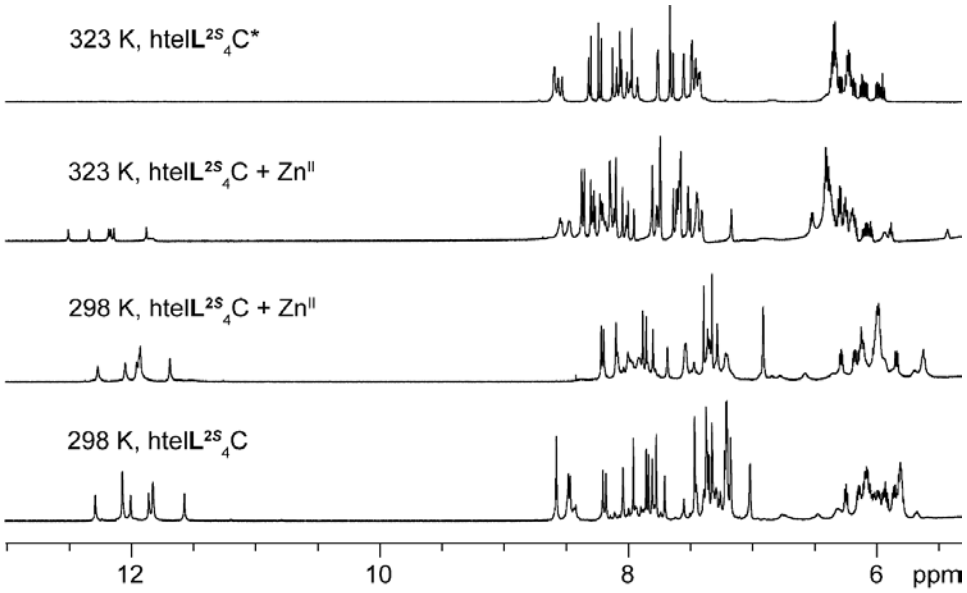

Figure 77. ^{1}H NMR (600/700 MHz, 95:5, H_2O:D_2O) of htel**L**$^{2S}_{4}$C in presence and absence of Zn^{II} at 298 and 323 K. Conditions: 0.5 mM htel**L**$^{2S}_{4}$C, 0.5 mM $ZnCl_2$, 10 mM K_2HPO_4/KH_2PO_4 pH 7.14, H_2O:D_2O, 95:5. *0.52 mM htel**L**$^{2S}_{4}$C, 9 mM K_2HPO_4/KH_2PO_4 pH 7.04, H_2O:D_2O, 9:1 .

Similarly, to acidifying the pH value, it was assumed, that addition of the Lewis-acid Zn^{II} would result in downfield shifted and sharper imidazole protons, since after Zn^{II} coordination a protonation of imidazole is not possible. In fact, this was not the case and after addition of Zn^{II} to htel**L**$^{2S}_{4}$C no imidazole protons could be identified in the ^{1}H NMR spectra. This could be explained with an exchange of the imidazole ligandosides with water or even the nucleobases. If this exchange was on the NMR timescale it would cause a broadening of the imidazole proton signals. Besides the broad imidazole protons, also for the imino-protons a slight broadening and a worse signal to noise ratio was observed. Surprisingly, integration showed only seven imino-protons instead of the expected eight, which could be a result of the broadening. Nevertheless, presence of the imino-protons was still indicative for a G-quadruplex formation, which was later supported by ^{1}H-^{1}H NOESY experiments. The stabilizing effect of Zn^{II} was proofed by VT ^{1}H NMR experiments. While in absence of Zn^{II} at 323 K no imino-protons were

observable, in presence Zn^{II} the imino-protons were still observed, showing the stabilizing effect of Zn^{II} (**Figure 77**).

Apart from the isolated imino-region the ^{1}H NMR spectra were strongly overlapping and not allowing to differentiate between the different protons. To dissect the ^{1}H NMR spectra ^{1}H-^{13}C Heteronuclear Single Quantum Coherence (HSQC) experiments were carried out to assign the strongly overlapping proton resonances to certain groups, e.g. the H4' (3.8 – 4.3 ppm) and H5'/H5'' (3.8 – 4.3 ppm) protons share very similar shifts, but the corresponding C4' (82 – 86 ppm) and C5' (63 – 68) carbons have very distinct chemical shifts, allowing to differentiate between the H4' and H5'/H5'' protons. According to the chemical shifts **Table 17** and **Figure 78**, proton resonances were assigned in the ^{1}H-^{13}C HSQC spectrum (**Figure 80**).[345,346]

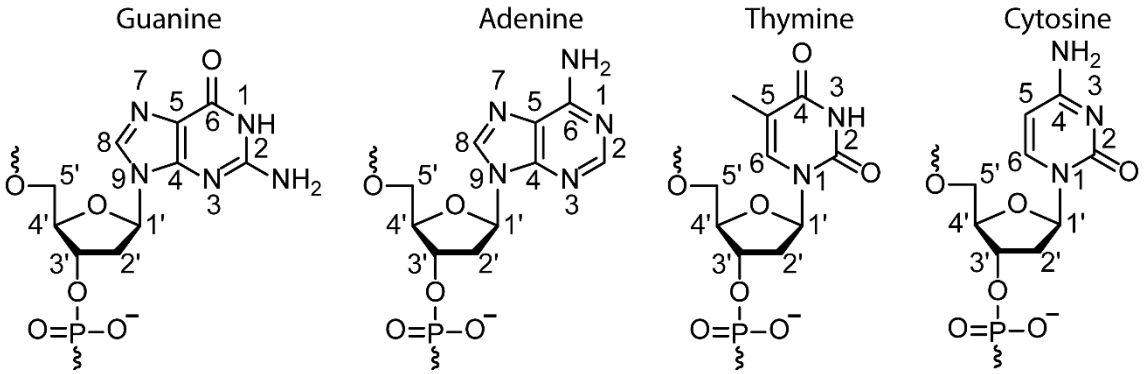

Figure 78. Numbering of the four canonical nucleobases in DNA, Guanine, Adenine, Thymine and Cytosine.

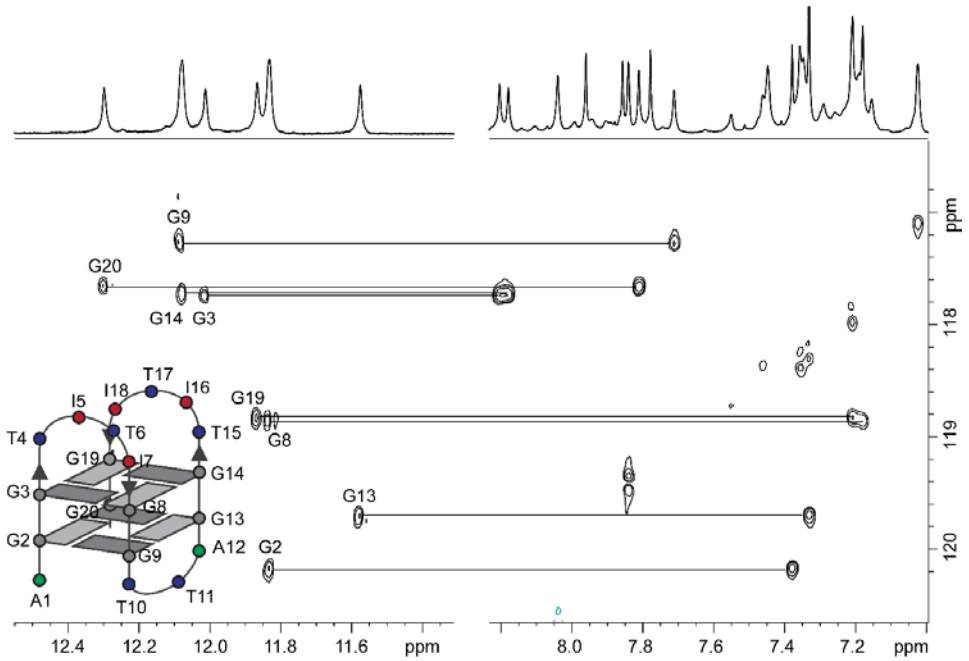

Figure 79. JR-HMBC (600 MHz, 90:10, H_2O:D_2O, 298 K) spectrum of htel**L**^{2S}$_4$C. Conditions: 0.5 mM htel**L**^{2S}$_4$C, 10 mM KCl, pH 7.0, 300 µL.

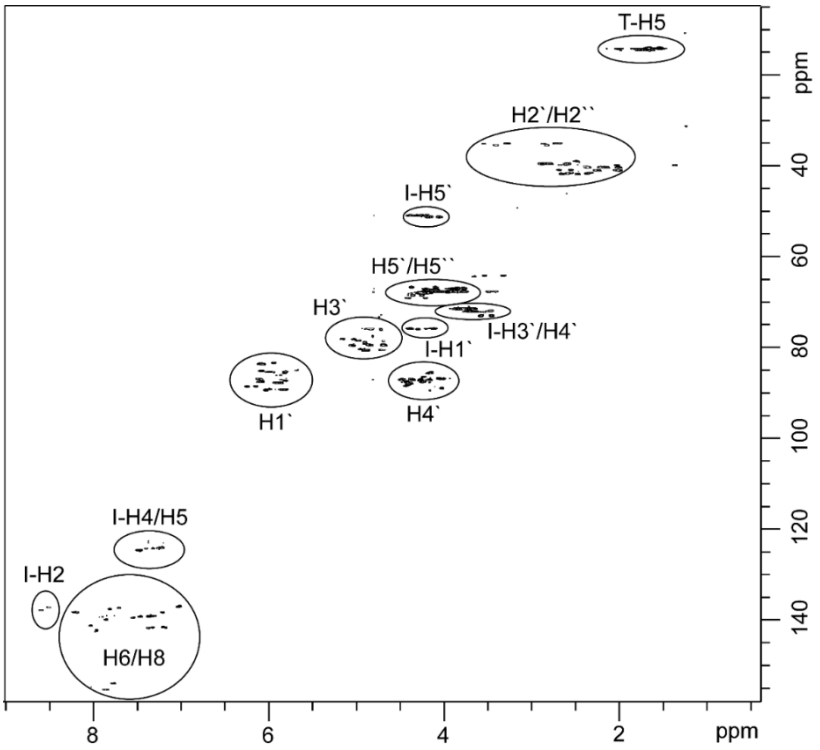

Figure 80. ^{1}H-^{13}C HSQC (700 MHz, D_2O, 298 K) of htel**L**$^{2S}_4$C and the assigned cluster for the aromatic base and aliphatic sugar protons. Conditions: 0.625 mM of htelL^{2S}_4C, 10 mM KCl, pH 7.0, D_2O, 240 µL.

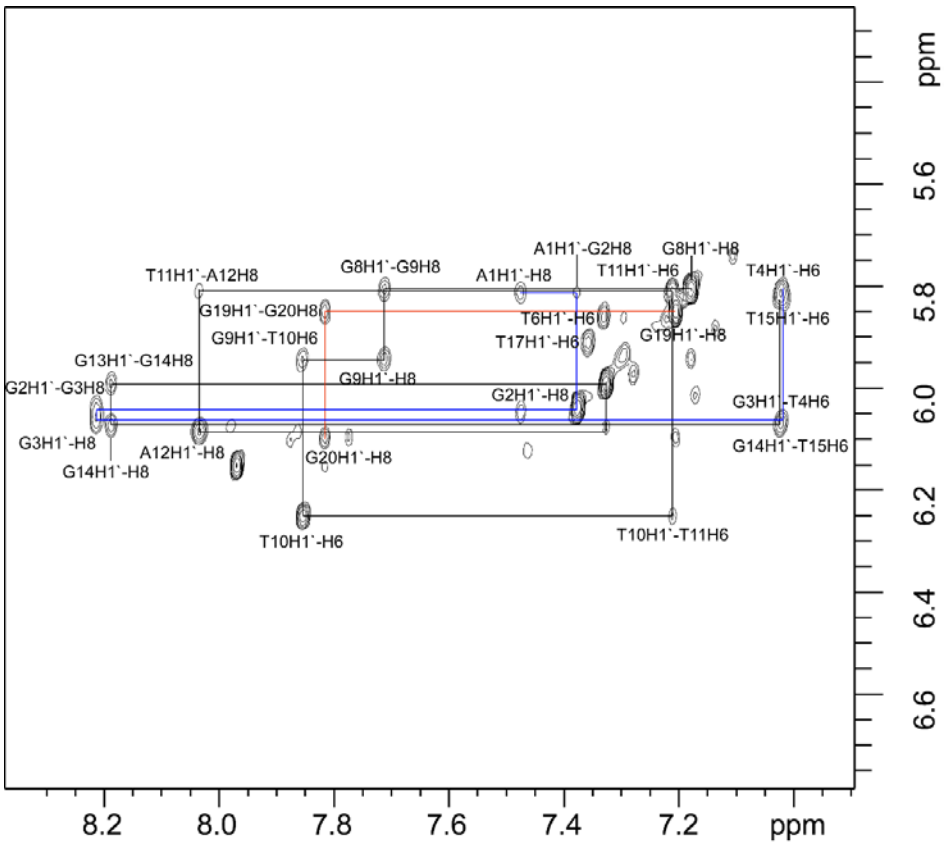

Figure 81. H6/8-H1' region of the ^{1}H-^{1}H NOESY NMR spectrum (700 MHz, D_2O, 298 K, 250 ms mixing time) of htel**L**$^{2S}_4$C. The lines indicate the sequential walk which is interrupted by the imidazole ligandosides. Conditions: 0.625 mM htel**L**$^{2S}_4$C, 10 mM KCl, pH 7.0, 240 µL.

After assigning the ^{1}H resonances to chemical groups in the ^{1}H-^{13}C HSQC spectrum, the proton chemical shifts were assigned to their nucleobases. For this purpose, a JR-HMBC experiment was recorded, allowing to correlate the imino-protons of the G-tetrads to the H8 protons of the respective guanine residue (**Figure 79)**.[347] This also allowed to differentiate overlapping imino-protons. Using the H8 protons of guanine as the starting point the sequential walk (**Figure 81**) of the H6/H8-H1' region was assigned by ^{1}H-^{1}H Nuclear Overhauser Enhancement Spectroscopy (NOESY). It was interrupted by the imidazole ligandosides due to a lack of the ribose backbone and missing cross-peaks between the aromatic imidazole protons and aliphatic glycol protons. The sequential walk was further approved from as second H8-H2' sequential walk region. Besides the sequential walk, from the H6/H8-H1' region also the glycosidic angle of the guanine residues was assigned. According to literature, in case of a *syn*-glycosidic angle very strong NOE cross-peaks between the H1'-H8 protons are observed, while in the *anti*-configuration weaker H1'-H8 cross-peaks are expected.[335] The reason is a closer distance of H1'-H8 protons in case of an *syn* glycosidic angle compared to *anti* (**Figure 73)**.[335] From the H8-H1' cross-peaks the glycosidic angle of G2, G8, G13 and G19 was assigned as *syn* and for G3, G9, G14 and G20 as *anti*. Interestingly, the H8 protons of the guanine residues with a *syn*-glycosidic angle were upfield-shifted compared to the ones with an *anti*-glycosidic angle and always two neighbouring guanine residues had the opposite glycosidic angle. This alternating arrangement of *syn-anti* glycosidic angles is typical for antiparallel G-quadruplexes. Together with the sequence derived from the sequential walk it could be concluded that an antiparallel G-quadruplex of the chair-type had formed.

The protons of the imidazole ligandosides were extremely difficult to assign since they appeared at neutral pH values very broad due to the previously mentioned interconverting protonation states and due to the very high flexibility of the linker and glycol backbone. The H2 imidazole protons were highfield shifted, which is in accordance with literature and not overlaying with the H6/H8 protons.[333] In contrast the H4 and H5 protons showed very similar shifts and were overlaying with the H6/H8 protons. Interestingly, the aromatic protons of the imidazole ligandosides I5 and I16 as well as I7 and I18 showed almost identical chemical shifts. This was due to the mirror like appearance of the loops 1 and 3 where the imidazole ligandosides are located. Only a few and weak inter residue cross-peaks between the aromatic imidazole protons and the nucleobases were observed. The ^{1}H-^{1}H NOESY in presence of Zn^{II} showed a lower resolution compared to the spectrum in absence of Zn^{II}, but in general the same cross-peaks were observed. This was expected, since Zn^{II} was not inducing structural changes

apart from the imidazole coordination. Also, the guanines with an *anti*-glycosidic angle were again downfield shifted compared to the guanines with a *syn*-glycosidic angle. Pleasingly, cross-peaks corresponding to the aromatic imidazole protons were much better resolved. It is assumed, this was reason of a fixation of the imidazole ligandosides after Zn^{II} coordination. Even more important, several inter residue cross-peaks between the imidazole ligandosides and the nucleobases were observed. Again, this was explained with the higher rigidity of the imidazole ligandosides after Zn^{II} coordination.

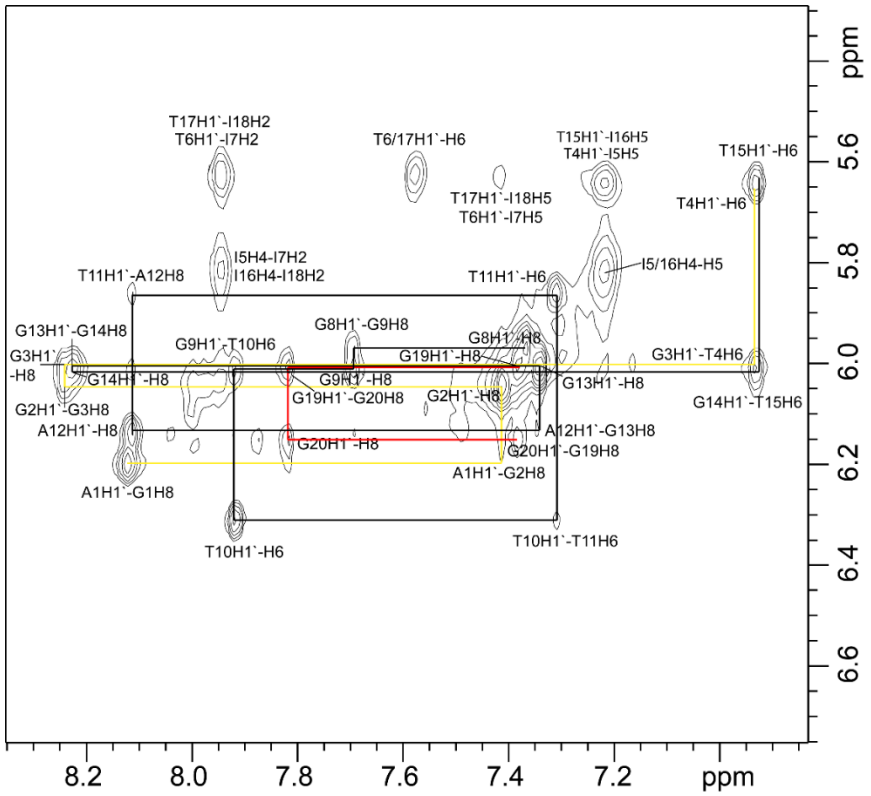

Figure 82. H6/8-H1' region of the ^{1}H-^{1}H NOESY (600 MHz, D_2O, 298 K, 250 ms mixing time) NMR spectrum of htel**L**$^{2S}_{4}$C in presence of Zn^{II}. The lines indicate the sequential walk which is interrupted by the imidazole ligandosides. Conditions: 0.71 mM htel**L**$^{2S}_{4}$C, 0.71 mM $ZnCl_2$, 2 mM KOH, 9 mM KH_2PO_4/K_2HPO_4, pH 7.0, 280 µL.

7.1 Structure calculation

Based on the data from the NMR experiments the solution structure of htel**L**$^{2S}_{4}$C was calculated. For structure calculations the software *xplor-NIH 3.1* was used, which employed the simulated annealing protocol.[348–353] In simulated annealing a single stranded sequence is heated to 3500°C and cooled to 25°C to simulate the annealing process of the secondary structure based on the experimental data. Partial charges were adopted from MD simulations, atom types, bonds, angles, and dihedrals were assigned in analogy to existing parameters.[333] Constraints were applied to maintain planar G-tetrads and hydrogen bond length involved in the Hoogsteen-base pairing.[340] If an *anti*

or *syn* glycosidic angle was unambiguously assigned an angle of 60° ± 70 (*syn*) or 240° ±70 (*anti*) was applied.[340] Distance restraints were calculated based on the integration of the NOE cross-peaks and were calibrated against the intramolecular H5-H6 distance in thymine. An overview of the applied restraints can be found in table **Table 12**. In total 400 structures were calculated using the simulated annealing protocol. The 40 lowest energy structures were used for the statistics in **Table 12**. From a total number of 2782 applied restraints an average number of 180 was violated, corresponding to a violation rate of 6 %. Espeacially the NOE distance restraints and angles show high numbers of violations, which must be carefully analysed and changed, if neccecary.

Table 12. Statistics of the restraints used in the structure calculation. The violations are based on the 40 lowest energy structure out of a total of 400 calculated structures.

Restraint	Average Violations	Number restraints
Total	180	2782
NOE distance	52	312
Torsion	4	77
Angle	46	1222
Bond	2	676
Impropers	6	439
Hydrogen bond restraints		32

To analyse the preliminary structures, the ten lowest energy structures were used. An overlay of these structures showed, that eight out of ten structures were folded in the same chair-type antiparallel topology (**Figure 83a,b**). Two structures seemed from chemical intuition unreasonable and were omitted in the alignment. Even more important, the G-tetrads nicely show an arrangement in two layers and from a top view, the ion pocket between the G-tetrads, where potassium is located, is visible (**Figure 83**). The central cation is missing, since it cannot be detected by NMR spectroscopy. Finally, the postion of the central cation will be calculated but first the G-quadruplex structures need a refinement. All in all the calcualted G-quadruplex structures look very reasonable, but still show some obviuos distortions e.g. the G-tetrad at the 5'-end shows obvious distortions (**Figure 83f**) and together with the violated restraints (180 on average) it becomes clear, that further optimizations will be necessary. The optimization process will involve a checkup of all NOE cross-peaks to validate the distance restraints. Espeacially strongly overlaying and weak cross-peaks need to be reassesed. Also, the number of interresidue NOE-contacts was comparably low and to find more would help to improve the structure calculation. After the number of violations is reduced to a minimum the next steps will involve the refinement of the lowest energy structures and the determination of the coordination geometry of the Zn^{II} cation. This will be challening, since no direct

evidence of Zn^{II} coordinaton could be derived from the NMR-experiments. The geometry has to be calculated from the NOE cross-peaks between the imidazole ligandosides, which suffer from a bad resolution.

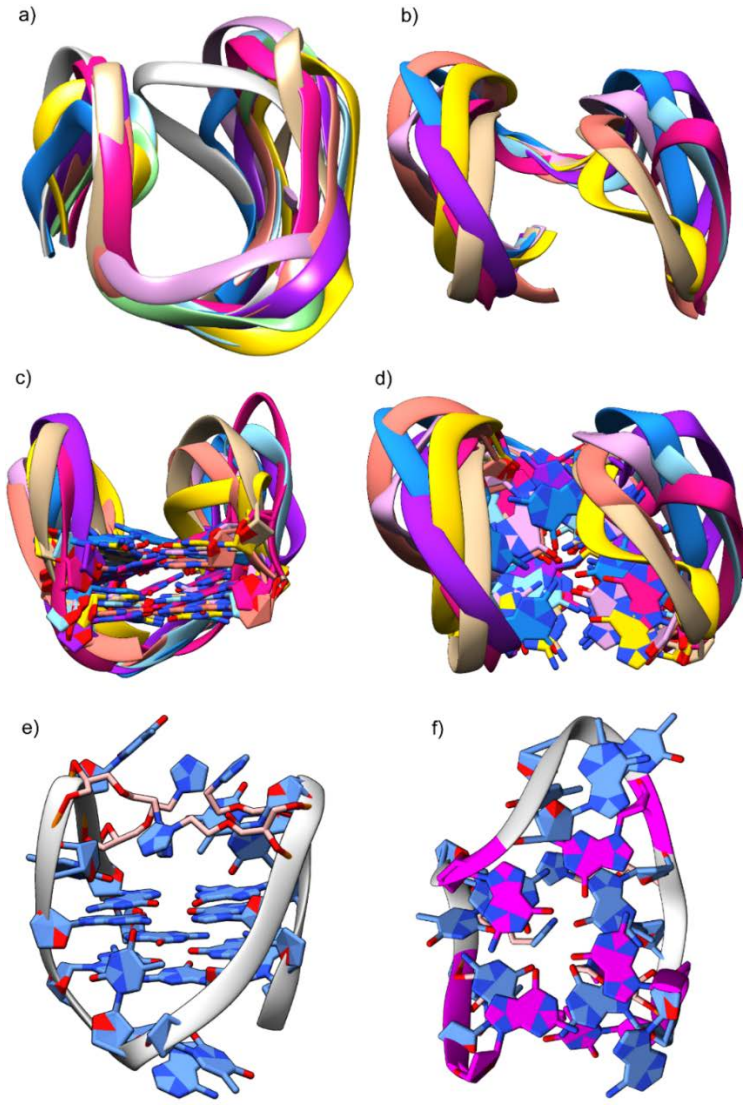

Figure 83. Preliminary calculated NMR solution structures of htel**L**$^{2S}{}_4$C. a,b) merged backbones of the 8 lowest energy structures, b) overlay of the G-tetrads and c) the best calculated structure in terms of NOE violations.

7.2 Summary

NMR based studies of htel**L**$^{2S}{}_4$C in solution could confirm the formation of a G-quadruplex in absence and presence of Zn^{II}. VT-NMR experiments showed a melting temperature of the G-quadruplex at T_m = 37 °C, which is in agreement with previous UV/Vis based thermal denaturation experiments. Also, the stabilizing effect of Zn^{II} could be confirmed by VT-NMR experiments. From ^{1}H-^{1}H NOESY experiments the formation of the proposed chair-type antiparallel topolgy was confirmed in absence and presence

of Zn^{II}. While the NOESY spectra were generally well resolved, the crosspeaks corresponding to the protons of the imidazole ligandsosides were very broad and badly resolved. This was dedicated to exchanging protonations states and the very flexible linkers of the imidazole ligandosides. Addition of Zn^{II} showed a silghtly improved resolution due to the fixation of the imidazole ligandsosides around the Zn^{II} centre. More important, additional interesidual NOE cross-peaks between the imidazole ligandosides and the nucleobases appeared, which will be mandatory for the calculation of the Zn^{II} coordination. For the structure calulations a total of 2782 restraints was applied, including 312 distance restraints. From the calculated 400 structure the 40 lowest energy structures showed an average of 180 violations, out of which 52 were NOE distance restraints. Further optimizations will be necesarry to reduce the number of violations to 0. Although still a high number of violations was observed, analysis of the calculated structures showed that 8 out of 10 structures showed the expected chair-type antiparallel topology. An overlay of the G-tetrads further showed the correct formation of planar G-tetrads with a central cavity that accomodates the cation, in this case K^+, although some of the G-tetrads still showed heavy distortions.

8 CONCLUSION AND OUTLOOK

In this dissertation the concept of metal-mediated DNA G-quadruplex structures was established in the field of DNAzymes and for asymmetric catalysis. Based on the pioneering work of David M. Engelhard, who incorporated pyridine ligandosides in tetra- and unimolecular G-quadruplexes, a new series of nature inspired imidazole ligandosides $\mathbf{L}^{1R/S}$, $\mathbf{L}^{2R/S}$ and $\mathbf{L}^{3R/S}$ was designed and synthesized.[24,26,29–31] In tetramolecular G-quadruplexes, the incorporation of $\mathbf{L}^{1R/S}$ allowed the complexation of a series of transition metal cations, including Cu^{II}, Ni^{II}, Zn^{II} and Co^{II}. Especially addition of Cu^{II} to the tetramolecular G-quadruplex $\mathbf{L}^{1R}G_4$ showed unprecedented high thermal stabilizations of up to $\Delta T_{1/2}$ = 51 °C and strongly accelerated association kinetics by two orders of magnitude. These enhanced properties led to the design of the tetramolecular G-quadruplex $\mathbf{L}^{1R}G_3$, which could be used as a Cu^{II} activated DNAzyme with a peroxidase like activity. While in absence of Cu^{II} $\mathbf{L}^{1R}G_3$ was to unstable, addition of equimolar amounts Cu^{II} strongly increased the stability and resulted in the formation of a tetramolecular G-quadruplex, catalysing after hemin addition the oxidation of ABTS in presence of H_2O_2. Further mass spectrometric experiments could clearly show the formation of the G-quadruplex/hemin complex.[29]

After established in tetramolecular G-quadruplexes, $\mathbf{L}^{1}$ and $\mathbf{L}^{2}$ were incorporated in unimolecular sequences. As it was found, that the linker in $\mathbf{L}^{1}$ was too short to allow a metal chelation, the $\mathbf{L}^{2}$ modified G-quadruplex htel$\mathbf{L}^{2}{}_4$ could complex a series of transition metal cations. Varying the number and position of $\mathbf{L}^{2}$ in the sequences led to the design of tailored coordination environments for different transition metal cations with respect to their preferred coordination geometry. In this respect, Cu^{II} preferred square planar arrangements, while for Ni^{II} coordination numbers between five and six were found ideal and in case of Zn^{II} the prearrangement of $\mathbf{L}^{2}$ in a tetrahedral geometry was highly beneficial. Interestingly, the incorporation of seven $\mathbf{L}^{2}$ allowed the complexation of a dinuclear Cu^{II} complex, which was proofed by native ESI-MS. It was found, that it catalysed in presence of O_2 the oxidation of *D*-Dopa, although compared to catechol oxidases with much slower reaction kinetics. Nevertheless, this might be an interesting starting point for the design of G-quadruplexes, mimicking catechol oxidases or even tyrosinases.

After $\mathbf{L}^{2}$ was established in unimolecular G-quadruplexes, it was mixed with a benzoate ligandoside $\mathbf{L}^{B}$ to create heteroleptic coordination environments. This could be exploited to further fine tune metal affinities, leading to sequences selectively binding Zn^{II} or Ni^{II},

according to the observed thermal stabilizations. This is an important step towards G-quadruplex structures, that bind selectively metal cations in complex systems.

The concept also allowed the design of G-quadruplexes with unsaturated coordination environments for Cu^{II}, potentially allowing the coordination of substrates for catalytic applications. Indeed, using a Cu^{II} catalysed Michael-Addition as benchmark reaction, in iterative rounds of sequence design and screening highly efficient G-quadruplexes were designed, catalysing the Michael-Addition between imidazole chalcone and dimethyl malonate in high conversions and enantioselectivities of up to 99 % *ee*. More importantly the concept allowed the design of G-quadruplexes for the enrichment of both enantiomers, without completely inverting the chirality of the DNA itself. From the iterative rounds of sequence design important structure activity relationships could be derived. This way, G-quadruplexes with one $\mathbf{L^2}$ in loop 1 and two $\mathbf{L^2}$ in loop 3 were in presence of KCl enriching the (*R*) enantiomer, while G-quadruplexes with two $\mathbf{L^2}$ in loop 1 in presence of NaCl led to an enrichment of the (*S*) enantiomer.

As a future prospect the work will continue to further develop and understand the system. Obviously, after only a single type of reaction was explored, it is planned to screen different types of reactions, like Friedel-Crafts reactions, sulfoxidations or even cyclopropanations. Early results of a Diels-Alder reaction showed already promising results in terms of conversion and enantioselectivity and will certainly be further investigated. Also, we are interested to find reactions, which are completely new in the context of DNA based catalysis and to extend the system to substrates, which we are so far not accessible. One idea is to incorporate hydrophobic phenyl or indole modifications into the loop regions to create discreate hydrophobic pockets for a substrate binding. Initial studies with a phenyl modification were already showing interesting results.

Besides the scope of reactions another interest is to further optimize the G-quadruplexes in terms of efficiency. In this respect we see a great potential to further investigate the co-solvent effects. As we already observed significant improvements after addition of 1M urea the next step will be to investigate the molecular reasons for the improvement by CD and NMR spectroscopy and other biophysical techniques. A detailed experimental knowledge about the molecular mechanisms will be the basis for the development of a computer aided sequence design in collaboration theoretical working groups. Currently QM/MM studies are planned to unveil the involvement of the neighbouring nucleobases in the catalytic mechanism. On a long term this should then allow in iterative rounds of computer aided sequence design and screening the identification of highly effective DNA G-quadruplexes, that can be applied for a broad range of reactions.

9 EXPERIMENTAL SECTION

9.1 Oligonucleotide Synthesis and Purification

Oligonucleotide synthesis, purification and spectroscopic experiments were performed as published previously. The protocols were adapted from the respective publications.[29–31]

9.1.1 Oligonucleotide Synthesis

All oligonucleotides were synthesized on a *K&A Laborgeraete GbR H-8* synthesizer on a 1 µMol scale using the standard phosphoramidite method and were following previously published procedures.[29,30] Standard phosphoramidites (DMT-dT-CEP, DMT-dA(Bz)-CEP and DMT-dG(iBu)-CEP) were used with cartridges containing controlled pore glass (CPG) solid supports (1000 Å, 25-35 µMol/g, DMT-dG(iBu)-CPG). The build in programs from the DNA synthesizer was used, following the standard protocols. The only difference was an extended coupling time for modified phosphoramidites. The composition of the used reagents is shown in **Table 13**. In a first step the cartridges were treated with DCA in CH_2Cl_2 to release the 5'-OH groups, followed by a washing step with ACN and argon. Subsequently the next phosphoramidite was coupled by mixing (0.1 M in ACN) with ACT (1:1, v/v). The coupling time was ~0.5 min for standard phosphoramidites and extended to ~3.5 min for the ligand-modified phosphoramidites. Then, the cartridge was treated with a 1:1 (v/v) mixture of Cap A and Cap B to deactivate unreacted 5'-OH groups and the synthesis cycle was finished by the oxidation with OXI. An additional washing step with ACN was introduced compared to the standard routine. After each individual step of the cycle, the cartridge was washed with ACN followed by a drying step with argon. The DNA solid phase cycle was repeated until the desired oligonucleotide was synthesized.[29–31]

Table 13. Reagents for DNA synthesis. Reprinted from Frontiers in Chemistry 2020.[30]

name	reagent	composition
DCA	detritylation	3% (v/v) dichloroacetic acid in anhydrous dichloromethane
ACT	activator	0.3 M 5-(benzylthio)-1H-tetrazole in anhydrous acetonitrile
Cap A	capping A	10% (v/v) N-methyl imidazole in anhydrous tetrahydrofurane
Cap B	capping B	2,6-lutidine / acetic anhydride / anhydrous tetrahydrofurane 1:1:8 (v/v/v)
OXI	Oxidizer	0.02 M iodine in tetrahydrofurane / pyridine / water 7:2:1 (v/v/v)
ACN		anhydrous acetonitrile

9.1.2 Oligonucleotide Purification

After DNA synthesis, the solid supports were removed from the cartridges and treated with 0.5 mL of concentrated ammonia at 55 °C for 16 h. The supernatant solution was filtered (*VWR* centrifugal filters) and the solid support was washed with 100 µL H_2O. To remove ammonia the sample volume was reduced to 300 µL using a *H. Saur Laborbedarf S-Concentrator BA-VC-300H* vacuum concentrator. Then oligonucleotides were purified using semipreparative reversed phase HPLC (**Table 14**) on an *Agilent Technologies 1260 Infinity II HPLC* system equipped with an autosampler, column oven, DAD detector and a *Macherey-Nagel VP 250/10 NUCLEODUR 100-5 C18ec* column (oven temperature: 40/60 °C, flow rate: 2/3 mL/min). Samples were lyophilized with a *Christ Alpha 2-4 LSCbasic* and redissolved in TEAA pH 7.2. The 5′-OH DMT protecting group was removed with 2 % TFA and oligonucleotides were desalted using *Waters Sep-Pak C18* cartridges. The cartridges were equilibrated with 2 x 2 mL ACN, 2 x 2 mL ACN:TEAA 100 mM pH 7.2, 1:1 and 2 x 2 mL 100 mM TEAA pH 7.2. Then the redissolved oligonucleotides were passed through two times, followed by a washing step with 2 x 2 mL 100 mM TEAA pH 7.2. Then 2 mL TFA (2 % aq.) were added followed by 2 mL 100 mM TEAA pH 9.2. To remove the salts, samples were then washed with 2 x 2 mL desalted H_2O and eluted with 2 mL H_2O:ACN, 1:1. The oligonucleotides were then lyophilized and stored as a solid or as 0.2–1 mM stock solution in water at –20 °C. The concentrations of all oligonucleotide stock solutions were determined *via* the absorbance at 260 nm at 25 °C with a *Thermo Scientific Nanodrop One* instrument.[29–31]

Table 14. Solvent gradient used for analytical (0.75/1 mL min^{-1}) and semipreparative (2/3 mL min^{-1}). A: 50 mM TEAA pH 7, B: 70:30 ACN/50 mM TEAA pH 7, C: H_2O, D: water.

Time / min	A / %	B / %	C / %	D / %
0	100	0	0	0
30	20	80	0	0
35	0	100	0	0
40	0	100	0	0
41	100	0	0	0
45	100	0	0	0

9.2 Oligonucleotide analytics

Oligonucleotides were analysed as previously published.[29–31]

9.2.1 Analytical RP-HPLC

After DNA synthesis and purification oligonucleotides were analysed by RP-HPLC. Therefore 5 µL samples were mixed 1:1 with TEAA 100 mM pH 7. RP-HPLC was performed on an *Agilent Technologies 1260 Infinity II* system equipped with an autosampler, column oven, DAD detector and a *Macherey-Nagel EC 250/4.6 NUCLEODUR 100-5 C18ec* column (oven temperature: 60 °C, flow rate: 0.75 mL/min or 1.00 mL/min, solvent A: 50 mM TEAA pH 7, solvent B: 70:30 ACN/50 mM TEAA pH 7). The RP-HPLC traces including the used solvent gradient are shown in the appendix.

9.2.2 Analytic ESI-MS

After DNA synthesis and purification oligonucleotides were analysed by ESI-MS. Therefore 5 µL samples were mixed 1:1 with TEAA 100 mM pH 7. Mass spectra were recorded on a *Bruker ESI-timsTOF* mass spectrometer (negative mode), which was calibrated using the *Agilent ESI-Low Concentration Tuning Mix*. Samples were automatically injected using the autosampler of an *Agilent Technologies 1260 Infinity* system (flow rate: 0.3 mL/min, solvent: ACN/H_2O 1:1).

9.2.3 MALDI-TOF

Oligonucleotides were analysed on a *Bruker ultrafleXtreme* MALDI-MS system in the negative mode. 0.5 µL of the HPA matrix solution (saturated solution with 3-HPA, 10 mg mL^{-1} diammonium hydrogen citrate, H_2O:ACN, 1:1) were deposition on a ground

steel MALDI target plate and allowed to dry. Then 0.5 µL of the sample solution were deposited on the matrix spot and allowed to dry. Prepared samples were then analysed using a laser intensity of 80 %.

9.3 UV/Vis and CD spectroscopy

Sample preparations and spectroscopic studies followed previously published protocols and were only adapted here.[29–31]

9.3.1 Sample preparation

For all UV-based thermal denaturation studies, tetramolecular G-quadruplex samples contained 3.75 (tetramolecular) or 1.88 (unimolecular) µM single-stranded DNA, 100 mM NaCl/KCl, 10 mM buffer and, if present, 0.98 µM transition metal salt. For all experiments, samples were prepared with ultrapure water (type I, 18.2 MΩ cm), obtained with a *VWR Puranity TU 3 UV*. Samples were heated to 85 °C for 10 min, slowly cooled to 4 °C with a cooling rate of 0.5 °C/min and then left at this temperature for several hours (typically overnight). To ensure full formation of tetramolecular G-quadruplexes, the respective samples were frozen at –20 °C for 1 h and thawed again to 4 °C.[29–31]

9.3.2 UV/Vis spectroscopy

UV spectra were recorded on a *Jasco V-650* or *Jasco V-750* UV-Visible Spectrophotometer equipped with a *PAC-743 6-cell* thermostat for temperature control. The temperature was controlled using a water filled reference cuvette. All UV experiments were performed in *Hellma Analytics114-QS* quartz glass cuvettes (1 cm path length). For thermal denaturation experiments always five samples were measured simultaneously to maintain constant heating rates between the experiments. In thermal denaturation experiments the temperature was increased with 0.5 °C min^{-1}, while the change of absorbance was recorded at 295 nm, indicative for a G-quadruplex denaturation. As a control the change of absorbance at 350 nm was recorded, which was subtracted to remove unspecific changes of the absorbance. Spectra were then normalized to fraction folded values between 1 and 0, corresponding to completely folded and unfolded G-quadruplexes, respectively. The melting temperature was graphically determined at the fraction folded value of 0.5 or by calculation of the first derivative from the melting curve, where the minimum was corresponding to the melting temperature. Note that for tetramolecular G-quadruplexes a non-equilibrium melting temperature $T_{1/2}$

is determined, while for unimolecular G-quadruplexes the equilibrium melting temperature T_m was determined.[29–31]

For Thermal difference spectra (TDS) a low temperature spectrum from 220 to 350 nm (data interval: 1 nm, bandwidth: 2.0 nm, response time: 0.96 sec, scan rate: 200 nm min^{-1}) was recorded at 0 or 4 °C, corresponding to a folded G-quadruplex. Then a high temperature spectrum was recorded at 85 or 95 °C, corresponding to a fully denatured G-quadruplex solution. From the high temperature spectrum, the low temperature spectrum was then subtracted to receive the TDS. The absorption at 350 nm was set to 0. A minimum in the TDS at 295±2 nm and maxima at 243±2 nm and 273±2 are indicative for the formation of G-quadruplexes.[29–31]

Table 15. Melting temperatures T_m in absence of transition metal cations and thermal stabilizations (ΔT_m) of unimolecular G-quadruplex forming sequences. Conditions: 1.88 µM ssDNA, 100 mM KCl, 10 mM LiCaco pH 7.2 and if present 1.88 or 3.75 µM transition metal cation.[29,31]

Sequence	No transition metal	$CuSO_4$	$NiSO_4$	ZnI_2	$Co(NO_3)_2$
htel**L**$^{1S}_4$	37	36 (-1)	36 (-1)	36 (-1)	37 (+0)
htel**L**$^{1R}_4$	29	29 (+0)	28 (-1)	29 (+0)	29 (+0)
htel**L**$^{2S}_2$	27	28 (+1)	27 (+0)	27 (+0)	26 (-1)
htel**L**$^{2S}_2$B in Na^I	53	55 (+2)	53 (+0)	54 (+1)	53 (+0)
htel**L**$^{2R}_2$	29	29 (+0)	29 (+0)	29 (+0)	28 (-1)
htel**L**$^{2R}_2$B in Na^I	52	52 (+0)	49 (-3)	52 (+0)	52 (+0)
htel**L**$^{2S}_3$	28	31 (+3)	28 (+0)	28 (+0)	27 (-1)
htel**L**$^{2S}_3$B in Na^I	50	56 (+6)	51 (+1)	52 (+2)	50 (+0)
htel**L**$^{2R}_3$	29	31 (+2)	28 (-1)	29 (+0)	30 (+1)
htel**L**$^{2R}_3$B in Na^I	45	49 (+4)	46 (+1)	49 (+4)	46 (+1)
htel**L**$^{2S}_4$	33	56 (+23)	45 (+12)	36 (+3)	35 (+2)
htel**L**$^{2S}_4$ 2 equiv. metal	33	53 (+20)	45 (+12)	35 (+2)	35 (+2)
htel**L**$^{2S}_4$B	37	60 (+23)	n.d.	56 (+19)	n.d.
htel**L**$^{2S}_4$C	42	63 (+21)	n.d.	63 (+21)	n.d.
htel**L**$^{2R}_4$	34	56 (+22)	45 (+11)	36 (+2)	36 (+2)
htel**L**$_4^{2R}$ 2 equiv. metal	34	51 (+17)	45 (+11)	37 (+3)	32 (-2)
htel**L**$^{2R}_4$B	36	62 (+26)	n.d.	52 (+16)	n.d.
htel**L**$^{2R}_4$C	43	66 (+23)	n.d.	55 (+12)	n.d.
htel**L**$^{2S}_5$	33	54 (+21)	55 (+22)	37 (+4)	37 (+4)
htel**L**$^{2S}_5$ 2 equiv. metal	33	46 (+13)	55 (+22)	38 (+5)	36 (+3)
htel**L**$^{2R}_5$	34	50 (+16)	47 (+13)	36 (+2)	35 (+1)
htel**L**$^{2R}_5$ 2 equiv. metal	34	47 (+13)	46 (+12)	37 (+3)	36 (+2)
htel**L**$^{2S}_6$	36	54 (+18)	59 (+23)	44 (+8)	44 (+8)
htel**L**$^{2S}_6$ 2 equiv. metal	34	52 (+ 18)	52 (+ 18)	42 (+ 8)	36 (+ 2)
htel**L**$^{2R}_6$	35	50 (+15)	51 (+16)	42 (+7)	41 (+6)
htel**L**$^{2R}_6$ 2 equiv. metal	35	51 (+16)	50 (+15)	44 (+9)	43 (+8)
htel**L**$^{2S}_7$	28	43 (+15)	46 (+18)	36 (+8)	36 (+8)
htel**L**$^{2S}_7$ 2 equiv. metal	28	46 (+18)	46 (+18)	38 (+10)	39 (+11)
htel**L**$^{2R}_7$	29	43 (+14)	44 (+15)	36 (+7)	30 (+1)
htel**L**$^{2R}_7$ 2 equiv. metal	29	46 (+17)	44 (+15)	39 (+10)	32 (+3)

9.3.3 CD spectroscopy

CD spectra were recorded on an *Applied Photophysics Chirascan qCD spectropolarimeter* (350 – 205 nm, 0.5 s time-per-point, step size 1 nm, bandwidth 0.5 nm, 3 repeats) at 7 °C. Temperature was controlled using a *Quantum Northwest* temperature control attached to a sample probe. A constant flow of dry N_2 was applied to avoid water condensation. To remove unspecific CD effects from the cuvettes, always background spectra with the same cuvette containing only buffer were recorded and subtracted. Spectra were generally smoothed with the build in software using Savitzky-Golay (5). The background was very noisy and was therefore smoothed with a factor of 10. The CD effect at 350 nm was set to 0.[29–31]

9.3.4 G-quadruplex association kinetics

Kinetic measurements following the G-quadruplex formation were performed as follows. Prepared sample solutions were heated to 95 °C for 10 min and transferred still hot to a cuvette. The cuvettes were cooled inside the spectrometer (UV or CD) to 7 °C and equilibrated for 120 s, before the measurement was started, following the change of the CD effect at 295 nm or the absorption at 295 nm.

The calculation of k_{on} was solely based on the CD spectroscopic measurements, since it was less influenced by water condensation and temperature dependent effects. The CD effect at 295 nm was converted to the G-quadruplex concentration with respect to the CD effect of a completely formed G-quadruplex solution. Using **Equation 3** k_{on} was calculated according to literature, where [A_4] is the G-quadruplex and [A] the single strand concentration.[29–31,260,275]

Table 16. Association kinetics k_{on} calculated from the CD based experiments with 8 and 16 µM ssDNA (**Figure 85**).

	Kon / M^{-3} s^{-1}	
	L^{1R}G$_4$	**L^{1S}G$_4$**
no metal	2.5 x 10^9	1.4 x 10^9
1 equiv. Cu^{II}	4.2 x 10^{11}	3.2 x 10^{11}
10 equiv. Cu^{II}	1.9 x 10^{11}	1.3 x 10^{11}
1 equiv. Zn^{II}	1.9 x 10^{10}	3.3 x 10^9

Equation 3.

$$\frac{d[A]}{dt} = -4\frac{d[A_4]}{dt} = -k_{on} * [A]^4$$

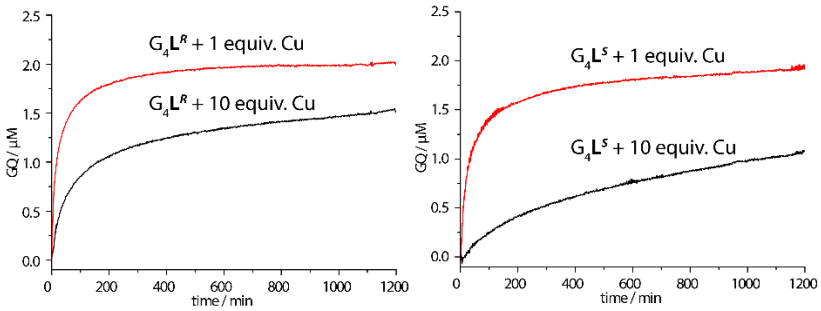

Figure 84. Kinetic G-quadruplex association studies with 8 µM ssDNA in presence of 1 (red) and 10 (black) equiv. Cu^{II}. Conditions: 8 µM ssDNA, 8 µM $CuSO_4$, 10 mM LiCaco pH 7.2, 100 mM NaCl.

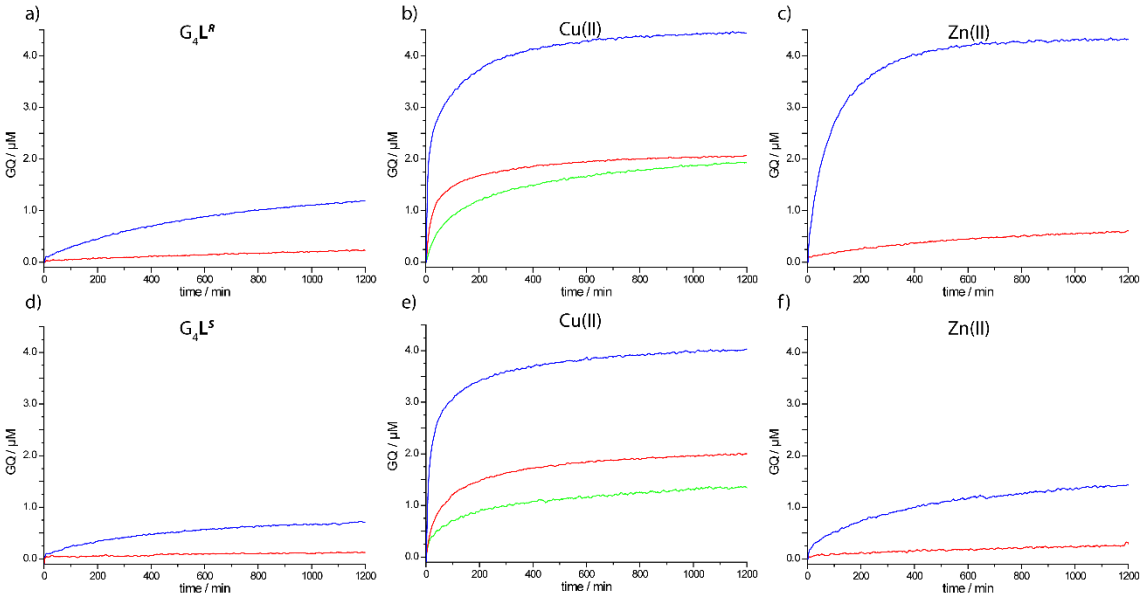

Figure 85. Kinetic G-quadruplex association studies of $\mathbf{L^{1R}}G_4$ (a-c) $\mathbf{L^{1S}}G_4$ (d-f) with 8 (red, green) and 16 (blue) µM ssDNA in absence and presence of 1 equiv. Zn^{II} and Cu^{II} or 10 equiv. (green) Cu^{II}. Conditions: 8 or 16 µM ssDNA, 10 mM LiCaco pH 7.2, 100 mM NaCl.

9.4 Catalytic studies

9.4.1 Enantioselective Michael-Addition

Samples were prepared as described in **9.3.1**. After the G-quadruplex samples were prepared the Michael-acceptor was added followed by dimethyl malonate (DMM) and incubated for three days at 5 °C unless otherwise stated. After three days the samples were extracted with Et_2O and the organic phase was dried over $MgSO_4$. Given that the sample volumes were very small this was done by adding $MgSO_4$ (tip of a spatula) to a centrifugal filter vial. On top was added the organic phase which was then filtered to remove the $MgSO_4$. The organic solvent was then removed using a *Saur Laborbedarf S-Concentrator BA-VC-300H* vacuum concentrator. The remaining solid was dissolved in Hexane/*i*POH, 70/30 and filtered again using a centrifugal filter vial. Conversion and

enantioselectivity were analysed by chiral normal phase HPLC using a *CHIRALPAK IA-3* column (Amylose tris(3,5-dimethylphenylcarbamate) immobilized on 3 µM silica-gel) and a *CHIRALPAK IC* guard column with a *n*Hexane/*i*POH, 80/20 solvent mixture and a flow rate of 1 mL min^{-1}. The signals corresponding to starting material and product were calibrated by injection of increasing volumes of 1 mM stock solution in DMSO (**Figure 86**).

9.4.2 Conversion and enantioselectivity

Table 3: Conversion and enantioselectivity of htel**L**$^{S}_{3}$A-htel**L**$^{S}_{3}$O. Conditions: 120 µM DNA, 100 µM $CuSO_4$, 100 mM KCl, 10 mM HEPES pH 8, 100 mM DMM, 1 mM Michael-acceptor **1**, DMSO (1 % v/v) at 5 °C for 3d.

Sequence	L in Loop 1	L in Loop 3	conversion [%]	*ee* [%]
htel**L**$^{S}_{3}$A	2	1	23	-29
htel**L**$^{S}_{3}$E	2	1	16	27
htel**L**$^{S}_{3}$F	2	1	8	11
htel**L**$^{S}_{3}$D	1	2	80	-91
htel**L**$^{S}_{3}$C	1	2	40	57
htel**L**$^{S}_{3}$G	1	2	66	44
htel**L**$^{S}_{3}$B	1	2	92	-96
htel**L**$^{S}_{3}$H	1	2	94	-83
htel**L**$^{S}_{3}$I	1	2	87	-91
htel**L**$^{S}_{3}$J	1	2	97	-91
htel**L**$^{S}_{3}$K	1	2	93	-86
htel**L**$^{S}_{3}$L	1	2	83	-93
htel**L**$^{S}_{3}$M	1	2	96	-90
htel**L**$^{S}_{3}$N	2	1	47	-32
htel**L**$^{S}_{3}$O	2	1	9	-37

Table 4: Conversion and enantioselectivity of htel**L**$^{S}_{3}$A-htel**L**$^{S}_{3}$O. Conditions: 120 µM DNA, 100 µM $CuSO_4$, 100 mM NaCl, 10 mM HEPES pH 8, 100 mM DMM, 1 mM Michael-acceptor **1**, DMSO (1 % v/v) at 5 °C for 3d.

Sequence	**L in Loop 1**	**L in Loop 3**	**conversion [%]**	***ee* [%]**
htel**L**$^{S}_{3}$A	2	1	12	3
htel**L**$^{S}_{3}$E	2	1	23	69
htel**L**$^{S}_{3}$F	2	1	3	14
htel**L**$^{S}_{3}$D	1	2	20	-68
htel**L**$^{S}_{3}$C	1	2	25	32
htel**L**$^{S}_{3}$G	1	2	11	48
htel**L**$^{S}_{3}$B	1	2	45	-55
htel**L**$^{S}_{3}$H	1	2	8	3
htel**L**$^{S}_{3}$I	1	2	22	-53
htel**L**$^{S}_{3}$J	1	2	36	-50
htel**L**$^{S}_{3}$K	1	2	10	-18
htel**L**$^{S}_{3}$L	1	2	61	-52
htel**L**$^{S}_{3}$M	1	2	12	-32
htel**L**$^{S}_{3}$N	2	1	12	-37
htel**L**$^{S}_{3}$O	2	1	8	-35

Table 5: Conversion and enantioselectivity of htel**L**$^{S}_{2}$A-htel**L**$^{S}_{2}$M. Conditions: 120 µM DNA, 100 µM $CuSO_4$, 100 mM NaCl, 10 mM HEPES pH 8, 100 mM DMM, 1 mM Michael-acceptor **1**, DMSO (1 % v/v) at 5 °C for 3d.

Sequence	**L in Loop 1**	**L in Loop 3**	**conversion [%]**	***ee* [%]**
htel**L**$^{S}_{2}$B	1	1	23	15
htel**L**$^{S}_{2}$C	1	1	56	-7
htel**L**$^{S}_{2}$D	1	1	16	4
htel**L**$^{S}_{2}$A	1	1	21	33
htel**L**$^{S}_{2}$E	1	1	16	14
htel**L**$^{S}_{2}$K	1	1	16	-11
htel**L**$^{S}_{2}$F	2	0	78	71
htel**L**$^{S}_{2}$G	2	0	61	67
htel**L**$^{S}_{2}$H	2	0	67	61
htel**L**$^{S}_{2}$I	0	2	43	44
htel**L**$^{S}_{2}$J	0	2	40	20
htel**L**$^{S}_{2}$L	1	1	14	-46
htel**L**$^{S}_{2}$M	1	1	6	-21

Table 6: Conversion and enantioselectivity of htel**L**$^{S}_{2}$A-htel**L**$^{S}_{2}$M. Conditions: 120 µM DNA, 100 µM $CuSO_4$, 100 mM KCl, 10 mM HEPES pH 8, 100 mM DMM, 1 mM Michael-acceptor **1**, DMSO (1 % v/v) at 5 °C for 3d.

Sequence	L in Loop 1	L in Loop 3	conversion [%]	*ee* [%]
htel**L**$^{S}_{2}$B	1	1	35	13
htel**L**$^{S}_{2}$C	1	1	61	-28
htel**L**$^{S}_{2}$D	1	1	52	-11
htel**L**$^{S}_{2}$A	1	1	28	31
htel**L**$^{S}_{2}$E	1	1	33	28
htel**L**$^{S}_{2}$K	1	1	68	-40
htel**L**$^{S}_{2}$F	2	0	75	46
htel**L**$^{S}_{2}$G	2	0	69	-29
htel**L**$^{S}_{2}$H	2	0	73	4
htel**L**$^{S}_{2}$I	0	2	97	-71
htel**L**$^{S}_{2}$J	0	2	92	44
htel**L**$^{S}_{2}$L	1	1	53	6
htel**L**$^{S}_{2}$M	1	1	18	-15

Table 7: Conversion and enantioselectivity of selected G-quadruplexes containing the **L**^{R} enantiomer. Conditions: 120 µM DNA, 100 µM $CuSO_4$, 100 mM electrolyte, 10 mM HEPES pH 8, 100 mM DMM, 1 mM Michael-acceptor **1**, DMSO (1 % v/v) at 5 °C for 3d.

Sequence	Number L	electrolyte	conversion [%]	*ee* [%]
htel**L**$^{R}_{2}$G	2	KCl	90	54
htel**L**$^{R}_{2}$I	2	KCl	92	-85
htel**L**$^{R}_{3}$G	3	KCl	60	4
htel**L**$^{R}_{3}$B	3	KCl	97	-84
htel**L**$^{R}_{3}$D	3	KCl	94	≥ 99 (-)
htel**L**$^{R}_{2}$F	2	KCl	94	30
htel**L**$^{R}_{2}$H	2	KCl	93	40
htel**L**$^{R}_{3}$H	3	KCl	95	-68
htel**L**$^{R}_{3}$I	3	KCl	98	-83
htel**L**$^{R}_{3}$J	3	KCl	96	-85
htel**L**$^{R}_{3}$K	3	KCl	94	-67
htel**L**$^{R}_{3}$L	3	KCl	96	-83
htel**L**$^{R}_{3}$M	3	KCl	98	-83
htel**L**$^{R}_{2}$G	2	NaCl	92	90
htel**L**$^{R}_{2}$I	2	NaCl	95	-7
htel**L**$^{R}_{2}$F	2	NaCl	93	86
htel**L**$^{R}_{2}$H	2	NaCl	93	56

Table 8: Conversion and enantioselectivity of selected G-quadruplexes containing no **L** or ≥ 4 times **L**. Conditions: 120 µM DNA, 100 µM $CuSO_4$, 100 mM electrolyte, 10 mM HEPES pH 8, 100 mM DMM, 1 mM Michael-acceptor **1**, DMSO (1 % v/v) at 5 °C for 3d.

Sequence	Number L	electrolyte	conversion [%]	*ee* [%]
-	-	NaCl	15	0
-	-	KCl	23	0
c-Myc	0	KCl	12	-1
$htel_{22}$	0	KCl	10	5
c-Myc	0	NaCl	5	6
$htel_{22}$	0	NaCl	7	0
htel$\mathbf{L}^{S}_{4}$A	4	KCl	10	-25
htel$\mathbf{L}^{S}_{4}$B	4	KCl	4	14
htel$\mathbf{L}^{S}_{4}$C	4	KCl	7	-28
htel$\mathbf{L}^{S}_{4}$B	4	NaCl	2	53
htel$\mathbf{L}^{S}_{4}$C	4	NaCl	0	0
htel$\mathbf{L}^{S}_{6}$	6	KCl	0	0
htel$\mathbf{L}^{S}_{7}$	7	KCl	17	-27

Table 9: Conversion and enantioselectivity of htel$\mathbf{L}^{R}_{3}$D and htel$\mathbf{L}^{R}_{2}$G in absence of transition metals and in presence of ZnI_2. Conditions: 120 µM DNA, 100 µM ZnI_2, 100 mM electrolyte, 10 mM HEPES pH 8, 100 mM DMM, 1 mM Michael-acceptor **1**, DMSO (1 % v/v) at 5 °C for 3d.

Sequence	Number L	electrolyte	transition metal salt	conversion [%]	*ee* [%]
htel$\mathbf{L}^{R}_{3}$D	3	KCl	ZnI2	-	-
htel$\mathbf{L}^{R}_{2}$G	2	NaCl	ZnI2	-	-
htel$\mathbf{L}^{R}_{3}$D	3	KCl	-	-	-
htel$\mathbf{L}^{R}_{2}$G	2	NaCl	-	-	-

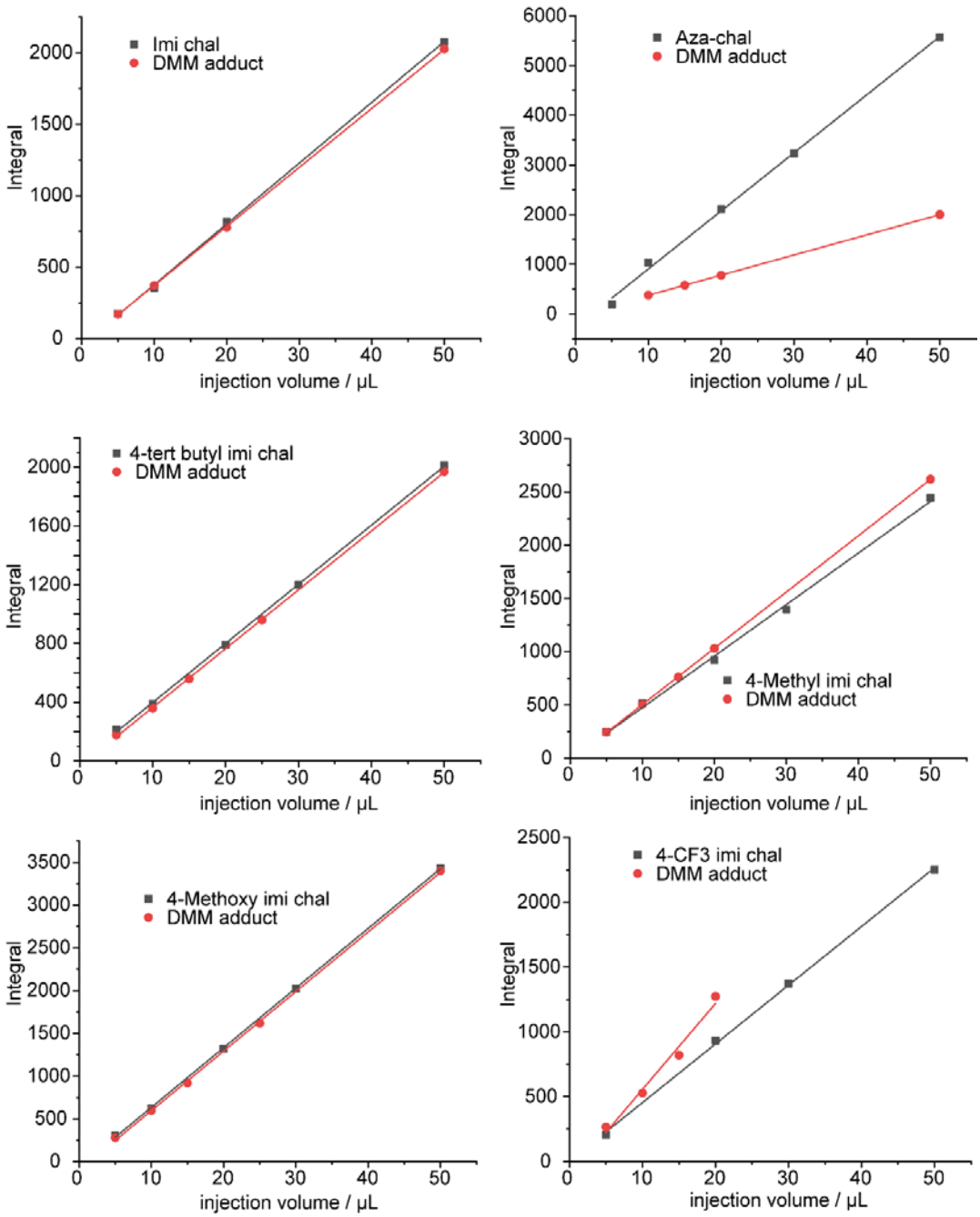

Figure 86. Calibration of the Michael-addition of chalcone derivatives and their DMM adducts. The signals corresponding to starting material and product were calibrated by injection of increasing volumes of 1 mM stock solution in *n* Hexane:*iso* propanol, 70/30.

9.5 Native ESI-MS

Native ESI-MS experiments followed the identical published protocol and the procedure was here adapted.[29–31] In native ESI-MS, mild conditions are applied during the ionization process to keep the secondary structure folded. To distinguish whether a G-quadruplex remains folded during ionization, two intrinsic properties are exploited. First, in case of tetramolecular G-quadruplexes is that they are only intact if signals corresponding to a tetramer are observed while single-stranded DNA corresponds to denatured G-quadruplexes. Second, in their native state G-quadruplexes always bind n-1 monovalent cations (n = number of G-tetrads) in their central pockets followed by a statistical distribution of additional unspecific adducts. For a denatured species, a statistical distribution of adducts would be expected, starting with zero cations.[264–266]

Native ESI-MS and Trapped Ion mobility measurements were performed on a *Bruker timsTOF* instrument combining a trapped ion mobility spectrometer (TIMS) with a time-of-flight (TOF) mass spectrometer in one instrument.

Measurement: TIMS and TOF were calibrated, using the commercial *Agilent ESI tuning mix*. The instrument was calibrated prior to each measurement. Ions were generated using electrospray ionization (ESI, analyte concentration: 12.5 µM G-quadruplex, 0.5 mM KCl and 50 mM TMAA (trimethyl ammonium acetate pH 6.8, solvent: acetonitrile-water, 1:1, capillary voltage: 4500 V, end plate offset voltage: 500 nebulizer gas pressure: 0.4/0.6 bar, dry gas flow rate: 6/9 l min-1, dry temperature: 303 K). The generated ions were then deflected into the entrance funnel and TIMS analyser (carrier gas: N2, temperature: 305 K, entrance pressure: 2.55 mbar, exit pressure: 0.89 mbar, IMS imeX ramp end: 1.66 1/K0, IMS imeX ramp start: 0.51 1/K0). In the TIMS analyser the ions were stationary trapped and accumulated for 70 or200 ms, before the electric field strength was stepwise reduced, leading to a release of ions, separated by their ion mobility. After release the ions were refoccussed and transferred to the TOF analyser.[270–272] Using the equation below, the ion mobility *K* was calculated from the electric field strength *E* and the velocity of the N_2 carrier gas stream *vg.*

$$K = \frac{v_g}{E} = \frac{A}{U_{release} - U_{out}} \quad (1)$$

A: calibration constant, $U_{release}$: voltage at which the ions are released, U_{out}: voltage applied to the exit of the tube. The ion mobility is corrected to standard gas density via

$$K_0 = K \frac{P}{1013\ \mathrm{hPa}} \frac{237\ \mathrm{K}}{T} \quad (2)$$

to obtain the reduced mobility K_0, where P is the pressure and T is the temperature. Using the Mason-Schamp equation, the collisional cross-section Ω can be calculated:

$$\Omega = \frac{(18\pi)^{\frac{1}{2}}}{16}\frac{ze}{(k_B T)^{\frac{1}{2}}}\left[\frac{1}{\mu}\right]^{\frac{1}{2}}\frac{1}{K_0}\frac{1}{N_0} \quad (3)$$

ze: ion charge, k_B: Boltzmann constant, μ: reduced mass of analyte and carrier gas, N_0: number density of the neutral gas.[29–31,270–272]

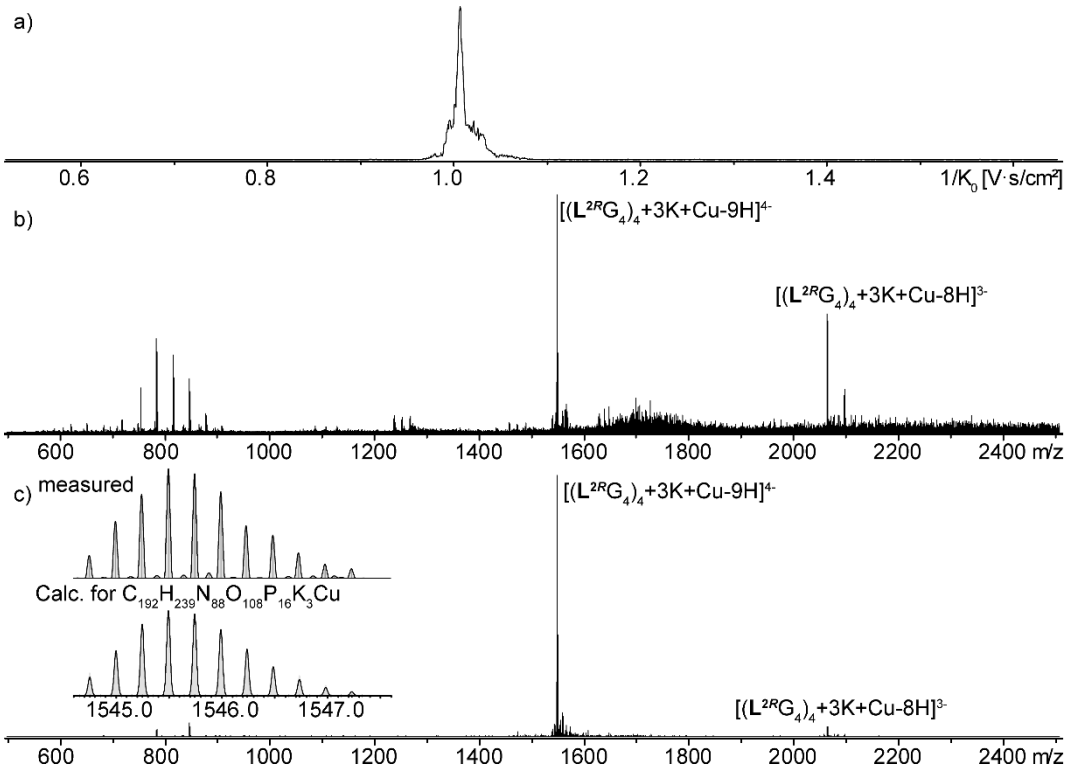

Figure 87. Native ESI-MS of **L^{2R}G$_4$** in presence of Cu^{II}. Conditions: 12.5 µM G-quadruplex, 0.5 mM KCl and 50 mM TMAA pH 6.8, solvent: acetonitrile-water, 1:1

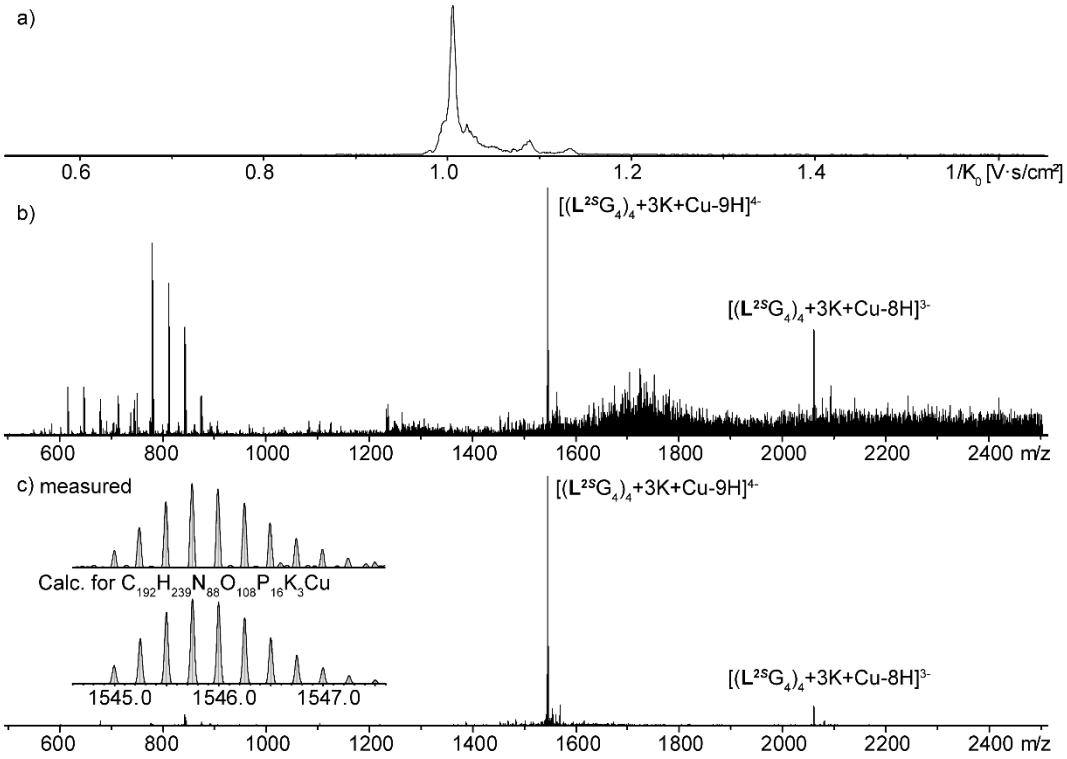

Figure 88. Native ESI-MS of $\mathbf{L^{2S}}G_4$ in presence of Cu^{II}. Conditions: 12.5 µM G-quadruplex, 12.5 µM $CuSO_4$, 0.5 mM KCl and 50 mM TMAA pH 6.8, solvent: acetonitrile-water, 1:1.

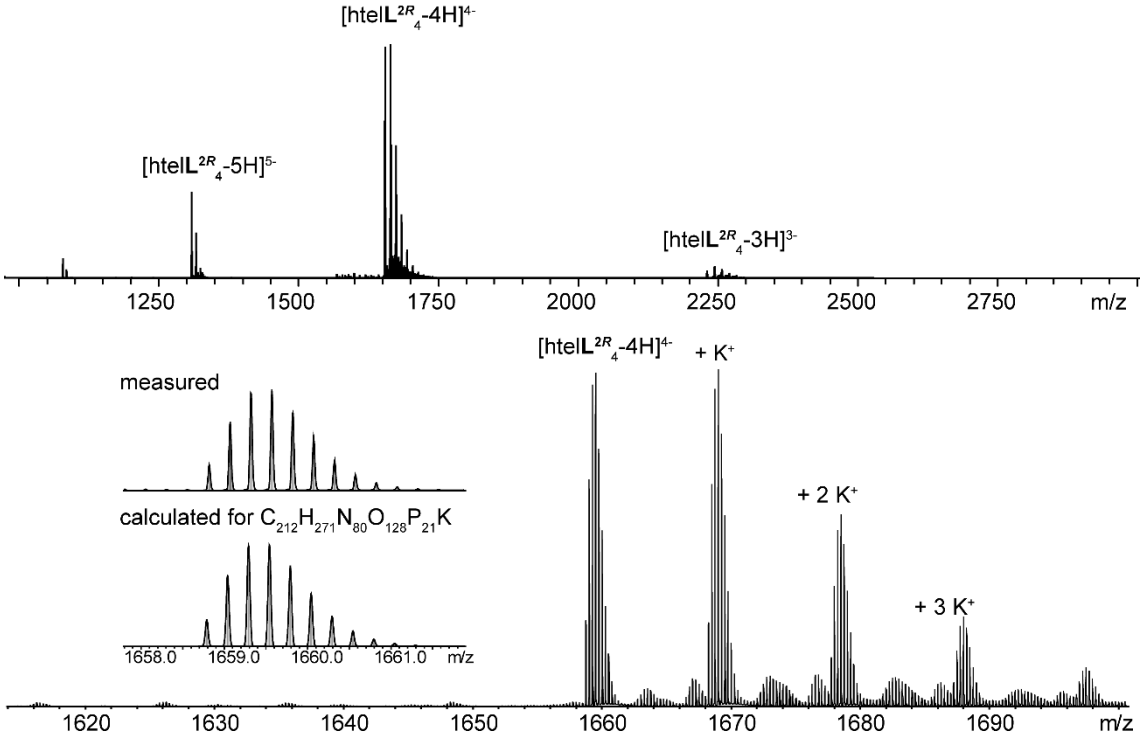

Figure 89. Native ESI-MS of htel$\mathbf{L^{2R}}_4$ in absence of transition metal cations. Conditions: 12.5 µM G-quadruplex, 0.5 mM KCl and 50 mM TMAA pH 6.8, solvent: acetonitrile-water, 1:1.

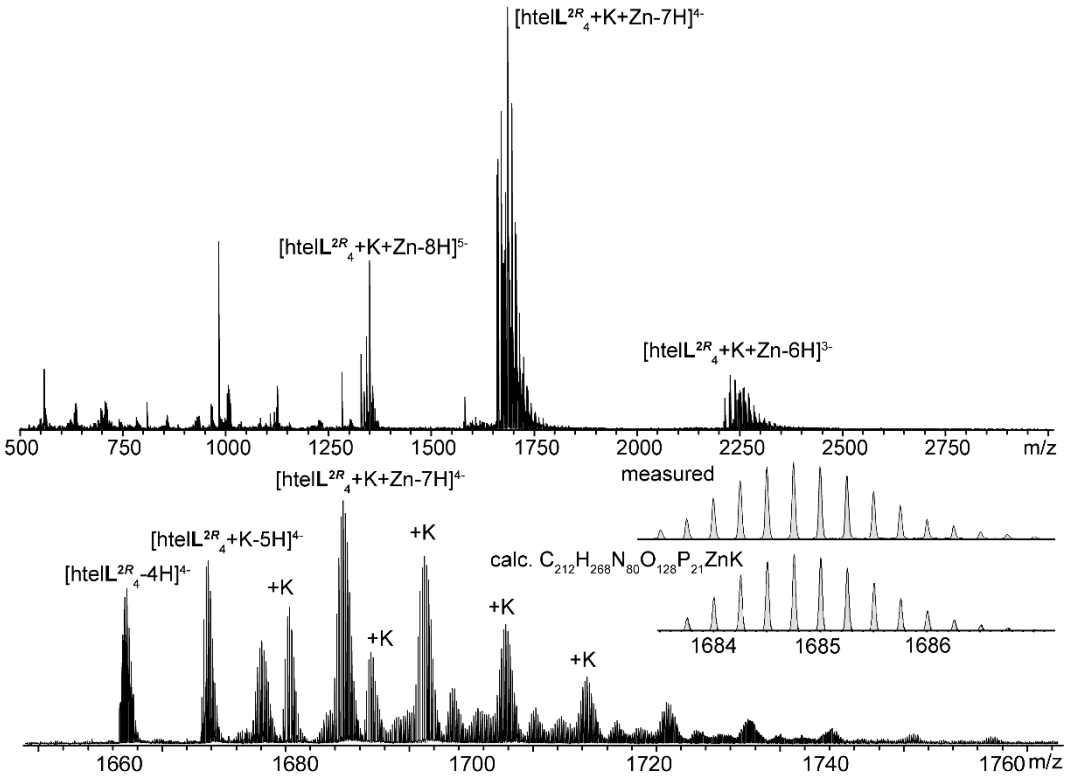

Figure 90. Native ESI-MS of htel**L**$^{2R}_4$ in presence of 1 equiv. Zn^{II}. Conditions: 12.5 µM DNA, 12.5 µM ZnI_2, 0.5 mM KCl, 50 mM TMAA, H_2O:ACN, 1:1.

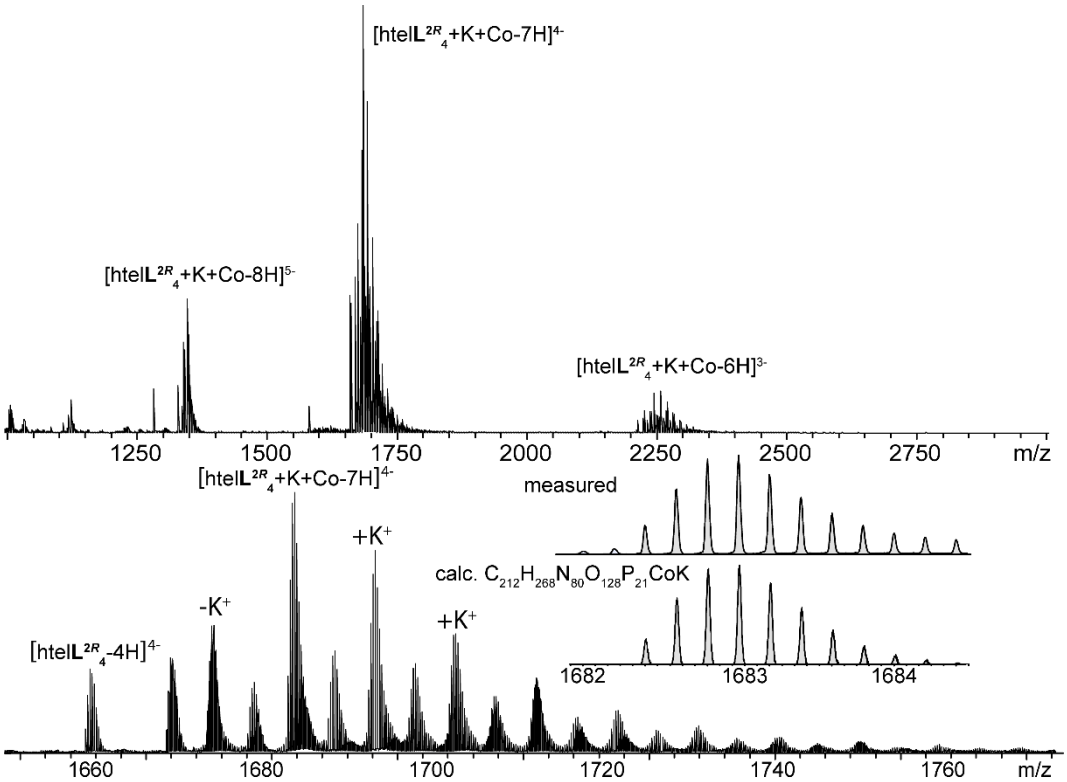

Figure 91. Native ESI-MS of htel**L**$^{2R}_4$ in presence of 1 equiv. Co^{II}. Conditions: 12.5 µM DNA, 12.5 µM $Co(NO_3)_2$, 0.5 mM KCl, 50 mM TMAA, H_2O:ACN, 1:1.

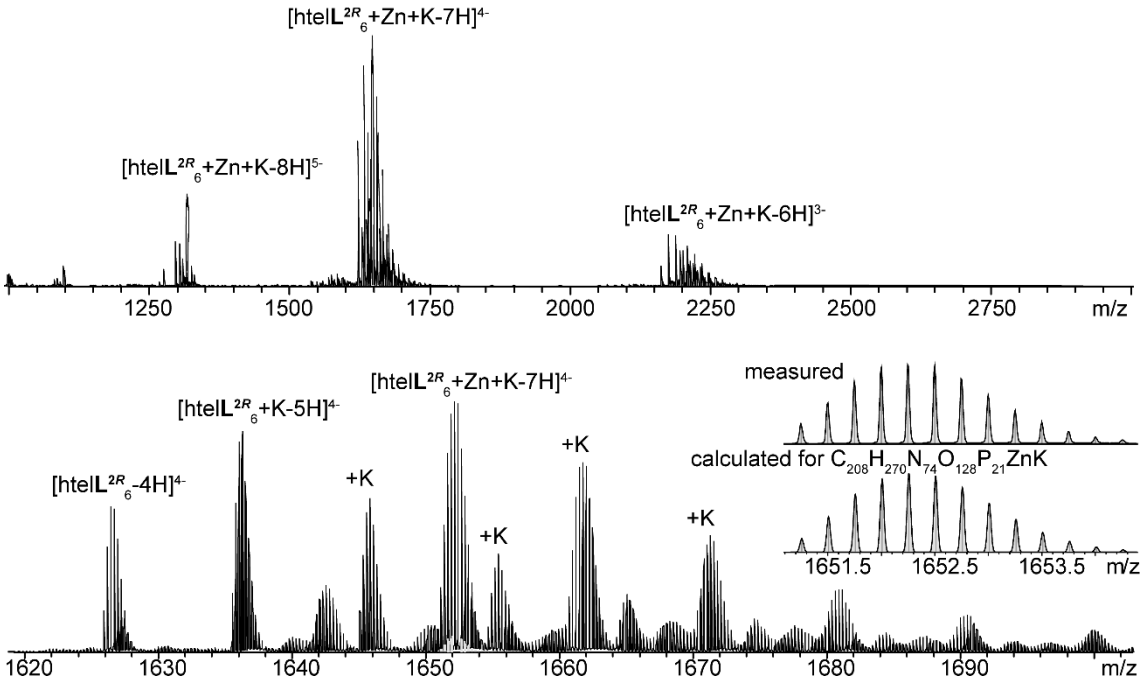

Figure 92. Native ESI-MS of htel**L**$^{2R}_6$ in presence of 1 equiv. Zn^{II}. Conditions: 12.5 µM DNA, 12.5 µM ZnI_2, 0.5 mM KCl, 50 mM TMAA, H_2O:ACN, 1:1.

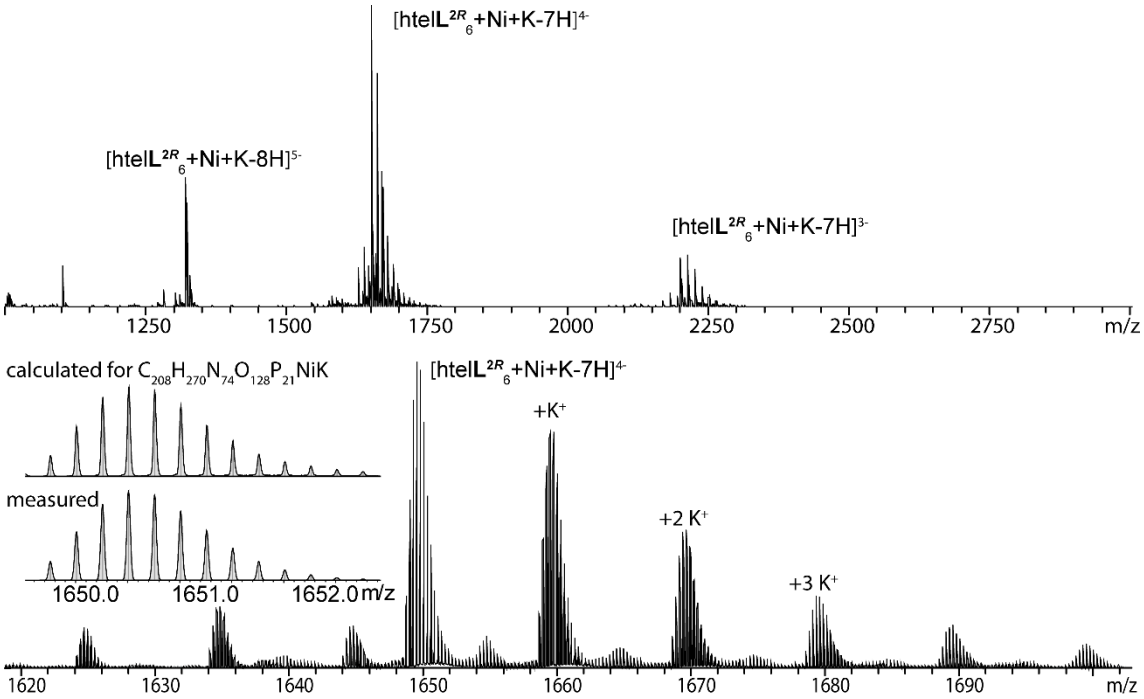

Figure 93. Native ESI-MS of htel**L**$^{2R}_6$ in presence of 1 equiv. Ni^{II}. Conditions: 12.5 µM DNA, 12.5 µM $NiSO_4$, 0.5 mM KCl, 50 mM TMAA, H_2O:ACN, 1:1.

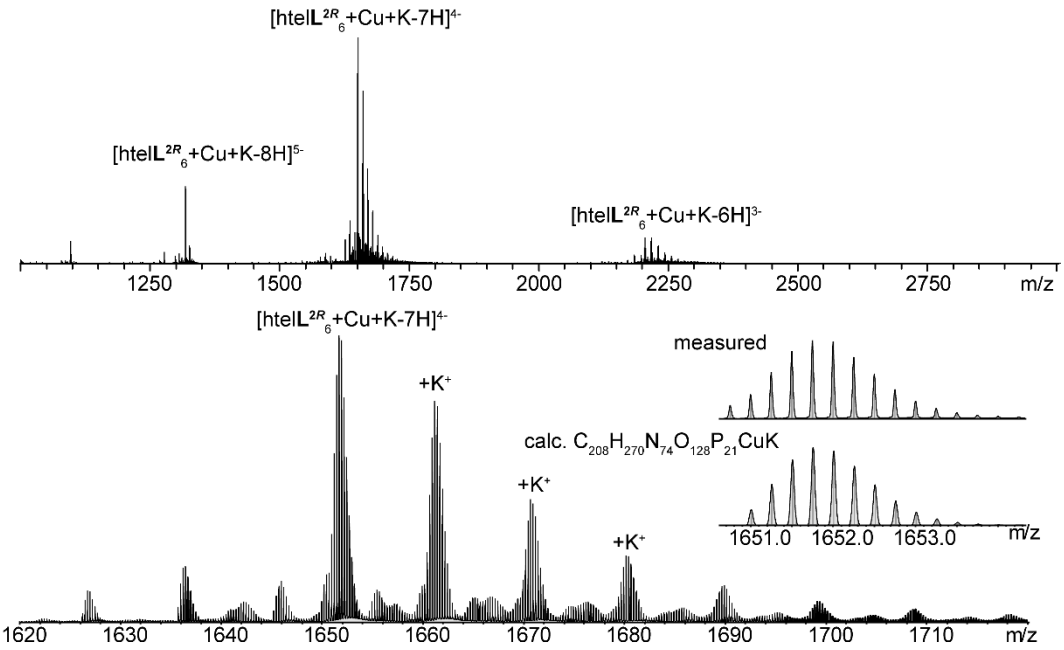

Figure 94. Native ESI-MS of htel$\mathbf{L}^{2R}_6$ in presence of 1 equiv. Cu^{II}. Conditions: 12.5 µM DNA, 12.5 µM $CuSO_4$, 0.5 mM KCl, 50 mM TMAA, H_2O:ACN, 1:1.

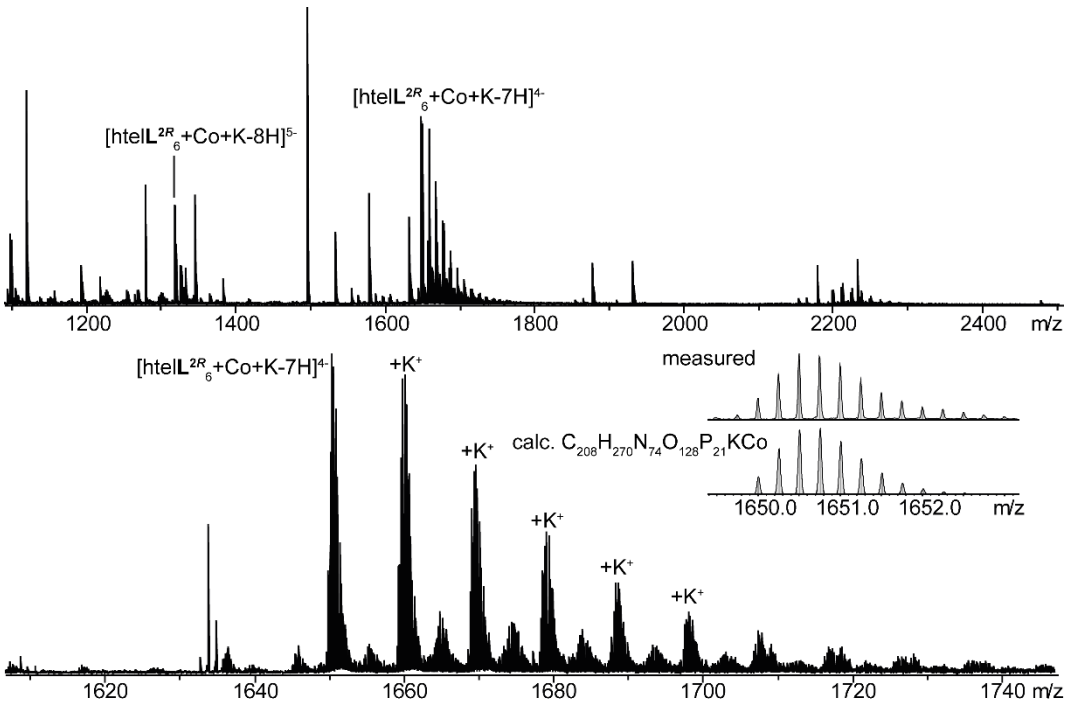

Figure 95. Native ESI-MS of htel$\mathbf{L}^{2R}_6$ in presence of 1 equiv. Co^{II}. Conditions: 12.5 µM DNA, 12.5 µM $Co(NO_3)_2$, 0.5 mM KCl, 50 mM TMAA, H_2O:ACN, 1:1.

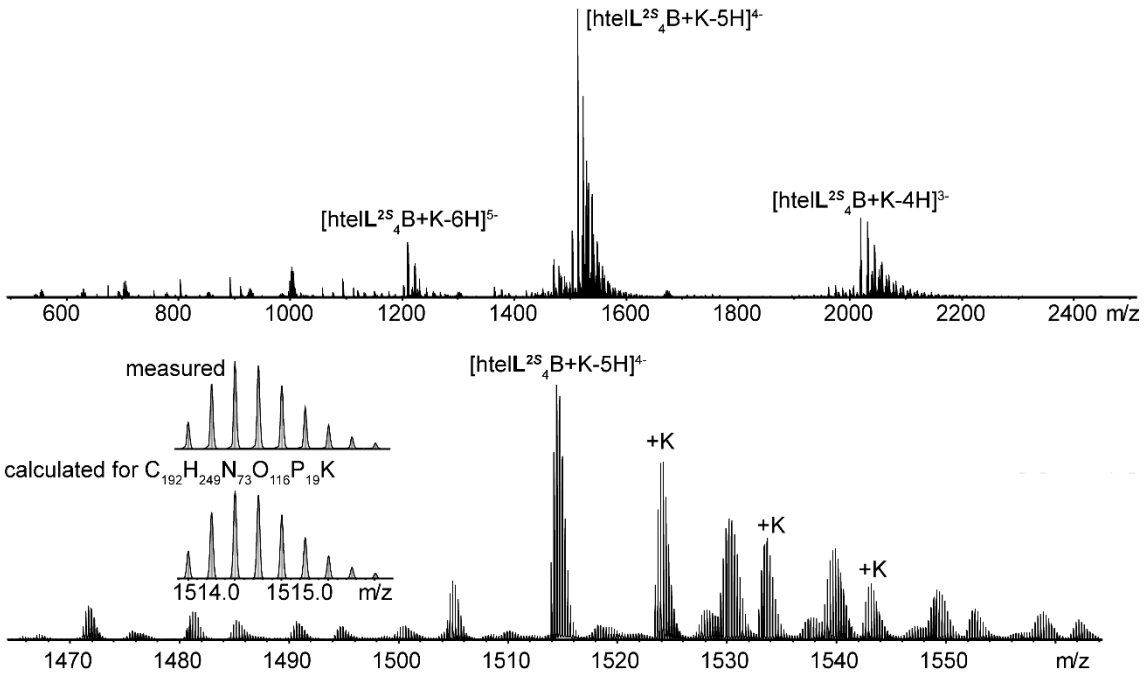

Figure 96. Native ESI-MS of htel**L**$^{2S}_4$B in absence of transition metal cations. Conditions: 12.5 µM DNA, 0.5 mM KCl, 50 mM TMAA, H_2O:ACN, 1:1.

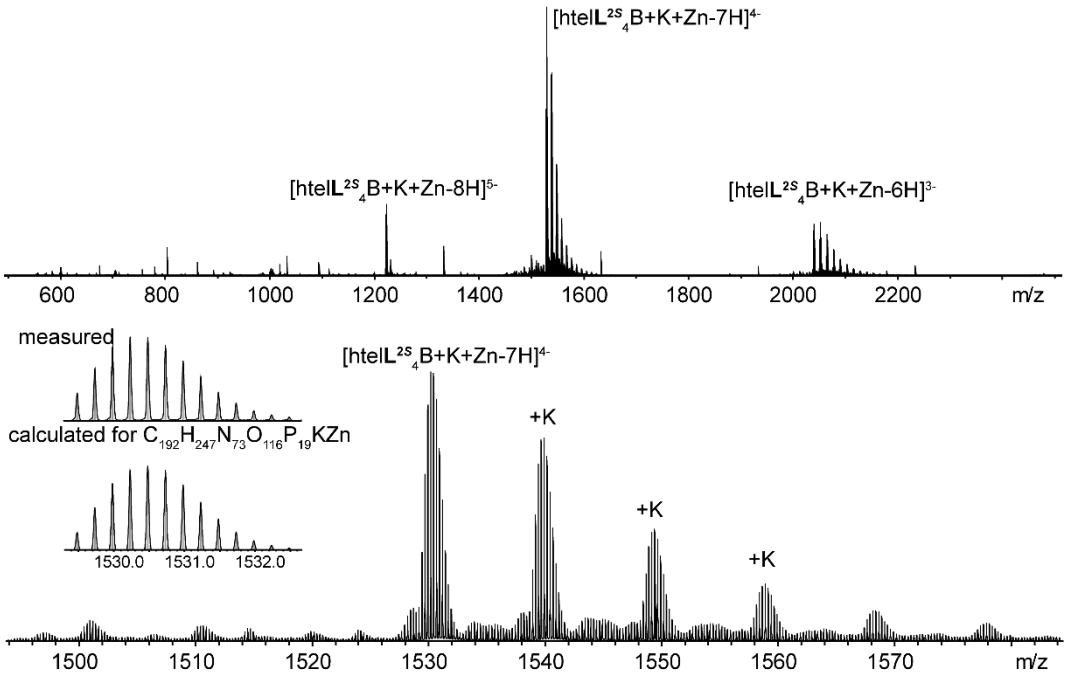

Figure 97. Native ESI-MS of htel**L**$^{2S}_4$B in presence of 1 equiv. Zn^{II}. Conditions: 12.5 µM DNA, 12.5 µM ZnI_2, 0.5 mM KCl, 50 mM TMAA, H_2O:ACN, 1:1.

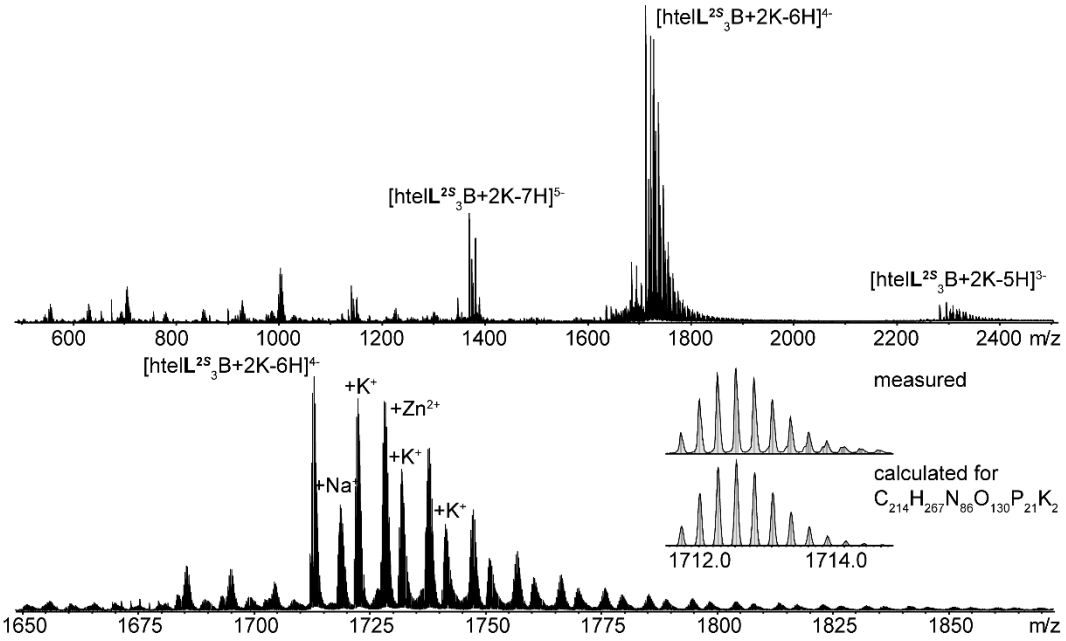

Figure 98. Native ESI-MS of htel**L**$^{2S}_{3}$B in absence of transition metal cations. Conditions: 12.5 µM DNA, 0.5 mM KCl, 50 mM TMAA, H_2O:ACN, 1:1.

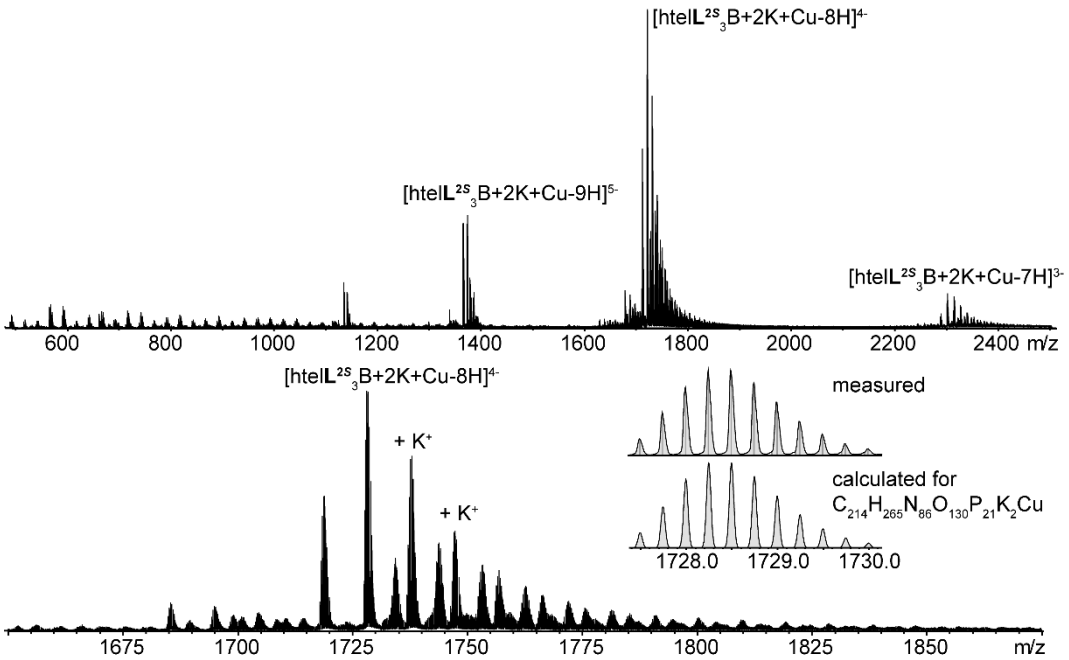

Figure 99. Native ESI-MS of htel**L**$^{2S}_{3}$B in presence of 1 equiv. Cu^{II}. Conditions: 12.5 µM DNA, 12.5 µM $CuSO_4$, 0.5 mM KCl, 50 mM TMAA, H_2O:ACN, 1:1.

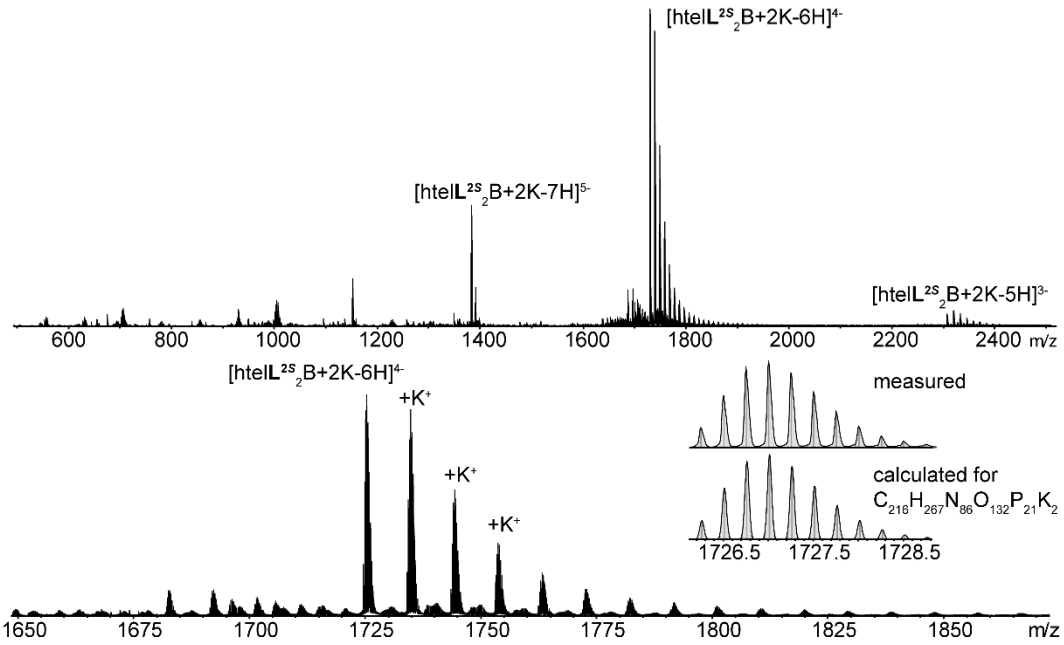

Figure 100. Native ESI-MS of htel**L**$^{2S}_2$B in absence of transition metal cations. Conditions: 12.5 µM DNA, 0.5 mM KCl, 50 mM TMAA, H_2O:ACN, 1:1.

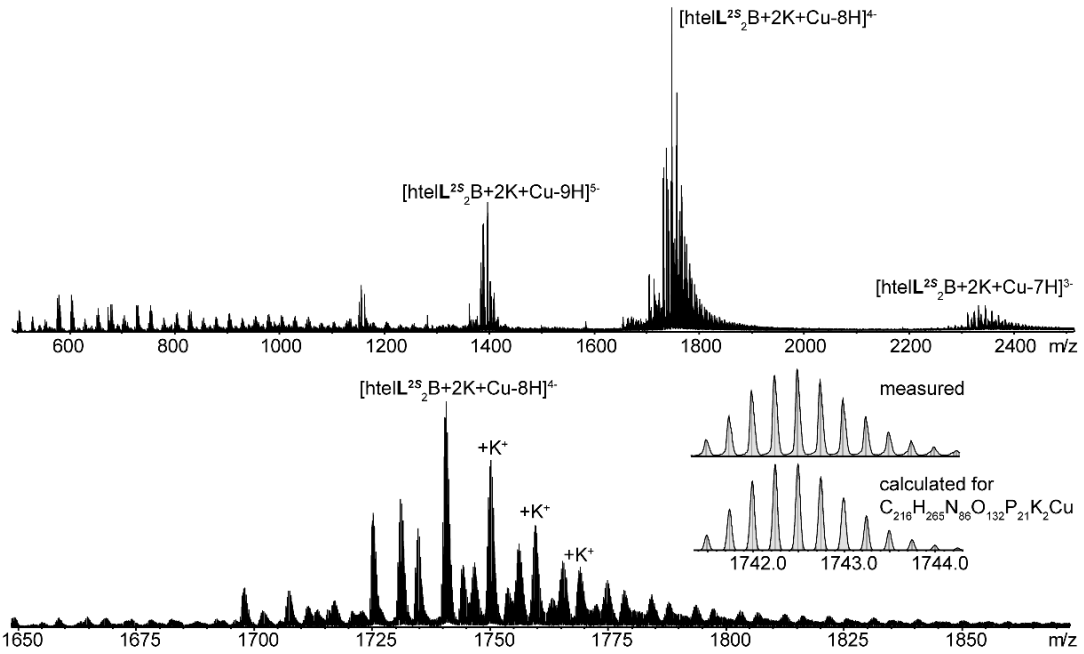

Figure 101. Native ESI-MS of htel**L**$^{2S}_2$B in presence of 1 equiv. Cu^{II}. Conditions: 12.5 µM DNA, 12.5 µM $CuSO_4$, 0.5 mM KCl, 50 mM TMAA, H_2O:ACN, 1:1.

9.6 MD simulations

Simulations were performed using GROMACS 2016.1/2020.[354–360] The AMBER force field ff99bsc1 was modified with new force field parameters for the imidazole ligandosides based on analogy to existing force field parameters.[361,362] For both enantiomers, the same set of parameters was used. Parameters regarding the Cu^{II} and Zn^{II} complex were estimated based on literature or calculated using MCPB.py and VFFDT (Visual Force Field Derivation Toolkit) with geometry optimized structures.[363–367] Adjacent ligands were named differently, to avoid ambiguity in the parameterization. Improper dihedrals were used to maintain coplanarity between the imidazole plane and the imidazole – metal plane. The respective parameters for Cu^{II} and Zn^{II} were estimated based on literature values.[366,367] The crystal structure of a tetramolecular parallel stranded (pdb: 2O4F) and unimolecular antiparallel basket- and chair-type (pdb: 143D, 1C35) G-quadruplex were modified with the Imidazole ligandosides to obtain the starting structure.[66,368,369] The modified starting structures were placed in a periodic rhombic bounding box and energy minimized for 2000 steps using steepest descent (600 kJ mol^{-1} nm^{1} tolerance). The system was solvated using a TIP3P water model and negative charges on the phosphates were neutralized with Na^+ or K^+ and the electrolyte concentration was set to 100 mM.

After neutralization, the structure was energy minimized using at first 500 steps of steepest descent with a tolerance of 500 kJ mol^{-1} nm^{-1}, followed by 3000 steps of conjugate gradient minimization with a tolerance of 300 kJ mol^{-1} nm^{-1}. A cut-off of the non-bonded Lennard Jones Potential was set to 1.3 nm. Coulombic interactions were treated using a Particle-mesh Ewald summation. Prior to the MD simulation, the starting structure was subjected to three rounds of energy minimization. In a first round using an NVT ensemble (NVT ensemble, constraints 1000 kJ mol^{-1} $Å^{-2}$, time step 2 fs; Temperature coupling modified Berendsen, 298 K) and positional constraints on heavy atoms was simulated for 100 ps, followed by 100 ps with additional pressure coupling (isotropic, Berendsen, 1 bar, time constant for coupling 0.1 ps, compressibility 4.5 10^{-5}) and in a last run 100 ps were simulated with lower applied positional constraints (100 kJ mol^{-1} $Å^{-2}$, Nose-Hoover temperature coupling 2 ps coupling, Parinello-Rahman isotropic pressure coupling, 2 ps coupling time). Prior to the production run a short MD simulation was run for 200 ps using the same settings as for the production run. The final simulation was simulated for 50/100 ns, writing coordinates after every 10 ps. After the production run, trajectories were centred and aligned. After clustering of the MD trajectory with Chimera, a representative snapshot was taken from one of the most abundant clusters. In the rmsd plots, the first frame was used as the reference.

9.6.1 RESP-charges

Partial point charges were calculated by RESP charge fitting, as described in ref.[24,29] from geometry optimized fragments (DFT B3LYP/6-31Gd). Using the capping scheme below, files were submitted to the REDServer-Development.[370–373] Inter- and intra-molecular charge constraints were applied to keep the correct total charge of the ligand. Exception was the **L²**-Zn^{II} complex, for which the RESP charges were calculated using the antechamber and respgen package.

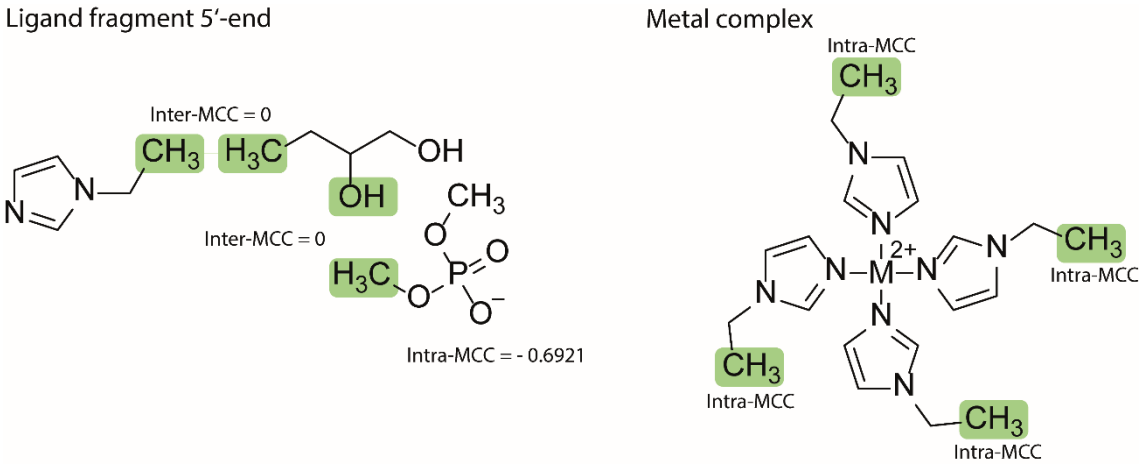

Figure 102. Applied Capping Scheme for **L¹**.

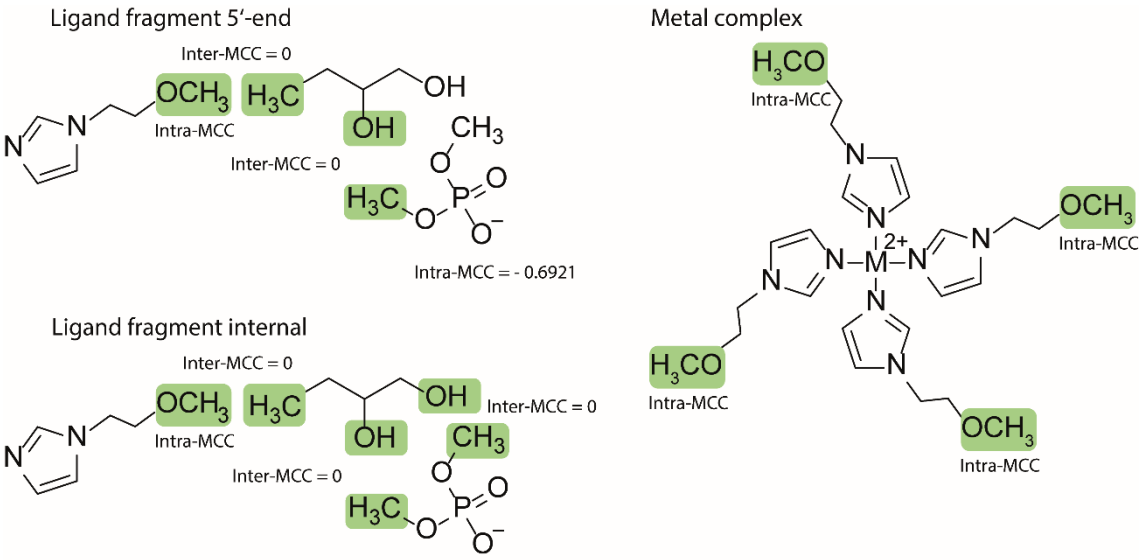

Figure 103. Applied Capping Scheme for **L²**.

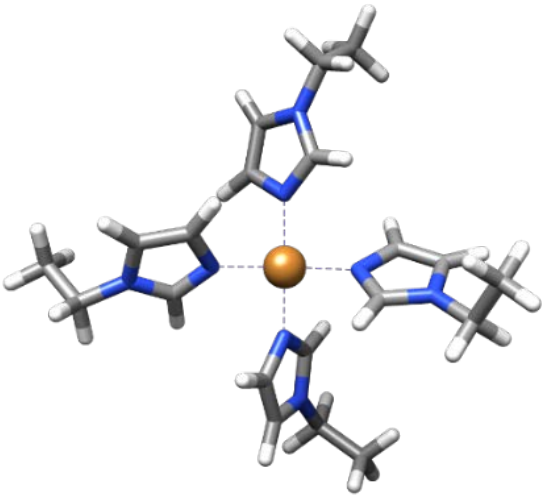

Figure 104. Geometry optimized complex of 1-ethyl-1H-imidazole with Cu^{II}. Gaussian09, DFT B3LYP/6-31Gd.

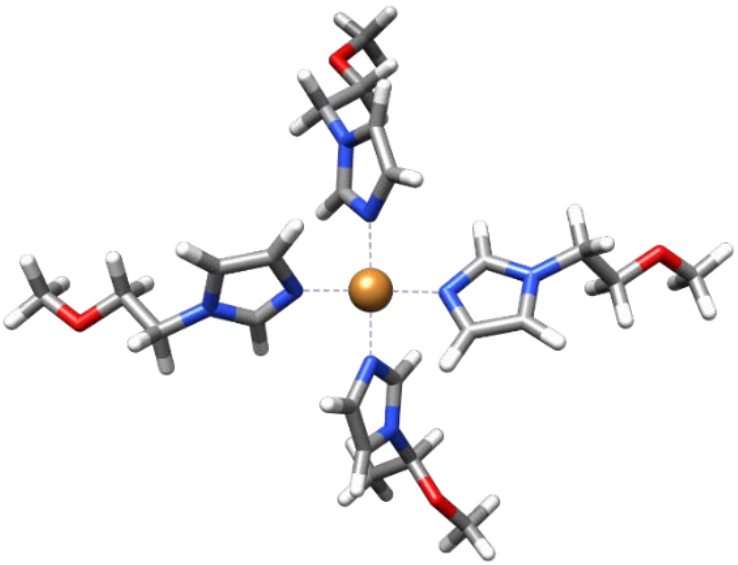

Figure 105. Geometry optimized complex of 1-(2-methoxyethyl)-1H-imidazole with Cu^{II}. Gaussian09, DFT B3LYP/6-31Gd.

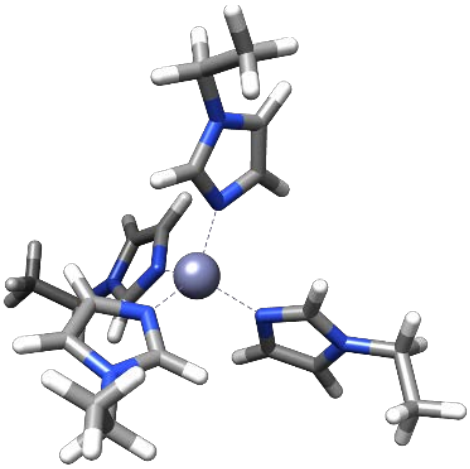

Figure 106. Geometry optimized complex of 1-ethyl-1H-imidazole with Zn^{II}. Gaussian09, DFT B3LYP/6-31Gd.

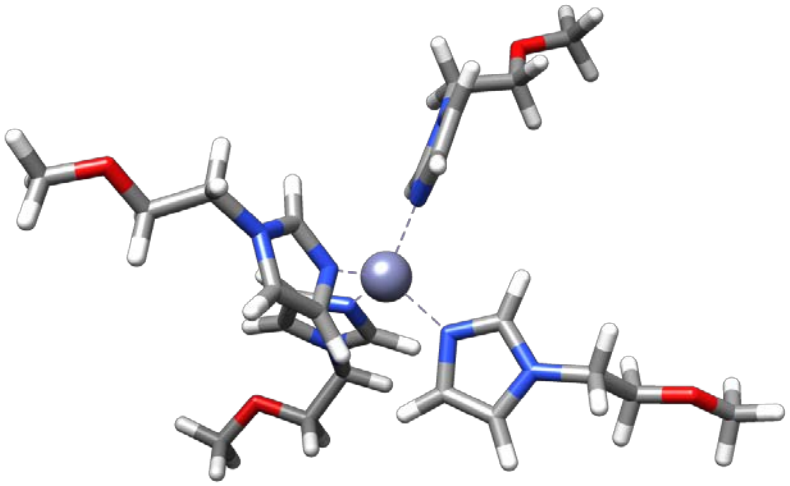

Figure 107. Geometry optimized complex of 1-(2-methoxyethyl)-1H-imidazole with Zn^{II}. Gaussian09, HF/6-31+G*.

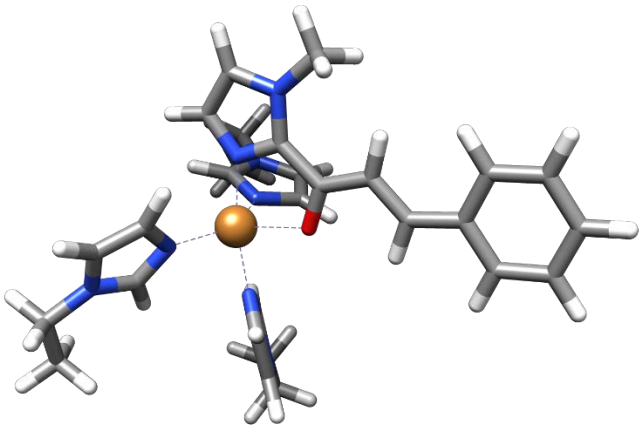

Figure 108. Geometry optimized complex of imidazole chalcone and N-ethyl-1H-imidazole with Cu^{II}. Gaussian16, DFT B3LYP/6-31Gd.

9.6.2 Simulations

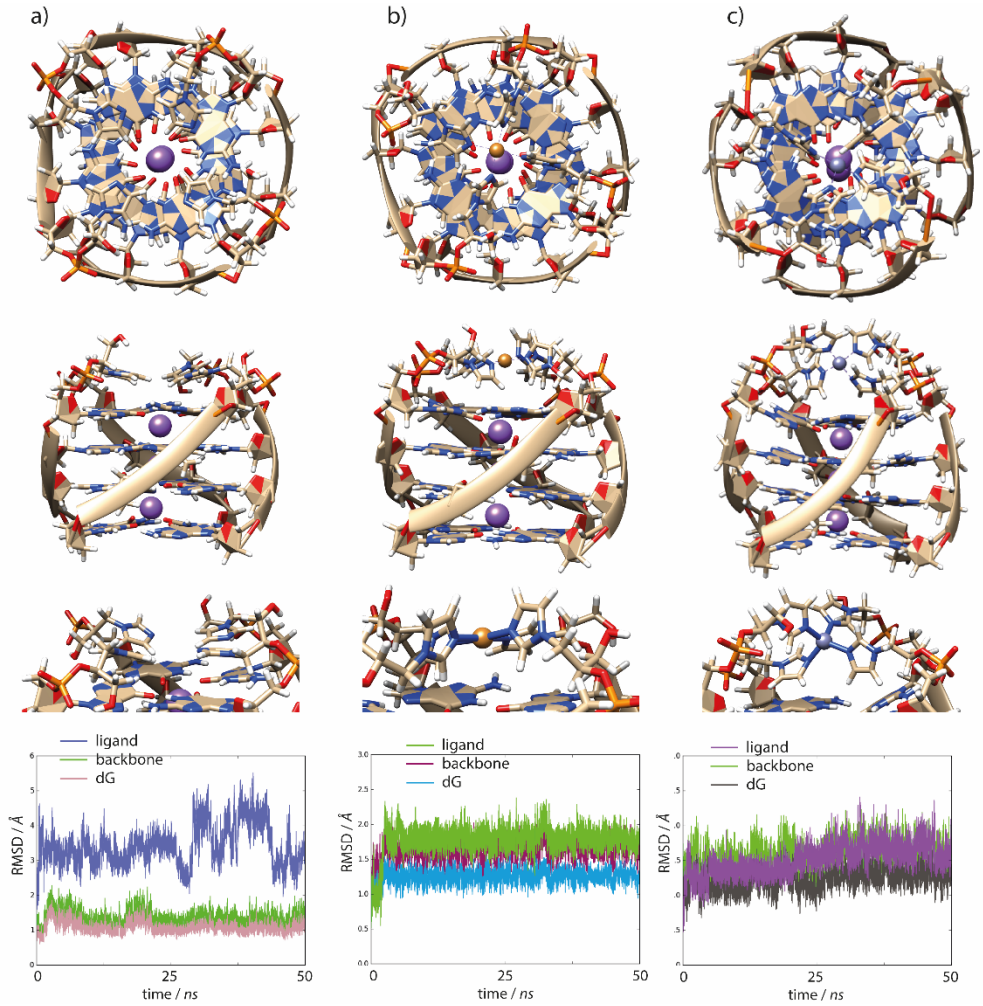

Figure 109. Representative Snapshots from the MD simulation of $\mathbf{L^{1S}G_4}$ in absence of transition metal cations and in solution. The corresponding RMSD graphs of the guanine residues, $\mathbf{L^{1S}}$ and the DNA backbone.

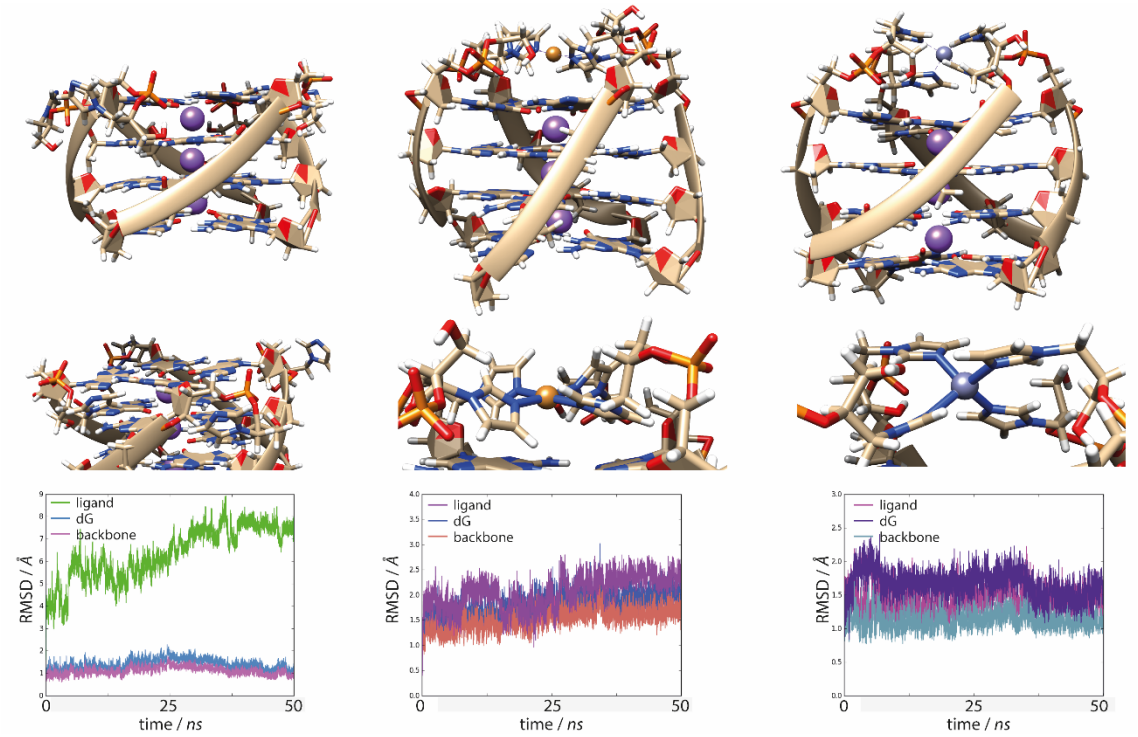

Figure 110. Representative Snapshots from the MD simulation of $\mathbf{L^{1R}}G_4$ in absence of transition metal cations and in solution. The corresponding RMSD graphs of the guanine residues, $\mathbf{L^{1R}}$ and the DNA backbone.

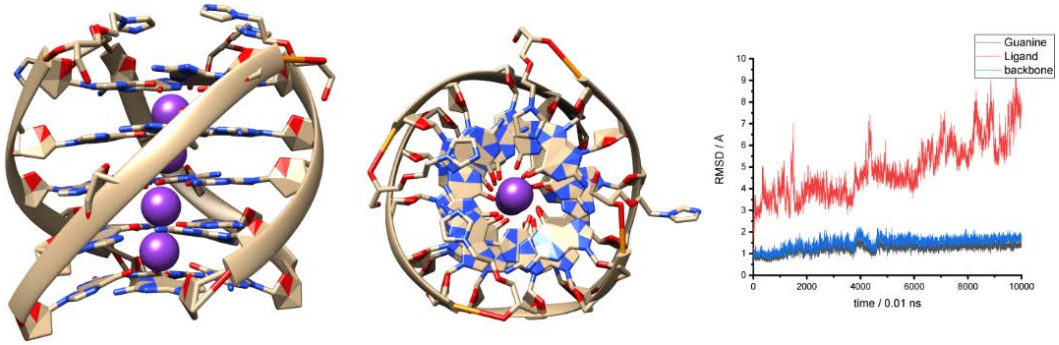

Figure 111. Representative Snapshots from the MD simulation of $\mathbf{L^{2R}}G_5$ in absence of transition metal cations and in solution. The corresponding RMSD graphs of the guanine residues, $\mathbf{L^{2R}}$ and the DNA backbone.

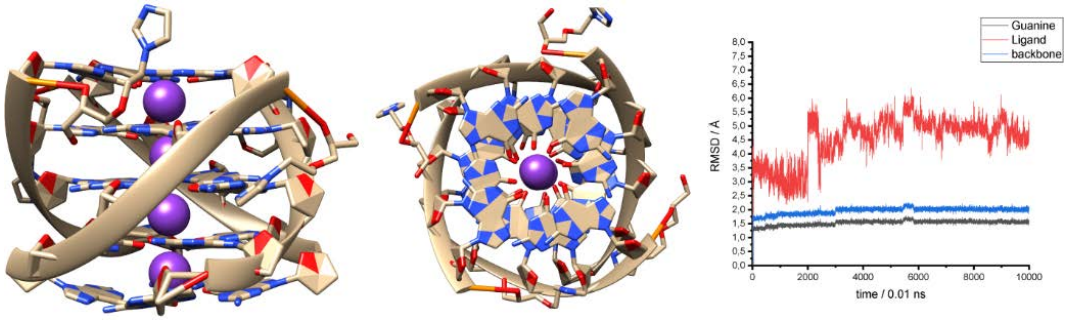

Figure 112. Representative Snapshots from the MD simulation of $\mathbf{L^{2R}}G_5$ in absence of Cu^{II} in the gas phase. Four negative charges were equally distributed along the phosphate backbone. The corresponding RMSD graphs of the guanine residues, $\mathbf{L^{RS}}$ and the DNA backbone.

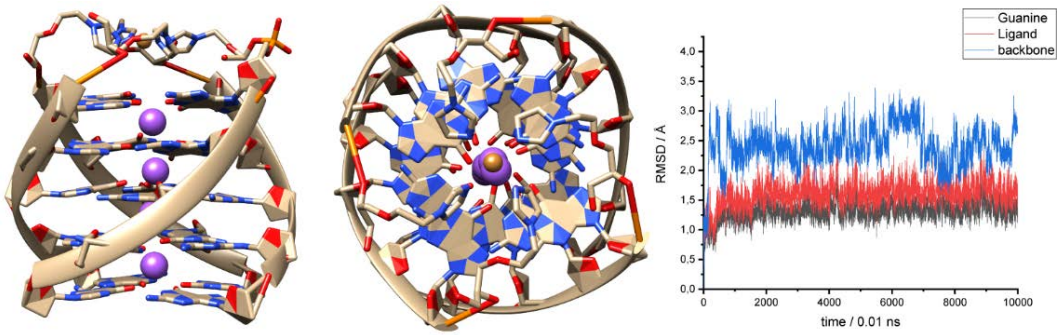

Figure 113. Representative Snapshots from the MD simulation of $\mathbf{L^{2R}}G_5$ in complex with Cu^{II} in solution. The corresponding RMSD graphs of the guanine residues, $\mathbf{L^{RS}}$ and the DNA backbone.

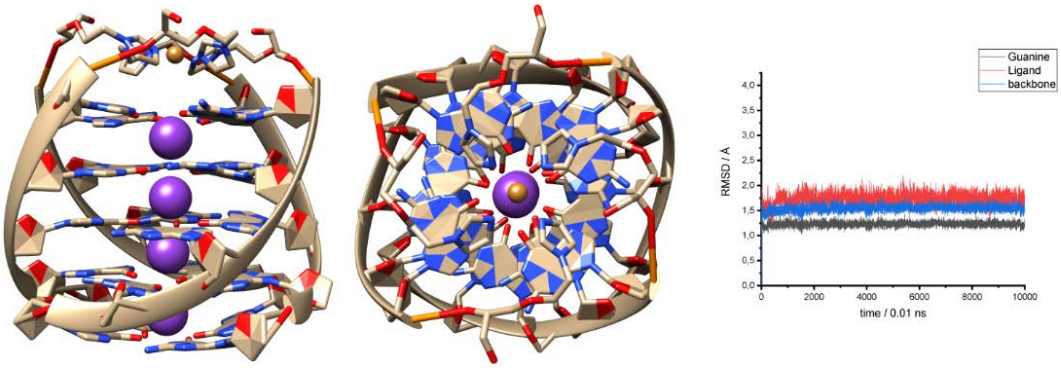

Figure 114. Representative Snapshots from the MD simulation of $\mathbf{L^{2R}}G_5$ in complex with Cu^{II} in the gas phase. Four negative charges were equally distributed along the phosphate backbone. The corresponding RMSD graphs of the guanine residues, $\mathbf{L^{2R}}$ and the DNA backbone.

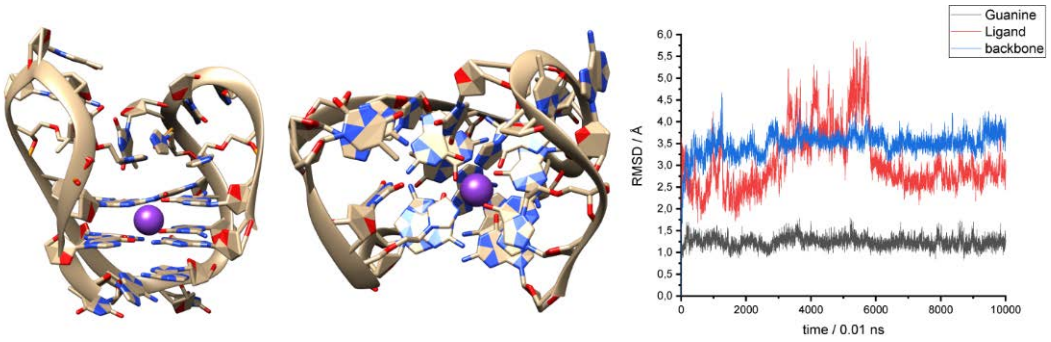

Figure 115. Representative Snapshots from the MD simulation of htel$\mathbf{L^{2S}}_4$ in absence of transition metal cations and the corresponding RMSD graphs of the guanine residues, $\mathbf{L^{2S}}$ and the DNA backbone.

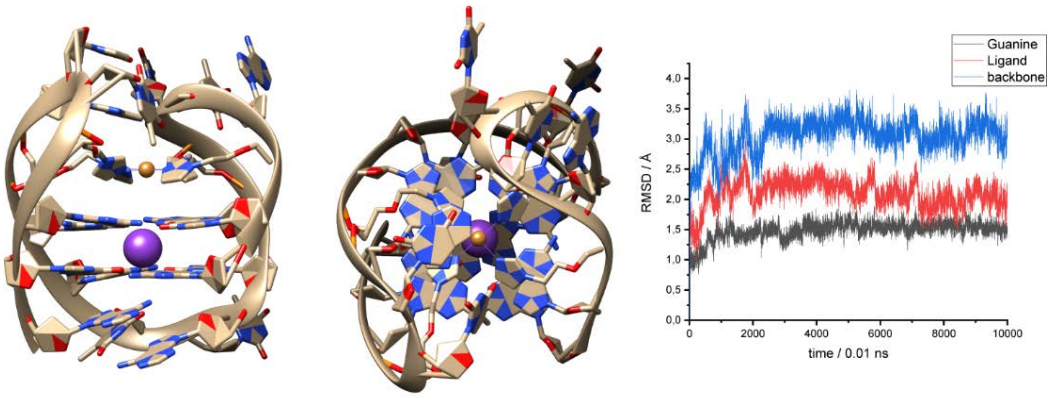

Figure 116. Representative Snapshots from the MD simulation of htel$\mathbf{L^{2S}}_4$ in absence of transition metal cations and the corresponding RMSD graphs of the guanine residues, $\mathbf{L^{2S}}$ and the DNA backbone.

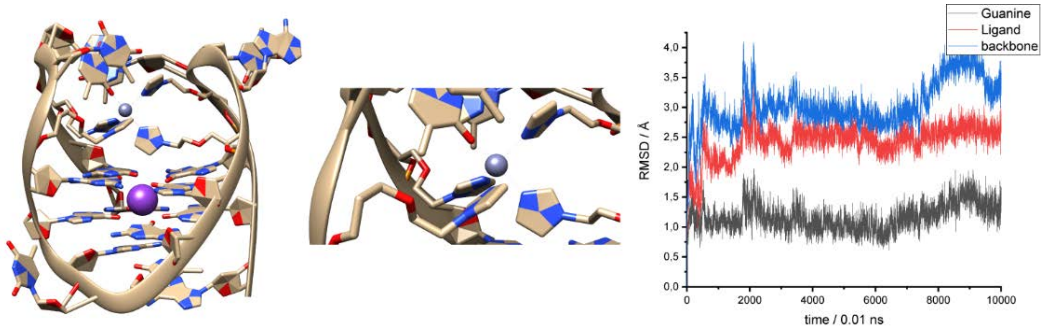

Figure 117. Representative Snapshots from the MD simulation of htel$\mathbf{L^{2S}}_4$ in complex with Zn^{II} and the corresponding RMSD graphs of the guanine residues, $\mathbf{L^{2S}}$ and the DNA backbone.

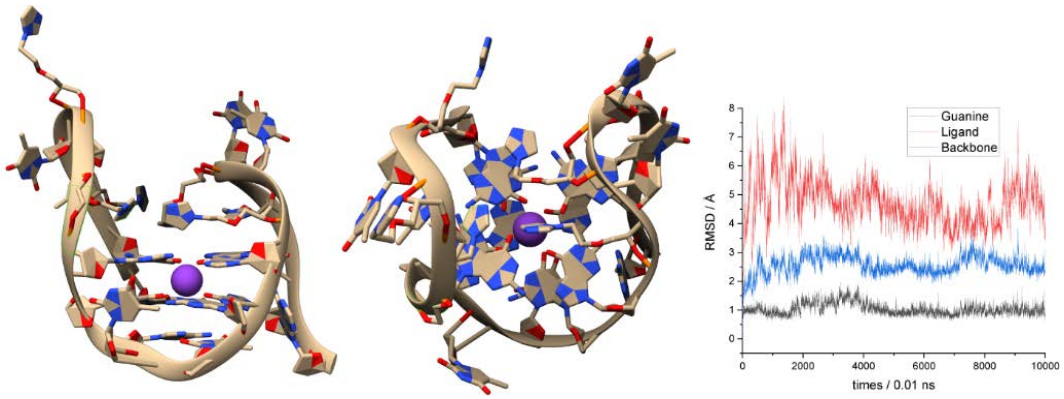

Figure 118. Representative Snapshots from the MD simulation of htel$\mathbf{L^{2S}}_6$ and the corresponding RMSD graphs of the guanine residues, $\mathbf{L^{2S}}$ and the DNA backbone.

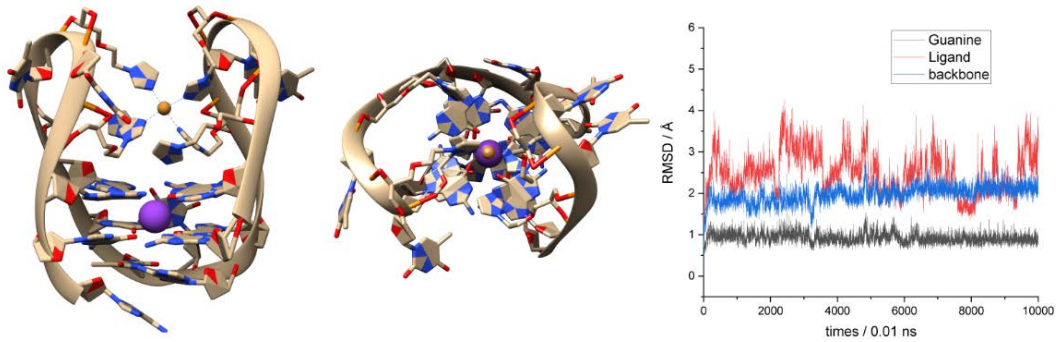

Figure 119. Representative Snapshots from the MD simulation of htel$\mathbf{L^{2S}}_6$ in complex with Cu^{II} and the corresponding RMSD graphs of the guanine residues, $\mathbf{L^{2S}}$ and the DNA backbone.

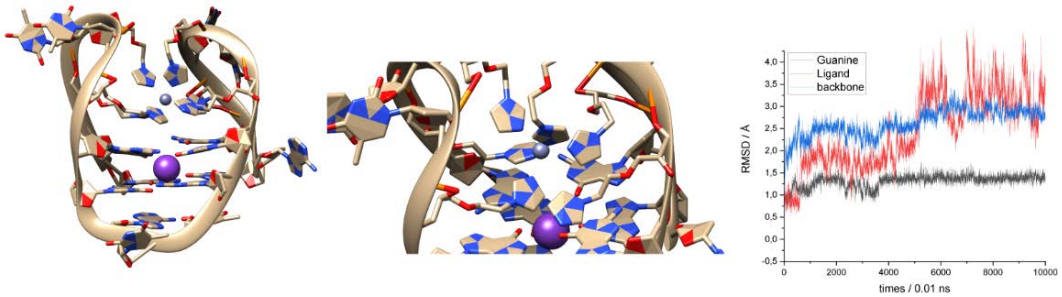

Figure 120. Representative Snapshots from the MD simulation of htel$\mathbf{L^{2S}}_6$ in complex with Zn^{II} and the corresponding RMSD graphs of the guanine residues, $\mathbf{L^{2S}}$ and the DNA backbone.

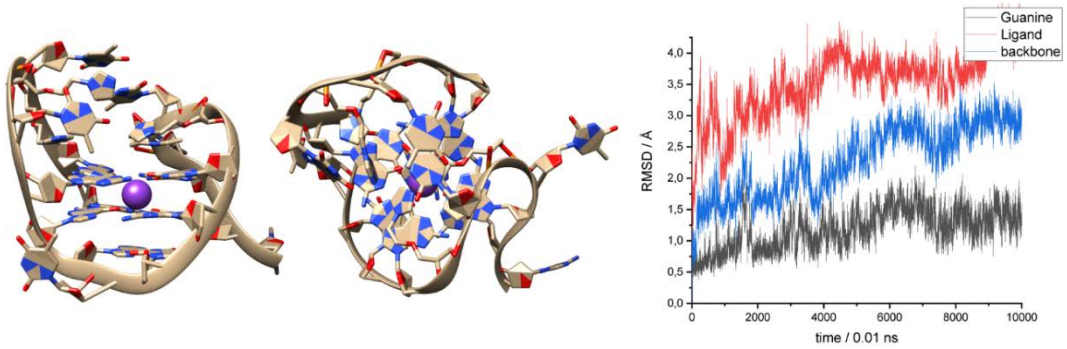

Figure 121. Representative Snapshots from the MD simulation of htel$\mathbf{L^{2S}}_4$C and the corresponding RMSD graphs of the guanine residues, $\mathbf{L^{2S}}$ and the DNA backbone.

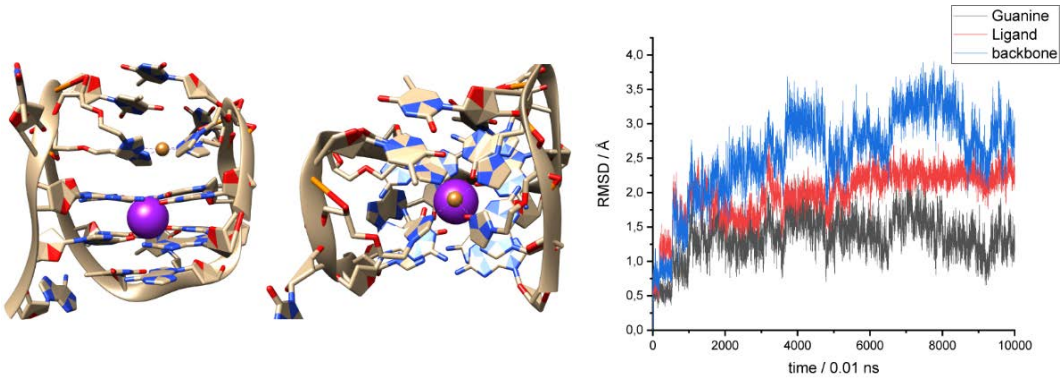

Figure 122. Representative Snapshots from the MD simulation of htel$\mathbf{L^{2S}}_4$C in complex with Cu^{II} and the corresponding RMSD graphs of the guanine residues, $\mathbf{L^{2S}}$ and the DNA backbone.

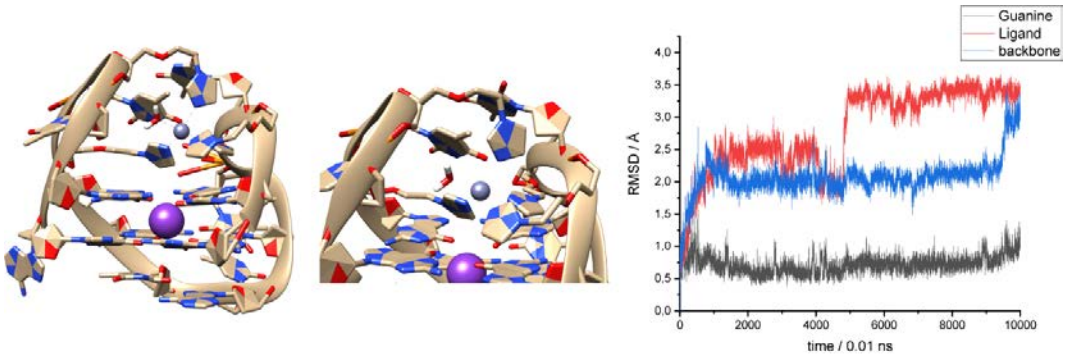

Figure 123. Representative Snapshots from the MD simulation of htel**L**^{2S}$_4$C in complex with Zn^{II} and the corresponding RMSD graphs of the guanine residues, **L**^{2S} and the DNA backbone.

9.7 NMR spectroscopy of DNA G-quadruplexes

9.7.1 Sample preparation

The lyophilized oligonucleotides were dissolved in 1 mL of water and desalted using size exclusion *NAP-10* columns from *GE Healthcare* to remove remaining triethyl ammonium acetate from solid phase synthesis. After desalting samples were lyophilized again and dissolved again in D_2O or H_2O for the sample preparation. G-quadruplex samples were prepared as described in **9.3.1**. The annealing step (85°C for 5 min, then cooling to 4°C with 0.5 °C min^{-1}) could be omitted since the NMR spectra seemed to be identical with and without annealing. The pH was adjusted using 10 mM HCl (DCl) or KOH (KOD).

9.7.2 NMR spectroscopy

Prepared samples were transferred into Shigemi-tubes with a matched magnetic susceptibility for D_2O. ^1H NMR spectra were recorded on a Bruker Avance 600 MHz spectrometer equipped with a TCI z-axis gradient CryoProbe or on a Bruker Avance 700 MHz spectrometer equipped with TXI z-axis gradient CryoProbe using excitation sculpting as water suppression.[339] For the structure determination non-exchangeable proton resonances were assigned by ^1H-^1H NOESY spectroscopy in D_2O (298 K, 60 or 250 ms mixing time). Exchangeable proton resonances were assigned by ^1H-^1H NOESY spectroscopy in H_2O:D_2O, 95:5/90:10 (298 K, 250 ms mixing time).

9.7.3 Structure calculation

From the assigned ^{1}H-^{1}H NOESY (250 ms mixing time, 298 K) spectra the peak volumes were determined by integration and calibrated to distances using a build in macro in DYANA.[374] Structure calculations were performed using the program XPLOR-NIH 3.0 using the standard forcefield parameters.[333,349] Parameters regarding the imidazole ligandosides were assigned in analogy to existing parameters from literature.[333] Starting from a stretched single strand, based on the sequence, using a simulated annealing protocol 400 structures were calculated. The calculation was based on NOE-, dihedral-, planarity-, and H-bond distance restraints. From the 400 calculated structures, the 40 lowest energy structures were used for the statistics.

Table 17. Proton and Carbon chemical shifts used to assign the four canonical DNA nucleobases thymidine, cytosine, adenine and guanine.

Name	Thymidine	Cytosine	Adenine	Guanine
H1’	5 – 6	5 – 6	5 – 6	5 – 6
H2’	1.7 – 2.3	1.7 – 2.3	2.3 – 2.9	2.3 – 2.9
H2’’	2.1 – 2.7	2.1 – 2.7	2.4 – 3.1	2.4 – 3.1
H3‘	4.4 – 5.0	4.4 – 5.0	4.4 – 5.2	4.4 – 5.2
H4’	3.8 – 4.3	3.8 – 4.3	3.8 – 4.3	3.8 – 4.3
H5’/H5’’	3.8 – 4.3	3.8 – 4.3	3.8 – 4.3	3.8 – 4.3
H6/8	6.8 – 7.9	6.8 – 7.9	7.7 – 8.5	7.5 – 8.3
H5	1.0 – 1.9	-	-	-
NH	13 – 14		-	12 – 13.6
NH_2	-	-	5 – 6	5 – 6
C1‘	83 – 89	83 – 89	83 – 89	83 – 89
C2‘	35 – 38	35 – 38	35 – 38	35 – 38
C3‘	70 – 78	70 – 78	70 – 78	70 – 78
C4‘	82 – 86	82 – 86	82 – 86	82 – 86
C5‘	63 – 68	63 – 68	63 – 68	63 – 68
C2	154	159	152 – 156	156
C4	169	166 – 168	149 – 151	152 – 154
C5	15 – 20	94 – 99	119 – 121	117 – 119
C6	137 – 142	136 – 144	157 – 158	161
C8	-	-	137 – 142	131 – 138

9.8 Synthesis

9.8.1 Synthesis of DMT-Glycidol

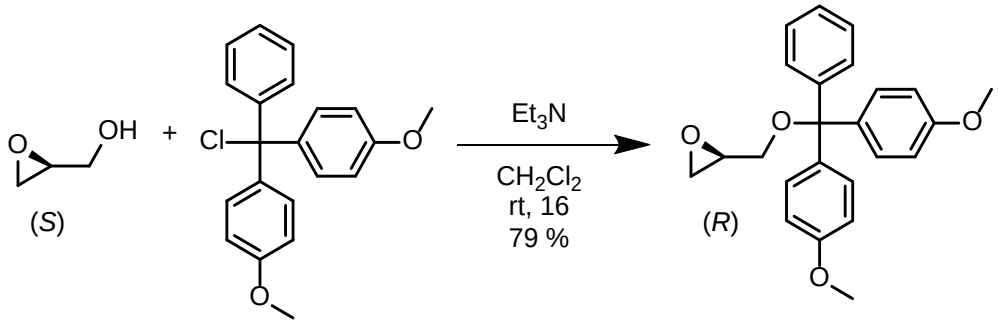

To a solution of (*S*)-glycidol (0.5 mL, 7.5 mM, 1.09 equiv.) and Et_3N (2.7 mL, 19.4 mM, 2.8 equiv.) in CH_2Cl_2 (17 mL) was added DMT-chloride (2.35 g, 6.9 mM, 1 equiv.) and stirred at rt for 16 h. The reaction mixture was washed with half saturated aq. $NaHCO_3$ (50 mL) and extracted with CH_2Cl_2 (3 × 30 mL). The combined organic layers were dried over $MgSO_4$ and the solvent was removed under reduced pressure to afford a dark red oil. The product was purified by column chromatography (cyclohexane/EtOAc, 98/2 → cyclohexane/EtOAc, 90/10) to afford DMT-(*R*)-glycidol as a viscous colourless oil (2.05 g, 5.4 mM, 79 %). The stereocentre is formally inverted due to the higher priority of the DMT-group.The synthesis of DMT-(*S*)-glycidol was identical. The ^{1}H NMR was in accordance with literature.[253]

^{1}H NMR (600 MHz, 298 K, $CDCl_3$): δ (ppm): 7.46 – 7.48 (m, 2H, CH), 7.34 – 7.37 (m, 4H, CH), 7.28 – 7. 31 (m, 2H, CH), 7.20 – 7.23 (m, 1H, CH), 6.82 – 6.85 (m, 4H, CH), 3.79 (s, 6H, -OCH3), 3.32 (dd, 1H, CH2), 3.13 (dd, 2H, CH2), 2.78 (dd, 1H, CH2), 2.63 (dd, 1H, CH2).

9.8.2 Glycol-based imidazole nucleoside 5

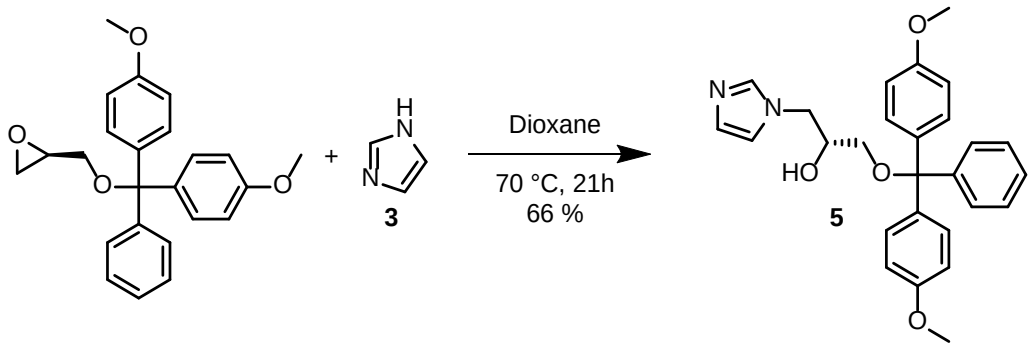

To a solution of imidazole **3** (0.54 g, 8 mM, 2 equiv.) in 1,4-dioxane (7.5 mL) a solution of DMT-glycidol in 1,4-dioxane (2.5 mL) was added. The reaction was stirred at 80 °C for 21 h until all starting material was consumed. The reaction mixture was washed with half saturated aq. $NaHCO_3$ (40 mL) and extracted with CH_2Cl_2 (2 × 30 mL). The combined organic layers were dried over $MgSO_4$ and the solvent was removed under reduced pressure to afford a yellow oil. The product was purified by flash chromatography (CH_2Cl_2/MeOH, 100/0 → CH_2Cl_2/MeOH, 90/10) followed by gel permeation chromatography ($CHCl_3$) to give the product (**5**) as a white foamy solid (1.16 g, 2.61 mM, 66 %). The synthetic procedure for (*S*)-**7** is identical.[29]

Chemical formula: $C_{27}H_{28}N_2O_4$

Molecular weight: 444.53 g mol^{-1}

HRMS (ESI, pos., Calc. [M+H]+ : 445.2122 ACN/water, 1/1, 0.1 % TFA) Found: m/z = 303.1365 [DMT]+ , 445.2109 [M+H]+

^{1}H NMR (600 MHz, 298 K, $CDCl_3$): δ (ppm): 7.43 – 7.41 (m, 2H, H_i), 7.35 (s, 1H, H_a) 7.32 – 7.29 (m, 6H, H_j,H_g), 7.24 – 7.22 (m, 1H, H_k), 6.88 (s, 1H, H_c), 6.85 – 6.82 (m, 5H, H_h, H_b), 4.07 (dd, ^3J = 13.7, 3.3, 1H, H_d), 3.99 – 3.94 (m, 1H, H_d), 3.96 – 3.91 (m, 1H, H_e), 3.79 (s, 6H, -OC*H*$_3$), 3.21 (dd, ^3J = 9.6, 5.4, 1H, H_f), 3.14 (dd, ^3J = 9.6, 5.4, 1H, H_f).

^{13}C NMR (150 MHz, 298 K, $CDCl_3$): δ (ppm): 159.0, 144.8, 138.0, 136.0, 130.3, 129.3, 128.4, 128.3, 127.3, 120.0, 113.6, 68.8, 70.5, 64.8, 55.6, 50.6.

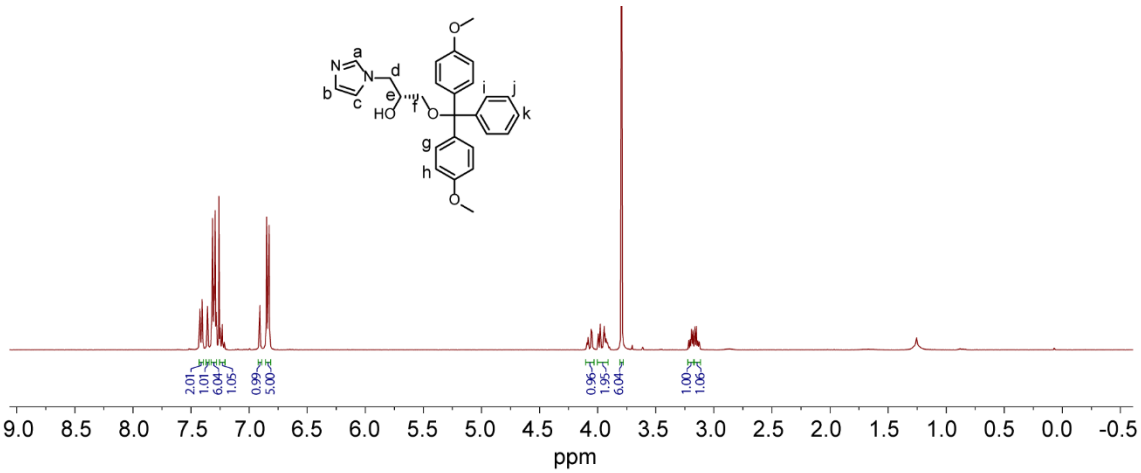

Figure 124. ^{1}H NMR (150 MHz, 298 K, $CDCl_3$) of Glycol-based imidazole nucleoside **5**.

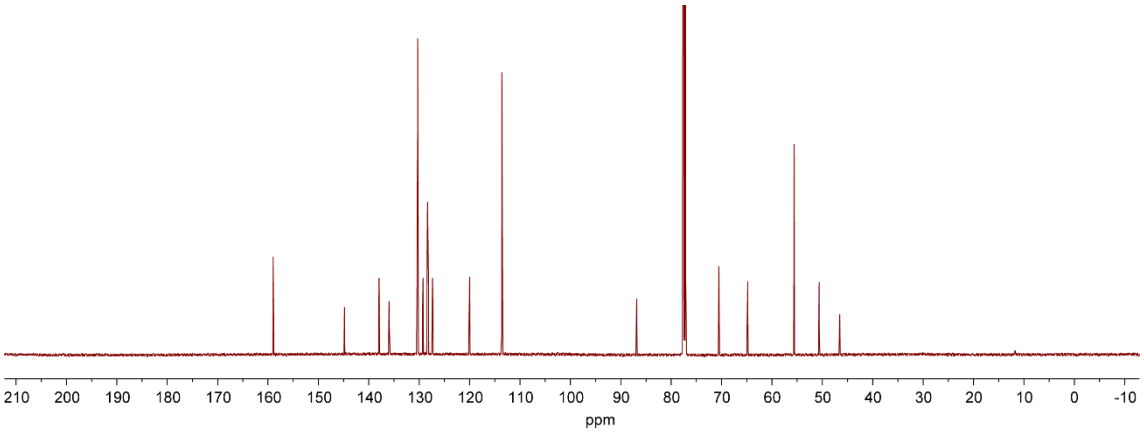

Figure 125. ^{13}C NMR (150 MHz, 298 K, $CDCl_3$) of Glycol-based imidazole nucleoside **5**.

9.8.3 Synthesis of phosphoramidite 7

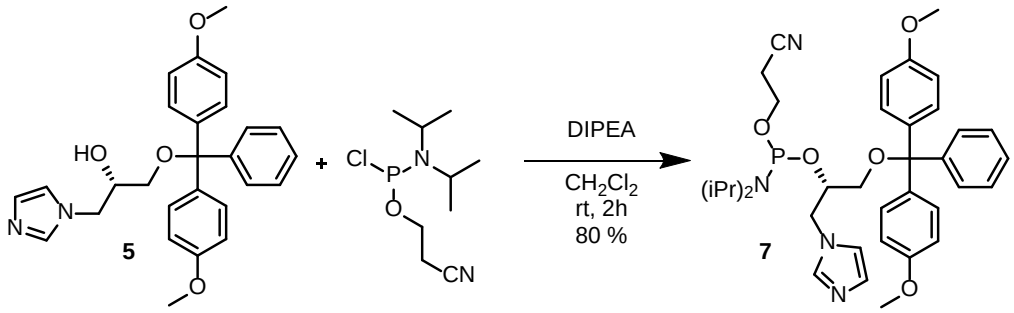

The synthesis was done in a glovebox under nitrogen atmosphere to exclude water and oxygen. To a stirring solution of (*S*)-**5** (355 mg, 0.8 mM, 1 equiv.) in CH_2Cl_2 (6.2 mL) was added at rt DIPEA (620 mg, 836 µL, 4.8 mM, 6 equiv.). To the solution CEDIP-Cl (189 mg, 178 µL, 0.8 mM, 1 equiv.) was added and the reaction was stirred for 90 minutes. After completion the solvent was removed under vacuum and the resulting crude phosphoramidite (*S*)-**7** was used for DNA synthesis, assuming a yield of 80 %. The synthetic procedure for (*R*)-**7** is identical.[29]

^{31}P NMR (122 MHz, 298 K, $CDCl_3$): δ (ppm): 149.8, 149.0.

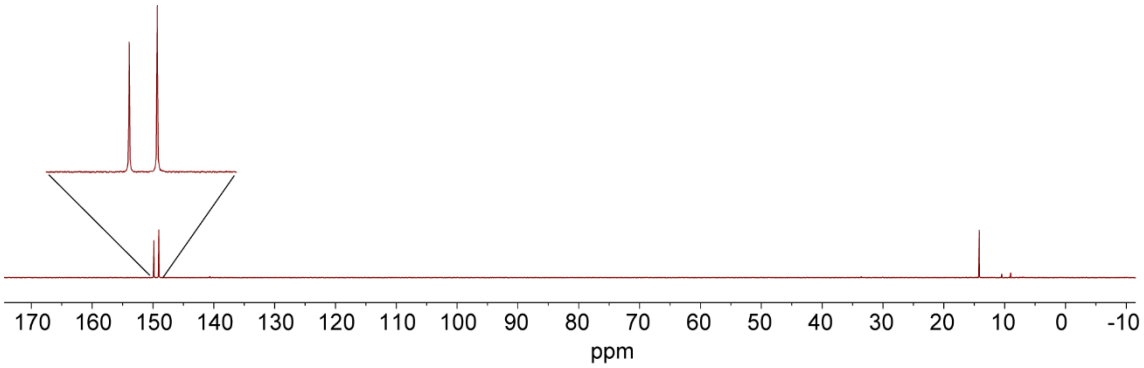

Figure 126. ^{31}P NMR (122 MHz, 298 K, $CDCl_3$) of phosphoramidite (S)-**7**.

9.8.4 Glycol-based imidazole nucleoside 6

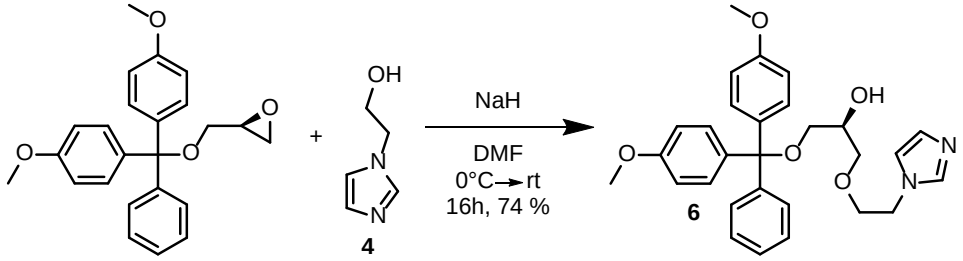

To a stirring suspension of NaH (200 mg, 60 *w/w* %, 5.31 mM, 4 equiv.) in DMF (2 mL) was added a solution of imidazole **4** (298 mg, 2.66 mM, 2 equiv.) in DMF (4mL) at 0°C. The reaction allowed to reach rt and was stirred for 60 min until no H_2 formation was observed. Then a solution of DMT-(*S*)-glycidol (500 mg, 1.33 mM, 1 equiv) in DMF (4 mL) was dropwise added and the reaction was stirred at 40 °C for 16 h.

After full conversion of the starting material a solution of half saturated aq. $NaHCO_3$ was added and the aqueous layer was extracted with CH_2Cl_2 (3 x 50 mL). The solvent was removed under reduced pressure and remaining yellow oil was purified by column chromatography ($CHCl_3$/MeOH, 100/0 → $CHCl_3$/MeOH, 90/10) followed by gel permeation chromatography to afford the Glycol-based imidazole nucleoside **6** as a foamy solid (480 mg, 0.98 mM, 74 %).[31]

Chemical formula: $C_{29}H_{32}N_2O_5$

Molecular weight: 488.58 g mol^{-1}

HRMS (ESI, pos., Calc. [M+H]+: 489.2384 ACN/water, 1/1, 0.1 % TFA): Found: m/z = 303.136 [DMT]+, 489.2381 [M+H]+

^{1}H NMR (700 MHz, 298 K, $CDCl_3$): δ (ppm): 7.46 (s, 1H, H_a), 7.42 – 7.41 (m, 2H, H_i), 7.31 – 7.29 (m, 4H, H_l), 7.30 – 7.28 (m, 2H, H_j), 7.23 – 7.20 (m, 1H, H_k), 7.01 (s, 1H, H_b),

6.89 (s, 1H, H_c), 6.84 – 6.82 (m, 4H, H_m), 4.06 (t, ^3J = 5.1 Hz, 2H, H_d), 3.93 – 3.90 (m, 1H, H_g), 3.79 (s, 6H, -OCH_3) 3.69 (t, ^3J = 5.2 Hz, 2H, H_e), 3.51 – 3.53 (dd, ^3J = 4.1, 9.9, 1H, H_f), 3.47 (dd, ^3J = 6.2, 9.8, 1H, H_f), 3.19 – 3.15 (m, 2H, H_h), 2.23 (s, 1H, O*H*).

^{13}C NMR (175 MHz, 298 K, $CDCl_3$): δ (ppm): 158.9, 145.0, 137.7, 136.2, 130.4, 129.6, 128.4, 128.2, 127.2, 119.7, 113.5, 86.5, 73.1, 71.0, 70.2, 64.7, 55.6, 47.3.

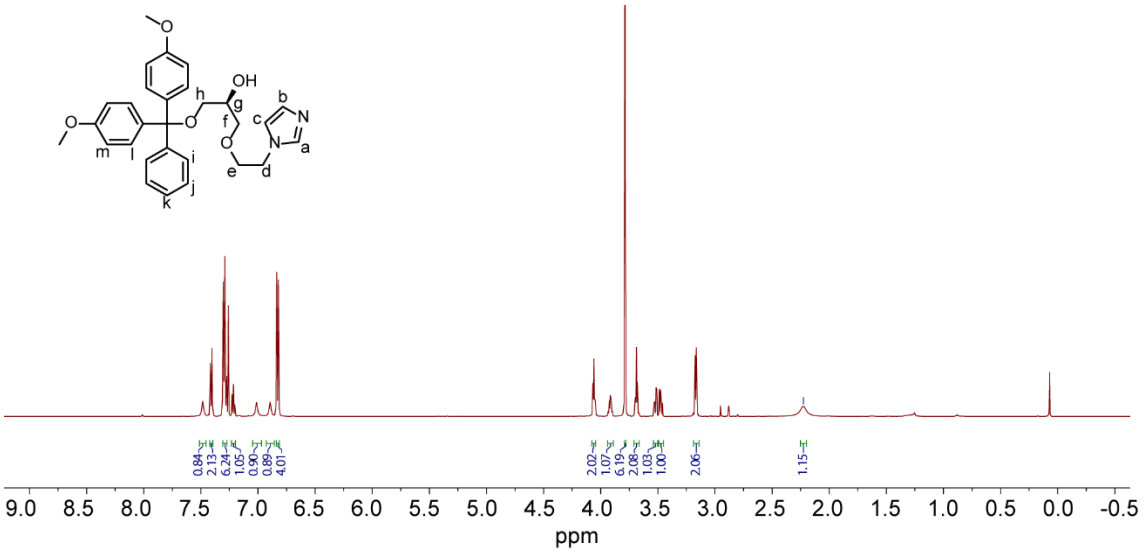

Figure 127. ^{1}H NMR (700 MHz, 298 K, $CDCl_3$) of Glycol-based imidazole nucleoside **6**.

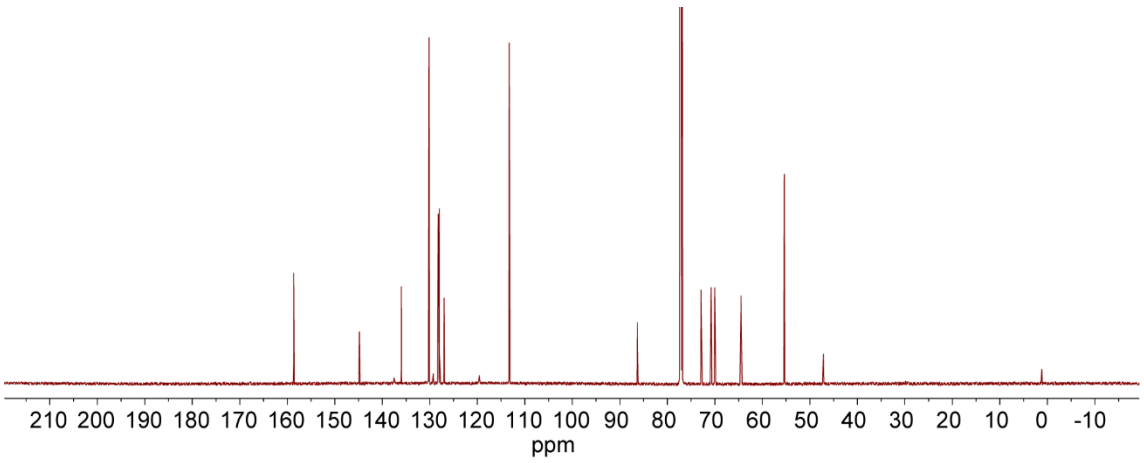

Figure 128. ^{13}C NMR (175 MHz, 298 K, $CDCl_3$) of Glycol-based imidazole nucleoside **6**. Note that the signals corresponding to the imidazole carbons are extremely small.

9.8.5 Synthesis of phosphoramidite 8

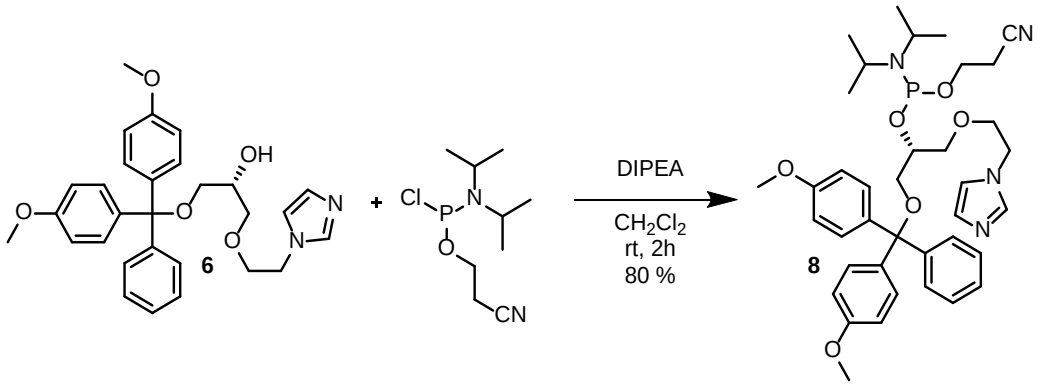

The synthesis was done in a glovebox under nitrogen atmosphere to exclude water and oxygen. To a stirring solution of (*R*)-**6** (650 mg, 1.33 mM, 1 equiv.) in CH_2Cl_2 (10 mL) was added at rt DIPEA (1.03 mg, 1.39 mL, 7.98 mM, 6 equiv.). To the solution CEDIP-Cl (315 mg, 297 µL, 1.33 mM, 1 equiv.) was added and the reaction was stirred for 90 minutes. After completion, the solvent was removed under vacuum and the resulting crude phosphoramidite (*R*)-**8** was used for DNA synthesis, assuming a yield of 80 %. The synthetic procedure for (*S*)-**8** is identical.[31]

HRMS (ESI, pos., Calc. [M+H]+: 689.3462, ACN): Found: m/z = 130.1624 [DIPEA]+, 303.1385 [DMT]+, 689.3466 [M+H]+

^{31}P NMR (202 MHz, 298 K, $CDCl_3$): δ (ppm): 149.4, 149.2.

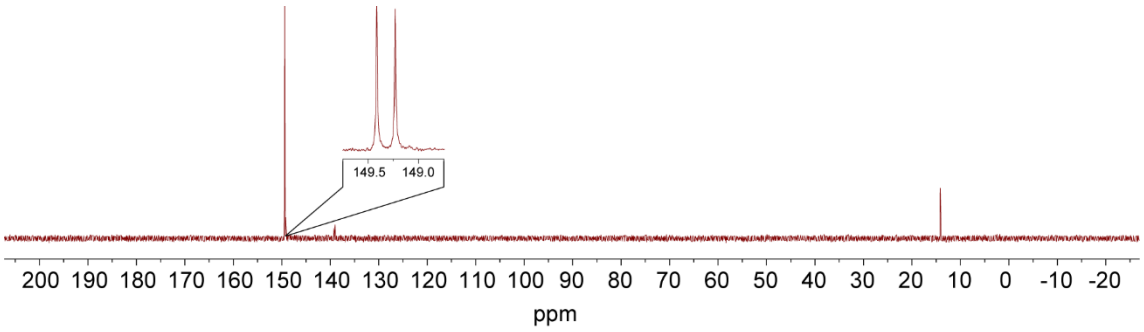

Figure 129. ^{31}P NMR (202 MHz, 298 K, $CDCl_3$) of phosphoramidite **8**.

9.8.6 Glycol-based imidazole nucleoside 1

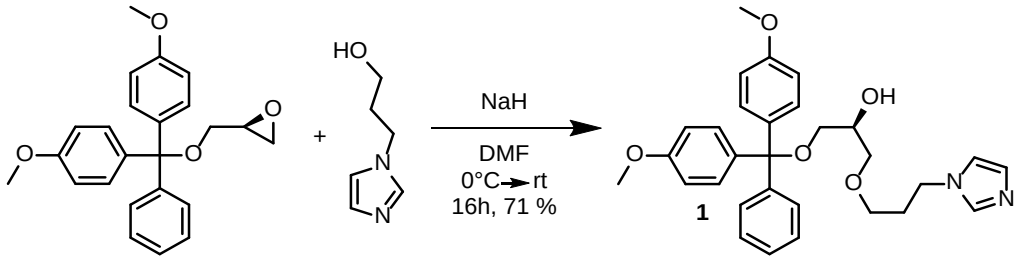

To a stirring suspension of NaH (200 mg, 60 *w/w* %, 5.31 mM, 4 equiv.) in DMF (2 mL) was added a solution of imidazole (336 mg, 2.66 mM, 2 equiv.) in DMF (4mL) at 0°C. The reaction allowed to reach rt and was stirred for 60 min until no H_2 formation was observed. Then a solution of DMT-(*R*)-glycidol (500 mg, 1.33 mM, 1 equiv) in DMF (4 mL) was dropwise added and the reaction was stirred at 40 °C for 16 h.

After full conversion of the starting material a solution of half saturated aq. $NaHCO_3$ was added and the aqueous layer was extracted with CH_2Cl_2 (3 x 50 mL). The solvent was removed under reduced pressure and remaining yellow oil was purified by column chromatography ($CHCl_3$/MeOH, 100/0 → $CHCl_3$/MeOH, 90/10) followed by gel permeation chromatography to afford the Glycol-based imidazole nucleoside (*R*)-**1** as a foamy solid (473 mg, 0.94 mM, 71 %). The synthetic procedure for (*S*)-**1** is identical.

Chemical formula: $C_{30}H_{34}N_2O_5$

Molecular weight: 502.61 g mol^{-1}

HRMS (ESI, pos., Calc. [M+H]+: 503.6110, ACN/water, 1/1, 0.1 % TFA): Found: m/z = 303.14 [DMT]+, 503.2542 [M+H]+

^{1}H NMR (600 MHz, 298 K, $CDCl_3$): δ (ppm): 7.45 (s, 1H, H_a), 7.44 – 7.41 (m, 2H, H_n), 7.33 – 7.29 (m, 4H, H_l), 7.30 – 7.27 (m, 2H, H_j), 7.23 – 7.19 (m, 1H, H_k), 7.05 (s, 1H, H_b), 6.88 (s, 1H, H_c), 6.84 – 6.81 (m, 4H, H_m), 3.97 (t, ^3J = 6.9 Hz, 2H, H_d), 3.96 – 3.92 (m, 1H, H_h), 3.78 (s, 6H, -OCH_3), 3.51 – 3.45 (m, 2H, H_g), 3.41 – 3.34 (m, 2H, H_f), 3.22 – 3.17 (m, 2H, H_i), 1.99 – 1.94 (m, 2H, H_e).

^{13}C NMR (150 MHz, 298 K, $CDCl_3$): δ (ppm): 158.9, 145.1, 137.7, 136.2, 130.4, 129.7, 128.4, 128.2, 127.2, 119.4, 113.5, 86.8, 72.7, 70.2, 67.6, 64.7, 55.6, 44.0, 31.4.

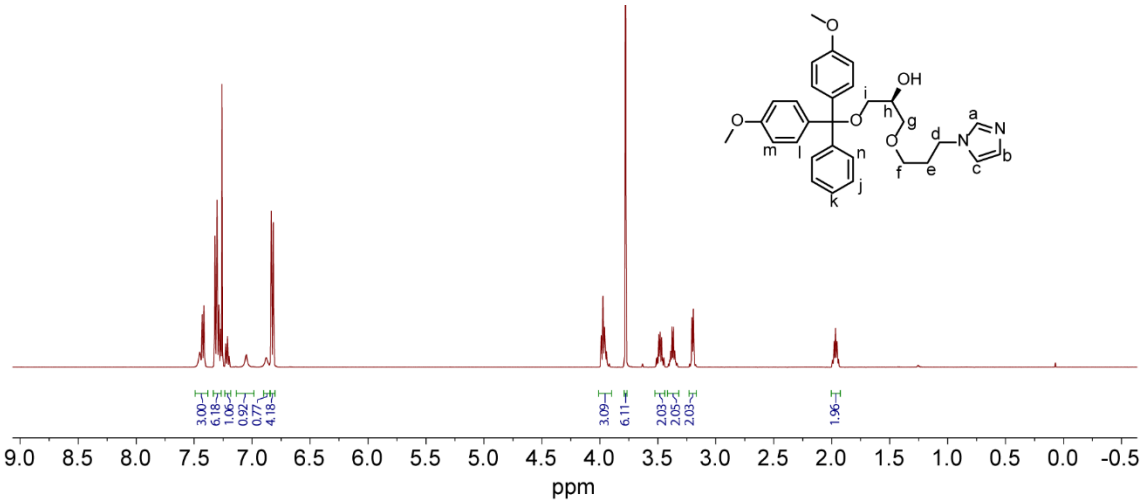

Figure 130. ^{1}H NMR (600 MHz, 298 K, $CDCl_3$) of glycol-based imidazole nucleoside **1**.

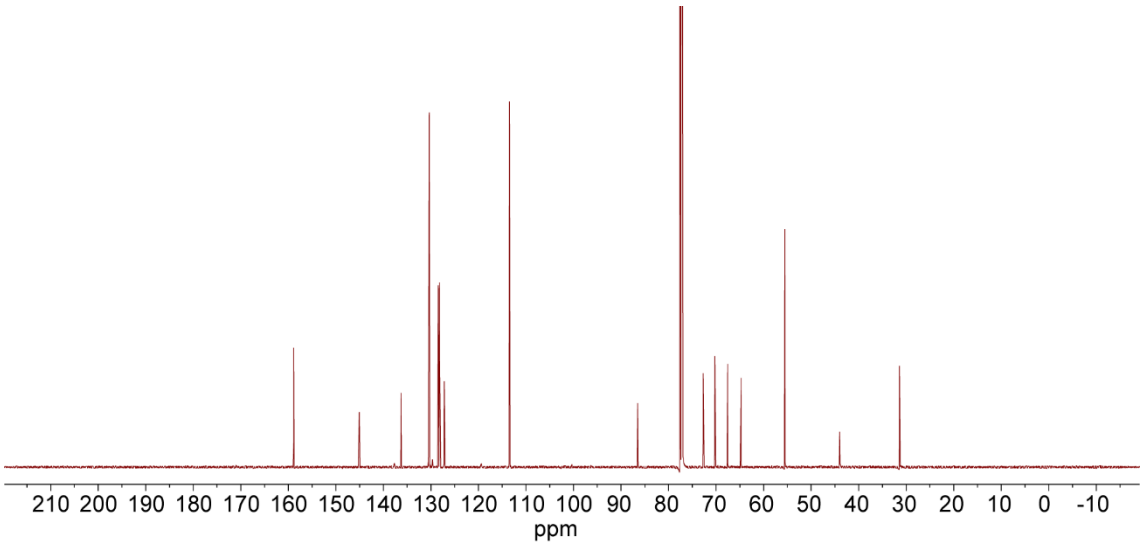

Figure 131. ^{13}C NMR (150 MHz, 298 K, $CDCl_3$) of glycol-based imidazole nucleoside **1**. Note that the signals corresponding to the imidazole carbons are extremely small.

9.8.7 Synthesis of phosphoramidite 2

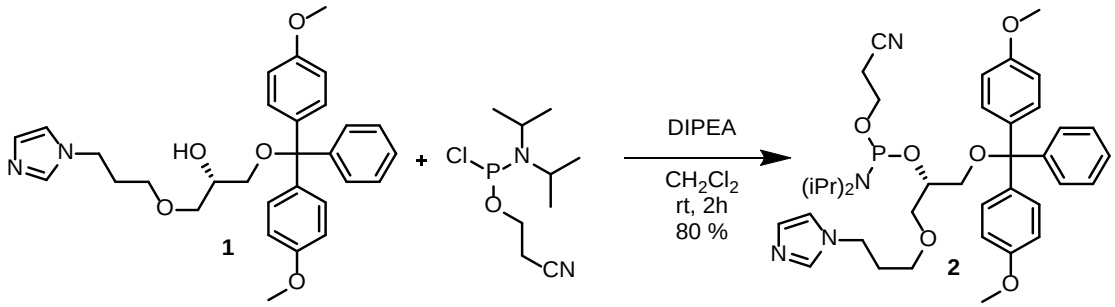

The synthesis was done in a glovebox under nitrogen atmosphere to exclude water and oxygen. To a stirring solution of (*S*)-**1** (402 mg, 0.8 mM, 1 equiv.) in CH_2Cl_2 (6.2 mL) was added at rt DIPEA (620 mg, 836 µL, 4.8 mM, 6 equiv.). To the solution CEDIP-Cl (189 mg, 178 µL, 0.8 mM, 1 equiv.) was added and the reaction was stirred for 90 minutes. After completion the solvent was removed under vacuum and the resulting crude phosphoramidite (*S*)-**2** was used for DNA synthesis, assuming a yield of 80 %. The synthetic procedure for (*R*)-**2** is identical.

Chemical formula: $C_{39}H_{51}N_4O_6P$

Molare Masse: 702.83 g mol-1

^{31}P NMR (162 MHz, 298 K, $CDCl_3$): δ (ppm): 149.2, 149.4.

9.8.8 Synthesis of 38

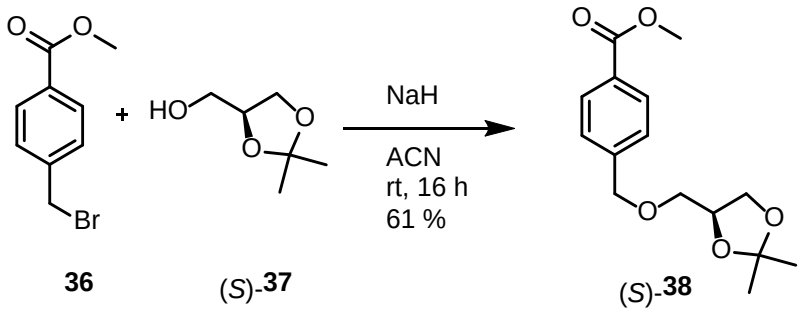

To a suspension of sodium hydride (60 % in mineral oil; 0.36 g, 8.42 mM, 1.1 equiv.) in dry acetonitrile (35 mL) (*S*)-(2,2-dimethyl-1,3-dioxolan-4-yl)methanol ((*S*)-**37**, 1.00 mL, 8.02 mM, 1.0 equiv.) was slowly added. The suspension was stirred at rt for 30 min and then cooled down to 0 °C before 4-(bromomethyl)benzoate (**36**, 1.84 g, 8.02 mM, 1.0 equiv.) was added. The reaction was allowed to reacht rt and was stirred overnight. After completion the solvent was removed under reduced pressure. The remaining solid was taken up in EtOAc (50 mL) and filtered. The filtrate was washed with water (50 mL). The

aqueous phase was extracted with EtOAc (3x 30 mL) and the combined organic layers were dried over $MgSO_4$. The solvent was removed under reduced pressure and the remaining oil was purified by column chromatography (*n*-pentane/ethyl acetate, 5:1) to afford (*S*)-**38** as a colourless oil (1.38 g, 4.93 mM, 61 %).[30]

^{1}H NMR (700 MHz, 298 K, $CDCl_3$): δ (ppm): (d, *J* = 8.4 Hz, 2H, 3-H and 7-H), 7.38 (d, *J* = 8.5 Hz, 2H, 4-H and 6-H), 4.62 (d, *J* = 12.9 Hz, 1H, 8-H_a), 4.59 (d, *J* = 12.8 Hz, 1H, 8-H_b), 4.32 – 4.27 (m, 1H, 2'-H), 4.05 (dd, *J* = 8.3 Hz, *J* = 6.5 Hz, 1H, 3'-H_a), 3.89 (s, 3H, $CO_2C\underline{H}_3$), 3.73 (dd, *J* = 8.3 Hz, *J* = 6.3 Hz, 1H, 3'-H_b), 3.55 (dd, *J* = 9.9 Hz, *J* = 5.7 Hz, 1H, 1'-H_a), 3.49 (dd, *J* = 9.9 Hz, *J* = 5.3 Hz, 1H, 1'-H_b), 1.40 (s, 3H, $C(C\underline{H}_3)_2$), 1.35 (s, 3H, $C(C\underline{H}_3)_2$).

^{13}C NMR (175 MHz, 298 K, $CDCl_3$): δ (ppm): 166.9 (C1), 143.4 (C5), 129.8 (C3 and C7), 129.5 (C2), 127.3 (C4 and C6), 109.6 ($\underline{C}(CH_3)_2$), 74.8 (C2'), 72.9 (C8), 71.5 (C1'), 66.8 (C3'), 52.1 ($CO_2\underline{C}H_3$), 26.8 ($C(\underline{C}H_3)_2$), 25.5 ($C(\underline{C}H_3)_2$).

HRMS (ESI, pos., Calc. [M+H]+: 303.1203, ACN): Found: m/z = 303.1198 [M+Na]+

Elemental analysis (%): Calc. for $C_{15}H_{20}O_5$: C 64.3, H 7.2; found: C 64.0, H 7.3.

9.8.9 Synthesis of 39

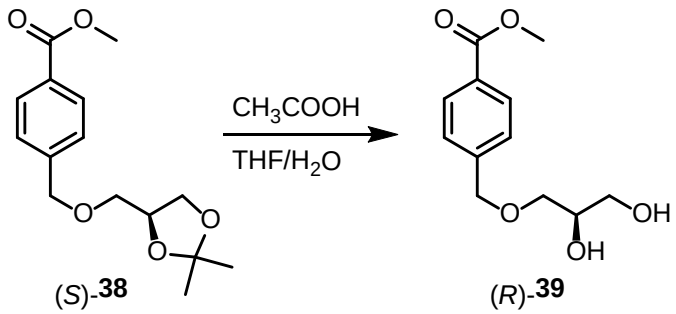

(*S*)-**38** (*R*)-**39**

Compound **38** was dissolved in THF before a mixture of acetic acid/water, 1/1, was added. The solution was heated to 60 °C and stirred overnight. The solvent was removed under reduced pressure and the remaining crude product was purified by column chromatography (dichloromethane/methanol, 10:1) to afford (*R*)-**39** as a white crystalline material (0.86 g, 3.60 mM, 96 %).[30]

^{1}H NMR (400 MHz, 298 K, $CDCl_3$): δ (ppm): 8.02 (d, *J* = 8.3 Hz, 2H, 3-H and 7-H), 7.38 (d, *J* = 8.2 Hz, 2H, 4-H and 6-H), 4.60 (s, 2H, 8-H), 3.96 – 3.88 (m, 4H, 2'-H and $CO_2C\underline{H}_3$), 3.72 (dd, *J* = 11.4 Hz, *J* = 3.9 Hz, 1H, 3'-H_a), 3.64 (dd, *J* = 11.4 Hz, *J* = 5.6 Hz, 1H, 3'-H_b), 3.61 – 3.53 (m, 2H, 1'-H_a and 1'-H_b), 2.46 (br s, 2H, 2'-O$\underline{H}$ and 3'-O$\underline{H}$).

^{13}C NMR (100 MHz, 298 K, $CDCl_3$): δ (ppm): 167.0 (C1), 143.1 (C5), 129.9 (C3 and C7), 129.7 (C2), 127.4 (C4 and C6), 73.1 (C8), 72.2 (C1'), 70.8 (C2'), 64.1 (C3'), 52.3 ($CO_2\underline{C}H_3$).

HRMS (ESI, pos., Calc. [M+H]+: 263.0890, ACN): Found: m/z = 263.0885 [M+Na]+

Elemental analysis (%): Calc. for $C_{12}H_{16}O_5$: C 60.0, H 6.7; found: C 59.9, H 6.7.

IR (ATR): $\tilde{\nu}$ = 3264, 2942, 2864, 1719, 1431, 1415, 1389, 1276, 1207, 1194, 1179, 1103, 1070, 1048, 1025, 1014, 954, 933, 866, 851, 763,712,529 cm^{-1}.

9.8.10 Synthesis of 40

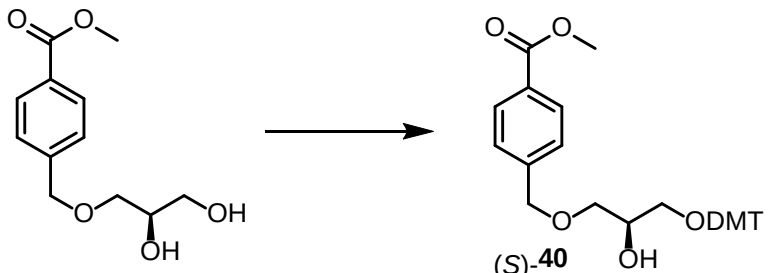

To a solution of (*R*)-**39** (1.18 g, 4.93 mM, 1.0 equiv.), *N*,*N*-diisopropylethylamine (1.68 mL, 9.86 mM, 2.0 equiv.) and 4-dimethylaminopyridine (0.04 g, 0.30 mM, 0.06 equiv.) in dry tetrahydrofuran (20 mL) at 0 °C a solution of 4,4'-dimethoxytrityl chloride (2.01 g, 5.92 mM, 1.2 equiv.) in dry tetrahydrofuran (10 mL) was added. The solution was allowed to warm to rt and was stirred overnight. The formed solid was filtered of and the solvent was removed under reduced pressure to obtain the crude product as a yellow oil. The product was purified by column chromatography (*n*-pentane/ethyl acetate, 5:1 + 0.5 % triethylamine to 2:1 + 0.5 % triethylamine) to afford (*S*)-**40** as a yellow oil (1.95 g, 3.59 mM, 73 %).[30]

^{1}H NMR (600 MHz, 298 K, CD_2Cl_2): δ (ppm): 8.00 – 7.96 (m, 2H, 3-H and 7-H), 7.44 – 7.41 (m, 2H, DMT-$\underline{H}_{ar}$), 7.38 – 7.34 (m, 2H, 4-H and 6-H), 7.32 – 7.26 (m, 6H, DMT-$\underline{H}_{ar}$), 7.24 – 7.20 (m, 1H, DMT-$\underline{H}_{ar}$), 6.85 – 6.80 (m, 4H, DMT-$\underline{H}_{ar}$), 4.57 (s, 2H, 8-H), 3.99 – 3.93 (m, 1H, 2'-H), 3.89 (s, 3H, $CO_2C\underline{H}_3$), 3.77 (s, 6H, DMT-$OC\underline{H}_3$), 3.60 (dd, *J* = 9.6 Hz, 4.4, 1H, 1'-H_a), 3.57 (dd, *J* = 9.6 Hz, 6.0, 1H, 1'-H_b), 3.18 (d, *J* = 5.4 Hz, 2H, 3'-H), 2.36 (d, *J* = 5.1 Hz, 1H, 2'-O$\underline{H}$).

^{13}C NMR (150 MHz, 298 K, CD_2Cl_2): δ (ppm): 167.2 (C1), 159.2 (DMT-C_{ar}), 145.6 (DMT-C_{ar}), 144.2 (C5), 136.5 (DMT-C_{ar}), 130.6 (DMT-C_{ar}), 130.0 (C3 and C7), 130.0 (C2), 128.6 (DMT-C_{ar}), 128.3 (DMT-C_{ar}), 127.7 (C4 and C6), 127.3 (DMT-C_{ar}), 113.6 (DMT-

C_{ar}), 86.6 (DMT-$\underline{C}(Ar)_3$), 73.1 (C8), 72.5 (C1'), 70.5 (C2'), 65.0 (C3'), 55.7 (DMT-O$\underline{C}H_3$), 52.5 ($CO_2\underline{C}H_3$).

HRMS (ESI, pos., ACN): *m/z* calc. for $C_{21}H_{19}O_2$ 303.1380 [DMT]$^+$, $C_{33}H_{34}O_7Na$ 565.2197 [M+Na]$^+$, $C_{33}H_{34}O_7K$ 581.1936 [M+K]$^+$; found 303.1373, 565.2196, 581.1936.

Elemental analysis (%)**:** Calc. for $C_{33}H_{34}O_7$: C 73.1, H 6.3; found: C 73.1, H 6.7.

9.8.11 Synthesis of phosphoramidite 41

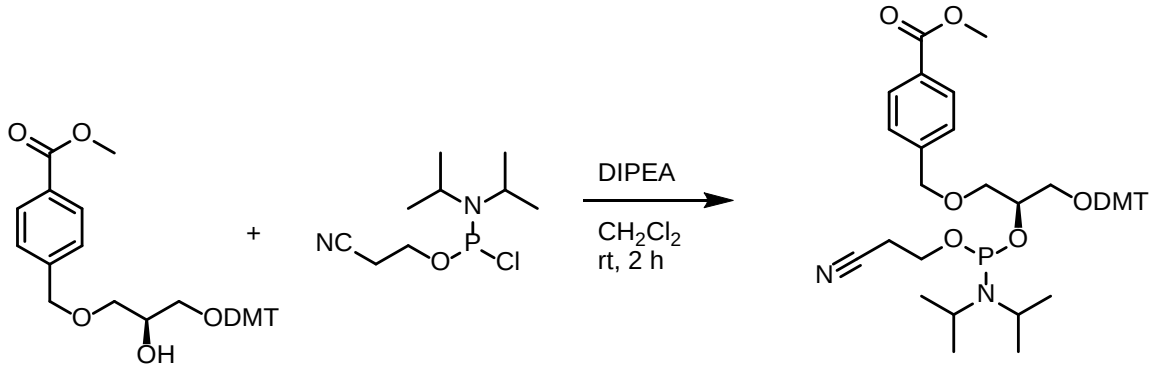

(*S*)-**40** (*S*)-**41**

The synthesis was done in a glovebox under nitrogen atmosphere to exclude water and oxygen. To a stirring solution of (*S*)-**40** (255 mg, 0.470 mM, 1.0 equiv.) in CH_2Cl_2 (10 mL) was added at rt DIPEA (112 µL, 0.705 mM, 1.5 equiv.). To the solution CEDIP-Cl (126 µL, 0.564 mM, 1.2 equiv.) was added and the reaction was stirred for 90 minutes. After completion the solvent was removed under vacuum and the resulting crude phosphoramidite (*S*)-**41** was used for DNA synthesis, assuming a yield of 80 %.[30]

Chemical formula: $C_{10}H_{10}O_3S$

Molecular weight: 210.25 g mol^{-1}

^{31}P NMR (162 MHz, 298 K, CD_2Cl_2): δ (ppm):149.4, 149.3.

HR-ESI MS (positive mode, MeCN)**:** *m/z* calc. for $C_{21}H_{19}O_2$ 303.1380 [DMT]$^+$, $C_{42}H_{52}N_2O_8P$ 743.3456 [M+H]$^+$, $C_{48}H_{67}N_3O_8P$ 844.4660 [M+$C_6H_{15}N$+H]$^+$; found 303.1378, 743.3453, 844.4657.

9.8.12 Michael-Acceptor MA1

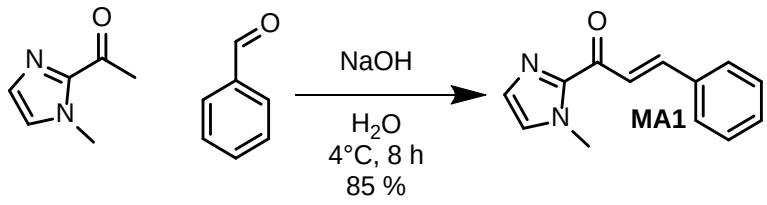

The synthesis of Michael-acceptor **MA1** was adapted from a literature procedure.[253] 1-(1-methyl-1H-imidazol-2-yl)ethan-1-one (340 mg, 2.74 mM, 1.1 equiv.) and benzaldehyde (264 mg, 2.49 mM, 1 equiv.) were added to distilled water (25 mL) and cooled to 4 °C. The mixture was shaken thoroughly to afford a fine emulsion. Then 10 mL of a 10 % aqueous NaOH solution was added and the mixture was shaken for ~30 seconds. The reaction was then left at 4 °C for 8 h. The resulting white solid was filtered, dried and the residue was recrystallized in 4 mL Ethanol to afford the product **MA1** as colorless needles (447 mg, 2.11 mM, 85 %). The ^{1}H NMR was in accordance with literature.[375]

Chemical Formula: $C_{13}H_{12}N_2O$

Molecular weight: 212.25 g mol^{-1}

HRMS (ESI, pos., Calc. [M+H]+: 213.1022, ACN): Found: m/z = 213.1030 [M+H]+, [2M+H]+.

^{1}H NMR (500 MHz, 298 K, $CDCl_3$): δ (ppm): 8.15 (d, ^{3}J = 15.9.0, 1H), 7.84 (d, ^{3}J = 15.9 Hz, 1H), 7.75 - 7.71 (m, 2H), 7.42 - 7.39 (m, 3H), 7.26 (d, ^{3}J = 2.4 Hz, 1H), 7.10 (s, 1H), 4.12 (s, 3H).

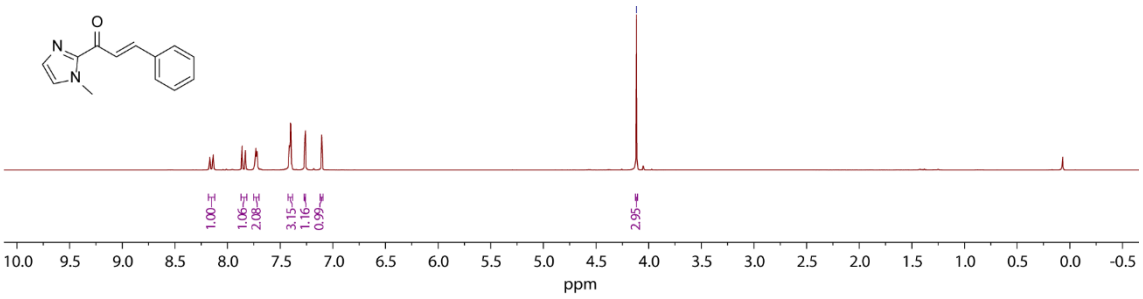

Figure 132. ^{1}H NMR (500 MHz, 298 K, $CDCl_3$) of Michael-acceptor **MA1**.

9.8.13 Michael-Acceptor MA2

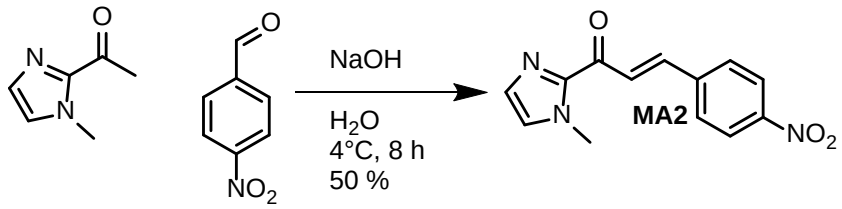

The synthesis of Michael-acceptor **MA2** was the same procedure as for Michael-acceptor **MA1** (47 mg, 0.18 mmol, 50 %)

Chemical Formula: $C_{13}H_{11}N_3O_3$

Molecular weight: 257.25 g mol^{-1}

HRMS (ESI, pos., Calc. [M+H]+: 258.0873 ACN): Found: m/z = 258.0873 [M+H]+.

^{1}H NMR (500 MHz, 298 K, DMSO-d^6): δ (ppm): 8.29 – 8.26 (m, 2H), 8.18 (d, *J* = 16.2 Hz, 1H), 8.08 – 8.05 (m, 2H), 7.82 (d, *J* = 16.1 Hz, 1H), 7.62 (s, 1H), 7.24 (s, 1H), 4.02 (s, 3H).

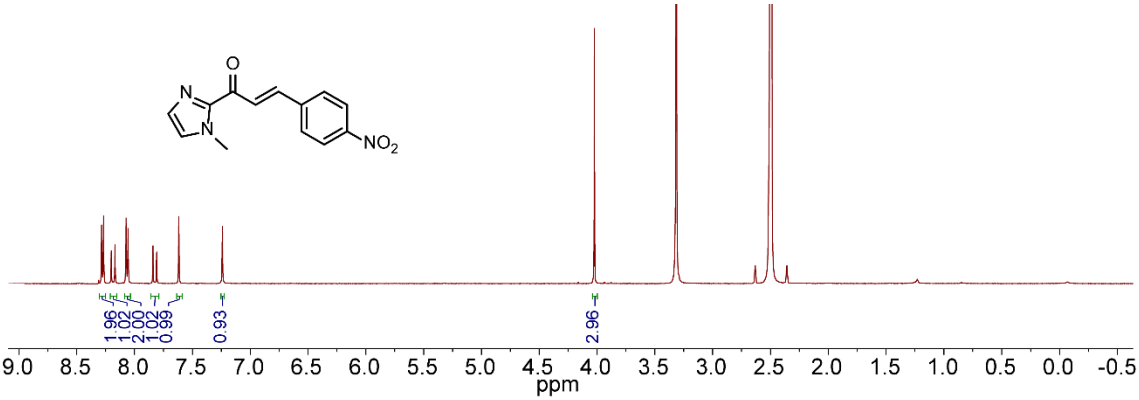

Figure 133. ^{1}H NMR (500 MHz, 298 K, DMSO-d^6) of Michael-acceptor **MA2**.

9.8.14 Michael-Acceptor MA3

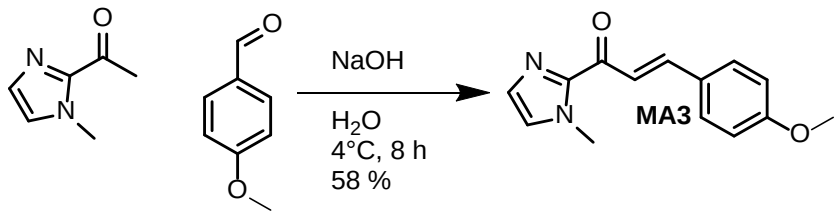

The synthesis of Michael-acceptor **MA2** was the same procedure as for Michael-acceptor **MA1** (52 mg, 0.21 mmol, 58 %)

Chemical Formula: $C_{14}H_{14}N_2O_2$

Molecular weight: 242.27 g mol^{-1}

HRMS (ESI, pos., Calc. [M+H]+: 243.1128 ACN): Found: m/z = 243.1123 [M+H]+, 243.1123 [2M+H]+

^{1}H NMR (500 MHz, 298 K, DMSO-d^6): δ (ppm): 7.92 (d, *J* = 15.9 Hz, 1H), 7.71 (d, *J* = 15.9 Hz, 1H), 7.73 (d, *J* = 8.7 Hz, 2H), 7.58 (s, 1H), 7.24 (s, 1H), 7.02 (d, *J* = 8.4, 2H), 4.00 (s, 3H), 3.82 (s, 3H).

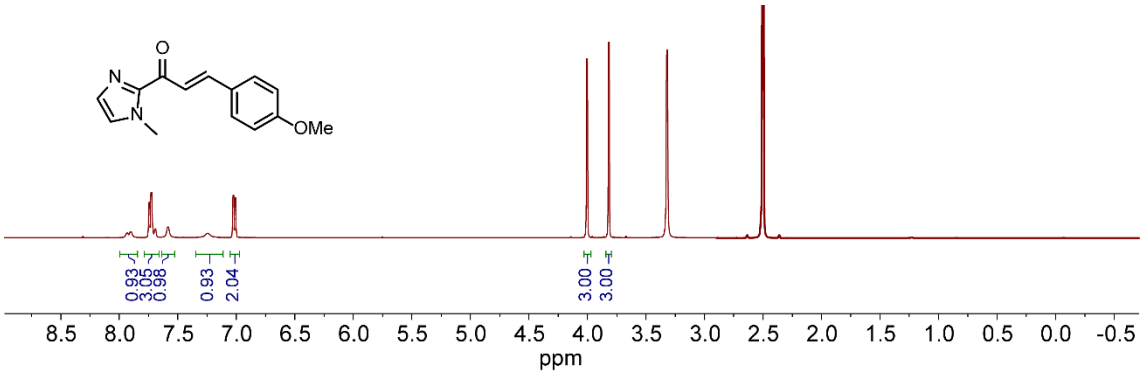

Figure 134. ^{1}H NMR (500 MHz, 298 K, DMSO-d^6) of Michael-acceptor **MA3**.

9.8.15 Michael-Acceptor MA4

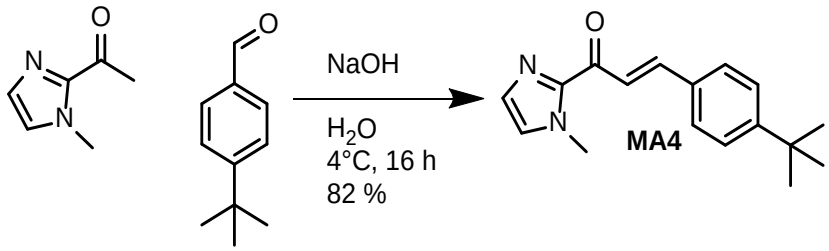

The synthesis of Michael-acceptor **MA4** was adapted from a literature procedure. 1-(1-methyl-1H-imidazol-2-yl)ethan-1-one (50 mg, 44 µL, 0.40 mM, 1.1 equiv.) and 4-tert-butylbenzaldehyde (59 mg, 57 µL, 0.37 mM, 1 equiv.) were added to distilled water (3.6 mL) and cooled to 4 °C. The mixture was shaken thoroughly to afford a fine emulsion. Then 1.4 mL of a 10 % aqueous NaOH solution was added and the mixture was shaken for ~30 seconds. The reaction was then left at 4 °C for 16 h. The emulsion was extracted with EtOAc (3 x 5 mL), the combined organic layers were dried over $MgSO_4$ and the solvent was removed under reduced pressure. The resulting yellow oil was purified by column chromatography (*n*Pentane/EtOAc, 90/10 → *n*Pentane/EtOAc, 70/30) to afford the product **MA4** as a colorless oil (81 mg, 0.30 mM, 82 %).

Chemical Formula: $C_{17}H_{20}N_2O$

Molecular weight: 268.36 g mol^{-1}

HRMS (ESI, pos., Calc. [M+H]+: 269.1648 ACN): Found: m/z = 269.1648 [M+H]+, 537.3225 [2M+H]+, 599.1442 [2M+Cu]+.

^{1}H NMR (600 MHz, 298 K, $CDCl_3$): δ (ppm): 8.05 (d, *J* = 16 Hz, 1H), 7.82 (d, *J* = 16 Hz, 1H), 7.65 – 7.62 (m, 2H), 7.43 – 7.40 (m, 2H), 7.21 (s, 1H), 7.06 (s, 1H), 4.08 (s, 3H), 1.33 (s, 9H).

^{13}C NMR (150 MHz, 298 K, $CDCl_3$): δ (ppm): 180.9, 154.4, 144.4, 143.8, 132.5, 129.5, 129.0, 127.5, 126.2, 122.2, 36.7, 35.3, 31.5.

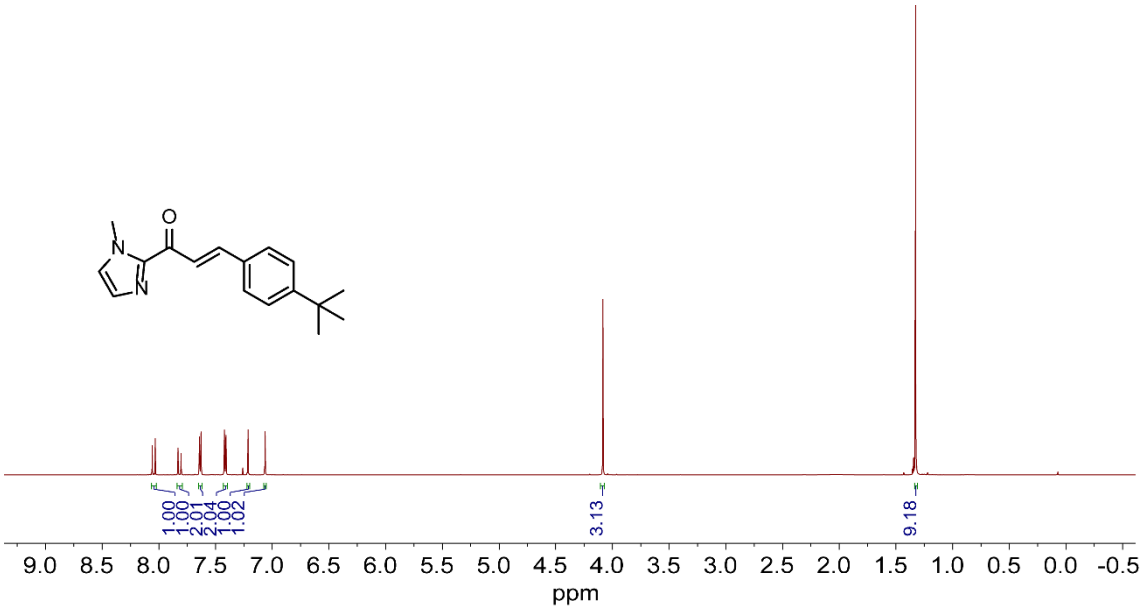

Figure 135. ^{1}H NMR (600 MHz, 298 K, $CDCl_3$) of Michael-acceptor **MA4**.

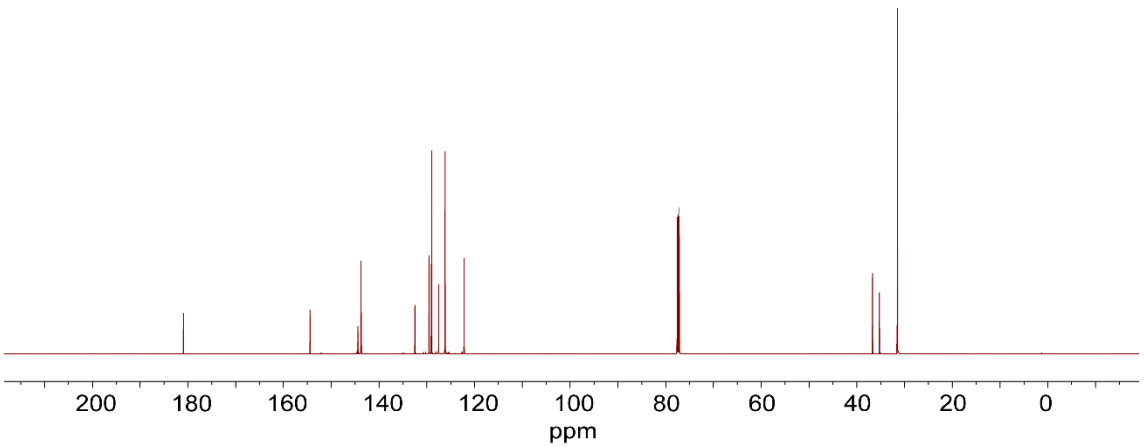

Figure 136. ^{13C} NMR (150 MHz, 298 K, $CDCl_3$) of Michael-acceptor **MA4**.

9.8.16 Michael-Acceptor MA5

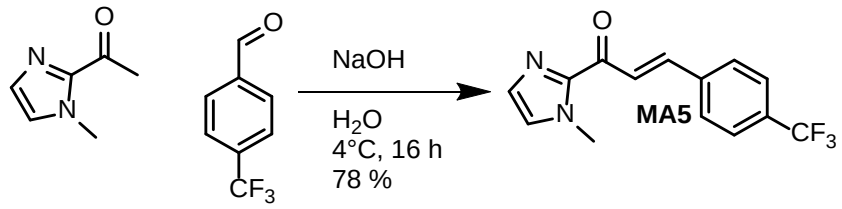

The synthesis of Michael-acceptor **MA5** was adapted from a literature procedure. 1-(1-methyl-1H-imidazol-2-yl)ethan-1-one (50 mg, 44 µL, 0.40 mM, 1.1 equiv.) and 4-(trifluoromethyl)benzaldehyde (64 mg, 61 µL, 0.37 mM, 1 equiv.) were added to distilled water (3.6 mL) and cooled to 4 °C. The mixture was shaken thoroughly to afford a fine emulsion. Then 1.4 mL of a 10 % aqueous NaOH solution was added and the mixture was shaken for ~30 seconds. The reaction was then left at 4 °C for 16 h. The resulting white solid was filtered, washed with water and dried To remove small impurities the product was in addition purified by column chromatography (*n*Pentane/EtOAc, 90/10 → *n*Pentane/EtOAc, 70/30) to afford the product **MA5** as a white solid (80 mg, 0.29 mM, 78 %).

Chemical Formula: $C_{14}H_{11}F_3N_2O$

Molecular weight: 280.25 g mol^{-1}

HRMS (ESI, pos., Calc. [M+H]+: 281.0896 ACN): Found: m/z = 281.0896 [M+H]+, 561.1722 [2M+H]+, 561.1722 [2M+Cu]+ 623.0939.

^{1}H NMR (600 MHz, 298 K, $CDCl_3$): δ (ppm): 8.16 (d, *J* = 16.0 Hz, 1H), 7.82 (d, *J* = 16.0 Hz, 1H), 7.8 – 7.78 (m, 2H), 7.67 – 7.64 (m, 2H), 7.25 (s, 1H), 7.11 (s, 1H), 4.11 (s, 3H).

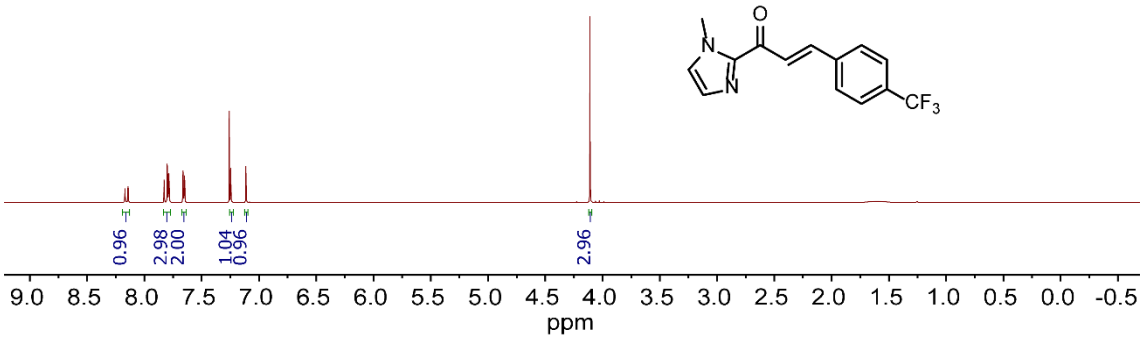

Figure 137. ^{1}H NMR (600 MHz, 298 K, $CDCl_3$) of Michael-acceptor **MA5**.

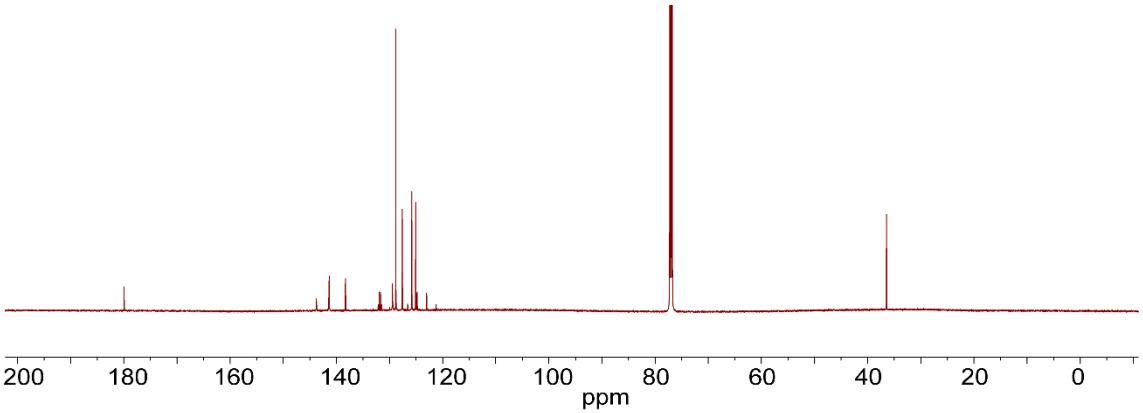

Figure 138. ^{1}H NMR (150 MHz, 298 K, $CDCl_3$) of Michael-acceptor **MA5**.

9.8.17 Michael-Acceptor MA6

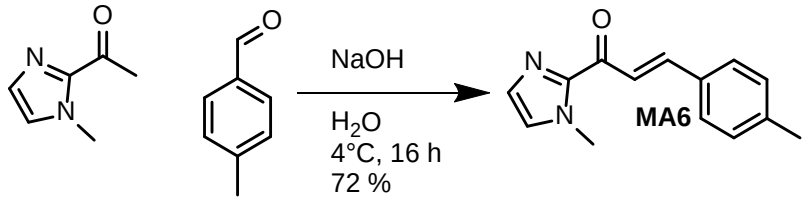

The synthesis of Michael-acceptor **MA6** was adapted from a literature procedure. 1-(1-methyl-1H-imidazol-2-yl)ethan-1-one (50 mg, 44 µL, 0.40 mM, 1.1 equiv.) and 4-methylbenzaldehyde (44 mg, 42 µL, 0.37 mM, 1 equiv.) were added to distilled water (3.6 mL) and cooled to 4 °C. The mixture was shaken thoroughly to afford a fine emulsion. Then 1.4 mL of a 10 % aqueous NaOH solution was added and the mixture was shaken for ~30 seconds. The reaction was then left at 4 °C for 16 h. The resulting white solid was filtered, washed with water and dried to afford the product **MA6** as white solid (60 mg, 0.27 mM, 72 %).

Chemical Formula: $C_{14}H_{14}N_2O$

Molecular weight: 226.28 g mol^{-1}

HRMS (ESI, pos., Calc. [M+H]+: 227.1179 ACN): Found: m/z = 227.1178 [M+H]+, 453.228 [2M+H]+, 515.1503 [M+Cu]+.

^{1}H NMR (500 MHz, 298 K, $CDCl_3$): δ (ppm): 8.04 (d, *J* = 16 Hz, 1H), 7.81 (d, *J* = 16 Hz, 1H), 7.62 – 7.58 (m, 2H), 7.22 – 7.19 (m, 3H), 7.08 (s, 1H), 4.09 (s, 3H), 2.38 (s, 3H).

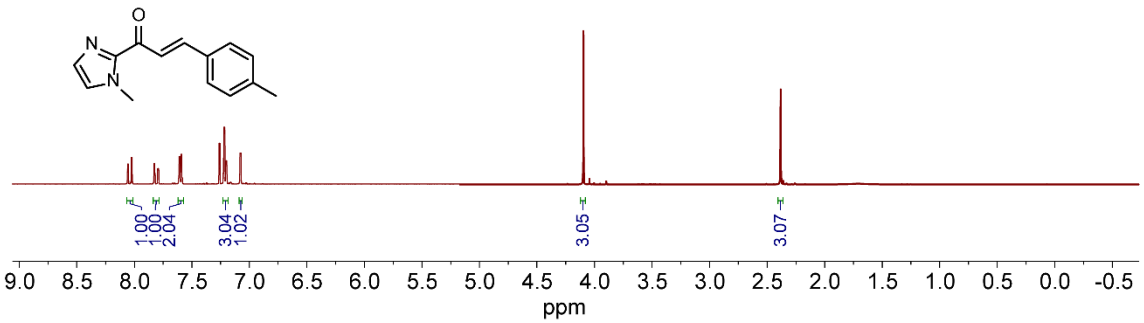

Figure 139. ^{1}H NMR (500 MHz, 298 K, $CDCl_3$) of Michael-acceptor **MA6**.

9.8.18 Michael-Acceptor MA7

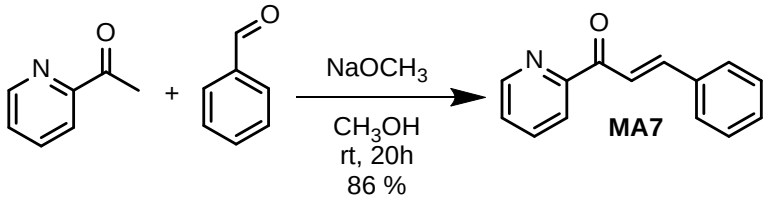

The synthesis of Michael-acceptor **MA7** was adapted from a literature procedure.[253] acetyl pyridine (332 mg, 2.75 mM, 1.1 equiv.) and benzaldehyde (265 mg, 2.50 mM, 1 equiv.) were added to distilled water (25 mL) and cooled to 4 °C. The mixture was shaken thoroughly to afford a fine emulsion. Then 10 mL of a 10 % aqueous NaOH solution was added and the mixture was shaken for ~30 seconds. The reaction was then left at 4 °C for 8 h. The resulting white solid was filtered, dried and the residue was recrystallized in 4 mL Ethanol to afford the product **MA7** as colourless needles (450 mg, 2.15 mM, 86 %).

The ^{1}H NMR was in accordance with literature.

Chemical Formula: $C_{14}H_{11}NO$

Molecular weight: 209.25 g mol^{-1}

HRMS (ESI, pos., Calc. [M+H]+: 210.0913, ACN): Found: m/z = 210.0912 [M+H]+, [2M+H]+.

^{1}H NMR (700 MHz, 298 K, $CDCl_3$): δ (ppm): 8.77 (ddd, *J* = 4.8, 1.8, 0.9 Hz, 1H), 8.34 (d, *J* = 16.0 Hz, 1H), 8.22 (dt, *J* = 7.8, 1.1 Hz, 1H), 7.96 (d, *J* = 16.0 Hz, 1H), 7.92 (td, *J* = 7.7, 1.7 Hz, 1H), 7.77 – 7.73 (m, 2H), 7.52 (ddd, *J* = 7.6, 4.8, 1.3 Hz, 1H), 7.46 – 7.39 (m, 3H).

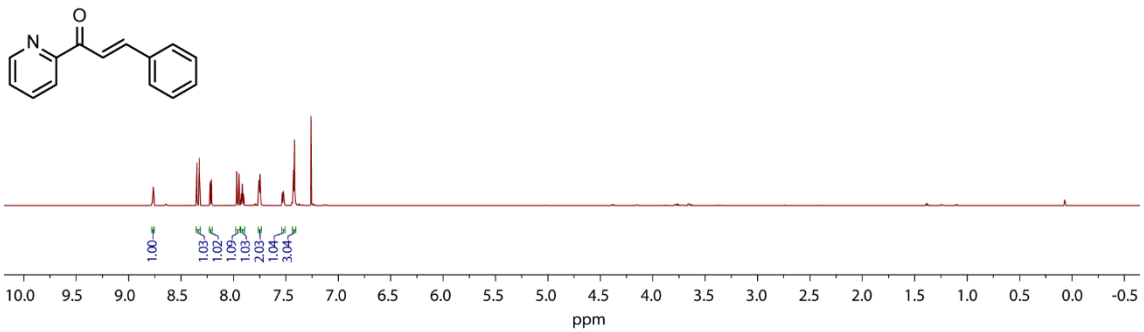

Figure 140. ^{1}H NMR (700 MHz, 298 K, $CDCl_3$) of Michael-acceptor **MA7**.

9.8.19 Michael-adduct A1

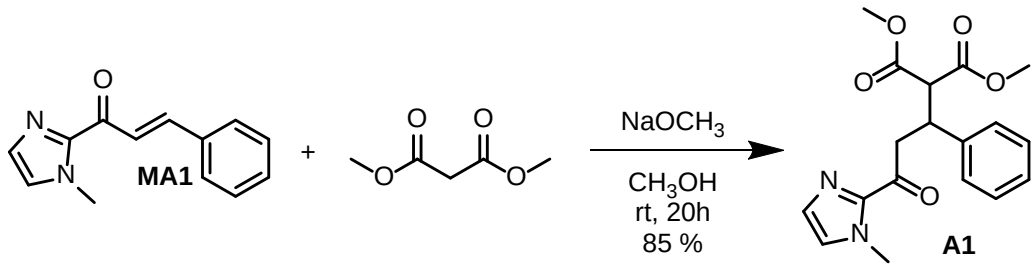

To a solution of dimethylmalonate (100 mg, 0.5 mM, 1 equiv.) and Michael-acceptor **MA1** (62 mg, 0.5 mM, 1 equiv.) in methanol (5 mL), sodium methoxide (0.05 mM, tip of a spatula) was added. The mixture was stirred at room temperature for 20 h. The solvent was removed and the remaining solid was purified by column chromatography (CH_2Cl_2 → CH_2Cl_2/MeOH, 90/5) to afford the Michael-adduct **A1** as a white solid (117 mg, 0.40 mM, 85 %). The ^{1}H NMR was in accordance with literature.[375]

Chemical Formula: $C_{18}H_{20}N_2O_5$

Molecular weight: 344.37 g mol^{-1}

HRMS (ESI, pos., Calc. [M+H]+: 345.1445 ACN): Found: m/z = 313.1180 [M+H-MeOH]+ 345.1442 [M+H]+, 367.1261 [M+Na]+, 407.0660 [M+Cu]+, 751.2029 [2M+Cu]+.

^{1}H NMR (500 MHz, 298 K, $CDCl_3$): δ (ppm): 7.31 - 7.29 (m, 2H), 7.26 - 7.22 (m, 2H), 7.18 - 7.14 (m, 1H), 7.10 (s, 1H), 6.95 (s, 1H), 4.16 (td, ^{3}J = 10.0 Hz, 4.4 Hz, 1H), 3.87 (s, 3H), 3.88 - 3.80 (m, 2H), 3.72 (s, 3H), 3.50 - 3.45 (m, 1H), 3.45 (s, 3H).

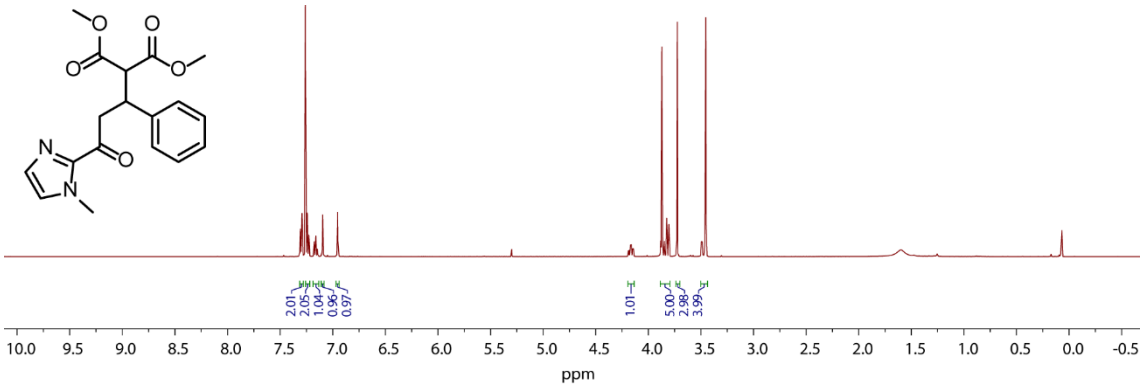

Figure 141. ^{1}H NMR (500 MHz, 298 K, $CDCl_3$) of Michael-adduct **A1**.

9.8.20 Michael-adduct A2

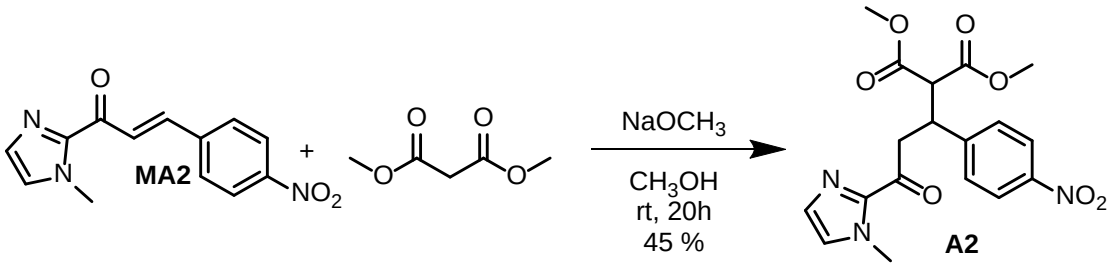

To a solution of dimethylmalonate (10.3 mg, 0.08 mM, 1 equiv.) and Michael-acceptor **MA2** (20 mg, 0.08 mM, 1 equiv.) in methanol (2 mL), sodium methoxide (0.05 mM, tip of a spatula) was added. The mixture was stirred at room temperature for 20 h. The solvent was removed and the remaining solid was purified by column chromatography (CH_2Cl_2 → CH_2Cl_2/MeOH, 90/5) to afford the Michael-adduct **A2** as a white solid (14 mg, 0.035 mM, 46 %).

Chemical Formula: $C_{18}H_{19}N_3O_7$

Molecular weight: 389.36 g mol^{-1}

HRMS (ESI, pos., Calc. [M+H]+: 390.1296, ACN): Found: m/z = 358.0310 [M+H-MeOH]+, 390.1293 [M+H]+, 841.1736 [2M+Cu]+

^{1}H NMR (500 MHz, 298 K, DMSO-d^{6}): δ (ppm): 8.12 – 8.09 (m, 2H), 7.63 – 7.60 (m, 2H), 7.45 (s, 1H), 7.08 (s, 1H), 4.21 (d, *J* = 10.1 Hz, 1H), 4.06 (td, *J* = 10.2, 3.8 Hz, 1H), 3.88 (dd, *J* = 17.5, 10.3 Hz, 1H), 3.78 (s, 3H), 3.67 (s, 3H), 3.41 (s, 3H), 3.36 – 3.33 (m, 1H).

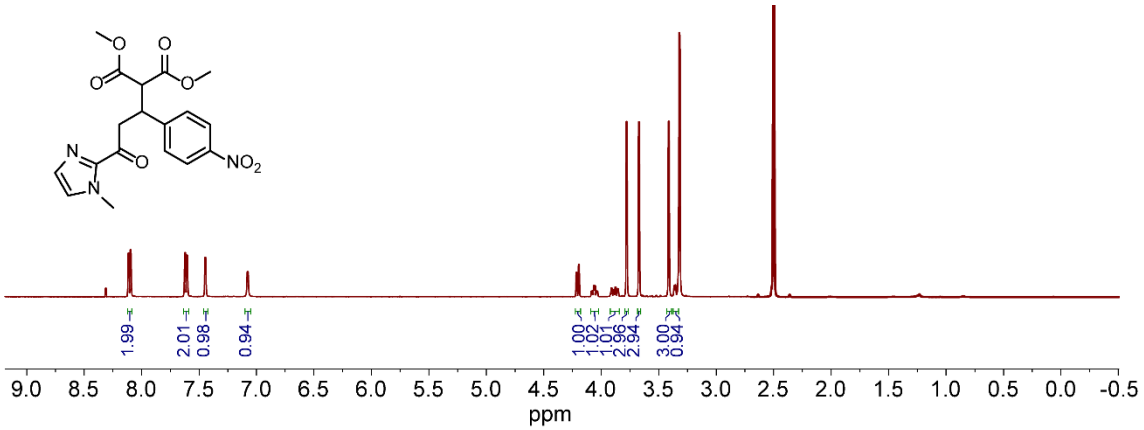

Figure 142. [1]H NMR (500 MHz, 298 K, DMSO-d6) of Michael-adduct **A2**.

9.8.21 Michael-adduct A3

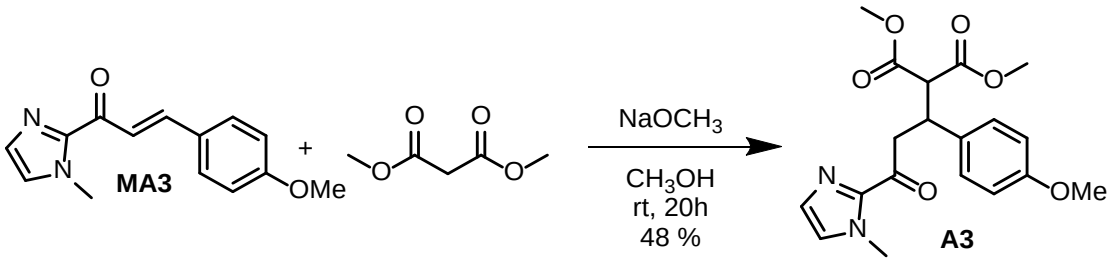

Michael-adduct **A3** was prepared as described in **9.8.20** to afford the product as colourless solid (15 mg, 0.04 mM, 48 %).

Chemical Formula: $C_{19}H_{22}N_2O_6$

Molecular weight: 374.39 g mol^{-1}

HRMS (ESI, pos., Calc. [M+H]+: 375.1551, ACN): Found: m/z = 375.1547 [M+H]+, 397.1367 [M+Na]+

^{1}H NMR (500 MHz, 298 K, DMSO-d^6): δ (ppm): 7.42 (s, 1H), 7.19 -7.16 (m, 2H), 7.07 (s, 1H), 6.78 – 6.75 (m, 2H), 3.97 (d, *J* = 10.0 Hz, 1H), 3.90 (td, *J* = 10.0, 3.5 Hz, 1H), 3.84 – 3.78 (m, 1H), 3.77 (s, 3H), 3.67 (s, 3H), 3.63 (s, 3H), 3.39 (s, 3H), 3.16 (dd, *J* = 16.8, 3.7 Hz, 1H).

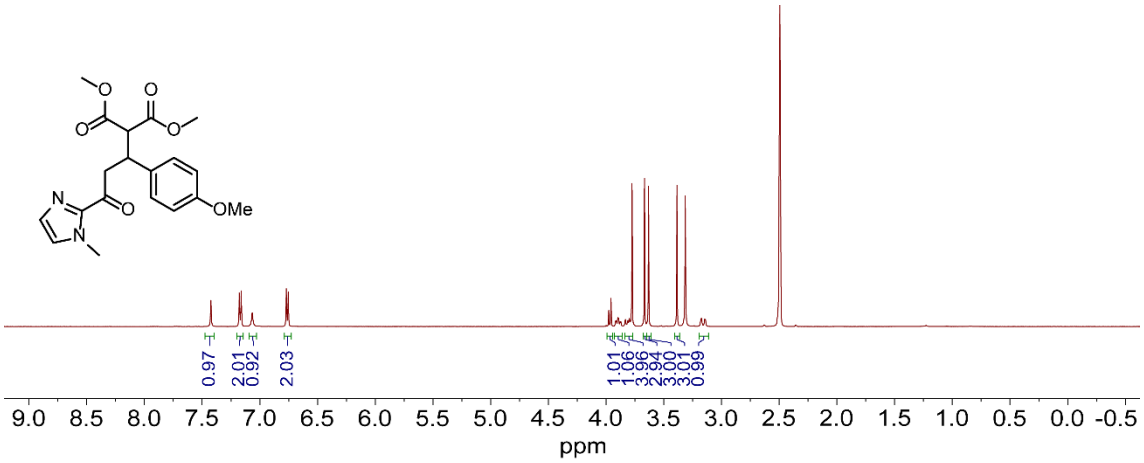

Figure 143. ^{1}H NMR (500 MHz, 298 K, DMSO-d6) of Michael-adduct **A3**.

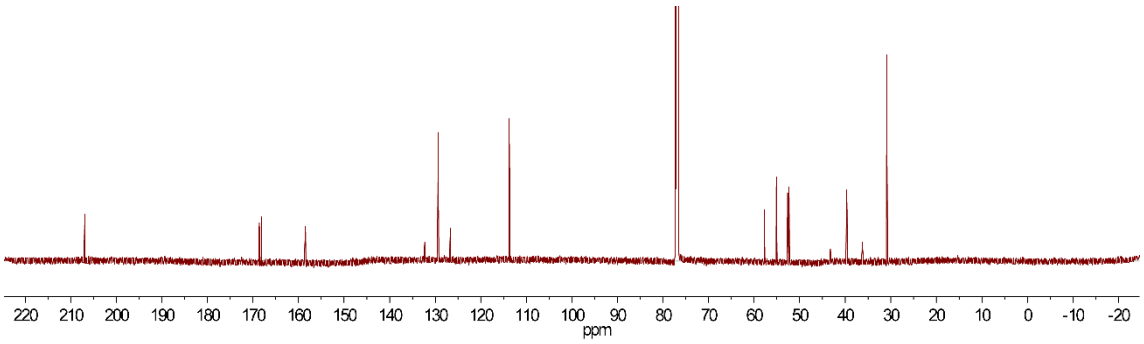

Figure 144: ^{1}H NMR (178 MHz, 298 K, $CDCl_3$) of Michael-adduct **A3**.

9.8.22 Michael-adduct A5

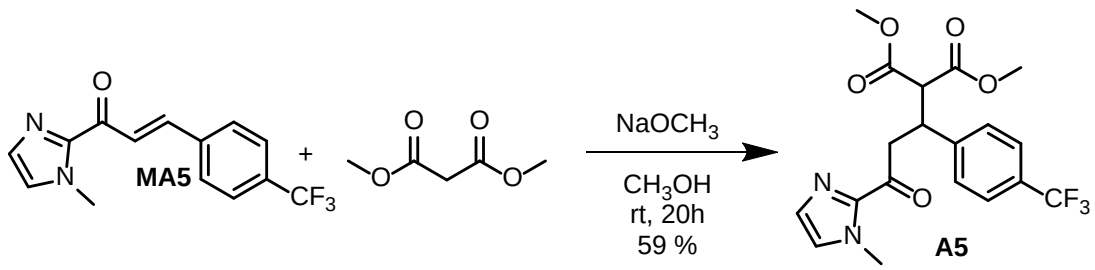

Michael-adduct **A5** was prepared as described in **9.8.20** to afford the product as colourless solid (17.5 mg, 0.04 mM, 59 %).

Chemical Formula: $C_{19}H_{19}F_3N_2O_5$

Molecular weight: 412.37 g mol^{-1}

HRMS (ESI, pos., Calc. [M+H]+: 413.1319, ACN): Found: m/z = 413.1315 [M+H]+, 435.1134 [M+Na]+

^{1}H NMR (700 MHz, 298 K, $CDCl_3$): δ (ppm): 7.5 (d, *J* = 8.0 Hz, 2H), 7.44 (d, *J* = 8.0 Hz, 2H), 7.10 (s, 1H), 6.97 (s, 1H), 4.23 (td, *J* = 10.0, 4.2 Hz, 1H), 3.89 – 3.82 (m, 2H), 3.88 (s, 3H), 3.74 (s, 3H), 3.50 – 3.47 (m, 1H), 3.47 (s, 3H).

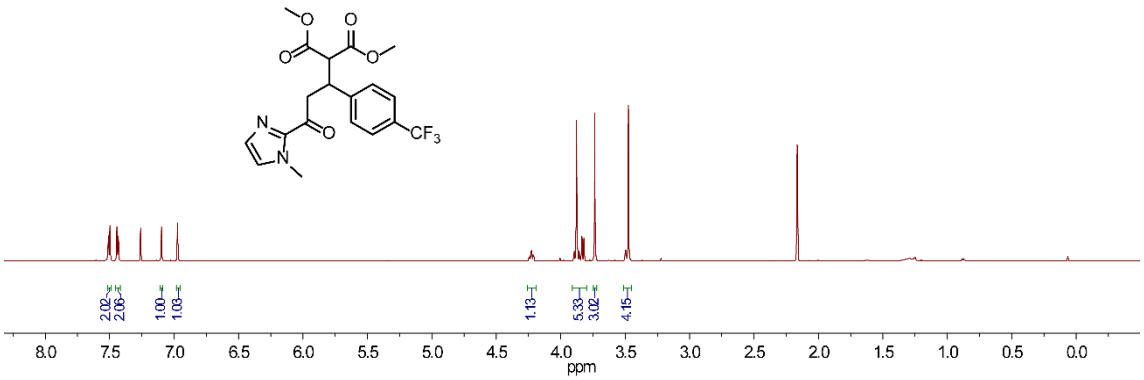

Figure 145. ^{1}H NMR (700 MHz, 298 K, $CDCl_3$) of Michael-adduct **A5**.

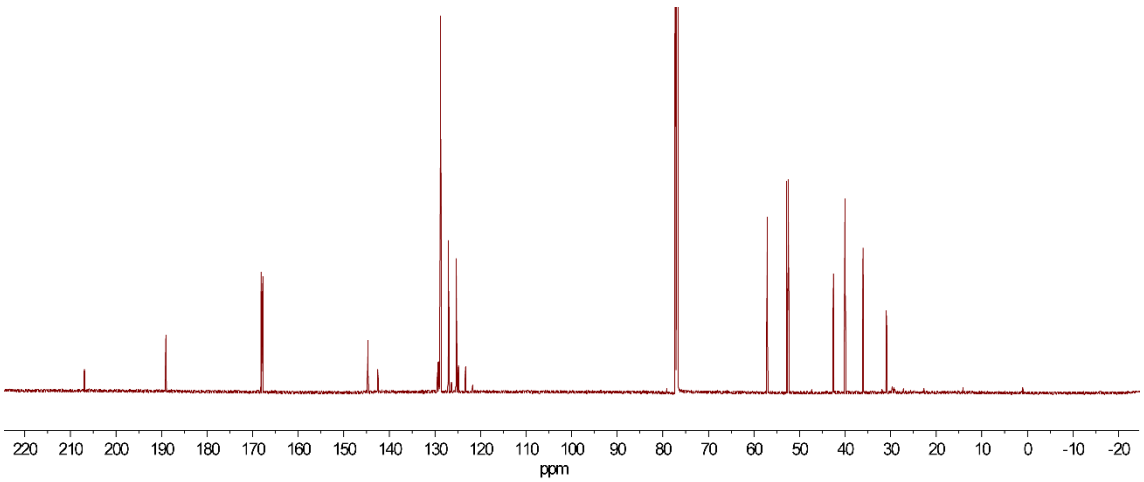

Figure 146. ^{13}C NMR (178 MHz, 298 K, $CDCl_3$) of Michael-adduct **A5**.

9.8.23 Michael-adduct A6

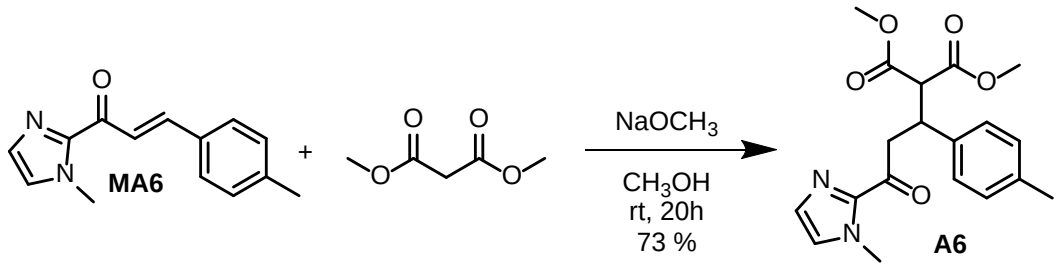

Michael-adduct **A6** was prepared as described in **9.8.20** to afford the product as colourless solid (17.5 mg, 0.06 mM, 73 %).

Chemical Formula: $C_{19}H_{22}N_2O_5$

Molecular weight: 358.39 g mol^{-1}

HRMS (ESI, pos., Calc. [M+H]+: 359.1601, ACN): Found: m/z = 359.1597 [M+H]+, 381.1416 [M+Na]+

^{1}H NMR (700 MHz, 298 K, $CDCl_3$): δ (ppm): 7.18 (d, *J* = 8.0 Hz, 2H), 7.12 (s, 1H), 7.04 (d, *J* = 8.0 Hz, 2H), 6.95 (s, 1H), 4.16 – 4.08 (td, *J* = 10, 4.3 Hz, 1H), 3.96 – 3.80 (m, 2H), 3.89 (s, 3H), 3.71 (s, 3H), 3.51 – 3.46 (m, 1H), 3.47 (s, 3H), 2.25 (s, 3H).

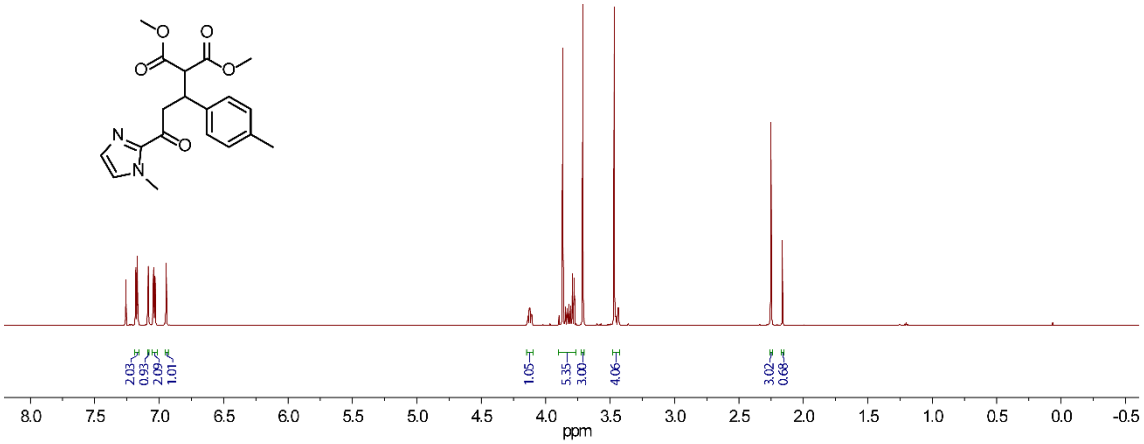

Figure 147. ^{1}H NMR (700 MHz, 298 K, $CDCl_3$) of Michael-adduct **A6**.

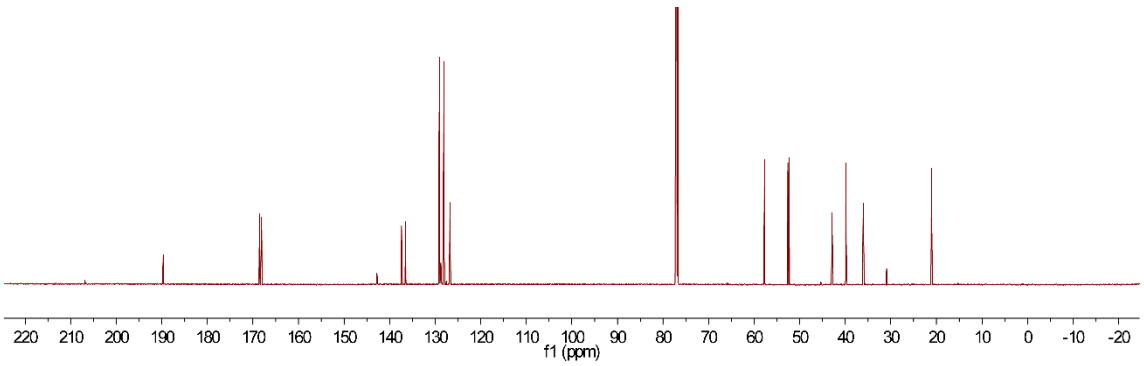

Figure 148. ^{1}H NMR (178 MHz, 298 K, $CDCl_3$) of Michael-adduct **A6**.

9.8.24 Michael-adduct A7

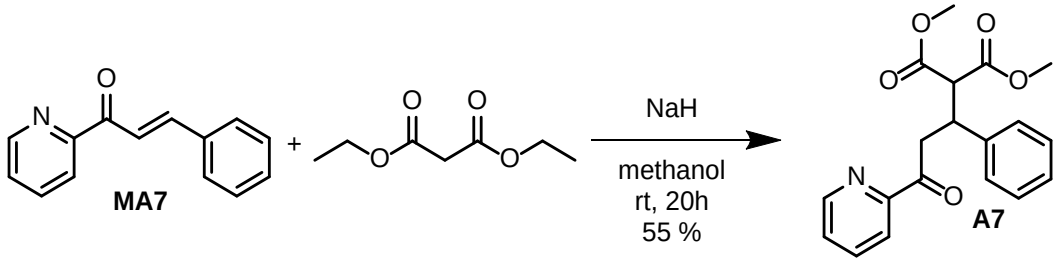

Michael-acceptor **A7** prepared as described in **9.8.20** to afford the product as colourless solid (101 mg, 0.27 mM, 55 %).

Chemical Formula: $C_{19}H_{19}NO_5$

Molecular weight: 341.13 g mol^{-1}

HRMS (ESI, pos., Calc. [M+H]+: 342.1336 ACN): Found: m/z = 342.1322 [M+H]+, 364.1155 [M+Na]+

^{1}H NMR (700 MHz, 298 K, $CDCl_3$): δ (ppm): 8.65 (d, *J* = 4.7 Hz, 1H), 7.91 (d, *J* = 7.8 Hz, 1H), 7.76 (td, *J* = 7.7, 1.7 Hz, 1H), 7.46 – 7.39 (m, 1H), 7.33 – 7.29 (m, 2H), 7.26 – 7.22 (m, 2H), 7.17 – 7.13 (m, 1H), 4.22 (td, *J* = 9.7, 4.3 Hz, 1H), 3.93 (dd, *J* = 17.9, 9.3 Hz, 1H), 3.86 (d, *J* = 10.2 Hz, 1H), 3.72 (s, 3H), 3.60 (dd, *J* = 18.0 Hz, 1H), 3.47 (s, 3H).

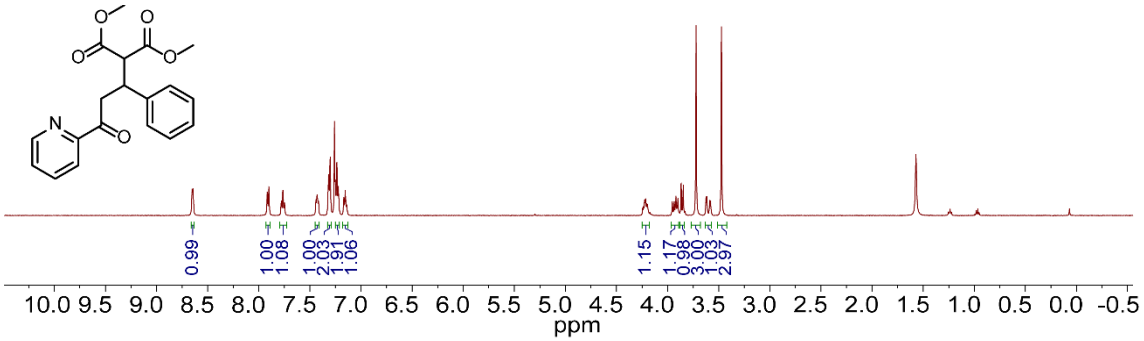

Figure 149. ^{1}H NMR (500 MHz, 298 K, $CDCl_3$) of Michael-acceptor **A7**.

9.8.25 Michael-adduct A8

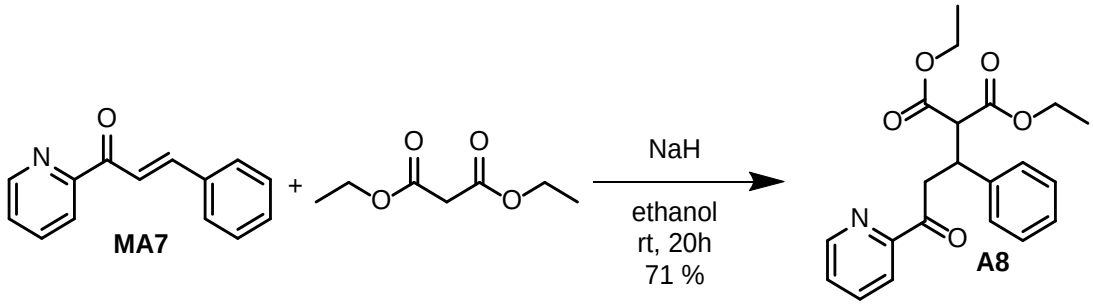

Michael-acceptor **A8** prepared as described in **9.8.20**, but with ethanol as the solvent to afford the product as colourless solid (130 mg, 0.35 mM, 71 %).

Chemical Formula: $C_{21}H_{23}NO_5$

Molecular weight: 369.42 g mol^{-1}

HRMS (ESI, pos., Calc. [M+H]+: 370.1649 ACN): Found: m/z = 370.1634 [M+H]+, 392.1454 [M+Na]+.

^{1}H NMR (500 MHz, 298 K, $CDCl_3$): δ (ppm): 8.65 – 8.63 (m, 1H), 7.92 – 7.89 (m, 1H), 7.76 (td, *J* = 7.7, 1.7 Hz, 1H), 7.42 (ddd, *J* = 7.5, 4.8, 1.3 Hz, 1H), 7.33 – 7.30 (m, 2H),

7.24 – 7.20 (m, 2H), 7.16 – 7.12 (m, 1H), 4.24 – 4.12 (m, 3H), 3.95 – 3.89 (m, 3H), 3.82 (d, *J* = 10.5 Hz, 1H), 3.60 (dd, *J* = 17.9, 4.2 Hz, 1H), 1.24 (t, *J* = 7.2 Hz, 3H), 0.98 (t, *J* = 7.1 Hz, 3H).

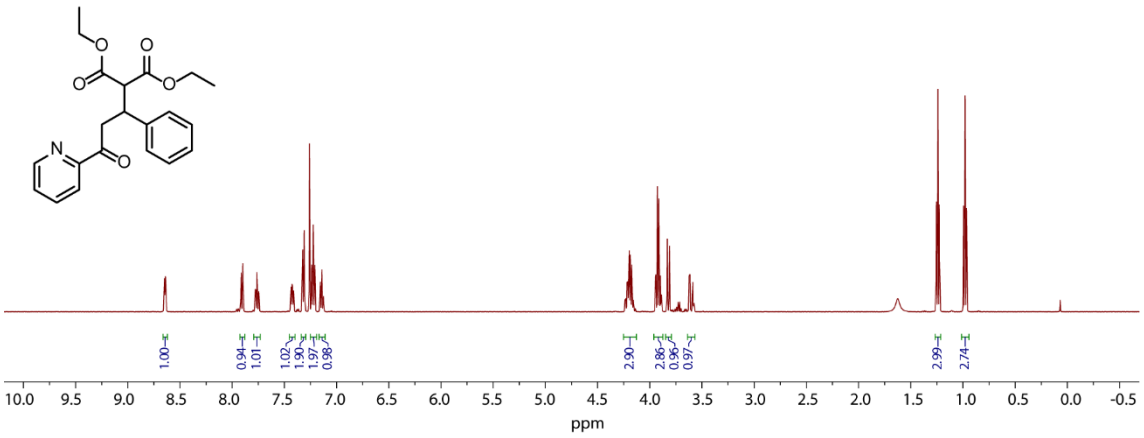

Figure 150. ^{1}H NMR (500 MHz, 298 K, $CDCl_3$) of Michael-acceptor **A8**.

10 APPENDIX

10.1 Additional spectroscopic data

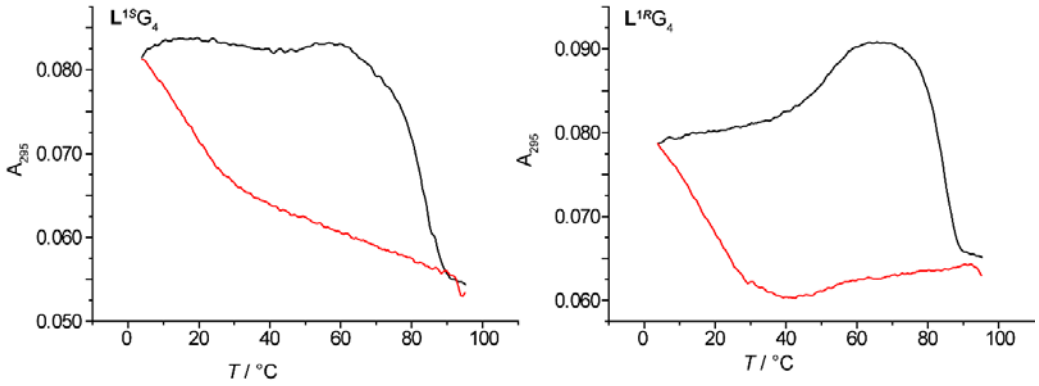

Figure 151. A strong hysteresis was observed for the melting (black) and renaturation (red) profiles of **L^{1S}**G$_4$ and **L^{1R}**G$_4$ in presence of Cu^{II}. Samples were heated or cooled with 0.5 °C min^{-1}. Conditions: 8 µM ssDNA, 8 µM CuSO$_4$, 10 mM LiCaco pH 7.2, 100 mM NaCl.

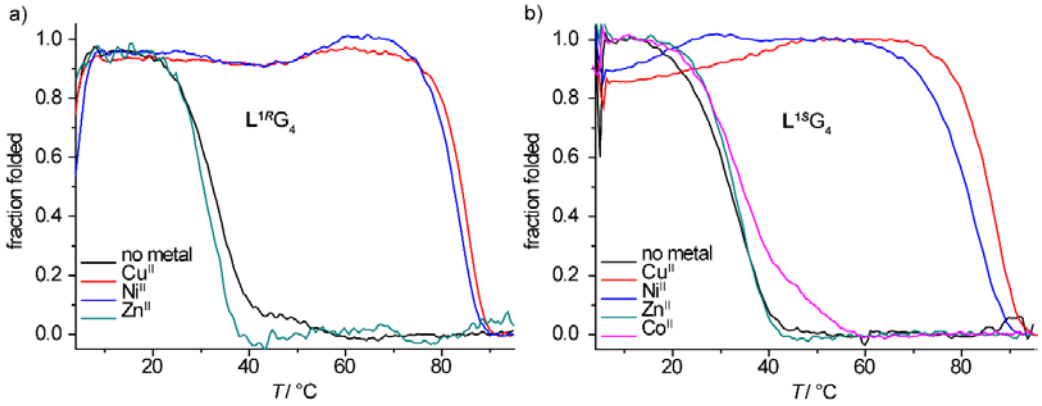

Figure 152. Melting profiles of a) **L^{1R}**G$_4$ and b) **L^{1S}**G$_4$ in presence of 10 equiv. EDTA. Conditions: 3.75 µM ssDNA, 0.94 µM transition metal salt, 10 µM EDTA, 100 mM NaCl, 10 mM LiCaco pH 7.2.

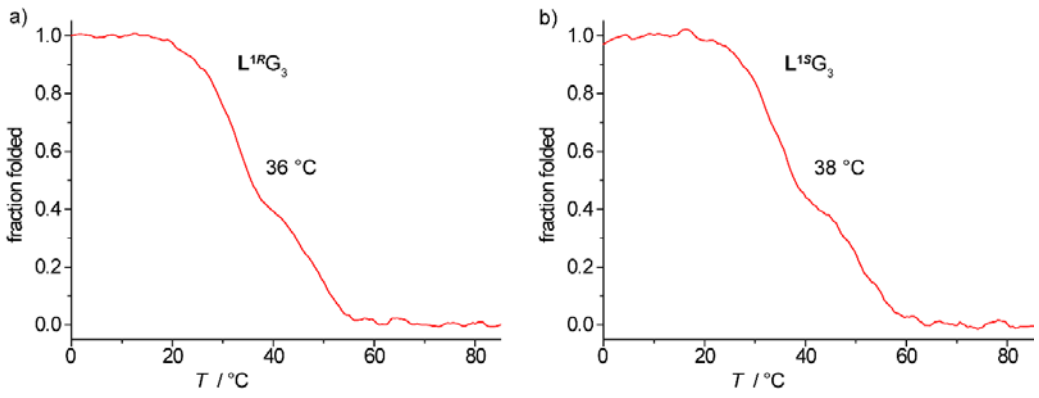

Figure 153. Melting profiles of a) **L^{1R}**G$_3$ and b) **L^{1S}**G$_3$ in presence of Cu^{II} and of 10 equiv. EDTA. Conditions: 3.75 µM ssDNA, 0.94 µM CuSO$_4$, 10 µM EDTA, 100 mM NaCl, 10 mM LiCaco pH 7.2.

10.2 Oligonucleotide Analytics

Name: Sequence (5'→3'):
L^BG_3 $L^BGG\ G$

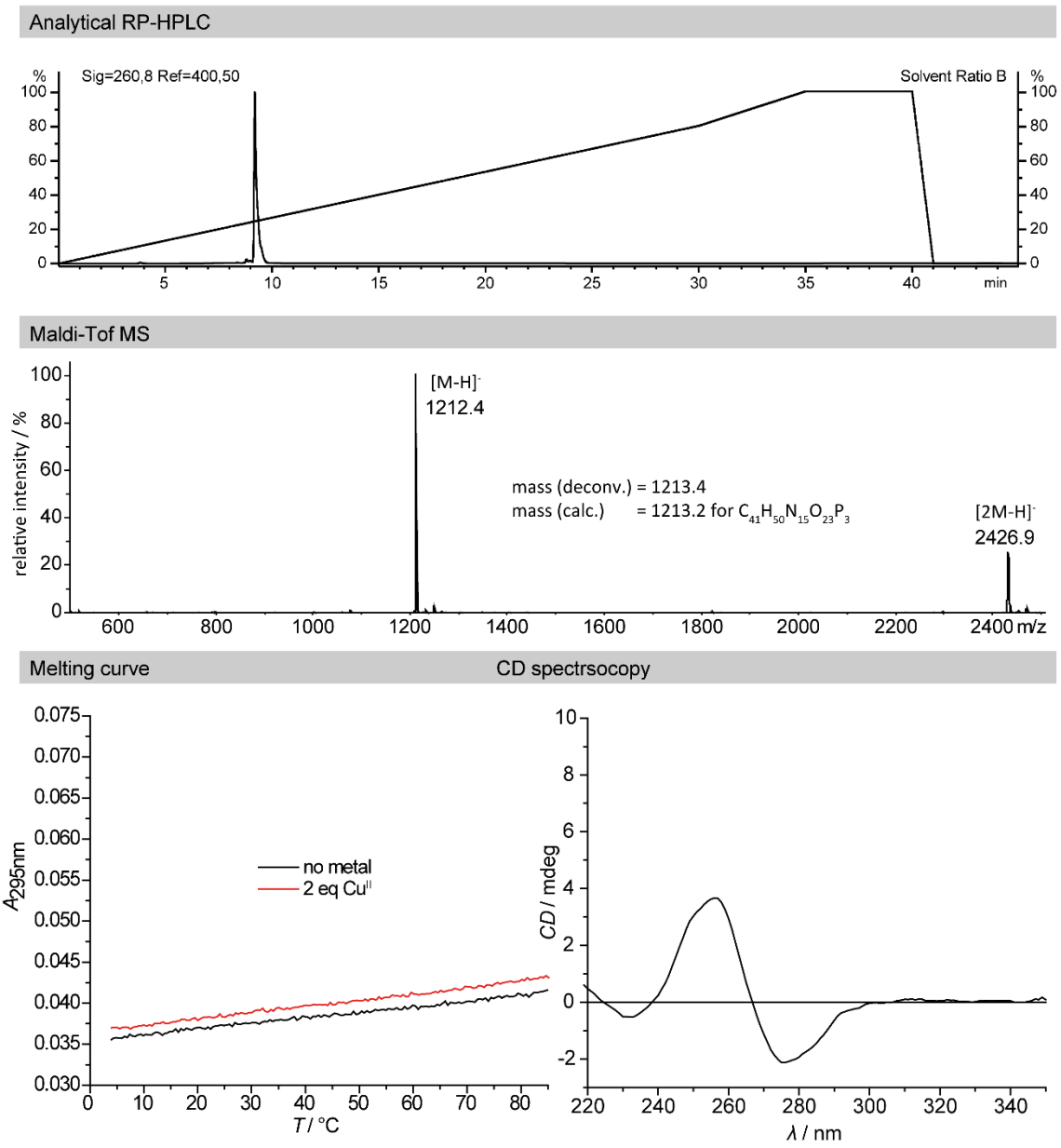

Figure 154. Analytic data of L^BG_3. Samples for thermal denaturation experiments and CD spectroscopy were prepared containing 4 µM ssDNA, 100 mM NaCl, 10 mM LiCaco pH 7.2.

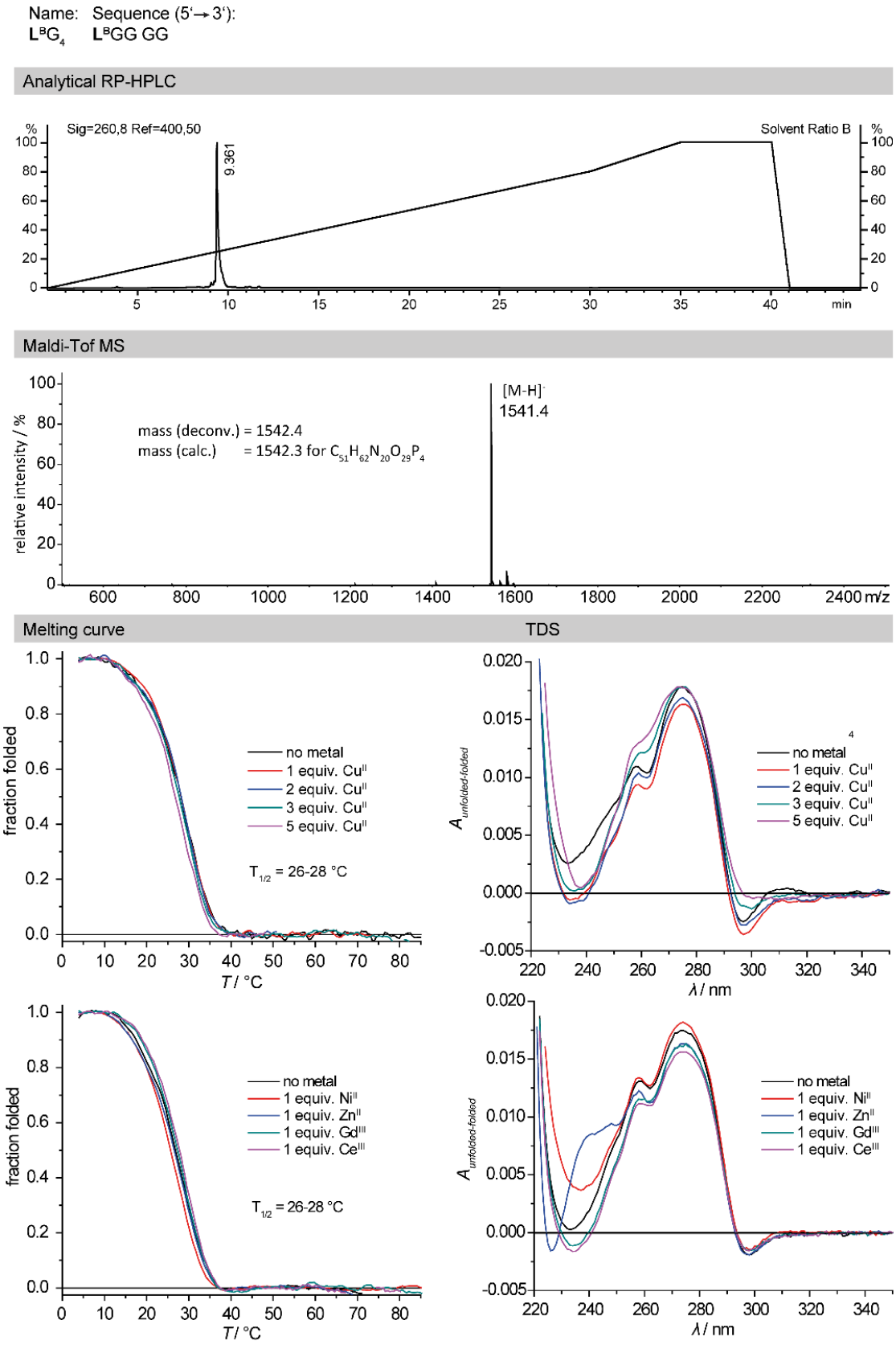

Figure 155. Analytic data of L^BG_4. Samples for thermal denaturation experiments and CD spectroscopy were prepared containing 4 µM ssDNA, 100 mM NaCl, 10 mM LiCaco pH 7.2.

Name: Sequence (5'→3'):
L^BG_5 L^BGG GGG

Analytical RP-HPLC

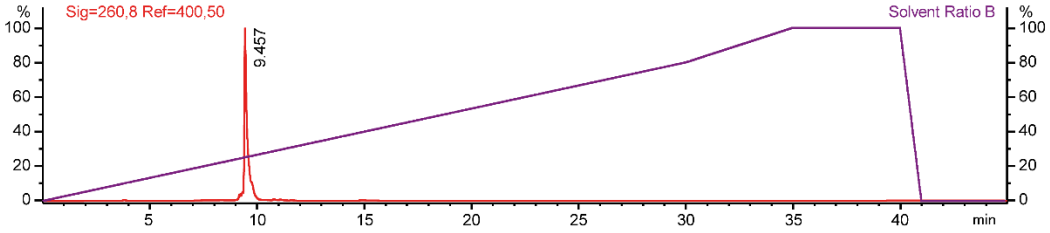

Maldi-Tof MS

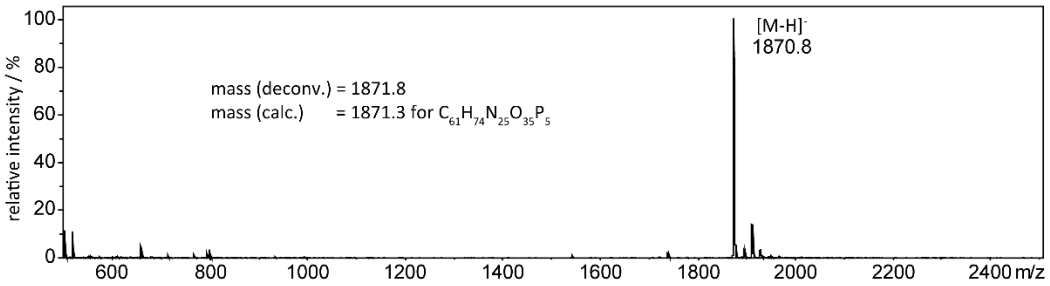

Melting curve TDS

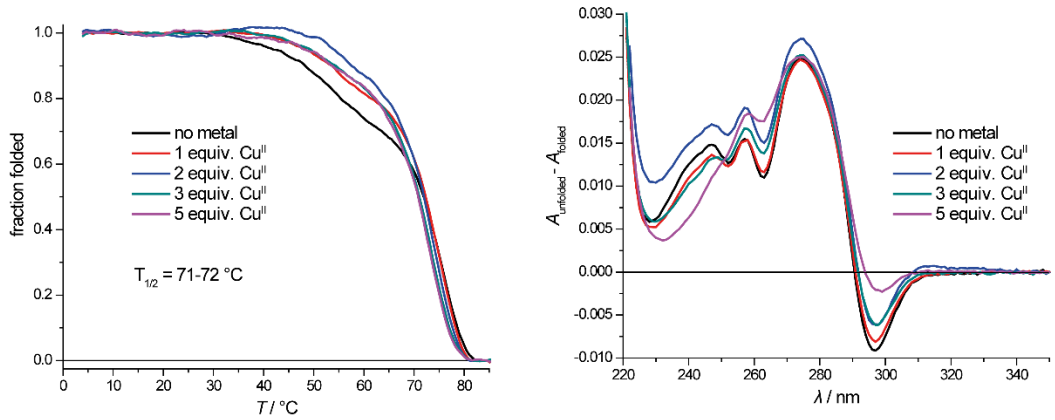

Figure 156. Analytic data of L^BG_5. Samples for thermal denaturation experiments and CD spectroscopy were prepared containing 4 µM ssDNA, 100 mM NaCl, 10 mM LiCaco pH 7.2.

Name: Sequence (5'→3'):
htelL^B_4 AGG L^BTT AL^BG GTT AGG L^BTT AL^BG G

Analytical RP-HPLC

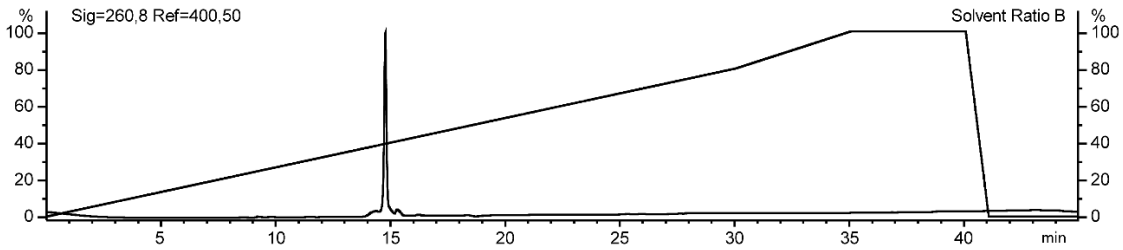

ESI-MS

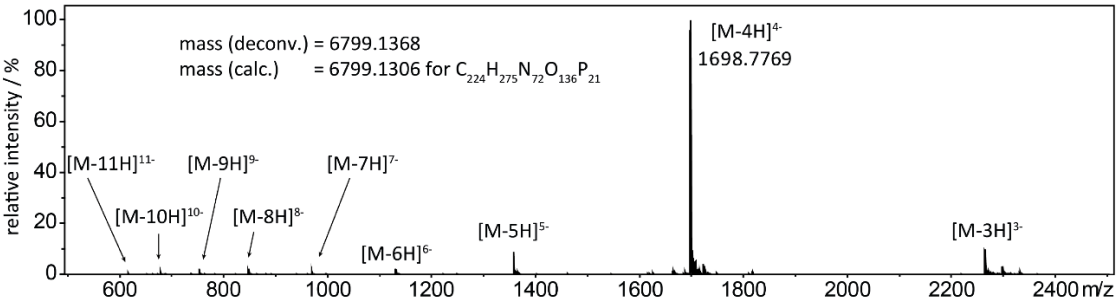

Melting curves

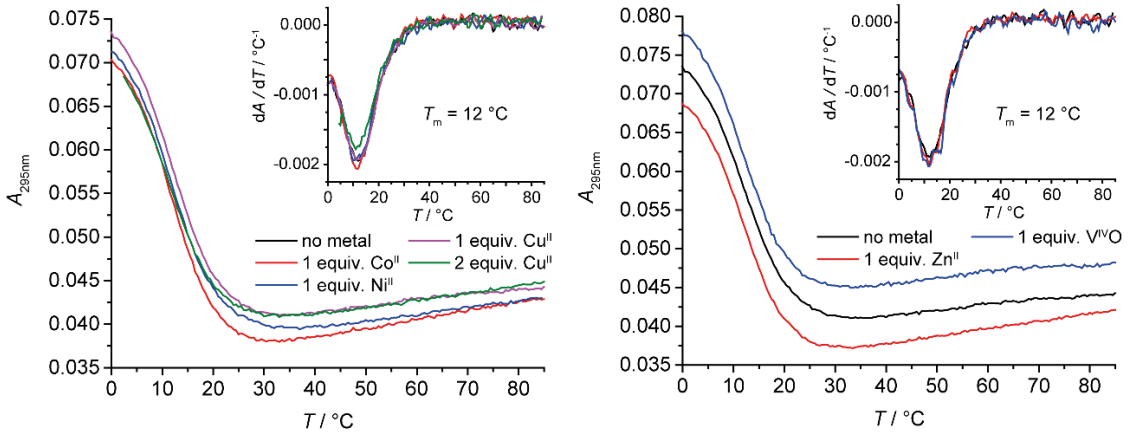

TDS CD

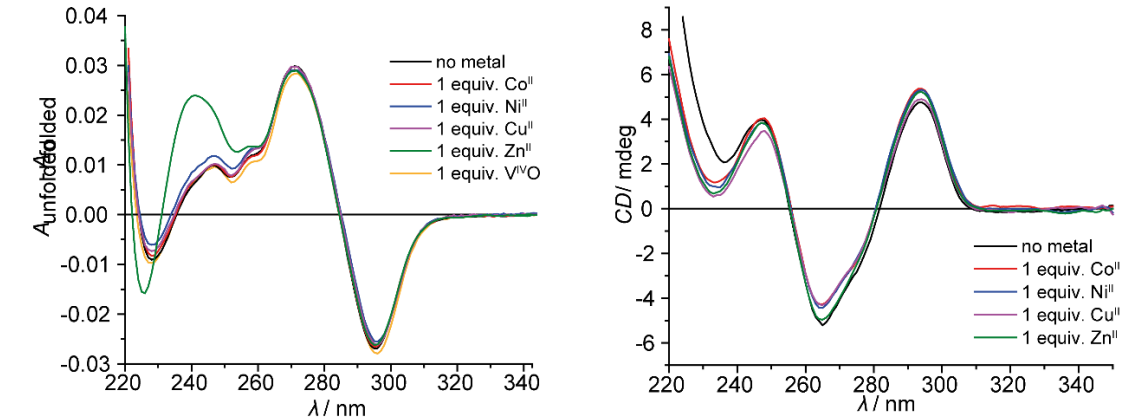

Figure 157. Analytic data of htel$\mathbf{L^B}_4$. Samples for thermal denaturation experiments, TDS and CD spectroscopy were prepared containing 1.875 µM ssDNA, 100 mM KCl, 10 mM LiCaco pH 7.2.

Name: Sequence (5'→3'):
htel$L^{B}_{3}L^{2S}$ AGG L^{2S}TT AL^{B}G GTT AGG L^{B}TT AL^{B}G G

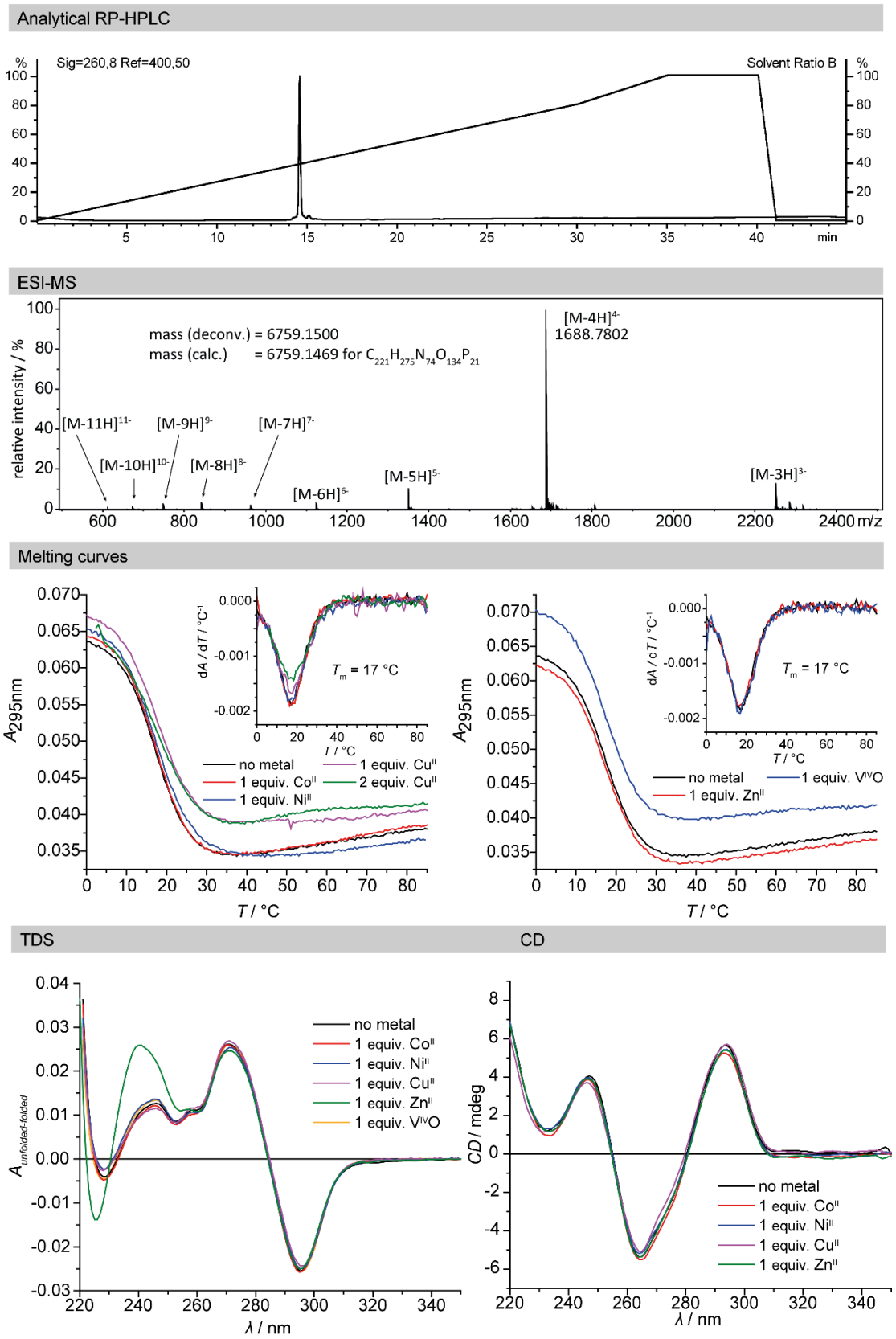

Figure 158. Analytic data of htel$L^{B}_{3}L^{2S}$. Samples for thermal denaturation experiments, TDS and CD spectroscopy were prepared containing 1.875 µM ssDNA, 100 mM KCl, 10 mM LiCaco pH 7.2.

Name: Sequence (5'→3'):
htel$L^{B}{}_{2}L^{2S}{}_{2}$ AGG L^{2S}TT AL^{B}G GTT AGG L^{2S}TT AL^{B}G G

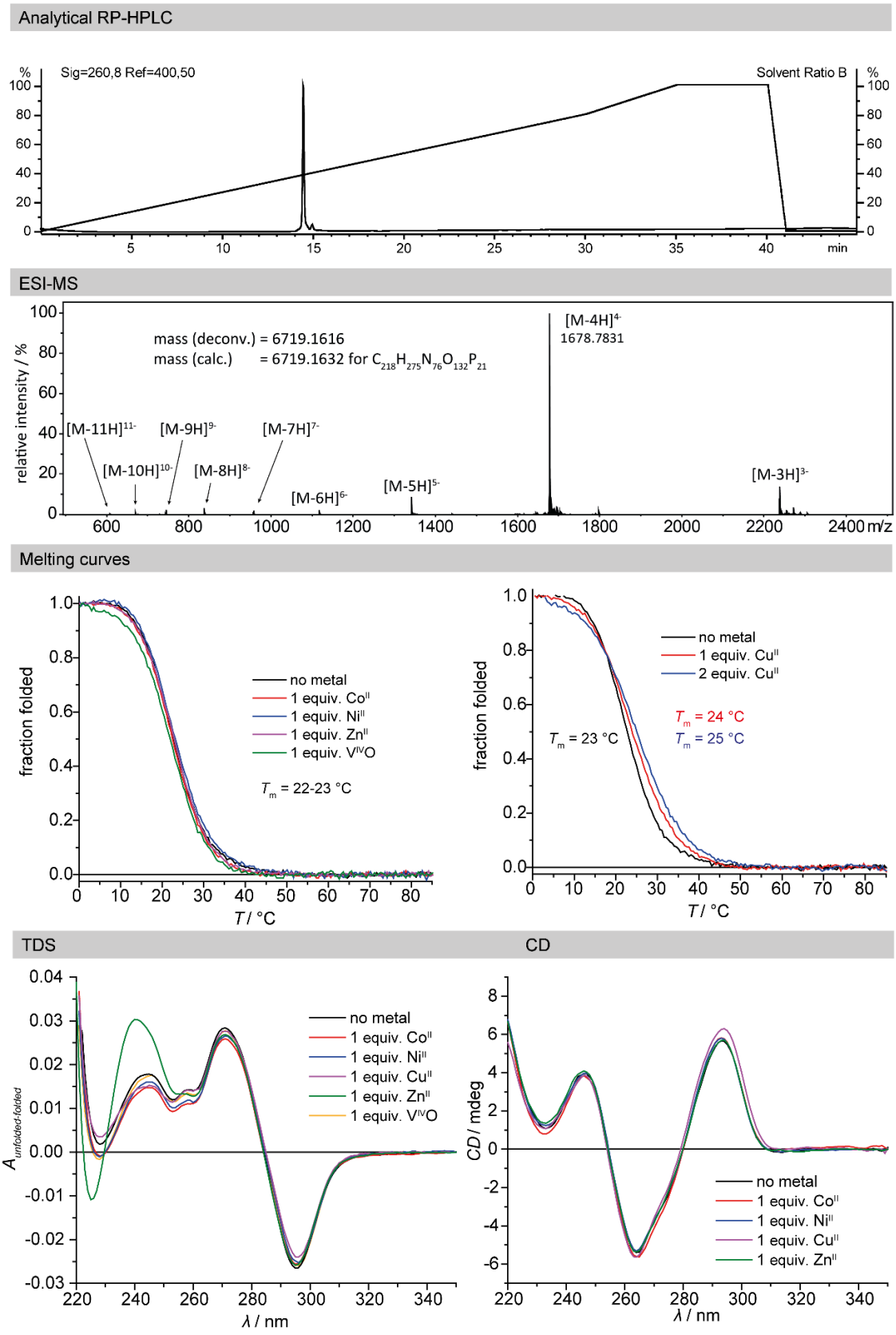

Figure 159. Analytic data of htel$L^{B}{}_{2}L^{2S}{}_{2}$. Samples for thermal denaturation experiments, TDS and CD spectroscopy were prepared containing 1.875 µM ssDNA, 100 mM KCl, 10 mM LiCaco pH 7.2.

Name: Sequence (5'→3'):
htel$L^{B}L^{2S}_{3}$ AGG L^{2S}TT AL^{2S}G GTT AGG L^{2S}TT AL^{B}G G

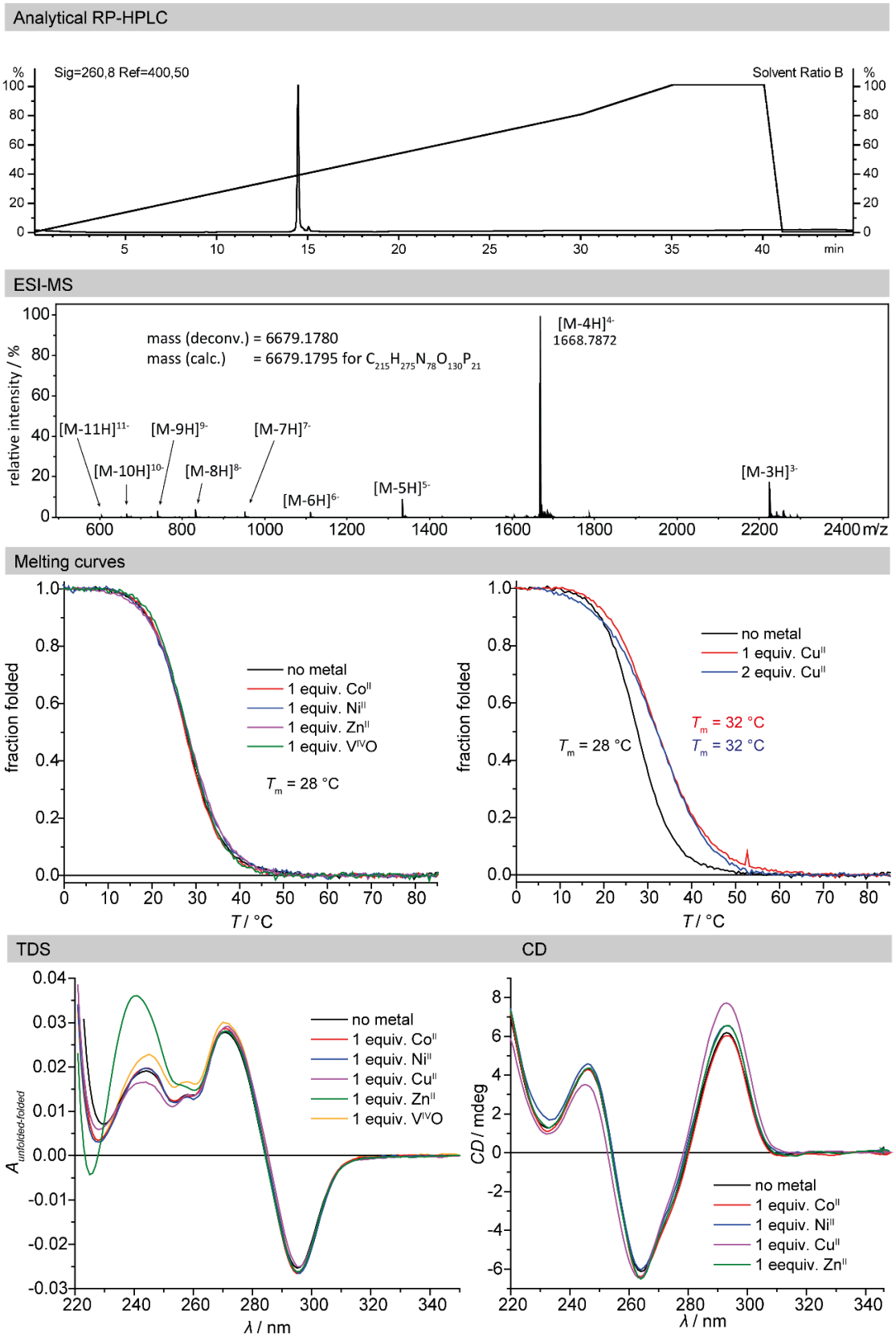

Figure 160. Analytic data of htel$L^{B}L^{2S}_{3}$. Samples for thermal denaturation experiments, TDS and CD spectroscopy were prepared containing 1.875 µM ssDNA, 100 mM KCl, 10 mM LiCaco pH 7.2.

Name: Sequence (5'→3'):
htel$L^{B}_{2}L^{2S}_{4}$ AGG $L^{2S}TL^{B}$ TL^{2S}G GTT AGG $L^{2S}TL^{B}$ TL^{2S}G G

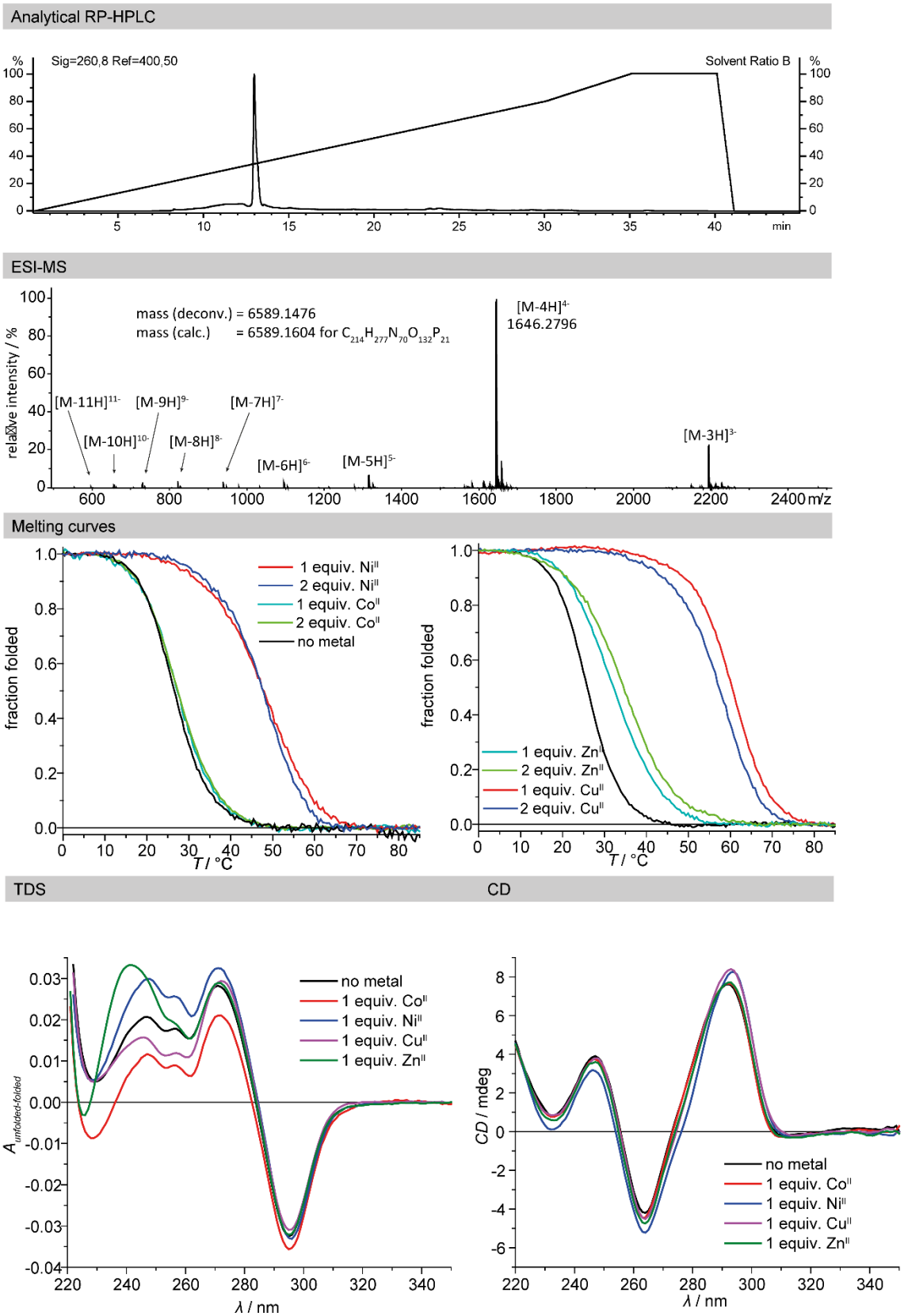

Figure 161. Analytic data of htel$L^{B}_{2}L^{2S}_{4}$. Samples for thermal denaturation experiments, TDS and CD spectroscopy were prepared containing 1.875 µM ssDNA, 100 mM KCl, 10 mM LiCaco pH 7.2.

Name: Sequence (5'→3'):
htel**L**$^{B}_{4}$**L**$^{2S}_{2}$ AGG **L**^{B}**TL**^{2S} **TL**^{B}G GTT AGG **L**^{B}**TL**^{2S} TL^{B}G G

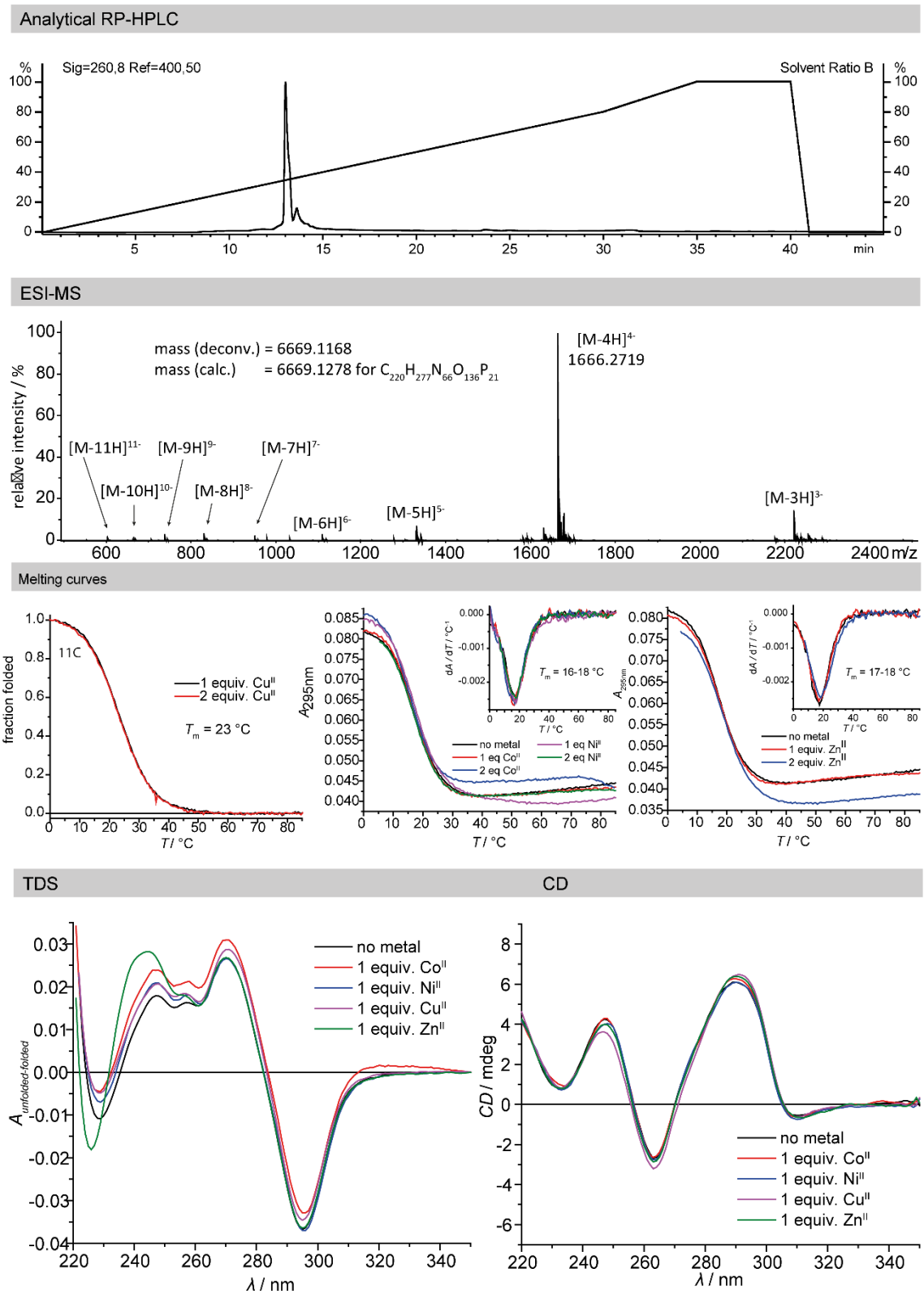

Figure 162. Analytic data of htel**L**$^{B}_{4}$**L**$^{2S}_{2}$. Samples for thermal denaturation experiments, TDS and CD spectroscopy were prepared containing 1.875 µM ssDNA, 100 mM KCl, 10 mM LiCaco pH 7.2.

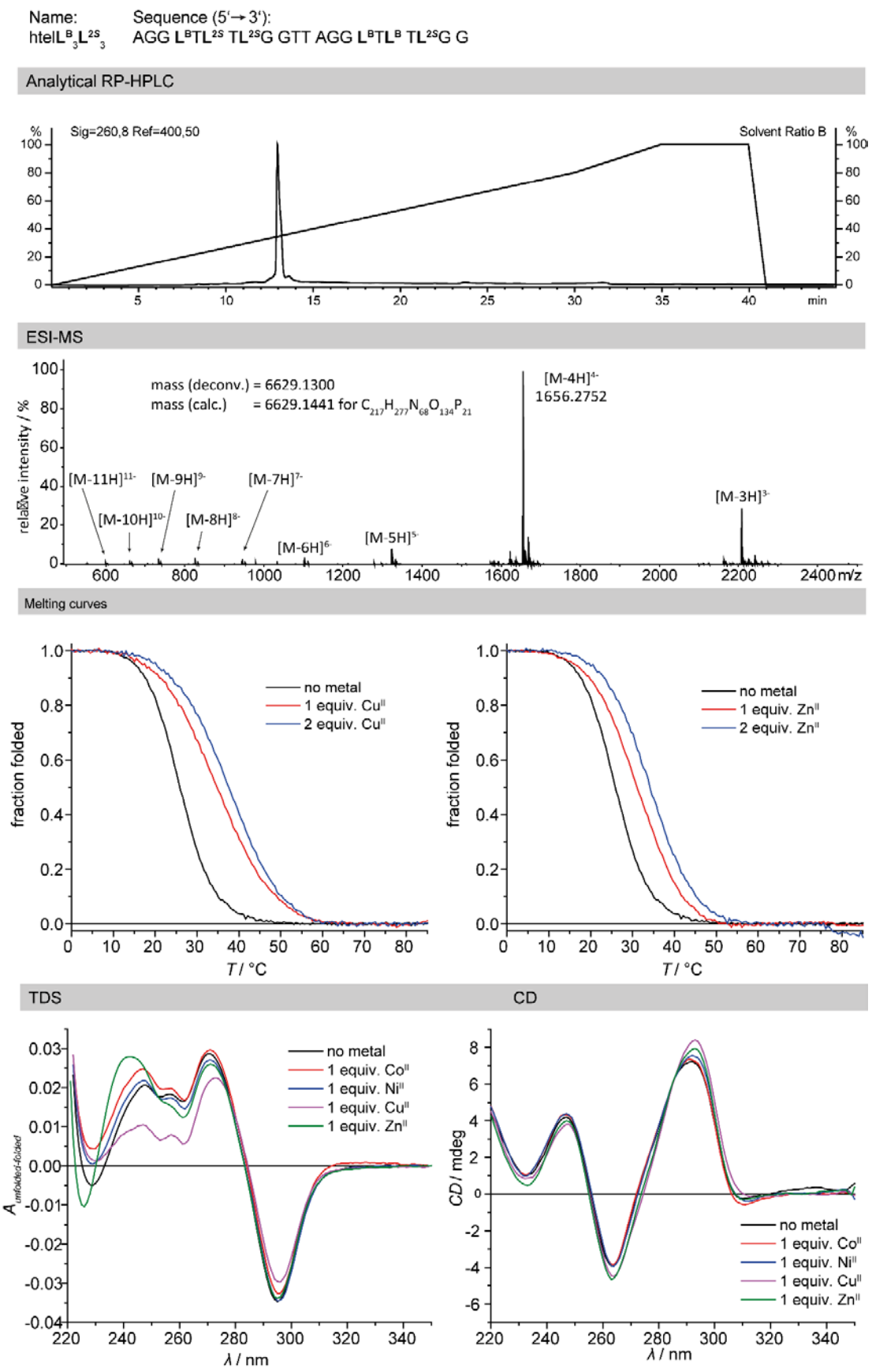

Figure 163 Analytic data of htel**L**$^{B}_{3}$**L**$^{2S}_{3}$. Samples for thermal denaturation experiments, TDS and CD spectroscopy were prepared containing 1.875 µM ssDNA, 100 mM KCl, 10 mM LiCaco pH 7.2.

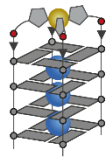

Name:
$L^{1R}G_3$

Sequence (5'→3'):
$L^{1R}GG\ G$

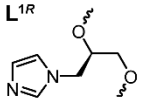

1 equiv.	-	Cu^{II}	Ni^{II}	Zn^{II}	Co^{II}
$T_{1/2}$	-	38	n. d.	n. d.	n. d.
$\Delta T_{1/2}$					

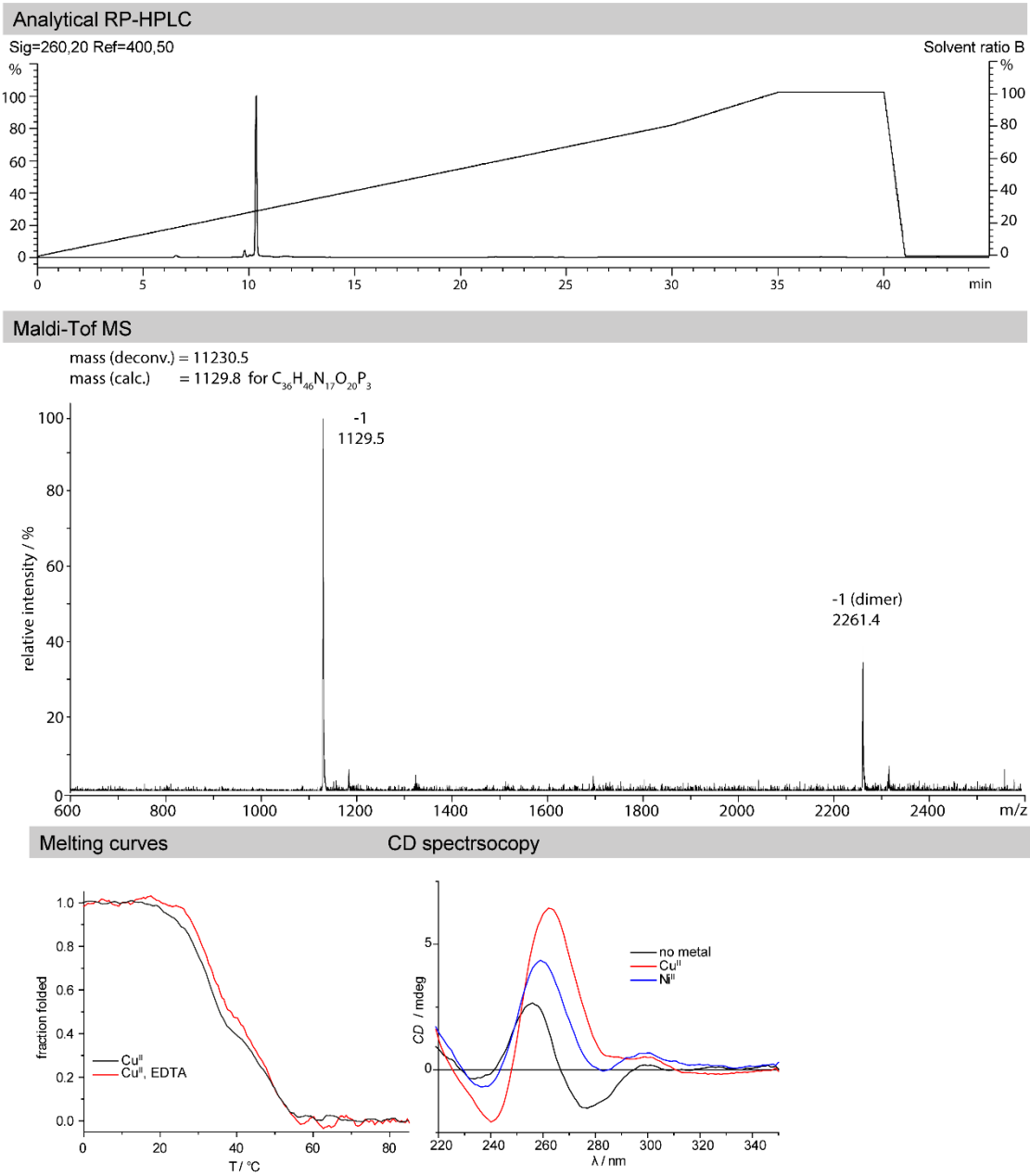

Figure 164. Analytic data of $L^{1R}G_3$. Samples for thermal denaturation experiments and CD spectroscopy were prepared containing 3.75 µM ssDNA, 0.98 µM transition metal salt, 100 mM NaCl, 10 mM LiCaco pH 7.2.

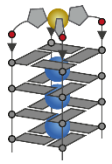

Name:
$L^{1S}G_3$

Sequence (5'→3'):
$L^{1S}GG\ G$

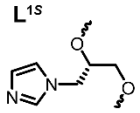

1 equiv.	-	Cu^{II}	Ni^{II}	Zn^{II}	Co^{II}
$T_{1/2}$	-	40	n. d.	n. d.	n. d.
$\Delta T_{1/2}$					

Analytical RP-HPLC

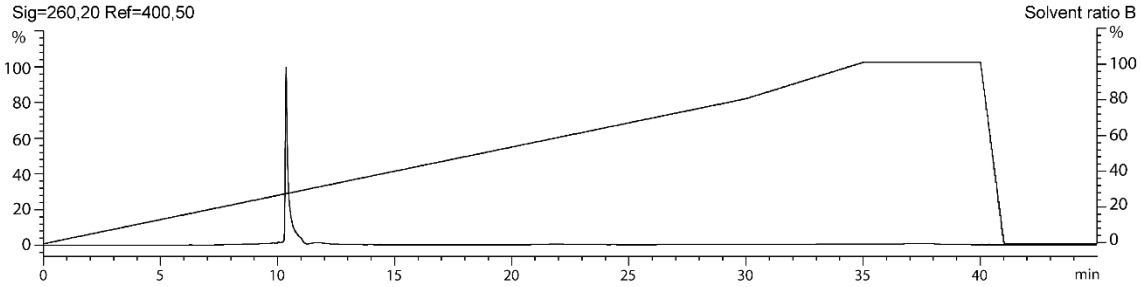

Maldi-Tof MS

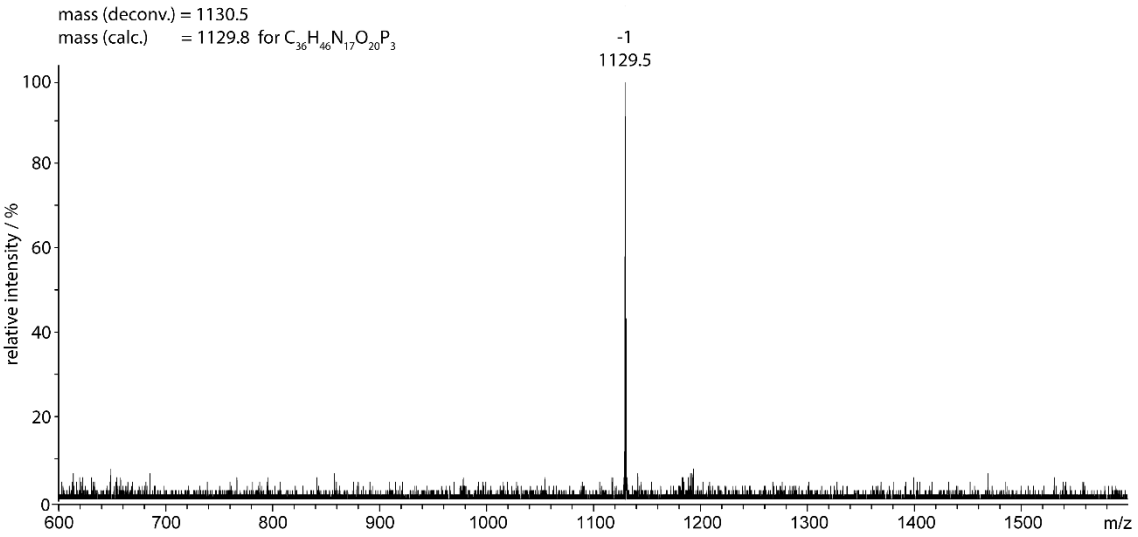

Melting curves

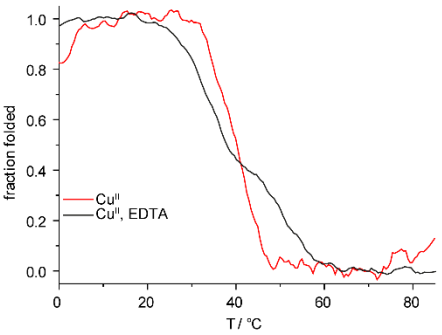

CD spectrsocopy

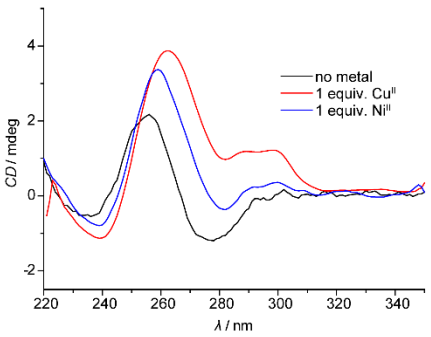

Figure 165. Analytic data of $L^{1S}G_3$. Samples for thermal denaturation experiments and CD spectroscopy were prepared containing 3.75 µM ssDNA, 0.98 µM transition metal salt, 100 mM NaCl, 10 mM LiCaco pH 7.2.

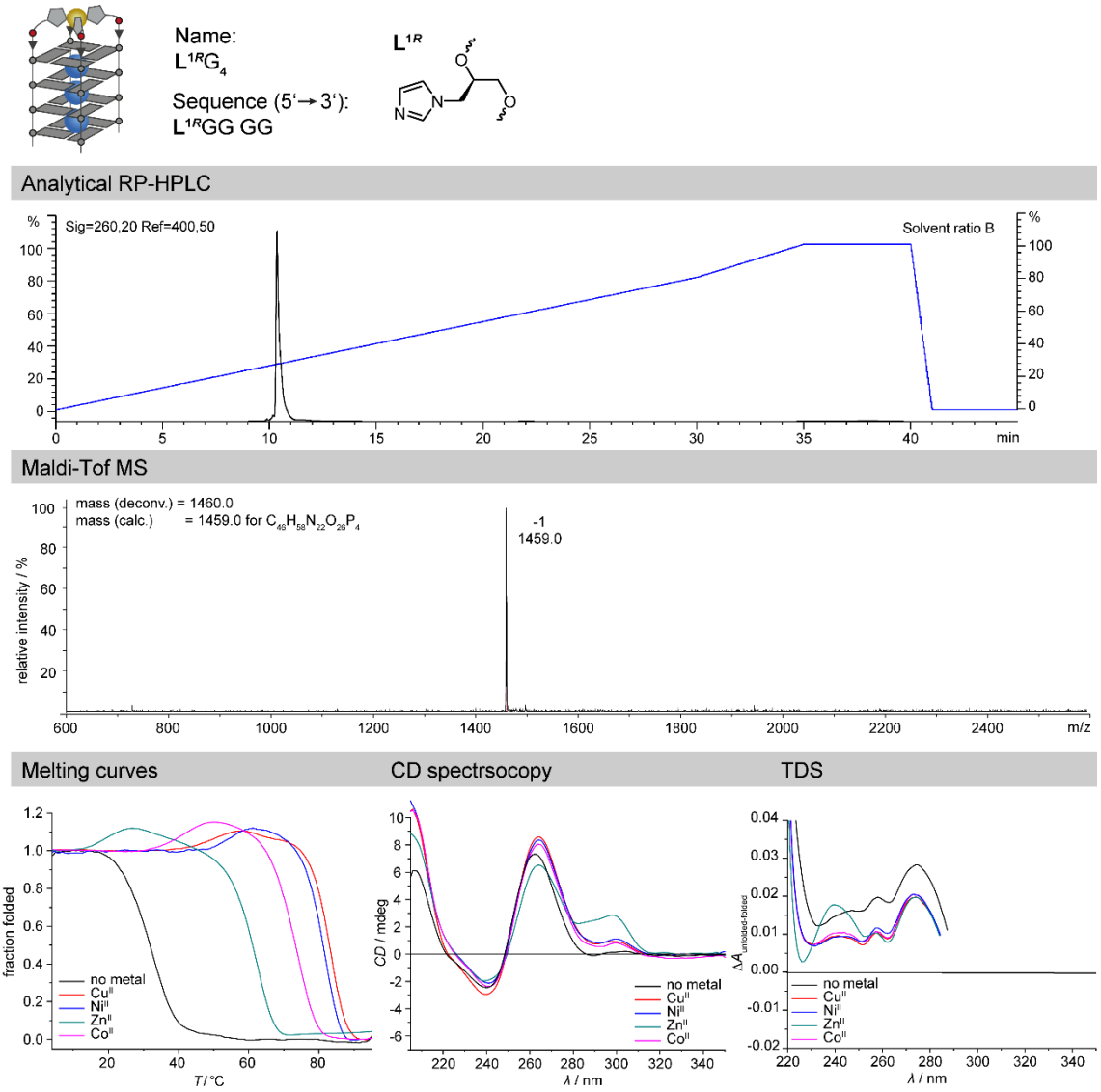

Figure 166. Analytic data of **L^{1R}G$_4$**. Samples for thermal denaturation experiments, TDS and CD spectroscopy were prepared containing 3.75 µM ssDNA, 0.98 µM transition metal salt, 100 mM NaCl, 10 mM LiCaco pH 7.2.

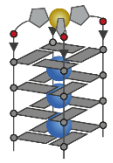

Name:
$L^{1S}G_4$

Sequence (5'→3'):
L^{1S}GG GG

L^{1S}

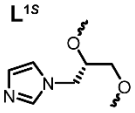

1 equiv.	-	Cu^{II}	Ni^{II}	Zn^{II}	Co^{II}
$T_{1/2}$	31	79	77	54	64
$\Delta T_{1/2}$	-	+ 48	+ 46	+ 23	+ 33

Analytical RP-HPLC

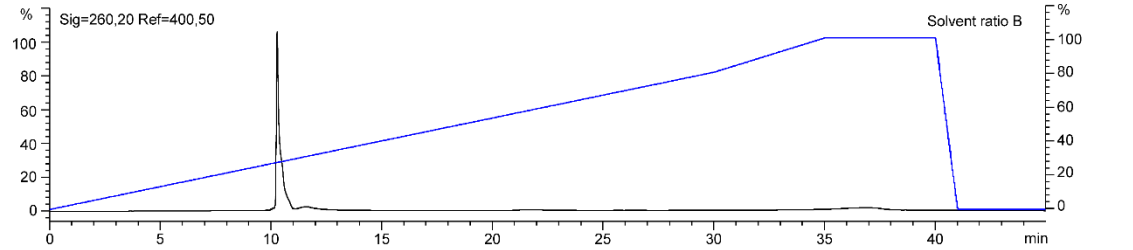

Maldi-Tof MS

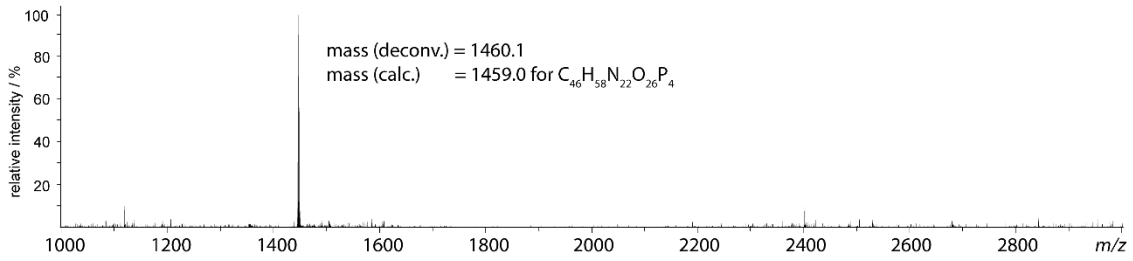

Melting curves | CD spectrsocopy | TDS

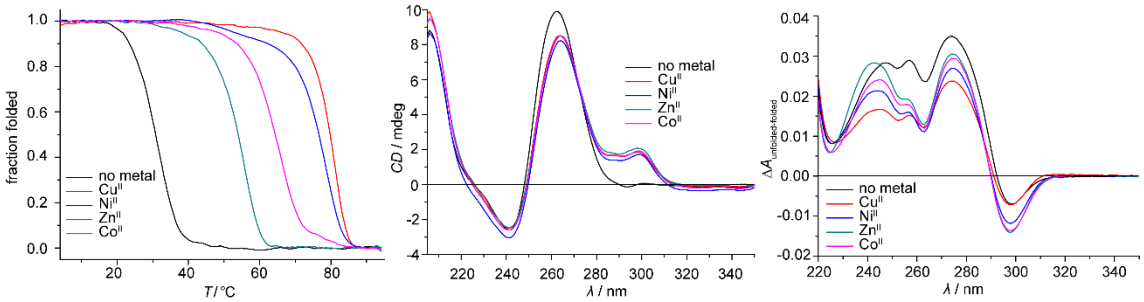

Figure 167. Analytic data of $L^{1S}G_4$. Samples for thermal denaturation experiments, TDS and CD spectroscopy were prepared containing 3.75 µM ssDNA, 0.98 µM transition metal salt, 100 mM NaCl, 10 mM LiCaco pH 7.2.

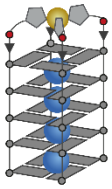

Name:
$L^{1R}G_5$

Sequence (5'→3'):
L^{1R}GG GGG

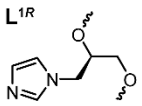

1 equiv.	-	Cu^{II}	Ni^{II}	Zn^{II}	Co^{II}
$T_{1/2}$	77	> 95	> 95	86	> 95
$\Delta T_{1/2}$				+9	

Analytical RP-HPLC

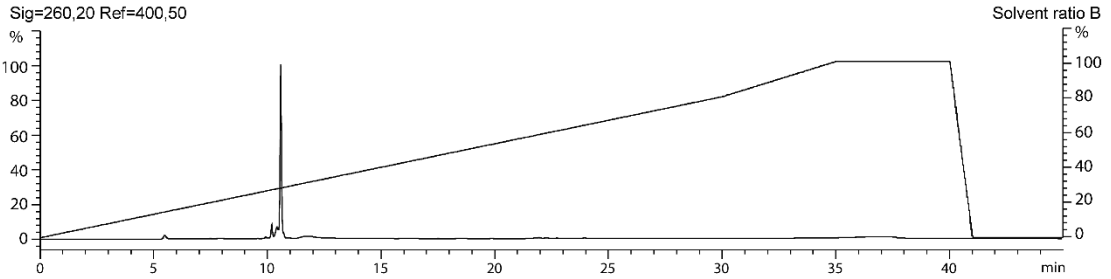

Maldi-Tof MS

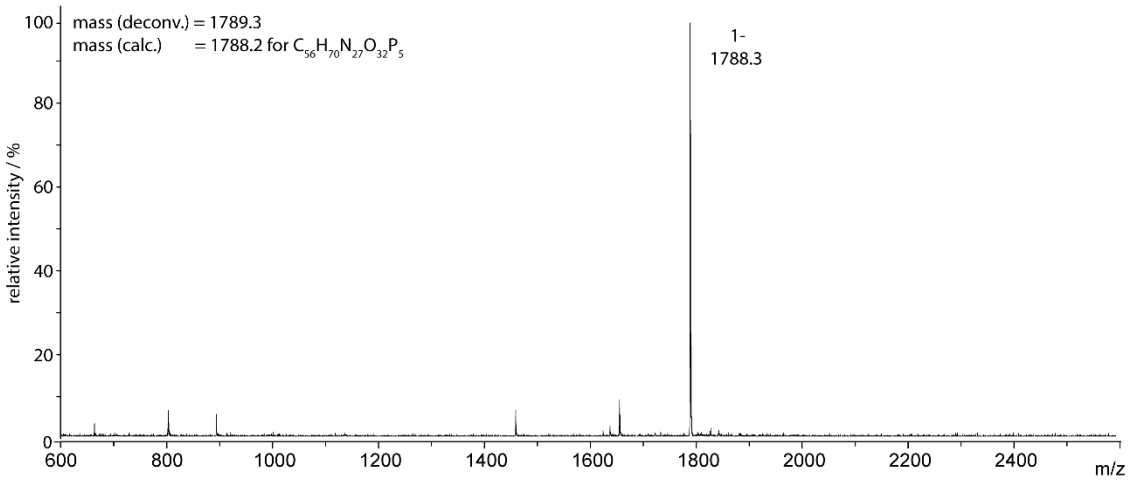

Melting curves | CD spectrsocopy | TDS

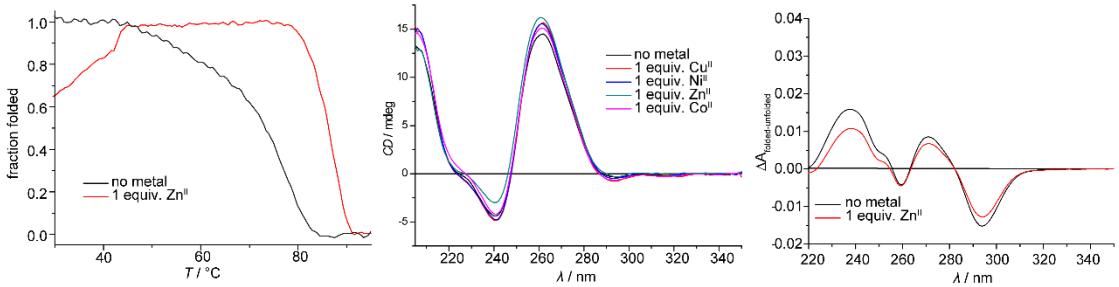

Figure 168. Analytic data of $L^{1R}G_5$. Samples for thermal denaturation experiments, TDS and CD spectroscopy were prepared containing 3.75 µM ssDNA, 0.98 µM transition metal salt, 100 mM NaCl, 10 mM LiCaco pH 7.2.

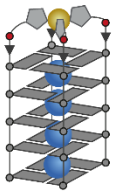

Name:
$L^{1S}G_5$

Sequence (5'→3'):
L^{1S}GG GGG

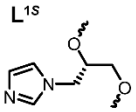

1 equiv.	-	Cu^{II}	Ni^{II}	Zn^{II}	Co^{II}
$T_{1/2}$	78	> 95	> 95	87	> 95
$\Delta T_{1/2}$				+9	

Analytical RP-HPLC

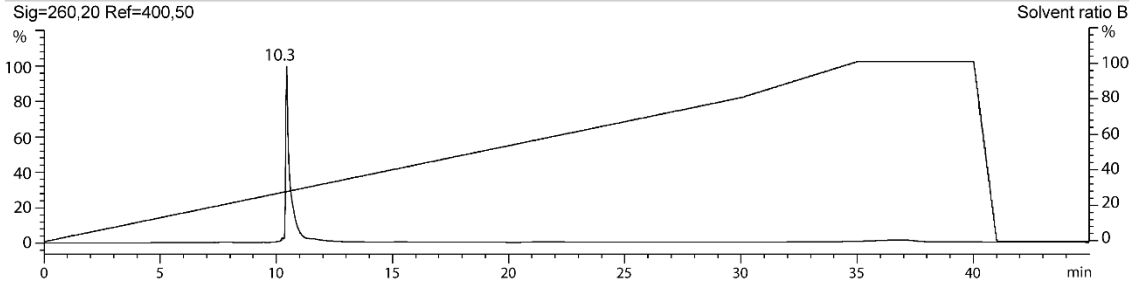

Maldi-Tof MS

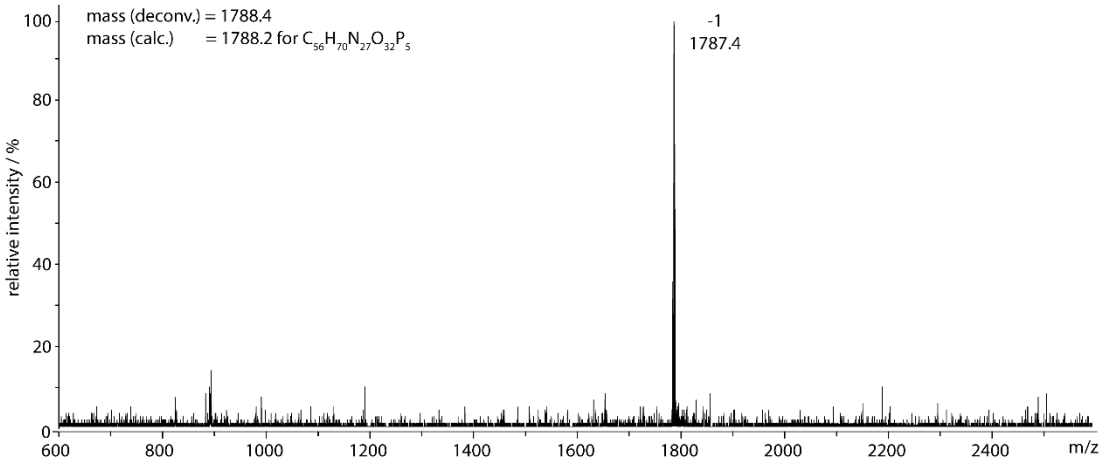

Melting curves | CD spectrsocopy | TDS

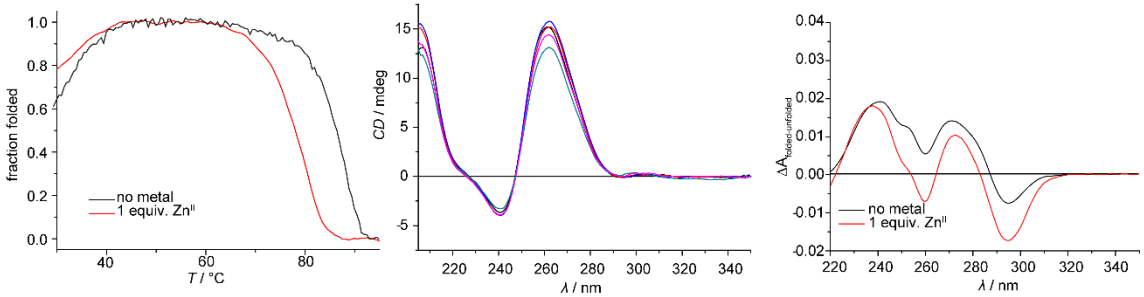

Figure 169. Analytic data of $L^{1S}G_5$. Samples for thermal denaturation experiments, TDS and CD spectroscopy were prepared containing 3.75 µM ssDNA, 0.98 µM transition metal salt, 100 mM NaCl, 10 mM LiCaco pH 7.2.

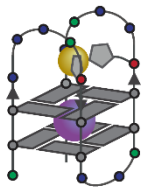

Name
htel$\mathbf{L^{2R}}_2$

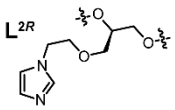

Sequence (5'→3')
AGG TTT A$\mathbf{L^{2R}}$G GTT AGG $\mathbf{L^{2R}}$TT ATG G

1 equiv.	-	Cu^{II}	Ni^{II}	Zn^{II}	Co^{II}
$T_{1/2}$	29	29	29	29	28
$\Delta T_{1/2}$		+0	+0	+0	-1

Analytical RP-HPLC

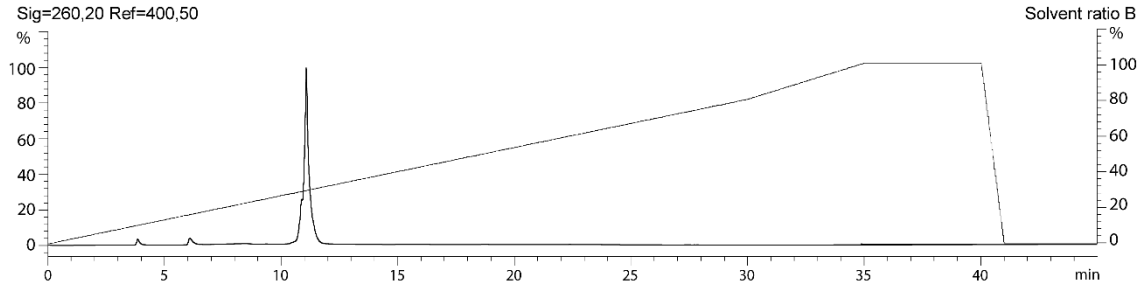

Maldi-Tof MS

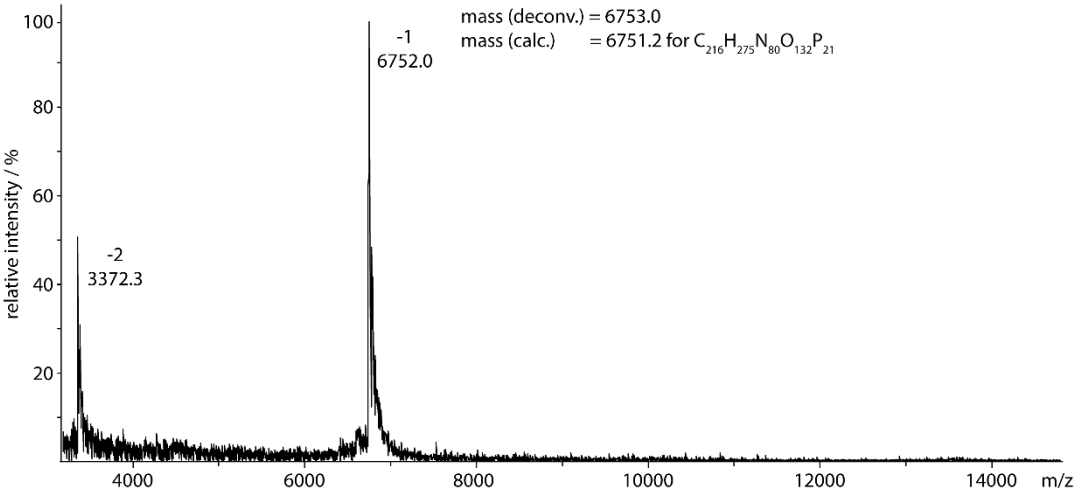

Melting curves | CD spectrsocopy | TDS

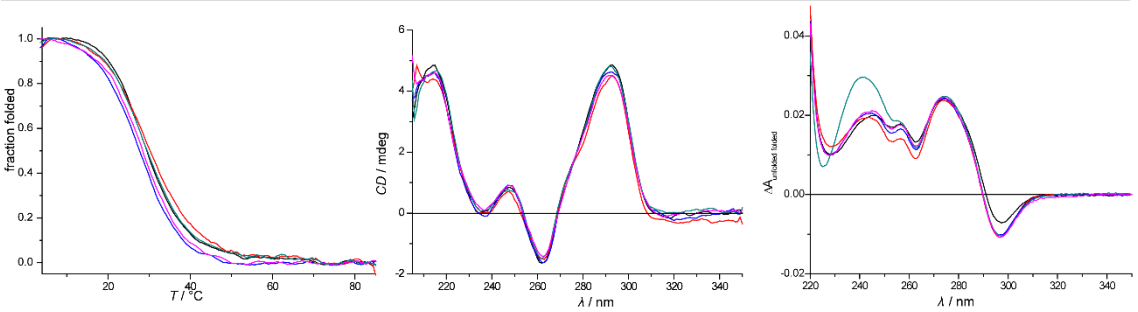

Figure 170. Analytic data of htel$\mathbf{L^{2R}}_2$. Samples for thermal denaturation experiments, TDS and CD spectroscopy were prepared containing 1.875 µM ssDNA, 1.875 µM transition metal salt, 100 mM KCl, 10 mM LiCaco pH 7.2.

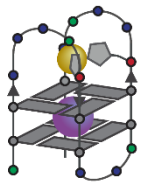

Name
htel**L**$^{2S}_{2}$

Sequence (5'→3')
AGG TTT A**L**^{2S}G GTT AGG **L**^{2S}TT ATG G

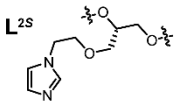

1 equiv.	-	Cu^{II}	Ni^{II}	Zn^{II}	Co^{II}
$T_{1/2}$	27	28	27	27	26
$\Delta T_{1/2}$		+1	+0	+0	-1

Analytical RP-HPLC

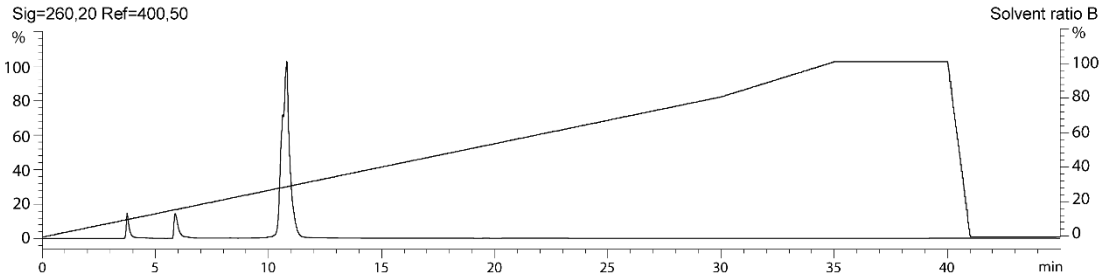

Maldi-Tof MS

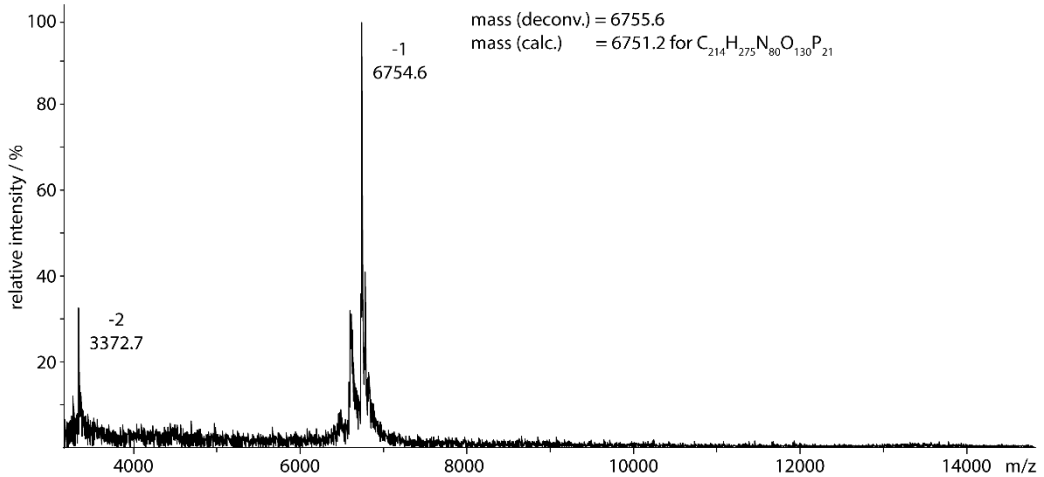

Melting curves | CD spectrsocopy | TDS

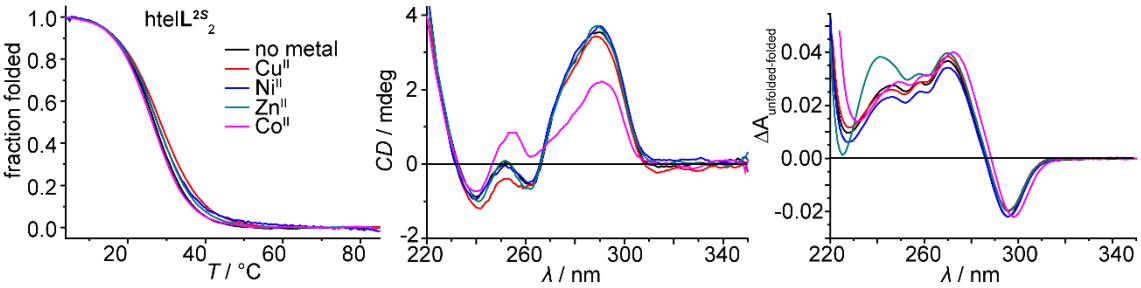

Figure 171. Analytic data of htel**L**$^{2S}_{2}$. Samples for thermal denaturation experiments, TDS and CD spectroscopy were prepared containing 1.875 µM ssDNA, 1.875 µM transition metal salt, 100 mM KCl, 10 mM LiCaco pH 7.2.

Name: Sequence (5'→3'):
htel**L**$^{2S}_{2}$B AGG GTL^{2S} TGG GTT AGG GTL^{2S} TGG G

Analytical RP-HPLC

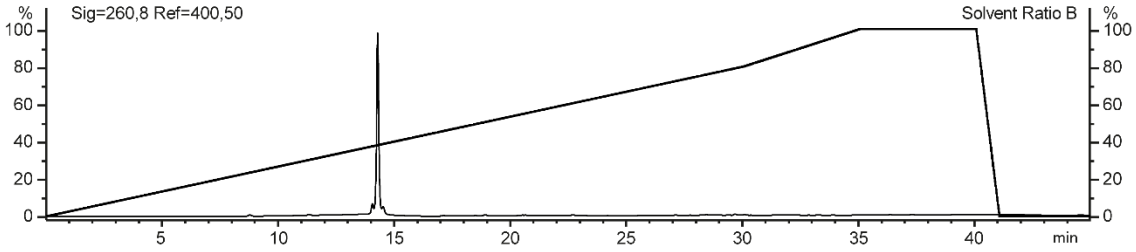

ESI-MS

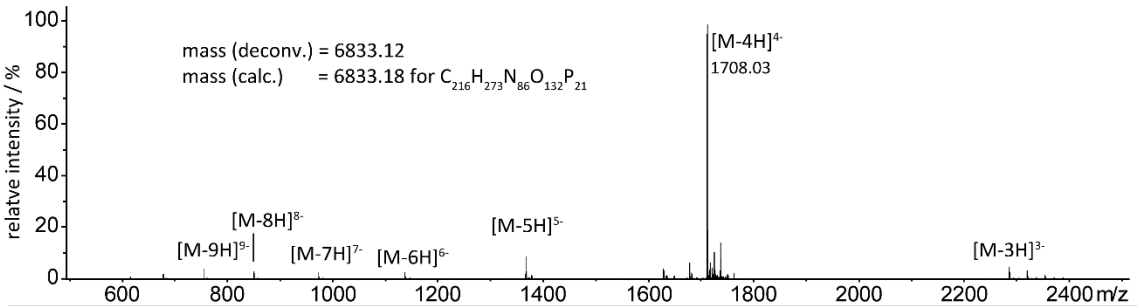

TDS

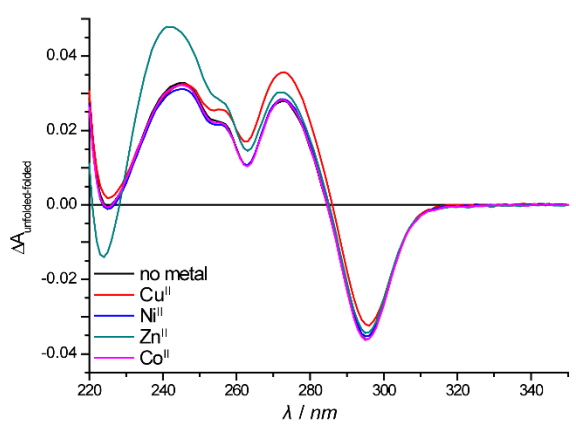

Melting Curves

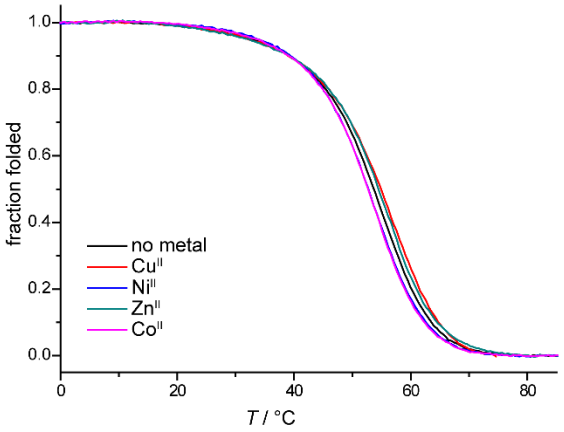

CD

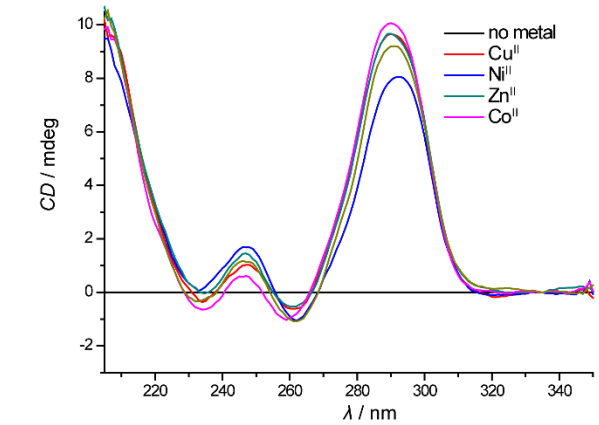

Figure 172. Analytic data of htel**L**$^{2S}_{2}$B. Samples for thermal denaturation experiments, TDS and CD spectroscopy were prepared containing 1.875 µM ssDNA, 1.875 µM transition metal salt, 100 mM NaCl, 10 mM LiCaco pH 7.2.

Name: Sequence (5'→3'):
htelL$^{2R}_{2}$B AGG GTL^{2R} TGG GTT AGG GTL^{2R} TGG G

Analytical RP-HPLC

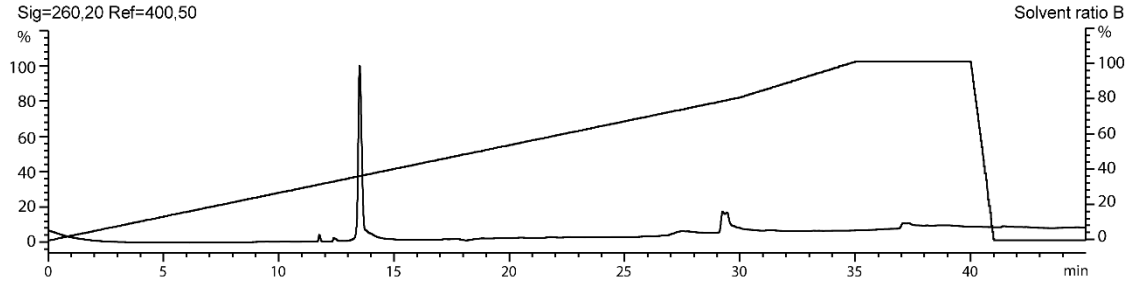

ESI-MS

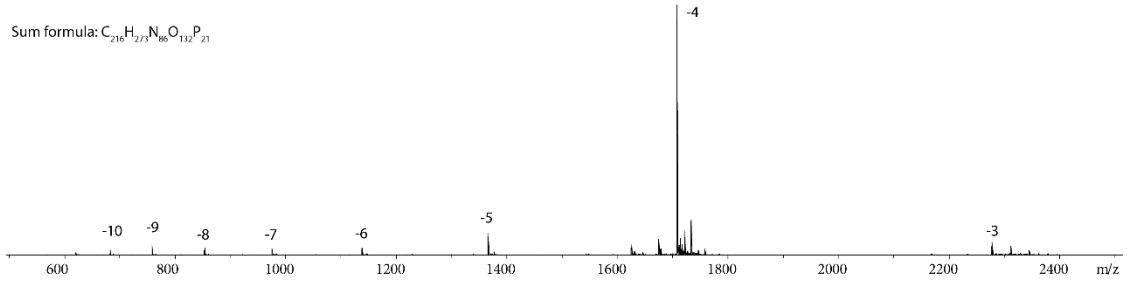

TDS

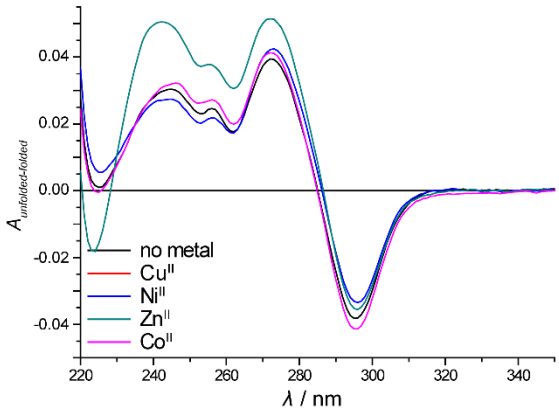

Melting Curves

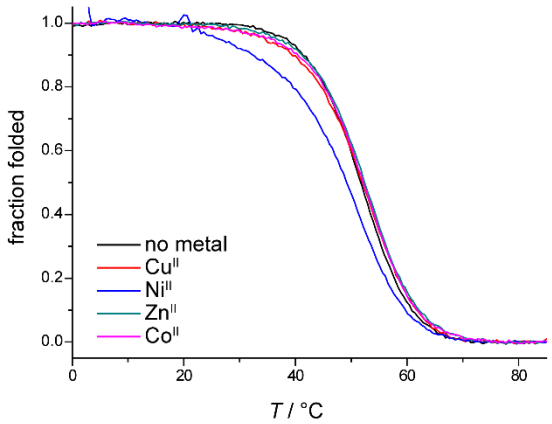

CD

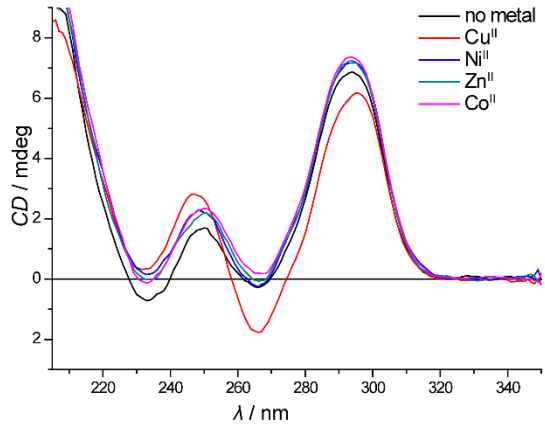

Figure 173. Analytic data of htel**L**$^{2R}_{2}$B. Samples for thermal denaturation experiments, TDS and CD spectroscopy were prepared containing 1.875 µM ssDNA, 1.875 µM transition metal salt, 100 mM NaCl, 10 mM LiCaco pH 7.2.

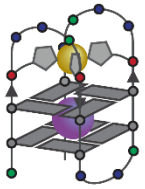

Name
htel**L**$^{2R}_3$

Sequence (5'→3')
AGG **L**^{2R}TT A**L**^{2R}G GTT AGG **L**^{2R}TT ATG G

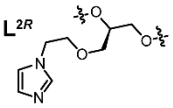

1 equiv.	-	Cu^{II}	Ni^{II}	Zn^{II}	Co^{II}
$T_{1/2}$	29	31	28	29	30
$\Delta T_{1/2}$		+2	-1	+0	+1

Analytical RP-HPLC

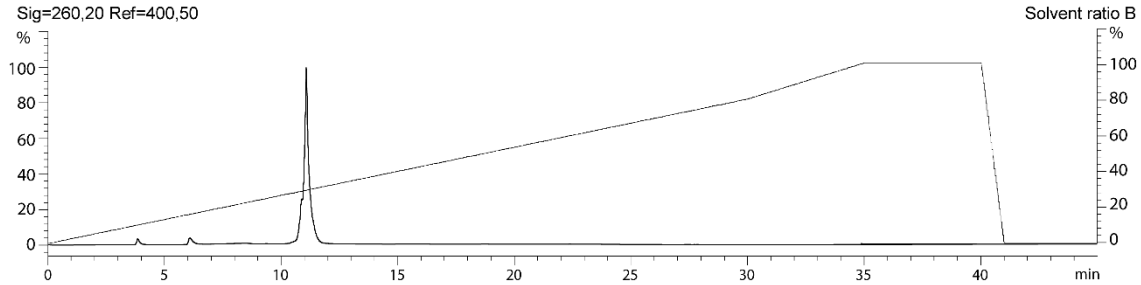

Maldi-Tof MS

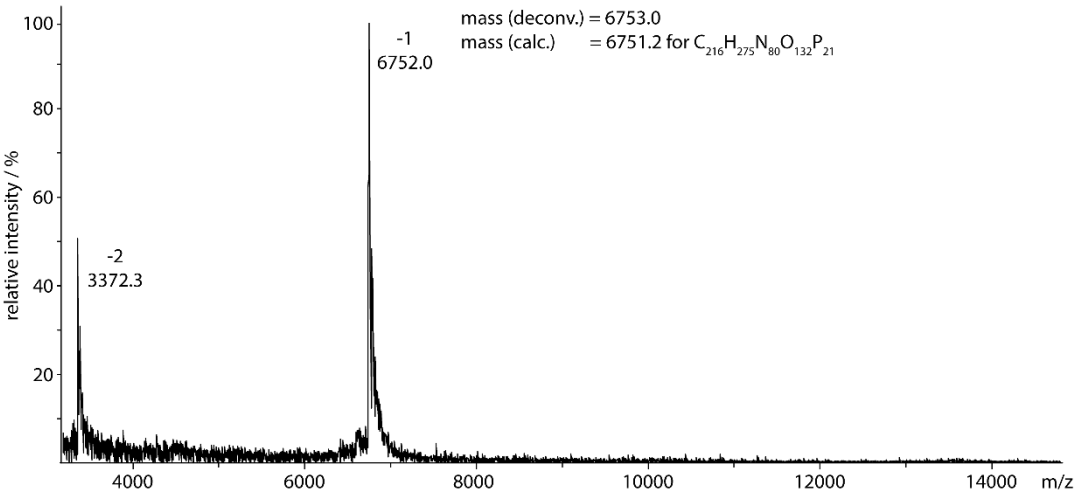

Melting curves | CD spectrsocopy | TDS

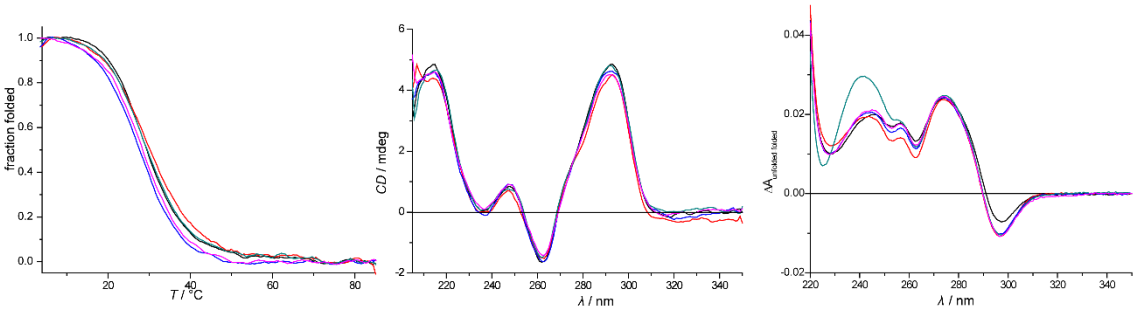

Figure 174. Analytic data of htel**L**$^{2R}_3$. Samples for thermal denaturation experiments, TDS and CD spectroscopy were prepared containing 1.875 µM ssDNA, 1.875 µM transition metal salt, 100 mM KCl, 10 mM LiCaco pH 7.2.

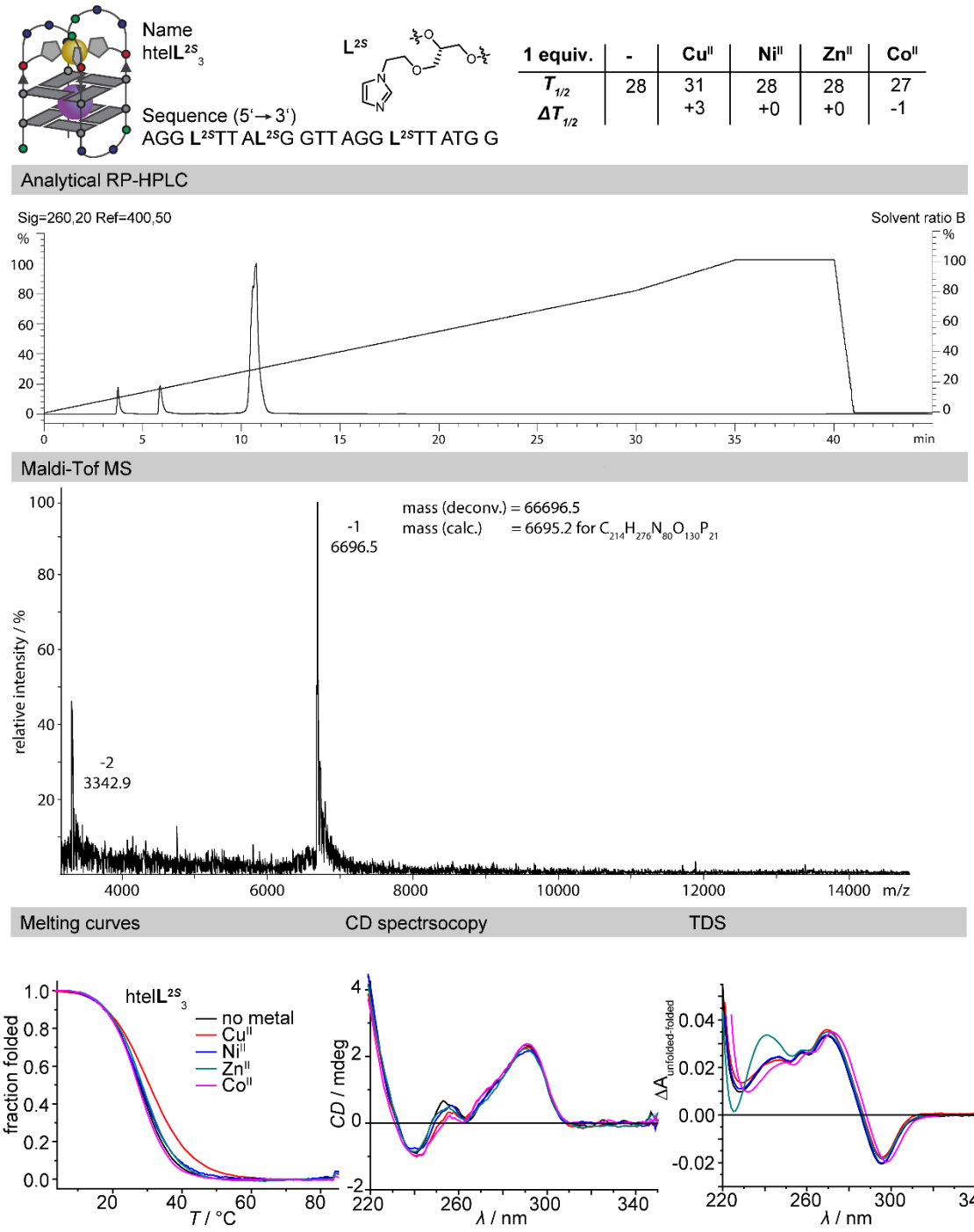

Figure 175. Analytic data of htel**L**$^{2S}_3$. Samples for thermal denaturation experiments, TDS and CD spectroscopy were prepared containing 1.875 µM ssDNA, 1.875 µM transition metal salt, 100 mM KCl, 10 mM LiCaco pH 7.2.

Name: Sequence (5'→3'):
htel**L**$^{2R}_{3}$B AGG GT**L**^{2R} TGG GTT AGG G**L**^{2R}T **L**^{2R}GG G

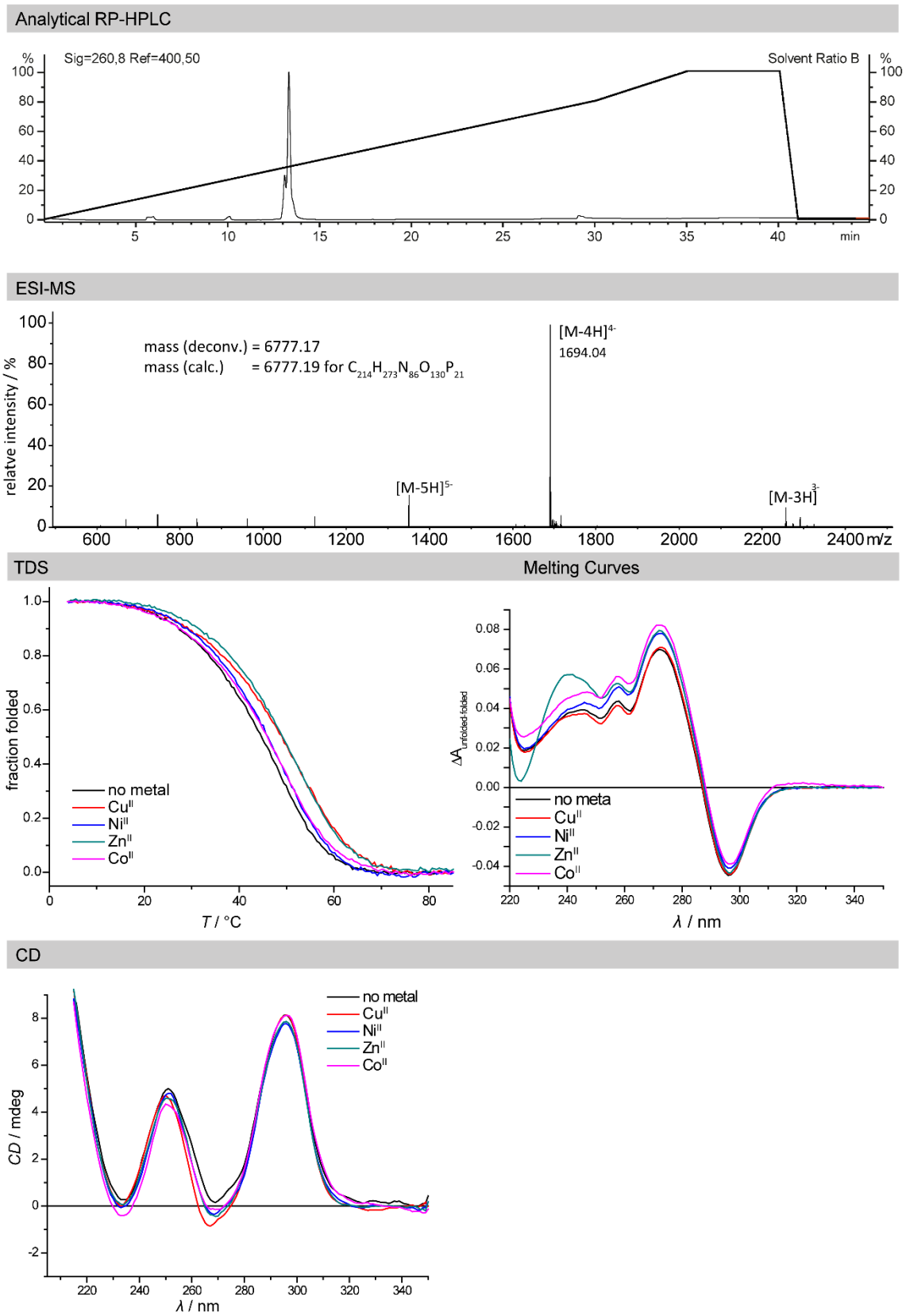

Figure 176. Analytic data of htel**L**$^{2R}_{3}$B. Samples for thermal denaturation experiments, TDS and CD spectroscopy were prepared containing 1.875 µM ssDNA, 1.875 µM transition metal salt, 100 mM NaCl, 10 mM LiCaco pH 7.2.

Name: Sequence (5'→3'):
htel**L**$^{2S}_{3}$B AGG GT**L**^{2S} TGG GTT AGG G**L**^{2S}T **L**^{2S}GG G

Analytical RP-HPLC

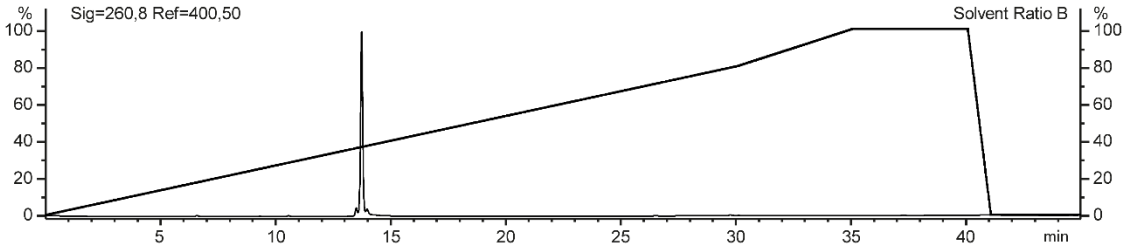

ESI-MS

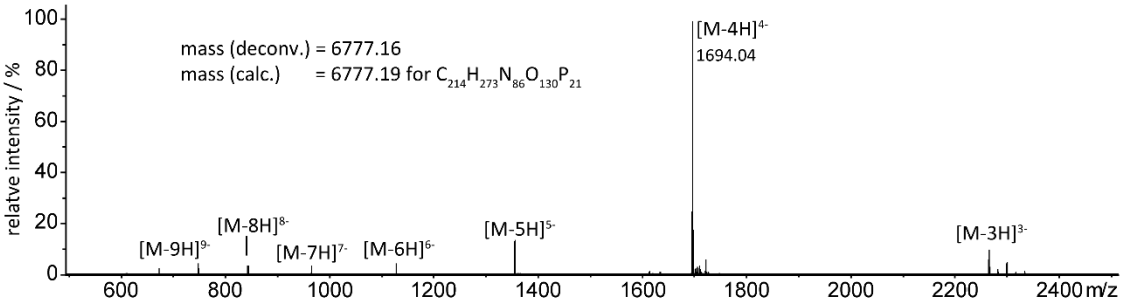

TDS

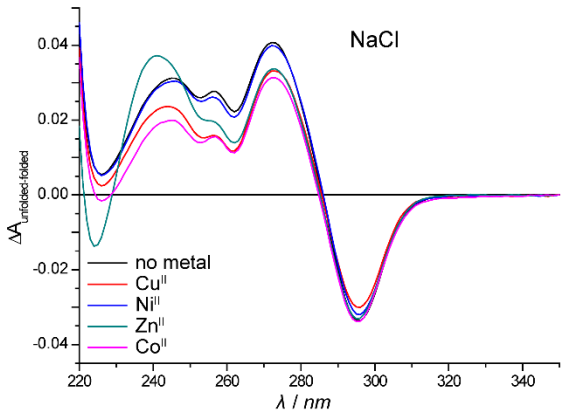

Melting Curves

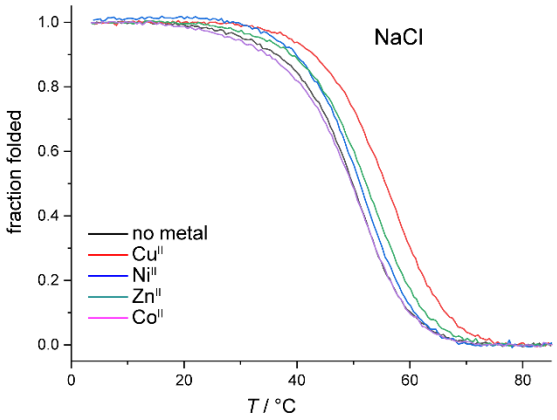

CD

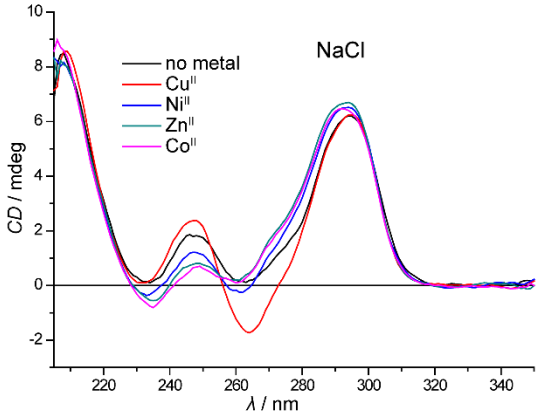

Figure 177. Analytic data of htel**L**$^{2S}_{3}$B. Samples for thermal denaturation experiments, TDS and CD spectroscopy were prepared containing 1.875 µM ssDNA, 1.875 µM transition metal salt, 100 mM NaCl, 10 mM LiCaco pH 7.2.

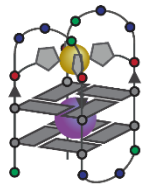

Name:
htel**L**$^{1R}_{4}$

Sequence (5'→3'):
AGG **L**^{1R}TT AL^{1R}G GTT AGG **L**^{1R}TT AL^{1R}G G

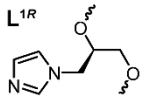

1 equiv.	-	Cu^{II}	Ni^{II}	Zn^{II}	Co^{II}
$T_{1/2}$	29	29	28	29	29
$\Delta T_{1/2}$		+0	-1	+0	+0

Analytical RP-HPLC

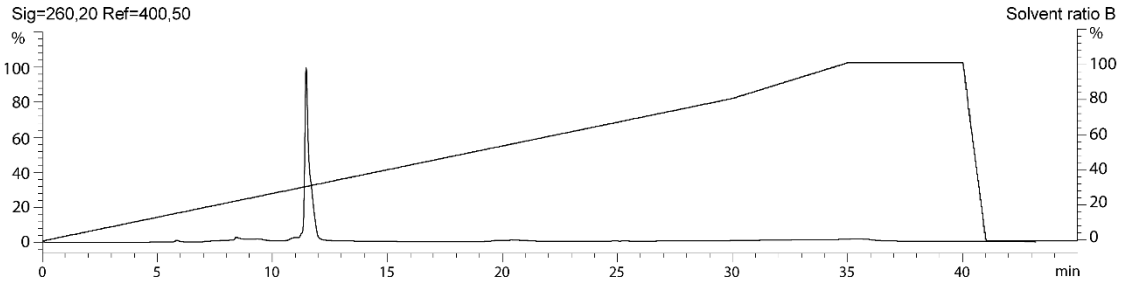

Maldi-Tof MS

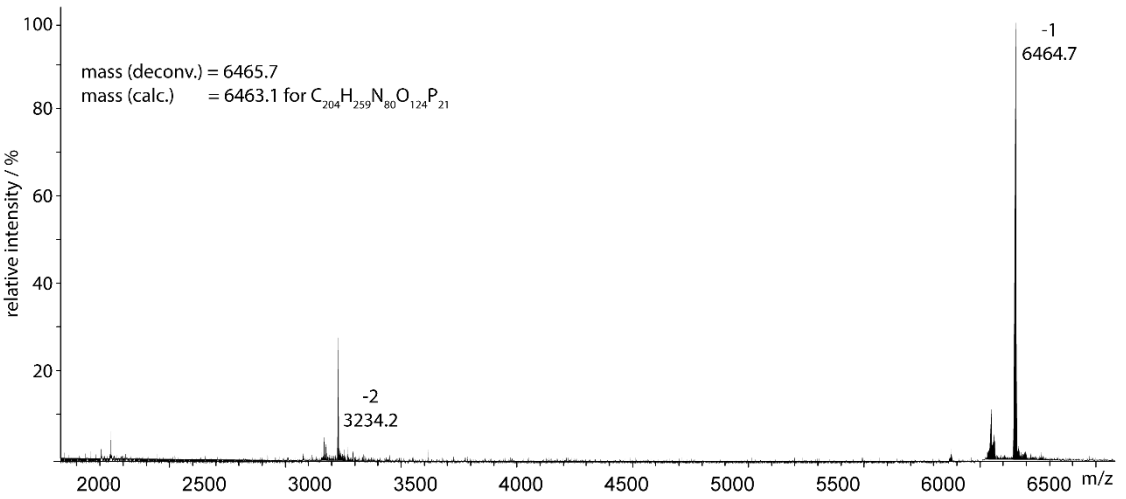

Melting curves | CD spectrsocopy | TDS

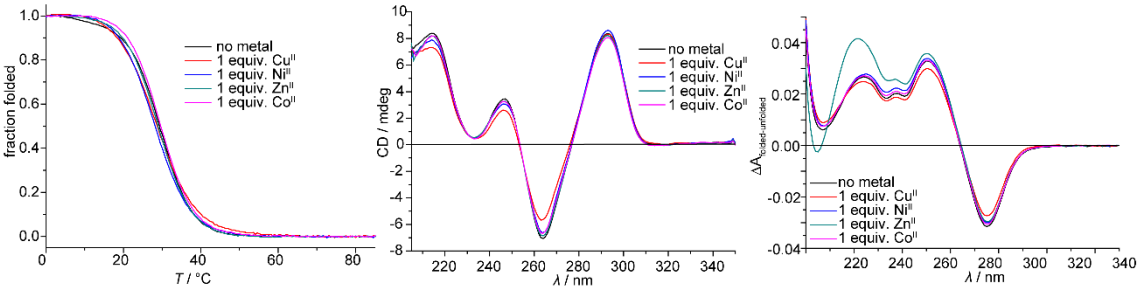

Figure 178. Analytic data of htel**L**$^{1R}_{4}$. Samples for thermal denaturation experiments, TDS and CD spectroscopy were prepared containing 1.875 µM ssDNA, 1.875 µM transition metal salt, 100 mM KCl, 10 mM LiCaco pH 7.2.

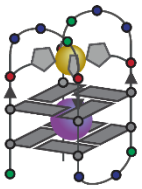

Name:
htel**L**$^{1S}_{4}$

Sequence (5'→3'):
AGG **L**^{1S}TT AL^{1S}G GTT AGG **L**^{1S}TT AL^{1S}G G

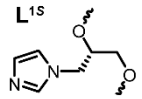

1 equiv.	-	Cu^{II}	Ni^{II}	Zn^{II}	Co^{II}
$T_{1/2}$	37	36	36	36	37
$\Delta T_{1/2}$		-1	-1	-1	+0

Analytical RP-HPLC

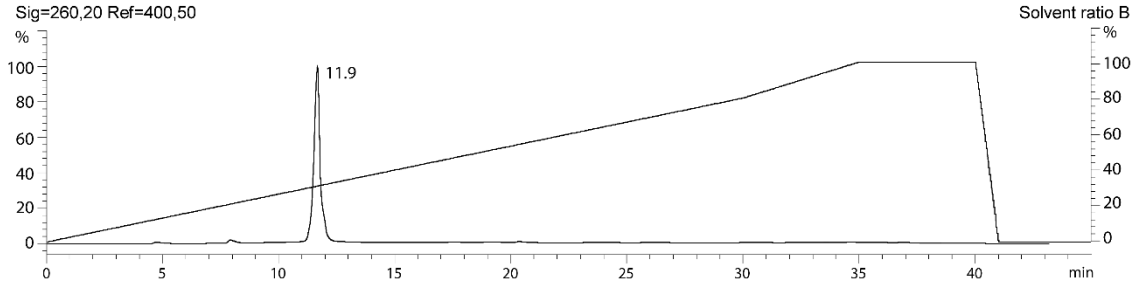

Maldi-Tof MS

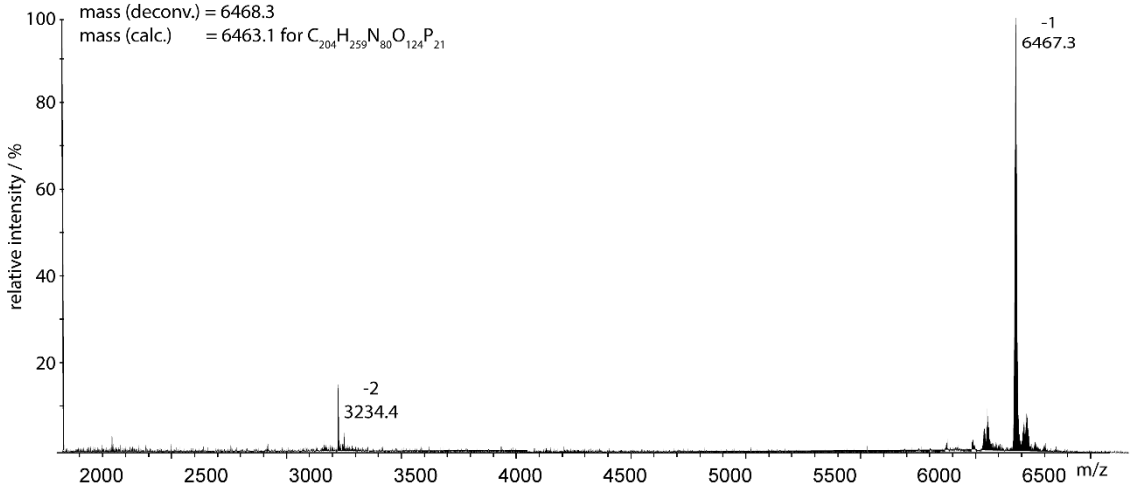

Melting curves | CD spectrsocopy | TDS

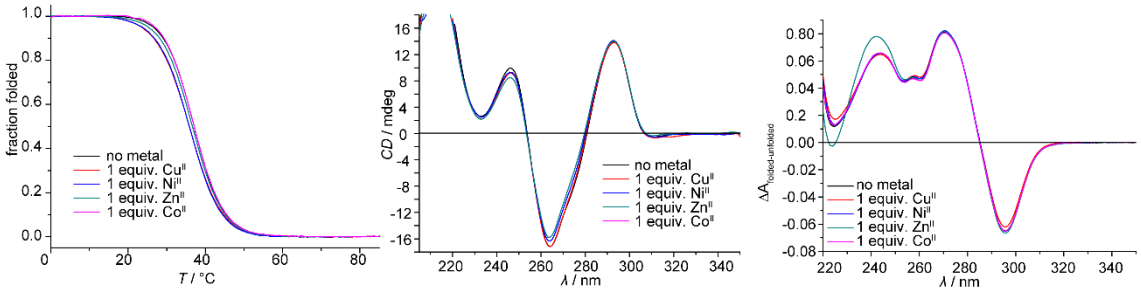

Figure 179. Analytic data of htel**L**$^{1S}_{4}$. Samples for thermal denaturation experiments, TDS and CD spectroscopy were prepared containing 1.875 µM ssDNA, 1.875 µM transition metal salt, 100 mM KCl, 10 mM LiCaco pH 7.2.

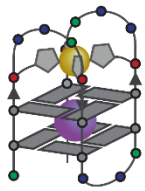

Name
htelL^{2R}_4

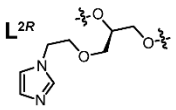

Sequence (5'→3')
AGG L^{2R}TT AL^{2R}G GTT AGG L^{2R}TT AL^{2R}G G

1 equiv.	-	Cu^{II}	Ni^{II}	Zn^{II}	Co^{II}
$T_{1/2}$	34	56	45	36	36
$\Delta T_{1/2}$		+22	+11	+2	+2

Analytical RP-HPLC

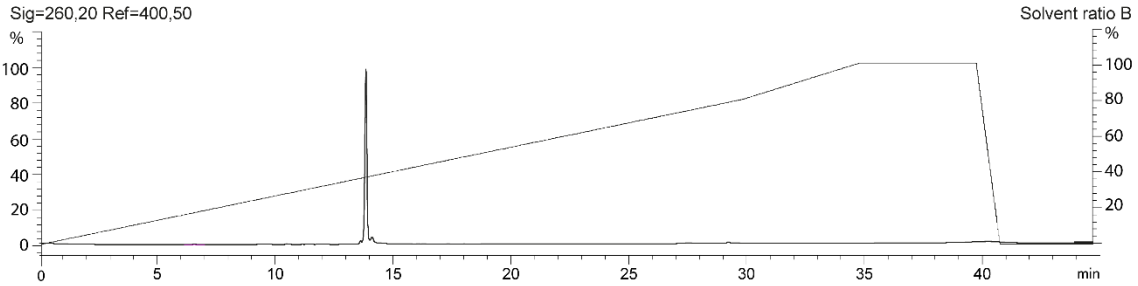

Maldi-Tof MS

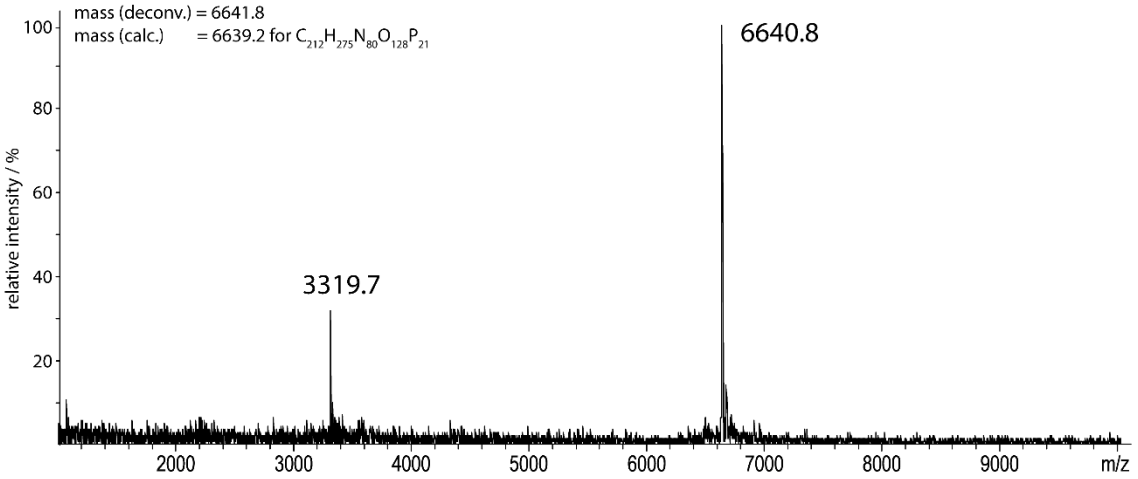

Melting curves | CD spectrsocopy | TDS

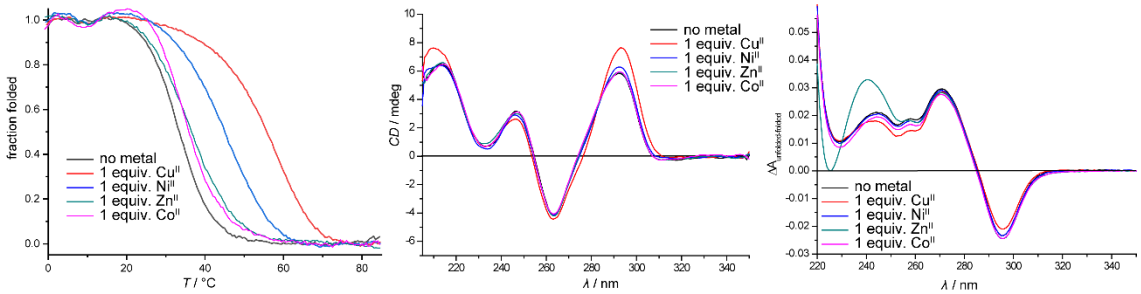

Figure 180. Analytic data of htelL^{2R}_4. Samples for thermal denaturation experiments, TDS and CD spectroscopy were prepared containing 1.875 µM ssDNA, 1.875 µM transition metal salt, 100 mM KCl, 10 mM LiCaco pH 7.2.

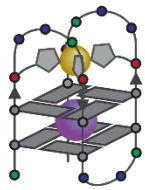

Name
htel**L**$^{2S}_{4}$

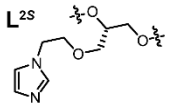

Sequence (5'→3')
AGG **L**^{2S}TT A**L**^{2S}G GTT AGG **L**^{2S}TT A**L**^{2S}G G

1 equiv.	-	Cu^{II}	Ni^{II}	Zn^{II}	Co^{II}
$T_{1/2}$	33	56	45	36	35
$\Delta T_{1/2}$		+23	+12	+3	+2

Analytical RP-HPLC

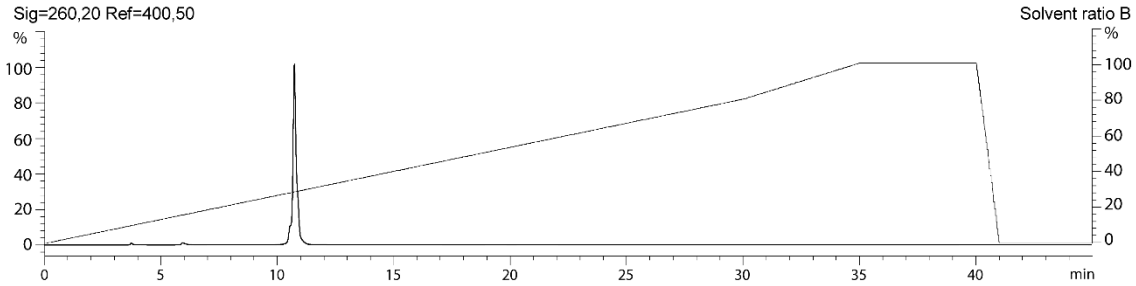

Maldi-Tof MS

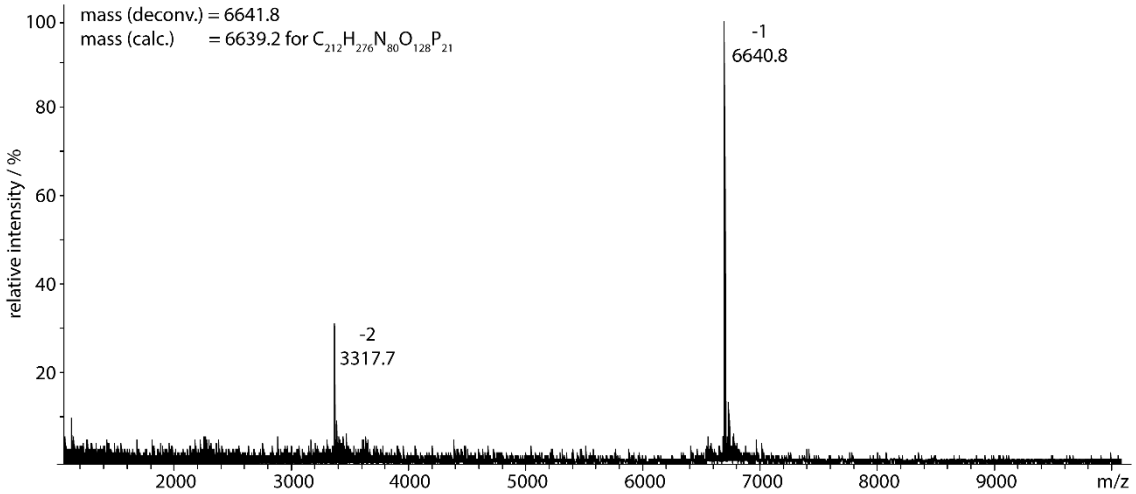

Melting curves | CD spectrsocopy | TDS

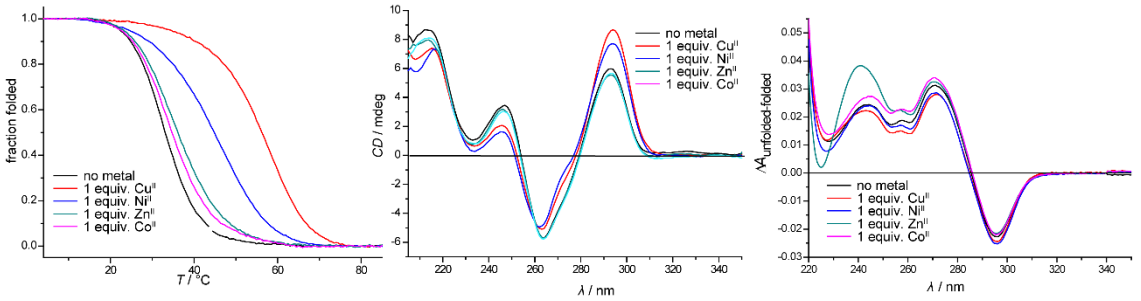

Figure 181. Analytic data of htel**L**$^{2S}_{4}$. Samples for thermal denaturation experiments, TDS and CD spectroscopy were prepared containing 1.875 µM ssDNA, 1.875 µM transition metal salt, 100 mM KCl, 10 mM LiCaco pH 7.2.

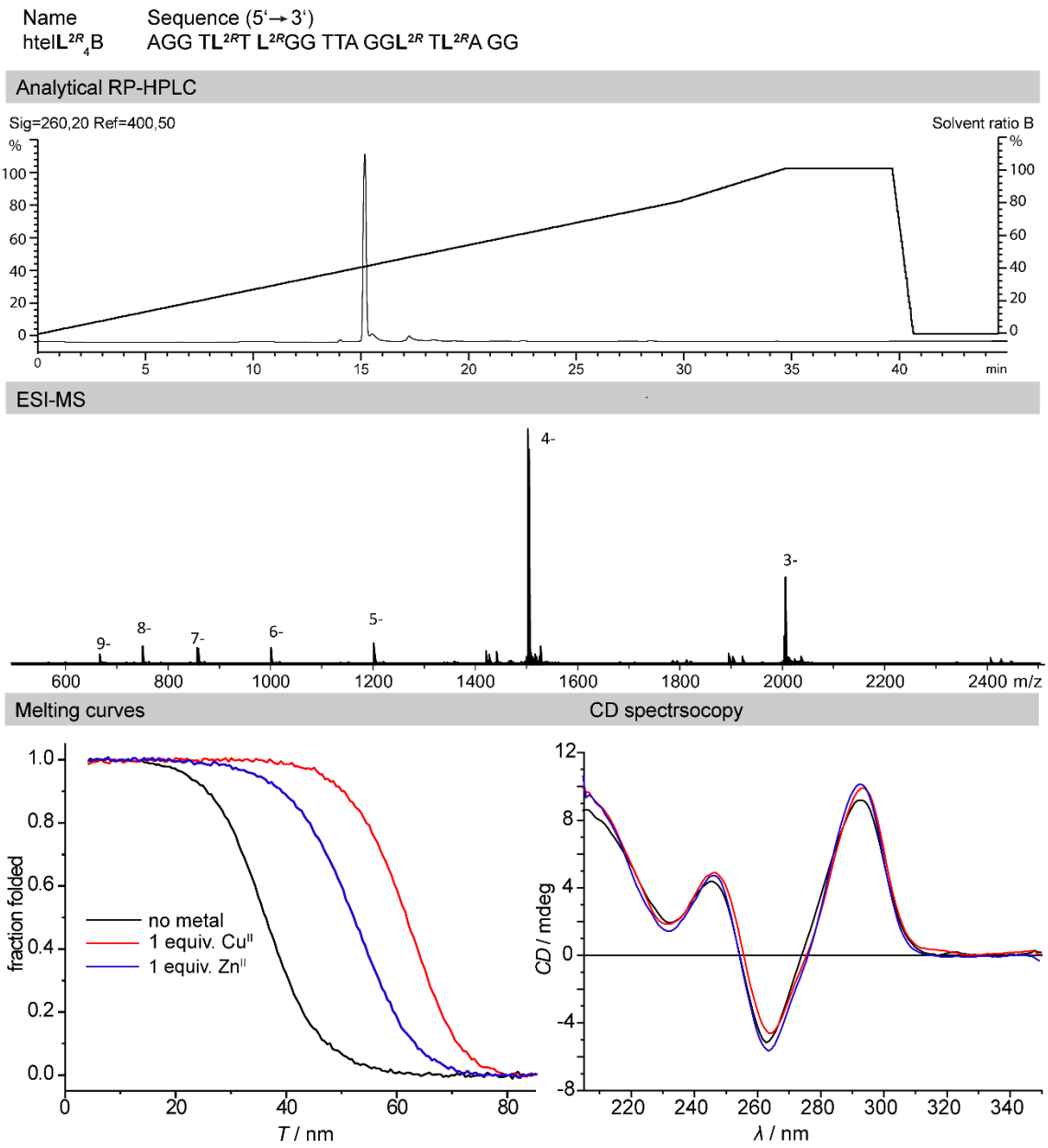

Figure 182. Analytic data of htel**L**^{2R}$_4$B. Samples for thermal denaturation experiments and CD spectroscopy were prepared containing 1.875 µM ssDNA, 1.875 µM transition metal salt, 100 mM KCl, 10 mM LiCaco pH 7.2.

Name
htel**L**$^{2S}_{4}$B

L^{2S} 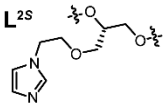

Sequence (5'→3')
AGG T**L**^{2S}T **L**^{2S}GG TTA GG**L**^{2S} T**L**^{2S}A GG

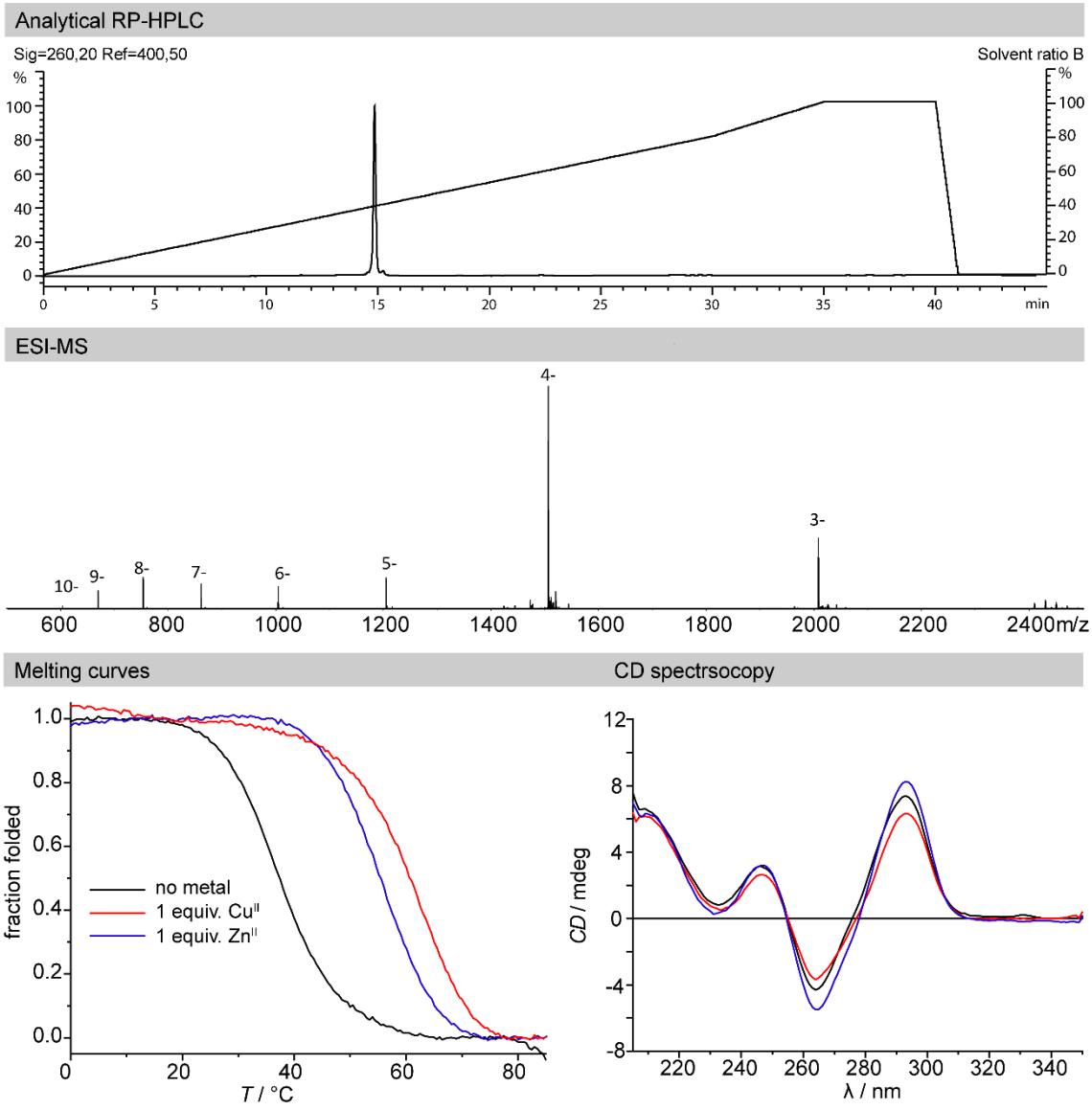

Figure 183. Analytic data of htel**L**$^{2S}_{4}$B. Samples for thermal denaturation experiments and CD spectroscopy were prepared containing 1.875 µM ssDNA, 1.875 µM transition metal salt, 100 mM KCl, 10 mM LiCaco pH 7.2.

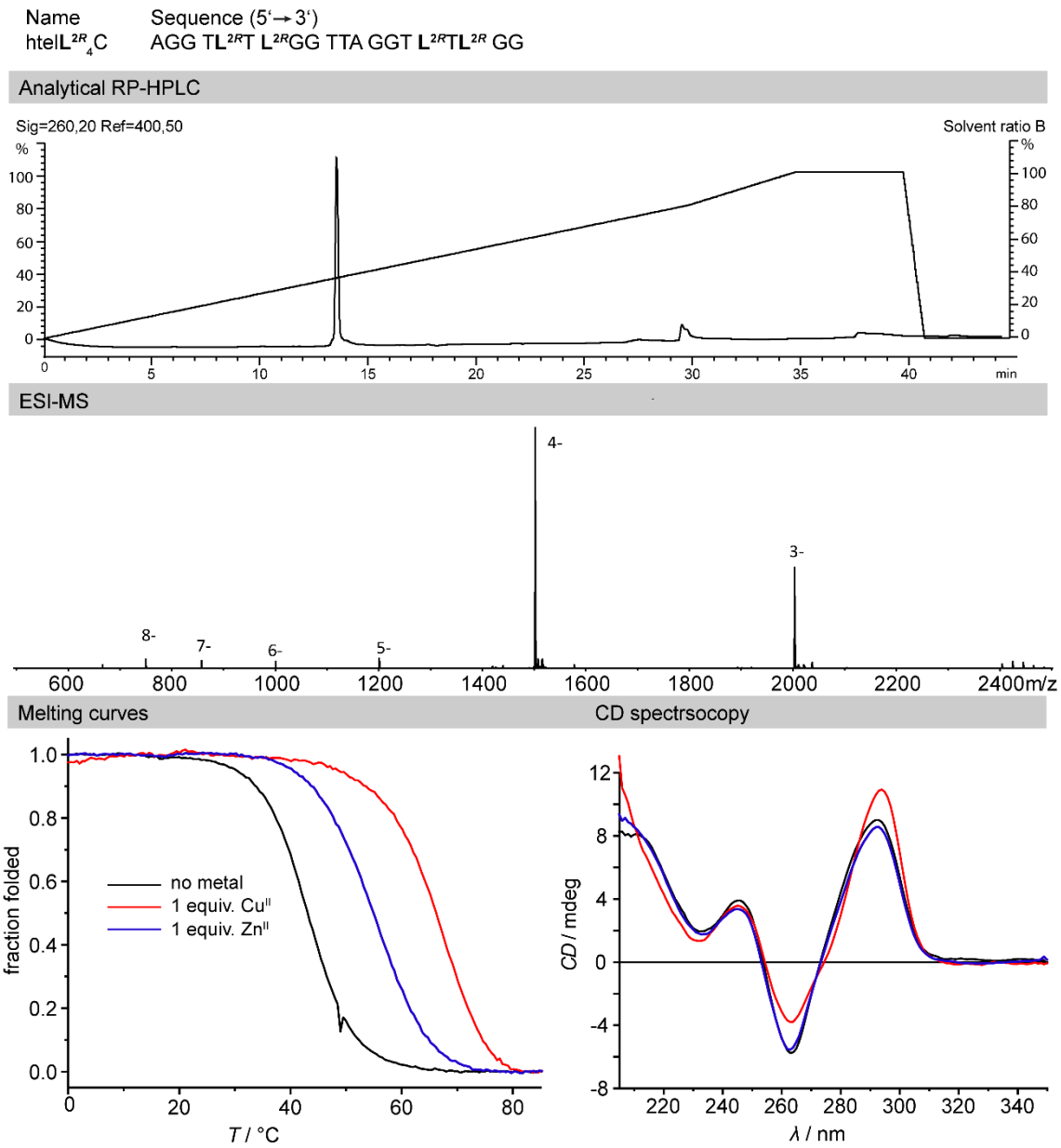

Figure 184. Analytic data of htel**L**$^{2R}_{4}$C. Samples for thermal denaturation experiments and CD spectroscopy were prepared containing 1.875 µM ssDNA, 1.875 µM transition metal salt, 100 mM KCl, 10 mM LiCaco pH 7.2.

Name
htel**L**$^{2S}_{4}$C

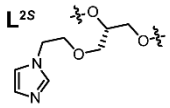

Sequence (5'→3')
AGG T**L**^{2S}T L^{2S}GG TTA GGT L^{2S}T**L**^{2S} GG

Analytical RP-HPLC

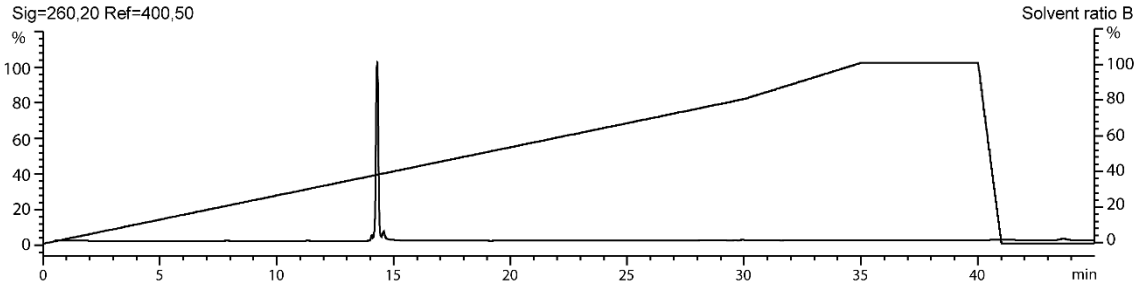

ESI-MS

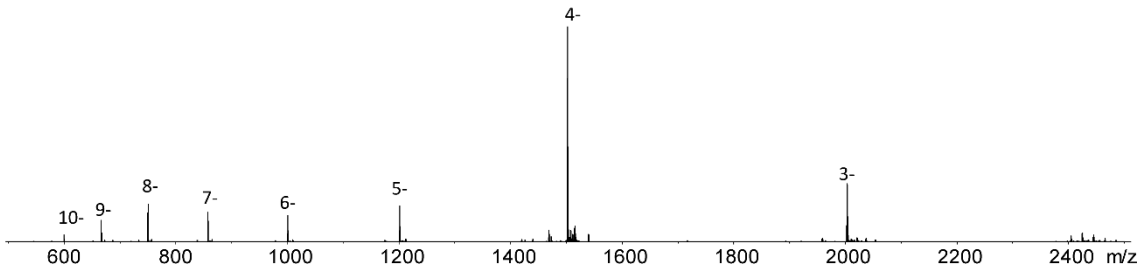

Melting curves

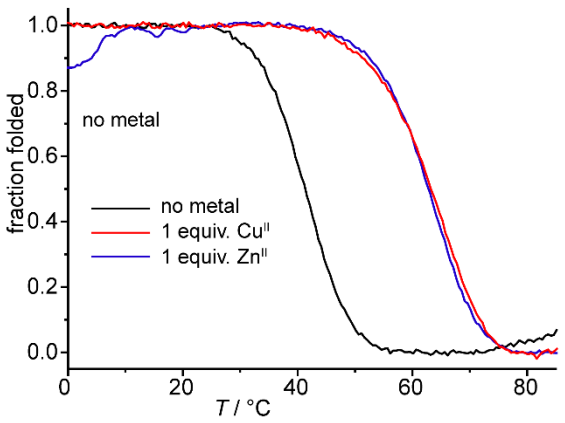

CD spectrsocopy

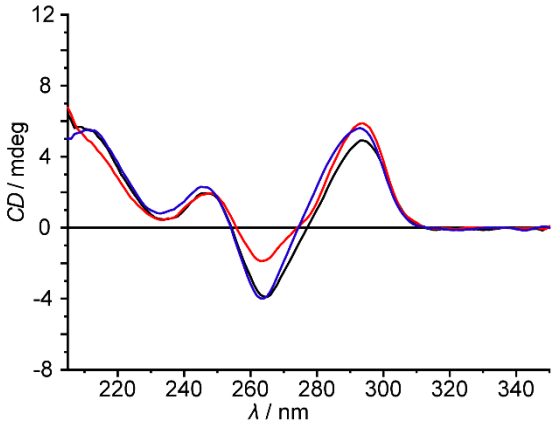

Figure 185. Analytic data of htel**L**$^{2S}_{4}$C. Samples for thermal denaturation experiments and CD spectroscopy were prepared containing 1.875 µM ssDNA, 1.875 µM transition metal salt, 100 mM KCl, 10 mM LiCaco pH 7.2.

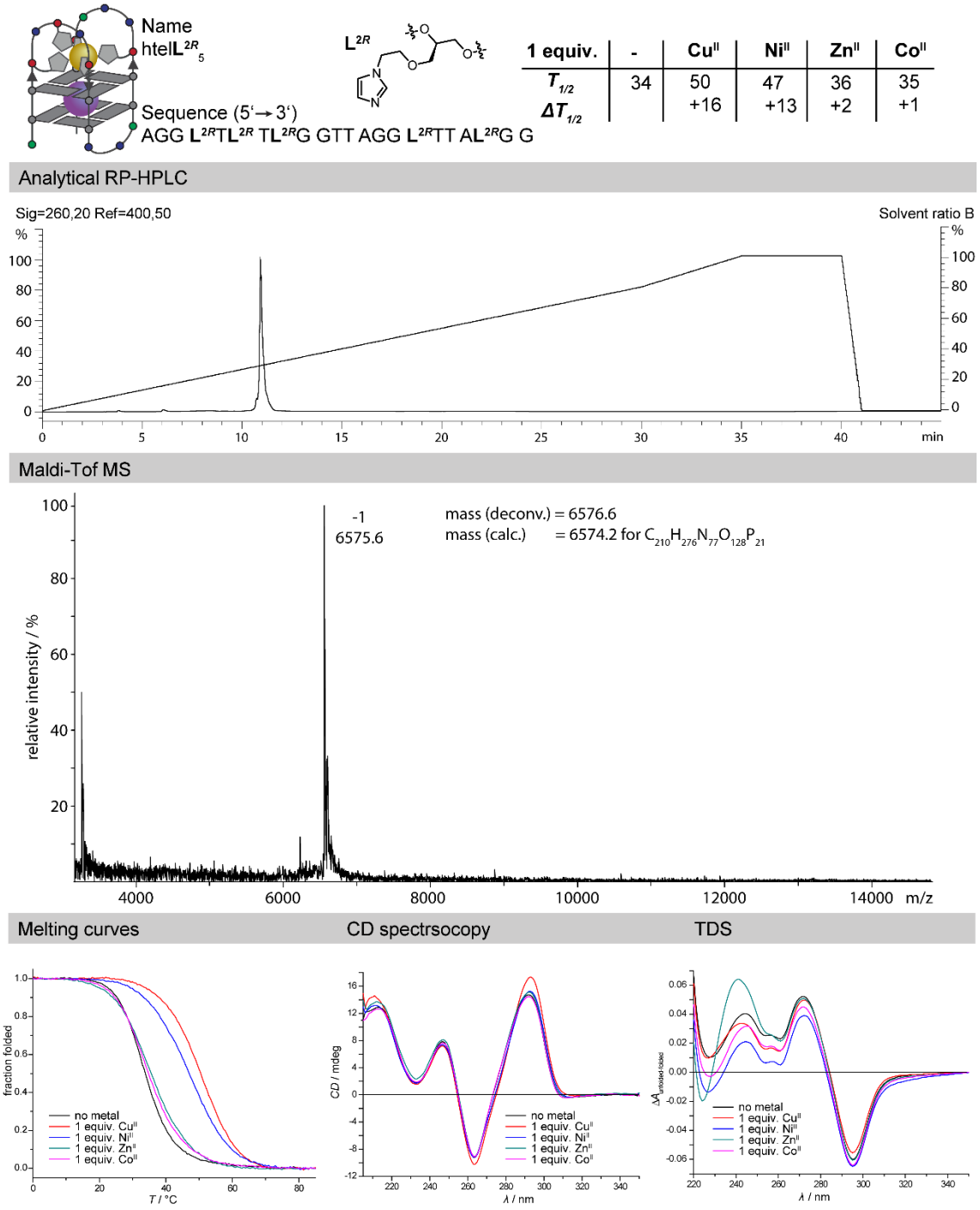

Figure 186. Analytic data of htel**L**$^{2R}_{5}$. Samples for thermal denaturation experiments, TDS and CD spectroscopy were prepared containing 1.875 µM ssDNA, 1.875 µM transition metal salt, 100 mM KCl, 10 mM LiCaco pH 7.2.

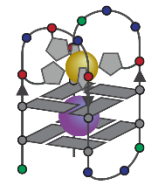

Name
htel$L^{2S}{}_5$

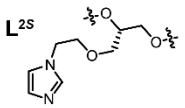

Sequence (5'→3')
AGG $L^{2S}TL^{2S}$ $TL^{2S}G$ GTT AGG $L^{2S}TT$ $AL^{2S}G$ G

1 equiv.	-	Cu^{II}	Ni^{II}	Zn^{II}	Co^{II}
$T_{1/2}$	33	54	55	37	37
$\Delta T_{1/2}$		+21	+22	+4	+4

Analytical RP-HPLC

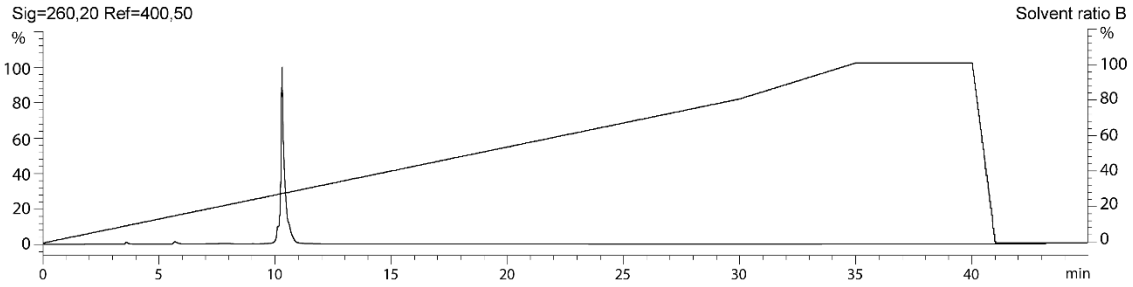

Maldi-Tof MS

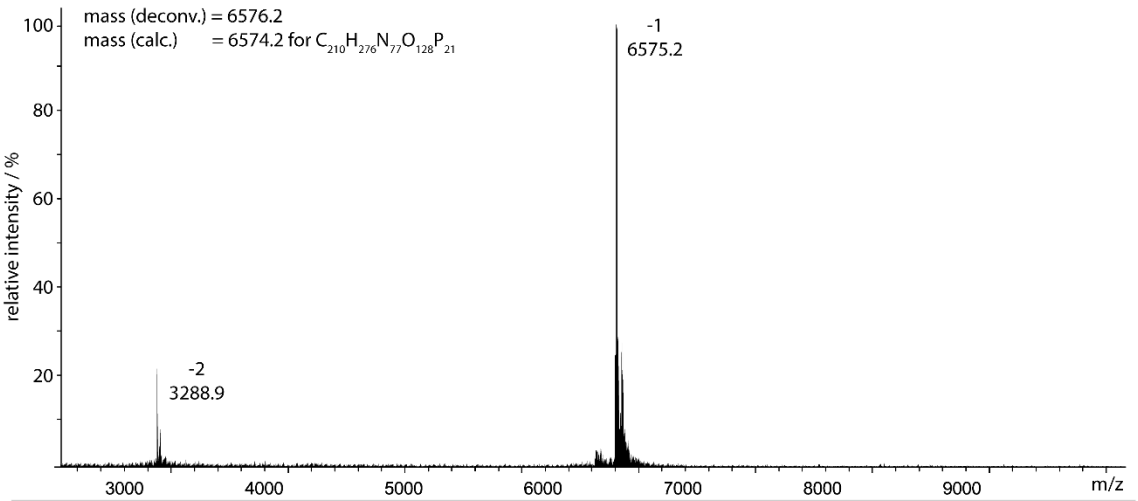

Melting curves | CD spectrsocopy | TDS

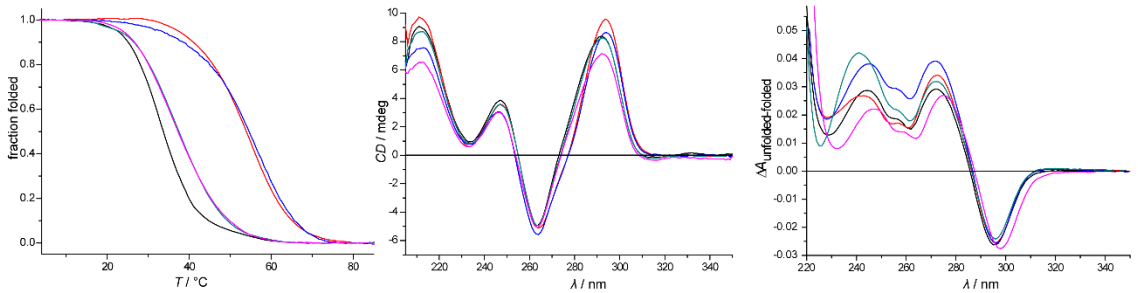

Figure 187. Analytic data of htel$\mathbf{L^{2S}}_5$. Samples for thermal denaturation experiments, TDS and CD spectroscopy were prepared containing 1.875 µM ssDNA, 1.875 µM transition metal salt, 100 mM KCl, 10 mM LiCaco pH 7.2.

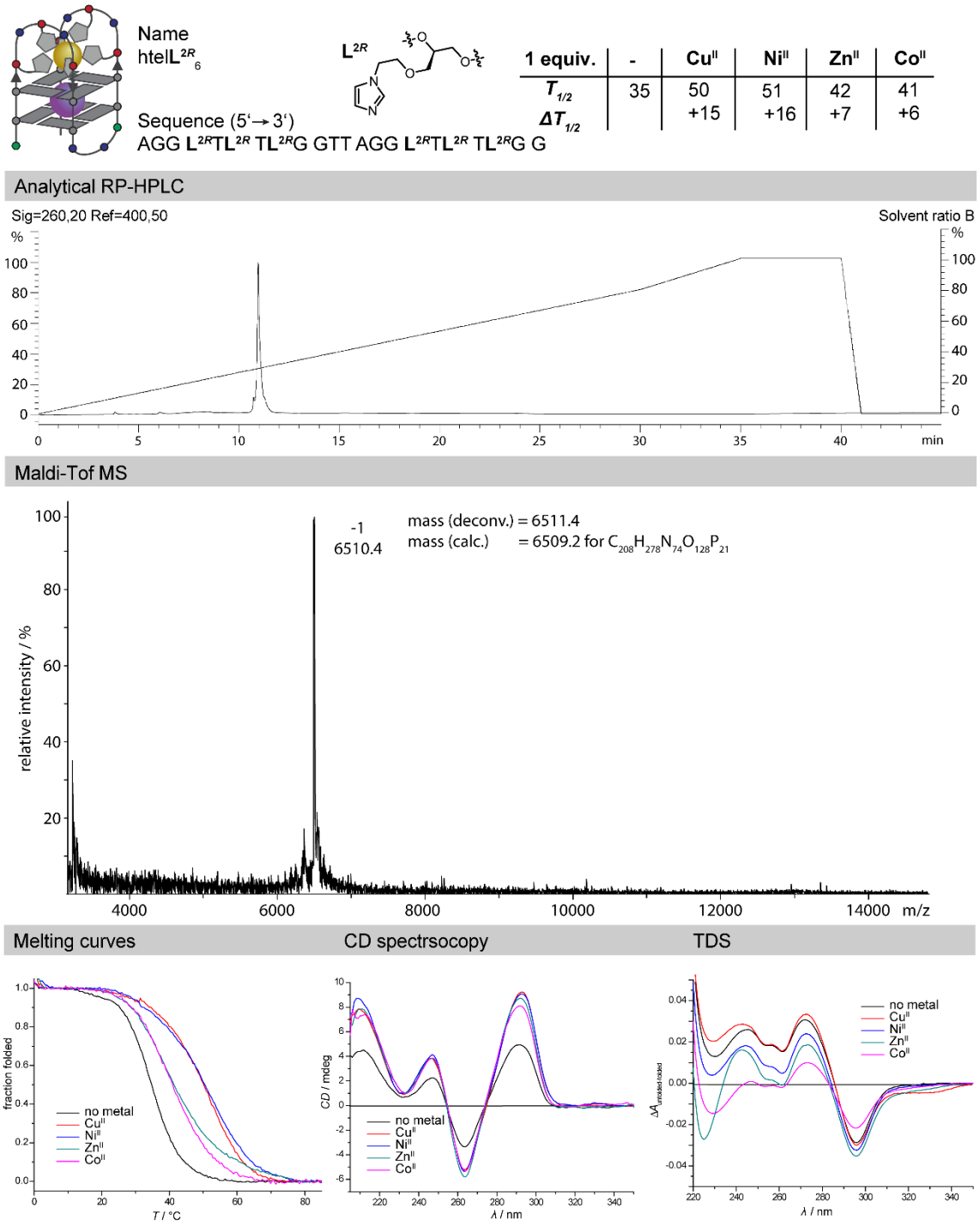

Figure 188. Analytic data of htel**L**$^{2R}_{6}$. Samples for thermal denaturation experiments, TDS and CD spectroscopy were prepared containing 1.875 µM ssDNA, 1.875 µM transition metal salt, 100 mM KCl, 10 mM LiCaco pH 7.2.

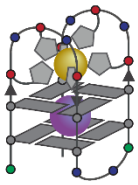

Name
htel$L^{2S}{}_6$

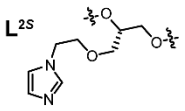

1 equiv.	-	Cu^{II}	Ni^{II}	Zn^{II}	Co^{II}
$T_{1/2}$	36	54	59	44	44
$\Delta T_{1/2}$		+18	+23	+8	+8

Sequence (5'→3')
AGG $L^{2S}TL^{2S}$ $TL^{2S}G$ GTT AGG $L^{2S}TL^{2S}$ $TL^{2S}G$ G

Analytical RP-HPLC

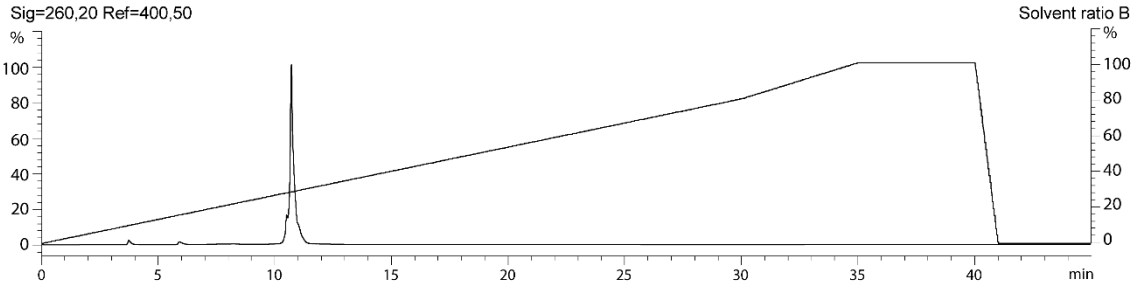

Maldi-Tof MS

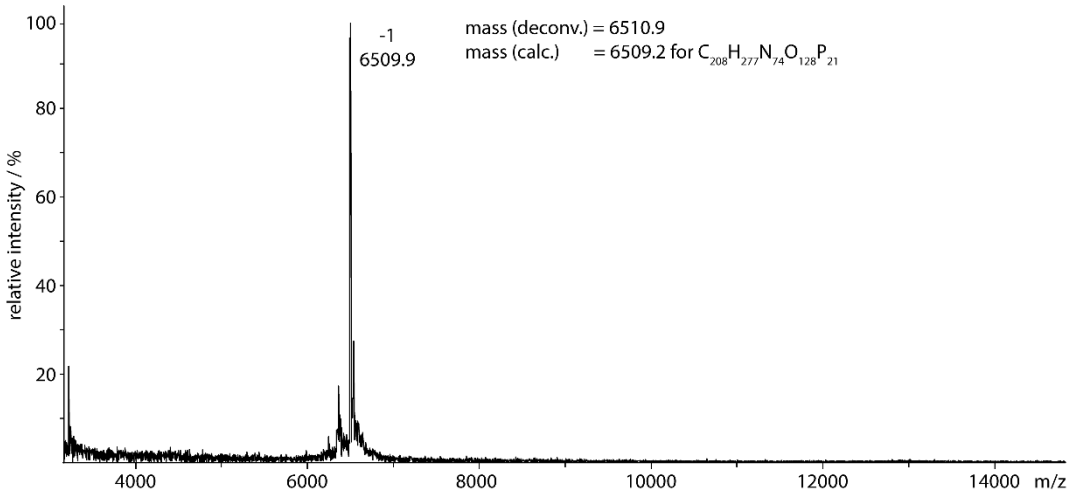

Melting curves | CD spectrsocopy | TDS

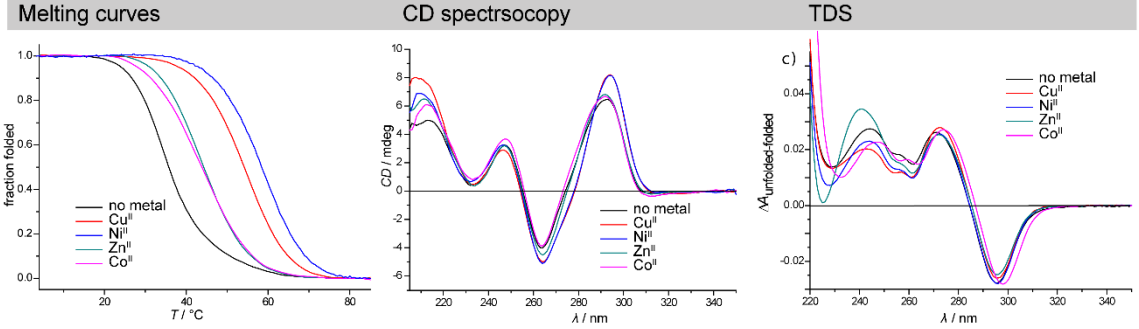

Figure 189. Analytic data of htel$\mathbf{L^{2S}}_6$. Samples for thermal denaturation experiments, TDS and CD spectroscopy were prepared containing 1.875 µM ssDNA, 1.875 µM transition metal salt, 100 mM KCl, 10 mM LiCaco pH 7.2.

Name
htel$L^{2R}{}_7$

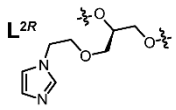

1 equiv.	-	Cu^{II}	Ni^{II}	Zn^{II}	Co^{II}
$T_{1/2}$	29	43	44	36	30
$\Delta T_{1/2}$		+14	+15	+7	+1

Sequence (5'→3')
AGG $L^{2R}TL^{2R}$ $L^{2R}TL^{2R}$ GGT TAG GL^{2R}T $L^{2R}TL^{2R}$ GG

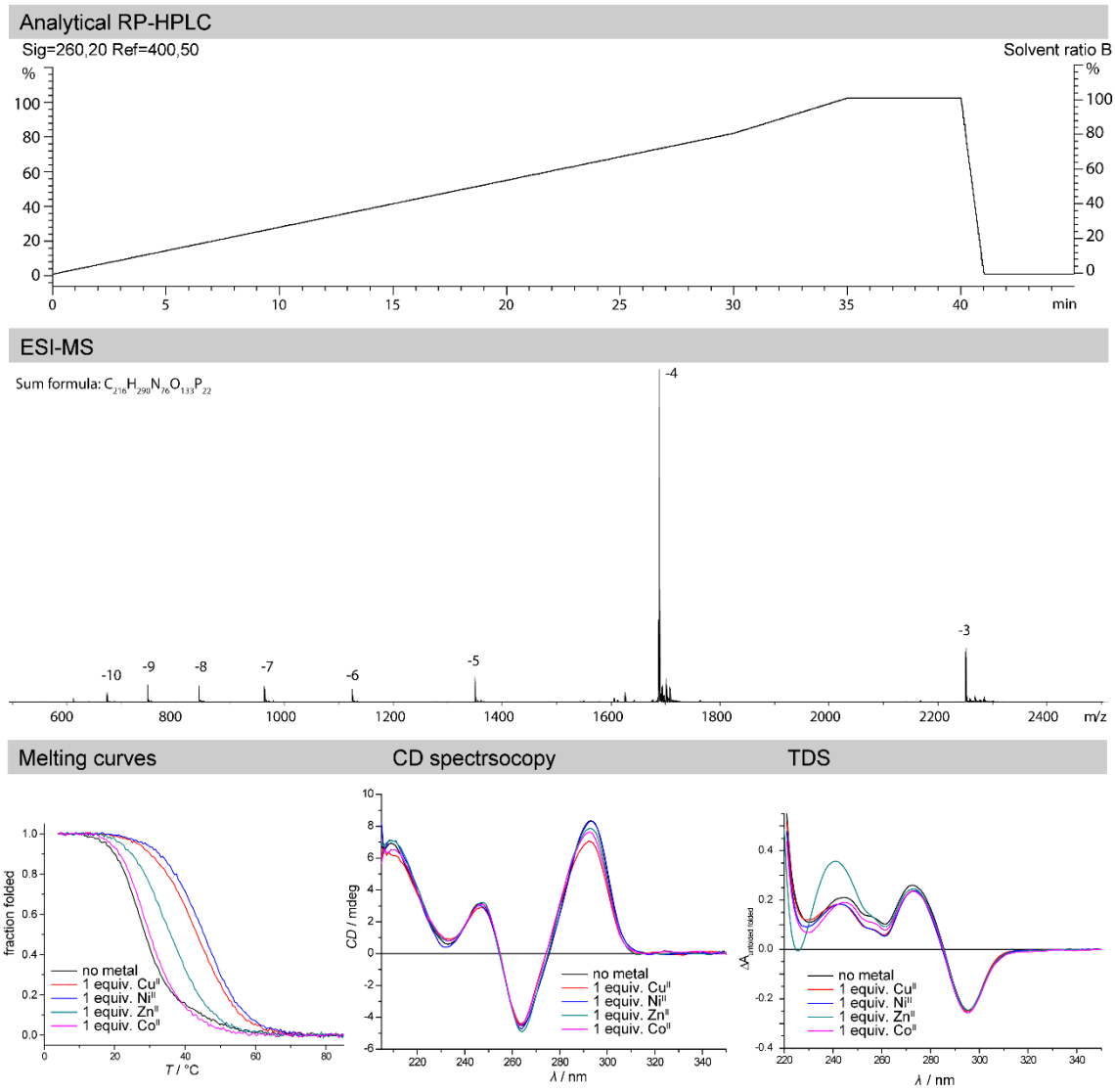

Figure 190. Analytic data of htel$L^{2R}{}_7$. Samples for thermal denaturation experiments, TDS and CD spectroscopy were prepared containing 1.875 µM ssDNA, 1.875 µM transition metal salt, 100 mM KCl, 10 mM LiCaco pH 7.2.

Name
htel**L**$^{2S}_{7}$

L^{2S} 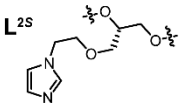

1 equiv.	-	Cu^{II}	Ni^{II}	Zn^{II}	Co^{II}
$T_{1/2}$	28	43	46	36	36
$\Delta T_{1/2}$		+15	+18	+8	+8

Sequence (5'→3')
AGG $L^{2S}TL^{2S}$ $L^{2S}TL^{2S}$ GGT TAG GL^{2S}T $L^{2S}TL^{2S}$ GG

Analytical RP-HPLC

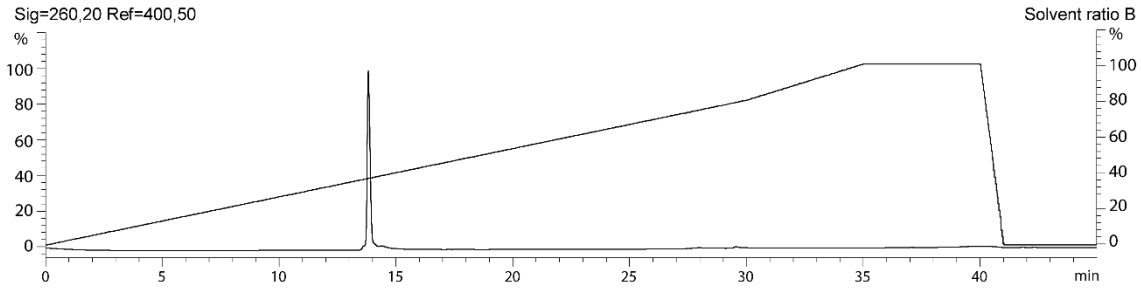

ESI-MS

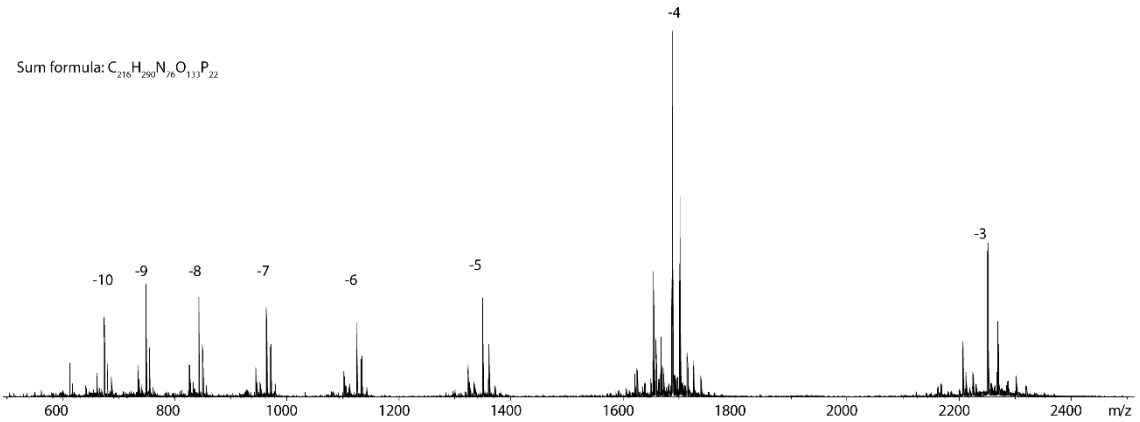

Melting curves | CD spectrsocopy | TDS

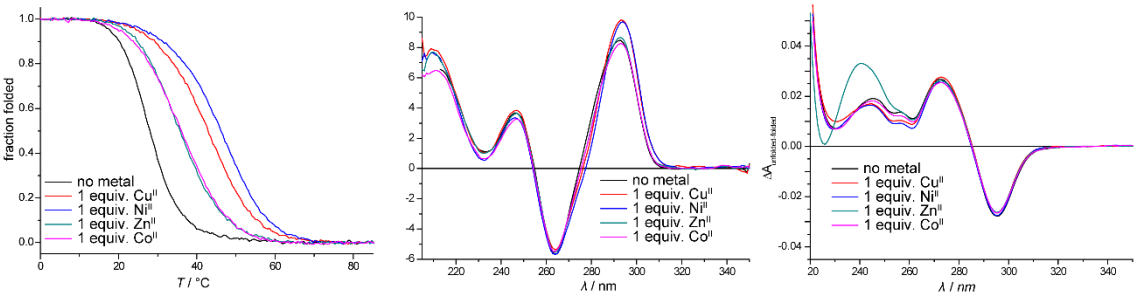

Figure 191. Analytic data of htel**L**$^{2S}_{7}$. Samples for thermal denaturation experiments, TDS and CD spectroscopy were prepared containing 1.875 µM ssDNA, 1.875 µM transition metal salt, 100 mM KCl, 10 mM LiCaco pH 7.2.

Name: Sequence (5'→3'):
htel$\mathbf{L^{2R}}_3$H AGG GT$\mathbf{L^{2R}}$ AGG GTT AGG G$\mathbf{L^{2R}}$T$\mathbf{L^{2R}}$GG G

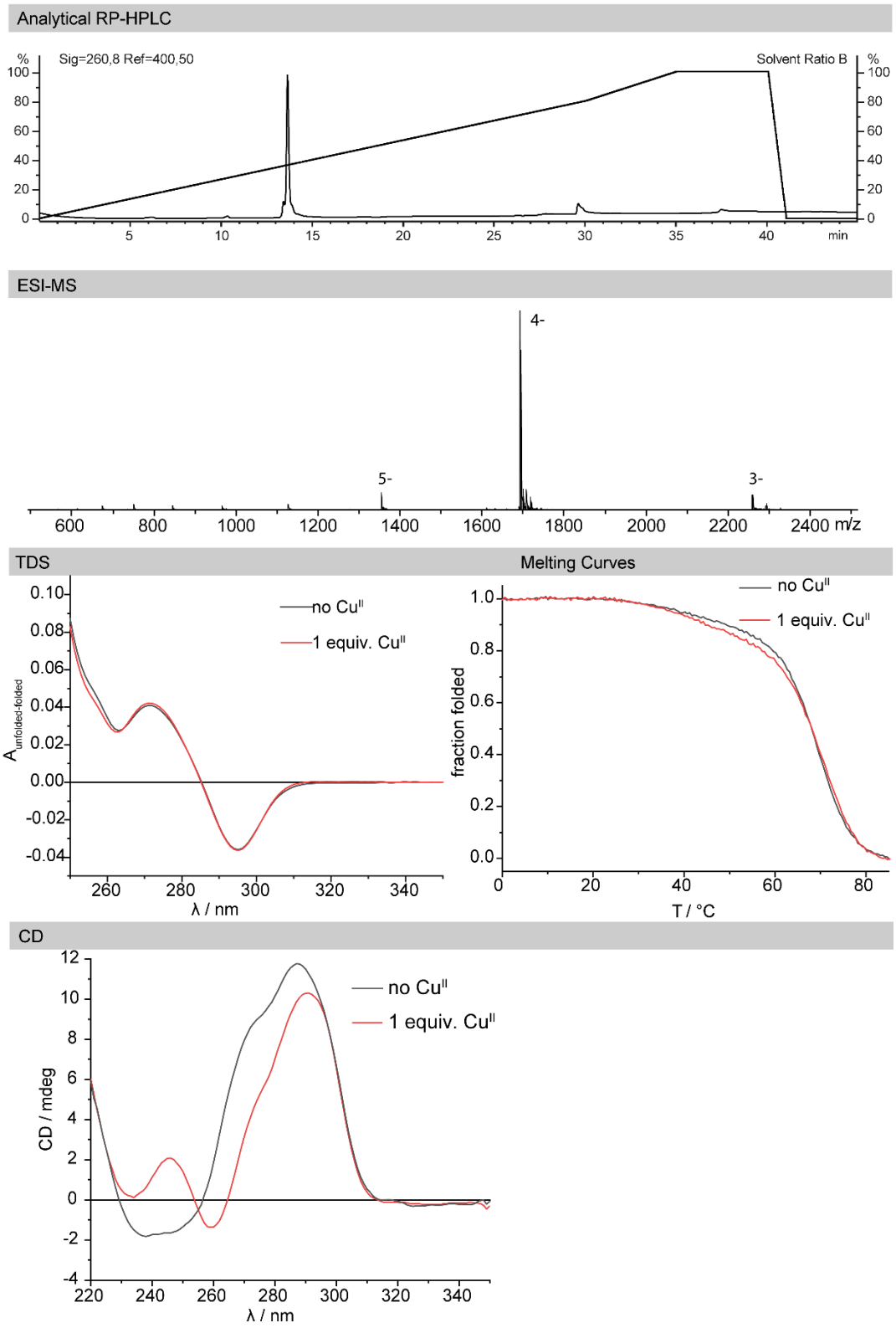

Figure 192. Analytic data of htel$\mathbf{L^{2R}}_3$H. Samples for thermal denaturation experiments, TDS and CD spectroscopy were prepared containing 2 µM ssDNA, 2 µM transition metal salt, 100 mM KCl, 10 mM HEPES pH 8.

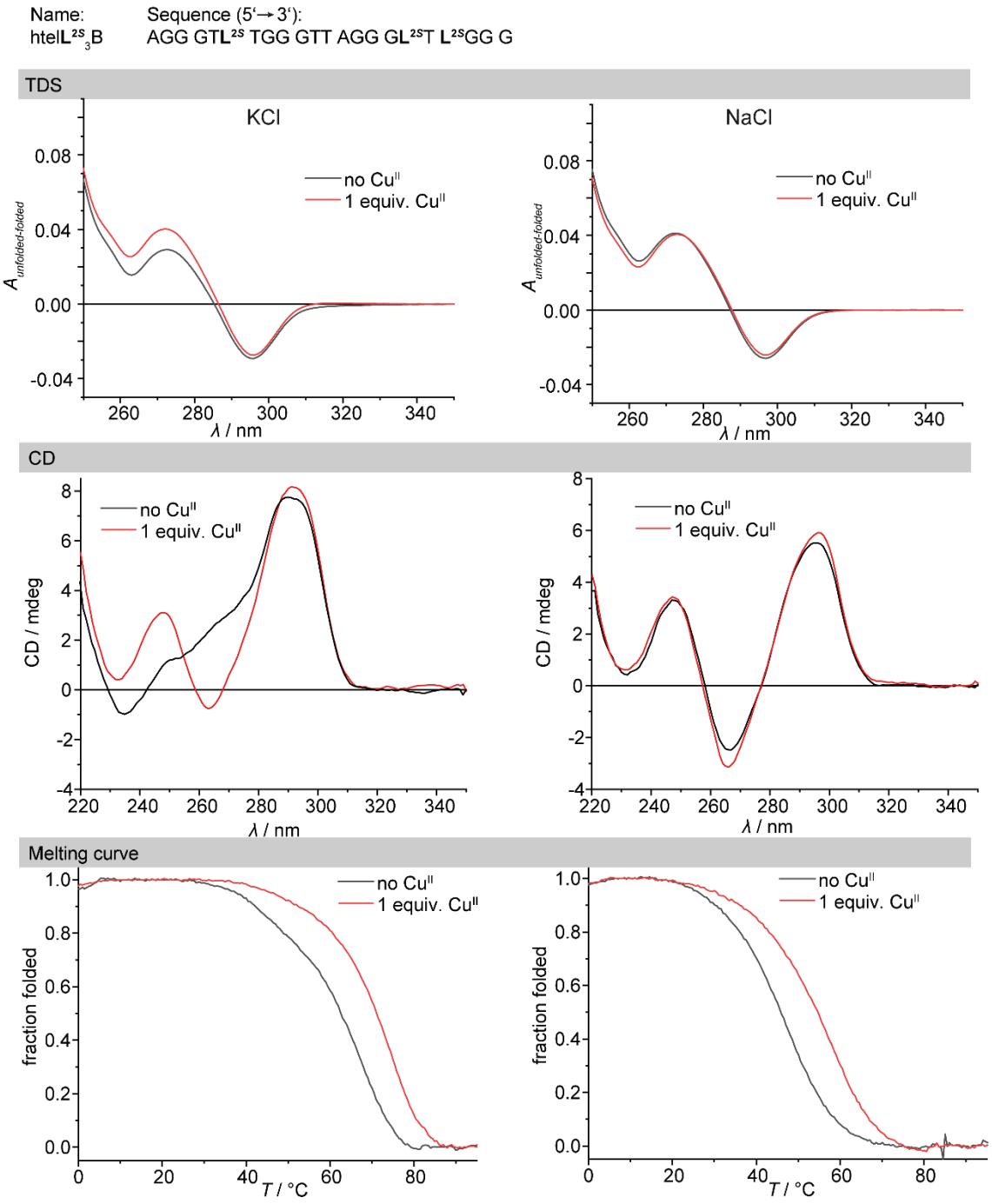

Figure 193. Analytic data of htel**L**^{2S}$_3$B. Samples for thermal denaturation experiments, TDS and CD spectroscopy were prepared containing 2 µM ssDNA, 2 µM transition metal salt, 100 mM KCl/NaCl, 10 mM HEPES pH 8. The analytical HPLC trace and ESI-MS are shown in **Figure 177**.

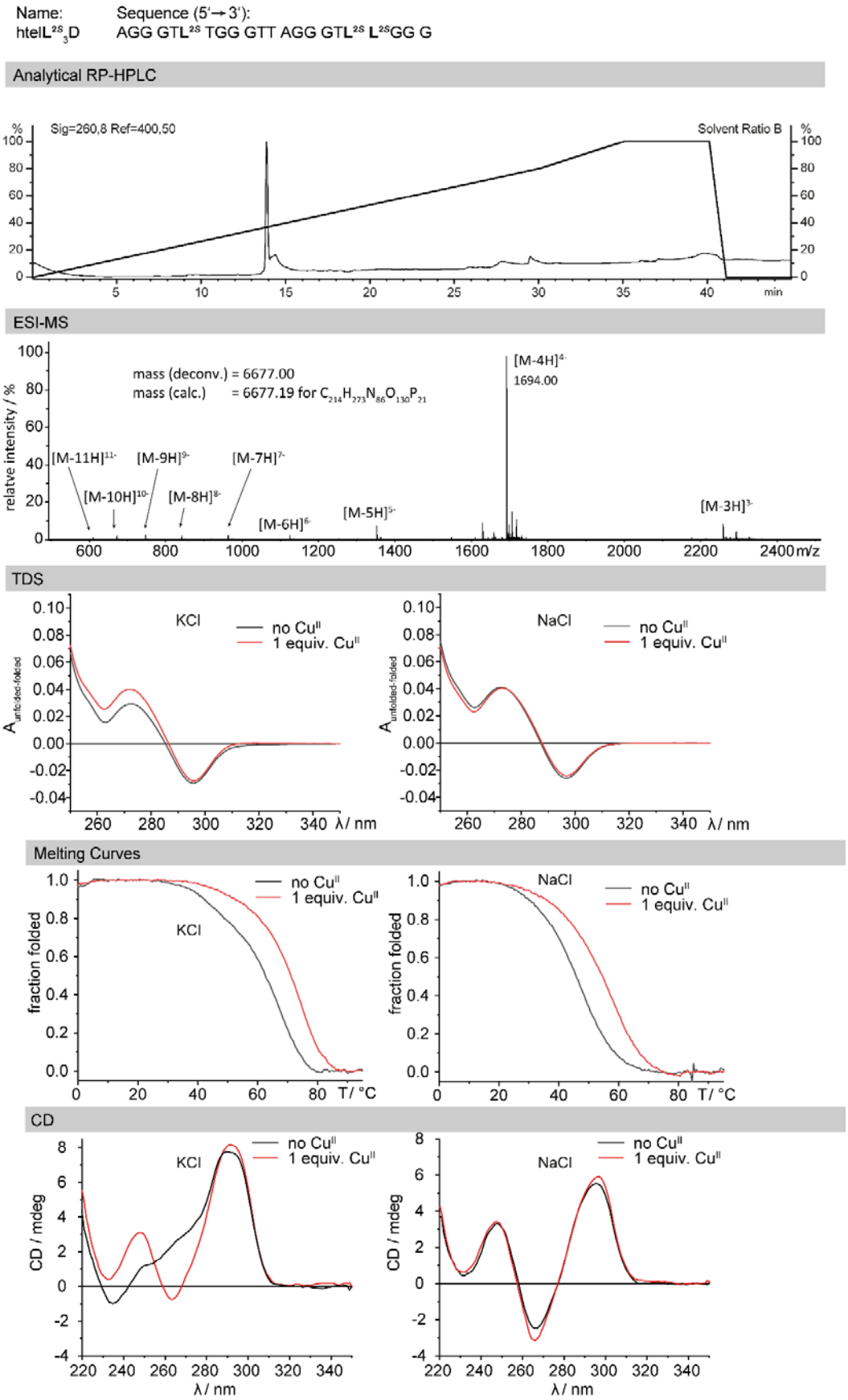

Figure 194. Analytic data of htel**L**^{2S}$_3$D. Samples for thermal denaturation experiments, TDS and CD spectroscopy were prepared containing 2 µM ssDNA, 2 µM transition metal salt, 100 mM KCl/NaCl, 10 mM HEPES pH 8.

Name: Sequence (5'→3'):
htel**L**^{2R}$_3$D AGG GT**L**^{2R} TGG GTT AGG GT**L**^{2R} **L**^{2R}GG G

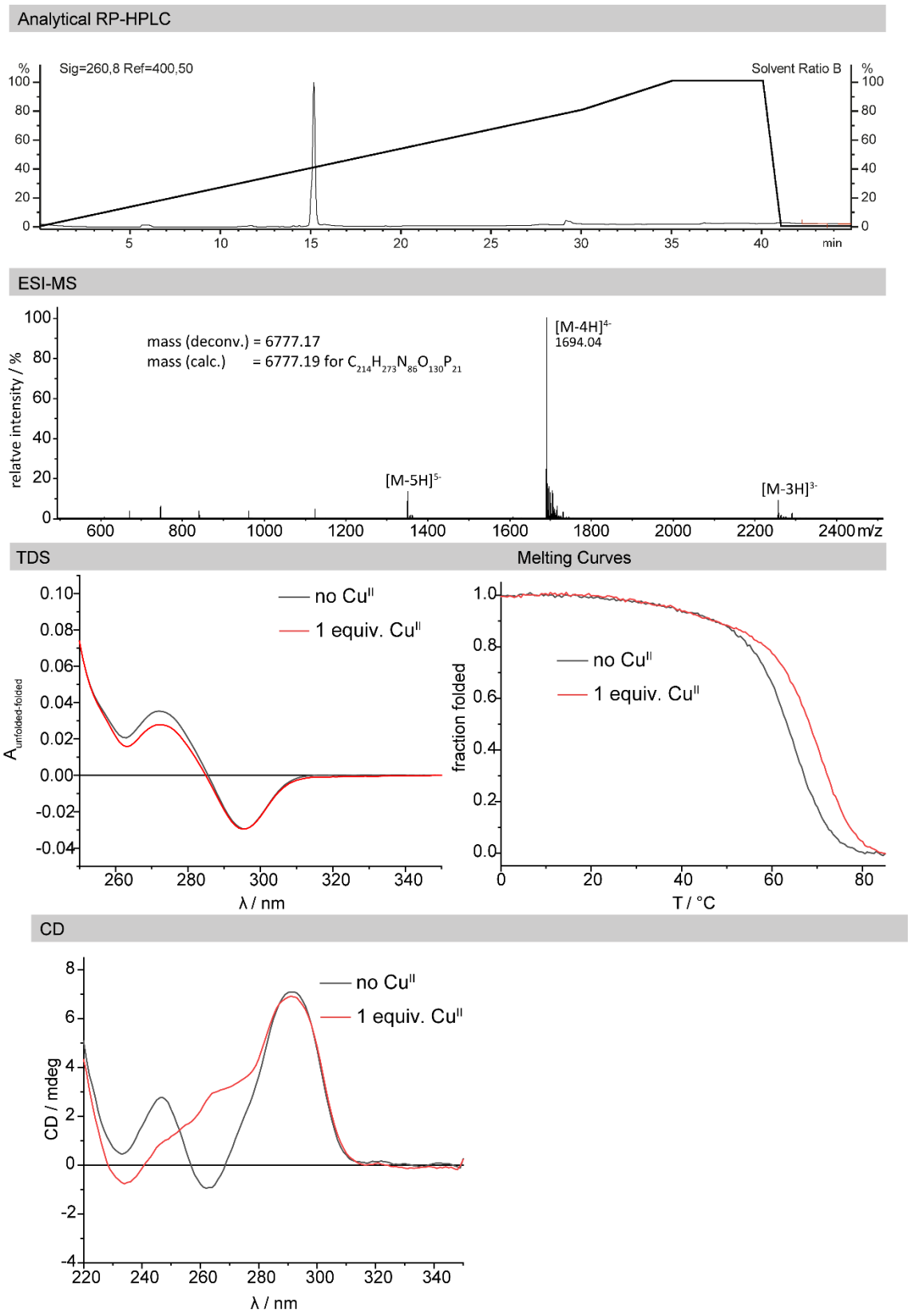

Figure 195. Analytic data of htel**L**^{2R}$_3$D. Samples for thermal denaturation experiments, TDS and CD spectroscopy were prepared containing 2 µM ssDNA, 2 µM transition metal salt, 100 mM KCl, 10 mM HEPES pH 8.

Name: Sequence (5'→3'):
htel**L**$^{2S}_{2}$F AGG G**L**^{2S}**L**^{2S} TGG GTT AGG GTT AGG G

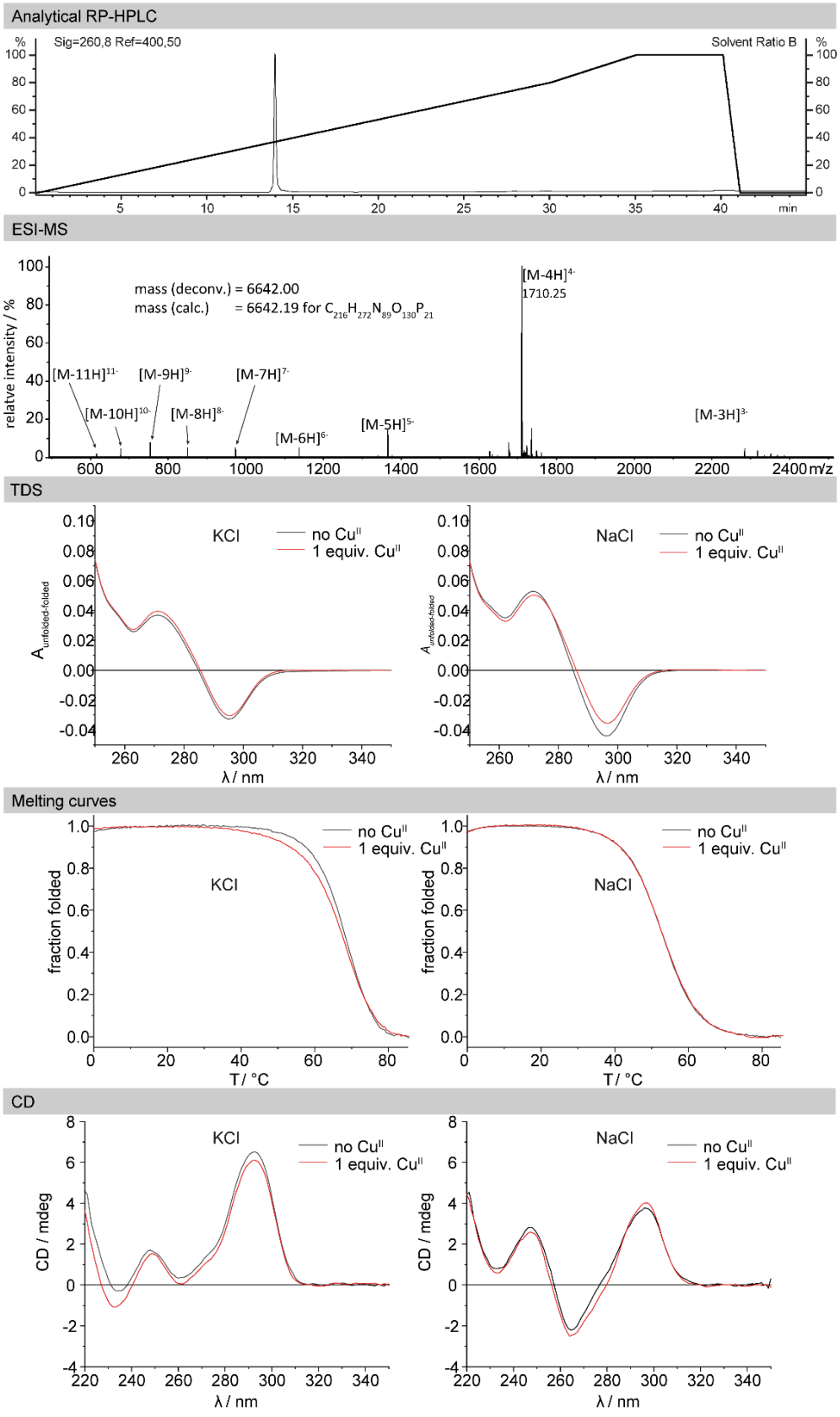

Figure 196. Analytic data of htel**L**$^{2S}_{2}$F. Samples for thermal denaturation experiments, TDS and CD spectroscopy were prepared containing 2 µM ssDNA, 2 µM transition metal salt, 100 mM KCl/NaCl, 10 mM HEPES pH 8.

Name: Sequence (5'→3'):
htel**L**$^{2R}_{2}$F AGG G**L**^{2R}**L**^{2R} TGG GTT AGG GTT AGG G

Analytical RP-HPLC

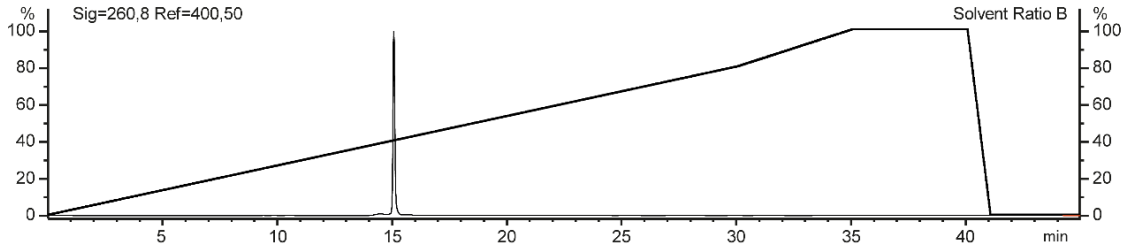

ESI-MS

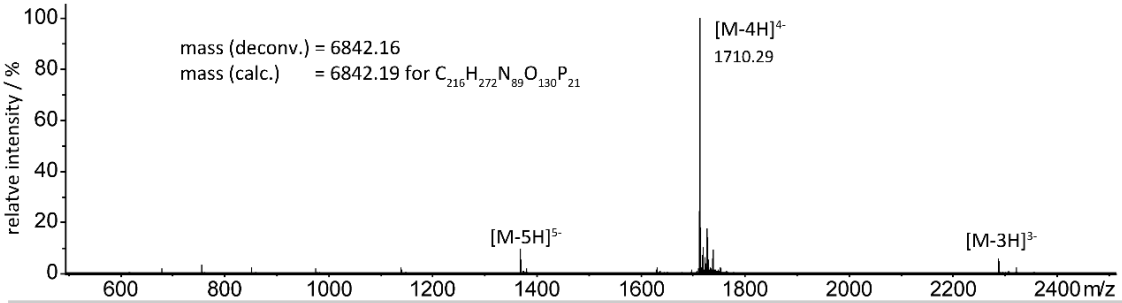

TDS

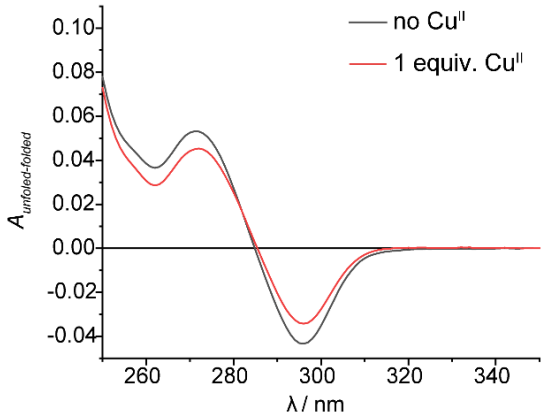

Melting Curves

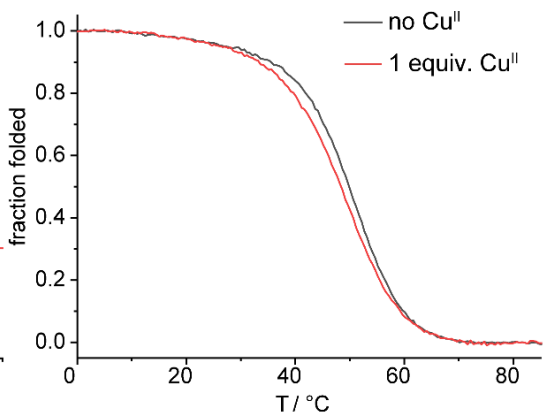

CD

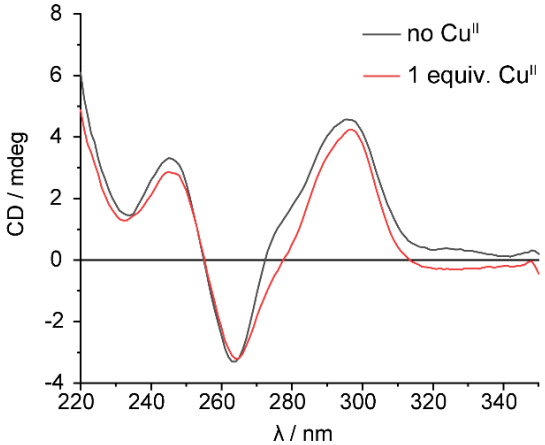

Figure 197. Analytic data of htel**L**$^{2R}_{2}$F. Samples for thermal denaturation experiments, TDS and CD spectroscopy were prepared containing 2 µM ssDNA, 2 µM transition metal salt, 100 mM NaCl, 10 mM HEPES pH 8.

Name: Sequence (5'→3'):
htel**L**$^{2R}_{2}$G AGG GT**L**^{2R} **L**^{2R}GG GTT AGG GTT AGG G

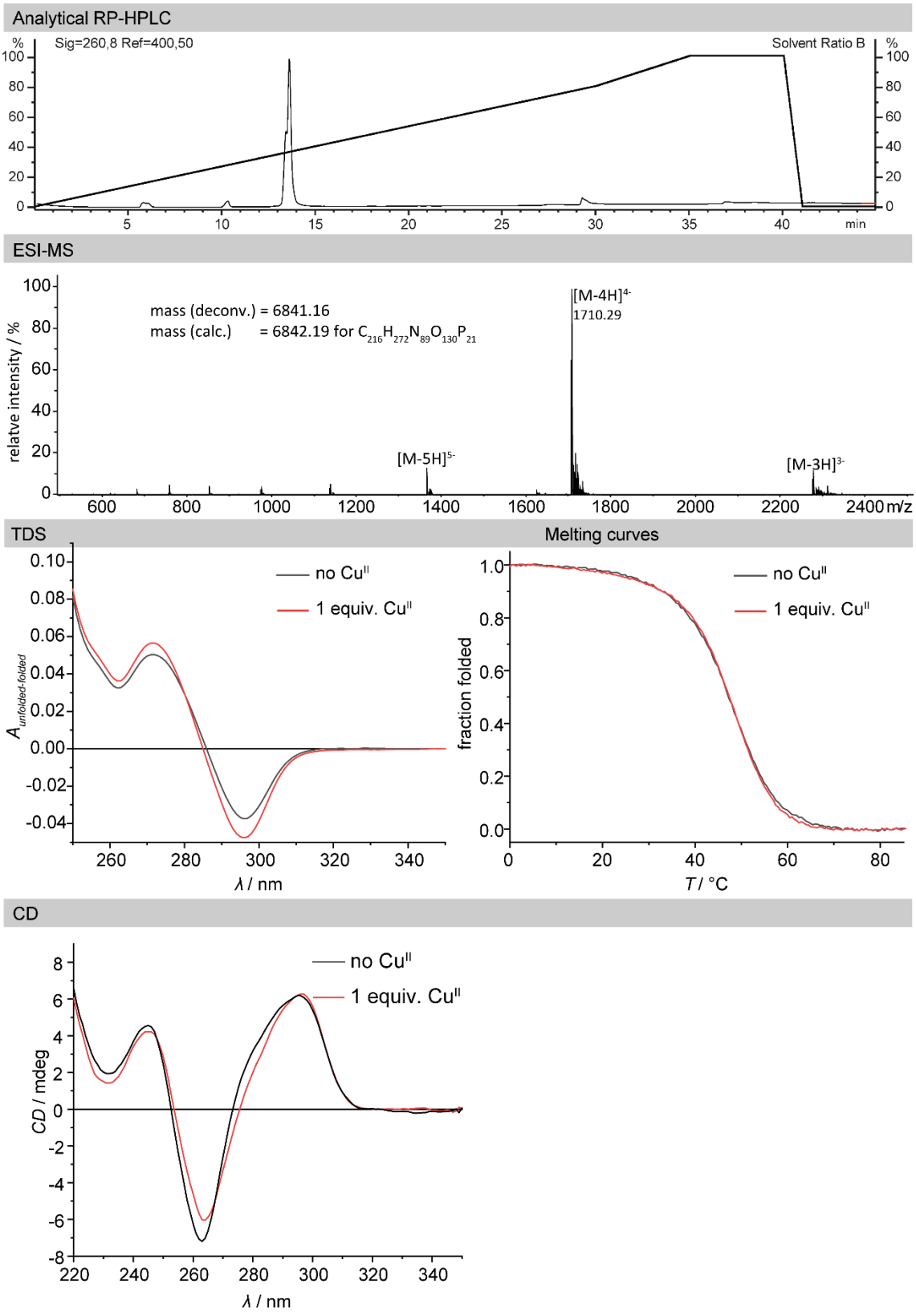

Figure 198. Analytic data of htel**L**$^{2R}_{2}$G. Samples for thermal denaturation experiments, TDS and CD spectroscopy were prepared containing 2 µM ssDNA, 2 µM transition metal salt, 100 mM NaCl, 10 mM HEPES pH 8.

Name: Sequence (5'→3'):
htel**L**$^{2S}_{2}$G AGG GT**L**^{2S} **L**^{2S}GG GTT AGG GTT AGG G

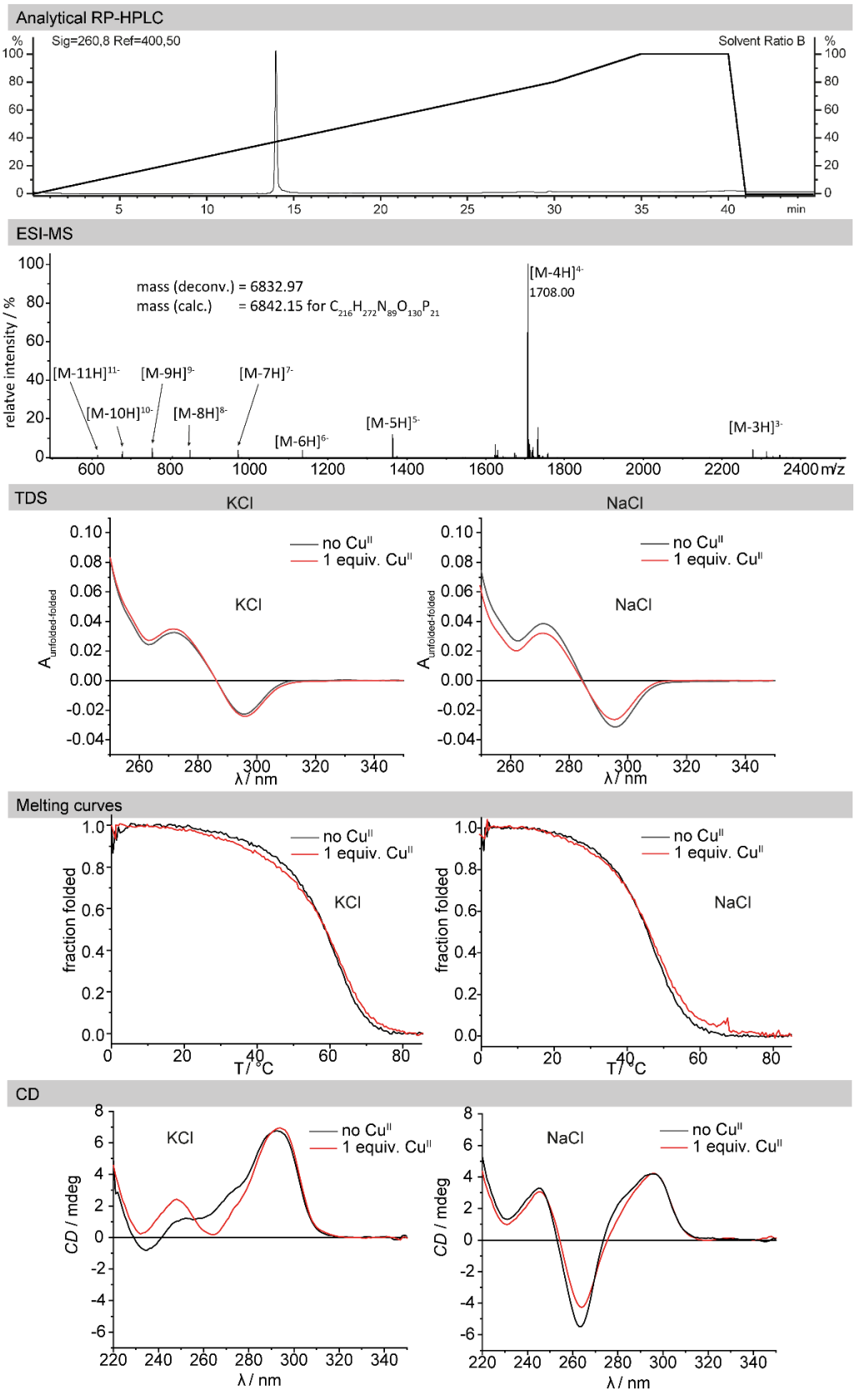

Figure 199. Analytic data of htel**L**$^{2S}_{2}$G. Samples for thermal denaturation experiments, TDS and CD spectroscopy were prepared containing 2 µM ssDNA, 2 µM transition metal salt, 100 mM KCl/NaCl, 10 mM HEPES pH 8.

10.3 Additional analytical ESI-MS

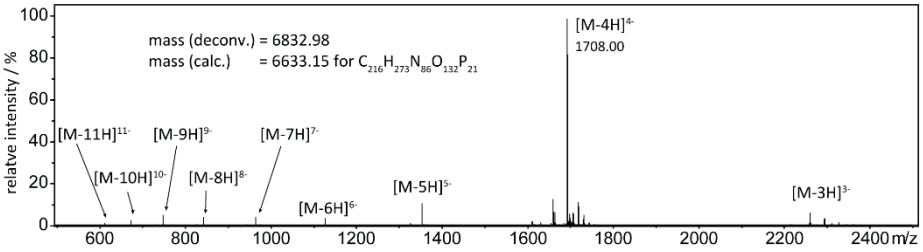

htel**L**$^{s}_{3}$M

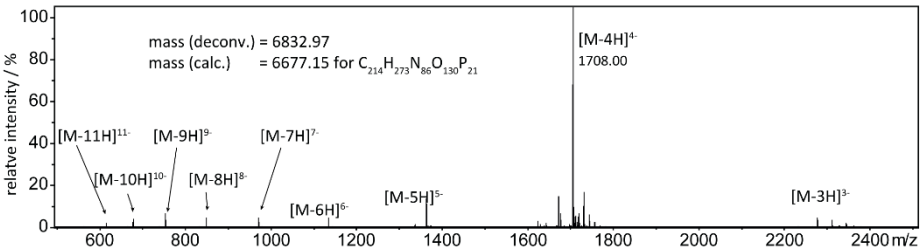

htel**L**$^{s}_{2}$K

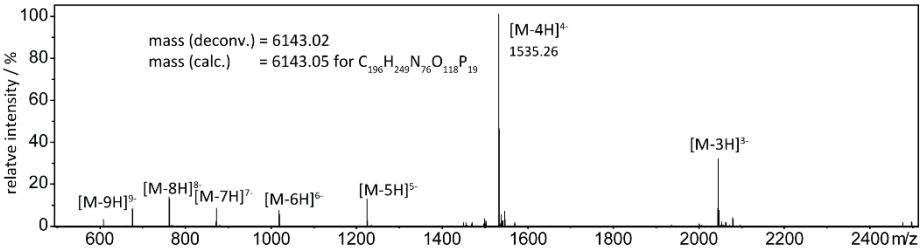

htel**L**$^{s}_{2}$L

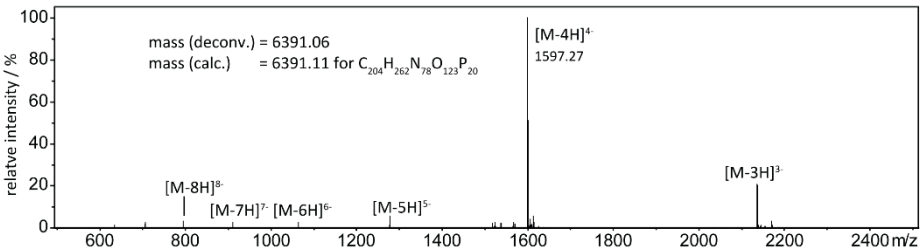

htel**L**$^{s}_{3}$N

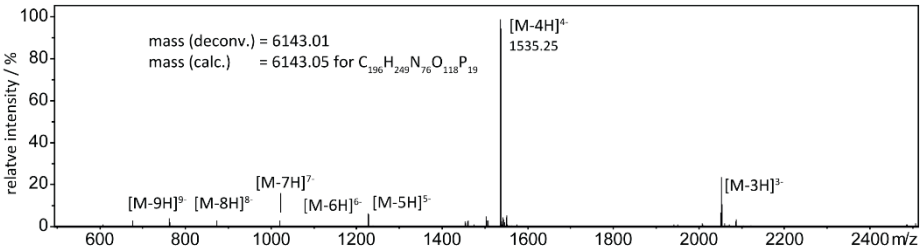

htel**L**$^{s}_{2}$M

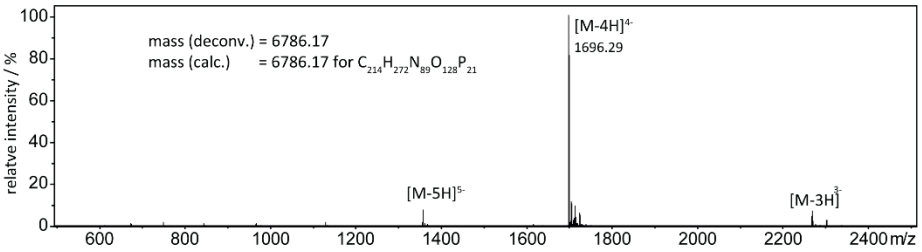

htelL$^{R}_{3}$I

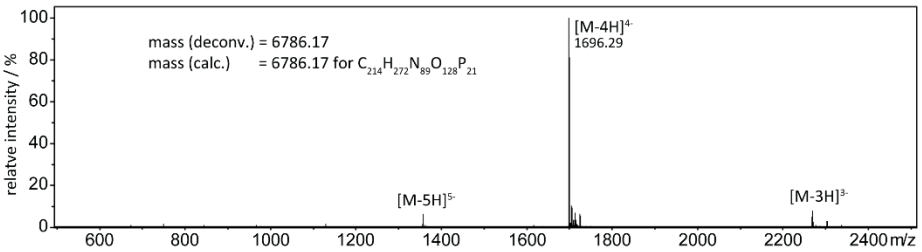

htelL$^{R}_{3}$J

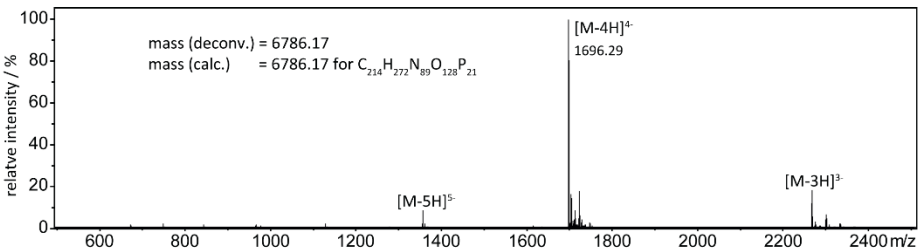

htelL$^{R}_{3}$K

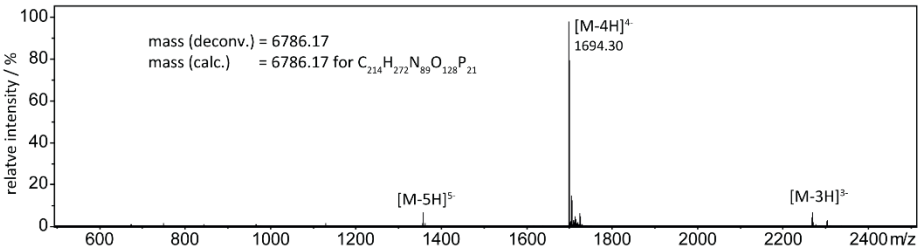

htelL$^{R}_{3}$L

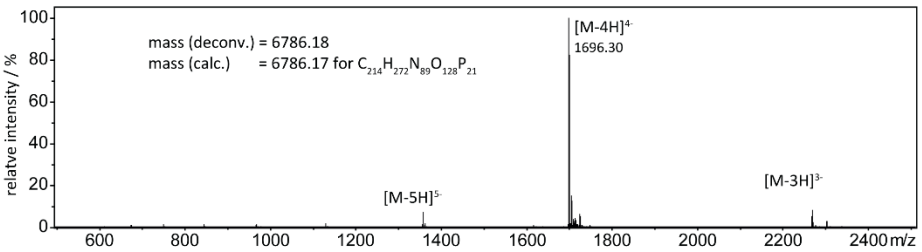

htelL$^{R}_{3}$M

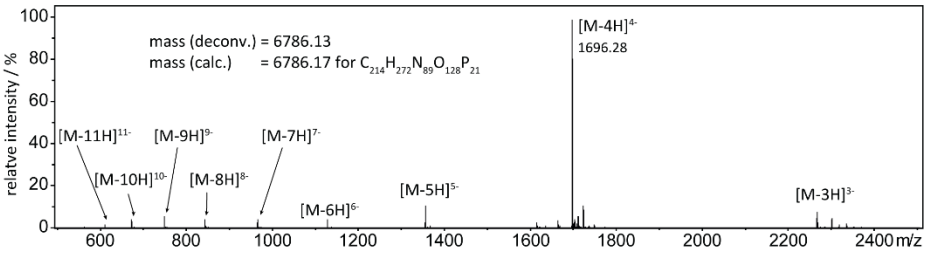

htel**L**$^{s}_{3}$H

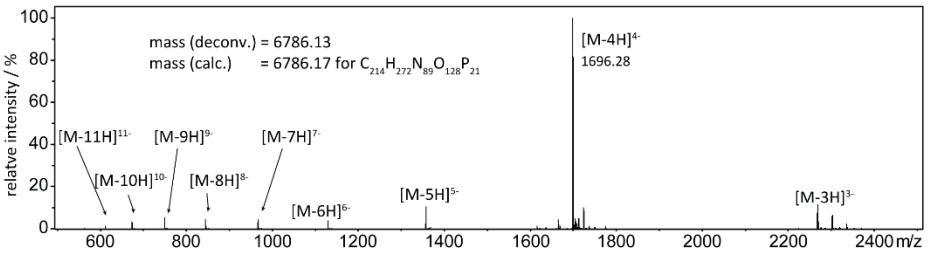

htel**L**$^{s}_{3}$I

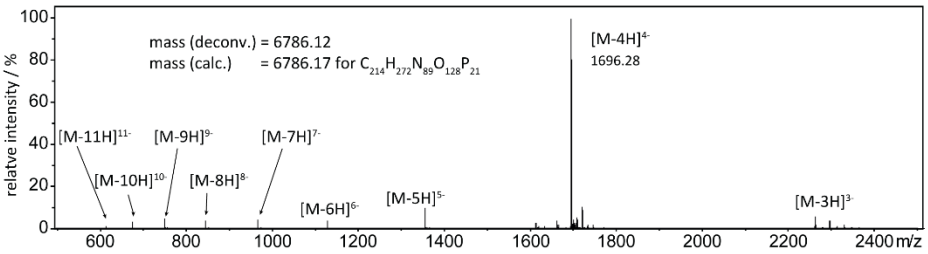

htel**L**$^{s}_{3}$J

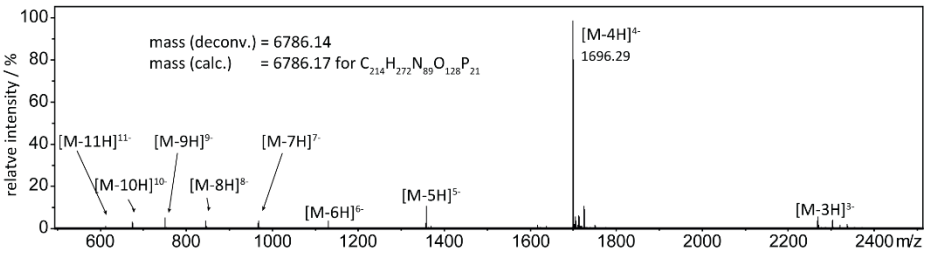

htel**L**$^{s}_{3}$K

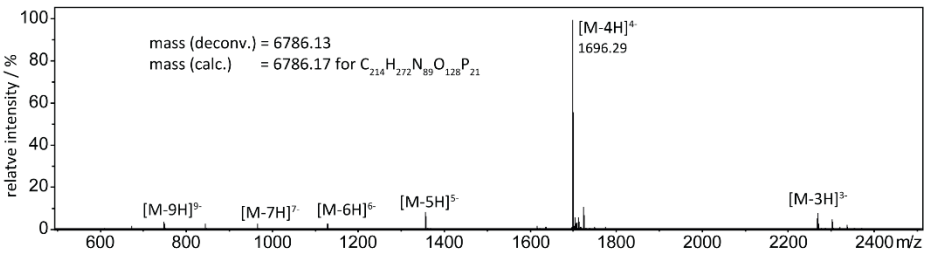

htel**L**$^{s}_{3}$L

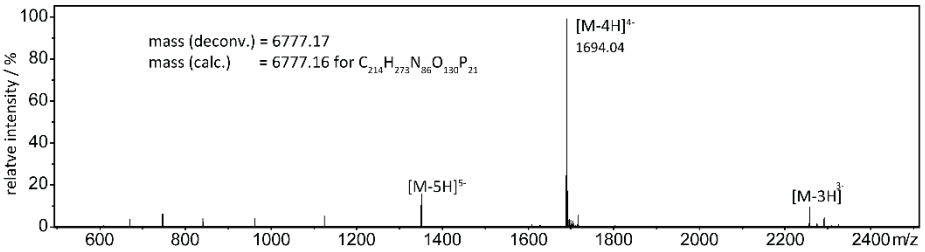

htel$\mathbf{L}^{R}_{3}$B

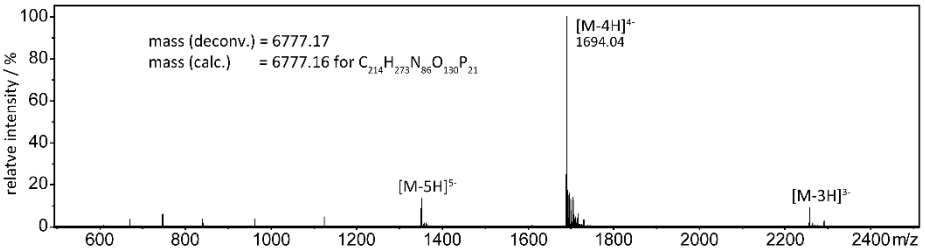

htel$\mathbf{L}^{R}_{3}$D

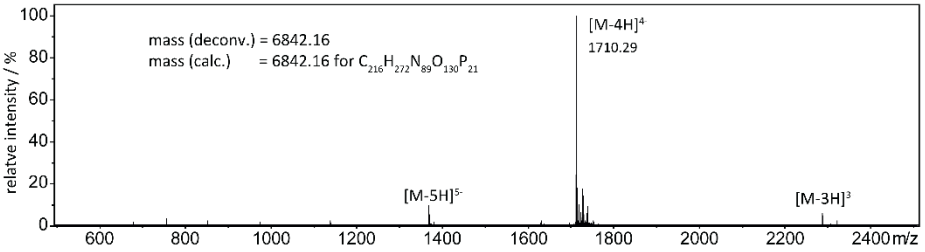

htel$\mathbf{L}^{R}_{2}$F

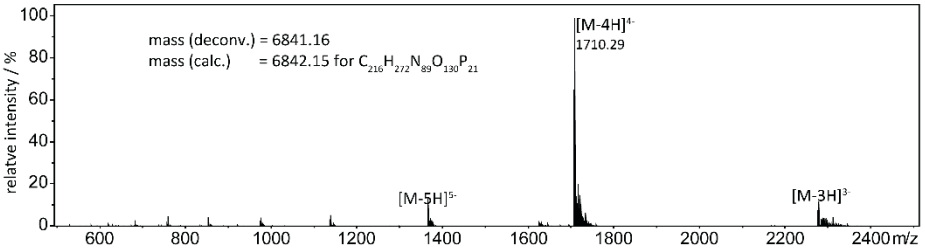

htel$\mathbf{L}^{R}_{2}$G

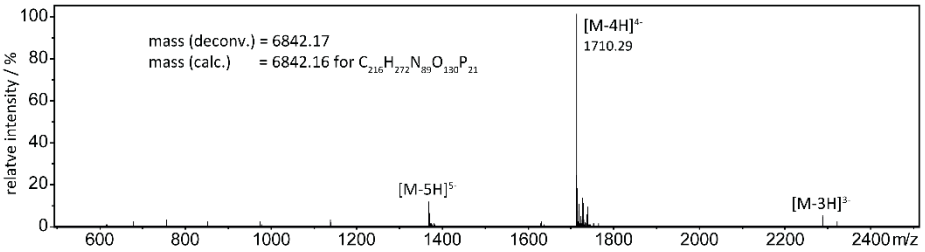

htel$\mathbf{L}^{R}_{2}$H

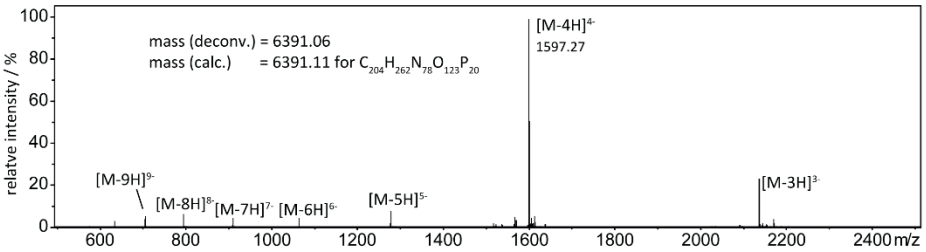

htel**L**$^{s}_{3}$O

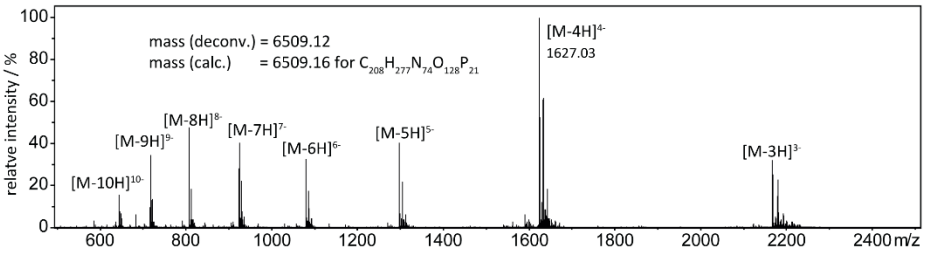

htel**L**$^{s}_{6}$

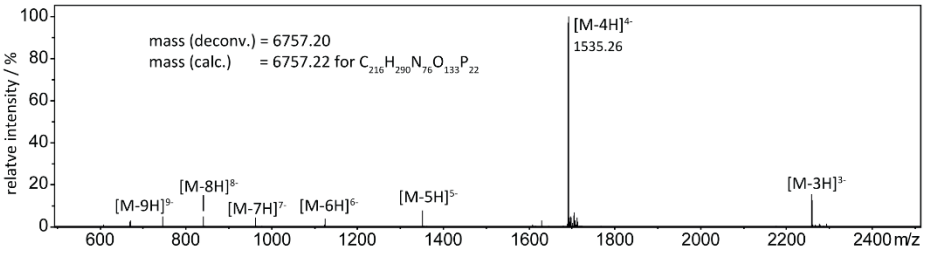

htel**L**$^{s}_{7}$

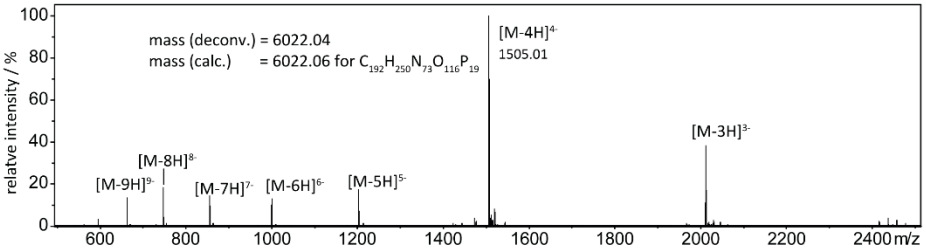

htel**L**$^{s}_{4}$B

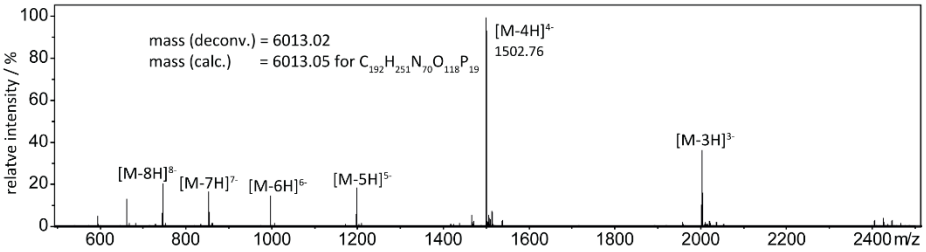

htel**L**$^{s}_{4}$C

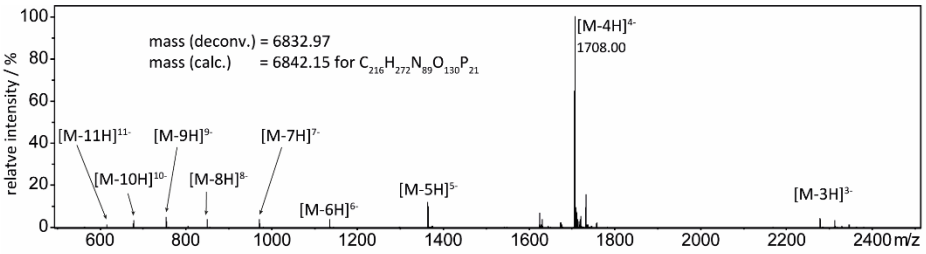

htel**L**$^{s}_{2}$G

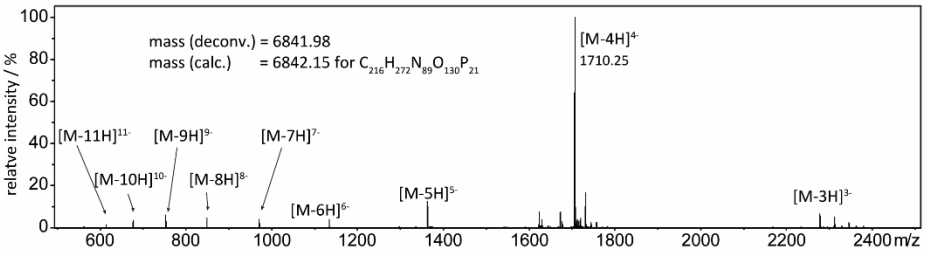

htel**L**$^{s}_{2}$H

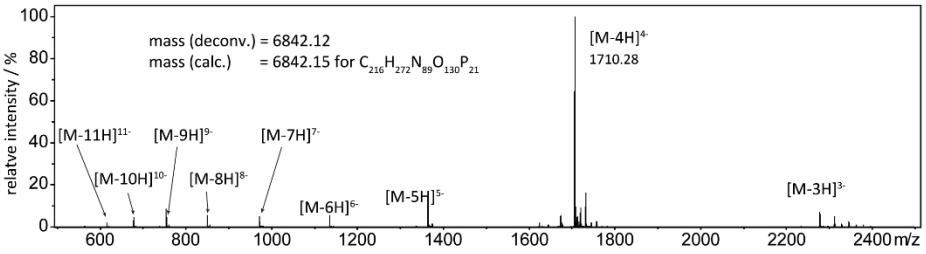

htel**L**$^{s}_{2}$I

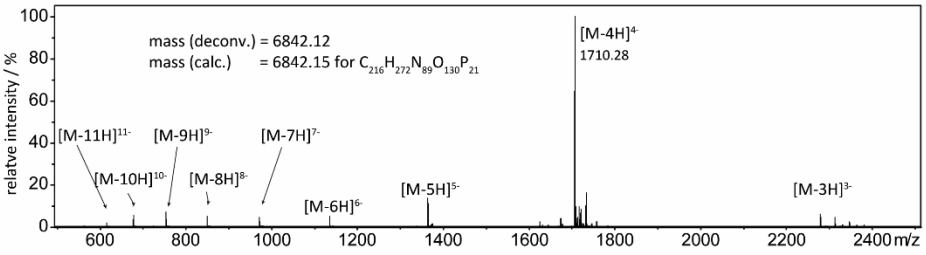

htel**L**$^{s}_{2}$J

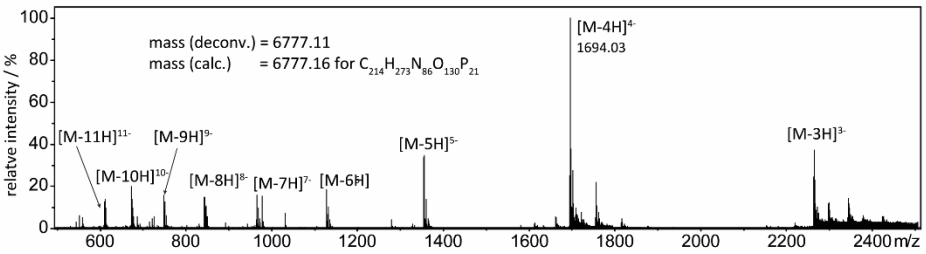

htel**L**$^{s}_{3}$G

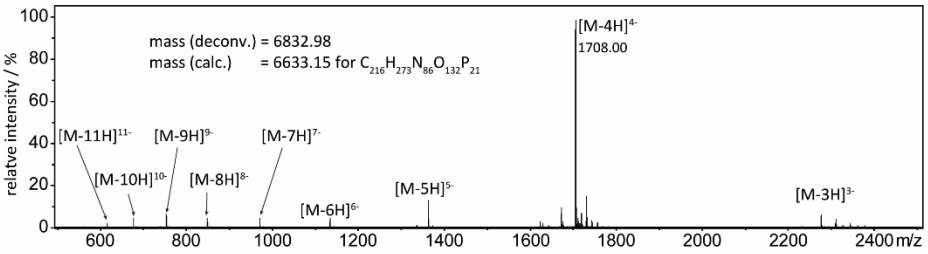

htel**L**$^{s}_{2}$C

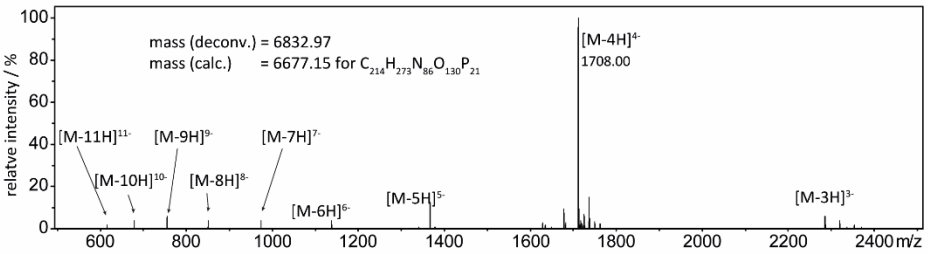

htel**L**$^{s}_{2}$D

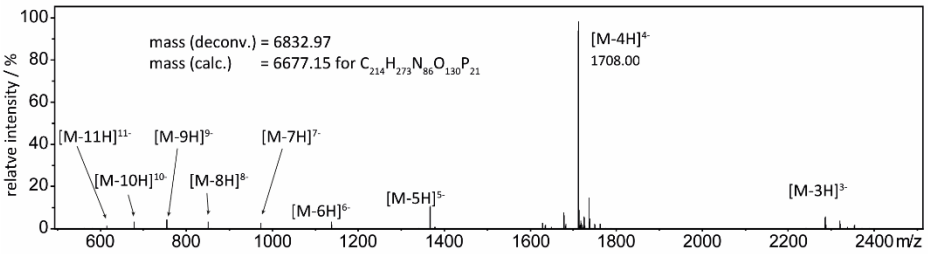

htel**L**$^{s}_{2}$A

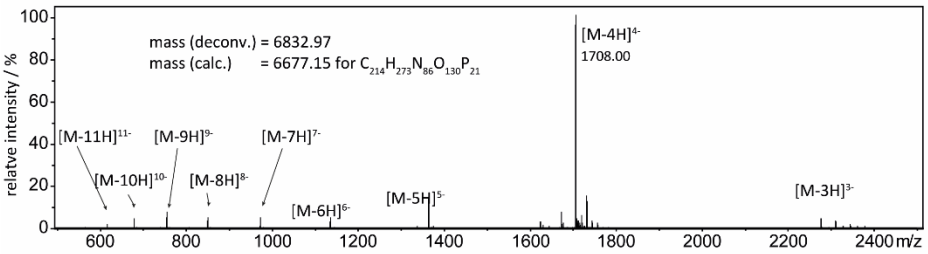

htel**L**$^{s}_{2}$E

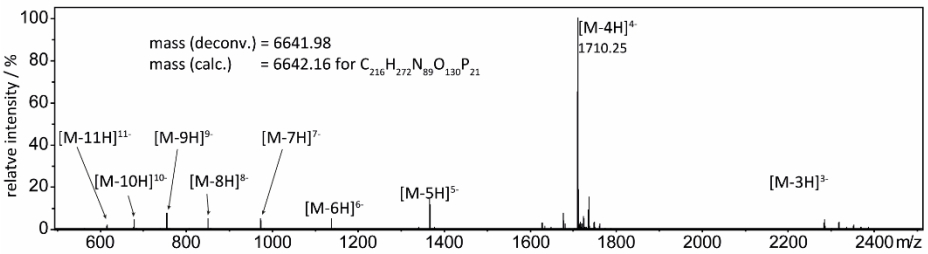

htel**L**$^{s}_{2}$F

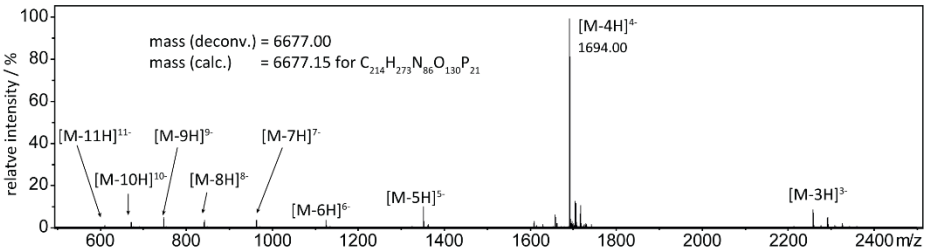

htel**L**$^{s}_{3}$A

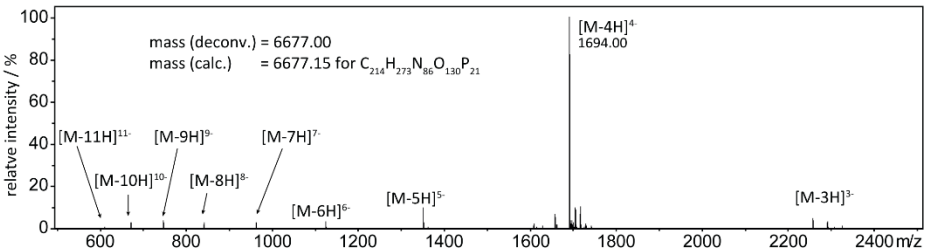

htel**L**$^{s}_{3}$C

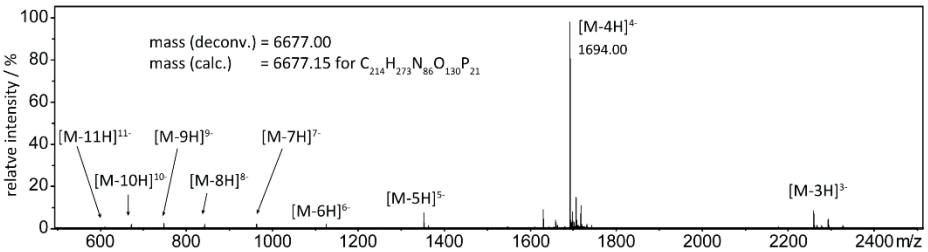

htel**L**$^{s}_{3}$D

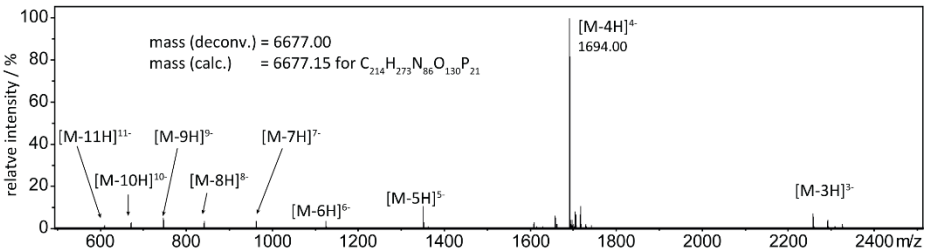

htel**L**$^{s}_{3}$E

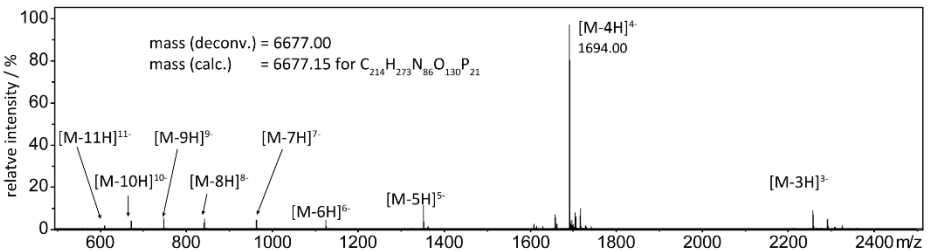

htel**L**$^{s}_{3}$F

10.4 Additional analytical HPLC traces

htelL$^{R}_{3}$M

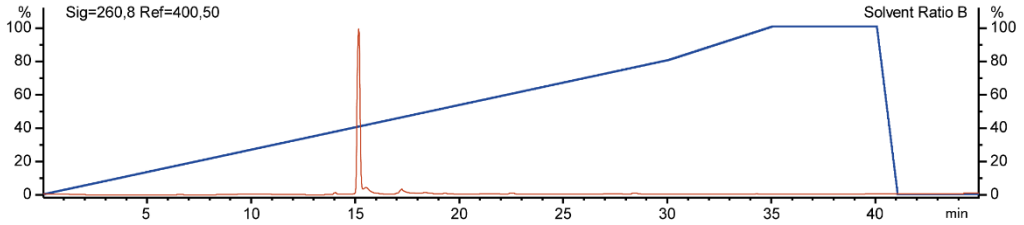

htelL$^{R}_{2}$F

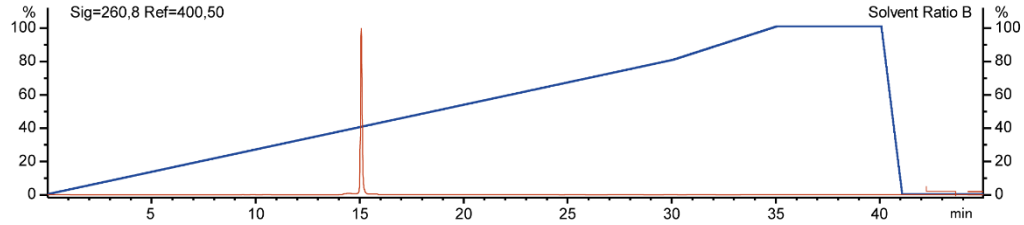

htelL$^{R}_{2}$G

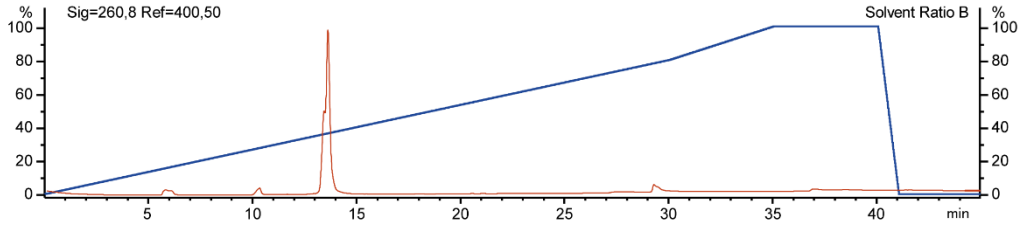

htelL$^{R}_{2}$H

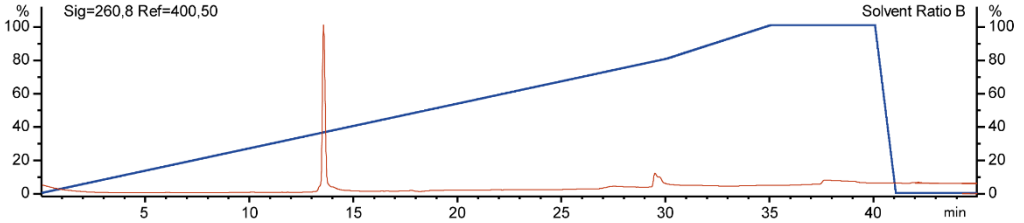

htelL$^{R}_{2}$I

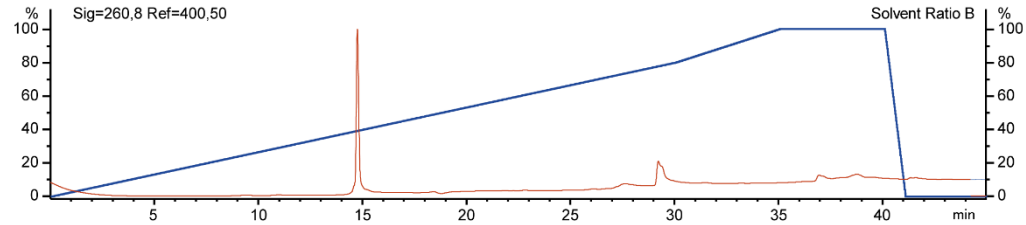

htelL$^{R}_{3}$G

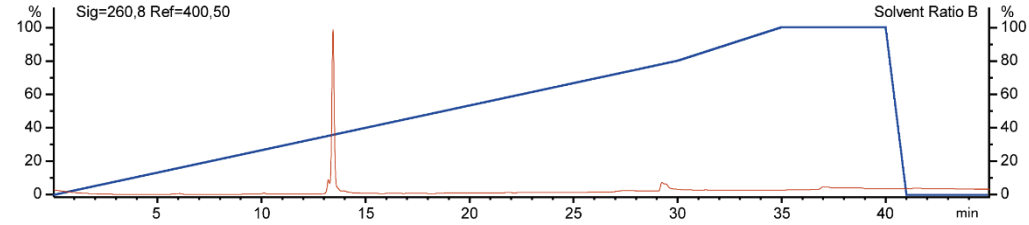

htelL$^{s}_{2}$I

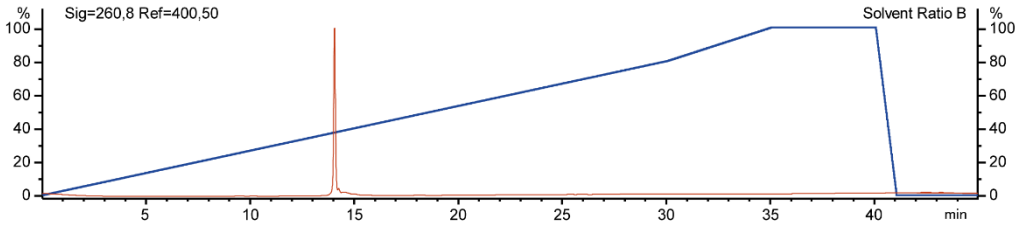

htelL$^{s}_{2}$J

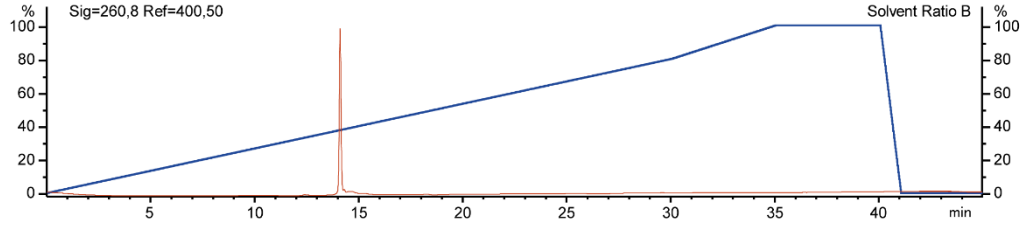

htelL$^{s}_{3}$G

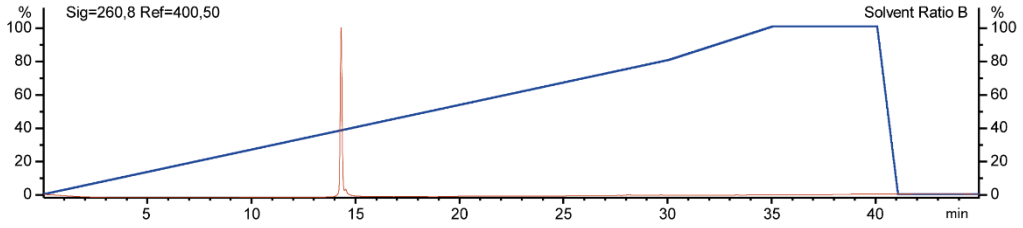

htelL$^{s}_{3}$H

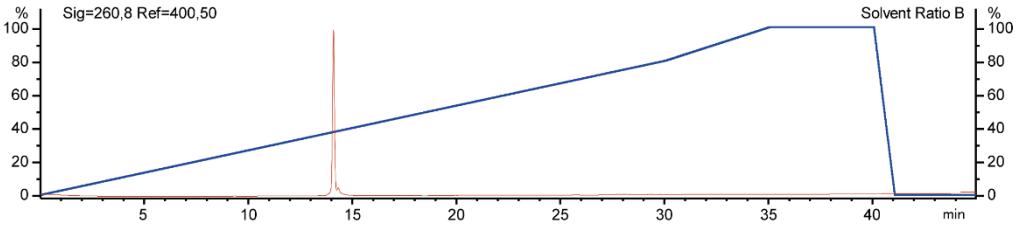

htelL$^{s}_{3}$I

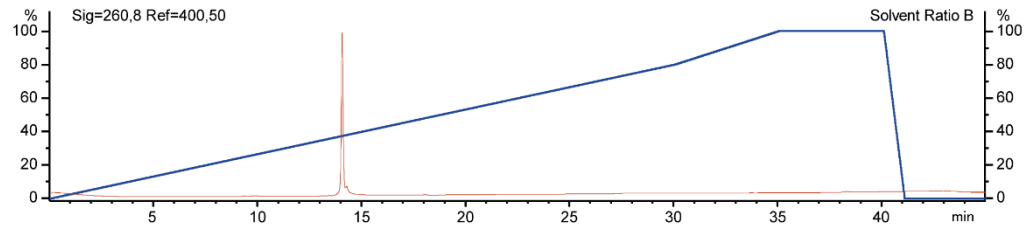

htelL$^{s}_{3}$J

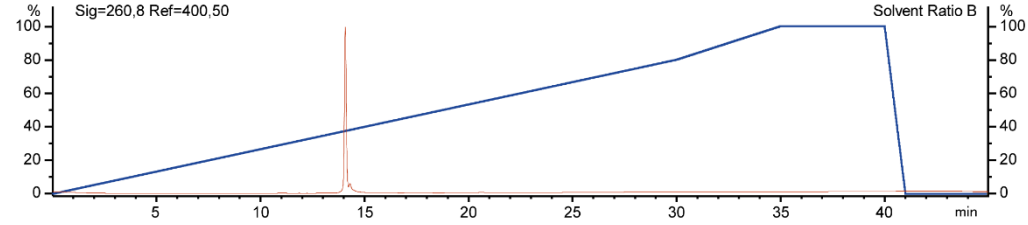

htel**L**$^{s}_{2}$C

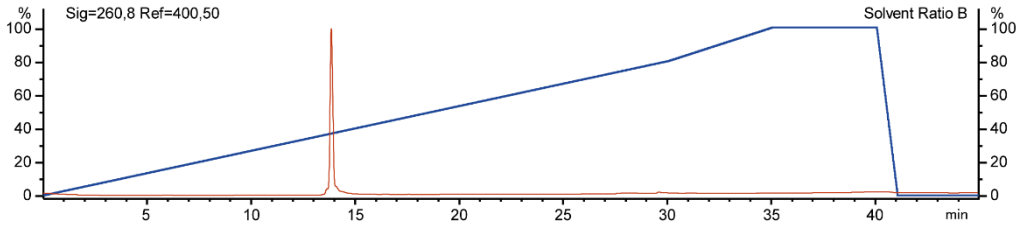

htel**L**$^{s}_{2}$D

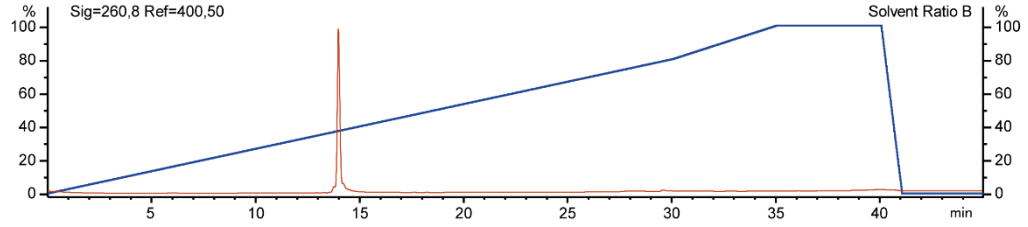

htel**L**$^{s}_{2}$A

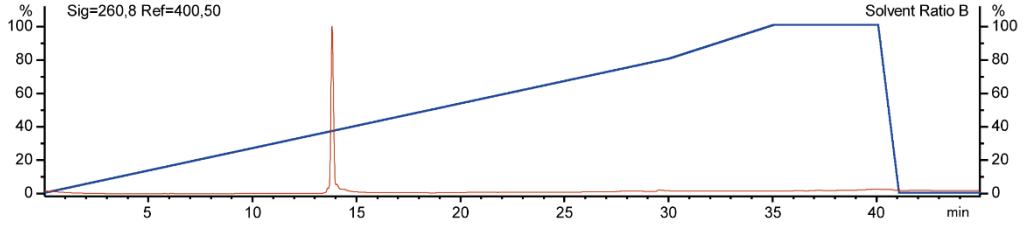

htel**L**$^{s}_{2}$E

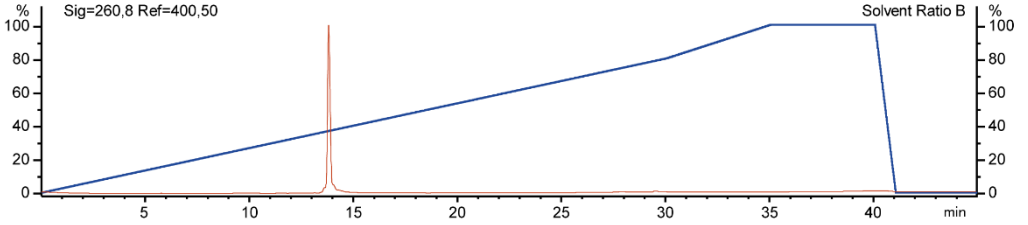

htel**L**$^{s}_{2}$F

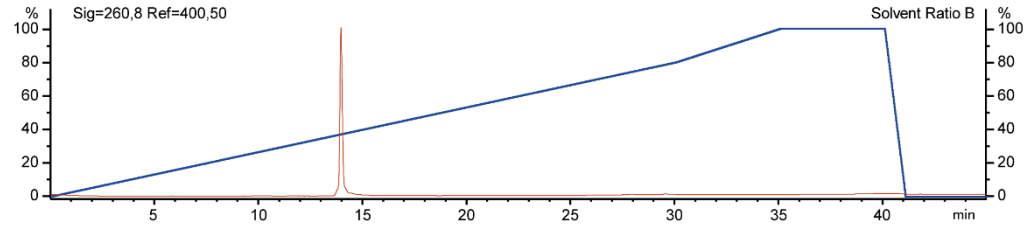

htel**L**$^{s}_{2}$G

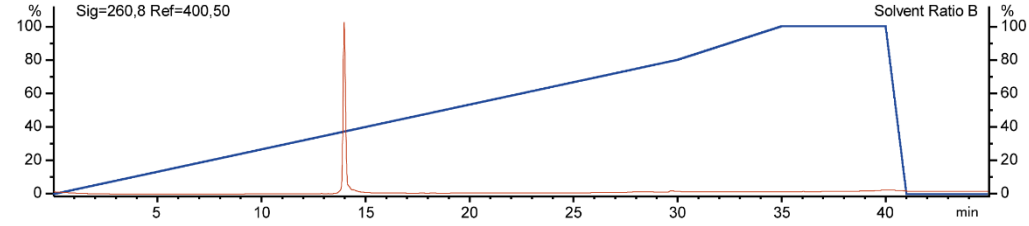

htel**L**$^{s}_{2}$H

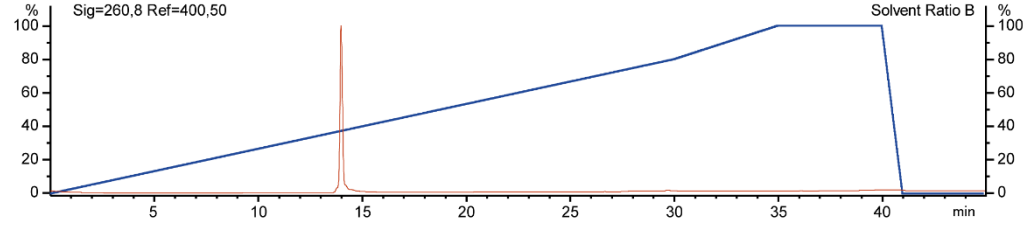

htelL$^{R}_{3}$B

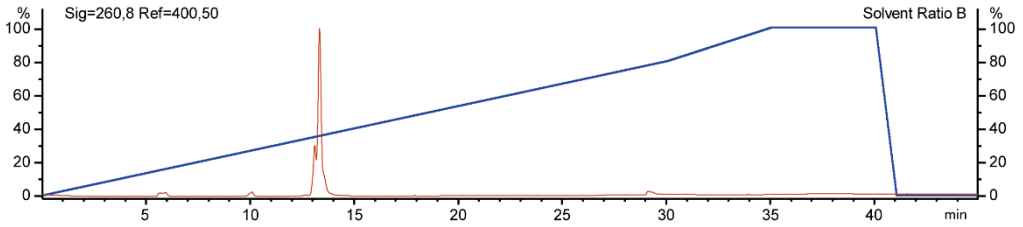

htelL$^{R}_{3}$D

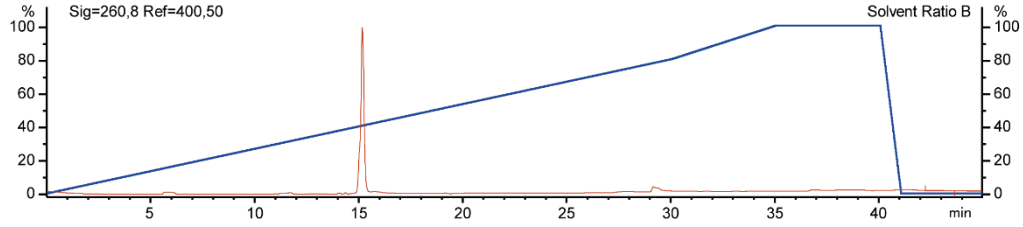

htelL$^{R}_{3}$H

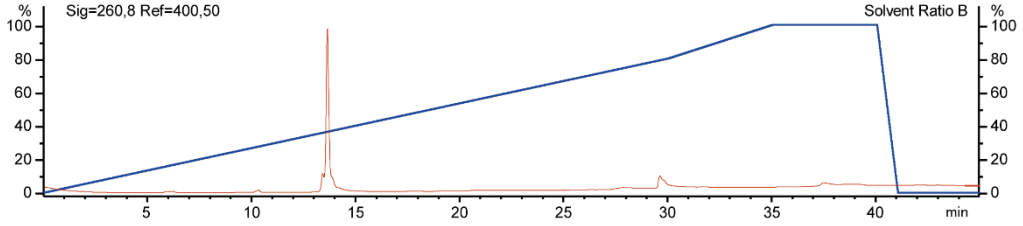

htelL$^{R}_{3}$I

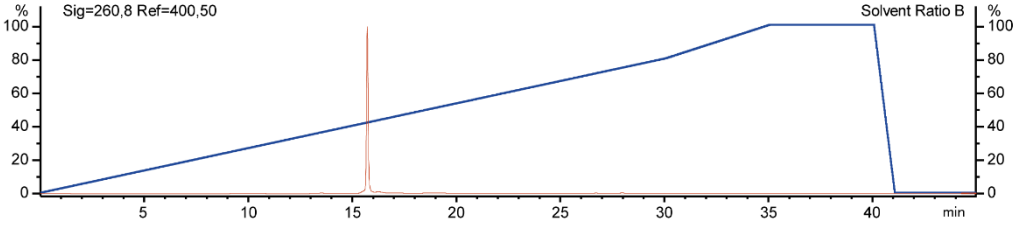

htelL$^{R}_{3}$J

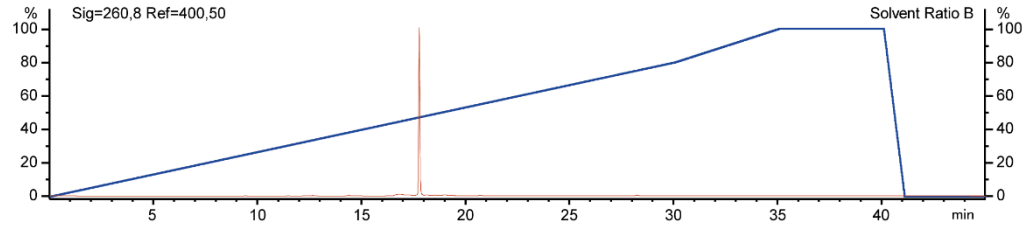

htelL$^{R}_{3}$K

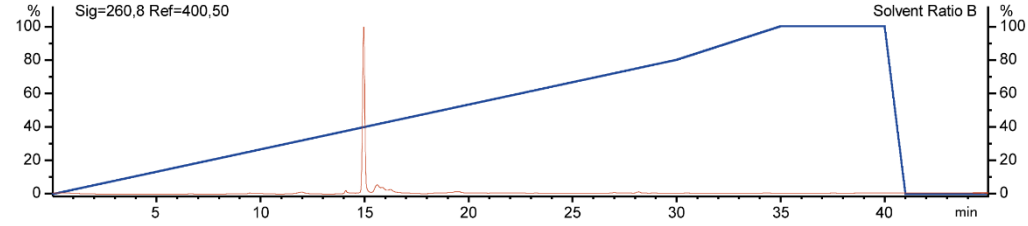

htelL$^{R}_{3}$L

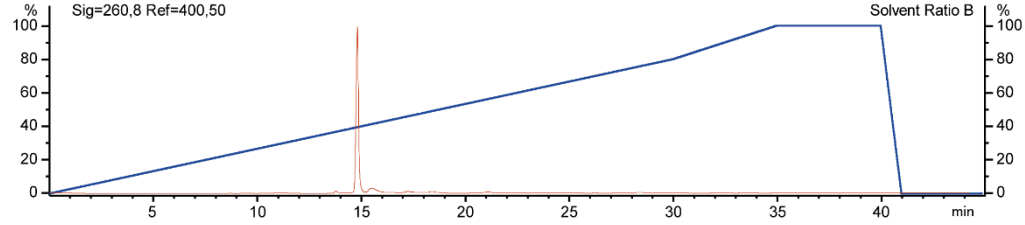

htelL$^{s}_{2}$B

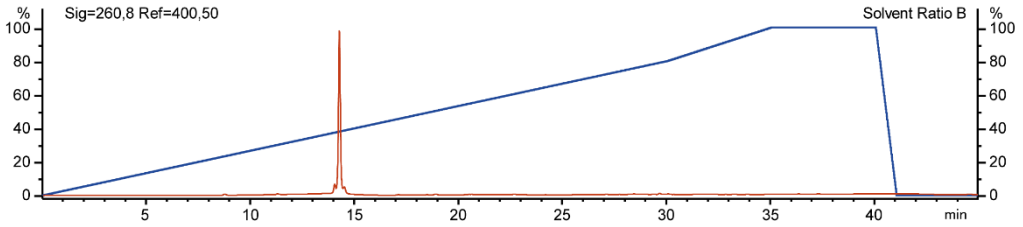

htelL$^{s}_{3}$B

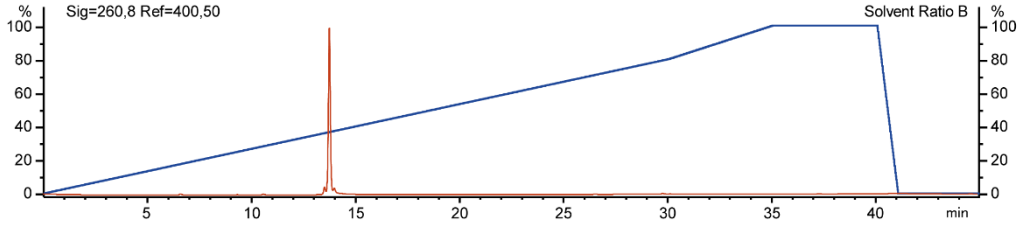

htelL$^{s}_{3}$A

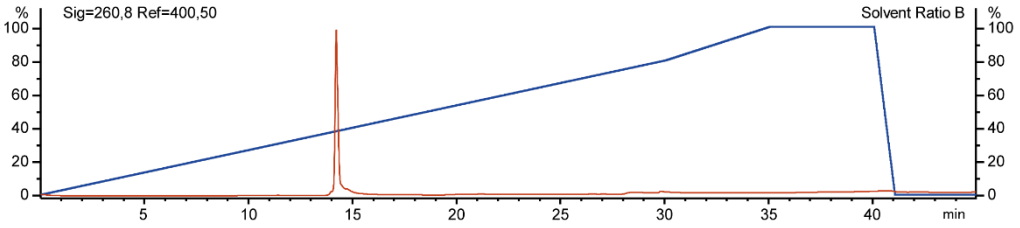

htelL$^{s}_{3}$C

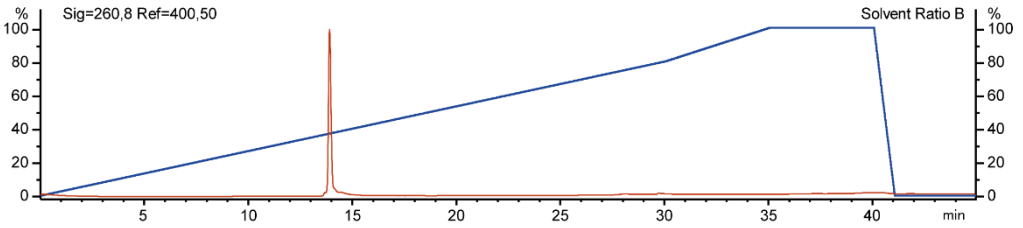

htelL$^{s}_{3}$D

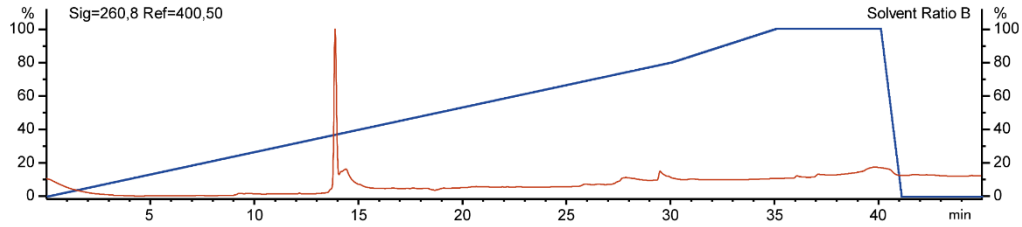

htelL$^{s}_{3}$E

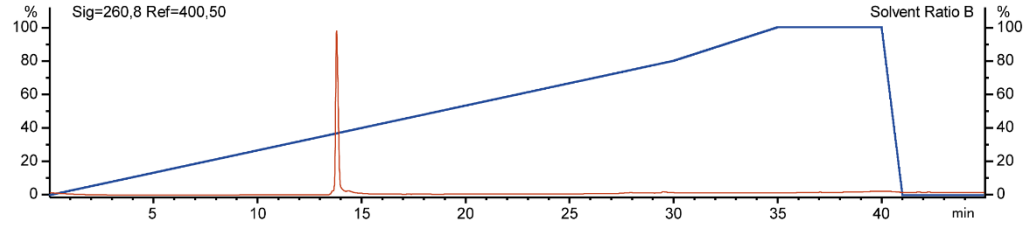

htelL$^{s}_{3}$F

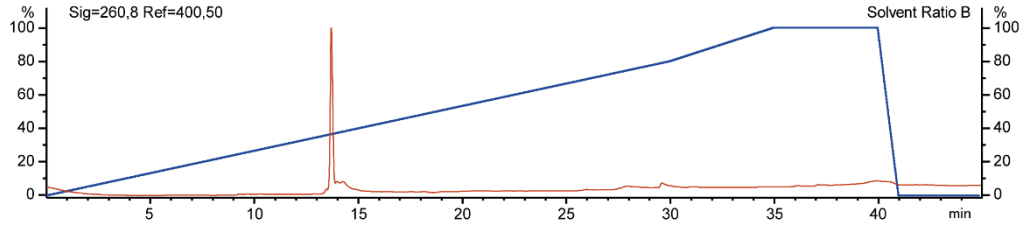

htelL$^{s}_{4}$A

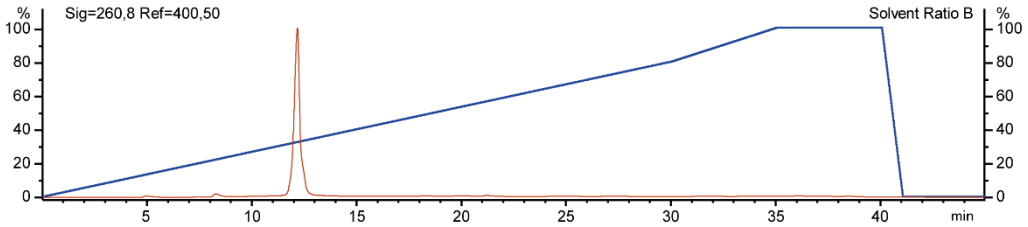

htelL$^{s}_{6}$

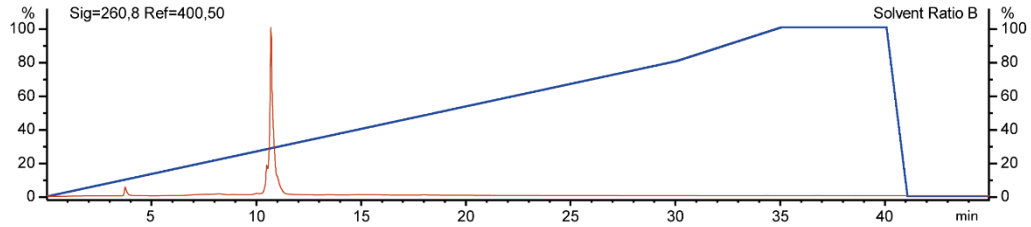

htelL$^{s}_{7}$

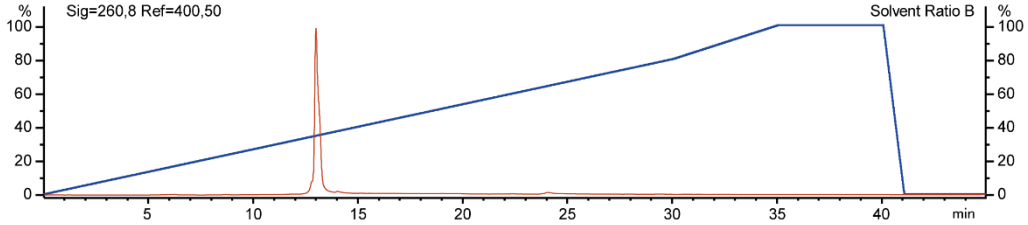

htelL$^{s}_{3}$K

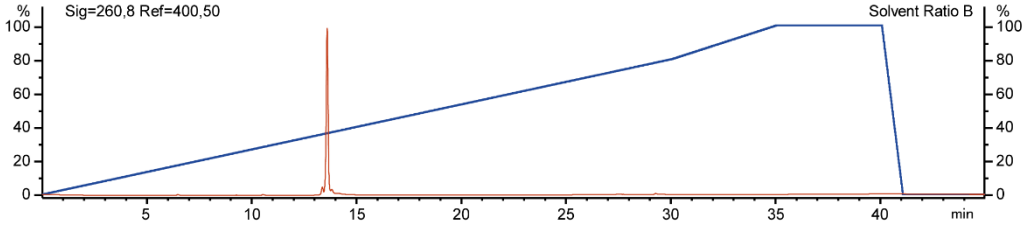

htelL$^{s}_{3}$L

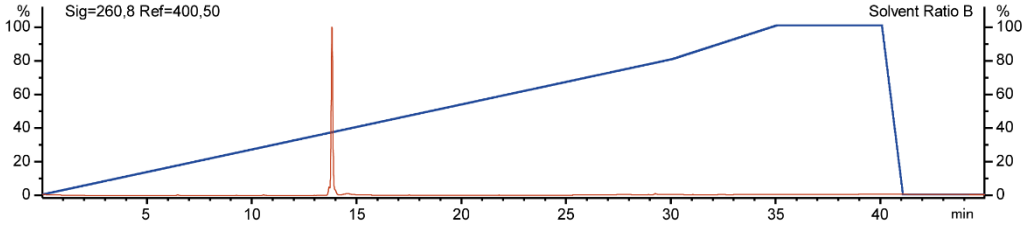

htelL$^{s}_{3}$M

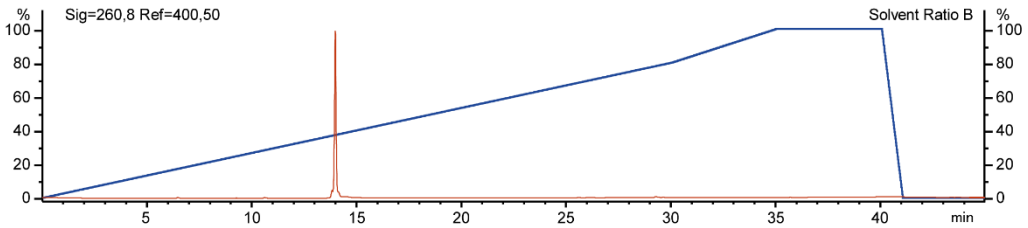

htel**L**$^{s}_{4}$B

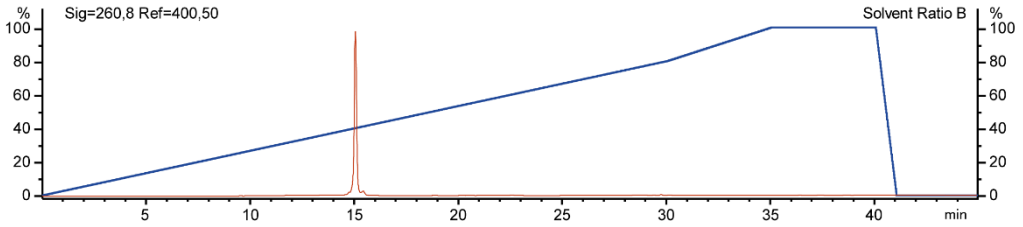

htel**L**$^{s}_{4}$C

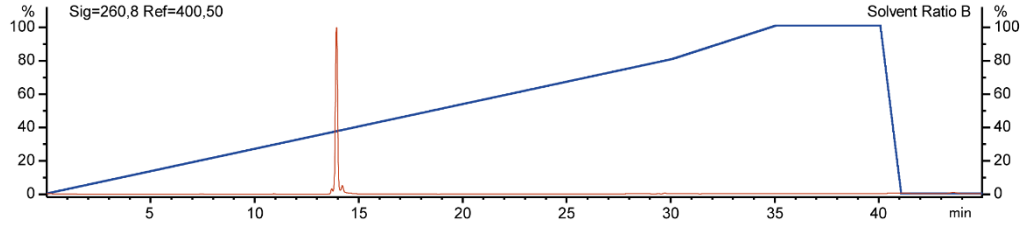

htel**L**$^{s}_{2}$K

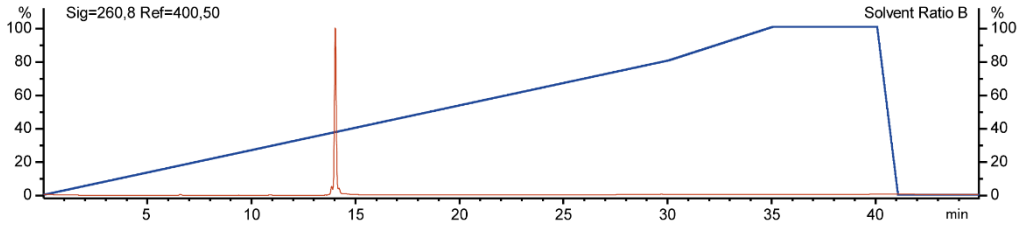

htel**L**$^{s}_{2}$L

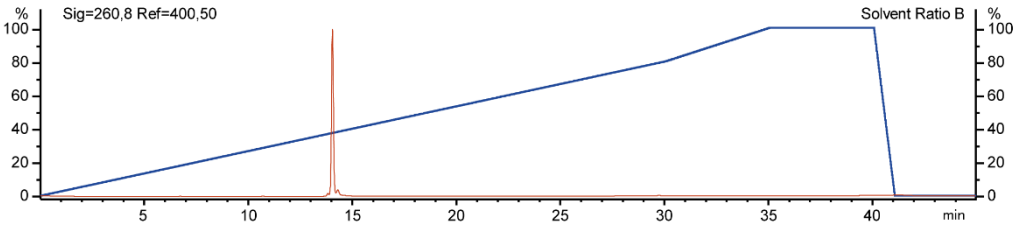

htel**L**$^{s}_{3}$N

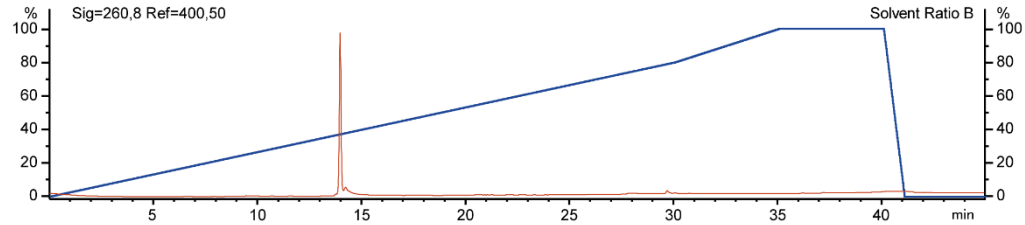

htel**L**$^{s}_{2}$M

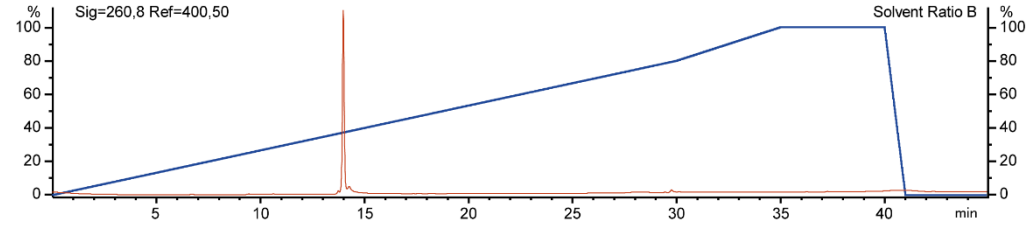

htel**L**$^{s}_{3}$O

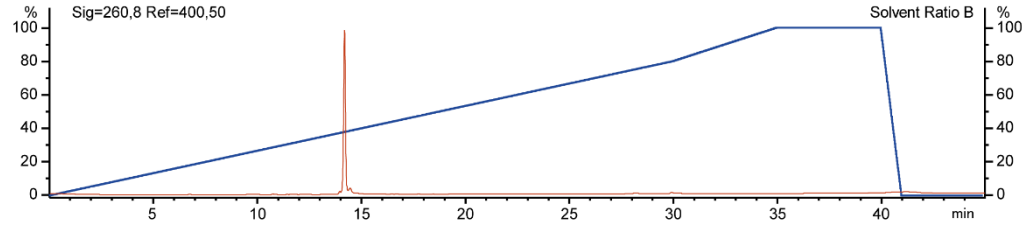

10.5 Abbreviations

3-HPA	3-hydroxypicolinic acid
A	adenine
ACN	acetonitrile
ATCUN	amino terminal Cu^{II}- and Ni^{II}-binding
Bp	base pair
BTT	5-(benzylthio)-1*H*-tetrazole
C	cytosin
CAP A/B	capping A/B
CCS	collisional cross section
CD	circular dichroism
CEDIP-Cl	2-Cyanoethyl *N,N*-diisopropylchlorophosphoramidite
CPG	controlled pore glass
DCA	dichloroacetic acid
DIPEA	diisopropyl ethyl amine
DMAP	4-dimethylamino pyridine
DMF	dimethyl formamide
DMSO	dimethyl sulfoxide
DMT	4,4-dimethoxytrityl
DNA	deoxyribonucleic acid
ds	double strand
EDTA	ethylenediaminetetraacetic acid
ESI-MS	Electron Spray Ionisation Mass Spectrometry
EPR	electron paramagnetic resonance
ESR	Elektronenspinresonanz
G	guanine
GHL	H-Gly-His-Lys-OH (tripeptide)
HP	hydroxypyridone
HPLC	high performance liquid chromatography
Htel	human telomeric repeat
Hz	Hertz
J	coupling constant
LiCaco	lithium cacodylate
MALDI-TOF	matrix-assisted laser desorption/ionization time of flight
MeOH	Methanol
MOF	metal organic framework
NEt_3	triethylamine
NMR	Nuclear Magnetic Resonance
ppm	parts per million
rt	room temperature
S	salen
SELEX	Systematic Evolution of Ligands by EXponential Enrichment

ss	single strand
$T_{1/2}$	non-equilibrium denaturation temperature
T	thymine
tba	thrombin binding aptamer
TDS	thermal difference spectra
TEAA	triethyl ammonium acetate
TIMS	trapped ion mobility spectrometry
TLC	thin layer chromatography
T_m	equilibrium denaturation temperature
ttel	*Tetrahymena* telomeric repeat
UV	ultraviolet-visible

NOTE OF THANKS

Special thanks to my supervisor Prof. Guido H. Clever for the great opportunity to work in an international group with the finest laboratory equipment. It was a great atmosphere, and I enjoyed the time being there.

Many thanks to Prof. Dr. Hannes Mutschler as co-examiner of my dissertation.

I would like to thank the hole Clever-Lab (außer Lukas) for the nice movie nights, group trips and so on.

A special thanks goes to Roland Sigel, Silke Johannsen and Zenghui Wang for the great time in Zurich and the help with NMR spectroscopy of DNA G-quadruplex structures.

I would like to thank my Bachelor students and my lab trainees for helping me in the lab and for their exciting results.

Further I would like to thank Prof. Waldmann for access to the MALDI-TOF spectrometer and Dr. Raphael Gasper-Schoenenbruecher for help with DNA crystallization setups.

Financial support from the Deutsche Forschungsgemeinschaft (DFG, German Research Foundation) under Germany's Excellence Strategy - EXC 2033 - 390677874 – RESOLV is thankfully acknowledged.

Meiner Freundin Vanessa möchte ich danken, dass sie immer mit mir Geduld hatte und zu mir gestanden hat, selbst wenn ich gestresst war oder wieder viel zu lange in der Uni geblieben bin.

Zum Schluss möchte ich meiner Familie für den bedingungslosen Rückhalt danken, besonders meinen Eltern, dass sie mir all das überhaupt erst ermöglicht haben, indem sie mich die ganzen Jahre motiviert und mit all ihren Möglichkeiten unterstützt haben.

Literature

[1] C. M. Dobson, C. M. Dobson, *Trends Biochem. Sci.* **1999**, *24*, 329–332.
[2] P. F. Xu, H. Noh, J. H. Lee, D. W. Domaille, M. A. Nakatsuka, A. P. Goodwin, J. N. Cha, *Mater. Today* **2013**, *16*, 290–296.
[3] J. Yang, I. Anishchenko, H. Park, Z. Peng, S. Ovchinnikov, D. Baker, *Proc. Natl. Acad. Sci.* **2020**, *117*, 1496–1503.
[4] M. L. Bochman, K. Paeschke, V. A. Zakian, *Nat. Rev. Genet.* **2012**, *13*, 770–780.
[5] N. Saini, Y. Zhang, K. Usdin, K. S. Lobachev, *Biochimie* **2013**, *95*, 117–123.
[6] H. Abou Assi, M. Garavís, C. González, M. J. Damha, *Nucleic Acids Res.* **2018**, *46*, 8038–8056.
[7] B. F. Eichman, M. Ortiz-Lombardía, J. Aymamí, M. Coll, P. S. Ho, *J. Mol. Biol.* **2002**, *320*, 1037–1051.
[8] A. Oleksi, A. G. Blanco, R. Boer, I. Usón, J. Aymamí, A. Rodger, M. J. Hannon, M. Coll, *Angew. Chem. Int. Ed.* **2006**, *45*, 1227–1231.
[9] J. Spiegel, S. Adhikari, S. Balasubramanian, *Trends Chem.* **2019**, *2*, 123–136.
[10] R. Hänsel-Hertsch, M. D. Antonio, S. Balasubramanian, *Nat. Rev. Mol. Cell. Bio.* **2017**, *18*, 279–284.
[11] V. T. Mukundan, N. Q. Do, A. T. Phan, *Nucleic Acids Res.* **2011**, *39*, 8984–8991.
[12] A. T. Phan, V. Kuryavyi, J.-B. Ma, A. Faure, M.-L. Andréola, D. J. Patel, *Proc. Natl. Acad. Sci.* **2005**, *102*, 634–639.
[13] D. J. Patel, A. T. Phan, V. Kuryavyi, *Nucleic Acids Res.* **2007**, *35*, 7429–7455.
[14] V. Esposito, L. Pirone, L. Mayol, E. Pedone, A. Virgilio, A. Galeone, *Biochimie* **2016**, *127*, 19–22.
[15] Y. Xu, *Chem. Soc. Rev.* **2011**, *40*, 2719–2740.
[16] S. Neidle, *Nat. Rev. Chem.* **2017**, *1*, 0041.
[17] M. Endo, H. Sugiyama, *Acc. Chem. Res.* **2014**, *47*, 1645–1653.
[18] J. S. Kahn, Y. Hu, I. Willner, *Acc. Chem. Res.* **2017**, *50*, 680–690.
[19] C.-H. Lu, X.-J. Qi, R. Orbach, H.-H. Yang, I. Mironi-Harpaz, D. Seliktar, I. Willner, *Nano Lett.* **2013**, *13*, 1298–1302.
[20] Y. Guo, J. Chen, M. Cheng, D. Monchaud, J. Zhou, H. Ju, *Angew. Chem. Int. Ed.* **2017**, *129*, 16863–16867.
[21] J. Wang, M. Cheng, J. Chen, H. Ju, D. Monchaud, J.-L. Mergny, J. Zhou, *Chem. Commun.* **2020**, DOI 10.1039/c9cc09237d.
[22] R. I. Adeoye, D. S. Osalaye, T. K. Ralebitso-Senior, A. Boddis, A. J. Reid, A. A. Fatokun, A. K. Powell, S. O. Malomo, F. J. Olorunniji, *Catalysts* **2019**, *9*, 613.
[23] S. Yang, W. Liu, R. Nixon, R. Wang, *Nanoscale* **2018**, *10*, 3626–3630.
[24] D. M. Engelhard, J. Nowack, G. H. Clever, *Angew. Chem. Int. Ed.* **2017**, *56*, 11640–11644.
[25] D. M. Engelhard, A. Meyer, A. Berndhäuser, O. Schiemann, G. H. Clever, *Chem. Commun.* **2018**, *54*, 7455–7458.
[26] D. M. Engelhard, R. Pievo, G. H. Clever, *Angew. Chem. Int. Ed.* **2013**, *52*, 12843–12847.
[27] D. M. Engelhard, L. M. Stratmann, G. H. Clever, *Chem. Eur. J.* **2018**, *24*, 2117–2125.
[28] L. M. Stratmann, Y. Kutin, M. Kasanmascheff, G. H. Clever, *Angew. Chem. Int. Ed.* **2020**, DOI 10.1002/anie.202008618.
[29] P. M. Punt, G. H. Clever, *Chem. Sci*. **2019**, *10*, 2513–2518.
[30] P. M. Punt, L. M. Stratmann, S. Sevim, L. Knauer, C. Strohmann, G. H. Clever, *Front. Chem.* **2020**, *8*, 26.
[31] P. M. Punt, G. H. Clever, *Chem. Eur. J.* **2019**, *25*, 13987–13993.
[32] J. M. M. Tan, E. S. P. Wong, K.-L. Lim, *Antioxid. Redox. Sign.* **2009**, *11*, 2119–2134.
[33] G. B. Irvine, O. M. El-Agnaf, G. M. Shankar, D. M. Walsh, *Mol. Med.* **2008**, *14*, 451–464.
[34] G. Ashraf, N. Greig, T. Khan, I. Hassan, S. Tabrez, S. Shakil, I. Sheikh, S. Zaidi, M. Akram, N. Jabir, C. Firoz, A. Naeem, I. Alhazza, G. Damanhouri, M. Kamal, *CNS. Neurol. Disord.* **2014**, *13*, 1280–1293.
[35] E. Nir, K. Kleinermanns, M. S. de Vries, *Nature* **2000**, *408*, 949–951.
[36] J. A. Walmsley, B. L. Sagan, *Biopolymers* **1986**, *25*, 2149–2172.
[37] M. Gao, B. Harish, M. Berghaus, R. Seymen, L. Arns, S. A. McCallum, C. A. Royer, R. Winter, *Sci. Rep.* **2017**, *7*, 9864.
[38] J. D. Watson, F. H. C. Crick, *Nature* **1953**, *171*, 737–738.
[39] J. D. Watson, F. H. C. Crick, *Nature* **1953**, *171*, 964–967.
[40] M. H. F. Wilkins, W. E. Seeds, A. R. Stokes, H. R. Wilson, *Nature* **1953**, *172*, 759–762.
[41] J. M. Berg, J. L. Tymoczko, G. J. G. jr., L. Stryer, *Stryer Biochemie* **2017**, 127–162.
[42] D. Voet, J. G. Voet, *Biochemistry, 4th Edition*, **2010**.
[43] D. R. Whelan, T. J. Hiscox, J. I. Rood, K. R. Bambery, D. McNaughton, B. R. Wood, *J. R. Soc. Interface* **2014**, *11*, 20140454.
[44] S. C. Ha, K. Lowenhaupt, A. Rich, Y.-G. Kim, K. K. Kim, *Nature* **2005**, *437*, 1183–1186.
[45] P. C. Champ, S. Maurice, J. M. Vargason, T. Camp, P. S. Ho, *Nucleic Acids Res.* **2004**, *32*, 6501–6510.
[46] D. R. Duckett, D. M. Lilley, *Embo J.* **1990**, *9*, 1659–1664.
[47] G. Laughlan, A. Murchie, D. Norman, M. Moore, P. Moody, D. Lilley, B. Luisi, *Science* **1994**, *265*, 520–524.
[48] M. D. Frank-Kamenetskii, S. M. Mirkin, *Annu. Rev. Biochem.* **2003**, *64*, 65–95.
[49] S. Haider, S. Neidle, *Meth. Mol. Biol.* **2009**, *608*, 17–37.

[50] S. Neidle, M. A. Read, *Biopolymers* **2001**, *56*, 195–208.
[51] A. Bedrat, L. Lacroix, J.-L. Mergny, *Nucleic Acids Res.* **2016**, *44*, 1746–1759.
[52] K. Hoogsteen, *Acta Cryst.* **1963**, *16*, 907–916.
[53] S. Neidle, *Nat. Rev. Chem.* **2017**, *1*, 0041.
[54] H. Masai, N. Kakusho, R. Fukatsu, Y. Ma, K. Iida, Y. Kanoh, K. Nagasawa, *J. Biol. Chem.* **2018**, *293*, 17033–17049.
[55] J. Gros, F. Rosu, S. Amrane, A. D. Cian, V. Gabelica, L. Lacroix, J.-L. Mergny, *Nucleic Acids Res.* **2007**, *35*, 3064–3075.
[56] M. L. Gill, S. A. Strobel, J. P. Loria, *Nucleic Acids Res.* **2006**, *34*, 4506–4514.
[57] F. W. Kotch, J. C. Fettinger, J. T. Davis, *Org. Lett.* **2000**, *2*, 3277–3280.
[58] D. Bhattacharyya, G. M. Arachchilage, S. Basu, *Front Chem* **2016**, *4*, 38.
[59] J. L. Huppert, S. Balasubramanian, *Nucleic Acids Res.* **2005**, *33*, 2908–2916.
[60] A. K. Todd, M. Johnston, S. Neidle, *Nucleic Acids Res.* **2005**, *33*, 2901–2907.
[61] A. Ambrus, D. Chen, J. Dai, T. Bialis, R. A. Jones, D. Yang, *Nucleic Acids Res.* **2006**, *34*, 2723–2735.
[62] J. Zhou, A. Bourdoncle, F. Rosu, V. Gabelica, J. Mergny, *Angew. Chem. Int. Ed.* **2012**, *51*, 11002–11005.
[63] C. Liu, B. Zhou, Y. Geng, D. Y. Tam, R. Feng, H. Miao, N. Xu, X. Shi, Y. You, Y. Hong, B. Z. Tang, P. K. Lo, V. Kuryavyi, G. Zhu, *Chem. Sci.* **2018**, *10*, 218–226.
[64] G. N. Parkinson, M. P. H. Lee, S. Neidle, *Nature* **2002**, *417*, 876–880.
[65] K. W. Lim, S. Amrane, S. Bouaziz, W. Xu, Y. Mu, D. J. Patel, K. N. Luu, A. T. Phan, *J. Am. Chem. Soc.* **2009**, *131*, 4301–4309.
[66] Y. Wang, D. J. Patel, *Structure* **1993**, *1*, 263–282.
[67] E. Largy, J.-L. Mergny, V. Gabelica, *Metal Ions Life Sci.* **2016**, *16*, 203–258.
[68] D. Bhattacharyya, G. M. Arachchilage, S. Basu, *Front. Chem.* **2016**, *4*, 38.
[69] C. C. Hardin, T. Watson, M. Corregan, C. Bailey, *Biochemistry* **1992**, *31*, 833–841.
[70] E. A. Venczel, D. Sen, *Biochemistry* **1993**, *32*, 6220–6228.
[71] Y. Ma, K. Iida, K. Nagasawa, *Biochem. Biophys. Res. Commun.* **2020**, *531*, 3–17.
[72] J.-L. Mergny, J. Li, L. Lacroix, S. Amrane, J. B. Chaires, *Nucleic Acids Res.* **2005**, *33*, e138.
[73] J.-L. Mergny, L. Lacroix, *Oligonucleotides* **2003**, *13*, 515–537.
[74] J. Mergny, L. Lacroix, *Curr. Protoc. Nucleic Acid Chem.* **2009**, *37*, 17.1.
[75] J. Kypr, I. Kejnovská, D. Renciuk, M. Vorlícková, *Nucleic Acids Res.* **2009**, *37*, 1713–1725.
[76] M. Vorlíčková, I. Kejnovská, J. Sagi, D. Renčiuk, K. Bednářová, J. Motlová, J. Kypr, *Methods* **2012**, *57*, 64–75.
[77] M. Vorlíčková, I. Kejnovská, K. Bednářová, D. Renčiuk, J. Kypr, *Chirality* **2012**, *24*, 691–698.
[78] R. del Villar-Guerra, J. O. Trent, J. B. Chaires, *Angew. Chem. Int. Ed.* **2018**, *57*, 7171–7175.
[79] A. Randazzo, G. P. Spada, M. W. da Silva, *Top. Curr. Chem.* **2012**, *330*, 67–86.
[80] P. Maleki, G. Mustafa, P. Gyawali, J. B. Budhathoki, Y. Ma, K. Nagasawa, H. Balci, *Nucleic Acids Res.* **2019**, *47*, 10744–10753.
[81] K. M. Rahman, K. Tizkova, A. P. Reszka, S. Neidle, D. E. Thurston, *Bioorg. Med. Chem. Lett.* **2012**, *22*, 3006–3010.
[82] R. del Villar-Guerra, J. O. Trent, J. B. Chaires, *Angew. Chem. Int. Ed.* **2018**, *57*, 7171–7175.
[83] Y. Geng, C. Liu, B. Zhou, Q. Cai, H. Miao, X. Shi, N. Xu, Y. You, C. P. Fung, R. U. Din, G. Zhu, *Nucleic Acids Res.* **2019**, *47*, 5395–5404.
[84] V. Singh, M. Azarkh, M. Drescher, J. S. Hartig, *Chem. Commun.* **2012**, *48*, 8258–8260.
[85] V. Singh, M. Azarkh, T. E. Exner, J. S. Hartig, M. Drescher, *Angew. Chem. Int. Ed.* **2009**, *48*, 9728–9730.
[86] A. T. Phan, V. Kuryavyi, J.-B. Ma, A. Faure, M.-L. Andréola, D. J. Patel, *Proc. Natl. Acad. Sci.* **2005**, *102*, 634–639.
[87] M. Adrian, B. Heddi, A. T. Phan, *Methods* **2012**, *57*, 11–24.
[88] L. Haase, J. Dickerhoff, K. Weisz, *Chem. Eur. J.* **2019**, *26*, 524–533.
[89] G. N. Parkinson, M. P. H. Lee, S. Neidle, *Nature* **2002**, *417*, 876–880.
[90] M. Gellert, M. N. Lipsett, D. R. Davies, *Proc. Natl. Acad. Sci.* **1962**, *48*, 2013–2018.
[91] R. Hänsel-Hertsch, M. D. Antonio, S. Balasubramanian, *Nat. Rev. Mol. Cell Biol.* **2017**, *18*, 279–284.
[92] G. Biffi, D. Tannahill, J. McCafferty, S. Balasubramanian, *Nat. Chem.* **2013**, *5*, 182–186.
[93] C. Lin, D. Yang, *Methods Mol Biol.* **2017**, *1587*, 171–196.
[94] A. D. Cian, G. Cristofari, P. Reichenbach, E. D. Lemos, D. Monchaud, M.-P. Teulade-Fichou, K. Shin-ya, L. Lacroix, J. Lingner, J.-L. Mergny, *Proc. Natl. Acad. Sci.* **2007**, *104*, 17347–17352.
[95] O. Mendoza, A. Bourdoncle, J.-B. Boulé, R. M. Brosh, J.-L. Mergny, *Nucleic Acids Res.* **2016**, *44*, 1989–2006.
[96] H. J. Lipps, D. Rhodes, *Trends Cell Biol.* **2009**, *19*, 414–422.
[97] K. Paeschke, S. Juranek, T. Simonsson, A. Hempel, D. Rhodes, H. J. Lipps, *Nat. Struct. Mol. Biol.* **2008**, *15*, 598–604.
[98] K. Paeschke, T. Simonsson, J. Postberg, D. Rhodes, H. J. Lipps, *Nat. Struct. Mol. Biol.* **2005**, *12*, 847–854.
[99] E. M. Rezler, J. Seenisamy, S. Bashyam, M.-Y. Kim, E. White, W. D. Wilson, L. H. Hurley, *J. Am. Chem. Soc.* **2005**, *127*, 9439–9447.
[100] S. Neidle, *FEBS J.* **2010**, *277*, 1118–1125.
[101] S. Lagah, I.-L. Tan, P. Radhakrishnan, R. A. Hirst, J. H. Ward, C. O'Callaghan, S. J. Smith, M. F. G. Stevens, R. G. Grundy, R. Rahman, *Plos One* **2014**, *9*, e86187.

[102] N. H. Campbell, G. N. Parkinson, A. P. Reszka, S. Neidle, *J. Am. Chem. Soc.* **2008**, *130*, 6722–6724.
[103] M. Porru, P. Zizza, M. Franceschin, C. Leonetti, A. Biroccio, *Biochimica Et Biophysica Acta Bba - Gen Subj* **2017**, *1861*, 1362–1370.
[104] C. Padgett, Quarfloxin in Patients With Low to Intermediate Grade Neuroendocrine Carcinoma, https://clinicaltrials.gov/ct2/show/NCT00780663, 12.**2020.**
[105] H. Xu, M. D. Antonio, S. McKinney, V. Mathew, B. Ho, N. J. O'Neil, N. D. Santos, J. Silvester, V. Wei, J. Garcia, F. Kabeer, D. Lai, P. Soriano, J. Banáth, D. S. Chiu, D. Yap, D. D. Le, F. B. Ye, A. Zhang, K. Thu, J. Soong, S. Lin, A. H. C. Tsai, T. Osako, T. Algara, D. N. Saunders, J. Wong, J. Xian, M. B. Bally, J. D. Brenton, G. W. Brown, S. P. Shah, D. Cescon, T. W. Mak, C. Caldas, P. C. Stirling, P. Hieter, S. Balasubramanian, S. Aparicio, *Nat. Commun.* **2017**, *8*, 14432.
[106] D. Drygin, A. Siddiqui-Jain, S. O'Brien, M. Schwaebe, A. Lin, J. Bliesath, C. B. Ho, C. Proffitt, K. Trent, J. P. Whitten, J. K. C. Lim, D. V. Hoff, K. Anderes, W. G. Rice, *Cancer Res.* **2009**, *69*, 7653–7661.
[107] J. Lavrado, H. Brito, P. M. Borralho, S. A. Ohnmacht, N.-S. Kim, C. Leitão, S. Pisco, M. Gunaratnam, C. M. P. Rodrigues, R. Moreira, S. Neidle, A. Paulo, *Sci. Rep.* **2015**, *5*, 9696.
[108] S. Mazzini, R. Gargallo, L. Musso, F. D. Santis, A. Aviñó, L. Scaglioni, R. Eritja, M. D. Nicola, F. Zunino, A. Amatulli, S. Dallavalle, *Int. J. Mol. Sci.* **2019**, *20*, 4927.
[109] S. Asamitsu, S. Obata, Z. Yu, T. Bando, H. Sugiyama, *Molecules* **2019**, *24*, 429.
[110] A. Siddiqui-Jain, C. L. Grand, D. J. Bearss, L. H. Hurley, *Proc. Natl. Acad. Sci.* **2002**, *99*, 11593–11598.
[111] S. Cogoi, A. E. Shchekotikhin, L. E. Xodo, *Nucleic Acids Res.* **2014**, *42*, 8379–8388.
[112] I. Pont, Á. Martínez-Camarena, C. Galiana-Roselló, R. Tejero, M. T. Albelda, J. González-García, R. Vilar, E. García-España, *Chembiochem* **2020**, *21*, 1167–1177.
[113] T. P. Garner, H. E. L. Williams, K. I. Gluszyk, S. Roe, N. J. Oldham, M. F. G. Stevens, J. E. Moses, M. S. Searle, *Org Biomol Chem* **2009**, *7*, 4194–4200.
[114] C. Marchetti, K. G. Zyner, S. A. Ohnmacht, M. Robson, S. M. Haider, J. P. Morton, G. Marsico, T. Vo, S. Laughlin-Toth, A. A. Ahmed, G. D. Vita, I. Pazitna, M. Gunaratnam, R. J. Besser, A. C. G. Andrade, S. Diocou, J. A. Pike, D. Tannahill, R. B. Pedley, T. R. J. Evans, W. D. Wilson, S. Balasubramanian, S. Neidle, *J Med Chem* **2018**, *61*, 2500–2517.
[115] J. Müller, *European Journal Of Inorganic Chemistry* **2008**, *2008*, 3749–3763.
[116] J. Müller, *Coordin Chem Rev* **2019**, *393*, 37–47.
[117] Y. Takezawa, J. Müller, M. Shionoya, *Chem Lett* **2017**, *46*, 622–633.
[118] S. Katz, *Biochim. Biophys. Acta* **1963**, *68*, 240–253.
[119] H. Liu, C. Cai, P. Haruehanroengra, Q. Yao, Y. Chen, C. Yang, Q. Luo, B. Wu, J. Li, J. Ma, J. Sheng, J. Gan, *Nucleic Acids Res.* **2016**, *45*, 2910–2918.
[120] D. A. Megger, J. Müller, *Nucleosides Nucleotides Nucleic Acids* **2009**, *29*, 27–38.
[121] N. M. Smith, S. Amrane, F. Rosu, V. Gabelica, J.-L. Mergny, *Chem. Commun.* **2012**, *48*, 11464–11466.
[122] Y. Tanaka, J. Kondo, V. Sychrovský, J. Šebera, T. Dairaku, H. Saneyoshi, H. Urata, H. Torigoe, A. Ono, *Chem. Commun.* **2015**, *51*, 17343–17360.
[123] H. Yamaguchi, J. Šebera, J. Kondo, S. Oda, T. Komuro, T. Kawamura, T. Dairaku, Y. Kondo, I. Okamoto, A. Ono, J. V. Burda, C. Kojima, V. Sychrovský, Y. Tanaka, *Nucleic Acids Res.* **2013**, *42*, 4094–4099.
[124] A. Ono, S. Cao, H. Togashi, M. Tashiro, T. Fujimoto, T. Machinami, S. Oda, Y. Miyake, I. Okamoto, Y. Tanaka, *Chem. Commun.* **2008**, *0*, 4825–4827.
[125] Y. Tanaka, J. Kondo, V. Sychrovský, J. Šebera, T. Dairaku, H. Saneyoshi, H. Urata, H. Torigoe, A. Ono, *Chem. Commun.* **2015**, *51*, 17343–17360.
[126] J. Kondo, Y. Tada, T. Dairaku, Y. Hattori, H. Saneyoshi, A. Ono, Y. Tanaka, *Nat. Chem.* **2017**, *9*, 956–960.
[127] S. Mandal, M. Hebenbrock, J. Müller, *Inorg. Chim. Acta* **2018**, *472*, 229–233.
[128] J. Müller, *Coord. Chem. Rev.* **2019**, *393*, 37–47.
[129] B. Jash, J. Müller, *Angew. Chem. Int. Ed.* **2018**, *57*, 9524–9527.
[130] I. Schönrath, V. B. Tsvetkov, T. S. Zatsepin, A. V. Aralov, J. Müller, *J. Biol. Inorg. Chem.* **2019**, *24*, 693–702.
[131] G. H. Clever, K. Polborn, T. Carell, *Angew. Chem. Int. Ed.* **2005**, *44*, 7204–7208.
[132] N. Sandmann, D. Defayay, A. Hepp, J. Müller, *J. Inorg. Biochem.* **2019**, *191*, 85–93.
[133] H. Weizman, Y. Tor, *Chem. Commun.* **2001**, 453–454.
[134] H. Urata, E. Yamaguchi, Y. Nakamura, S. Wada, *Chem. Commun.* **2011**, *47*, 941–943.
[135] K. Tanaka, A. Tengeiji, T. Kato, N. Toyama, M. Shiro, M. Shionoya, *J. Am. Chem. Soc.* **2002**, *124*, 12494–12498.
[136] M. Hande, O. Saher, K. Lundin, C. Smith, R. Zain, T. Lönnberg, *Molecules* **2019**, *24*, 1180.
[137] H. Räisälä, T. Lönnberg, *Chem. Eur. J.* **2019**, *25*, 4751–4756.
[138] G. H. Clever, K. Polborn, T. Carell, *Angew. Chem. Int. Ed.* **2005**, *44*, 7204–7208.
[139] G. H. Clever, S. J. Reitmeier, T. Carell, O. Schiemann, *Angew. Chem. Int. Ed.* **2010**, *49*, 4927–4929.
[140] G. H. Clever, Y. Söltl, H. Burks, W. Spahl, T. Carell, *Chem. Eur. J.* **2006**, *12*, 8708–8718.
[141] G. H. Clever, T. Carell, *Angew. Chem. Int. Ed.* **2006**, *46*, 250–253.
[142] K. Tanaka, G. H. Clever, Y. Takezawa, Y. Yamada, C. Kaul, M. Shionoya, T. Carell, *Nat. Nanotechnol.* **2006**, *1*, 190–194.

[143] S. Liu, G. H. Clever, Y. Takezawa, M. Kaneko, K. Tanaka, X. Guo, M. Shionoya, *Angew. Chem. Int. Ed.* **2011**, *50*, 8886–8890.
[144] J. C. Léon, Z. She, A. Kamal, M. H. Shamsi, J. Müller, H. Kraatz, *Angew. Chem. Int Ed* **2017**, *56*, 6098–6102.
[145] M. Hollenstein, C. Hipolito, C. Lam, D. Dietrich, D. M. Perrin, *Angew. Chem. Int. Ed.***2008**, *47*, 4346–4350.
[146] M. J. E. Resendiz, J. C. Noveron, H. Disteldorf, S. Fischer, P. J. Stang, *Org. Lett.* **2004**, *6*, 651–653.
[147] C.-K. Chiang, C.-C. Huang, C.-W. Liu, H.-T. Chang, *Anal. Chem.* **2008**, *80*, 3716–3721.
[148] J. C. Léon, D. González-Abradelo, C. A. Strassert, J. Müller, *Chem. Eur. J.* **2018**, *24*, 8320–8324.
[149] B. Jash, J. Müller, *J. Inorg. Biochem.* **2018**, *186*, 301–306.
[150] Y. Takezawa, W. Maeda, K. Tanaka, M. Shionoya, *Angew. Chem. Int. Ed.***2009**, *48*, 1081–1084.
[151] J. H. A. Duprey, Y. Takezawa, M. Shionoya, *Angew. Chem. Int. Ed.***2013**, *52*, 1212–1216.
[152] K. Tanaka, Y. Yamada, M. Shionoya, *J. Am. Chem. Soc.* **2002**, *124*, 8802–8803.
[153] M. A. Abdelhamid, L. Fábián, C. J. MacDonald, M. R. Cheesman, A. J. Gates, Z. A. Waller, *Nucleic Acids Res.* **2018**, *46*, 5886–5893.
[154] M. A. Abdelhamid, L. Fábián, C. J. MacDonald, M. R. Cheesman, A. J. Gates, Z. A. Waller, *Nucleic Acids Res.* **2018**, *46*, gky390.
[155] D. Miyoshi, H. Karimata, Z.-M. Wang, K. Koumoto, N. Sugimoto, *J. Am. Chem. Soc.* **2007**, *129*, 5919–5925.
[156] Y. Xu, Y. Suzuki, T. Lönnberg, M. Komiyama, *J. Am. Chem. Soc.* **2009**, *131*, 2871–2874.
[157] D. M. Engelhard, R. Pievo, G. H. Clever, *Angew. Chem. Int. Ed.* **2013**, *52*, 12843–12847.
[158] D. M. Engelhard, L. M. Stratmann, G. H. Clever, *Chem. Eur. J.* **2018**, *24*, 2117–2125.
[159] D. M. Engelhard, A. Meyer, A. Berndhäuser, O. Schiemann, G. H. Clever, *Chem. Commun.* **2018**, *54*, 7455–7458.
[160] D. M. Engelhard, J. Nowack, G. H. Clever, *Angew. Chem. Int. Ed.* **2017**, *56*, 11640–11644.
[161] R. H. Holm, P. Kennepohl, E. I. Solomon, *Chem. Rev.* **1996**, *96*, 2239–2314.
[162] K. J. Waldron, J. C. Rutherford, D. Ford, N. J. Robinson, *Nature* **2009**, *460*, 823–830.
[163] J. A. Raven, M. C. W. Evans, R. E. Korb, *Photosynth. Res.* **1999**, *60*, 111–150.
[164] J. T. Rubino, K. J. Franz, *J. Inorg. Biochem.* **2012**, *107*, 129–143.
[165] S. B. J. Kan, R. D. Lewis, K. Chen, F. H. Arnold, *Science* **2016**, *354*, 1048–1051.
[166] H. J. Davis, T. R. Ward, *ACS Cent. Sci.* **2019**, *5*, 1120–1136.
[167] *Angew. Chem.* **2018**, *130*, 14895–14895.
[168] H. J. Davis, T. R. Ward, *ACS Cent. Sci.* **2019**, *5*, 1120–1136.
[169] H. M. Key, P. Dydio, D. S. Clark, J. F. Hartwig, *Nature* **2016**, *534*, 534–537.
[170] L. Villarino, K. E. Splan, E. Reddem, L. Alonso-Cotchico, C. G. de Souza, A. Lledós, J. Maréchal, A. W. H. Thunnissen, G. Roelfes, *Angew. Chem. Int. Ed.***2018**, *57*, 7785–7789.
[171] J. Zhao, D. G. Bachmann, M. Lenz, D. G. Gillingham, T. R. Ward, *Catal. Sci. Technol.* **2018**, *8*, 2294–2298.
[172] W. J. Song, F. A. Tezcan, *Science* **2014**, *346*, 1525–1528.
[173] L. A. Churchfield, F. A. Tezcan, *Acc. Chem. Res.* **2019**, *52*, 345–355.
[174] P. Srivastava, H. Yang, K. Ellis-Guardiola, J. C. Lewis, *Nat. Commun.* **2015**, *6*, 7789.
[175] W. Ghattas, V. Dubosclard, A. Wick, A. Bendelac, R. Guillot, R. Ricoux, J.-P. Mahy, *J. Am. Chem. Soc.* **2018**, *140*, 8756–8762.
[176] Z. Zhou, G. Roelfes, *Nat. Catal.* **2020**, 1–6.
[177] M. Jeschek, R. Reuter, T. Heinisch, C. Trindler, J. Klehr, S. Panke, T. R. Ward, *Nature* **2016**, *537*, 661–665.
[178] Y. Lu, N. Yeung, N. Sieracki, N. M. Marshall, *Nature* **2009**, *460*, 855–862.
[179] C. Guerrier-Takada, K. Gardiner, T. Marsh, N. Pace, S. Altman, *Cell* **1983**, *35*, 849–857.
[180] K. Kruger, P. J. Grabowski, A. J. Zaug, J. Sands, D. E. Gottschling, T. R. Cech, *Cell* **1982**, *31*, 147–157.
[181] H. S. Bernhardt, *Biol. Direct* **2012**, *7*, 23.
[182] K. L. Vay, H. Mutschler, *Emerg. Top. Life Sci.* **2019**, *3*, 469–475.
[183] E. Y. Song, E. I. Jiménez, H. Lin, K. L. Vay, R. Krishnamurthy, H. Mutschler, *Angew. Chem. Int. Ed.* **2020**, DOI 10.1002/anie.202010918.
[184] H. G. Kloepfer, *Chemie Unserer Zeit* **1973**, *7*, 49–58.
[185] J. de la Cruz, K. Karbstein, J. L. W. Jr., *Annu. Rev. Biochem.* **2015**, *84*, 1–37.
[186] C. J. Hutchins, P. D. Rathjen, A. C. Forster, R. H. Symons, *Nucleic Acids Res.* **1986**, *14*, 3627–3640.
[187] H. W. Pley, K. M. Flaherty, D. B. McKay, *Nature* **1994**, *372*, 68–74.
[188] F. D. Steffen, M. Khier, D. Kowerko, R. A. Cunha, R. Börner, R. K. O. Sigel, *Nat. Commun.* **2020**, *11*, 104.
[189] R. R. Breaker, G. F. Joyce, *Chem. Biol.* **1994**, *1*, 223–229.
[190] B. Cuenoud, J. W. Szostak, *Nature* **1995**, *375*, 611–614.
[191] Y. Li, D. Sen, *Nat. Struct. Biol.* **1996**, *3*, 743–747.
[192] G. Liang, Y. Man, A. Li, X. Jin, X. Liu, L. Pan, *Microchem. J.* **2017**, *131*, 145–153.
[193] D. Morrison, M. Rothenbroker, Y. Li, *Small Methods* **2018**, *2*, 1700319.
[194] W. Ren, P.-J. J. Huang, D. de Rochambeau, W. J. Moon, J. Zhang, M. Lyu, S. Wang, H. Sleiman, J. Liu, *Biosens. Bioelectron.* **2020**, *165*, 112285.
[195] J. Liu, Y. Lu, *Angew. Chem. Int. Ed.***2007**, *46*, 7587–7590.
[196] T. Lan, K. Furuya, Y. Lu, *Chem. Commun.* **2010**, *46*, 3896–3898.

[197] J. Li, Y. Lu, *J. Am. Chem. Soc.* **2000**, *122*, 10466–10467.
[198] Y. Takezawa, T. Nakama, M. Shionoya, *J. Am. Chem. Soc.* **2019**, *141*, 19342–19350.
[199] Y. Takezawa, L. Hu, T. Nakama, M. Shionoya, *Angew. Chem. Int. Ed.***2020**, DOI 10.1002/anie.202009579.
[200] W. Li, Y. Li, Z. Liu, B. Lin, H. Yi, F. Xu, Z. Nie, S. Yao, *Nucleic Acids Res.* **2016**, *44*, 7373–7384.
[201] J. Kosman, B. Juskowiak, *Anal. Chim. Acta* **2011**, *707*, 7–17.
[202] I. Willner, B. Shlyahovsky, M. Zayats, B. Willner, *Chem. Soc. Rev.* **2008**, *37*, 1153–1165.
[203] J. Wang, L. Yue, Z. Li, J. Zhang, H. Tian, I. Willner, *Nat. Commun.* **2019**, *10*, 4963.
[204] X. Zhou, S. Guo, J. Gao, J. Zhao, S. Xue, W. Xu, *Biosens. Bioelectron.* **2017**, *98*, 83–90.
[205] J. Chen, Y. Zhang, M. Cheng, J.-L. Mergny, Q. Lin, J. Zhou, H. Ju, *Microchim. Acta* **2019**, *186*, 786.
[206] D.-M. Kong, N. Wang, X.-X. Guo, H.-X. Shen, *Analyst* **2010**, *135*, 545–549.
[207] C. Tuerk, L. Gold, *Science* **1990**, *249*, 505–510.
[208] A. D. Ellington, J. W. Szostak, *Nature* **1990**, *346*, 818–822.
[209] E. Golub, H. B. Albada, W.-C. Liao, Y. Biniuri, I. Willner, *J. Am. Chem. Soc.* **2016**, *138*, 164–172.
[210] M. Smietana, S. Arseniyadis, *Chimia Int. J. Chem.* **2018**, *72*, 630–634.
[211] J. J. Marek, R. P. Singh, A. Heuer, U. Hennecke, *Chem. Eur. J.* **2017**, *23*, 6004–6008.
[212] S. Dey, A. Jäschke, *Angew. Chem. Int. Ed.***2015**, *54*, 11279–11282.
[213] M. Cheng, Y. Li, J. Zhou, G. Jia, S.-M. Lu, Y. Yang, C. Li, *Chem. Commun.* **2016**, *52*, 9644–9647.
[214] A. J. Boersma, B. L. Feringa, G. Roelfes, *Angew. Chem. Int. Ed.***2009**, *48*, 3346–3348.
[215] D. Coquière, B. L. Feringa, G. Roelfes, *Angew. Chem. Int. Ed.***2007**, *46*, 9308–9311.
[216] G. Roelfes, A. J. Boersma, B. L. Feringa, *Chem. Commun.* **2006**, *0*, 635–637.
[217] A. Rioz-Martínez, J. Oelerich, N. Ségaud, G. Roelfes, *Angew. Chem. Int. Ed.***2016**, *55*, 14136–14140.
[218] J. Oelerich, G. Roelfes, *Chem. Sci.* **2013**, *4*, 2013–2017.
[219] M. Wilking, U. Hennecke, *Org Biomol Chem* **2013**, *11*, 6940–6945.
[220] J. J. Marek, U. Hennecke, *Chem. Eur. J.* **2017**, *23*, 6009–6013.
[221] P. Fournier, R. Fiammengo, A. Jäschke, *Angew. Chem. Int. Ed.***2009**, *48*, 4426–4429.
[222] S. Dey, C. L. Rühl, A. Jäschke, *Chem. Eur. J.* **2017**, *23*, DOI 10.1002/chem.201785068.
[223] A. J. Boersma, D. Coquière, D. Geerdink, F. Rosati, B. L. Feringa, G. Roelfes, *Nat Chem* **2010**, *2*, 991–995.
[224] J. Mansot, S. Aubert, N. Duchemin, J.-J. Vasseur, S. Arseniyadis, M. Smietana, *Chem. Sci.* **2019**, *10*, 2875–2881.
[225] J. Mansot, J. Lauberteaux, A. Lebrun, M. Mauduit, J. Vasseur, R. M. de Figueiredo, S. Arseniyadis, J. Campagne, M. Smietana, *Chem. Eur. J.* **2020**, *26*, 3519–3523.
[226] J. Oelerich, G. Roelfes, *Chem. Sci.* **2013**, *4*, 2013–2017.
[227] G. Roelfes, B. L. Feringa, *Angew. Chem. Int. Ed.***2005**, *44*, 3230–3232.
[228] P. Fournier, R. Fiammengo, A. Jäschke, *Angew. Chem. Int. Ed.***2009**, *48*, 4426–4429.
[229] S. Roe, D. J. Ritson, T. Garner, M. Searle, J. E. Moses, *Chem. Commun.* **2010**, *46*, 4309–4311.
[230] Wang, C., Jia, G., Zhou, J., Li, Y., Liu, Y., Lu, S., Li, C. *Angew. Chem. Int. Ed.* **2012**, *51*, 9352–9355. https://dx.doi.org/10.1002/anie.201204850 [231] M. Wilking, U. Hennecke, *Org. Biomol. Chem.* **2013**, *11*, 6940–6945.
[232] S. Dey, A. Jäschke, *Molecules* **2020**, *25*, 3121.
[233] S. Dey, C. L. Rühl, A. Jäschke, *Chem. Eur. J.* **2017**, *23*, 12162–12170.
[234] C. Wang, G. Jia, J. Zhou, Y. Li, Y. Liu, S. Lu, C. Li, *Angew. Chem. Int. Ed.***2012**, *51*, 9352–9355.
[235] J. Hao, W. Miao, Y. Cheng, S. Lu, G. Jia, C. Li, *ACS Catal.* **2020**, *10*, 6561–6567.
[236] M. Cheng, Y. Li, J. Zhou, G. Jia, S.-M. Lu, Y. Yang, C. Li, *Chem. Commun.* **2016**, *52*, 9644–9647.
[237] J. H. Yum, S. Park, H. Sugiyama, *Org. Biomol. Chem.* **2019**, DOI 10.1039/c9ob01876j.
[238] B. Cuenoud, J. W. Szostak, *Nature* **1995**, *375*, 611–614.
[239] A. K. Behera, K. J. Schlund, A. J. Mason, K. O. Alila, M. Han, R. L. Grout, D. A. Baum, *Biopolymers* **2013**, *99*, 382–391.
[240] R. R. Breaker, G. F. Joyce, *Chem. Biol.* **1994**, *1*, 223–229.
[241] T. D. Canale, D. Sen, *Biochim. Biophy. Acta* **2017**, *1861*, 1455–1462.
[242] D. Coquière, B. L. Feringa, G. Roelfes, *Angew. Chem. Int. Ed.***2007**, *46*, 9308–9311.
[243] B. Lippert, P. J. S. Miguel, *Inorg. Chim. Acta* **2018**, *472*, 207–213.
[244] G. H. Clever, M. Shionoya, *Coord. Chem. Rev.* **2010**, *254*, 2391–2402.
[245] L. Mazzei, M. Cianci, F. Musiani, G. Lente, M. Palombo, S. Ciurli, *J. Inorg. Biochem.* **2017**, *166*, 182–189.
[246] P. Kumar, V. Reithofer, M. Reisinger, S. Wallner, T. Pavkov-Keller, P. Macheroux, K. Gruber, *Sci Rep-uk* **2016**, *6*, 23787.
[247] G. S. Kachalova, A. C. Shosheva, G. P. Bourenkov, A. A. Donchev, M. I. Dimitrov, H. D. Bartunik, *J. Inorg. Biochem.* **2012**, *115*, 174–181.
[248] K. Rohlf, *Bachelor thesis*, Imidazol-Basierte Metallbasentetraden in G-Quadruplexstrukturen – Synthese & Charakterisierung, **2017**.
[249] D. M. Engelhard, *Dissertation*, Synthesis and coordination chemistry of tetradentate chelators based on ligand-appended G-quadruplex structures **2016**.
[250] Y. Lu, Proc. Natl. Acad. Sci. **2010**, *107*, 1811–1812.
[251] E. Aronoff-Spencer, C. S. Burns, N. I. Avdievich, G. J. Gerfen, J. Peisach, W. E. Antholine, H. L. Ball, F. E. Cohen, S. B. Prusiner, G. L. Millhauser, *Biochemistry* **2000**, *39*, 13760–13771.
[252] O. L. Acevedo, R. S. Andrews, *Tetrahedron Lett.* **1996**, *37*, 3931–3934.

[253] L. Zhang, A. E. Peritz, P. J. Carroll, E. Meggers, *Synthesis* **2006**, *2006*, 645–653.
[254] L. J. McBride, M. H. Caruthers, *Tetrahedron Lett.* **1983**, *24*, 245–248.
[255] S. L. Beaucage, M. H. Caruthers, *Tetrahedron Lett.* **1981**, *22*, 1859–1862.
[256] J. E. Marugg, A. Burik, M. Tromp, G. A. van der Marel, J. H. van Boom, *Tetrahedron Lett.* **1986**, *27*, 2271–2274.
[257] T. Simonsson, *Biol. Chem.* **2001**, *382*, 621–628.
[258] L. Joly, F. Rosu, V. Gabelica, *Chem. Commun.* **2012**, *48*, 8386–8388.
[259] Q. Zhai, M. Deng, L. Xu, X. Zhang, X. Zhou, *Bioorg. Med. Chem. Lett.* **2012**, *22*, 1142–1145.
[260] J.-L. Mergny, A. D. Cian, A. Ghelab, B. Saccà, L. Lacroix, *Nucleic Acids Res.* **2005**, *33*, 81–94.
[261] B. Jash, J. Müller, *J. Inorg. Biochem.* **2018**, *186*, 301–306.
[262] S.-S. Chen, *CrystEngComm* **2016**, *18*, 6543–6565.
[263] M. Lõkov, S. Tshepelevitsh, A. Heering, P. G. Plieger, R. Vianello, I. Leito, *Eur. J. Org. Chem.* **2017**, *2017*, 4475–4489.
[264] V. D'Atri, M. Porrini, F. Rosu, V. Gabelica, *J. Mass Spectrom.* **2015**, *50*, 711–726.
[265] A. Marchand, V. Gabelica, *J. Am. Soc. Mass Spectrom.* **2014**, *25*, 1146–1154.
[266] M. J. Lecours, A. Marchand, A. Anwar, C. Guetta, W. S. Hopkins, V. Gabelica, *Biochi. Biophys. Acta* **2017**, *1861*, 1353–1361.
[267] R. Cumeras, E. Figueras, C. E. Davis, J. I. Baumbach, I. Gràcia, *Analyst* **2014**, *140*, 1376–1390.
[268] H. E. Revercomb, E. A. Mason, *Anal. Chem.* **1975**, *47*, 970–983.
[269] A. Ahmed, Y. J. Cho, M. No, J. Koh, N. Tomczyk, K. Giles, J. S. Yoo, S. Kim, *Anal. Chem.* **2011**, *83*, 77–83.
[270] F. A. Fernandez-Lima, D. A. Kaplan, M. A. Park, *Rev. Sci. Instrum.* **2011**, *82*, 126106.
[271] D. R. Hernandez, J. D. DeBord, M. E. Ridgeway, D. A. Kaplan, M. A. Park, F. Fernandez-Lima, *Analyst* **2014**, *139*, 1913–1921.
[272] J.-F. Greisch, J. Chmela, M. E. Harding, D. Wunderlich, B. Schäfer, M. Ruben, W. Klopper, D. Schooss, M. M. Kappes, *Phys. Chem. Chem. Phys.* **2017**, *19*, 6105–6112.
[273] S. Godlewska, J. Jezierska, K. Baranowska, E. Augustin, A. Dołęga, *Polyhedron* **2013**, *65*, 288–297.
[274] W.-H. Wang, X.-Y. Su, Z.-H. Mao, J.-S. You, R.-G. Xie, *Acta Crystallogr. E* **2006**, *62*, m445–m447.
[275] J. R. Wyatt, P. W. Davis, S. M. Freier, *Biochemistry* **1996**, *35*, 8002–8008.
[276] S. C. Hoops, K. W. Anderson, K. M. Merz, *J. Am. Chem. Soc.* **1991**, *113*, 8262–8270.
[277] Y. Li, D. Sen, *Biochemistry* **1997**, *36*, 5589–5599.
[278] E. Golub, R. Freeman, I. Willner, *Angew. Chem. Int. Ed.* **2011**, *50*, 11710–11714.
[279] A. Niazov-Elkan, E. Golub, E. Sharon, D. Balogh, I. Willner, *Small* **2014**, *10*, 2883–2891.
[280] G. Pelossof, R. Tel-Vered, J. Elbaz, I. Willner, *Anal. Chem.* **2010**, *82*, 4396–4402.
[281] E. Sharon, E. Golub, A. Niazov-Elkan, D. Balogh, I. Willner, *Anal. Chem.* **2014**, *86*, 3153–3158.
[282] R. Freeman, X. Liu, I. Willner, *J. Am. Chem. Soc.* **2011**, *133*, 11597–11604.
[283] H. Ibrahim, P. Mulyk, D. Sen, *ACS Omega* **2019**, *4*, 15280–15288.
[284] T. Li, B. Li, E. Wang, S. Dong, *Chem. Commun.* **2009**, *0*, 3551–3553.
[285] P. M. Punt, G. H. Clever, *Chem. Sci.* **2019**, *10*, 2513–2518.
[286] M. A. Aleman-Garcia, R. Orbach, I. Willner, *Chem. Eur. J.* **2014**, *20*, 5619–5624.
[287] S. E. W. Opitz, S. Smrke, B. A. Goodman, C. Yeretzian, Foods **2014**, 253–264.
[288] A. Risitano, K. R. Fox, *Biochemistry* **2003**, *42*, 6507–6513.
[289] E. Largy, J.-L. Mergny, V. Gabelica, *Metal Ions Life Sciences* **2016**, *16*, 203–258.
[290] O. Mendoza, M. Porrini, G. F. Salgado, V. Gabelica, J. Mergny, *Chem. Eur. J.* **2015**, *21*, 6732–6739.
[291] S. Burge, G. N. Parkinson, P. Hazel, A. K. Todd, S. Neidle, *Nucleic Acids Res.* **2006**, *34*, 5402–5415.
[292] Y. Wang, D. J. Patel, *Structure* **1994**, *2*, 1141–1156.
[293] S. J. F. Degen, E. W. Davie, *Biochemistry* **1987**, *26*, 6165–6177.
[294] S. Amrane, R. W. L. Ang, Z. M. Tan, C. Li, J. K. C. Lim, J. M. W. Lim, K. W. Lim, A. T. Phan, *Nucleic Acids Res.* **2009**, *37*, 931–938.
[295] W. Li, A. Kaplan, G. Grant, J. Toole, L. Leung, *Blood* **1994**, *83*, 677–682.
[296] F. Rosu, E. D. Pauw, V. Gabelica, *Biochimie* **2008**, *90*, 1074–1087.
[297] K. W. Lim, S. Amrane, S. Bouaziz, W. Xu, Y. Mu, D. J. Patel, K. N. Luu, A. T. Phan, *J. Am. Chem. Soc.* **2009**, *131*, 4301–4309.
[298] Y. Wang, D. J. Patel, *Structure* **1993**, *1*, 263–282.
[299] C. Löw, P. Neumann, H. Tidow, U. Weininger, C. Haupt, B. Friedrich-Epler, C. Scholz, M. T. Stubbs, J. Balbach, *J. Mol. Biol*. **2010**, *398*, 375–390.
[300] S. Godlewska, J. Jezierska, K. Baranowska, E. Augustin, A. Dołęga, *Polyhedron* **2013**, *65*, 288–297.
[301] J. Reedijk, G. A. van Albada, B. Limburg, I. Mutikainen, U. Turpeinen, *Acta Crystallogr. E* **2011**, *68*, m90–m90.
[302] H. Irving, R. J. P. Williams, *Nature* **1948**, *162*, 746–747.
[303] J. T. Rubino, K. J. Franz, *J. Inorg. Biochem.* **2012**, *107*, 129–143.
[304] C. J. Coates, J. Nairn, *Dev. Comp. Immunol.* **2014**, *45*, 43–55.
[305] I. A. Koval, P. Gamez, C. Belle, K. Selmeczi, J. Reedijk, *Chem. Soc. Rev.* **2006**, *35*, 814–840.
[306] L. Calabrese, J. Rotilio, **1977**, 180–184.
[307] Y. Cui, Y.-H. Hu, F. Yu, J. Zheng, L.-S. Chen, Q.-X. Chen, Q. Wang, *Int. J. Biol. Macromol.* **2017**, *95*, 1289–1297.
[308] J. Di, S. Bi, *Spectrochim. Acta A Mol. Biomol. Spectrosc.* **2003**, *59*, 1689–1696.
[309] F. Solano, J. C. García-Borrón, J. A. Lozano, P. Aroca, *Pigment Cell Res.* **1991**, *4*, 255–6.
[310] J. M. Pawelek, *Pigment Cell Res.* **1991**, *4*, 53–62.

[311] T. Kobayashi, W. D. Vieira, B. Potterf, C. Sakai, G. I. and V. J. Hearing, *J. Cell Sci.* **1995**, *108*, 2301–2309.
[312] M. Jarenmark, H. Carlsson, E. Nordlander, *C. R. Chim.* **2007**, *10*, 433–462.
[313] A. Hoffmann, S. Herres-Pawlis, *Encyclopedia of inorganic and bioinorganic chemistry* **2017**, 1–15.
[314] B. Dicke, A. Hoffmann, J. Stanek, M. S. Rampp, B. Grimm-Lebsanft, F. Biebl, D. Rukser, B. Maerz, D. Göries, M. Naumova, M. Biednov, G. Neuber, A. Wetzel, S. M. Hofmann, P. Roedig, A. Meents, J. Bielecki, J. Andreasson, K. R. Beyerlein, H. N. Chapman, C. Bressler, W. Zinth, M. Rübhausen, S. Herres-Pawlis, *Nat. Chem.* **2018**, *10*, 355–362.
[315] J. H. Yum, S. Park, R. Hiraga, I. Okamura, S. Notsu, H. Sugiyama, *Org. Biomol. Chem.* **2019**, *17*, 2548–2553.
[316] S. Park, H. Matsui, K. Fukumoto, J. H. Yum, H. Sugiyama, *RSC Adv.* **2020**, *10*, 9717–9722.
[317] L. Gjonaj, G. Roelfes, *Chemcatchem* **2013**, *5*, 1718–1721.
[318] N. S. Oltra, G. Roelfes, *Chem. Commun.* **2008**, *0*, 6039–6041.
[319] A. J. Boersma, B. de Bruin, B. L. Feringa, G. Roelfes, *Chem. Commun.* **2012**, *48*, 2394–2396.
[320] D. Renčiuk, I. Kejnovská, P. Školáková, K. Bednářová, J. Motlová, M. Vorlíčková, *Nucleic Acids Res.* **2009**, *37*, 6625–6634.
[321] P. B. Lawrence, J. L. Price, *Curr. Opin. Chem. Biol.* **2016**, *34*, 88–94.
[322] D. R. Canchi, A. E. García, *Phys. Chem.* **2013**, *64*, 273–293.
[323] R. P. Megens, G. Roelfes, *Org. Biomol. Chem.* **2010**, *8*, 1387–1393.
[324] J. Knop, S. Patra, B. Harish, C. A. Royer, R. Winter, *Chem. Eur. J.* **2018**, *24*, 14346–14351.
[325] L. Aslanyan, J. Ko, B. G. Kim, I. Vardanyan, Y. B. Dalyan, T. V. Chalikian, *J. Phys. Chem. B* **2017**, *121*, 6511–6519.
[326] Y. Ueda, Y. Zouzumi, A. Maruyama, S. Nakano, N. Sugimoto, D. Miyoshi, *Sci. Technol. Adv. Mat.* **2016**, *17*, 753–759.
[327] M. Dutta, *J. Indian. Inst. Sci.* **2018**, *98*, 231–245.
[328] S. J. Opella, F. M. Marassi, *Arch. Biochem. Biophys.* **2017**, *628*, 92–101.
[329] G. Wu, A. Wong, Z. Gan, J. T. Davis, *J. Am. Chem. Soc.* **2003**, *125*, 7182–7183.
[330] S. K. Vasa, H. Singh, K. Grohe, R. Linser, *Angew. Chem. Int. Ed.***2019**, *58*, 5758–5762.
[331] D. Wei, G. N. Parkinson, A. P. Reszka, S. Neidle, *Nucleic Acids Res.* **2012**, *40*, 4691–4700.
[332] O. P. Schmidt, S. Jurt, S. Johannsen, A. Karimi, R. K. O. Sigel, N. W. Luedtke, *Nat. Commun.* **2019**, *10*, 4818.
[333] S. Johannsen, N. Megger, D. Böhme, R. K. O. Sigel, J. Müller, *Nat. Chem.* **2010**, *2*, 229–234.
[334] M. K. Schlegel, L.-O. Essen, E. Meggers, *J. Am. Chem. Soc.* **2008**, *130*, 8158–8159.
[335] M. Adrian, B. Heddi, A. T. Phan, *Methods* **2012**, *57*, 11–24.
[336] A. E. Kelly, H. D. Ou, R. Withers, V. Dötsch, *J. Am. Chem. Soc.* **2002**, *124*, 12013–12019.
[337] T. Horiuchi, M. Takahashi, J. Kikuchi, S. Yokoyama, H. Maeda, *J. Magn. Reason.* **2005**, *174*, 34–42.
[338] D. G. Gadian, F. N. H. Robinson, *J. Magn. Reason. 1969* **1979**, *34*, 449–455.
[339] T. L. Hwang, A. J. Shaka, *J. Magn. Reason.* **1995**, *112*, 275–279.
[340] F. R. Winnerdy, P. Das, B. Heddi, A. T. Phan, *J. Am. Chem. Soc.* **2019**, *141*, 18038–18047.
[341] T. A. Early, D. R. Kearns, J. F. Burd, J. E. Larson, R. D. Wells, *Biochemistry* **1977**, *16*, 541–551.
[342] D. R. Kearns, D. J. Patel, R. G. Shulman, *Nature* **1971**, *229*, 338–339.
[343] K. Ebel, H. Koehler, A. O. Gamer, R. Jäckh, *Ullmann's Encyclopedia of Industrial Chemistry,* John Wiley & Sons **2013**.
[344] S. Johannsen, N. Megger, D. Böhme, R. K. O. Sigel, J. Müller, *Nat. Chem.* **2010**, *2*, 229–234.
[345] J. L. Markley, A. Bax, Y. Arata, C. W. Hilbers, R. Kaptein, B. D. Sykes, P. E. Wright, K. Wüthrich, *J. Biomol. NMR* **1998**, *12*, 1–23.
[346] K. Wüthrich, *NMR of Proteins and Nucleic Acids*, John Wiley & Sons, **1991**.
[347] A. T. Phan, *J. Biomol. NMR* **2000**, *16*, 175–178.
[348] C. D. Schwieters, J. J. Kuszewski, N. Tjandra, G. M. Clore, *J. Magn. Reson.* **2003**, *160*, 65–73.
[349] C. D. Schwieters, J. J. Kuszewski, G. M. Clore, *Prog. Nucl. Mag. Reson. Spectrosc.* **2006**, *48*, 47–62.
[350] M. Nilges, G. M. Clore, A. M. Gronenborn, *Febs Lett.* **1988**, *229*, 317–324.
[351] M. Nilges, A. M. Gronenborn, A. T. Brünger, G. M. Clore, *Protein Eng. Des. Sel.* **1988**, *2*, 27–38.
[352] M. Nilges, G. M. Clore, A. M. Gronenborn, *Febs Lett.* **1988**, *239*, 129–136.
[353] G. M. Clore, A. M. Gronenborn, *Crit. Rev. Biochem. Mol.* **2008**, *24*, 479–564.
[354] S. Pronk, S. Páll, R. Schulz, P. Larsson, P. Bjelkmar, R. Apostolov, M. R. Shirts, J. C. Smith, P. M. Kasson, D. van der Spoel, B. Hess, E. Lindahl, *Bioinformatics* **2013**, *29*, 845–854.
[355] D. V. D. Spoel, E. Lindahl, B. Hess, G. Groenhof, A. E. Mark, H. J. C. Berendsen, *J. Comput. Chem.* **2005**, *26*, 1701–1718.
[356] B. Hess, H. Bekker, H. J. C. Berendsen, J. G. E. M. Fraaije, *J. Comput. Chem.* **1997**, *18*, 1463–1472.
[357] G. Bussi, D. Donadio, M. Parrinello, *J. Chem. Phys.* **2007**, *126*, 014101.
[358] P. Szilárd, M. J. Abraham, C. Kutzner, B. Hess, E. Lindahl, **2015**, 3–27.
[359] M. J. Abraham, T. Murtola, R. Schulz, S. Páll, J. C. Smith, B. Hess, E. Lindahl, *Softwarex* **2015**, *1–2*, 19–25.
[360] B. Hess, C. Kutzner, D. van der Spoel, E. Lindahl, *J. Chem. Theory Comput.* **2008**, *4*, 435–47.
[361] I. Ivani, P. D. Dans, A. Noy, A. Pérez, I. Faustino, A. Hospital, J. Walther, P. Andrio, R. Goñi, A. Balaceanu, G. Portella, F. Battistini, J. L. Gelpí, C. González, M. Vendruscolo, C. A. Laughton, S. A. Harris, D. A. Case, M. Orozco, *Nat. Methods* **2016**, *13*, 55–58.
[362] A. Pérez, I. Marchán, D. Svozil, J. Sponer, T. E. Cheatham, C. A. Laughton, M. Orozco, *Biophys. J.* **2007**, *92*, 3817–3829.

[363] M. J. Frisch, G. W. Trucks, H. B. Schlegel, G. E. Scuseria, M. A. Robb, J. R. Cheeseman, G. Scalmani, V. Barone, G. A. Petersson, H. Nakatsuji, X. Li, M. Caricato, A. V. Marenich, J. Bloino, B. G. Janesko, R. Gomperts, B. Mennucci, H. P. Hratchian, J. V. Ortiz, A. F. Izmaylov, J. L. Sonnenberg, D. Williams-Young, F. Ding, F. Lipparini, F. Egidi, J. Goings, B. Peng, A. Petrone, T. Henderson, D. Ranasinghe, V. G. Zakrzewski, J. Gao, N. Rega, G. Zheng, W. Liang, M. Hada, M. Ehara, K. Toyota, R. Fukuda, J. Hasegawa, M. Ishida, T. Nakajima, Y. Honda, O. Kitao, H. Nakai, T. Vreven, K. Throssell, J. A. Montgomery, Jr., J. E. Peralta, F. Ogliaro, M. J. Bearpark, J. J. Heyd, E. N. Brothers, K. N. Kudin, V. N. Staroverov, T. A. Keith, R. Kobayashi, J. Normand, K. Raghavachari, A. P. Rendell, J. C. Burant, S. S. Iyengar, J. Tomasi, M. Cossi, J. M. Millam, M. Klene, C. Adamo, R. Cammi, J. W. Ochterski, R. L. Martin, K. Morokuma, O. Farkas, J. B. Foresman, and D. J. Fox, *Gaussian 16, Revision C.01*, Gaussian, Inc., Wallingford CT, **2016**.
[364] D. A. Case, I. Y. Ben-Shalom, S. R. Brozell, D. S. Cerutti, T. E. Cheatham, III, V. W. D. Cruzeiro, T. A. Darden, R. E. Duke, D. Ghoreishi, M. K. Gilson, H. Gohlke, A. W. Goetz, D. Greene, R. Harris, N. Homeyer, S. Izadi, A. Kovalenko, T. Kurtzman, T. S. Lee, S. LeGrand, P. Li, C. Lin, J. Liu, T. Luchko, R. Luo, D. J. Mermelstein, K. M. Merz, Y. Miao, G. Monard, C. Nguyen, H. Nguyen, I. Omelyan, A. Onufriev, F. Pan, R. Qi, D. R. Roe, A. Roitberg, C. Sagui, S. Schott-Verdugo, J. Shen, C. L. Simmerling, J. Smith, R. Salomon-Ferrer, J. Swails, R. C. Walker, J. Wang, H. Wei, R. M. Wolf, X. Wu, L. Xiao, D. M. Y. and P. A. Kollman, *AMBER 2018*, University of California, San Francisco, **2018**.
[365] P. Li, K. M. Merz, *J. Chem. Inf. Model.* **2016**, *56*, 599–604.
[366] M. B. Peters, Y. Yang, B. Wang, L. Füsti-Molnár, M. N. Weaver, K. M. Merz, *J. Chem. Theory Comput.* **2010**, *6*, 2935–2947.
[367] R. Mera-Adasme, K. Sadeghian, D. Sundholm, C. Ochsenfeld, *J. Phys. Chem. B* **2014**, *118*, 13106–13111.
[368] C. Creze, B. Rinaldi, R. Haser, P. Bouvet, P. Gouet, *Acta Crystallogr. D* **2007**, *63*, 682–688.
[369] V. M. Marathias, P. H. Bolton, *Nucleic Acids Res.* **2000**, *28*, 1969–1977.
[370] E. Vanquelef, S. Simon, G. Marquant, E. Garcia, G. Klimerak, J. C. Delepine, P. Cieplak, F.-Y. Dupradeau, *Nucleic Acids Res.* **2011**, *39*, W511-7.
[371] F. Wang, J.-P. Becker, P. C. & F.-Y. Dupradeau, R.E.D. Python: Object oriented programming for Amber force fields, Université de Picardie - Jules Verne, Sanford Burnham Prebys Medical Discovery Institute, **2013**.
[372] F.-Y. Dupradeau, A. Pigache, T. Zaffran, C. Savineau, R. Lelong, N. Grivel, D. Lelong, W. Rosanski, P. Cieplak, *Phys. Chem. Chem. Phys.* **2010**, *12*, 7821–39.
[373] C. I. Bayly, P. Cieplak, W. Cornell, P. A. Kollman, *J. Phys. Chem.* **1993**, *97*, 10269–10280.
[374] P. Güntert, C. Mumenthaler, K. Wüthrich, *J. Mol. Biol.* **1997**, *273*, 283–298.
[375] J. Wang, E. Benedetti, L. Bethge, S. Vonhoff, S. Klussmann, J. Vasseur, J. Cossy, M. Smietana, S. Arseniyadis, *Angew. Chem. Int. Ed.* **2013**, *52*, 11546–11549.